

**Novel Electromagnetic Space Applications:
Electron-Based Touchless Potential Sensing and
Low-Gravity Magnetohydrodynamics**

by

Álvaro Romero-Calvo

B.Sc., Universidad de Sevilla, 2016

M.Sc., Universidad de Sevilla, 2019

M.Sc., Politecnico di Milano, 2019

A thesis submitted to the Faculty of
the Graduate School of the University of Colorado
in partial fulfillment of the requirements for the degree of
Doctor of Philosophy

Department of Aerospace Engineering Sciences

2022

Committee Members:

Prof. Hanspeter Schaub

Prof. Zoltan Sternovsky

Prof. Allison Anderson

Prof. Miguel Herrada

Dr. William West

Romero-Calvo, Álvaro (Ph.D., Aerospace Engineering Sciences)

Novel electromagnetic space applications: electron-based touchless potential sensing and low-gravity magnetohydrodynamics

Thesis directed by Prof. Hanspeter Schaub

The commercialization of the sub-orbital environment, the ambition to make humans a multi-planetary species, and the urgent need for sustainable space operations are driving the development of a new generation of space systems. The use of electromagnetic forces (and electromagnetism, in general) is proposed in this dissertation to enable mid-distance, contactless actuation and sensing for space technology development. Following this paradigm, two applications are explored: electron-based touchless spacecraft potential sensing, and low-gravity magnetohydrodynamics.

The electron-based touchless potential sensing method was recently introduced to characterize the electrostatic state of non-cooperative objects in GEO and deep space. Applications span from arcing prevention to space debris removal. Although the fundamentals of this approach were studied in previous works, several open questions remained regarding the effect of complex geometries and differential charging on the sensing process. Such questions are here addressed with efficient numerical tools and vacuum chamber experiments, providing key insights into the behavior of realistic spacecraft formations. In addition, new active photoelectron-based sensing strategies are proposed that overcome some of the challenges of previous implementations.

The concept of low-gravity magnetohydrodynamics is also introduced as a way to actuate low-gravity fluid mechanics systems using magnetic forces. The theoretical foundations of the field are established from the analytical, numerical, and experimental perspectives with particular attention to the equilibrium, stability, and modal response of gas-liquid interfaces. Specific features of bubbles and droplets are also explored. Finally, the use of magnetic polarization and Lorentz forces in low-gravity fluid systems is discussed together with some of their applications, which include phase separation, magnetic positive positioning, and low-gravity electrolysis. The development of such technologies is initiated with support from microgravity research campaigns at ZARM's drop tower and Blue Origin's New Shepard suborbital rocket.

Dedication

A mi familia, porque gracias a ellos escribo estas líneas. A Hanspeter, Maestro Jedi, por acogerme como estudiante y prepararme para lo que está por llegar. Y a Maricruz, porque su amor no entiende de fronteras.

Acknowledgements

There are no words to thank Dr. Hanspeter Schaub enough for his tremendous support. His guidance, encouragement, and generosity have made me a better researcher, a better person, and set an example that I will follow for the rest of my career. Thank you for being such an extraordinary human being.

This dissertation is the product of many hours of work with many exceptional individuals. I thank Dr. Gabriel Cano-Gómez and Dr. Miguel Herrada for supporting me all these years: first as instructors, then as collaborators, and now as friends. I am grateful to Dr. Katharina Brinkert, Ömer Akay, and Ffion James for giving me the chance to join their team and demonstrate some of the coolest concepts of this dissertation. I also thank Dr. Filippo Maggi, Dr. Elena Castro-Hernández, and my teammates at StELIUM and The Ferros for two exciting microgravity campaigns at ZARM's drop tower, where we were lucky to have Dr. Thorben Könemann and the rest of the ZARM team on our side. It has been an honor to work with Dr. Will West, Keith Billings, and Connor Nogales on our New Shepard experiment, which was manufactured thanks to the support from Nathan Coyle, Katie Rae, Paul Koenig, Ian Peck, and Matt Rhode. Thanks to the remaining members of my committee, Dr. Allie Anderson and Dr. Zoltan Sternovsky, for their guidance. I also want to acknowledge the strong economic support from the La Caixa and Rafael del Pino foundations, and from the Air Force Office of Scientific Research (AFOSR).

I feel extremely lucky to have shared some of the best years of my life with the amazing group of people that composes the AVS Lab. It has been a real pleasure to fight (and be repeatedly defeated by) the Spirit of the Chamber together with Dr. Kieran Wilson, Dr. Miles Bengtson, Julian Hammerl, and Kaylee Champion. Special thanks go to Connor, Avi, Michael, Andrea, and the Spanish & Associates crew for the great adventures we lived together, but not less important, for their endless supply of M&Ms.

Finally, I want to thank my family, because they are the reason why I could pursue this exciting career and the reference I always followed. Maricruz, you were 8 hours ahead, but you always made me feel close. You are my best friend, but most importantly, you are my team. Thanks for everything.

Contents

Chapter

1	Introduction	1
1.1	Motivation	1
1.2	Touchless potential sensing	4
1.2.1	Concept	4
1.2.2	Complex shapes and heterogeneous charging	5
1.2.3	Electron beam modeling	6
1.2.4	Photoelectron-based sensing strategies	7
1.3	Low-gravity magnetohydrodynamics	9
1.3.1	Definition and scope	9
1.3.2	Analytical perspective	10
1.3.3	Numerical perspective	11
1.4	Applications of low-gravity magnetohydrodynamics	12
1.4.1	Phase separation	12
1.4.2	Magnetic positive positioning	14
1.4.3	Launch vehicle restart	15
1.4.4	Magnetically enhanced electrolysis	18
1.5	Main contributions	21

I	Electron-based touchless potential sensing	23
2	Preliminary considerations	24
2.1	Electrostatic framework	24
2.1.1	Maxwell equations	24
2.1.2	Particle dynamics	25
2.1.3	Space environment	25
2.2	Surface processes	27
2.2.1	Secondary Electron Emission	28
2.2.2	Photoelectron emission	29
2.2.3	Backscattered electron emission	31
2.3	The ECLIPS space environments simulation facility	32
2.3.1	Overview	33
2.3.2	Sources	35
2.3.3	Probes	38
2.3.4	Ancillary equipment	40
2.3.5	Other components	45
2.4	Collaborators	45
3	Complex shapes and differential charging	46
3.1	Particle Tracing Model	46
3.1.1	Electrostatic framework	47
3.1.2	Implementation of secondary electron emission	48
3.1.3	A note on backscattered electrons	49
3.2	Materials and methods	49
3.2.1	Experimental setup	49
3.2.2	Material Properties	51
3.2.3	Measurement of secondary electron flux	51

3.2.4	Configuration of SIMION model	52
3.3	Results and discussion	54
3.3.1	Overview of electron trajectories	54
3.3.2	Calibration	55
3.3.3	Complex shapes	56
3.3.4	Differential charging	58
3.3.5	Target observability	60
3.3.6	Source regions and sensing strategy	62
4	A quasi-analytical approach to electron beam modeling	64
4.1	Context and strategy	64
4.2	Electron beam model	66
4.2.1	Physical model	66
4.2.2	Mathematical model	66
4.3	Performance analysis	72
4.3.1	Verification	72
4.3.2	Validation	73
4.4	Uncertainty in active spacecraft charging scenario	78
4.4.1	Problem statement	78
4.4.2	Uncertainty quantification analysis	81
4.4.3	Results	82
4.5	Collaborators	86
5	Active photoelectron-based sensing strategies	87
5.1	Simulation of active photoemission	87
5.1.1	Implementation	87
5.1.2	Effective values	89
5.1.3	Superparticle method	89

5.2	Material properties	90
5.2.1	Secondary electron emission	90
5.2.2	Backscattered electron yield	91
5.2.3	Photoelectric yield	91
5.2.4	Normal reflectance	92
5.3	Analysis of complex geometries	93
5.3.1	Experimental setup	93
5.3.2	Configuration of SIMION model	94
5.3.3	Calibration	94
5.3.4	Results and discussion	96
5.4	Applications	98
5.4.1	Critical analysis of previous methods	98
5.4.2	Touchless potential sensing	100
5.4.3	Charge control	100
5.4.4	Material identification	101
5.5	Collaborators	102
II	Low-gravity magnetohydrodynamics	103
6	Preliminary considerations	104
6.1	Forces on magnetically polarized media	105
6.2	Stress tensor and force distribution	106
6.3	Governing equations for a magnetic, viscous, incompressible fluid	107
6.3.1	Volume equations	107
6.3.2	Boundary conditions	108
6.4	Formulation of mass-force potentials	109

7	An analytical perspective	110
7.1	Problem definition	110
7.2	Equilibrium	111
7.2.1	Dimensional formulation	111
7.2.2	Nondimensional formulation	113
7.3	Stability	113
7.4	Modal response	116
7.4.1	Nonlinear formulation	116
7.4.2	Linear equations	117
7.4.3	Dimensionless linear equations	119
7.4.4	Variational formulation	120
7.4.5	Ritz method	120
7.4.6	Finite differences method	123
7.4.7	Limitations	124
8	Bubble dynamics	125
8.1	Effective total force	126
8.2	Growth	127
8.3	Detachment	128
8.4	Displacement	129
8.4.1	Dynamic regime	129
8.4.2	Bubble force balance	130
8.4.3	Terminal velocity	131
8.5	Application to liquid droplets	131
8.6	Collaborators	133
9	Experimental validation	134
9.1	ZARM's drop tower	135

9.2	Axisymmetric free surface oscillations	136
9.2.1	The ESA <i>Drop Your Thesis!</i> 2017 - <i>The Ferros</i> project	136
9.2.2	Experimental setup	137
9.2.3	Visualization system	138
9.2.4	Liquid properties	140
9.2.5	Operation	141
9.2.6	Results	141
9.3	Lateral free surface oscillations	148
9.3.1	The UNOOSA DropTES 2019 - <i>StELIUM</i> project	148
9.3.2	Experimental setup	148
9.3.3	Visualization system	149
9.3.4	Liquid properties	152
9.3.5	Operation	152
9.3.6	Results	153
9.4	Free floating ferrofluid droplet	156
10	Fully coupled interface-tracking magnetohydrodynamic model	160
10.1	Numerical method	161
10.1.1	Problem formulation	161
10.1.2	Axisymmetric Navier-Stokes equations	162
10.1.3	Magnetic potentials for axisymmetric problem	162
10.1.4	Boundary conditions	164
10.1.5	Discretization of the simulation domain	168
10.1.6	Sloshing modes and free surface stability	171
10.2	Verification and validation	173
10.2.1	Field-free solution	173
10.2.2	Magnetic model	175

10.2.3	Equilibrium and virtual magnet substitution	177
10.2.4	Modal shapes	179
10.2.5	Dynamic response	180
10.3	Extended capabilities	183
10.3.1	Global stability	183
10.3.2	Time-dependent analysis	184
10.4	Generalization	186
10.5	Collaborators	189
III	Applications of low-gravity magnetohydrodynamics	190
11	Magnetic phase separation	191
11.1	Materials and Methods	192
11.1.1	Experimental setup	192
11.1.2	Experimental matrix	193
11.1.3	Liquid properties	194
11.1.4	Magnetic environment	194
11.1.5	Bubble tracking algorithm	195
11.2	Results and discussion	198
11.2.1	Overview	198
11.2.2	Terminal velocity	200
11.2.3	Wall-bubble interactions	202
11.2.4	Bubble-bubble interactions	203
11.3	Collaborators	204
12	Magnetic positive positioning	205
12.1	Fundamental MP ² architectures	205
12.1.1	Classification based on type of actuation	205

12.1.2	Classification based on scope	207
12.2	Performance analysis	208
12.2.1	Case of analysis	208
12.2.2	Equilibrium, stability, and modal response	210
12.2.3	System scaling	214
12.3	Technical feasibility	216
12.3.1	Thermal stability of ferrofluids	216
12.3.2	Radiation stability of ferrofluids	218
12.3.3	Impact of ferrofluid-enriched propellants on the propulsion subsystem	220
12.4	Collaborators	222
13	Application of magnetic positive positioning to launch vehicle restart	223
13.1	Launcher characteristics	224
13.1.1	Overview	224
13.1.2	Propellant behavior during stage separation	225
13.1.3	Engine restart conditions	226
13.2	Magnetic Positive Positioning	228
13.2.1	Implementation	228
13.2.2	Passive retention strategy	229
13.2.3	Recovery strategy	230
13.2.4	Magnetic trap	233
13.2.5	Magnetic field generation	235
13.2.6	Fuel tank	238
13.3	Propellant Gasification System	240
13.4	Hybrid Magnetic Gasification	241
13.5	Summary	243
13.6	Collaborators	244

14 Magnetically enhanced electrolysis	245
14.1 Fundamental architectures	245
14.1.1 Diamagnetically enhanced electrolysis	246
14.1.2 Lorentz-force enhanced electrolysis	247
14.2 Numerical study	248
14.2.1 Electrically neutral media	248
14.2.2 Effect of magnetic field in unbalanced electrolyte	253
14.2.3 Scale-up process	254
14.3 ASGSR Ken Souza Magnetically Enhanced Electrolysis Experiment	255
14.3.1 Scientific Objectives	256
14.3.2 Requirements	256
14.3.3 Experimental setup	257
14.3.4 Preliminary test	265
14.4 Short-term microgravity experiments	270
14.4.1 LiMo Project	270
14.4.2 Experimental setup	270
14.4.3 Preliminary results	272
Conclusions	279
Bibliography	283
Appendix	
A Magnetic force distribution	313
B Magnetic Comsol Multiphysics model	316

Tables

Table

2.1	Magnetic control system configuration.	36
4.1	Uncertainty analysis parameters.	82
4.2	Comparison of output variances between the full 702 parameters and the reduced 15 parameters MC analyses.	84
4.3	Normalized sensitivity indices from FAST sensitivity analysis with 15 inputs and 5 outputs. The values are scaled by a factor of 10 for convenience.	85
5.1	Emission parameters for selected materials [1, 2].	90
5.2	Representative parameters of commercial-off-the-Shelf UV lasers.	100
9.1	Physical properties of the ferrofluid solution employed in the ESA <i>Drop Your Thesis!</i> 2017 experiment with their standard deviations [3].	140
9.2	Current intensities for each drop.	141
9.3	Damping ratios for the first two axisymmetric oscillation modes computed by means of the half-power bandwidth method. The uncertainty is represented by the standard deviation. . .	147
9.4	StELIUM test matrix.	152
9.5	Experimental results for contact angle, fundamental oscillation frequency and damping ratios for axisymmetric and lateral waves, and lateral hysteresis parameter.	153
10.1	Fourth-order finite difference coefficients.	171

10.2 Intermediate results for representative positions in domain A as a function of the applied current intensity.	178
10.3 Complex fundamental axisymmetric frequencies as a function of mesh density in region A ($n_s \times n_{\eta_A}$) for different current intensities.	183
10.4 Complex second axisymmetric frequencies as a function of mesh density in region A ($n_s \times n_{\eta_A}$) for different current intensities.	183
10.5 Fitting parameters defined in Eq. 10.25 for the time evolution of the center of the free surface reported in Fig. 10.13 for different step loads.	186
11.1 Experimental matrix.	194
11.2 Bubbles tracked during 4.7 s of free fall. Labels are assigned for the left (L) and right (R) magnets and the first (1) or second (2) experiment with Milli-Q water.	201
12.1 Physical properties of CH_4 (l) enriched with a 0.53% volume of Fe_3O_4 nanoparticles, and of O_2 (l) at cryogenic storage temperature [2, 4, 5].	209
12.2 Maximum particle diameter as given by key energy balances.	217
13.1 Geometrical and inertial parameters of the launch vehicle.	224
13.2 Stage acceleration, settling time, and minimum initial oxidizer and fuel masses for different restart configurations of Falcon 9's first and second stages.	228
13.3 Mass and power budget for different magnetic configurations.	237
13.4 Mass from different components required for the flip around and settling maneuvers in the first and second stages.	242
13.5 Comparison of different propellant settling approaches and mass budgets for first and second stages.	243
14.1 Relevant physicochemical properties of water, gas hydrogen, and gas oxygen at 25°C and 1 atm [2].	248
14.2 Level-1 requirements.	257

14.3 Quasi-steady-state current density values of independent magnetic and non-magnetic platinum foil electrodes measured after 8.5 s of microgravity conditions. 274

A.1 Equivalent total magnetic force expressions. 315

Figures

Figure

1.1	Artistic illustration of Gateway in lunar orbit with the SpaceX Dragon XL logistics module on approach to docking. Credit: NASA.	2
1.2	Solomon S. Papell's conceptualization of the magnetic positive positioning concept in his 1963 US Patent 3,215,572 [6].	3
1.3	Conceptual representation of the secondary electrons and x-ray-based electrostatic potential measurement processes.	4
1.4	Charge distribution and secondary electron trajectories for isolated spacecraft geometry [7, 8].	5
1.5	Conceptual representation of the combined photoelectron and x-ray generation processes. . .	8
1.6	Spring-mass-damper mechanical sloshing analogies for different propellant tanks.	10
1.7	Conceptual representation of a diamagnetic standalone phase separator. Blue arrows represent the liquid/gas flow, while red arrows denote the magnetization vector of the magnet.	13
1.8	Examples of magnetic positive positioning and magnetic liquid sloshing.	15
1.9	Examples of magnetic positive positioning and magnetic liquid sloshing.	17
1.10	Water electrolysis in microgravity.	19
2.1	The ECLIPS Space Environments Simulation Facility.	33
2.2	Electron gun mounted onto the side of the ECLIPS chamber.	35
2.3	Installation of vertical coils inside the vacuum chamber.	37
2.4	Analysis of the magnetic disturbances induced by an IMG-300 UHV IMG in the radial cross-section passing through the center of the IMG.	38

2.5	Phosphor screen and RPA. The size and shape of the electron beam are observed in blue for a particular gun configuration and electromagnetic environment.	39
2.6	Residual Gas Analyzer mounted onto the side of the ECLIPS chamber.	41
2.7	Bakeout infrared emitter in operation during a touchless potential sensing experiment.	41
2.8	Rotational stage with first translational stage mounted atop it.	43
2.9	Power supplies and control infrastructure for the chamber. The server rack at top right contains the HVPS and controllers for the electron and ion guns.	44
3.1	Experimental setup.	50
3.2	Estimated secondary emission properties of aluminum.	51
3.3	SIMION model geometry.	53
3.4	Electron beam trajectory for different electrode heading angles α	55
3.5	Centering and calibration of the electron beam.	56
3.6	Secondary electrons spectrum for a range of electrode potentials and rotation angles.	57
3.7	Secondary electron trajectories between the electrodes.	58
3.8	Electron current fluxes at selected energy levels.	59
3.9	Electron trajectories from panel (red) and bus (green) electrodes for different heading angles and potential configurations.	60
3.10	Observability matrix of the system for different heading angles and panel-bus potentials. Missing angles are not observable.	61
3.11	Source region of secondary electrons reaching the RPA for a heading of 80° and an electrode potential of -800 V.	62
4.1	Comparison between simulation framework and SIMION's beam repulsion model [9] for $E = 1$ eV, $\delta = -16.7^\circ$, and $I_0 = 3.47 \mu\text{A}$	73
4.2	Experimental setup inside the ECLIPS chamber.	74
4.3	Electron beam spot in the phosphor screen under different electrode potentials.	75
4.4	Experimental electron flux distribution as a function of the applied electrode potential.	76

4.5	Electron beam spot in the phosphor screen under different electrode rotation angles at -100 V.	77
4.6	MSM representation of the experimental setup with electron beam propagation at -500 V. . .	78
4.7	Validation metrics \mathcal{R} and θ as a function of the electrode potential and heading angle.	79
4.8	Geometry of the 2-SC problem for the basic simulation parameters (see Table 4.1).	79
4.9	Validation metrics \mathcal{R} and θ as a function of the target spacecraft potential V and beam energy E_b for the nominal active spacecraft charging scenario.	80
4.10	Beam radius evolution as a function of divergence angle for the nominal active spacecraft charging scenario.	81
4.11	Result of the Monte Carlo simulation.	83
4.12	Trajectory of 100 secondary electrons generated in the beam-target intersection region described by the Monte Carlo analysis in Fig. 4.11(b).	85
5.1	SIMION examples of photons (white) being generated and reflected, leading to the emission of photoelectrons (green) and secondary electrons (blue).	88
5.2	Backscattered electron yield for selected materials as a function of the impacting electron energy [10].	91
5.3	Photoelectric yield for selected materials as a function of the impacting photon energy [11–13].	92
5.4	Normal reflectance for selected materials as a function of the impacting photon energy [2, 13, 14].	92
5.5	Experimental setup.	93
5.6	Normalized spectrum of the Hamamatsu L10706-S2D2 UV light source [15].	94
5.7	Calibration of the position and heading of the UV light.	95
5.8	Overview of photoelectron trajectories (green) generated by the UV source (white) as a function of the electrode assembly heading angle. The first iteration of reflected photons is shown for -25° and removed for clarity in the other cases.	96

5.9	Comparison of experimental and simulated currents from the electrode assembly as a function of its potential and heading angle. The currents correspond to the electron flux entering the RPA in the ± 50 eV band around the electrode potential.	97
7.1	Framework of analysis for the study of magnetic liquid interfaces in low-gravity [16].	111
7.2	Mesh employed to discretize a ferrofluid interface in a cylindrical tank using the finite differences solution procedure.	124
8.1	Conceptual stages of single bubble evolution when subject to an inhomogeneous magnetic field in microgravity. Detachment occurs when the vertical momentum balance is no longer satisfied, inducing a microconvection flow in the surrounding liquid. The bubble subsequently accelerates until viscous drag \mathbf{F}_ν compensates the magnetic buoyancy force, reaching the terminal velocity.	125
9.1	ZARM's drop tower.	135
9.2	Acceleration profile of ZARM's drop tower drop and catapult capsules. Disturbances during the microgravity window are caused by the payload.	136
9.3	From left to right, ZARM's drop tower, drop capsule, and setup of the ESA <i>Drop Your Thesis!</i> 2017 <i>The Ferros</i> experiment [3]. The setup has a mobile structure (red labels) with two identical assemblies that include (a) cylindrical ferrofluid containers, (b) magnetic coils, and (c) detection systems. The structure slides over a fixed frame (blue labels) with (d) a stepper engine actuator, and (e) two linear modules, as indicated by the orange arrow.	137
9.4	Geometry of the ESA <i>Drop Your Thesis!</i> 2017 <i>The Ferros</i> liquid tank.	138
9.5	Frame of one of the video records. The central point, laser pattern lines and light reflections can be observed.	139
9.6	Measured magnetization curve of the 1:10 vol EMG-700 ferrofluid solution.	140
9.7	Theoretical meniscus profile for upper (red) and lower (blue) containers for 0, 11, and 22 A computed using the coupled equilibrium model (Sec. 7.2).	141

9.8	Experimental vertex to border vertical distance f' as a function of current intensity I , measured 4 seconds after launch and comparison with coupled (solid) and uncoupled (dashed) theoretical frameworks. The measurements have a resolution of ± 1.8 mm.	142
9.9	Magnetic Bond number Bo_{mag} at the meniscus as a function of the dimensionless radius and coils current intensity for coupled (solid) and uncoupled (dashed) magnetic models.	143
9.10	Normalized first and second axisymmetric modes as a function of the dimensionless radius R for the free (light) and stuck (dark) edge conditions, the coupled (solid) and uncoupled (dashed) physical models, and $I = 20$ A.	143
9.11	Fundamental axisymmetric oscillation frequency for experimental (Exp.), coupled model (solid), and uncoupled model (dashed) values as a function of coils current intensity for upper and lower containers. The error bars denote the standard deviation of the measurements, to which a linear regression (dotted) is superposed. The free edge condition is assumed in the computations.	144
9.12	Second axisymmetric oscillation frequency for experimental (Exp.), coupled model (solid), and uncoupled model (dashed) values as a function of coils current intensity for upper and lower containers. The error bars denote the standard deviation of the measurements, to which a linear fitting (dotted) is superposed. The free edge condition is assumed in the computations.	147
9.13	Experimental setup (not in scale).	149
9.14	Surface line laser evolution of a StELIUM container in microgravity. On the top, the time evolution of different surface points is depicted. The first and second columns represents the top and lateral reconstructions of the ferrofluid surface. On the third column, synchronized lateral images are shown.	150
9.15	Fast Fourier Transform of the laser line for axisymmetric and lateral oscillations of the upper container.	151
9.16	Axisymmetric (left) and lateral (right) fundamental frequencies as a function of the coils current intensity.	154

9.17	Sequence captured by a lateral camera showing the ferrofluid droplet formation and evolution after the application of the vertical percussion. a) -2.5 s; b) -1 s; c) -0.5 s; d) 0 s; e) 0.5 s; f) 1 s; g) 1.5 s; h) 2 s; i) 2.5 s.	157
9.18	Measured and integrated height of the droplet as a function of time for the total force distribution (Eq. A.6 + Eq. A.11) and the Kelvin force alone (Eq. A.6). The error bands represent the standard deviation.	158
10.1	Schematic of the problem under study and numerical simulation domain with mapped regions and interfaces. The dashed rectangle E_c denotes the virtual coil domain.	161
10.2	Eigenfrequencies spectrum for $I = 10$ A. The first three dynamic modes are labeled.	172
10.3	Real fundamental axisymmetric frequency as a function of the contact angle and gravity level compared with analytical results from Yeh [17].	173
10.4	Numerical results for the dimensionless frequency as a function of the Ohnesorge number and contact angle compared with envelope data from Gerstmann and Dreyer [18].	174
10.5	Numerical results for the damping ratio as a function of the Ohnesorge number and contact angle compared with envelope data from Gerstmann and Dreyer [18].	175
10.6	Magnetic field comparison for $I = 20$ A.	176
10.7	Force density module comparison for $I = 20$ A.	176
10.8	Comparison of pressure and magnetic field lines for a paramagnetic fluid with $\chi^{\text{vol}} = 0.1$ at $I = 1$ A.	177
10.9	Comparison of magnetic fields and meniscus produced by a 3 mm height, 27.5 mm external radius magnet with a central 5 mm radius hole located 1 mm below the container. The virtual magnet substitution method described in Sec. 10.1.4.1 is employed.	179
10.10	Comparison of first two fundamental modes for $I = 20$ A.	179
10.11	First two axisymmetric natural sloshing frequencies compared with the quasi-analytical model Sec. 7.4 and experimental measurements obtained during the ESA <i>Drop Your Thesis!</i> 2017 campaign and reported in Chapter 9.	181

10.12	Fundamental axisymmetric frequency as a function of the applied destabilizing inertial acceleration for magnetic ($I = 22$ A) and non-magnetic ($I = 0$ A) cases.	184
10.13	Time evolution of the center of the free surface after the application of magnetic (top) and inertial (bottom) step loads in microgravity. The modal fits reported in Eq. 10.25 and Table 10.5 are superposed.	185
10.14	Streamlines after the application of magnetic (5-20 A) and inertial (0.53 m/s^2) step loads in microgravity. Successive time points reflect the first node (0), minimum ($T/4$), second node ($T/2$), and maximum ($3T/4$) of the displacement of the center of the surface, as indicated in Fig. 10.13.	187
10.15	Mesh employed in the study of the growth and detachment of bubbles immersed in ferrofluids.	188
11.1	Conceptual representation of a magnetic standalone and surface-tension enhanced diamagnetic phase separator. Blue arrows represent the liquid/gas flow, while red arrows denote the magnetization vector.	191
11.2	Experimental setup and syringe sample container located inside a ZARM's drop tower capsule.	193
11.3	Magnetic environment inside the syringe when filled with MilliQ water and 1 mm diameter air bubbles. The white bar at the top represents the gas injector.	195
11.4	Bubble detection algorithm steps applied to the original video frame image.	196
11.5	Unfiltered bubble trajectories resulting from the application of the bubble detection algorithm to a 4.7 s drop tower experiment. The color of the markers reflects the time of flight. Their size is scaled between 0.35 and 3.4 mm radius as indicated by the legend.	197
11.6	Control experiments for MilliQ water showing the injection and displacement of air bubbles in the absence of magnetic forces.	198
11.7	Overview of experimental results for the five drop experiments. Videos are labeled depending on whether the magnet is located at the left (L) or right (R) of the image.	199
11.8	Scaled bubble velocities as a function of the horizontal magnetic force compared with Eqs. 8.24 and 8.26 during the 4.7 s microgravity flight. The legend indicates the bubble ID from Table 11.2.	200

11.9	Bubble coalescence events at the wall for the L-01, R-02, and R-04 experiments. The red arrow indicates the ejection of a small gas bubble after bubble coalescence.	202
11.10	Bubble dragging example for the R-02 MilliQ water solution in microgravity. The red arrow indicates the velocity of the smaller bubble as the larger one drags it.	204
12.1	Conceptual representation of passive and active MP ² devices.	206
12.2	Modal spring-mass mechanical analogy for inviscid liquid sloshing.	208
12.3	Magnetization curves of liquid CH_4 enriched with a 0.53% volume of Fe_3O_4 nanoparticles (ferromagnetic) and liquid O_2 (paramagnetic).	209
12.4	Sketch of the 1U propellant tank considered in the analysis. Units in mm.	210
12.5	Axisymmetric meniscus profile and magnetic Bond number (color scale) for different filling ratios.	212
12.6	Axisymmetric meniscus profile as a function of the filling ratio (FR).	213
12.7	Magnetic Bond number at the axisymmetric meniscus as a function of the filling ratio (FR).	213
12.8	Fundamental free-edge sloshing frequencies as a function of the filling ratio (FR).	213
12.9	Dependence of the critical Bond number with the magnetization of the magnet in Fig. 12.4 for the LOX tank and 5 cm filling height.	214
12.10	$B_{o_{mag}}$ distribution (color scale) in a CH_4 -based ferrofluid with FR=80% and a flat surface.	215
12.11	Analysis of the combustion of $LCH_4/LOX/Fe_3O_4$	221
13.1	Geometrical parameters of a launch vehicle stage.	224
13.2	Estimated acceleration profile of the 1 st and 2 nd stages after separation.	225
13.3	Top view of the second-stage LOX tank of SpaceX's Falcon 9 during the CRS-5 mission. Source: www.youtube.com/watch?v=mVAGoWJuDKk	226
13.4	Magnetic Positive Positioning.	228
13.5	Magnetic acceleration contours induced on LOX by a 35 cm diameter coil operating at 1 At.	229

13.6	Time required by a LOX droplet to reach the bottom of the tank as a function of its distance to the coil and the applied current intensity. The minimum tank settling length required by the single engine (S.E.), minimum thrust (Min. T.) and maximum thrust (Max. T.) configurations is superposed.	232
13.7	Conceptual magnetic trap system for Falcon 9's first stage LOX tank. Red and blue arrows indicate the propellant flux in hyper- and microgravity conditions, respectively.	234
13.8	Magnetic acceleration field induced by a 5 cm radius 10 cm height praseodymium magnet magnetized at 1300 kA/m.	235
13.9	Propellant Gasification System.	241
13.10	Hybrid Propellant Gasification System.	241
13.11	Time required by a LOX droplet to reach the bottom of the tank as a function of its initial position and velocity when subject to a 10^4 At coil located at the tank outlet. The minimum tank settling length required by the single engine (S.E.), minimum thrust (Min. T.) and maximum thrust (Max. T.) configurations is superposed.	242
14.1	Conceptual representation of a magnetically enhanced electrolysis cell. Blue arrows represent the liquid/gas flow, while red arrows denote the magnetization vector.	246
14.2	Alkaline cell where the charge unbalance in the OH^- transport region leads to a magnetic Lorentz buoyancy effect in the presence of an out-of-plane magnetic field \mathbf{B}	247
14.3	Radial cross-section of the magnetic force density induced by a cylindrical magnet in an O_2 gas bubble. The red arrows, solid lines, and dashed lines represent the non-scaled force vector, the constant force contours, and the magnetic flux lines, respectively.	249
14.4	Radial cross-section of the Stokes terminal velocity v_t induced by a cylindrical magnet in an O_2 gas bubble with 1 mm radius in water. The red arrows, solid lines, and dashed lines represent the non-scaled velocity vector, the constant velocity contours, and the magnetic flux lines, respectively.	250

14.5	Two-dimensional simulation with 1 cm depth of the microgravity terminal velocity v_t induced by an array of magnets in an O_2 gas bubble with 1 mm radius in water. The black arrows, red arrows, solid lines, and dashed lines represent the magnetization direction, non-scaled velocity vector, the constant velocity contours, and the magnetic flux lines, respectively.	251
14.6	(a) Radial cross-section of the break-of diameter d_0 induced by a 10 mm radius, 5 mm height cylindrical magnet in an O_2 gas bubble in water with $\theta_c = 5^\circ$. The solid and dashed lines represent the constant break-of diameter contours and the magnetic flux lines, respectively. (b) Break-of diameter in the axis of symmetry for different gas-liquid combinations.	252
14.7	Two-dimensional simulation with 10 cm depth of the microgravity terminal velocity v_t induced by an array of magnets in an O_2 gas bubble with 1 mm radius in water. The hypothetical location of the Membrane Electrode Assemblies is represented by light gray areas. Black arrows, red arrows, and solid lines represent the magnetization direction, non-scaled velocity vector, and constant velocity contours, respectively.	254
14.8	Architecture tree.	258
14.9	Final design of the Magnetically Enhanced Electrolysis experiment.	259
14.10	Magnetic electrolytic cell assembly.	260
14.11	Magnetic environment inside the left section of the magnetic cell.	261
14.12	Power and electronics subsystem.	262
14.13	Nominal acceleration profile during Blue Origin's New Shepard flight [19].	263
14.14	Sample electrochemical data from a single cell during on-ground testing.	264
14.15	Overview of experimental setup before integration.	266
14.16	Sample camera image during on-ground testing.	266
14.17	External structure. The white bolt in subfigure (b) blocks the hydraulic circuit and is removed before flight.	267
14.18	Detail of the magnetic cell and gas accumulators.	267
14.19	Detail of the mirrors.	268
14.20	Drop tower test of the magnetic electrolytic cell.	269

14.21	Experimental setup of the LIMO experiment.	271
14.22	Magnetic environment of the LIMO experimental setup in the $y = 0$ plane defined by the working electrode (W.E.) and the counter electrode (C.E.).	272
14.23	Electrochemical performance of platinum foil and mesh electrodes with and without magnetic fields during a 9.3 s catapult drop.	273
14.24	Non-magnetic platinum foil electrode with hydrogen bubbles.	275
14.25	Magnetic platinum foil electrode with hydrogen bubbles.	276
14.26	Non-magnetic platinum mesh electrode with hydrogen bubbles.	277
14.27	Magnetic platinum mesh electrode with hydrogen bubbles.	278
B.1	Mesh employed by the magnetic Comsol Muliphysics model.	317

Chapter 1

Introduction

1.1 Motivation

In 1985 Ronald E. Rosensweig wrote this in the preface of his reference textbook, *Ferrohydrodynamics*, “*my initial studies with my colleagues were motivated by engineering endeavors and the hope that adding a magnetic term to the equations of fluid motion would lead to interesting and useful consequences*” [20]. In light of the vast impact of his work, Rosensweig’s hopes were certainly justified. Unlike surface tension or mechanical interactions, electromagnetic forces enable mid-distance, contactless actuation and sensing. This is the distinctive characteristic that sparked my curiosity when I started studying the dynamics of ferrofluids, and also the underlying motivation that pushed me to explore more applications of electromagnetism in space. There are countless problems where the “addition of a magnetic term” can result in new architectures or performance enhancements and, in most cases, I found a surprisingly early stage of development.

Many different systems fall into the definition of “space electromagnetics”. AstroScale’s docking plates employ magnetic actuators to enable docking during servicing operations, and a similar approach is being explored by ALTIUS Space Machines using electropermanent magnets. TESSERA’s project at MIT’s Space Exploration Initiative implements electromagnetic actuators to self-assemble space structures. ETA Space aims at demonstrating cryogenic management technologies in orbit, and magnetic slosh control was considered during the design of LOXSAT-1. In the academic realm, Prof. Mason A. Peck’s works on magnetic de-spinning [21], eddy-current actuation for on-orbit inspection [22], or electrodynamic tethers for chipsats [23] have introduced some interesting ideas for electromagnetic actuation in space. The use of



Figure 1.1: Artistic illustration of Gateway in lunar orbit with the SpaceX Dragon XL logistics module on approach to docking. Credit: NASA.

electron beams and electrostatic repulsion for lunar dust mitigation is also gathering significant attention in the life support community [24].

In this context, the first part of this Ph.D. dissertation deals with the touchless sensing of target spacecraft potentials in Geosynchronous Equatorial Orbits (GEO) and deep space. Knowledge of a target's electrostatic potential is critical when spacecraft charging is significant and multiple spacecraft are involved (i.e. for close proximity operations at high altitude). Rendezvous events have historically taken place in the Low Earth Orbit (LEO), but the increasing need for active space debris removal makes GEO operations necessary. Moreover, the ambition to make humans a multi-planetary species is shifting our interest from LEO to the cislunar environment, the best example being the (hopefully) upcoming Lunar Gateway station depicted in Fig. 1.1. It is in these new environments with low-density high-temperature plasma where spacecraft charging becomes a major concern or, from a more optimistic perspective, a great opportunity for concepts like the electrostatic tractor [25]. The electron-based touchless potential sensing technology covered in Part I is ultimately aimed at supporting these new ideas.

Ferrofluids were invented in 1963 by NASA's engineer Solomon S. Papell [6] and they have found application in fields as diverse as printing, medicine, tribology, heat transfer, or even art. It is usually forgotten is that Papell's US Patent 3,215,572 introduced ferrofluids as a mechanism to control rocket

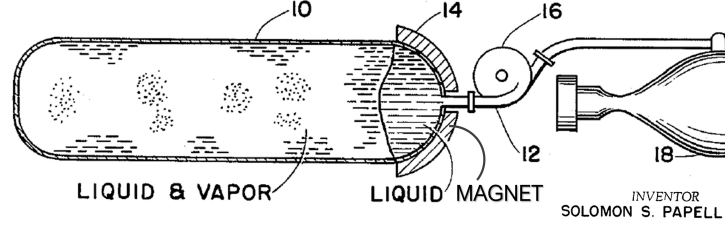


Figure 1.2: Solomon S. Papell’s conceptualization of the magnetic positive positioning concept in his 1963 US Patent 3,215,572 [6].

propellant sloshing in an approach that is nowadays known as Magnetic Positive Positioning (MP^2 , see Chapters 12 and 13). Papell illustrated the concept with the drawing in Fig. 1.2, that is found in the first page of his patent. In spite of the originality of his invention, magnetic positive positioning systems have not yet flown to space and the maturity of this technology remains below a technology readiness level (TRL) of 5. Propulsion engineers probably thought that the risk and cost of developing magnetic propellants was not worth the effort given the existence of solutions with flight heritage, like surface-tension-based propellant management devices (PMDs). However, space exploration faces an age where classical technologies are being pushed to their limits and more efficient approaches are required for new missions. For instance, traditional PMDs will generally fail to store and transfer cryogenics extracted from In-Situ Resource Utilization (ISRU) due to the weak surface tension forces. Analogous problems are observed in the design of conformal tank geometries for SmallSats, where volume is even more limited than mass and where MP^2 can potentially lead to significant reductions in both.

The list of electromagnetic technologies enabled by new missions (and the list of mission concepts enabled by such technologies) goes on and on and includes the ideas explored in this dissertation. The challenges that we face in the new age of space exploration will push our sector to expand its traditional limits. It is in this context where an opportunity is presented to leverage previously unexplored electromagnetic concepts and create a new generation of space systems. What follows is a brief introduction to the ones explored in this dissertation: **electron-based touchless spacecraft potential sensing** and **low-gravity magnetohydrodynamics**.

1.2 Touchless potential sensing

1.2.1 Concept

The use of secondary electrons [26] and x-rays [27–29] has been recently proposed to touchlessly sense the electrostatic potential of non-cooperative objects in GEO and deep space. These approaches, illustrated in Fig. 1.3, make use of a positively charged servicing craft that directs a high-energy electron beam at the object of interest so that low-energy secondary electrons and x-rays are emitted from the surface. The secondary electron flux is accelerated toward the servicing craft and arrives with an energy equal to the potential difference between the two bodies. The servicing craft measures the electron and photon energy spectrum and, knowing its own potential, infers that of the target [30]. Potential levels of the order of 10s of keV and beam currents of up to 1 mA are considered in these scenarios [31].

Several novel GEO and deep space applications are enabled by this approach, including those dealing with the electrostatic detumbling [32] and reorbiting [25, 33–35] of debris, Coulomb formations [36], virtual structures [37], electrostatic inflation [38], and the mitigation of arcing during rendezvous, docking, and proximity operations [39]. Coulomb formations can also be established in LEO by exploiting the plasma

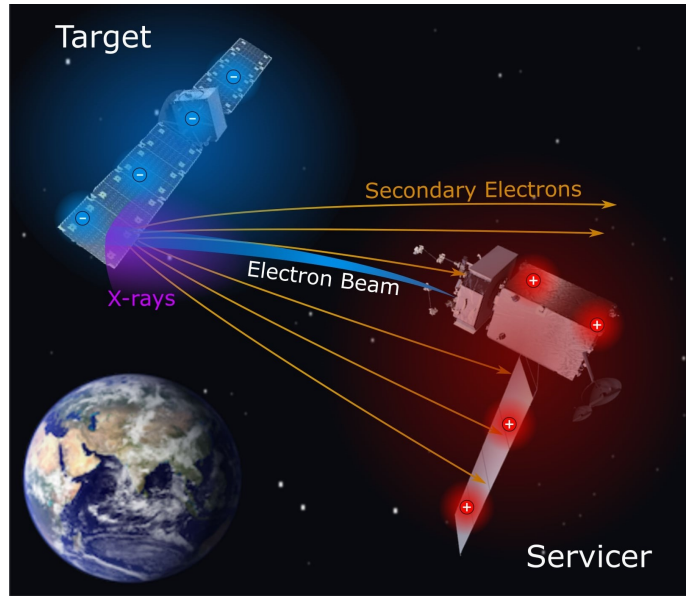


Figure 1.3: Conceptual representation of the secondary electrons and x-ray-based electrostatic potential measurement processes.

wake of the leading spacecraft [40]. In addition, X-ray sensing methods have been proposed for arcing detection in GEO [41].

This dissertation focuses on the electron-based touchless potential sensing method and its associated challenges. For further details on the x-ray method, the reader is referred to Ref. 42.

1.2.2 Complex shapes and heterogeneous charging

The validation of electron-based touchless electrostatic potential sensing methods has been addressed in previous works with flat plates, which simplify experimental procedures and ease data interpretation [26, 43, 44]. However, a flat surface is not representative of a standard spacecraft, whose complex geometry leads to a highly inhomogeneous electric field that determines the trajectories of low-energy particles [45–48]. Recent work exemplifies the importance of this effect by making use of two-dimensional shape primitives in vacuum chamber and numerical experiments, showing how concave geometries and internal corners focus the flux of secondary electrons, while convex surfaces and external corners have the opposite effect [8]. This is illustrated in Fig. 1.4. The detectability of secondary electrons at a servicing spacecraft is thus determined by the target’s geometry and relative position [8] and the interaction with the impinging electron beam [49]. The problem is further complicated when differential charging (i.e. multiple potentials) is considered.

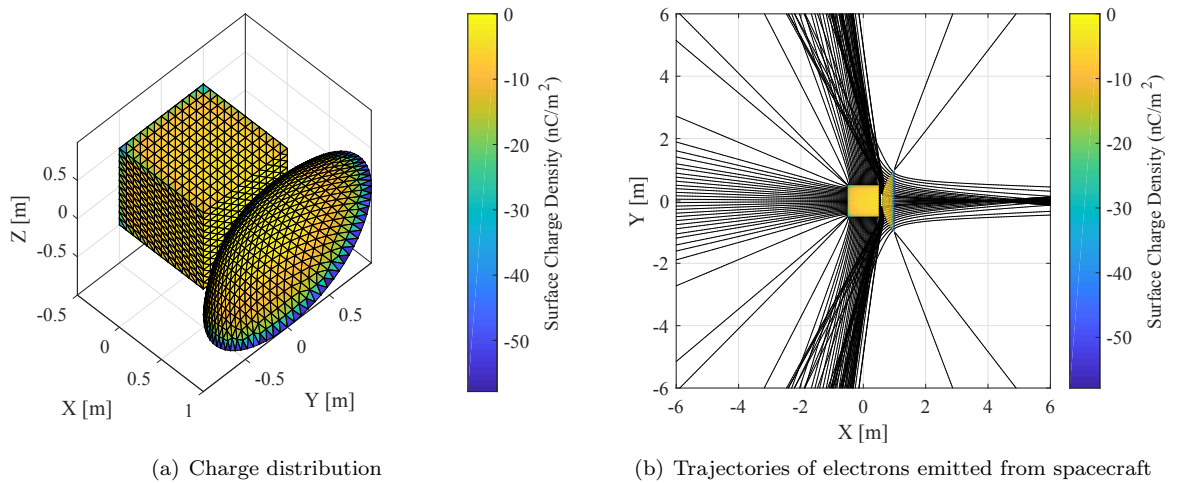


Figure 1.4: Charge distribution and secondary electron trajectories for isolated spacecraft geometry [7, 8].

Although modern design best practices recommend all exterior surfaces to be connected to a common ground [50], this is often hard to achieve in the daily practice, ultimately leading to arcing events [51–54]. On one hand, a differentially-charged body steers the electrons in different directions with respect to the uniform potential scenario. On the other, their observability may be severely compromised due to the generation of potential traps [55].

Chapter 3 addresses the detectability of spacecraft potentials using the secondary electron method in realistic targets. Its primary goal is to identify the geometrical configurations for which the flux of secondaries is observable and its magnitude. A second goal is to develop and validate an efficient particle tracing simulation framework that enables high-fidelity simulations of the sensing process. Previously unexplored mechanisms, like the coupling between electron beam propagation and secondary electron generation, are addressed. Moreover, the effects of differential charging on the secondary electron flux generated on a complex space-like geometry are studied for the first time. Vacuum chamber experiments are carried out at the Electrostatic Charging Laboratory for Interactions between Plasma and Spacecraft (ECLIPS) simulation facility [56] to support the study. A relatively straightforward three-dimensional numerical implementation is achieved by making use of SIMION, a popular particle tracing simulator used in the design of ion optics [9] which is particularly appropriate for space applications where space charge effects remain negligible.

1.2.3 Electron beam modeling

Chapter 3 shows that the detection of secondary electrons from a target spacecraft is conditioned by its geometry, position with respect to the servicer, charging state, and electron source region [8]. From a technical perspective, the intersection between the electron beam and the target object defines the area where secondaries are generated. The ability to focus the electron beam on a specific spot of the target not only finds application in potential sensing, but also in the identification of surface materials and the characterization of differentially-charged objects. Therefore, the efficient and physically accurate modeling of the electron beam is key for pre-flight studies and in-situ operation. Past missions have operated electron beams in space, with some examples being SCATHA [57] or the Electron Drift Instruments at GEOS [58], Freja [59], Cluster [60], and MMS [61]. Since beam repulsion effects were negligible or irrelevant in most cases,

very basic electron beam models could be employed. This would not be appropriate for the technologies discussed in Part I.

The application of the particle tracing framework introduced in Chapter 3 to model the electron beam dynamics is appropriate in most cases, but (i) fails to implement the electromagnetic expansion effects in high-intensity beams, and (ii) doubles the computational cost of the simulation by propagating electron trajectories from the servicer to the target. The computational aspect is critical for in-situ operations. In addition, the detection process is subject to significant uncertainties that must be accounted for in the design, making efficient models necessary for uncertainty quantification.

Chapter 4 takes advantage of the the active potential sensing environment to introduce a simplified, computationally efficient electron beam model suitable for onboard flight algorithms. The model is employed to study the uncertainty in the propagation of electron beams in an active potential sensing scenario by means of highly efficient Monte Carlo simulations.

1.2.4 Photoelectron-based sensing strategies

Chapters 3 and 4 will show that uncertainty mitigation is one of the major challenges in the electron-based touchless potential sensing method. Unmodeled geometries, a particularly complex differential charging scenario, or servicer-target positioning errors can bring the electron sensor away from the flux of secondaries predicted by onboard models, hence losing their signal. Analytical and experimental studies have already highlighted this issue and suggested the combined measurement of secondary electrons and x-rays to enhance the robustness of the sensing process [44, 49]. However, the physics of each problem are not favorable to the simultaneous generation of these signals: while secondary electrons are mainly released at moderate electron beam energies [55], the generation of x-rays is favored by energetic particle impacts [27]. In addition, and as shown in Chapter 4, low-energy electron beams are steered in the presence of the inhomogeneous electrostatic field generated by the servicer-target system, increasing the sources of uncertainty of the problem. From a technical perspective, it would be convenient to develop a sensing strategy that uncouples both mechanisms and optimizes the generation and control of secondary electrons and x-rays while minimizing the current fluxes imparted on the target.

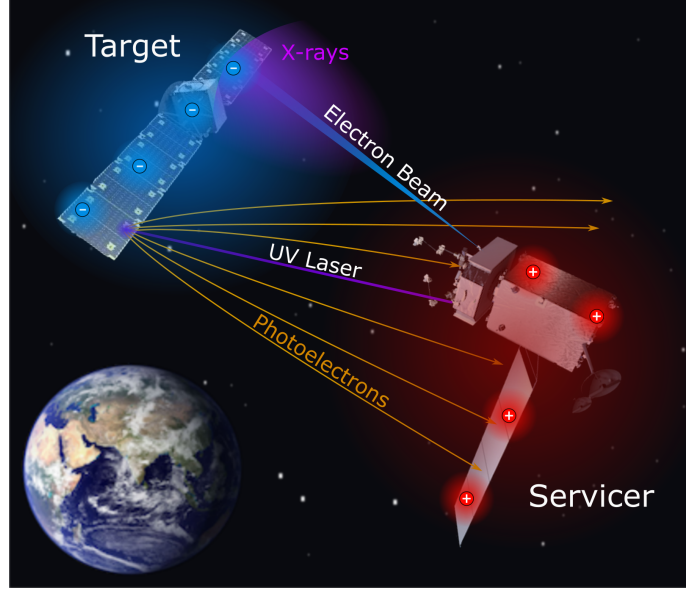


Figure 1.5: Conceptual representation of the combined photoelectron and x-ray generation processes.

The use of ultraviolet (UV) sources is explored in Chapter 5 to generate an environment-independent electron release method. In particular, the simultaneous application of ultraviolet (UV) lasers and high-energy electron beams is proposed to excite the emission of photoelectrons and x-rays in non-cooperative GEO objects. Figure 1.5 shows a conceptual representation of this strategy where both systems operate independently and impact (if needed) different areas of the target. Major sources of uncertainty are eliminated with this approach due to the high directivity of quasi-relativistic electron beams and the rectilinear trajectories of photons which, unlike electron beams, remain unaffected by the complex electrostatic environment. In addition, independently controlled positive (photoelectrons) and negative (electron beam) currents are added to the target spacecraft charge balance, enabling a promising new method to touchlessly sense the electrostatic potential of an object without changing its equilibrium state.

The photoelectric effect has been considered for decades in the spacecraft charging community and is usually treated from a current-balance perspective [55]. Recent works have also explored the use of solar light as a way to excite photoelectric emission and passively sense the target potential [7]. In contrast, Chapter 5 focuses on active photoemission sensing and adopts a particle-centered strategy to extend the framework introduced in Chapter 3 to the modeling of UV laser beams. The outcomes of the simulation are compared

with experimental results to inform the design of future systems.

1.3 Low-gravity magnetohydrodynamics

1.3.1 Definition and scope

In contrast with the term “magnetohydrodynamics”, which refers to the interaction between magnetic fields and fluid conductors of electricity, the word “ferrohydrodynamics” is closely related to the volume force density that arises when a ferrofluid is polarized. The polarization force is not only observed in ferrofluids, but also in natural liquids such as water or liquid oxygen [62]. However, it is so weak that terrestrial applications are almost nonexistent¹. In microgravity, however, even the slightest disturbance can determine the behavior of a fluid system [63]. This has led to the formulation of several potential space applications, including mass transfer [64–68], thermomagnetic convection [69, 70], micropropulsion [71, 72], phase separation [73], or sample holding [74], among others. Earth systems employing ferrofluids are also numerous and cover bubble and droplet studies [75–77], T-junctions [78–80], or energy harvesters [81–83]. In other words, the application of magnetic forces leads to alternative fluid management approaches in microgravity and on Earth.

None of the aforementioned terms (magneto/ferrohydrodynamics) fully identifies the domain of physics dealing with the magnetic polarization force in both ferrofluids and natural liquids. While the first is commonly associated with Lorentz forces arising in fluid conductors of electricity, the second is bounded to ferrofluids. Due to the lack of a better candidate, and with permission from Prof. Alfvén [84], I will subsequently refer to the intersection between low-gravity fluid mechanics, magnetic polarization forces, and Lorentz forces as *low-gravity magnetohydrodynamics (LG-MHD)*.

Although Lorentz forces will be considered in Chapter 14, Parts II and III will focus mainly on magnetic polarization and its applications in low-gravity fluid mechanics. There are important reasons behind this decision: (i) magnetic polarization forces have historically been ignored in the study of low-gravity fluid mechanics, creating a gap of knowledge that needs to be filled, (ii) magnetic polarization forces can be treated with quasi-analytical tools, enabling fast technology development, and (iii) Lorentz forces are

¹ Still, it has been employed to levitate frogs or grasshoppers (who, let’s be honest, don’t seem very happy about it) <https://youtu.be/KlJsVqc0yWM?t=34>. Consulted on: 14/04/2022.

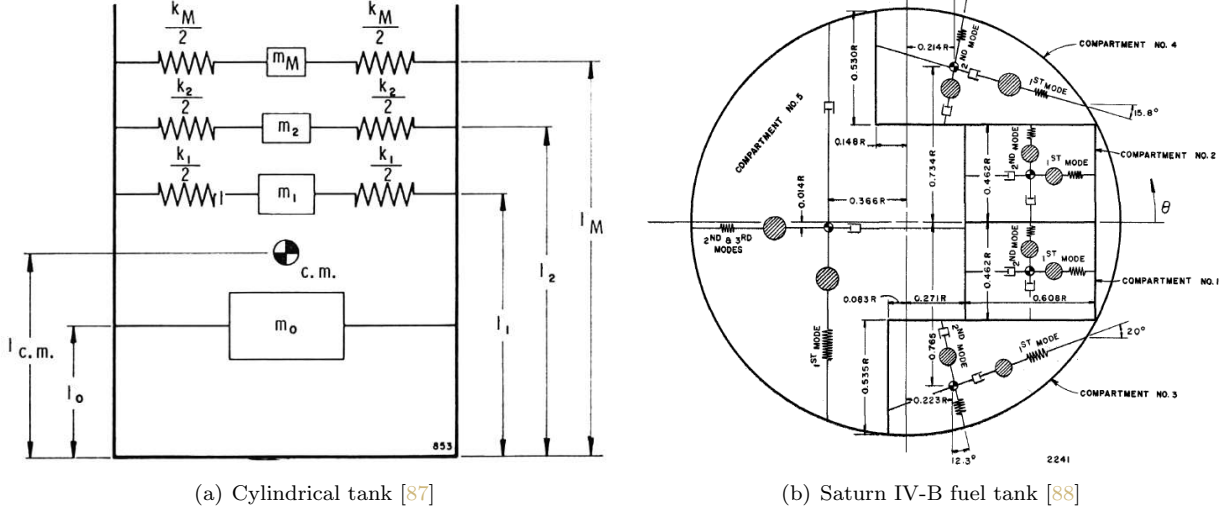


Figure 1.6: Spring-mass-damper mechanical sloshing analogies for different propellant tanks.

far less common and, when applicable, lead to complex magnetohydrodynamic flows that require dedicated numerical simulations.

1.3.2 Analytical perspective

The study of liquid interfaces in low-gravity has traditionally focused on three basic concepts: equilibrium, stability, and modal response [85]. All three became essential for the development of PMDs in the early 1960s, with the latter resulting in mechanical analogies under different gravity levels [86] like those depicted in Fig. 1.6. The very few publications studying surface tension-dominated liquid interfaces subject to magnetic polarization, on the contrary, have only made use of numerical methods, somehow skipping that essential body of knowledge. The reasons behind this are unclear, but may be related to the inherent complexity of the problem and the widespread availability of computational resources by the time magnetic actuation became a realistic possibility (i.e. after the popularization of neodymium magnets and low-temperature superconductors). However, a more classical approach to LG-MHD pays off in terms of computational efficiency and fundamental understanding.

Three-dimensional low-gravity fluid mechanics problems usually fall beyond the capabilities of analytical methods. Software suites like K. A. Brakke's Surface Evolver have become extremely popular in

the low-gravity fluid physics community to compute interfacial static equilibria [89], while dynamic systems are usually treated by means of interface-capturing and interface-tracking numerical frameworks (more on this in Chapter 10). In order to exploit the advantages of analytical methods while keeping them practical enough for a technical application, the formulations derived in Chapter 7 are restricted to axisymmetric liquid-gas problems (including lateral oscillations). Axisymmetric interfaces are ubiquitous in low-gravity fluid systems, from pipes to propellant tanks, and enable a simpler two-dimensional analysis. Once the physics of axisymmetric interfaces are understood, the three-dimensional extension becomes almost trivial using modern numerical methods. In addition, and due to their importance as elemental multiphase flow units, specific features regarding bubble and droplet dynamics are addressed in Chapter 8. An experimental validation of these formulations is given in Chapter 9 using a series of drop tower experiments.

1.3.3 Numerical perspective

The quasi-analytical tools developed in Chapters 7 and 8 are particularly hard to extend to viscous flows or complex three-dimensional geometries. In addition, they also involve some important simplifications. It is in this context where numerical magnetohydrodynamic multiphase simulation frameworks can make a difference by enhancing our understanding and modeling capabilities.

A classification of previous numerical magnetohydrodynamic frameworks may consider two key characteristics: solution procedure and multiphase flow modeling approach. In the first category, and excluding implementations where the fluid-magnetic coupling is ignored or heavily simplified, *partitioned* schemes that iteratively solve the fluid-magnetic equations seems predominant [16, 90–95]. In contrast, *monolithic* approaches solve all equations simultaneously within a global system of nonlinear equations and have also been implemented using the finite elements method [96–98]. Although monolithic approaches deal with the inversion of a large Jacobian, require more memory, and renounce to the modularity of partitioned schemes, they are also more robust and generally more computationally efficient than iterative implementations, particularly for complex multiphysics problems [99–102]. From the multiphase flow modeling perspective, the Lattice Boltzmann [93, 95, 103, 104], level set [94], phase field [105], and volume of fluid methods [91, 98], or a combination of the previous [92] have been employed. The last three can be categorized as interface-

capturing, meaning that an auxiliary function is introduced in a fixed spatial domain to determine the location of the interface. Although their versatility has made them extremely popular in the multiphase flow community, interface-capturing methods face significant challenges when dealing with the formulation and implementation of surface tension [106]. This includes the mitigation of numerical diffusion at the interface, the computation of surface normals and curvatures, or the imposition of a discrete balance of surface tension and pressure gradient terms [107]. In contrast, interface-tracking methods employ meshes that follow the fluid surface by advecting with the flow a discrete set of points distributed along the interface. This approach avoids numerical diffusion, provides a seamless implementation of surface tension forces, and leads to simpler boundary conditions, which makes it particularly appropriate for capillary and low-gravity fluid problems. However, the geometrical transformation employed to transition from the uniform computational domain to the deformed mesh complicates the final expression of the governing equations and limits their applicability to relatively simple geometries [108].

Interface-tracking methods for coupled, capillary magnetohydrodynamic systems remain, to the best knowledge of the author, completely unexplored. Their development is highly desirable for the study of a wide variety of fundamental and applied problems, ranging from bubble and droplet studies to microfluidic and low-gravity systems. To cover this knowledge gap, Chapter 10 introduces the very first of such models and validates it with the experimental measurements introduced in Chapter 9.

1.4 Applications of low-gravity magnetohydrodynamics

1.4.1 Phase separation

The third and last part of this dissertation introduces several cases of application of low-gravity magnetohydrodynamics. The first of them is phase separation, which is a crucial process for a wide variety of space technologies. Those include propellant management devices, heat transfer and life support systems comprising the production of oxygen, fuels and other chemicals as well as the removal of carbon dioxide from cabin air and the recycling of waste water, among many others.

Numerous phase separation methods have been developed for microgravity conditions. Centrifuges

[109, 110], forced vortical flows [111–115], rocket firing [116–118], membranes [119, 120], and surface-tension-based technologies [121, 122], which include wedge geometries [123–126], springs [127], eccentric annuli [128], microfluidic channels [129] or porous substrates [130, 131], among others, are the most traditional solutions. As an alternative, the use of electrohydrodynamic forces has been studied since the early 1960s [132] and successfully tested for boiling, two-phase flow management [133–135], and conduction pumping [136] applications. Hydroacoustic forces arising from the application of ultrasonic standing waves [137] have been applied to enhanced a wide variety of terrestrial processes [138] and also proposed to control bubbly flows in propellant tanks [139, 140] and life support systems [141]. Small amplitude vibrations can also be employed to manage multiphase flows and induce phase separation in microgravity [142] by selecting viscoequilibrium configurations [143] or exploiting frozen wave instabilities [144]. These approaches present unique characteristics that affect aspects like their operational lifespan, reliability, performance and intrusiveness [141].

Complementary to the aforementioned methods, the inherent magnetic properties of liquids can be employed for passive phase separation. A conceptual representation of this approach is shown in Fig. 1.7. As shown in Chapter 6, inhomogeneous magnetic fields induce a weak polarization force in continuous media that, due to the differential magnetic properties between phases, results in a net buoyancy force. This phenomenon is known as *magnetic buoyancy* and has been applied to terrestrial boiling experiments with ferrofluids [145, 146]. Previous works on low-gravity magnetohydrodynamics have explored, for instance, the diamagnetic manipulation of air bubbles in water [64, 65], the positioning of diamagnetic materials [74], air-water separation [73], protein crystal growth [147], or combustion enhancement [65]. The use of

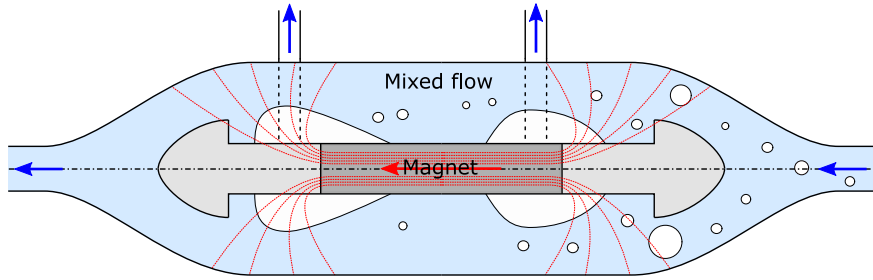


Figure 1.7: Conceptual representation of a diamagnetic standalone phase separator. Blue arrows represent the liquid/gas flow, while red arrows denote the magnetization vector of the magnet.

magnetic buoyancy in phase separation under microgravity conditions remains, however, largely unexplored and motivates the work presented in Chapter 11.

1.4.2 Magnetic positive positioning

Magnetic positive positioning is the second application explored in this work. Propellant sloshing represents a major concern for aerospace engineers due to its capacity to disturb the dynamics of space vehicles. During launch, the uncontrolled movement of liquids may lead to a total or partial mission failure [148]. In microgravity, sloshing is characterized by its highly stochastic nature, which complicates the design of propellant management systems and induces additional spacecraft attitude disturbances [86]. PMDs are commonly employed to ensure a gas-free expulsion of propellant, fix the center of mass of the fluid and tune its free surface frequencies and damping ratios [63, 149]. However, they also increase the inert mass of the vehicle and complicate numerical simulations [150].

An interesting alternative to classical PMDs and active settling methods relies on the application of electromagnetic fields to generate a gravity-equivalent acceleration. The use of dielectrophoresis, a phenomenon on which an electric force is exerted on dielectric materials, was explored by the US Air Force with suitable propellants in 1963. The study highlighted the risk of electrical arcing and the need for large, heavy and noisy power sources [132]. Most of these concerns are no longer valid sixty years afterwards and, indeed, several groups are currently exploring the application of electric polarization forces to space technology [134, 135, 151–153]. The magnetic equivalent, Magnetic Positive Positioning (MP²), has also been suggested to exploit the magnetic polarization force on paramagnetic, diamagnetic, and ferromagnetic liquids [6].

As shown in Chapter 11, MP² devices must deal with the rapid decay of magnetic fields with distance, that limits their applicability to relatively small regions. This difficulty may be compensated by employing ferrofluids. Terrestrial works have explored the natural frequency shifts due to the magnetic interaction [155], axisymmetric sloshing [156, 157], two-layer sloshing [158], liquid swirling [159] or the development of tuned magnetic liquid dampers [160, 161]. Low-gravity contributions include the gravity compensation experiments performed by Dodge in 1972, who indirectly addressed the low-gravity sloshing of ferrofluids

subjected to quasi-uniform magnetic forces [162]. Motivated by the advent of stronger permanent magnets and high-temperature superconductors, the NASA Magnetically Actuated Propellant Orientation (MAPO) experiment validated in 2001 the magnetic positioning of ferrofluid solutions in a series of parabolic flights [163]. Such ferrofluids were selected to approximate the linear magnetization curve of liquid oxygen for different magnetic field intensities. Subsequent publications presented refined numerical models and numerical results of technical relevance [154, 164–171]. The axisymmetric and lateral sloshing of water-based ferrofluids was characterized in microgravity when subjected to an inhomogeneous magnetic field as part of the ESA Drop Your Thesis! 2017 [77, 172, 173] and UNOOSA DropTES 2019 [174–177] campaigns reported in Chapter 9.

In spite of the existence of recent works on MP², the TRL of this approach is still below 5. Chapter 12 outlines the basic MP² architectures and discusses their technical feasibility employing the tools introduced in Chapters 7 and 8.

1.4.3 Launch vehicle restart

The exploration and commercialization of space has led to the increasing contamination of the LEO environment by non-functional man-made objects. Space debris represents a serious safety hazard for current and future satellites due to the risk of in-orbit collisions, and a concern for the general population during

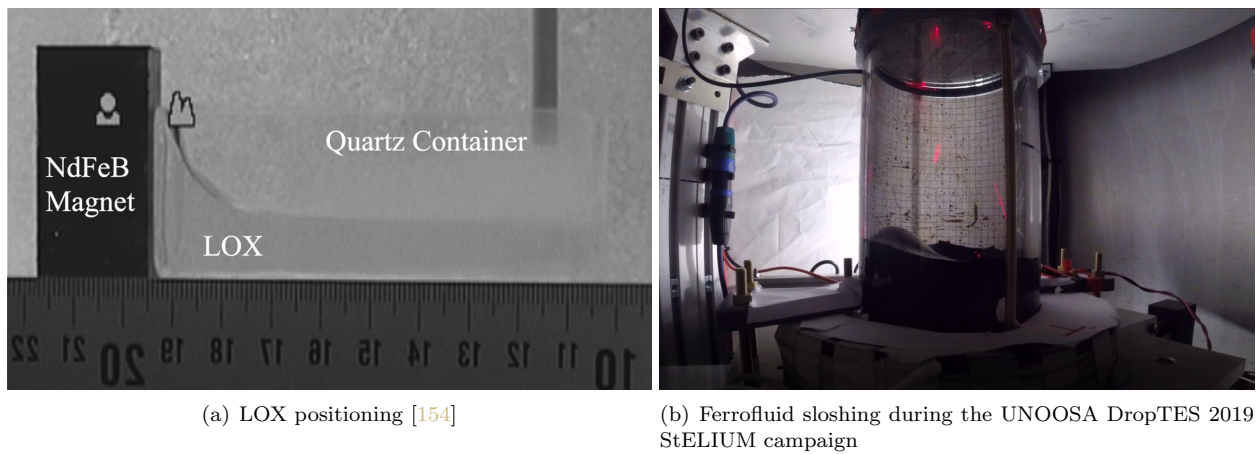


Figure 1.8: Examples of magnetic positive positioning and magnetic liquid sloshing.

uncontrolled re-entry events. The minimization of debris release during normal operations has consequently become a major goal for the international space community [178].

Launch vehicles (LVs) represent more than 42% of the abandoned intact objects in orbit and account for 57% of the abandoned mass [179]. Recent studies have identified the most dangerous elements in an attempt to guide future active debris removal efforts [179–181], resulting in a list that includes 290 second stages of the Soviet/Russian “Cosmos-3M” LV, 7 of which have been considered among the 50 most concerning space debris objects [181], 110 third stages of the Soviet/Russian “Cyclone-3” LV, 54 units of the American first and second stages of the “Delta” LV, as well as 38 third stages of the Chinese “CZ-4” and “CZ-2D” LVs. Further concerns arise due the presence of propellant residuals in the tanks, which account for up to $\sim 3\%$ of the initial fuel mass [182]. During the long stay of a stage in orbit, the remaining fuel evaporates under the influence of solar radiation, which leads to an increased risk of explosion and, therefore, to the generation of space debris [178]. The uncontrolled descent of first LV stages in sensitive drop areas can also lead to environmental pollution caused by the depressurization of toxic fuels, fires in the drop sites, and the contamination of water bodies. This problem is more relevant for Russian LVs like “Soyuz”, “Proton”, and “Angara”, where most of the drop zones are located on land [183, 184].

Modern launch vehicle operations are subject to strict space debris mitigation policies [178]. When graveyard orbits are not attainable, the orbital lifetime is limited and systems are passivated by removing all energy sources. Active deorbiting represents a highly attractive alternative to those strategies, but it is not exempt from risks and technical challenges [185]. Among them, proper engine restart conditions must be provided once the stage is separated from the rest of the vehicle in order to ensure a safe reorbiting or reentry. This decoupling induces strong disturbances on the propellant residuals and leads to highly non-linear sloshing dynamics, compromising the operation of the engine feed system [186].

Propellant management devices (PMDs) like porous traps [187, 188], troughs [189–191], or start baskets [192, 193] have been employed to safely restart rocket engines against moderate accelerations (particularly, in upper launcher stages with storable propellants), but these approaches do not easily apply to cryogenics due to their complex heat transfer mechanisms and low surface tension. In fact, screen channel liquid acquisition devices (Fig. 1.9(a)) are the only type of PMD with cryogenic flight heritage [194]. Although



(a) Total communication screen channel liquid acquisition device [194]



(b) Ullage engine from Saturn IV-B at NASA Johnson Space Center

Figure 1.9: Examples of magnetic positive positioning and magnetic liquid sloshing.

significant efforts are being devoted to the design of cryogenic liquid acquisition systems [195], the inertial (or active) settling approach is far more extended. Ullage engines have been traditionally employed during insertion, orbital coast, or on-orbit operations. These independent rockets induce accelerations that can be as weak as 10^{-4} to 10^{-3} m/s^2 and involve solid, mono-propellant, bi-propellant, or cold gas technologies, sometimes fed by vaporized propellant vented from the main tanks [196]. Some examples include the Saturn IV-B's hypergolic liquid bi-propellant Auxiliary Propulsion System (APS) [116, 117] pictured in Fig. 1.9(b), the APS at the Centaur upper stage [197], SpaceX's Falcon 9 nitrogen cold gas thrusters for coast attitude control [198], or the two *Sistema Obespecheniya Zapuska* (SOZ) ullage engines of the Blok DM-2 Proton upper stage. This last unit has raised concerns in the space debris community after being responsible for up to 50 on-orbit explosions between 1984 and 2019 [199].

The technical specifications of ullage engines are not usually accessible to the scientific community, which hampers any effort to perform an “external” evaluation of these systems. However, numerous reports from the Apollo era can still be consulted. The two Saturn IV-B APSs were usually fired in three consecutive ullaging burns for a total of ~ 245 s, consuming ~ 13.5 kg of propellant ($\sim 23.5\%$ of the total propellant mass of each APS) [200]. The dry mass of the APS is unknown to the author but seems of the order of several hundred kilograms judging by the volume of the system. The dry mass of Saturn IV-B was about 13.5 t.

On the other hand, each one of the two SOZ units of the Block DM-2 upper stage had a dry mass of ~ 106 kg and a total propellant mass of up to 114 kg, while the stage itself weighted 2.1 t. Although determined by the characteristics of the vehicle and its mission profile, the total mass of ullage rocket systems is usually of the order of hundreds of kilograms [201]. With a Falcon 9's launch cost to LEO of ~ 2700 \$/kg [202], an economic penalty per launch and stage of up to ~ 500.000 USD may be estimated. This value is doubled for GEO orbits, and multiplied by an even larger factor in a Mars mission.

Even though ullage engines are a robust and well-established solution to deal with the restart of rocket engines in microgravity conditions², lower mass penalties and/or enhanced reliability may be found in different technical alternatives. In Chapter 13, the passive Magnetic Positive Positioning approach introduced in Chapter 12 is expanded and particularized for this problem alone and in combination with an on-board Propellant Gasification System (PGS) [203]. The historical background of each system is presented together with a preliminary technical analysis.

1.4.4 Magnetically enhanced electrolysis

The last application of low-gravity magnetohydrodynamics covered in this dissertation deals with one key technology for space exploration: water electrolysis, which refers to the electrochemical decomposition of water into hydrogen and oxygen. The reaction was first performed by Troostwijk and Deiman in 1789 [204, 205] and was already considered for space applications in the early 1960s [206]. A wide range of environmental control and life support systems [207], space propulsion technologies [208–210], or energy conversion and storage mechanisms [211, 212] rely on this process. Furthermore, future interplanetary missions are likely to employ water as a commodity acquired and processed by In Situ Resource Utilization (ISRU) methodologies to produce propellants, thereby reducing vehicle launch mass [213, 214].

Water electrolysis technologies can be classified according to the nature of the electrolyte. Three chemistries are considered for space applications: alkaline/acidic, proton exchange membrane (PEM), and solid oxide ceramics. Of these, the low temperature alkaline/acidic and PEM electrolytes require phase separation at the electrode. The liquid alkaline technology employs two metallic electrodes separated by a

² With exceptions! See this report on the Centaur AC-3 launched on June 30, 1964: www.nasaspaceflight.com/2022/05/centaur-turns-60/. Consulted on 09/05/2022.

porous material and immersed in a conductive aqueous solution, usually prepared with KOH or $NaOH$. The cell separator allows the exchange of the OH^- groups and prevents the recombination of H_2 and O_2 into water. PEM cells, on the contrary, are fed with pure water and make use of a proton-conducting polymer electrolyte. PEM cells allow high current densities, prevent the recombination of oxygen and hydrogen (and so, are safer), and produce high-purity gases. However, they lack the long-term heritage of alkaline cells and are sensitive to water impurities [215].

The operation of alkaline and PEM cells in low-gravity is severely complicated by the absence of strong buoyancy forces, resulting in increased complexity, mass, and power consumption. Dedicated microgravity experiments have shown how the weak buoyancy force gives rise to a layer of gas bubbles over the electrodes, shielding the active surface and limiting mass transport [216–218]. This effect is shown in Fig. 1.10(a). Gas bubbles tend to be larger than in normal-gravity conditions due to the longer residence time and the absence of bubble departure. Besides, and unlike in normal-gravity, the bubble departure diameter increases with increasing current intensity [219]. A forced water flow can be employed to flush this structure, but this approach complicates the architecture of the system and has a limited efficiency [119]. Most types of electrolytic cells also require a liquid/gas phase separation stage. Among those reviewed in Sec 1.4.1,

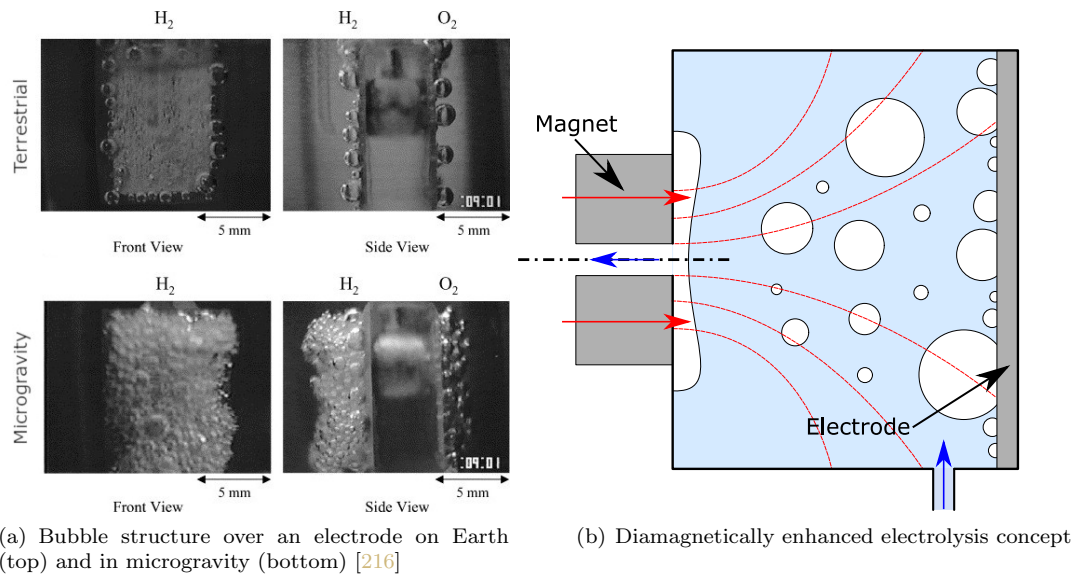


Figure 1.10: Water electrolysis in microgravity.

centrifuges [109, 110] and gas-liquid separation membranes [119, 120] are nowadays preferred. However, they present some important drawbacks: while centrifuges add to the mass and power budgets and induce g-jitter, membranes have limited lifetime and tend to clog in the presence of water impurities [208, 220].

Both alkaline and PEM technologies have flown to space and dealt with the phase separation problem in different ways. The Russian Elektron module, first operated at Mir and then at the ISS, makes use of a circulating alkaline electrolyte (25 %wt KOH) and a fluid circuit with gas/liquid static separators and heat exchangers [221]. The operation of the system has been compromised in the past by notorious malfunction events [222–224]. NASA’s Oxygen Generation System (OGS), installed at the ISS in July 2006, makes use of a cathode-fed PEM and a rotary phase separator and absorber modules to produce dry oxygen. Unlike anode-fed PEMs, cathode feeding avoids the humidification of O_2 due to proton-induced electro-osmosis [208]. Technical problems associated with the management of two-phase flows in the OGS in microgravity have also been reported [109, 225]. JAXA has recently developed a cathode-fed PEM cell for O_2 generation. The system relies on the removal of the electrode gas cover by means of forced convection. The separation of gas hydrogen and liquid water is performed by means of a membrane-type phase separator [119, 120, 226]. Subsequent versions of the cathode-fed cell rely on an internal water/gas separation function that makes water circulation and phase separator unnecessary, creating a simple, energy-efficient, and lightweight system. However, difficulties were found to reach a stable phase separation process [227–229]. As a way to remove the water purification and phase separation stages, substantial efforts have been devoted to the development of Static Water Feed (SWF) electrolytic cells, which avoid the phase separation stage by means of a second PEM. Technological demonstrators by *Life Systems* were tested on the STS-69 Endeavor (1995) and the STS-84 Atlantis (1997) for NASA [230–235], being followed by relatively modern systems [208, 236]. In spite of its inherent advantages, this approach requires larger cells to deliver a specific gas output due to the presence of a second membrane, that increases the water gradient, and the adoption of a cathode-fed configuration for the second membrane [208, 226].

This review unveils the numerous challenges associated with the low-gravity gas/liquid separation process in electrolytic cells and shows important limitations in current and foreseen technologies. As a complement or substitution of previous methods, the magnetic polarization forces discussed throughout this

dissertation may be employed not only to induce phase separation in an independent module, as done in Chapter 11, but also to promote the detachment of bubbles from the electrodes, as illustrated in Fig. 1.10(b). This would reduce the bubble departure diameter, induce convective bubbly flows, enlarge the effective electrode surface, and minimize mass transport limitations and associated cell efficiency losses. Some of these effects have already been observed in terrestrial boiling experiments with ferrofluids, where a significant influence of the magnetic field on the surface bubble coverage and heat transfer coefficient is reported [145, 146]. In other words, this approach would lead to simple and lightweight cells with no moving parts. The same benefits would be obtained for low-gravity boiling devices, with the boiling surfaces being equivalent to the electrodes. However, the use of magnetic buoyancy in low-gravity electrolysis and boiling remains essentially unexplored.

The applications of magnetic buoyancy in low-gravity electrolysis is introduced in Chapter 14, where both experimental and numerical studies are presented. In particular, the design of a long-term magnetically enhanced electrolysis experiment onboard Blue Origin’s New Shepard is discussed together with short-term acidic cell tests at ZARM’s drop tower.

1.5 Main contributions

The goals of this dissertation can be summarized as follows:

- (1) Provide modeling capabilities and assess the feasibility of secondary-electron-based touchless potential sensing methods:
 - (a) Study the flux of secondaries in complex active spacecraft charging scenarios (Chapter 3).
 - (b) Develop and validate onboard algorithms to model the dynamics of electron beams in GEO+ orbits (Chapter 4).
 - (c) Model and exploit the photoelectric effect in active sensing scenarios (Chapter 5).
- (2) Address low-gravity magnetohydrodynamics (LG-MHD) as a separate field with distinctive characteristics:

- (a) Develop the analytical (Chapters 6 to 8) and numerical (Chapter 10) fundamentals of the field.
 - (b) Validate fundamental results by means of microgravity experiments (Chapter 9).
- (3) Apply the LG-MHD theory to develop novel space technologies:
- (a) Demonstrate the use of magnetic polarization forces in phase separation (Chapter 11).
 - (b) Assess the feasibility of magnetic positive positioning systems (Chapters 12 & 13).
 - (c) Assess the feasibility of magnetically enhanced electrolysis technologies (Chapter 14).

Part I

Electron-based touchless potential sensing

Chapter 2

Preliminary considerations

The study of the electron-based touchless potential sensing technology introduced in Sec. 1.2 is based on a series of fundamental physical processes and experimental procedures. The former can be modeled by means of a simplified subset of Maxwell equations and a series of technical approximations to the surface processes of interest. The complexity of the problem motivates its study in experimental facilities like the ECLIPS vacuum chamber employed in this dissertation. This chapter provides a basic background on these aspects.

2.1 Electrostatic framework

2.1.1 Maxwell equations

In the problems under study in Part I, quasi-static magnetic fields are considered in the absence of electrically polarizable media. These conditions lead to the simplified Gauss and Faraday equations

$$\nabla \cdot \mathbf{E} = \frac{\rho_v}{\epsilon_0}, \quad (2.1a)$$

$$\nabla \times \mathbf{E} = 0, \quad (2.1b)$$

where \mathbf{E} is the electric field, ρ_v is the free charge density, and ϵ_0 is the permittivity of vacuum. As a consequence of Eq. 2.1b, the electric field derives from the electrostatic potential V through

$$\mathbf{E} = -\nabla V. \quad (2.2)$$

In addition, it is interesting to note that the integral form of Eq. 2.1b leads to \mathbf{E} being normal to the interface between a conductor (for which $\mathbf{E} = 0$) and free space [7].

The free charge density ρ_v is zero in a neutral plasma, but the presence of a charged spacecraft disrupts this equilibrium state and generates a charge distribution around the body. Still, for the low-density ($0.1\text{-}1$ particles per cm^{-3}) GEO environment, the effect of ρ_v is usually negligible at distances of tens of meters and $\rho_v \approx 0$ can be safely assumed (see Sec. 2.1.3). Under this condition, Eq. 2.1a reduces to Laplace's equation

$$\nabla^2 V = 0, \quad (2.3)$$

which features significant computational advantages when solved in combination with Dirichlet or Neumann boundary conditions for V .

2.1.2 Particle dynamics

The relativistic change in momentum of a charged particle is given by the balance

$$\frac{d(\gamma m \mathbf{v})}{dt} = \mathbf{F}, \quad (2.4)$$

with \mathbf{F} denoting the Lorentz force

$$\mathbf{F} = q(\mathbf{v} \times \mathbf{B} + \mathbf{E}) \quad (2.5)$$

and where \mathbf{v} , q , and m are the particle velocity, charge, and mass, respectively, $\gamma = (1 - \beta^2)^{-1/2}$ is the Lorentz factor, $\beta = v/c$, c is the speed of light, \mathbf{E} is the electric field, \mathbf{B} is the magnetic flux density, t is the time, and an inertial time derivative is considered. It should be noted that, in accordance with the special theory of relativity, the inertia of a particle with respect to a reference frame depends on its speed with respect to such frame. Consequently, the term γm defines the apparent mass of the particle. The position \mathbf{x} in the inertial reference frame can be computed by integrating

$$\frac{d\mathbf{x}}{dt} = \mathbf{v}. \quad (2.6)$$

2.1.3 Space environment

In the presence of charged spacecraft, the surrounding plasma tends to relocate under the influence of the perturbed electrostatic field following a process known as Debye screening [237]. For a sphere with radius R_{SC} and low surface potential $V_{SC} (\ll k_B T_e / q_e)$, the electrostatic potential field is damped under

the Debye Hückel approximation [238]

$$V(r) = -\frac{V_{SC}R_{SC}}{r}e^{-\frac{r-R_{SC}}{\lambda_D}}, \quad (2.7)$$

where

$$\lambda_D = \sqrt{\frac{\epsilon_0 k_B T_e}{n_e q_e^2}} \quad (2.8)$$

is a characteristic distance known as Debye length, r is the radial coordinate, k_B is Boltzmann's constant, T_e is the electron temperature, n_e is the electron density, and q_e is the elementary charge. The radial electric field is computed with Eq. 2.2 from Eq. 2.7, becoming

$$E(r) = \frac{V_{SC}R_{SC}}{r^2}e^{-\frac{r-R_{SC}}{\lambda_D}} \left(1 + \frac{r}{\lambda_D}\right). \quad (2.9)$$

The nominal value of λ_D in GEO is ~ 200 m [238], implying that the damping factors in Eqs. 2.7 and 2.9 have a second order effect on the electron detection process for distances of the order of tens of meters. In other words, the unperturbed electrostatic potential obtained by solving Eq. 2.3 offers a good approximation of the actual electrostatic environment while minimizing computational costs.

Even though overall space charge effects can be neglected in a first-order approximation, localized charge accumulation may also influence the sensing process. For instance, a number of works have reported the existence of electrostatic barriers that prevent the detection of low-energy particles and the release of photoelectrons from a spacecraft surfaces [239–242]. These barriers appear when “*the photoelectron density at the surface of the spacecraft greatly exceeds the ambient plasma density, the spacecraft is significantly larger than the local Debye length of the photoelectrons, and the thermal electron energy is much larger than the characteristic energy of the escaping photoelectrons*” [241]. The effect is important near the Sun but becomes far less concerning for distances beyond 0.3 AU [241, 242]. In the problem addressed by this work, the target spacecraft can charge negatively up to several kV under the influence of a well-localized electron beam. The beam landing spot generates low-energy secondary electrons that can produce their own electrostatic barrier [243]. Using a spot radius of 10 cm, unit yield, and average secondary energy of 2 eV, the number densities of secondaries near the surface range between 200 and $2 \cdot 10^5 \text{ cm}^{-3}$, resulting in secondary Debye lengths between 70 and 2 cm. These rough computations indicate that well-focused high-current beams may lead

to localized electrostatic barriers. Poisson solvers and particle-in-cell simulations are needed to explore this issue in further detail. From a practical perspective, a mild electrostatic barrier may reduce the number of secondaries escaping the surface, but should not significantly influence their trajectory. The models employed in Part I should then offer a good approximation to the problem in most cases of technical interest.

Regarding electron-plasma interactions, it should be noted that the GEO plasma is low density ($0.1\text{-}1\text{ cm}^{-3}$) and high-energy (up to many keV), excluding quiet days without significant solar activity where higher densities ($\sim 100\text{ cm}^{-3}$) and lower energies (few tens of eV) are observed [55]. As a consequence, the mean free path is of the order of 100 AU, and the GEO environment can be considered collisionless. The same occurs in high-vacuum (10^{-7} Torr), where the mean free path is about 1 km. On the other hand, the detectability of incoming flux of secondaries is not compromised by the environment because it is several orders of magnitude larger than the background plasma both in active and passive potential sensing scenarios [7].

Changes in temperature can also influence the work function of the surface material [244] and its secondary electron yield [245, 246]. Given that the operational temperature of space antennas and solar panels ranges between -100°C and 100°C [247], the thermal environment may significantly alter the secondary electron flux magnitude during the potential sensing process. However, this does not affect the spatial distribution of secondary electrons or the detectability of the target. The electron beam is, by itself, another heat source. In the laboratory setups presented in Chapter 3 and 4, a $\sim 0.01\text{ W}$ electron beam directed toward an aluminum target with an emissivity of ~ 0.1 and a surface area of $\sim 500\text{ cm}^2$ results in a temperature variation of less of 1 K under the black body assumption. Thus, the electron-beam-induced temperature increase can be neglected in this work and, most likely, in the vast majority of technical applications.

2.2 Surface processes

Several fundamental surface processes are at the core of the touchless potential sensing technologies introduced in Sec. 1.2. Those include secondary electron, photoelectric, and backscattered electron emissions. X-ray generation is thoroughly covered in Ref. 42 and is left out of this discussion, which focuses on the basic technical aspects of electron generation phenomena.

2.2.1 Secondary Electron Emission

When a sufficiently energetic primary electron impacts a surface, part of its energy is shared with neighboring particles, leading to the release of secondary electrons (also named *secondaries*) [55]. This process is dependent on the secondary electron yield, primary electron impact, angular distribution, and energy distribution through complex physical mechanisms that are subsequently approached with simplified, technical models.

2.2.1.1 Secondary electron yield

The probability of emission of secondaries per incoming primary electron is given by the secondary electron yield δ . This value depends on the incidence energy E of the impinging particle in a relation that can be approximated by the Sanders and Inouye yield model [248]

$$\delta(E, 0) = c \left[e^{-E/a} - e^{-E/b} \right], \quad (2.10)$$

where $a = 4.3E_{\max}$, $b = 0.367E_{\max}$, and $c = 1.37\delta_{\max}$. The parameters δ_{\max} and E_{\max} define the maximum yield point, characterize the surface, and depend strongly on the surface structure and conditions [249–251], which may be particularly unpredictable after a prolonged exposition to the GEO environment [252]. It should be noted that $\delta(E, 0)$ may be greater than 1 between the crossover points E_1 and E_2 , with $E_1 < E_{\max} < E_2$. Consequently, an incoming particle may generate more than one secondary electron [55]. Alternative models have been proposed and an excellent review of them can be found in Sec. 2.2 of Ref. 253.

2.2.1.2 Effect of incident primary electron angle

The emission of secondaries is also dependent on the incidence angle of the impinging electrons. Darlington and Cosslett propose the relation [254]

$$\delta(E, \phi) = \delta(E, 0)e^{\beta_s(E)(1-\cos \phi)}, \quad (2.11)$$

with ϕ being the primary incidence angle, $\delta(E, 0)$ the secondary electron yield obtained from Eq. 2.10, and

$$\beta_s(E) = e^\zeta, \quad (2.12a)$$

$$\zeta = 0.2755(\xi - 1.658) - \left\{ [0.2755(\xi - 1.658)]^2 + 0.0228 \right\}^{1/2}, \quad (2.12b)$$

$$\xi = \ln(E/E_{\max}), \quad (2.12c)$$

empirical factors proposed by Laframboise and Kamitsuma [55, 255].

2.2.1.3 Angular distribution

The angular release of secondary electrons follows approximately Lambert's cosine law and is nearly independent of the angle of incidence of the impinging particle [256]. At the particle level, the polar angle can be computed from a uniform 0-1 random variable x through [257]

$$\theta = \frac{1}{2} \arccos(1 - 2x), \quad (2.13)$$

while the azimuth angle follows a uniform distribution between 0° and 360° .

2.2.1.4 Energy distribution

The energy E_s of a secondary electron with respect to the vacuum level is of the order of a few eV and follows a characteristic distribution with a peak at one third of the work function φ of the material. The Chung-Everhart normalized probability density function (PDF)

$$f(E_s) = \frac{6\varphi^2 E_s}{(E_s + \varphi)^4} \quad (2.14)$$

is commonly employed to approximate this distribution [258].

2.2.2 Photoelectron emission

Photoelectrons can be regarded as a particular case of secondary electrons for which the impinging particle is a photon. The physics behind photoelectron emission are thus very similar, but some important differences must be accounted for.

2.2.2.1 Photoelectric yield

The probability of emission of a photoelectron per collision is determined by the photoelectric yield [55]

$$Y(\omega, \phi, R) = Y^*(\omega, \phi)(1 - R), \quad (2.15)$$

where $Y^*(\omega, \phi)$ is the yield per absorbed photon, ω is the photon energy, ϕ is in this case the photon incidence angle, and $R(\omega, \phi, \sigma)$ is the surface reflectance, which depends on the photon energy, incidence angle, and root mean square surface roughness σ . Opaque surfaces are implicitly assumed. The incidence angle effect on the yield is of the form [259]

$$Y^*(\omega, \phi) \approx \frac{Y^*(\omega, 0)}{\cos \phi}, \quad (2.16)$$

but since $1 - R(\omega, \phi, \sigma)$ also has the approximate dependence [260, 261]

$$1 - R(\omega, \phi, \sigma) \approx [1 - R(\omega, 0, \sigma)] \cos \phi, \quad (2.17)$$

both $\cos \phi$ terms cancel in Eq. 2.15. Therefore, $Y(\omega, R)$ is not, in first-order approximation, a function of the photon incidence angle [55].

2.2.2.2 Total reflectance

The total reflectance is distinctively associated with the simulation of photoelectron emission. It can be expressed as the sum of specular (R_s) and diffuse (R_d) reflectances

$$R(\omega, 0, \sigma) = R_s(\omega, 0, \sigma) + R_d(\omega, 0, \sigma), \quad (2.18)$$

which are defined as [262]

$$R_s(\omega, 0, \sigma) = R_0(\omega) \exp \left[\frac{-(4\pi\sigma)^2}{\lambda^2} \right], \quad (2.19a)$$

$$R_d(\omega, 0, \sigma) = R_0(\omega) \frac{(4\pi\sigma)^2}{\lambda^2}, \quad (2.19b)$$

with $R_0(\omega)$ being the normal reflectance of a perfectly smooth surface of the impacted material, $\lambda = hc/\omega$ the photon wavelength, h Planck's constant, and c the speed of light. The ratio of diffuse to specular reflectances is given by

$$\frac{R_d}{R_s} = \frac{(4\pi\sigma)^2}{\lambda^2} \exp \left[\frac{(4\pi\sigma)^2}{\lambda^2} \right], \quad (2.20)$$

implying that for small wavelength and large surface roughness the diffuse term is the major contributor to the total reflectance. Reflected photons experience negligible energy variations [261] and can generate photoelectrons at different surfaces.

2.2.2.3 Angular distribution

Since photoelectrons are a particular case of secondary electrons, their angular emission distribution follows approximately Lambert's cosine law, which can be implemented following Eq. 2.13.

2.2.2.4 Energy distribution

Photoelectrons are usually considered very low-energy particles in spacecraft charging studies. Their maximum emission energy is given by

$$E_p = \omega - \varphi. \quad (2.21)$$

It is important to note that the Ly- α line (121.6 nm, 10.2 eV) is dominant in the solar spectrum, and hence photoelectrons will be generated with a maximum energy of about 5 to 6 eV after subtracting the work function of the material. Therefore, a small positive spacecraft potential will act as a potential dwell and prevent their release [263].

2.2.3 Backscattered electron emission

Backscattered electrons are primary electrons reflected off the target surface [55]. They have approximately the same energy as the impinging particle and are hence easy to distinguish from secondary electrons in the overall energy spectrum. Although they do not play a central role in the touchless measurement of target spacecraft potentials, they can influence the magnitude and source regions of secondary electron fluxes.

2.2.3.1 Backscattered electron yield

Following the same approach as with secondary electrons, it is possible to define the backscattered electron yield η as the probability of reflection of an incoming electron. For sufficiently high impact energies,

η depends on the atomic number Z and the impact angle ϕ , and is virtually independent of the primary electron energy E . In this regime, Everhart proposes the model [264]

$$\eta(Z, 0) = \frac{a - 1 + 0.5^a}{a + 1}, \quad (2.22)$$

with $a(Z) = 0.045Z$ being an experimentally fitted parameter. The minimum electron energy (in eV) that makes this approach valid is shown to be

$$E_{\min} \geq 13.7Z^{4/3} \tan(\theta/2), \quad (2.23)$$

with $180^\circ - \theta$ being the deflection angle of the electron in the material. To establish this value, Everhart suggests using $\theta = 45^\circ$.

2.2.3.2 Angular distribution

Darlington and Cosslett's model can also be employed to compute the influence of the incidence angle of the primary electrons on the generation of backscattered electrons, resulting in [254]

$$\eta(Z, \phi) = \eta(Z, 0)e^{\beta_b(1 - \cos \phi)}, \quad (2.24)$$

with $\eta(Z, 0)$ being the backscattered electron yield obtained from Eq. 2.22, and where

$$\beta_b = 7.37Z^{-0.56875}, \quad (2.25)$$

is an empirical factor proposed by Laframboise and Kamitsuma [55].

2.3 The ECLIPS space environments simulation facility

The Electrostatic Charging Laboratory for Interactions between Plasma and Spacecraft (ECLIPS) research vacuum chamber allows conducting experiments relevant to charged astrodynamics in a space-like environment. The facility includes a range of sources to provide electron, ion, and photon fluxes, probes to characterize electron fluxes, x-rays, and potentials, and a variety of ancillary components to ensure the safe operation of the system, such as 3-axis motion stages, a magnetic environment control system, or a residual gas analyzer, among others. ECLIPS can be considered part of the reduced group of facilities intended to

study spacecraft charging, which include the JUMBO chamber at the Air Force Research Laboratory [265], the Sirene facility [266], or the test chambers at Utah State University [267] or Pennsylvania State University [268], among others.

The ECLIPS facility is extensively used in subsequent chapters and briefly described in this section, which is limited to the components of relevance for Part I for simplicity. Further details can be found in Ref. 56.

2.3.1 Overview

The bell-jar style vacuum chamber pictured in Fig. 2.1(a), with 75 cm in diameter and 1 meter in height, was donated to the AVS Laboratory by the Air Force Research Laboratory (AFRL) in 2016. It is



Figure 2.1: The ECLIPS Space Environments Simulation Facility.

made of stainless steel and has an o-ring interface between the bell and the base, which includes a grid of $1/4$ –20 holes to fix internal components. The chamber operates in the 10^{-7} – 10^{-6} Torr range, and is connected to a two-stage pumping system composed of an Agilent IDP-15 scroll pump and an Agilent Turbo-V 1001 Navigator turbomolecular pump. Important improvements have been made since its donation, including the addition of a range of KF and CF flanges of varying diameters, which are used to accommodate the required viewports, sources, probes, and feedthroughs. The viewports facilitate visual observation of electrostatic actuation, motion control, and related processes. A current view of the ECLIPS chamber is shown in Fig. 2.1(b).

Sudden power failures could prove catastrophic for the turbomolecular pump, as well as electron and ion guns. To protect the equipment against this eventuality, the facility is connected to two CyberPower 1500PFCLCD uninterruptible power supplies, which provide up to 20 minutes of battery-based runtime in the event of a power failure. This period is more than adequate to allow the building’s backup power generators to come online and continue to provide support power to critical systems. All mechanical parts and electronic components are connected to a common ground and checked before the execution of a chamber experiment. The common ground is established by a copper grounding bar connected to the building ground.

The top of the bell jar is raised and lowered by two column lift mechanisms that provide access to the chamber. These FLT-12 units from Progressive Automations can provide up to 30 cm of vertical actuation with 11500 N of lifting capacity, and are driven by a remote controller that can be programmed to specific heights. Slotted flanges welded to the exterior of the chamber enable interaction with the column lift, and also ensure that the full weight of the chamber lid rests on the o-ring interface with the base for optimal sealing. Furthermore, the two lifts are electronically controlled to ensure that the chamber lid is always lifted level, and the fully-constrained nature of the system ensures that the chamber lid is repeatably positioned between runs. For safety reasons, the system is automatically disabled while the pumps are operated.

Additional sources, probes, and ancillary components of relevance to this dissertation are subsequently addressed.

2.3.2 Sources

A series of sources for electrons, ions, photons, and magnetic fields have been integrated into the chamber, enabling an accurate reproduction of the space environment. In most experiments, the electron beam is used to generate secondary electrons, study charged beam dynamics and generate x-rays for material characterization and potential sensing, while the vacuum ultra-violet (VUV) lamp is used to stimulate photoelectric emission for charging and potential sensing applications.

2.3.2.1 Electron Gun

The primary electron gun of the facility is a Kimball Physics EMG-4212D, which is capable of accelerating electrons up to 30 keV with currents from 10 nA up to 100 μ A. The beam location and focus can be adjusted through integrated optics, leading to spot sizes from 500 μ m up to 25 mm at a typical working distance of 150 mm. It implements pulsing capabilities of up to 5 kHz, which finds application in some active spacecraft charging scenarios. In addition, the current level can be kept stable in time using a dedicated operation mode. The quasi-collimated beam is characterized by a Gaussian distribution, and is mounted onto the side of the ECLIPS chamber as shown in Fig. 2.2.

A 38 mm diameter Kimball Physics Rugged Phosphor Screen (later shown in Fig. 2.5) is used to

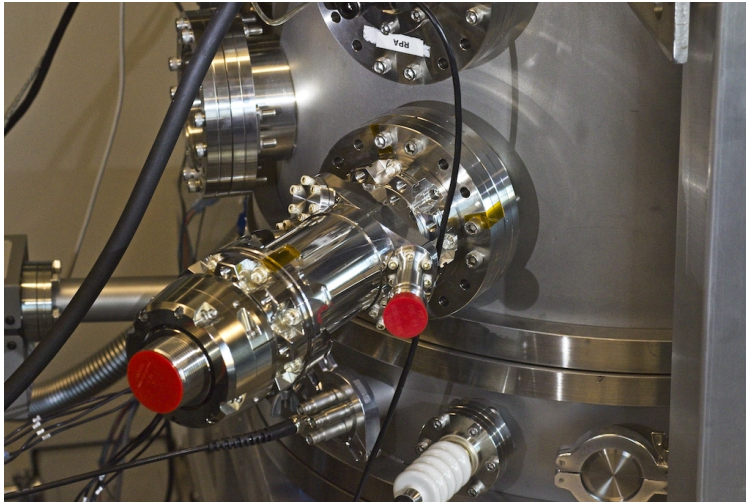


Figure 2.2: Electron gun mounted onto the side of the ECLIPS chamber.

center the electron beam and set its configuration. Once the desired set of parameters is fixed, the result is stored in the internal memory of the electron gun, allowing for repeatable experiments.

2.3.2.2 Vacuum Ultraviolet Lamp

A Hamamatsu L10706-S2D2 VUV light source, composed of a deuterium bulb with a MgF_2 window, is used to excite photoelectron emission from targets of interest. This source is flange mounted, and relies on an external air supply to provide cooling. The deuterium bulb and MgF_2 window result in a peak emission wavelength of 160 nm, with a total emission range of 115 to 400 nm. The lamp requires a constant supply of cooling air, provided by a building-wide compressed air supply. The air flow is also activated during bakeout.

2.3.2.3 Magnetic environment control system

The ECLIPS chamber has a dedicated set of coils designed to generate a specific magnetic environment. Even though they were not used in this dissertation, the design was led by the author and is subsequently described. Several experiments may benefit from magnetic control, like those requiring the cancellation of Earth's magnetic field, the imposition of LEO/GEO-like environments, or the study of specific plasma regimes, particularly when low-energy secondary electrons are considered. Similar setups can be found at larger scales worldwide, such as IABG's Magnetic Field Simulation Facility in Germany [269] or NASA's Spacecraft Magnetic Test Facility in Maryland [270].

The system is designed to generate a uniform, 3-axis controllable magnetic field in a 5 cm radius cylindrical region inside the vacuum chamber. Three pairs of coils arranged in a quasi-Helmholtz configuration are considered, with the vertical ones being located inside the chamber and the horizontal ones in the outside. The specifications of the final design are given in Table 2.1, with R being the coil radius, L the distance between coils, I_{\max} the maximum current intensity, B_{\max} the maximum magnetic flux density, N

Table 2.1: Magnetic control system configuration.

Coils	R [mm]	L [mm]	I_{\max} [A]	B_{\max} [μT]	N [#]	B_{step} [nT]	R_e- [cm]	T_{eq} [
Int.	298	298	5	600	40	121	56	59
Ext.	298	760	5	60	12	10	562	48

the number of wire turns, B_{step} the resolution achieved by the controller, R_{e-} the electron gyro-radius, and T_{eq} the equilibrium temperature with maximum current intensity, computed with a lumped heat transfer model. A 5 A constant current JUNTEK DPM-8605 power source is employed. The horizontal assemblies are designed to cancel Earth's magnetic field ($\sim 51.6 \mu\text{T}$ in 2022 in Boulder, Colorado, according to the WMM-2020 model), while the vertical coils produce a stronger magnetic environment. This choice is motivated by the highly demanding geometrical constraints of the chamber.

The internal coils, which follow the specifications in Table 2.1, are pictured in Fig. 2.3. Each coil is attached to an aluminum platform that imposes a circular profile and acts as a heat sink. The vertical distance between the coils is controlled by means of four 80/20 frames that serve as supports, and the assembly is connected to the power source by means of a dedicated feedthrough.

Besides the Earth's influence, the coils should also compensate the magnetic disturbances produced by the instruments and hardware of the facility. A simplified 3D Finite-Elements Model (FEM) testbed is available in Comsol Multiphysics to simulate the magnetic environment of specific experiments. The chamber is made of stainless steel, and is assumed to have a relative permeability of 1.002. A case of application of the magnetic testbed is shown in Fig. 2.4. The purpose of this specific simulation is to quantify the magnetic

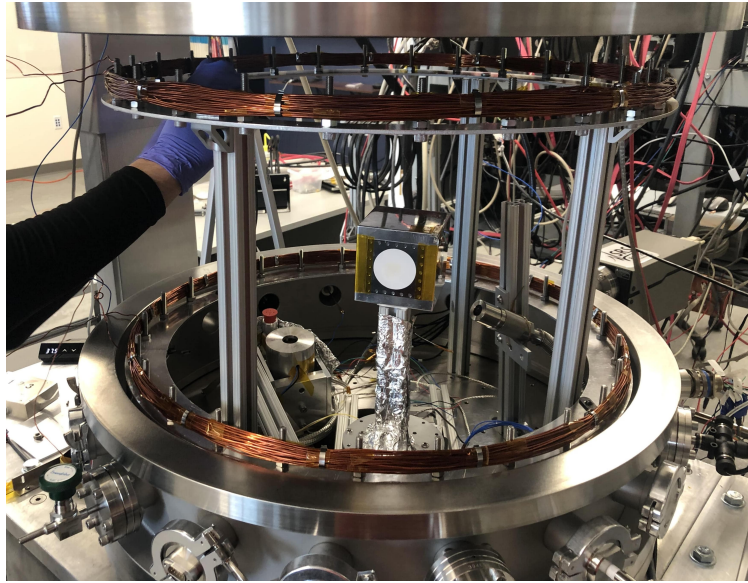


Figure 2.3: Installation of vertical coils inside the vacuum chamber.

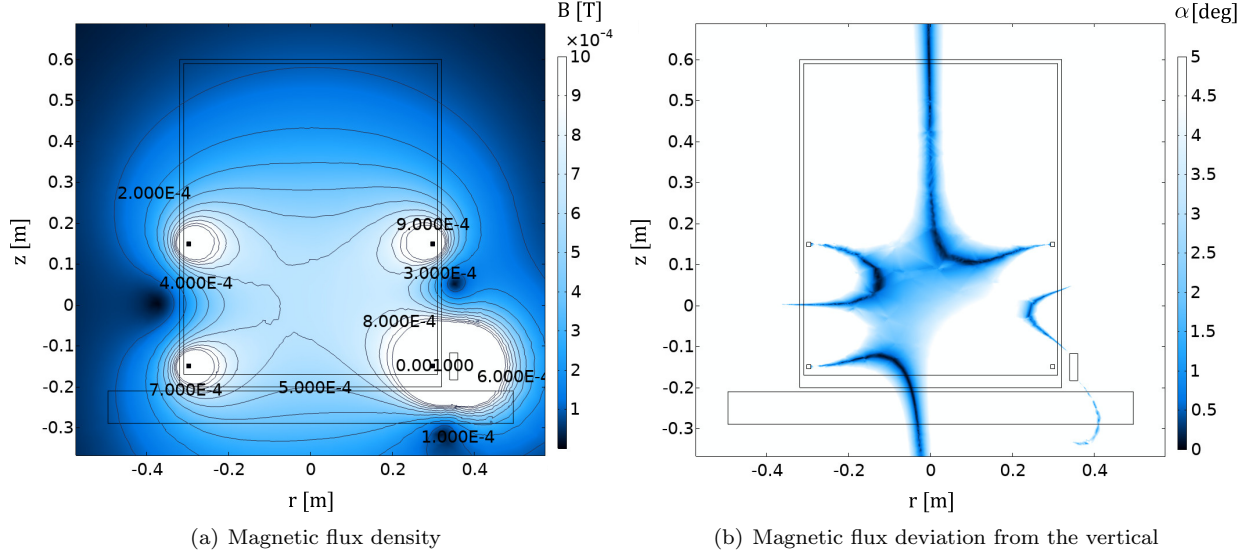


Figure 2.4: Analysis of the magnetic disturbances induced by an IMG-300 UHV IMG in the radial cross-section passing through the center of the IMG.

disturbance induced by the Agilent IMG-300 UHV Inverted Magnetron Gauge (IMG) while the internal coils operate at 5 A. The figure shows the magnetic flux density and the vertical deviation angle α of the magnetic field in a radial cross-section passing through the center of the IMG. The inhomogeneous field distribution reflects the strong influence of the IMG, that may disturb sensitive experiments in one side of the testing volume.

2.3.3 Probes

Most scientific and technical results are obtained with just three probes: an RPA, a set of multimeters, and an x-ray spectrometer. Only the first and second are used in this dissertation.

2.3.3.1 Retarding Potential Analyzer (RPA)

The custom-made RPA is essentially a gridded Faraday cup with a 1.2 cm diameter circular aperture. The device, depicted in Fig. 2.5 next to the small phosphor screen, consists of a front grounded grid and a second discriminating grid to which high-voltages can be applied. The discriminating grid creates an approximately equipotential plane and the front grid contains the electric fields within the instrument. When

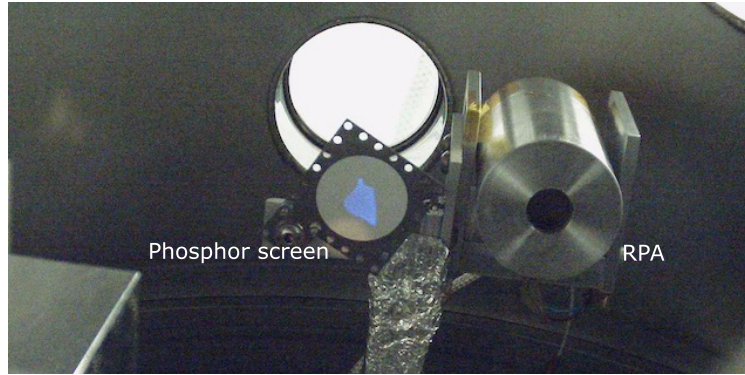


Figure 2.5: Phosphor screen and RPA. The size and shape of the electron beam are observed in blue for a particular gun configuration and electromagnetic environment.

no voltage is applied to the discriminating grid, an electron with any energy can pass through the instrument and into the detector. As a negative voltage is applied, electrons with lower energies cannot overcome the potential barrier and are hence repelled from the system. Thus, the electron energy distribution is obtained by sweeping through voltages applied to the grid. The collector itself is a hollow cylinder (closed at the back) which helps to prevent secondary or backscattered electrons generated on the collector from escaping back out the front of the instrument. The current is recorded using a Keithley 2401 SourceMeter picoammeter and one of the high-voltage power supplies is used to set the potential of the discriminating grid. Several noise floor measurements have been taken in which the electron energy analyzer is installed in the chamber, but none of the sources are turned on, so there is no source of electrons. The measured noise current of the electron energy analyzer and picoammeter system has a mean of 12.4 pA and a standard deviation of 33.9 pA.

2.3.3.2 Multimeters

The accurate monitoring of potentials is fundamental for the direct observation of the object under study or as a secondary measurement from a primary instrument (e.g. the RPA). The ECLIPS facility includes a Keithley DMM6500, that can measure potentials up to 1000 V, and a Keithley 2401 SourceMeter picoammeter. Both are computer controlled, enabling rapid measurements and development of automation routines that can feedback on detected currents or potentials.

The 1000 V range limitation of the Keithley DMM6500 is partially overcome by means of the internal voltmeters included with the power sources, which are in fact designed to operate at high voltages. In floating potential experiments, where an external element cannot be attached, the object of interest is grounded through a large 100 G Ω resistor which reduces the drain current to 0.3 μ A at 30 kV. This value is significantly smaller than the 10 μ A-level electron beam current employed in most experiments, and has a reduced impact in the operation of the system. The potential is then indirectly measured by means of the Keithley 2401 SourceMeter picoammeter, exhibiting errors of \sim 100 V for voltages below 20 kV.

2.3.4 Ancillary equipment

In addition to the pumps, batteries, and mechanisms described in Sec. 2.3.1, several other ancillary components ensure the nominal operation of the chamber and related instruments. However, they are not specific to any particular experimental configuration.

2.3.4.1 Pressure gauges

The pressure of the chamber is continuously monitored with an Agilent ConvecTorr gauge from atmosphere up to 10^{-4} Torr, and with an Agilent IMG-100 IMG below 10^{-3} Torr. Both gauges are connected to an Agilent XGS-600 gauge controller, and in tandem provide accurate measurements of chamber pressure for the full range of operation. These measurements are employed in the Chamber Control Interface (see Sec. 2.3.4.7) to monitor the state of the facility and ensure a safe operation.

2.3.4.2 Residual Gas Analyzer

An SRS RGA-200 Stanford Research Systems residual gas analyzer with a 200 amu range is used to monitor the molecular environment in the chamber. The device is represented in Fig. 2.6. It provides useful diagnostic information in cases of high outgassing, such as during extended stepper motor operation, or for evaluating the performance of the bakeout system.

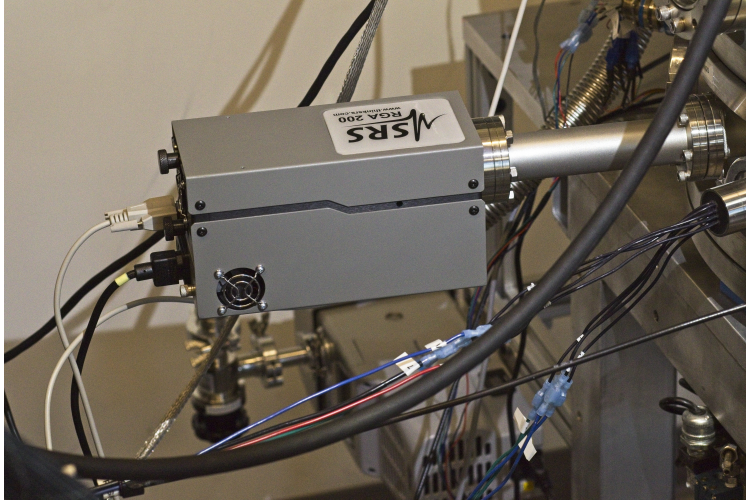


Figure 2.6: Residual Gas Analyzer mounted onto the side of the ECLIPS chamber.

2.3.4.3 Bakeout system

A VB-1 Vacuum Bakeout Package with one IRB-600 infrared emitter is employed to accelerate the pump down process and clean the internal surfaces of the chamber. A type J thermocouple located at ~ 15 cm from the source provides temperature feedback to the controller, which imposes a pre-defined temperature during bakeout. The heat emitter, shown in Fig. 2.7, is located in one of the CF flanges of the lateral wall, and irradiates the different components with a surface power density that decays with the square of the



Figure 2.7: Bakeout infrared emitter in operation during a touchless potential sensing experiment.

distance to the source.

The bakeout temperature determines the outgassing speed of different species following an exponential law. Higher temperatures are more effective in removing contaminants from the surface; however, the maximum value is limited by the survivability of the different instruments inside the chamber. Although most of them are not directly illuminated by the infrared emitter and only receive heat through the walls of the chamber, others (e.g. the x-ray sensor) are positioned close to the source. As a safety measure, a 70°C limit is imposed.

2.3.4.4 Magnetometer

Magnetic fields are measured in the range of $\pm 200 \mu\text{T}$ and DC to 1 kHz with a vacuum-rated Stefan-Mayer 3-axis FLC3-70 fluxgate magnetometer. The instrument is formatted as a compact cylinder 3 cm length and 1 cm diameter, so it can be operated within the chamber and located at any point of interest. In addition, a manual Latnex MF-30K AC/DC magnetometer is employed to characterize magnetic fields between 0 and 3 T.

2.3.4.5 Motion stages

Many experiments conducted in the ECLIPS facility have geometrical dependencies, whether a desire to sample electron populations at different points relative to a target or examine the structure of a spacecraft wake under different charging conditions. This led to the development of the 3-axis translation system shown in Fig. 2.8, with axes moving according to cylindrical coordinates. The assembly is composed of a Newmark Systems RM-3 rotational stage mounted on the base and two custom-built linear stages. The latter employ the same vacuum-safe stepper motors as the Newmark Systems RM-3 stage and are mounted on the rotational stage, allowing for any arbitrary movement to be conducted in the chamber. The cylindrical design was chosen to maximize the use of space within the chamber, allowing translations right up to the chamber walls in each direction. The position of each stage is measured by linear and rotary high-vacuum Renishaw Tonic encoders¹ with 5 μm resolution. The encoders are connected to the Chamber Control Interface (see

¹ <https://www.renishaw.com/en/tonic-encoder-series--37824>. Consulted on: 06/07/2022.

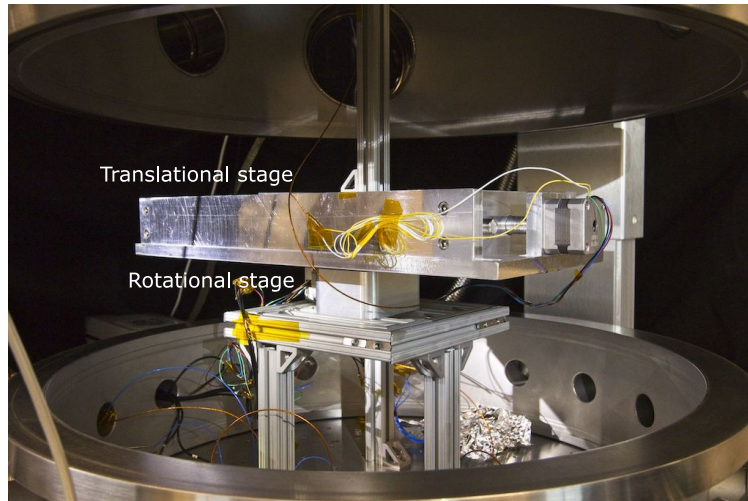


Figure 2.8: Rotational stage with first translational stage mounted atop it.

Sec. 2.3.4.7) and feed a closed-loop position controller. This assembly is dismounted when needed to test different configurations.

The steppers quickly warm up during operation in vacuum, outgassing primarily water with some contribution from carbon dioxide. For this reason, the vacuum gauge controller keeps track of the pressure and disconnects the steppers when a predetermined threshold is reached. This is important to ensure a safe operation of delicate components, such as electron or ion sources, rated for use only below 10^{-6} Torr.

2.3.4.6 Power systems

A major focus of chamber research is the touchless characterization of spacecraft charging. This requires the ability to simultaneously control the potential of a range of systems, from the RPA grids to a series of target objects. Therefore, several power supplies are integrated into the chamber facility, as seen in Fig. 2.9. Two Matsusada AU-30R1 High-Voltage Power Supplies (HVPS) provide high quality potentials up to 30 kV. These units are controlled via fiber optic connections to the primary computer, reducing the risk of electrical interference. In addition, several other HVPS are available for experiments, including two Spellman CZE2000 units with a maximum voltage and current of 30 kV and 0.3 mA, respectively, and two Spellman SL300 power supplies with a maximum voltage of 3 kV and a maximum current of 10 mA. Additionally, a Keysight E3631A low-voltage power supply is used to power the stepper motors at 12 V.

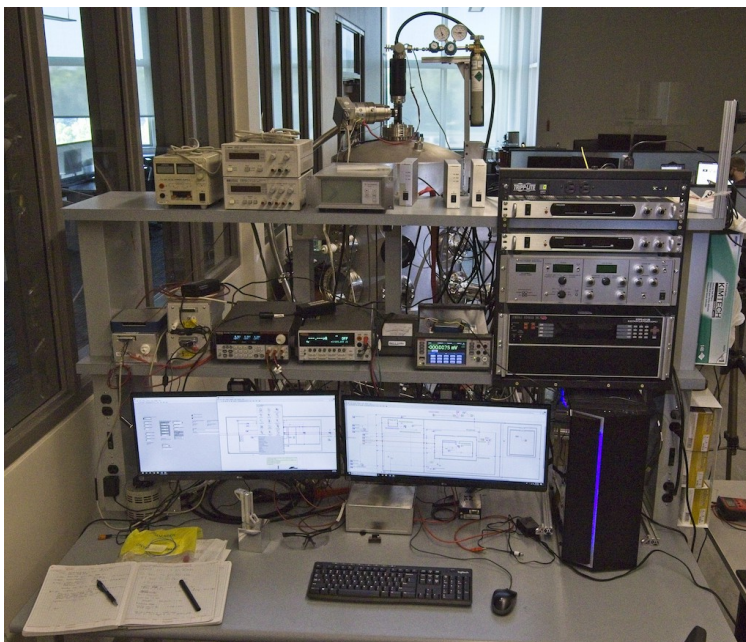


Figure 2.9: Power supplies and control infrastructure for the chamber. The server rack at top right contains the HVPS and controllers for the electron and ion guns.

2.3.4.7 Chamber Control Interface

All chamber systems are controlled from a workstation computer with a series of LabView Virtual Instruments (VIs). A Chamber Control Interface keeps track of the pressure and temperature levels and monitors the pump down and venting processes, implementing partially automated checklists that are followed by the operator. The interface can also issue email and phone alerts when dangerous events are detected (e.g. unexpected overpressure, excessive temperature during bakeout, or abnormal instrument performance). VNC and SCP servers are available to remotely access the workstation and fix critical issues. A series of cameras that monitor the interior of the chamber and its surroundings can also be accessed from the workstation. One of the goals of the system is to enable safe overnight experiments.

In addition to the Chamber Control Interface, several dedicated sub-VIs are available to perform specific tasks. Those include a motion stage controller employed to manually position the experiment and process encoder readings, an interface for the RGA, or a full control and metering suite for the electron gun, among others. Although the user develops specific VIs for specific experiments, an extensive library of sub-VIs is available to configure and operate all the instruments in the chamber

2.3.5 Other components

The ECLIPS chamber also incorporates a 1402 Ion Gun from Non Sequitur Technologies, a broad spectrum electron gun designed by Dr. Miles Bengtson and Dr. Kieran Wilson, and an Amptek X123 x-ray spectrometer that were not used in this dissertation or listed above. However, they are thoroughly described in Ref. 56.

2.4 Collaborators

The development of the ECLIPS facility is an ongoing multi-year process that counted with the participation of several individuals. Those include graduated Ph.D. students (Dr. Kieran Wilson, Dr. Miles Bengtson, Dr. Jordan Maxwell, Dr. Joe Hughes), current Ph.D. students (Julian Hammerl, Kaylee Champion, James Walker, Andrea López), CU Boulder technicians (Matt Rhode, Nathan Coyle), and undergraduate researchers (Dalton Turpen, Ryan Block, and Charlie Lipscomb).

Chapter 3

Complex shapes and differential charging

Previous works have validated the basic operation of the electron-based touchless potential sensing method employing flat plates in a vacuum chamber environment [26, 43, 44]. However, the technological maturation from such well-controlled laboratory experiments to the actual space implementation must be addressed with dedicated technical studies. Those must necessarily deal with complex spacecraft geometries and differential charging. The former determines the trajectories of secondary electrons generated at the surface, and therefore, the detectability of the system [8]. Differential charging produces the same effect, but it is much harder to characterize, model, and compensate for. This chapter explores the influence of both factors and introduces a particle tracing framework that implements the physical mechanisms described in Chapter. 2.

3.1 Particle Tracing Model

The study of the effect of complex shapes and differential charging on the touchless electrostatic potential sensing problem requires advanced numerical simulation models that must be able to implement the basic physical processes described in Sec. 2.2. In general, particle tracing simulators are particularly well suited for this task. Although many different approaches could be adopted for this task, the model here introduced is implemented in SIMION by means of user-defined functions programmed in Lua language. SIMION eases geometrical calculations and implements a well-established toolset that speeds up the development process.

3.1.1 Electrostatic framework

The trajectory of each charged particle is computed in SIMION from Newton's second law in Eq. 2.4. SIMION, however, assumes $\gamma = 1$ by default, applying relativistic corrections only when $\gamma > 10^{-10}$. The electric field is derived by solving Eqs. 2.3 and 2.2 in the simulation domain. A regular Cartesian mesh is employed with the boundary conditions being determined by the predefined potentials of each electrode (Dirichlet) or by the zero-derivative of V (Neumann). The potential of the electrodes, named *potential arrays* in SIMION, can be adjusted individually by taking advantage of the additive property of the Laplace equation. The overall potential is then computed as the superposition of each solution, enabling faster simulations.

The geomagnetic field in GEO orbit is ~ 100 nT, resulting in gyroradii of 100-3000 m for electron energies from 10 to 10^4 eV. Although weak, this effect can slightly deviate the secondary electrons and should be considered in GEO simulations. In the case of application described in Sec. 3.2, however, the geomagnetic field is almost perfectly aligned with the electron velocities (specifically, with the electron beam), the gyroradius is several times larger than the characteristic length of the experiment, and the electric force is one order of magnitude larger than the magnetic force. For these reasons, the magnetic contribution has been neglected.

It is important to note that SIMION, by default, does not solve Poisson's equation to account for the space-charge effects represented by ρ_v in Eq. 2.1a. This implies that the electrostatic environment is fully determined by the configuration of the potential arrays, that the electrostatic field is computed before each simulation, and that the magneto-electrostatic interaction between particles is not considered. Electron beams, however, can include approximate beam repulsion models. From a practical perspective, neglecting space charge effects results in significant computational advantages that may be critical for the development of future on-board algorithms. Further details on the implications of this assumption in spacecraft charging scenarios can be found in Sec. 2.1.3.

3.1.2 Implementation of secondary electron emission

The secondary emission effect described in Sec. 2.2.1 is not included by default in SIMION and should be properly implemented to enable the study of active spacecraft charging. Since SIMION is a particle tracing simulation framework, all surface processes are faced from the particle perspective rather than using integral formulations. User-defined Lua functions are written to complement the standard toolset.

The computation of the number of secondaries released per impinging electron represents the first process of interest. The secondary electron yield, calculated in this dissertation from the Sanders and Inouye yield model in Sec. 2.2.1.1, is a macroscopic quantity. At the particle level, however, it seems natural to treat this event as a Poisson point process, and thus a Poisson distribution with parameter $\lambda = \delta(E)$ is implemented using Knuth's algorithm [271]. Unlike the existing SIMION examples¹, where an impacting primary electron is either terminated or steered to match a yield below 1, the model here presented employs the new experimental SIMION 8.1/8.2 function `simion.experimental.add_particles()` to create an undefined number of particles from a collision event.

The energy of a secondary is computed in a dedicated Lua library by applying the inversion method to the cumulative distribution function (CDF) of the PDF defined by the Chung-Everhart model in Eq. 2.14, resulting in

$$g(E_s) = \frac{\varphi}{3(E_s + \varphi)^3} - \frac{1}{2(E_s + \varphi)^2} + \frac{1}{6\varphi^2}. \quad (3.1)$$

The desired E_s is obtained by entering the CDF with a value of g sampled from a uniform distribution. However, it is not possible to derive an analytical $E_s(g)$ from Eq. 3.1, and thus Newton's method is implemented to compute E_s for a given g . This process is implemented in Lua taking $\varphi/3$ as an initial estimate, reaching the desired energy value within a few iterations with a tolerance of ± 0.01 eV.

The effect of the incidence angle (Sec. 2.2.1.2) and the angular emission distribution (Sec. 2.2.1.3) can be directly implemented in SIMION, which facilitates a low-level control of each particle.

¹ The interested reader is referred to the `readme.html` file in the `examples/secondary` folder of SIMION 2020

3.1.3 A note on backscattered electrons

Backscattered electrons may also be produced due to the impact of a primary electron, as described in Sec. 2.2.3. However, the backscattered electron yield drops below 20% for the aluminum targets employed in this chapter (see Fig. 5.2 and Ref. 10), and has limited influence on the overall secondary electron flux and follow-up interactions. In addition, they are easy to remove from the overall energy spectrum due to their energetic nature. For the sake of simplicity, backscattered electrons are neglected in the analysis. Applications dealing with high atomic number materials, for which much larger yields may be present [264], should consider using the aforementioned SIMION function `simion.experimental.add_particles()` to model backscattered particles and follow-up interactions using normal incidence measurements at low impact energies [10] or the Everhart model at high impact energies [264] together with the Darlington and Cosslett angular distribution model and the empirical factors proposed by Laframboise and Kamitsuma [55, 254, 255].

3.2 Materials and methods

3.2.1 Experimental setup

The experimental vacuum chamber setup pictured in Fig. 3.1 is employed to study the observability of secondary electrons in complex differentially-charged targets using the ECLIPS vacuum chamber described in Sec. 2.3. It is composed of a $70 \times 70 \times 70$ mm³ spacecraft-like bus electrode and a 145×60 mm² panel electrode assembly that is actuated by a stepper engine. Both electrodes together resemble the geometry of a spacecraft and are charged independently up to -800 V by a Matsusada AU-30R1 and a Spellman SL300 high voltage power supply. The assembly is irradiated by a Kimball Physics EMG-4212D electron gun configured to produce an electron beam of 1307 eV and 10 μ A. This beam energy value is chosen to maximize the production of secondaries (see Sec. 3.2.2). The resulting flux of secondary electrons is measured by a Retarding Potential Analyzer (RPA) that forms an angle of $\sim 16^\circ$ with the electron beam and stays at least 95 mm away from the tip of the panel electrode. The angular position of the electrode assembly is monitored by means of an incremental rotary high-vacuum Renishaw Tonic encoder.

The experiment is designed to measure the energy spectrum of electrons arriving at the RPA for a given bus and panel electrode potentials and assembly rotation angle. A 3.8 cm diameter Kimball Physics Rugged Phosphor Screen is employed to set the unperturbed electron beam configuration and provide a reference point for the numerical simulation. The beam reaches both electrodes with a ~ 2.5 cm final beam diameter. Secondary electrons are thus generated over both surfaces, enabling the study of differential charging problems.

A key difference between the setup represented in Fig. 3.1 and an actual spacecraft charging scenario is the existence of a grounded vacuum chamber wall (essentially, a Faraday cage) around the experiment. Its presence disturbs the electrostatic potential around the electrodes, and must be taken into account in the definition of the numerical simulation framework. Furthermore, the small scale of the experiment makes results particularly sensitive to geometrical and beam pointing errors.

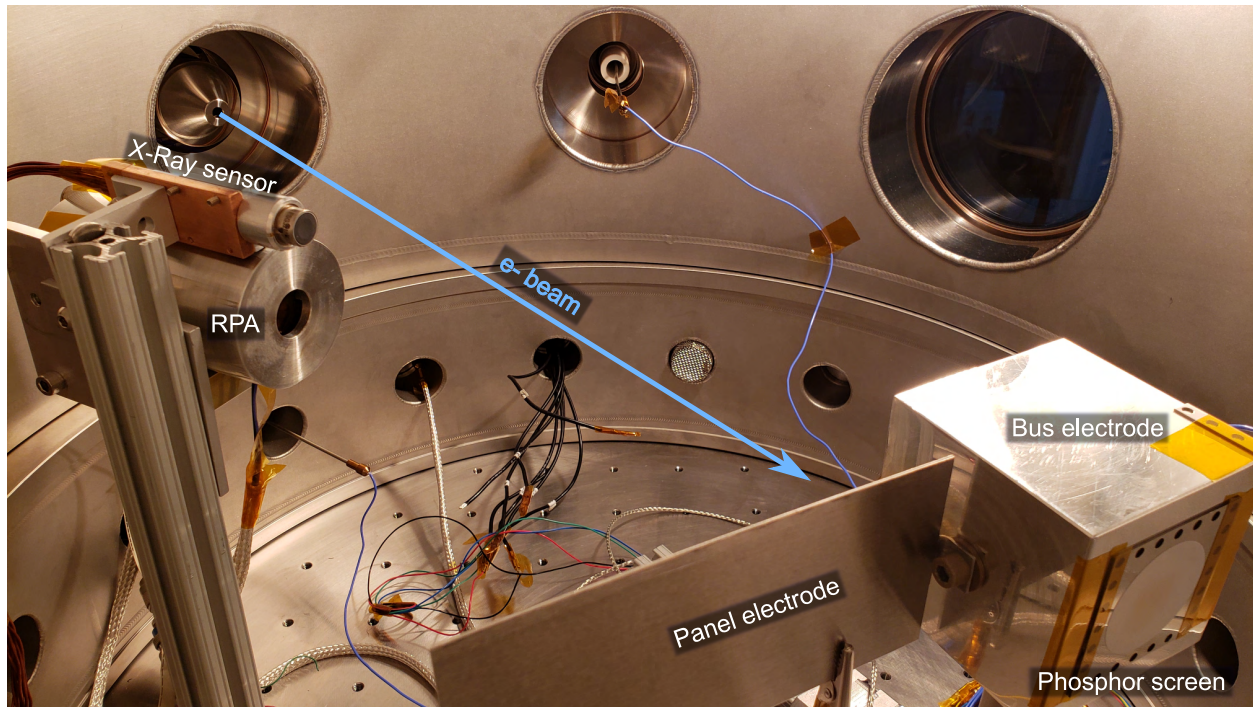


Figure 3.1: Experimental setup.

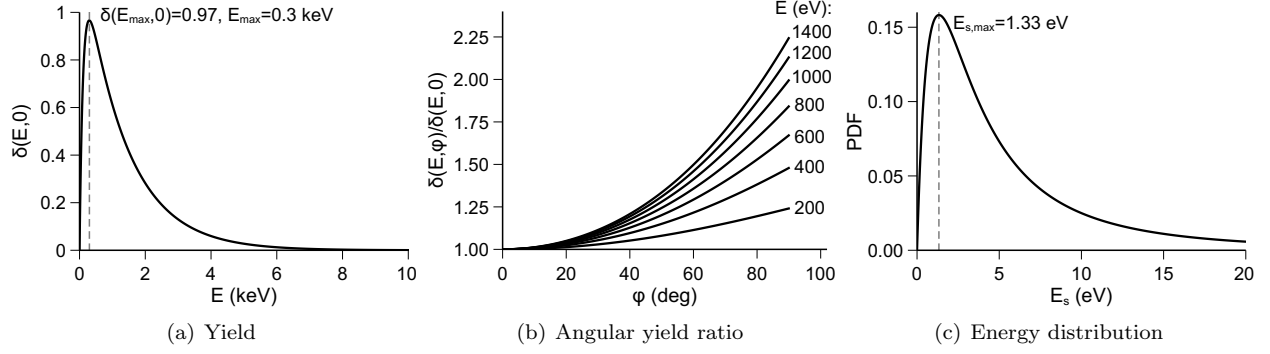


Figure 3.2: Estimated secondary emission properties of aluminum.

3.2.2 Material Properties

The electrodes are made of aluminum, which is characterized by the parameters $E_{\max} \approx 300$ eV, $\delta_{\max} \approx 0.97$ [55], and $\varphi \approx 4$ eV [258]. As noted in Sec. 2.2.1, these estimations depend strongly on surface conditions that are usually characterized in a laboratory environment [249–252] but are hard to estimate in space, and should thus be taken as a rough estimate. This difficulty does not prevent the numerical framework from being applied to active spacecraft charging scenarios, because it is in the angular dependence of the result and not in their absolute value where most of the technical interest lies.

Figure 3.2 represents the secondary electron yield as a function of the energy of a normal incident primary electron (Sec. 2.2.1.1), the angular yield ratio as a function of the angle and incidence of the primary electron (Sec. 2.2.1.2), and the PDF of secondary electron energies (Sec. 2.2.1.4). These relations are implemented in the Lua library of the SIMION model and motivate the selection of an electron beam of ~ 1300 eV to irradiate the target with landing energies close to the yield peak.

3.2.3 Measurement of secondary electron flux

The flux and spectrum of the secondaries generated over the electrodes is measured using the in-house RPA described in Sec. 2.3. The RPA features an entrance grid at ground potential, and a second discriminating grid controlled by a Matsusada AU-30R1 high-voltage power supply. A Keithley DMM6500 multimeter is connected to the grid to measure its voltage and correct the small bias induced by the source.

After the grids, a Faraday cup connected to a Keithley 2401 SourceMeter picoammeter is employed to measure the current flux at different energy levels. Electron currents of at least 10 pA with energies up to 1000 eV can be detected with this configuration. Based on previous measurements [49], the RPA efficiency is roughly estimated to be 20%, although this value should be expected to vary with the direction and intensity of the incoming flux of electrons. For simplicity, a 0.2 correction factor is considered in all simulations.

The RPA is operated in two different modes. In the first, the cumulative secondary electron energy spectrum is obtained by sweeping energy levels from -150 V below the minimum applied potential up to 150 V above the maximum with steps of 1 V and taking the average of 45 samples. The resulting curve is then differentiated to obtain the energy spectrum, as done in Sec. 3.3.3. In the second mode, the total current is measured at ± 50 eV of the expected energy peak. Both values are subtracted to determine the flux of electrons associated with that energy band. Although this approach provides less information on the population of electrons, it is much faster than the former and eases angular dependence studies like those presented in Sec. 3.3.4. Both methods are applied in an identical way in SIMION.

3.2.4 Configuration of SIMION model

The SIMION simulation framework introduced in Sec. 3.1 is tailored, without any loss of generality, for the assembly presented in Fig. 3.1. A single geometry file (`.gem`) is used to implement the setup described in Sec. 3.2.1, resulting in the $301 \times 301 \times 301$ mesh (2 mm/grid unit) depicted in Fig. 3.3. Each point of the domain requires about 10 bytes of RAM, and up to 20 billion points can be simulated. The floor, walls, main structural supports, and RPA casing are grounded, while the bus and panel electrodes are modeled as fast arrays with adjustable potentials. From a numerical perspective, the walls of the chamber impose a Dirichlet external boundary condition to the Laplace equation (see Sec. 3.1.1).

Because SIMION employs a Cartesian mesh, curved geometries introduce jags that may distort the local electric field and even prevent secondaries from escaping the surface. This problem is overcome by rotating the system while leaving the electrodes aligned with the axes of the model². Previous implementations by the main SIMION programmer, David Manura, integrate the trajectories of secondary electrons

² As the old saying says, “If the mountain will not come to Mohammed, Mohammed will go to the mountain” (Francis Bacon, Essays, 1625)

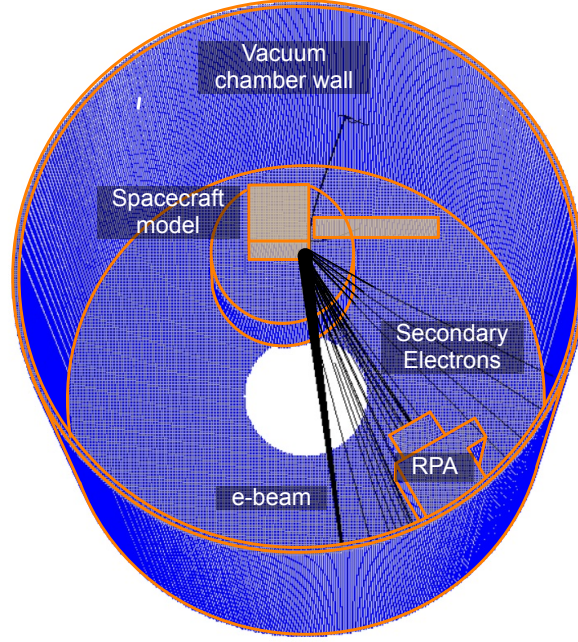


Figure 3.3: SIMION model geometry.

to displace the source region a few units away from the surface. That approach is particularly effective for generic geometries but is not employed in this chapter.

The determination of surface normal vectors is a critical step for several processes involved in the generation of secondaries, from the imposition of a Lambertian angular distribution to the proper quantification of the secondary electron yield. In this chapter, the different directions are determined analytically after identifying the impact location of the primary electron. However, it is also possible to estimate the surface normals by taking advantage of the fact that the electric field *should* be orthogonal to the surface. The reasons why this may not always be the case are the inherent numerical errors associated with the computation of ∇V , and the presence of jags in curved geometries. These issues may be partially corrected if the gradient is computed a few units away from the surface, but the accuracy of the results is strongly dependent on the geometry and electrostatic environment under study. Analytical solutions are consequently implemented in this work.

Matlab is employed to configure and launch the SIMION simulation and also to analyze its outcomes. The SIMION model exports a text file with the kinetic energy of the electrons that reach the interior of

the RPA. The collision is detected using SIMION's `segment.terminate()` function, from where the final position of the electron is extracted. If the position is within the RPA detector volume, the energy of the incoming electron is recorded for future analysis.

The new physical processes implemented in the model have been verified by comparing the numerical outcomes with the analytical formulations in Sec. 2.2.1. In order to guarantee the stability of the solution, the electrostatic field is set to converge with a relative error of 10^{-4} , while the electron trajectories are integrated using a fourth-order Runge-Kutta method with a maximum step size of one grid unit and a trajectory quality factor of 3 (see Ref. 9 for further details on this parameter). The secondary electron current flux resulting from this configuration varies less than 5% with respect to equivalent high-fidelity simulations showing virtually no changes in the predicted energy spectrum.

3.3 Results and discussion

The experiment pictured in Fig. 3.1 is tested at the ECLIPS Space Environments Simulation Facility [56] to validate the numerical simulation framework introduced in Sec. 2.2.1. Numerical and experimental results are presented in this section to understand the detection process and assess the validity of the SIMION model, extracting relevant conclusions for future applications.

3.3.1 Overview of electron trajectories

Although charged particles and optical systems are usually considered analogous, the former, unlike the latter, cannot be directly observed. Tracing particle simulation frameworks help overcome this issue with trajectory visualization tools, offering key insights into the behavior of the system.

The trajectories of 100 randomly sampled electron beam particles are represented in Fig. 3.4 for electrode rotation angles between -40° and 80° with respect to the beam axis and a common electrode potential of -800 V. As explained in Sec. 3.2.4, the rotation of the electrode assembly is applied to the rest of the model, keeping the electrodes aligned with the geometrical axes to avoid jags in the surfaces where secondaries are generated. Three clear regimes of operation can be observed: (i) the beam is deflected before reaching the target ($\alpha = -40^\circ, 0^\circ$), (ii) the beam reaches the target, but the resulting secondaries

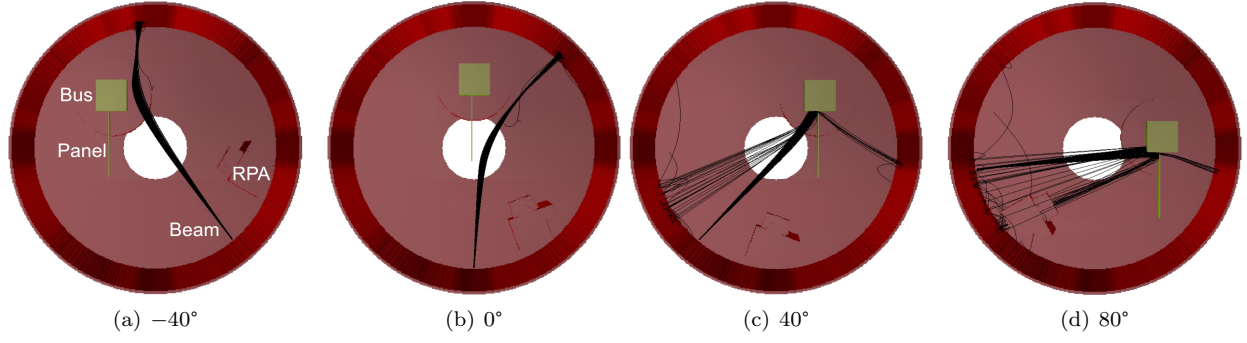


Figure 3.4: Electron beam trajectory for different electrode heading angles α .

do not reach the detector ($\alpha = 40^\circ$), and (iii) the beam reaches the target and the resulting electrons do reach the detector ($\alpha = 80^\circ$). The same focusing effect that has been characterized in previous works [8] is present in the corner between the panel and the bus, concentrating the trajectories of the secondaries and restricting their detectability to narrow regions. It is interesting to note that some trajectories result in more than one secondary electron, and some of them are also sources of second-generation particles. If generated at grounded surfaces, those particles do not have a particular interest in the detection of the electrode potentials because they arrive at the RPA with very small energies. However, in the differential charging scenario, some of those second-generation particles may be created over the surface of the electrode with the highest potential, therefore affecting the detection process. The generation of secondaries over grounded surfaces is thus forbidden in the model in order to improve its computational efficiency.

3.3.2 Calibration

A small divergence in the geometrical or electrostatic parameters of the model with respect to the experiment can result in qualitatively different results. This is due, among other factors, to the small scale of the system under study. Even though the SIMION geometry carefully resembles the experimental setup, the vacuum chamber environment does not facilitate taking measurements and some errors are almost unavoidable. In particular, the steering and expansion of the electron beam determine the *effective emission area* of secondary electrons. The beam configuration is thus centered by observing its footprint over the phosphor screen with an electrode heading of -40° . The SIMION beam particles configuration file (.fly2)

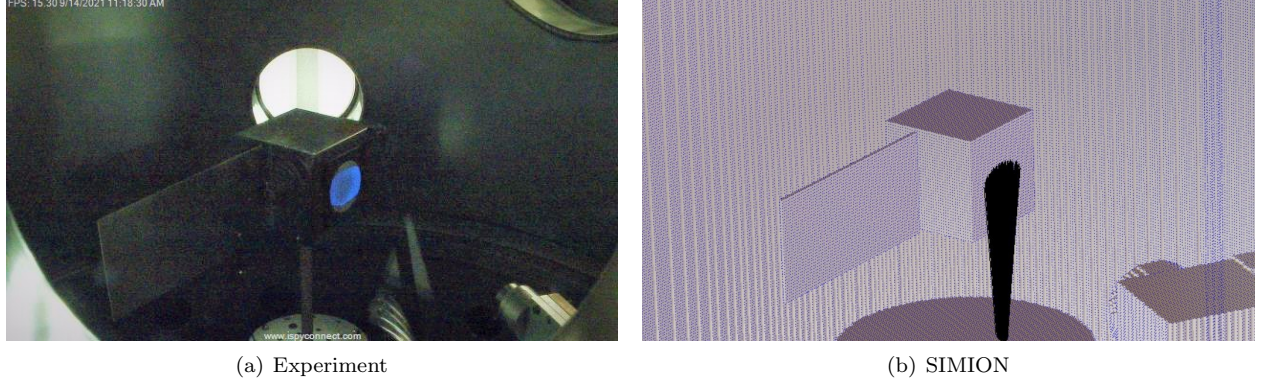


Figure 3.5: Centering and calibration of the electron beam.

is then tuned manually to achieve the matching exemplified in Fig. 3.5.

3.3.3 Complex shapes

The first set of experiments focuses on the detectability of the spacecraft-like assembly when both electrodes are charged to the same potential. This should be the standard case for modern spacecraft, whose external surfaces are generally designed to remain grounded [48, 50], even though this is hard to achieve in practice. In order to reduce the uncertainty of the measurements, both electrodes are connected to the Spellman SL300 high voltage power source, whose potential is set and verified manually before each run. The electron gun is operated at 1307 eV, 10 μA , and centered as shown in Fig. 3.5.

Figure 3.6 shows the electron distribution measured by the RPA and predicted by the model for rotation angles from -30° to 80° and electrode potentials from -600 V to -800 V. The secondary electron signal is detected only at 70° and 80° for both the model and the experiments, and hence the -30° to 50° data is removed from the plots, leaving the 60° case as a reference. In spite of the presence of numerous sources of uncertainty, the model is able to predict the location and intensity of the peaks with remarkable accuracy. The relative magnitude of the 70° measurements with respect to their 80° counterparts is captured as well.

A constant bias of ~ 20 V is observed in the experiments with respect to the electrode potential. Furthermore, the experimental peaks are almost symmetric, a feature that is not reproduced by SIMION

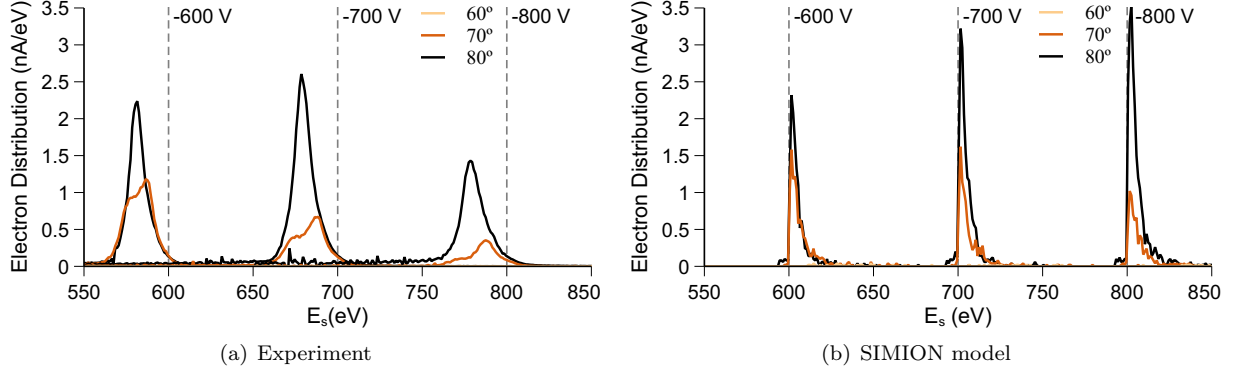


Figure 3.6: Secondary electrons spectrum for a range of electrode potentials and rotation angles.

and that is not considered in the physical model described in Sec. 3.1. Since the same multimeter is used to set the electrode potential and measure the RPA grid voltage, an equipment-induced bias should be discarded in the detection process. There are, however, two additional sources of error that may explain the peak shift and its unexpected symmetry. The first is the presence of oxide or contamination over the electrodes. Previous research has shown that this thin layer can induce spatially inhomogeneous surface potential losses of the order of a few volts [250]. The second refers to the performance of the RPA itself, whose internal configuration may result in an apparent plasma heating and wider energy distributions. Although interesting from a purely scientific viewpoint, these errors do not represent a concern for the applications here considered. In particular, a robust RPA calibration process will likely solve most of these problems, limiting the detection error to tens of volts.

It should finally be noted that the experiments reflect a higher total electron current, computed as the area under the distribution curve, than SIMION. Disagreements in the electron flux magnitude can be attributed to a myriad of factors that have not been thoroughly characterized in this work, from the secondary electron yield to the detector efficiency. The observed disagreement is a direct consequence of such sources of uncertainty, but still, the model is able to provide the correct order of magnitude estimate. From a technical perspective, the ability of the model to predict the electron flux magnitude is not as relevant as its capacity to determine the orientations for which secondary electrons can be detected. It is clear from Fig. 3.6 that this primary objective is achieved and that, if an educated estimate of the target surface and

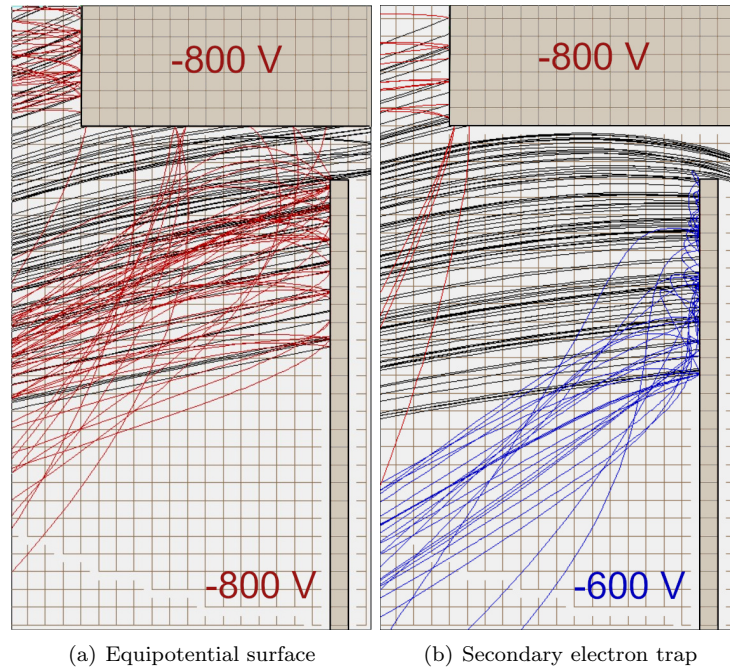


Figure 3.7: Secondary electron trajectories between the electrodes.

detector properties is available, the incoming flux can be reasonably approximated.

3.3.4 Differential charging

The differential charging scenario is characterized by a complex potential field in the surroundings of the charged object. Unlike the homogeneous case discussed in the previous section, a potential hill appears between the electrodes (see Chapter 6 in Ref. 55), which due to Eq. 2.4 and noting the negative charge of the electrons may result in an overall attractive force and a well-localized electron trap [8]. The effect is shown in Fig. 3.7(b), where most of the secondaries are not able to get out of the panel surface in the presence of a 200 V potential difference. As a consequence, the steering and expansion of the electron beam determine the effective emission area, which can vary significantly with small pointing errors. In order to mitigate this effect and reduce the uncertainty of the experimental setup, a wide 3° half-angle electron beam at 1307 eV and $10 \mu\text{A}$ is subsequently employed with the same pointing configuration as before. Future spacecraft systems may adopt the same approach when differential charging is suspected.

Figure 3.8 shows the experimental and numerical electron current fluxes from a range of secondary

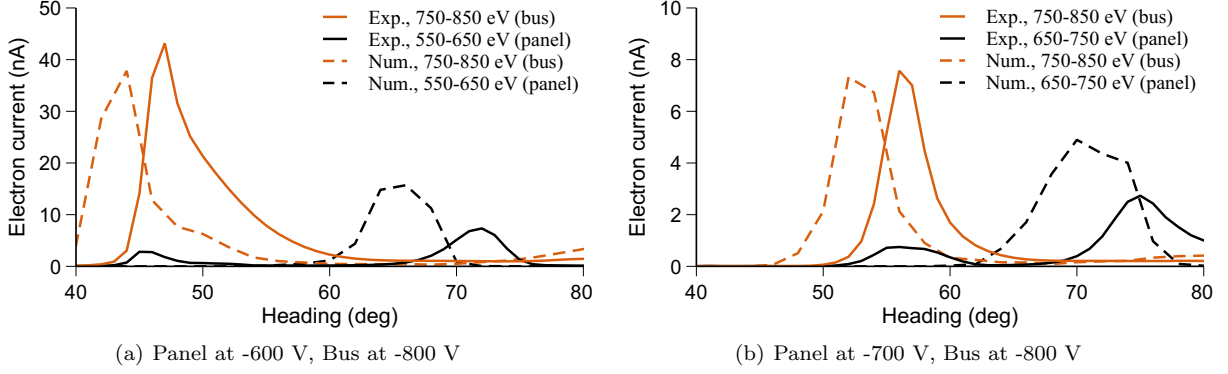


Figure 3.8: Electron current fluxes at selected energy levels.

electron energies as a function of the electrode assembly heading and charging state. The bus is set to -800 V, while the -600 V and -700 V panel potentials are explored. The secondary electron energy range is chosen to match the potentials of the electrodes within a band of ± 50 eV (see Sec. 3.2.3). Experimental results are in good agreement with the simulation but shifted by a constant $\sim 3^\circ$ in each case. The independence of this value with the applied electrode potential points to the accumulation of errors in the transcription of the experimental geometry to the SIMION model. Such errors are always hard to avoid in a vacuum chamber experiment, where access is complicated, but do not represent a major technical concern. It is also important to note how, for the first peak, both potentials can be easily determined. This contrasts with the difficulties experienced by the x-ray method in the determination of multiple potentials [272].

More interesting is, however, the absence of a signal from the panel between 40° and 60° in the simulations and the relatively large peak magnitude errors in the 70° - 80° range. To shed light on this issue, Fig. 3.9 depicts the secondary electron trajectories for several heading angles and both potential combinations. Electrons reaching the RPA come from the south face of the bus in the 45° and 55° cases, while secondaries generated at the root of the panel are easily deflected. Since both electrodes generate particles with very similar energy distributions, it can be readily concluded that the experimental signal from the panel should come from a region close to the bus. A careful examination of the setup depicted in Fig. 3.1 shows that there is an unmodeled geometry that satisfies this characteristic: the small support of the panel. The higher current flux in the 65° to 75° experimental peaks is harder to explain but may be

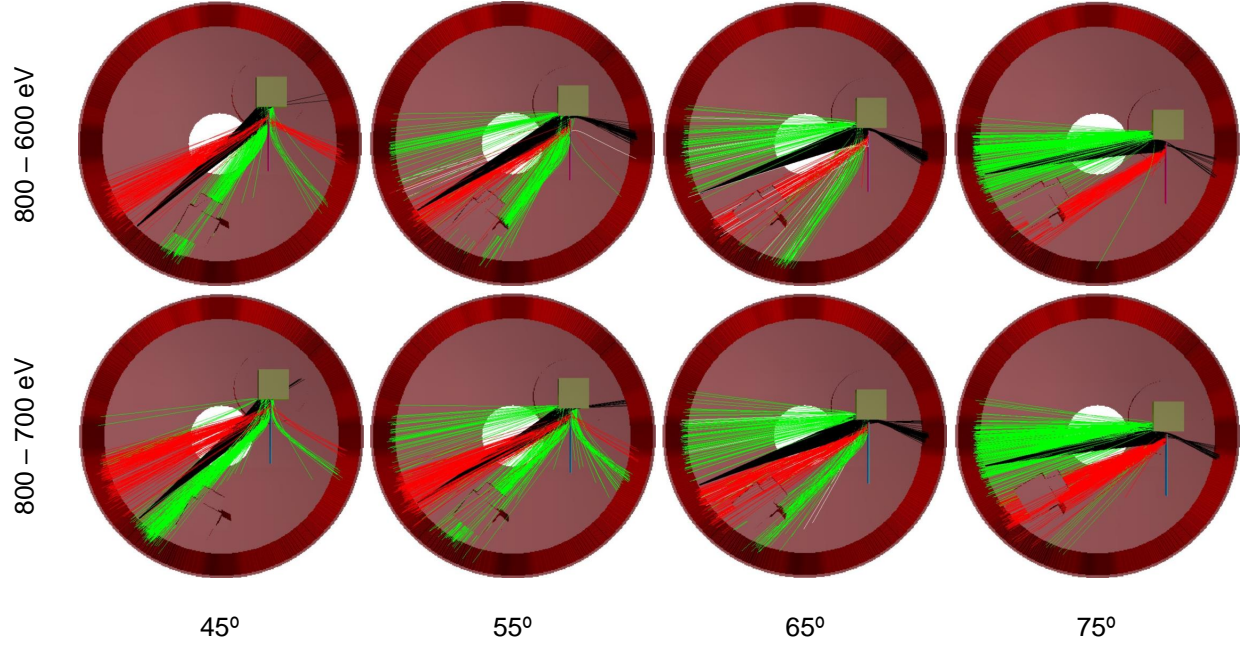


Figure 3.9: Electron trajectories from panel (red) and bus (green) electrodes for different heading angles and potential configurations.

attributed to (i) a higher than expected electron beam density in the intersection with the panel, (ii) a small horizontal deflection error of the beam, or (iii) the presence of the unmodeled panel support.

The discussion on the geometrical disagreements between the model and reality reflects the sensitivity of the electron-based touchless potential sensing method to apparently insignificant features of the target geometry and electron beam properties in a differential charging scenario. This observation is in agreement with the results reported in Ref. 49 and motivates the development of this model and its future application in closed-loop detection algorithms.

3.3.5 Target observability

The observability space of the experimental setup is explored numerically in Fig. 3.10 for electrode potentials ranging from -500 V to -800 V, heading angles from 0° to 80° , and the electron beam configuration employed in Sec. 3.3.4. The incoming electron current is quantified for each electrode energy range as described in Sec. 3.2.3. Not surprisingly, the observable states conform to a small subset of the search space, restricted mostly to the 50° to 80° range. Equipotential surfaces are generally easier to observe, as they avoid

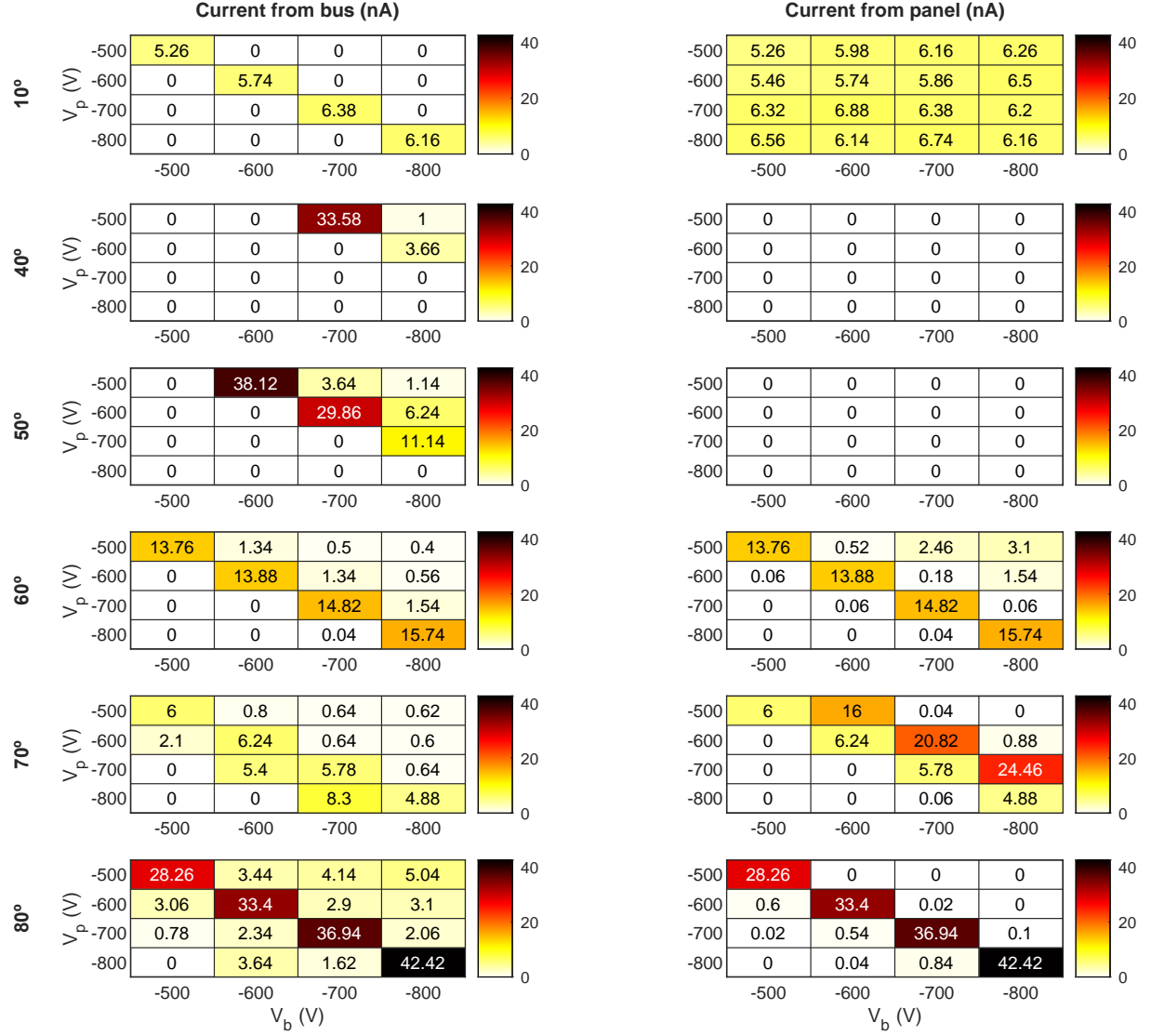


Figure 3.10: Observability matrix of the system for different heading angles and panel-bus potentials. Missing angles are not observable.

the generation of electron traps between the electrodes, increasing the effective secondary emission area. It is also important to note that, for those cases where the equipotential state is observable (60° to 80°), the current (or, equivalently, the trajectories of the secondaries) becomes remarkably stable with the applied voltage. Since secondary electrons are created with small initial energies (see Fig. 3.2(c)), the beginning of their trajectories closely follows the electrostatic field lines, which determine their future evolution far away from the assembly. Thus, for a sufficiently large electrode potential, the resulting trajectories and measured

current will behave as noted.

An interesting feature is also observed for a heading of 10° , where the observability of the panel seems almost independent of the applied potentials. This is just a consequence of the intersection between the electron beam and the tip of the plate, which results in a direct flux of secondaries moving toward the RPA. The effect is overestimated in the SIMION framework due to the relatively coarse Cartesian grid of the model (2 mm/grid unit), which assigns a thickness to the panel of about 4 times the real value.

3.3.6 Source regions and sensing strategy

In the analysis carried out in the previous section, a given geometrical and electrostatic configuration is assumed to compute the incoming flux of secondary electrons. Although this approach provides useful information on the coupled dynamics of the active sensing problem, its computational cost is prohibitive for most applications. Instead, future missions are likely to apply a different strategy: (i) determine the *source regions*, defined as the areas of the target where electrons detected at the RPA are generated, and (ii) aim the electron beam at such regions. Particle tracing simulation frameworks like the one here introduced can implement this approach and its associated control algorithms. As an example, Fig. 3.11 shows the source regions for an 80° heading angle and a homogeneous electrode potential to -800 V. The electron beam should

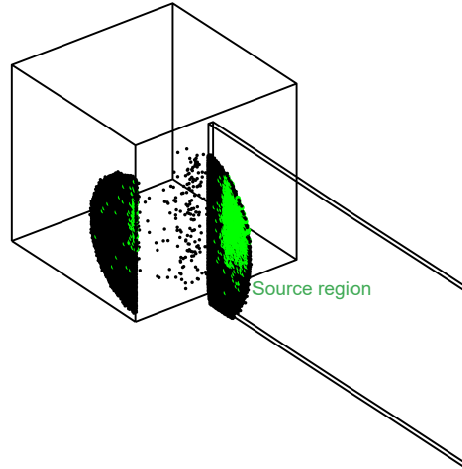


Figure 3.11: Source region of secondary electrons reaching the RPA for a heading of 80° and an electrode potential of -800 V.

be aimed at the green points in order to detect a signal and measure the target properties.

Because the potential distribution of a target spacecraft is unknown beforehand, the determination of source regions is complicated in the initial stages of the sensing process. Qualitative diagnostic information would be helpful to bound the solution space and discover, for instance, if a particular component of the target is electrically detached from the structure. Broad electron beams like the one implemented in Sec. 3.3.4 may be used to excite large portions of the target surface, enabling the measurement of multiple potentials and overcoming electron traps. X-rays-sensing [27] is independent of the electrostatic environment and exhibits optimum observability properties [272], which makes it appropriate for diagnostic purposes. However, it also leads to larger potential errors than electron sensing [44]. A combination of both methods is thus ideal to achieve a robust and accurate detection, as highlighted by previous studies [44, 49].

Chapter 4

A quasi-analytical approach to electron beam modeling

As exemplified in Chapter 3, the detection of secondary electrons is determined by the geometry, charging state, and electron beam configuration of the touchless potential sensing problem. The electron beam plays a key role in this and other applications, but the forces involved in its propagation go beyond Lorentz’s law in Eq. 2.5. Electromagnetic repulsion effects can also be relevant for high-current beams and are generally ignored by particle tracing simulators (which, as pointed out in Chapter 2, do not usually consider space-charge effects). In addition, particle tracers assign similar computational costs to the propagation of each electron within the beam and to the resulting secondaries, effectively doubling the computational cost of the simulation. This may not be concerning for on-ground studies, where computational power is readily available, but can hamper the development of flight algorithms.

The purpose of this chapter is twofold: firstly, to introduce and test a quasi-analytical, uncoupled, and computationally efficient electron beam expansion and deflection model for active charging applications and in-situ operations; and secondly, to characterize the uncertainty in the beam-target intersection properties, which condition the measurement of secondary electrons.

4.1 Context and strategy

Existing electron beam models may be divided into two families: those that fully implement the space-charge effects induced by the beam, and those that ignore such interaction [9]. In the former, the electric field depends on the trajectory of the particles and is hence computed by solving Poisson’s equation in the simulation domain, leading to accurate results but large computational costs. Particle-In-Cell (PIC)

simulations are commonly employed for this purpose, and have been widely used to study the injection and long-term propagation of electron beams in plasma environments [273–277]. Charged Particle Optics (CPO¹) Boundary Element Method (BEM) [278] in combination with the space-charge cell and tube methods [279] has also been applied to all sorts of electrostatic problems [280]. In the models that ignore space-charge effects, on the contrary, particle trajectories are propagated under the unperturbed electrostatic potential generated by the electrodes. Some representative approaches are SIMION’s Coulombic and Beam repulsion models, that approximate the beam expansion dynamics by computing the electrostatic repulsion forces in the beam cross-section at each time step [9]. Simplified analytical results for the beam expansion process can also be found in the literature [281].

The appropriateness of a certain beam model depends on its scenario of application. In the active spacecraft charging problem, servicer and target spacecraft are separated a few 10s of meters and employ focused electron beams of 10s of kV. This implies that the beam will deflect only slightly before reaching the target. In fact, the short propagation distance makes it remain in the initial expansion phase, where the beam density is much larger than the GEO plasma density and the expansion dynamics are driven by the radial electric field in the beam cross section [282]. With GEO Debye lengths of ~ 200 m [238], plasma interactions can be safely ignored (see Sec. 2.1.3), but the beam evolution is determined by the electric field from nearby charged bodies.

A solution that can be regarded as an intermediate approach between the analytical expansion equations described by Humphries in Ref. 281 and SIMION’s repulsion models [9] is here presented. By taking advantage of the particular active spacecraft charging environment, a simplified framework of analysis that uncouples electron beam expansion and deflection processes is developed and combined with the Multi-Spheres Method (MSM) for the estimation of electric fields [283]. The result is an accurate particle-tracing-like model that overcomes the one introduced in Chapter 3 in terms of computational efficiency, making it suitable for onboard flight algorithms.

¹ <https://simion.com/cpo/>. Consulted on: 09/05/2022.

4.2 Electron beam model

4.2.1 Physical model

The propagation of electron beams in space is subject to several internal and external electromagnetic interactions. The quasi-analytical physical model introduced in this chapter assumes (i) negligible space-charge effects, (ii) small beam deflection angles θ , (iii) small radial expansion, (iv) axisymmetric distribution of geometry and loads within the beam cross-section, and (v) negligible plasma interactions.

The first two assumptions are key for developing a computationally efficient simulation framework because they uncouple the beam-electrode system and the expansion and deflection processes. As explained in Sec. 4.4.1, small beam deflection angles are produced when the potential difference between servicer and target spacecraft is significantly smaller than the electron beam energy. This is the case of interest for remote sensing applications; otherwise, the beam may be deflected enough to completely avoid the target. The third and fourth assumptions reduce the cross-section electrostatic surface integrals to one dimension by allowing the implementation of an infinite cylindrical beam framework of analysis. Such approach is appropriate for small beam divergence angles and leads to large computational gains with respect to existing particle tracing simulations. Finally, and since the separation between servicer and target spacecraft is of the order of 10s of meters, which represents a fraction of the GEO Debye length of 100-1000 m, the electron beam dynamics can be reasonably studied without taking into account complex plasma interactions.

4.2.2 Mathematical model

In what follows, the deflection of the beam is assumed to be produced by the electromagnetic environment, while its expansion is a consequence of the distribution of charge in the beam cross-section and the initial beam divergence angle. The model simultaneously and independently addresses both problems by integrating the trajectories of the beam centroid (deflection) and a series of electrons distributed along the axisymmetric beam cross-section (expansion). In both cases, Lorentz's force defines the electromagnetic force on each particle through Eq. 2.5. The relativistic change in momentum of the particle is given by Eq. 2.4 and the position \mathbf{x} in the inertial reference frame is computed from Eq. 2.6.

For the sake of clarity, the *internal* fields, that drive the expansion problem, are subsequently denoted by lowercase variables, while the *external* fields, that determine the deflection dynamics, are given by uppercase letters.

4.2.2.1 Expansion of cylindrical electron beams

In the beam expansion problem, the radial trajectories of a set of electrons are integrated at different radii of the beam cross-section using Eqs. 2.5-2.6. The internal electromagnetic fields and forces generated by axisymmetric cylindrical beams must consequently be computed. This is done under the infinite length approximation, leading to good estimates when the characteristic longitudinal (propagation) distance is much larger than the characteristic radius of the beam. The main advantage of this approach is the large reduction in computational cost achieved by expressing a 3D problem in the axisymmetric domain.

Axisymmetric cylindrical beams generate radial electric and azimuthal magnetic fields. The first is readily derived from Gauss's law, resulting in [281]

$$\mathbf{e}(r, t) = \frac{q}{\epsilon_0 r} \int_0^r dr' n(r', t) r' \mathbf{u}_r, \quad (4.1)$$

where q is the electron charge, $n(r)$ denotes the volume density distribution of electrons, and $\{\mathbf{u}_r, \mathbf{u}_\psi, \mathbf{u}_z\}$ describes a cylindrical reference system centered in the axis of the beam and whose z component is aligned with the velocity. Similarly, Ampère's law gives the azimuthal magnetic field [281]

$$\mathbf{b}(r, t) = \frac{\mu_0 q v_z(t)}{r} \int_0^r dr' n(r', t) r' \mathbf{u}_\psi, \quad (4.2)$$

with μ_0 being the permeability of free space, and v_z the propagation velocity of the beam (assumed to be uniform in the cross-section). The modules of the electric and magnetic fields are related through $e = (c/\beta)b$. By applying Eq. 2.5 to these fields, the internal electromagnetic force becomes

$$\mathbf{f}(r, t) = \frac{q^2}{r\epsilon_0} (1 - \beta(t)^2) \int_0^r dr' n(r', t) r' \mathbf{u}_r, \quad (4.3)$$

where the z component of the force, caused by the radial expansion velocity, has been neglected. The magnetic and electric forces are related through $F_{\text{mag}} = -\beta^2 F_{\text{el}}$. For relativistic electron beams, both terms are approximately compensated ($\beta \rightarrow 1$), allowing long-distance transport at high current levels [281, 284].

The initial beam velocity profile is approximated in two steps. First, the velocity of propagation $v_z(0)$ is computed from the initial relativistic beam energy, $E_b = (\gamma - 1)m_0c^2$, by solving for γ and β . Then, the initial divergence angle δ , which is not caused by the electromagnetic repulsion between particles but by the optical configuration of the electron gun itself, is imposed as

$$\mathbf{v}(r, 0) \sim \frac{r\delta}{R_b}v_z(0)\hat{\mathbf{u}}_r + v_z(0)\hat{\mathbf{u}}_z, \quad (4.4)$$

where R_b is the beam radius and a quasi-collimated beam is assumed ($\delta \ll 1$). The initial electron density function, $n(r, 0)$, is modeled following a pre-defined statistical distribution (e.g. quasi-Gaussian, uniform, etc) that satisfies the electron beam current intensity I_b and energy E_b . The condition

$$\int_0^{R_b} dr' 2\pi r' n(r', t) = \frac{I_b}{qv_z(t)} \quad (4.5)$$

is then imposed at each time step to conserve the electron beam current. This expression assumes a uniform v_z component computed in a plane perpendicular to the axis of the beam, which is consistent with the small radial expansion assumption of the model. Uniform beams can be discretized with a single external electron in the axisymmetric beam cross-section, while more complex profiles (e.g. Gaussian) should employ a finer discretization to capture the evolution of the distribution. A convergence analysis should be carried out in each case; in particular, high-intensity beams require more points to accurately simulate the electromagnetic repulsion effect.

It should be noted that, although Eqs. 4.1-4.5 are given as a function of time (describing the movement of a particle), they are actually associated with a steady-state solution. Time is related to the arc parameter s along the beam centroid through $\delta s = v_z \delta t$. In a straight beam, $s = z$, and each of these expressions can be written in terms of the cylindrical coordinates r and z . The ratio β also changes depending on the beam propagation velocity, which is computed in the deflection problem independently of the expansion algorithm.

4.2.2.2 Deflection of cylindrical electron beams

The deflection of the beam is here represented by the trajectory of the centroid of the cross-section, which is integrated using Eqs. 2.5-2.6 for given external electric and magnetic fields. While the first is

mainly produced by the potential difference between both spacecraft, the second is imposed by the magnetic environment.

The charge Q of a conducting body is related to its capacitance C through $Q = C V$, where V is the potential with respect to the ambient plasma. The identification of the zero potential with the ambient plasma is a common choice in the spacecraft charging community [55] that has been adopted in this work. If V is known, then the capacitance can be used to determine the total charge of the conducting body, from which the electric field at distant points can be computed. However, objects in close proximity exhibit mutual capacitance effects [285] which must be accounted for to accurately determine the total charge, its distribution, and the nearby electric field. Capacitance is a function of the geometry of the system, but analytical solutions are only available for a limited number of shapes (such as spheres or round plates). Therefore, a numerical solution scheme must be used to find the capacitance of the system. The Method of Moments is generally employed for that purpose and, based on its solution, the Multispheres Method (MSM) has been developed as a computationally efficient alternative to approximate the resulting charge distribution [283, 286]. The MSM performs such approximation by discretizing the geometry using equivalent charged spheres [283, 286]. Given the potential on each sphere and its location with respect to the rest, the charge distribution is computed by solving the linear system

$$\begin{pmatrix} V_1 \\ V_2 \\ \vdots \\ V_n \end{pmatrix} = k_c \begin{bmatrix} 1/R_1 & 1/r_{1,2} & \dots & 1/r_{1,n} \\ 1/r_{2,1} & 1/R_2 & \dots & 1/r_{2,n} \\ \vdots & \vdots & \ddots & \vdots \\ 1/r_{n,1} & 1/r_{n,2} & \dots & 1/R_n \end{bmatrix} \begin{pmatrix} q_1 \\ q_2 \\ \vdots \\ q_n \end{pmatrix}, \quad \mathbf{V} = [\mathbf{S}]\mathbf{Q}, \quad (4.6)$$

where $k_c = 1/(4\pi\epsilon_0)$ is the Coulomb constant, R_i is the radius of each sphere, $r_{i,j}$ is the distance between spheres i and j , and $[\mathbf{S}]$ denotes the elastance matrix [285], which is the inverse of the capacitance matrix. If both spacecraft are assumed to be conducting bodies in electrostatics equilibrium, each of them must have an equipotential surface, and so all V_i belonging to the same surface must equal. This assumption is appropriate for a GEO spacecraft since modern design specifications require all outer surfaces to be electrically connected [50], although it can be relaxed for differential charging studies. The charge vector \mathbf{Q} constitutes a model of the charge distributions on the spacecraft, which allows calculating the electric field \mathbf{E} created by these

distributions as the superposition of the one produced by each individual charge q_j , given by

$$\mathbf{E}_j(r) = \frac{q_j}{4\pi\epsilon_0 p^3} \mathbf{p}, \quad p \geq R_j, \quad (4.7)$$

where \mathbf{p} denotes the radial position vector, and R_j is the radius of the sphere. An arbitrary number of spheres can be placed and their radii adjusted to match the capacitance of the MSM to the true value.

In relation to the magnetostatic interaction, this work assumes an arbitrarily oriented GEO magnetic field of 100 nT. Its large characteristic length of variation ($\sim 10^3$ km), the small characteristic time of the beam deflection process ($\sim 10^{-6}$ s), and the small influence of the field in the problem under consideration justify its treatment as a fixed parameter.

4.2.2.3 Nondimensional formulation

The numerical conditioning of the electron beam expansion and deflection problem can be largely improved by employing a dimensionless formulation of Eqs. 2.5-2.6, which become

$$\mathcal{F} = (\mathbf{v} \times \mathcal{B} + \mathcal{E}), \quad (4.8)$$

$$\frac{d(\gamma \mathbf{v})}{d\tau} = \mathcal{F}, \quad (4.9)$$

$$\frac{d\mathbf{x}}{d\tau} = \mathbf{v}, \quad (4.10)$$

where

$$\mathbf{x} = \frac{\mathbf{x}}{x_{\text{ref}}}, \quad \tau = \frac{t}{t_{\text{ref}}}, \quad \mathbf{v} = \frac{t_{\text{ref}}}{x_{\text{ref}}} \mathbf{v}, \quad \mathcal{B} = \frac{q_{\text{ref}} t_{\text{ref}}}{m_{\text{ref}}} \mathbf{B}, \quad \mathcal{E} = \frac{q_{\text{ref}} t_{\text{ref}}^2}{m_{\text{ref}} x_{\text{ref}}} \mathbf{E}, \quad \mathcal{F} = \frac{t_{\text{ref}}^2}{m_{\text{ref}} x_{\text{ref}}} \mathbf{F}. \quad (4.11)$$

The electron mass and charge are taken as a reference ($m_{\text{ref}}, q_{\text{ref}}$), with the characteristic time being $t_{\text{ref}} = 10^{-6}$ s. The characteristic length x_{ref} is equal to the initial electron beam radius R_b and the mean spacecraft separation L_c for the expansion and deflection processes, respectively. In other words, two different dimensionless problems are solved simultaneously.

4.2.2.4 Validity metrics

As noted in Sec. 4.2.1, the analytical model introduced in this section is valid while the beam deflection angle

$$\theta = \arccos \left[\frac{\mathbf{v}(0) \cdot \mathbf{v}(t_f)}{|\mathbf{v}(0)| |\mathbf{v}(t_f)|} \right], \quad (4.12)$$

is small, with t_f denoting the final simulation time. The additional dimensionless parameter

$$\mathcal{R} = \frac{\gamma m v^2}{|q L_c (\mathbf{v} \times \mathbf{B} + \mathbf{E})_\perp|} = \frac{\gamma v^2}{|(\mathbf{v} \times \mathbf{\mathcal{B}} + \mathbf{\mathcal{E}})_\perp|} \quad (4.13)$$

is defined to describe the ratio between the instantaneous electromagnetic gyroradius and the characteristic spacecraft separation L_c , with \perp denoting the force component perpendicular to the electron trajectories and the different variables referring to the deflection problem. The metric \mathcal{R} reflects the influence of the electromagnetic environment on the trajectory of the centroid. A small value of \mathcal{R} implies that its gyroradius is comparable to the characteristic spacecraft separation, which ultimately leads to the focusing of the beam. The reader may visualize this scenario with a simple geometrical problem: if two identical circumferences are initially superposed and then separated slightly, two intersection points will be generated. The same happens with an electron beam when $\mathcal{R} \leq 1$. This effect is not contemplated in the model, which explains why $\mathcal{R}(\theta)$ must be significantly greater (smaller) than 1.

4.2.2.5 Numerical integration scheme

The integration of Eqs. 2.5-2.6 must conserve the total energy of the system. Common integrators, such as the 4th order Runge-Kutta (RK) method, carry a certain truncation error with each time step, resulting in unbounded divergences in the long term. This has made the Boris algorithm, which is an explicit, time-centered integrator that conserves the phase space volume and bounds the global energy error, the standard for particle physics simulations [287]. However, in short-term applications (like the one discussed in this manuscript) RK integrators still offer an appropriate solution. In the simulations that follow, a variable-step, variable-order Adams-Bashforth-Moulton PECE solver of orders 1 to 13 is implemented by means of Matlab's routine `ode113` [288], resulting in relative total energy errors below 0.001%.

4.3 Performance analysis

4.3.1 Verification

Every model should be tested to verify its implementation, a step that is summarized here by independently focusing on the deflection and expansion processes. As described in Sec. 4.2.2.5, the predicted trajectories pass the energy conservation test. Besides, they also match the analytical electron gyroradius and gyrofrequency in the presence of a constant magnetic field. Particle dynamics in combination with the MSM representation of charged bodies have been thoroughly addressed in previous works [7], leaving the beam expansion dynamics as the last module to be verified.

SIMION's documentation includes a case of analysis² where its Coulombic and Beam repulsion models are validated with coupled space-charge results from CPO [9]. The example consists on an isolated beam of 1 eV that originates in a 3 mm circle with a uniform distribution of 1000 electrons and a deflection angle of $\delta = -16.7^\circ$. The beam current is set as a multiple of the maximum value $I_0 = 3.47 \mu\text{A}$ sustained by the system, leading to the results depicted in Fig. 4.1. The same scenario is simulated with the beam model presented in Sec. 4.2, showing an overall excellent agreement with SIMION. Small differences between both sets of results should be attributed to simplifying assumptions. For instance, the initial beam velocity profile in Eq. 4.4, leads to a set of particles with unequal kinetic energies. Although appropriate for small deflection angles (like the ones used in active spacecraft charging scenarios), this approximation performs worse with $\delta \gg 1$. However, while the computational cost of each SIMION simulation scales with the square of the number of particles [9], just a few trajectories are required by the proposed framework: the centroid, and a certain number of points in the axisymmetric cross-section that are employed to recompute the volume distribution of electrons. Since in this case such distribution is uniform, a single electron is needed to capture the evolution of the beam envelope; however, 50 particles are simulated for illustrative purposes. This computational advantage, together with the reduction of a complex problem to a small set of parameters, are the main advantage of the simplified model here introduced.

² The interested reader is referred to the `readme.html` file in the `examples/repulsion` folder of SIMION 2020

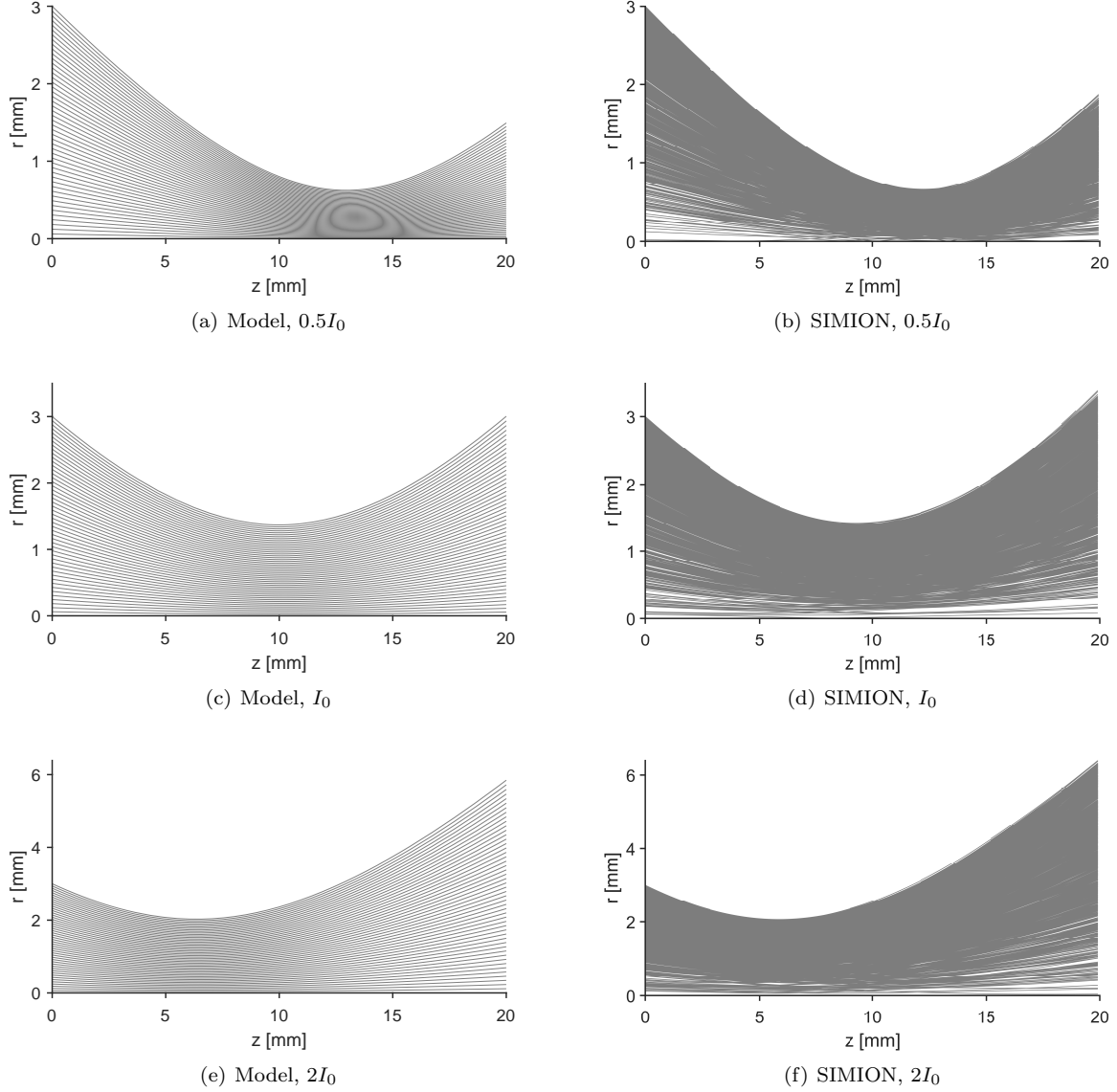


Figure 4.1: Comparison between simulation framework and SIMION's beam repulsion model [9] for $E = 1$ eV, $\delta = -16.7^\circ$, and $I_0 = 3.47 \mu\text{A}$.

4.3.2 Validation

The physical mechanisms involved in the electron beam expansion and deflection processes have been very well understood for decades, and the validation of fundamental particle dynamics has consequently little technical value. On the contrary, future applications depend on the proper application of the model presented in Sec. 4.2, which relies on a number of assumptions that limit its validity space. Provided that

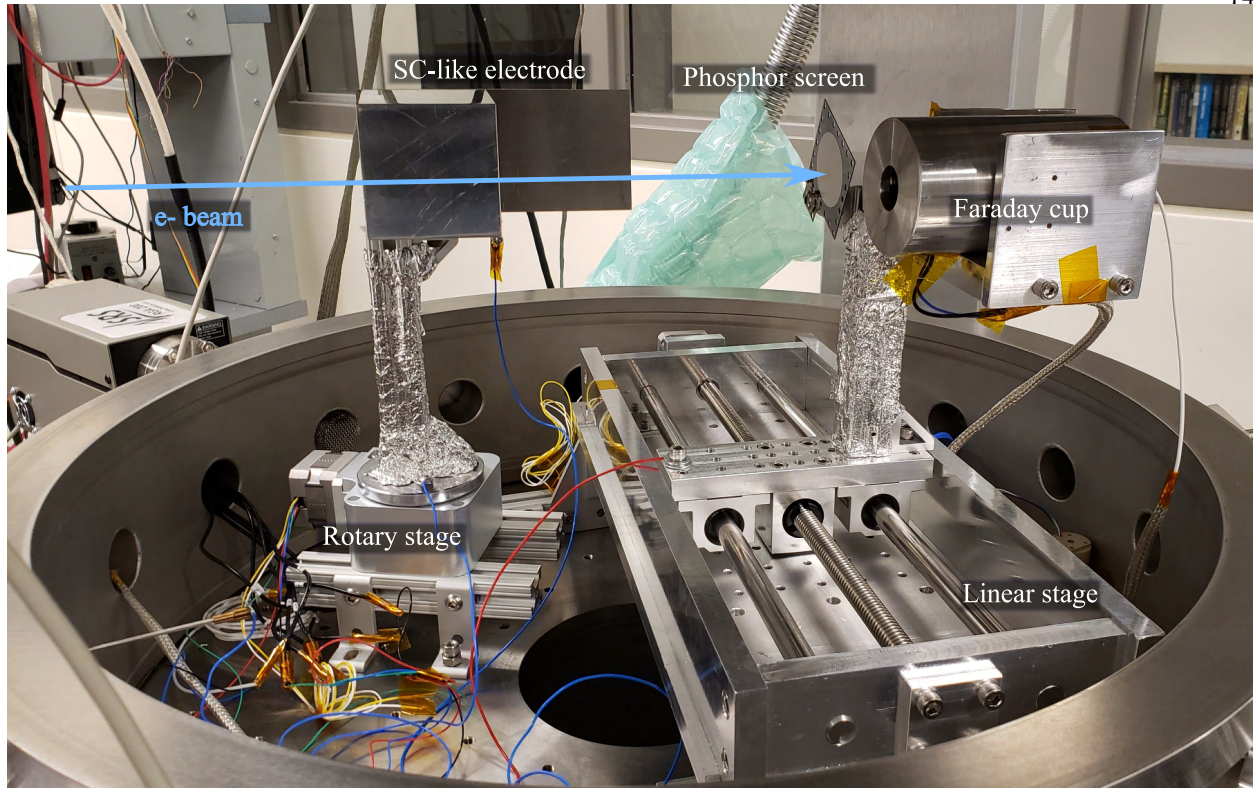


Figure 4.2: Experimental setup inside the ECLIPS chamber.

such assumptions are met, a computationally efficient and powerful analysis tool is obtained.

With the purpose of exploring the performance of the model in a worst-case scenario, the experimental setup shown in Fig. 4.2 is tested in the ECLIPS Space Environment Simulation Facility [289]. The assembly exposes an electron beam from a Kimball Physics EMG-4212D electron gun to the electric field generated by a charged spacecraft-like electrode mounted on a rotary stage. The shape and location of the beam spot at approximately 35 cm from the gun orifice are observed with a 3.81 cm diameter rugged phosphor screen, and the spatial distribution is obtained with a Retarding Potential Analyzed (RPA) mounted on a linear stage. The beam is configured at 1 keV energy and $10 \mu A$ current, while the electrode is set at -100 to -500 V employing a Matsusada AU-30R1 high-voltage power supply. The electron flux at the RPA is measured with a Keithley 2400 multimeter. Finally, the system is automated by means of a LabView VI.

Figure 4.3 shows the beam spot profiles at the phosphor screen for electrode potentials ranging from -100 to -500 V. Because the gun orifice is slightly below the symmetry plane of the electrode, a voltage

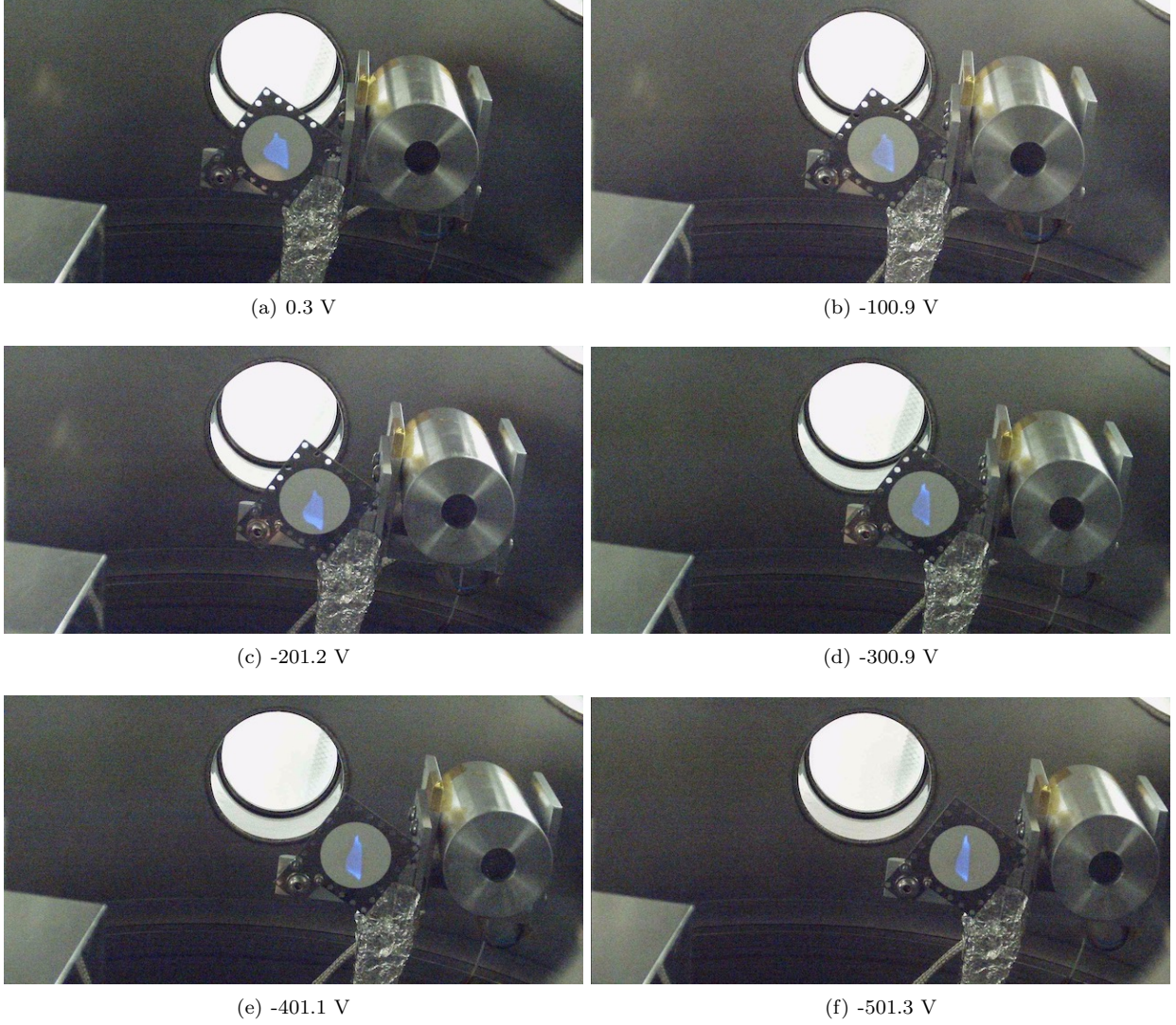


Figure 4.3: Electron beam spot in the phosphor screen under different electrode potentials.

decrease leads to a slight downwards deflection. This is compensated with a fine tuning of the vertical gun deflection settings, which do not alter the horizontal position or shape of the spot. Figure 4.3(a) shows a ~ 13 mm diameter beam cross-section, which is considerably larger than the initial ~ 3 mm diameter beam. Tests with different beam current intensities give the same spot shape, which demonstrates that the expansion is not induced by the electrostatic repulsion between electrons, but by the initial beam spread angle δ . As the voltage decreases, the beam is deflected away from the electrode and its cross-section is elongated vertically. The spot shape is deformed significantly below -300 V, indicating the existence of small

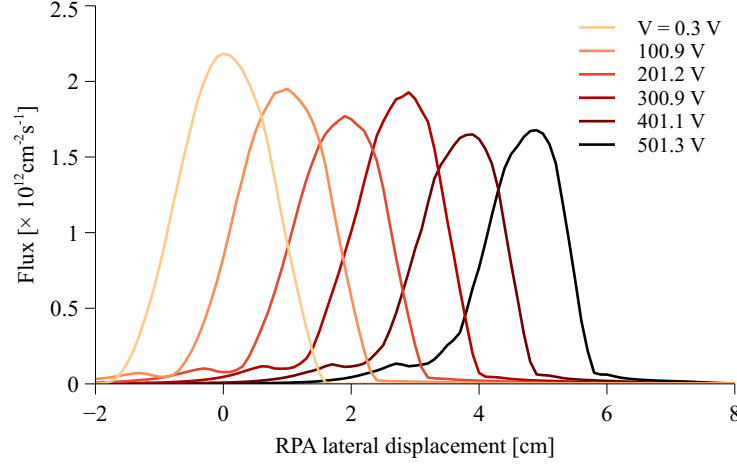


Figure 4.4: Experimental electron flux distribution as a function of the applied electrode potential.

gyro radii with $\mathcal{R} \sim 1$. These observations are complemented with the electron flux distribution computed with the RPA in Fig. 4.4, where the narrowing process reduces the width of the flux peak and its amplitude. Based on the 0 V case, the spread angle is estimated to be $\delta \sim 2.5^\circ$. It should be noted that the apparent beam radius shown in Fig. 4.3(a) is smaller than the one reported in Fig. 4.4. This is due to limitations imposed by the power density threshold of the phosphor screen and the effective aperture of the RPA³.

The influence of the electrode rotation angle α on the beam deflection and spot shape is also explored in Fig. 4.5 for $V = -100$ V and $\alpha = 10^\circ$ to 50° . Although the beam is deflected and the cross section is modified, these effects are much less pronounced than in Fig. 4.3, implying that the \mathcal{R} metric is significantly larger. In other words, the uncoupled model is far more appropriate for this case.

The framework of analysis introduced in Sec. 4.2 is not designed to predict the elongation of the beam cross-section, but still gives accurate estimations for those cases where the beam deflection angle is small. In order to evaluate the validity metrics defined in Sec. 4.2.2.4, the experimental setup is reproduced with a 934-spheres MSM representation of the spacecraft-like electrode. The result is shown in Fig. 4.6 for an electrode potential of -500 V, that corresponds to the case in Fig. 4.3(f), and a beam expansion angle $\delta = 2.5^\circ$.

The validity metrics \mathcal{R} and θ are reported in Fig. 4.7(a) as a function of the electrode potential V and

³ The variations in light intensity at the phosphor screen are caused by the Electron-Beam-Induced-Deposition (EBID) of carbon and heavy molecules over the surface, and not by variations in the distribution of electrons in the beam cross-section.

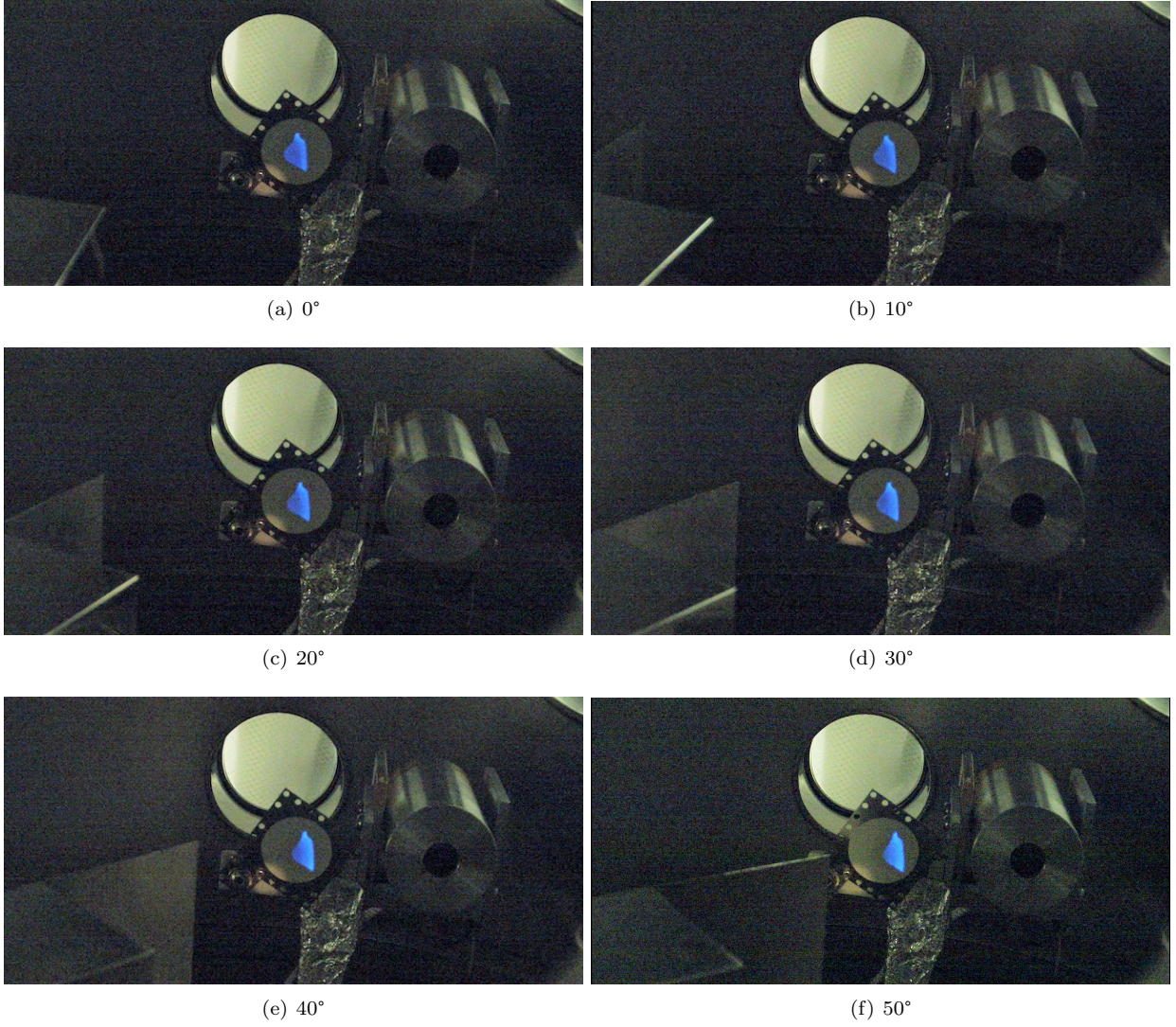


Figure 4.5: Electron beam spot in the phosphor screen under different electrode rotation angles at -100 V.

in Fig. 4.7(b) in terms of the electrode rotation angle α . An increase in the electrode potential decreases the minimum \mathcal{R} value and increases the deflection angle θ , reaching $\sim 3^\circ$ and 9.5° , respectively, for the limit case of -300 V. Larger values lead to significant beam cross-section deformations, as shown in Figs. 4.3(e)-4.3(f). Similarly, the rotation of the electrode creates a second minimum in the \mathcal{R} plot (i.e. a second maximum in the electromagnetic force), but since this minimum is larger than in the -200 V case, its effects on the beam cross-section are less significant. Due to the large beam expansion angle δ , the magneto-electrostatic repulsion between electrons plays virtually no role in the expansion dynamics of the beam.

The experiment demonstrates the appropriateness of the expansion/deflection decoupling when the validation metrics \mathcal{R} and θ adopt sufficiently large values. In such cases, the beam cross-section becomes practically independent of the external electromagnetic force. Although the assumptions of the model significantly constraint its validity range, it is precisely in the spacecraft charging scenario where this computationally efficient framework can be better exploited.

4.4 Uncertainty in active spacecraft charging scenario

4.4.1 Problem statement

Once the validity of the beam model has been contrasted with experimental observations, the base scenario of analysis is introduced in Fig. 4.8. The GOES-R⁴ and SSL-1300⁵ spacecraft MSM models are shown together with the e^- beam centroid evolution in the global reference system $\{\hat{x}, \hat{y}, \hat{z}\}$. The target spacecraft (-2.5 V) is negatively charged with respect to the servicer (0 kV) due to the current unbalance induced by the electron beam, generating a net electrostatic force that tends to deflect and slow down the 5 keV, 10 μ A electrons from $4.2 \cdot 10^7$ m/s to $3.2 \cdot 10^7$ m/s. The electron beam energy must be larger than the absolute potential difference to allow the electrons to reach the target surface. The \mathcal{R} parameter depends quadratically on the propagation speed and approximately linearly on the beam energy (see Eq. 4.13), and

⁴ <https://www.goes-r.gov/spacesegment/spacecraft.html>. Consulted on: 07/06/2022.

⁵ http://sslmda.com/html/1300_series_platform.php. Consulted on: 07/06/2022.

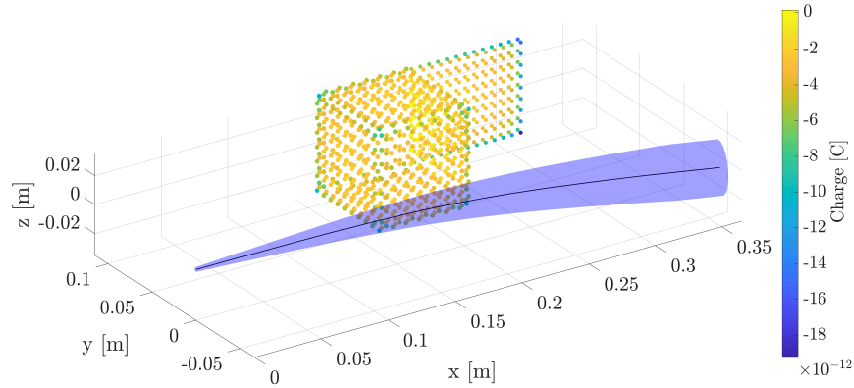


Figure 4.6: MSM representation of the experimental setup with electron beam propagation at -500 V.

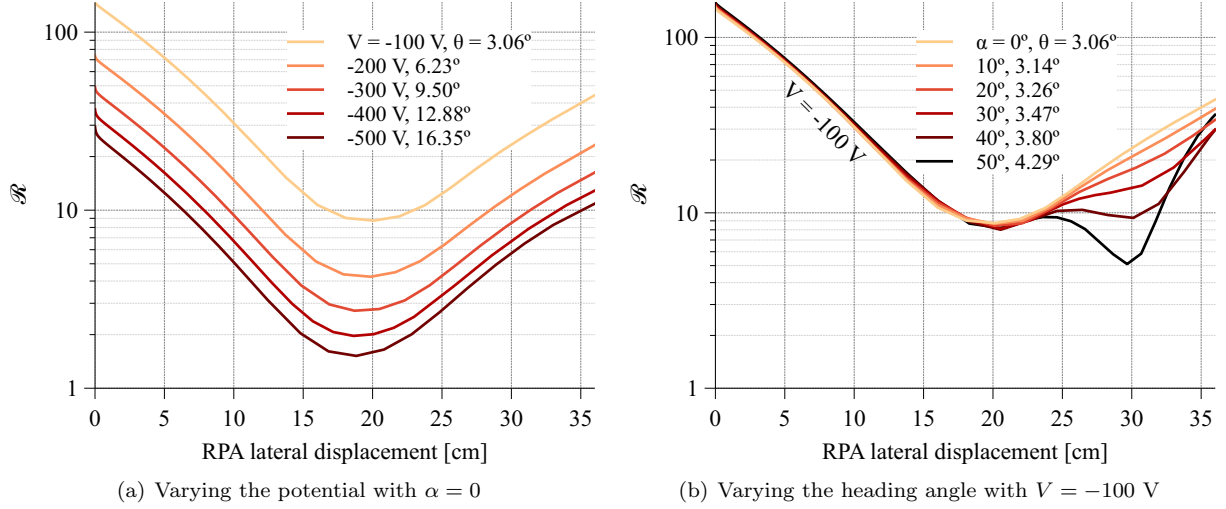


Figure 4.7: Validation metrics \mathcal{R} and θ as a function of the electrode potential and heading angle.

hence the physical model here adopted is particularly well suited for high beam energy applications.

The trade-off between beam energy and spacecraft potential is analyzed in Fig. 4.9 by comparing the validity metrics along the beam trajectory in three different scenarios. As expected, an increase in beam energy leads to larger \mathcal{R} and smaller θ values, while a decrease in the target spacecraft potential has the opposite effect. In the nominal case ($E_b = 5$ keV, $V = -2.5$ kV), a deflection angle $\theta = 5.33^\circ$ and a minimum

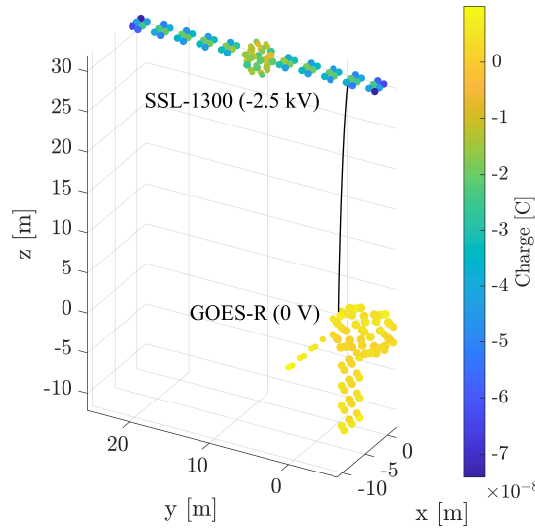


Figure 4.8: Geometry of the 2-SC problem for the basic simulation parameters (see Table 4.1).

$\mathcal{R} = 4$ are reached, satisfying the validity range of the model. These values are analogous, in terms of \mathcal{R} and θ , to the experimental -200 V case pictured in Fig. 4.3(c) and analyzed in Fig. 4.7.

Figure 4.10 explores the beam expansion dynamics for different deflection angles. When a stream of collimated electrons ($\delta = 0$) exits the gun, the magneto-electrostatic repulsion expands the beam radius from 2.5 to 40 mm in the 30 m flight. The trajectory of those electrons is non-linear, but as the initial δ angle is increased, a linear expansion is achieved. This qualitatively different behavior reflects the existence of *repulsive* and *inertial* expansion regimes. Although in the second case the expansion dynamics become practically irrelevant, a larger beam-target intersection is also obtained. This may not be convenient for the characterization of the target.

A discretization of 50 radial points is employed to model the expansion process, deviating less than a 0.01% from a 200-points model in the worst-case collimated beam regime. An MSM model with 172 spheres is applied to the deflection problem, resulting in errors below 5 cm in the final beam centroid position with respect to a high-fidelity 1976 spheres MSM simulation. These results are acceptable for the problem here discussed.

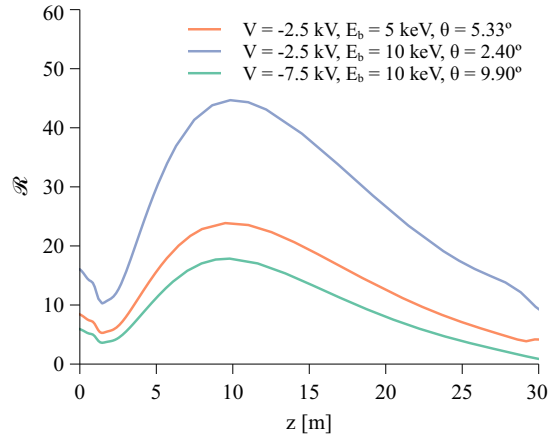


Figure 4.9: Validation metrics \mathcal{R} and θ as a function of the target spacecraft potential V and beam energy E_b for the nominal active spacecraft charging scenario.

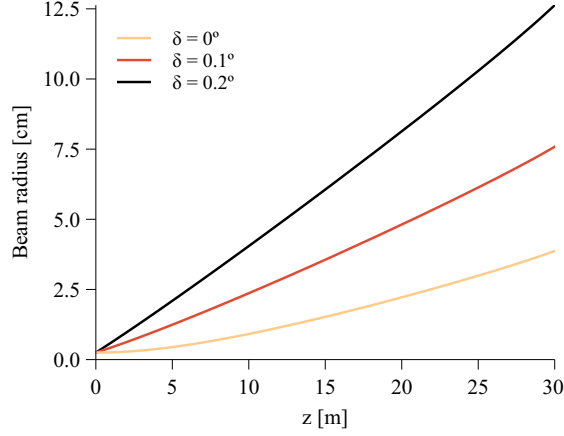


Figure 4.10: Beam radius evolution as a function of divergence angle for the nominal active spacecraft charging scenario.

4.4.2 Uncertainty quantification analysis

The model built in Sec. 4.2 is, because of its computational efficiency, particularly well suited to quantify the uncertainty in the beam-target intersection position in an active spacecraft charging scenario. The analysis is designed from the perspective of a servicing spacecraft that seeks to steer the beam toward a particular spot of the target. A total of 702 uncertain variables are considered, with 688 being associated to the MSM spheres that approximate the charge distribution of the two-spacecraft system. The list of input variables and their distribution is detailed in Table 4.1. The outputs of the analysis are (i) the radius of the beam cross section at the end of flight, (ii) the centroid landing position in the target plane, which is perpendicular to the line of sight between both spacecraft, (iii) the landing energy, and (iv) the time of flight.

Due to the large number of parameters and reduced computational cost of the simulation, a Monte Carlo analysis is chosen over other uncertainty quantification methods. The relative influence of each input parameter on the output metrics is measured by means of sensitivity indices, computed with a Fourier Amplitude Sensitivity Testing (FAST) suite⁶ from Ref. 290.

⁶ <https://www.mathworks.com/matlabcentral/fileexchange/40759-global-sensitivity-analysis-toolbox>. Consulted on: 07/06/2022.

Table 4.1: Uncertainty analysis parameters.

Variable	Distribution	Mean	STD	Unit
Beam current (I_b)	Normal	10	0.1	μA
Beam energy (E_b)	Normal	5	0.05	keV
Initial divergence angle (δ)	Uniform	0.1	Lims: [0, 0.2]	deg
Initial particle density STD (σ_b)	Normal	0.83	0.083	mm
Servicer potential (V_{ser})	Normal	0	0.05	kV
Servicer, Euler-313 ($\psi_{\text{ser}}, \theta_{\text{ser}}, \phi_{\text{ser}}$)	Normal	[0,90,0]	[0.1,0.1,0.1]	deg
Target potential (V_{tar})	Normal	-2.5	0.25	kV
Target, Euler-313 ($\psi_{\text{tar}}, \theta_{\text{tar}}, \phi_{\text{tar}}$)	Normal	[0,180,0]	[5,5,5]	deg
Relative Position (r_x, r_y, r_z)	Normal	[0,10,32]	[0.5,0.5,1]	m
Capacitances (x172)	Normal	Dataset	1%	C
Spheres pos. (x516)	Normal	Dataset	1%	m
Initial beam radius	Fixed	2.5	0	mm

4.4.3 Results

The Monte Carlo analysis is carried out with 10^4 random realizations generated from the distributions reported in Table 4.1, which are conservative estimations of the different sources of error. Each simulation takes approximately 0.6 s after parallelizing the code with 7 CPU threads in Matlab 2021 (Intel Core i7-7820HQ CPU at 2.90 GHz, 32 Gb RAM). The solution converges in mean and variance for the expansion and deflection problems.

Results in Fig. 4.11 depict the Probability Density Functions (PDFs) of the model outputs: (a) final beam radius $R_{b,f}$, (b) final centroid position $p_{x,f}$ and $p_{y,f}$, (c) time of flight t_f , and (d) final beam energy $E_{b,f}$. The first follows a quasi-uniform distribution, clearly influenced by the uniform sampling of the initial deflection angle δ , and spans from 4 to 13 cm. These expansion values, computed for $\delta \subseteq [0^\circ, 0.2^\circ]$, are small in comparison with the spread of the beam centroid shown in Fig. 4.11(b), where the target [0.11, -1.26] m is marked as a red cross. The landing positions follow a multi-Gaussian distribution with mean [0.07, -1.20] m and covariance [0.20, -0.006; -0.006, 0.28] m². This implies that the beam centroid has a 93.9% probability of intercepting the SSL-1300 solar panel, represented as a rectangle in the figure, while the chances of hitting a 20 cm diameter circle surrounding the target are just a 0.3%. The time of flight PDF is represented in Fig. 4.11(c) and follows a log-normal distribution with logarithmic mean 14.07 μs and variance $2.14 \cdot 10^{-4} \mu\text{s}^2$. This result is relevant for applications employing pulsed beam modulations to filter

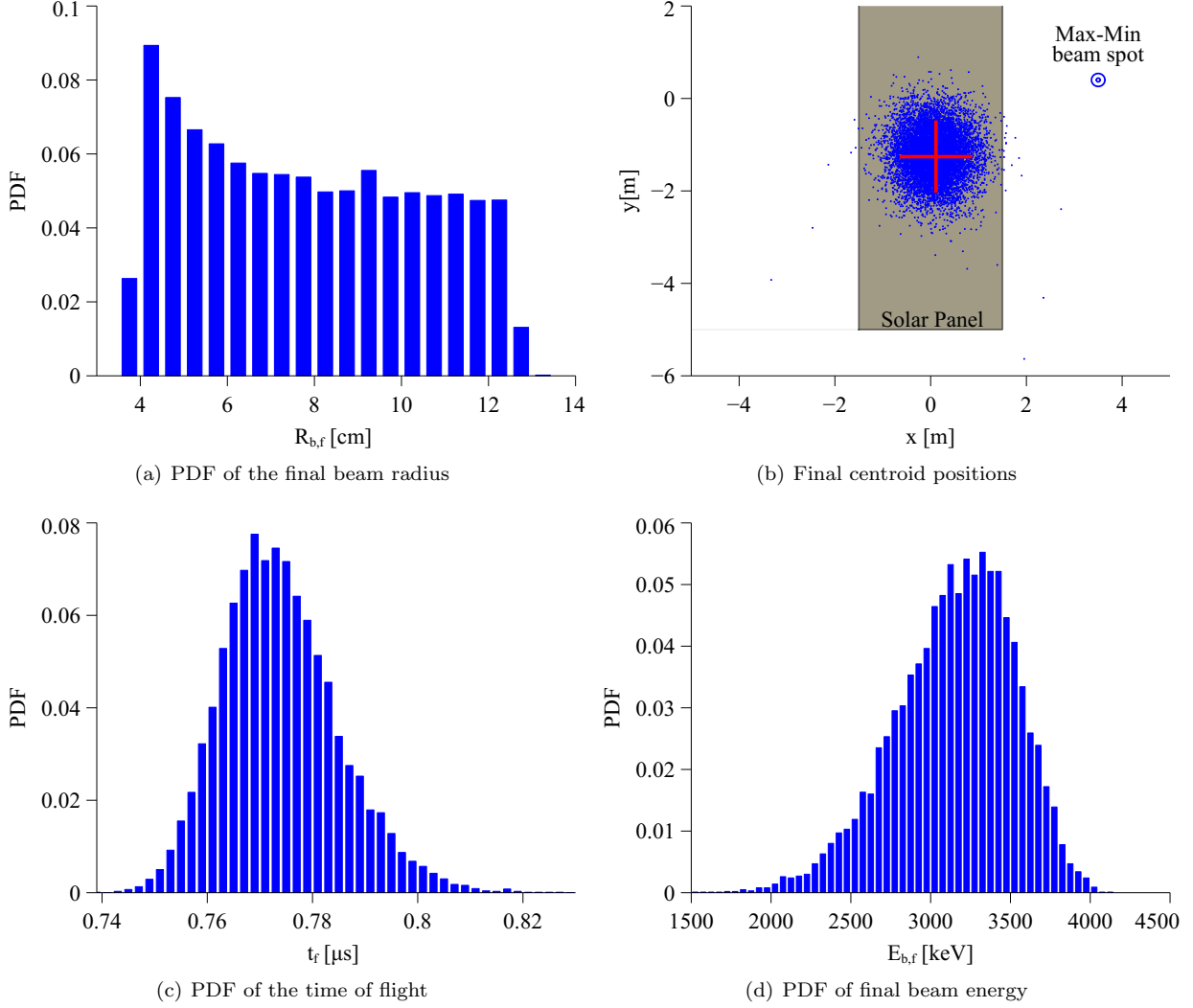


Figure 4.11: Result of the Monte Carlo simulation.

the returning secondary electron flux from the target. Modulated electron beams have been employed in previous space instruments, such as the Electron Drift Instrument of MMS [61]. Finally, the landing energy PDF is shown in Fig. 4.11(d) and fitted with a Weibull distribution (scale 3309.98, shape 9.97) with mean 3148.55 keV and variance 144294 keV². The landing energy determines the SE yield, and is hence important for defining the resulting SE flux [26]. It also determines the X-ray spectrum profile and intensity [291].

In order to determine the influence of each input on the outcomes reported in Fig. 4.11, a Fourier Amplitude Sensitivity Testing (FAST) Global Sensitivity Analysis (GSA) is conducted. The analysis is limited to the 15 non-MSM inputs in Table 4.1 to minimize its computational cost. Although 688 MSM

variables are removed, Table 4.2 shows how the total variances remain practically identical, denoting that such uncertain inputs have a negligible effect in the final distributions.

Table 4.3 reports the sensitivity coefficients for 10^4 realizations. The five outputs of the model (final beam radius $E_{b,f}$, beam-target intersection coordinates $p_{x,f}$ and $p_{y,f}$, final energy $E_{b,f}$, and time of flight t_f) are listed in the rows, while the inputs are shown in the columns. Bold fonts are employed to highlight the largest sensitivities, showing that each output variance can be almost completely explained with less than two inputs. For instance, the final beam radius is mainly dependent on the initial divergence angle, while the final positions are related to the uncertainties in their corresponding relative spacecraft position component. The output $p_{y,f}$ is also dependent on the target potential, which promotes the lateral deflection of the beam, as shown in Fig. 4.3. Although the results seem to indicate that the variance in $p_{x,f}$ is also explained by the beam current I_b , this should be attributed to numerical errors, because the model uncouples the expansion and deflection problems. The final beam energy $E_{b,f}$ and time of flight t_f are depend on the initial beam energy E_b and target spacecraft potential V_{tar} , whose relative influence is strongly influenced by the uncertainty bands selected in Table 4.1. The attitude of each spacecraft does not seem to have a large influence in any output variable; however, this is caused by the small attitude disturbance angles selected in Table 4.1, which would increase with less accurate attitude determination sensors.

It should be noted that, among the most influential input parameters, only the target potential and relative positions are not predefined. An obvious conclusion is that the targeting of specific regions is limited by the accuracy in the measurement of the relative position between the two spacecraft. Although this problem may be addressed with better sensing equipment, the strong influence of the target potential raises additional issues. In order to obtain a first measurement, the electron beam needs to intercept the target, but such interception can only be guaranteed if an estimate of V_{tar} is available. The problem may be solved

Table 4.2: Comparison of output variances between the full 702 parameters and the reduced 15 parameters MC analyses.

	$V(R_{b,f})$ [m ²]	$V(p_{x,f})$ [m ²]	$V(p_{y,f})$ [m ²]	$V(E_{b,f})$ [keV ²]	$V(t_f)$ [s ²]
Full	6.830e-4	0.204	0.276	1.387e5	1.301e-16
Reduced	6.790e-4	0.203	0.269	1.456e5	1.319e-16

Table 4.3: Normalized sensitivity indices from FAST sensitivity analysis with 15 inputs and 5 outputs. The values are scaled by a factor of 10 for convenience.

	I_b	E_b	σ_b	V_{tar}	V_{ser}	r_x	r_y	r_z	ϕ_{tar}	θ_{tar}	ψ_{tar}	ϕ_{ser}	θ_{ser}	ψ_{ser}	δ
$R_{b,f}$	0.053	0.112	0.011	0.306	0.044	0.009	0.019	0.121	0.005	0.001	0.015	0.056	0.318	0.365	8.563
$p_{x,f}$	<i>1.208</i>	0.204	0.009	0.016	0.004	8.284	0.001	0.003	0.233	0.002	0.005	0.002	0.025	0.002	0.002
$p_{y,f}$	0.004	0.030	0.033	1.550	0.354	0.003	7.888	0.109	0.001	0.003	0.001	0.003	0.020	0.001	0.001
$E_{b,f}$	0.056	1.541	0.021	7.122	0.554	0.071	0.126	0.226	0.117	0.138	0.006	0.005	0.005	0.013	0.001
t_f	0.028	3.524	0.005	4.661	0.760	0.006	0.024	0.741	0.010	0.238	0.001	0.000	0.001	0.001	0.001

by temporarily increasing the beam expansion angle δ to irradiate larger areas, enhancing the chances of collision, or by employing a more directive beam with higher energy E_b . An X-ray sensor oriented toward the irradiated region would then be used to obtain the first target voltage estimation, which would then be followed by more accurate SE estimations.

However, the availability of target potential measurements using the SE method, which is significantly more accurate than the X-ray approach [43], is strongly dependent on the geometry of the system [8]. The spatial distribution reported in Fig. 4.11(b) for the beam-target intersection has a critical influence on the

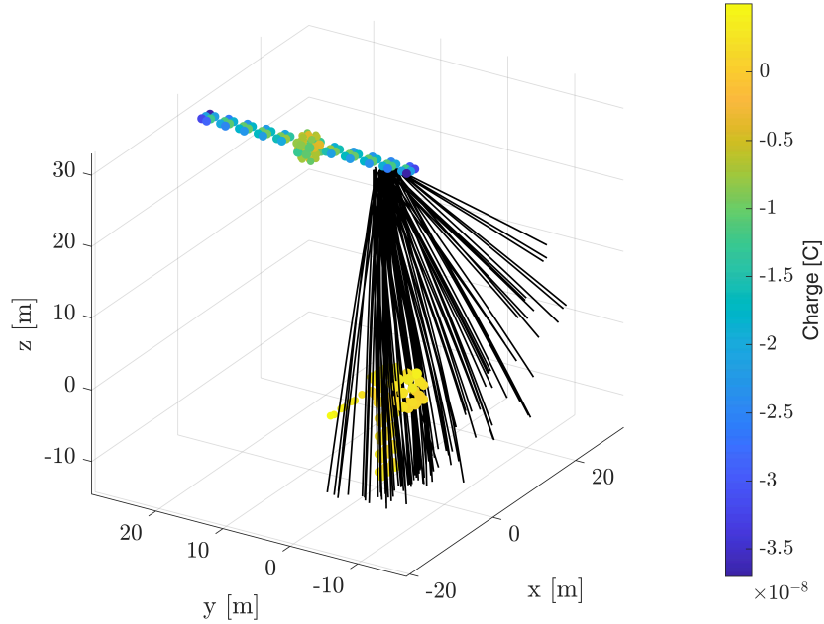


Figure 4.12: Trajectory of 100 secondary electrons generated in the beam-target intersection region described by the Monte Carlo analysis in Fig. 4.11(b).

flux of SEs. Figure 4.12 depicts the trajectories of 100 SEs uniformly generated in a circle with 1.5 m radius (3σ interval) and whose center matches the origin of the Monte Carlo final beam centroid distribution ($x = 0.07$ m, $y = -1.20$ m, $z = 30$ m). Since they are created with energies of the order of just a few eV [258], SEs are assumed to start their trajectory with zero velocity. The SEs are able to reach the servicer only when the beam hits a very specific area of the target, named *source region* in Chapter 3, so it can be readily concluded that a limited subspace of the Monte Carlo solution domain will be detectable. That is, an RPA mounted in the servicer and aimed at a suitable target region is not guaranteed to detect SEs with the statistical distributions reported in Table 4.1, concluding that the combination of X-ray and SE measurements is necessary to ensure a robust and accurate estimation of the target spacecraft potential. A feedback control loop may be employed to actively steer the beam and guarantee the measurement of SEs, following an implementation analogous to the Electron Drift Instrument of MMS [61].

4.5 Collaborators

The electron beam model presented in this chapter was developed in collaboration with Prof. Gabriel Cano-Gómez, whose contributions are gratefully acknowledged. The author also thanks Prof. Alireza Doostan for his comments on Sec. 4.4.

Chapter 5

Active photoelectron-based sensing strategies

The active exploitation of photoelectron emission for touchless spacecraft potential sensing is explored in this chapter by means of UV light sources. In contrast with previous works [7, 55], the photoelectric effect is not treated from the current balance perspective, but with a particle-centered scheme. This enables the inclusion of photoelectrons in the SIMION model introduced in Chapter 3, which is expanded and compared with experimental results to assess the feasibility and challenges of this new sensing framework.

Several new applications are enabled by this approach, from material identification to charge control. In particular, the simultaneous use of UV lasers and high-energy electron beams is proposed to excite the emission of photoelectrons and x-rays in non-cooperative GEO objects. The ultimate goal of this strategy is to reduce the sources of uncertainty identified in previous chapters by employing highly directive quasi-relativistic electron beams and the rectilinear laser trajectories.

5.1 Simulation of active photoemission

A necessary preliminary step for the study of active photoemission problems is the development of particle tracing simulators. With this goal, the model introduced in Sec. 3.1 is adapted to include photons, photoelectrons, and secondary electrons resulting from the impact of the latter on the electrode surfaces.

5.1.1 Implementation

The particle tracing model shares the same electrostatic framework and secondary electron implementation already discussed in Sec. 3.1. However, UV lamps are also considered as particle sources. Photons

are modeled in SIMION as particles with zero charge and arbitrary mass and velocity that follow rectilinear trajectories.

The impact of a photon with a charged surface is followed by the application of Eq. 2.17 to determine whether it is reflected or not. If the photon is absorbed into the material, photoelectrons can be generated based on the photoelectric yield in Eq. 2.16. This mechanism is implemented adopting the Poisson point process described in Sec. 3.1.2. Lambert's cosine law, described by Eq. 2.13, is considered for the angular distribution of emitted photoelectrons, which are released with fixed initial energy. Photoelectrons that impact a different surface may generate a secondary electron following the procedures described in Sec. 3.1.2. The normal incidence parameters $R_0(\omega)$ and $Y^*(\omega, 0)$ and the work function φ are taken as external inputs.

Reflected photons keep flying under specular or diffuse schemes, depending on the ratio given by Eq. 2.20. Specular reflections are trivial to implement in SIMION, while diffuse reflections are modeled following Lambert's cosine law in Eq. 2.13. A maximum number of successive reflections can be imposed for computational efficiency. An overview of the processes implemented in the model is given in Fig. 5.1 for a single emitted photon.

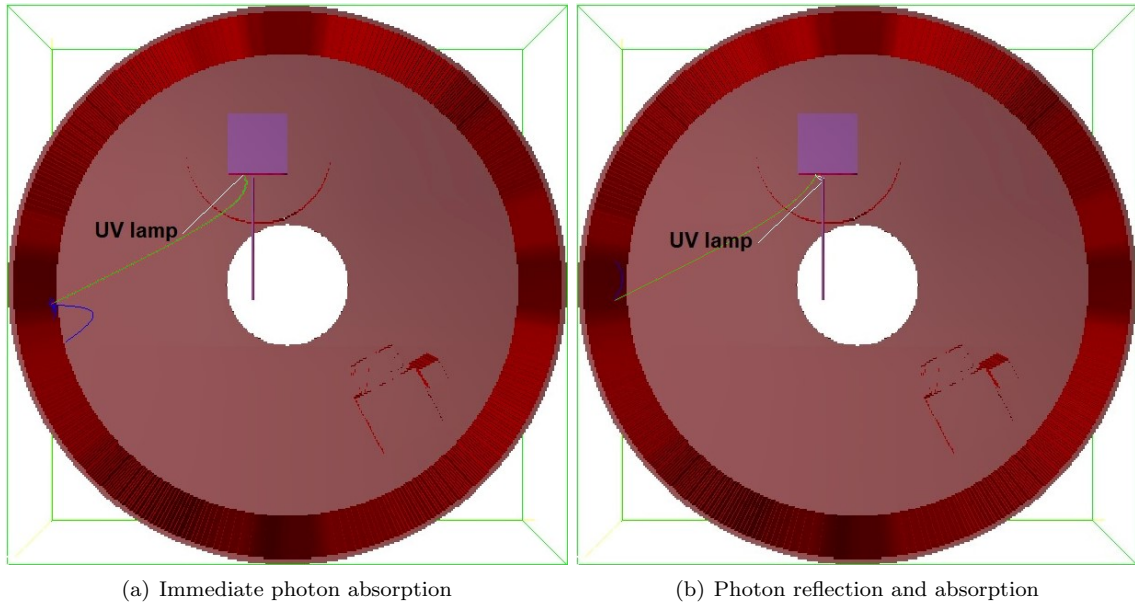


Figure 5.1: SIMION examples of photons (white) being generated and reflected, leading to the emission of photoelectrons (green) and secondary electrons (blue).

5.1.2 Effective values

The photoelectric yield $Y^*(\omega, 0)$ and initial photoelectron energy $E_p(\omega)$ depend on the energy ω of the incident photon. However, photons are implemented as particles with arbitrary mass and speed, so they do not contain any spectral information. Although this would certainly be easy to correct in SIMION, a simpler and more computationally efficient approach is adopted in this work.

Knowing the normalized spectrum $S(\omega)$ of the UV source, the *effective* photoelectric yield

$$Y_{\text{eff}}^*(0) = \int_0^\infty Y^*(\omega, 0) S(\omega) d\omega, \quad (5.1)$$

with “0” denoting the normal incidence angle, can be computed as the average number of photoelectrons released per impinging photon. This value faithfully reproduces the response of the system due to the large number of photons involved in the process. In addition, the mean photon energy

$$\overline{E}_p = \int_0^\infty \omega S(\omega) d\omega \quad (5.2)$$

is adopted for each photoelectron released in SIMION. This simplification is appropriate because initial photoelectron energies are of the order of few eVs, but given that the electrostatic environment is dominated by large spacecraft potentials, small variations in this value have a negligible effect in the overall result.

5.1.3 Superparticle method

The photoelectric yield is of the order of 10^{-7} for most materials and low photon energies, as shown in Fig. 5.3, meaning that a large number of photons have to be generated in SIMION to release a single photoelectron. To overcome this issue, the effective photoelectric yield computed in Eq. 5.1 is multiplied by a scale factor κ to accelerate the simulation, leading to the *virtual* photoelectric yield

$$Y_{\text{virt}}^*(0) = \kappa Y_{\text{eff}}^*(0). \quad (5.3)$$

Each photon is thus treated as a *superphoton* that represents κ particles. As a consequence, the current measured by the RPA as predicted by the simulation needs to be adjusted accordingly. The photon flux coming out of the UV source per second is

$$n_{\text{ph}} = \frac{P_{\text{ph}}}{\overline{E}_p}, \quad (5.4)$$

where P_{ph} is the power of the source. If n_{sim} photons are simulated with a scale factor κ and a number $n_{\text{e-, det}}$ of electrons enter the detector during the simulation, then the actual measured current is calculated as

$$j_{\text{ph}} = \eta_{\text{det}} \frac{n_{\text{ph}}}{\kappa n_{\text{sim}}} q_e n_{\text{e-, det}} \quad (5.5)$$

with η_{det} being the efficiency of the detector.

5.2 Material properties

The secondary electron, x-ray, and photoelectron emission processes depend on a series of surface properties that must be characterized in a laboratory environment. Although the experiments performed in this chapter only employ aluminum targets, this section presents standard values for a range of space materials that will be later used in Sec. 5.4.

5.2.1 Secondary electron emission

The parameters δ_{max} and E_{max} define the shape of the Sanders and Inouye secondary electron yield curve and its angular dependence according to the Darlington and Cosslett model, while the work function φ of the conductive material determines the Chung-Everhart secondary electron energy distribution. The electron affinity χ defines the energy separation between the lowest possible state for any excited electron in a dielectric material and the vacuum level, and it may be used in place of the work function when analyzing dielectrics [1]. Table 5.1 reports these values together with the first (E_1) and second (E_2) crossover points (for which $\delta = 1$) for selected materials [1, 2]. Although the Sanders and Inouye yield model is adopted in

Table 5.1: Emission parameters for selected materials [1, 2].

Material	Z	φ/χ [eV]	δ_{max}	E_{max} [eV]	E_1 [eV]	E_2 [eV]
Aluminum	13	4.20	1.0	300	300	300
Gold	79	5.47	1.4	800	150	>2000
Copper	29	5.10	1.3	600	200	1500
Iron	26	4.67	1.3	400	120	1400
Kapton	4.7	5.8	1.67	280	50	750
Teflon	3.8	4.1	2.4	350	50	180

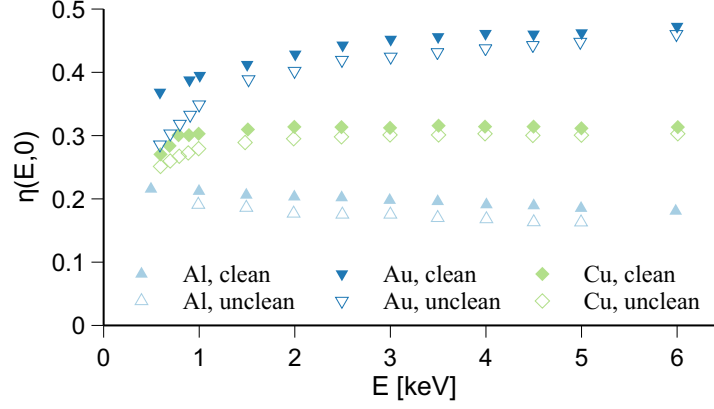


Figure 5.2: Backscattered electron yield for selected materials as a function of the impacting electron energy [10].

this work, some materials exhibit high-energy yields that may be significantly larger than those predicted by Eq. 2.10. For instance, gold has a yield of ~ 0.7 at ~ 20 keV [292].

5.2.2 Backscattered electron yield

Equation 2.22 provides a good estimation of the backscattered electron yield for energies above the limit given by Eq. 2.23 as a function of the Z values listed in Table 5.1. However, it is also important to characterize how $\eta(E, 0)$ evolves for $E < E_{\min}$. Figure 5.2 depicts the yield values below 6 keV for clean (ion bombarded) and unclean samples of aluminum, gold, and copper from Ref. 10. As expected, clean and unclean values converge and the measurements stabilize as E grows. The backscattered electron yield can reach up to 50%, highlighting the importance of this effect for some materials. In the experiments presented in this chapter, however, energetic electrons do not impact the electrode assembly and backscattered electrons are not considered.

5.2.3 Photoelectric yield

The photoelectric yield $Y^*(\omega, 0)$ is usually characterization by means of well-controlled laboratory experiments. Results for aluminum, gold, Kapton, and Teflon are presented in Fig. 5.3 as a function of the photon impact energy. Kapton and Teflon are backed by silver [11]. In the case of aluminum and gold, the

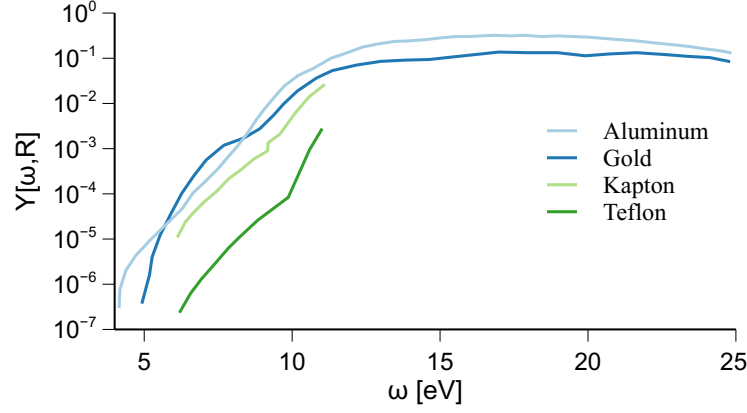


Figure 5.3: Photoelectric yield for selected materials as a function of the impacting photon energy [11–13].

yield increases with the impinging photon energy until it reaches a plateau at 10^{-1} and about 12 eV.

5.2.4 Normal reflectance

Similarly to the photoelectric yield, the normal reflectance of a perfectly smooth surface should be characterized experimentally. Figure 5.4 shows the value of $R_0(\omega)$ for selected materials as a function of the impinging photon energy [2]. Kapton is backed by aluminum, as it would be on multi-layer insulators [13], and Teflon is backed by silver. The reflectance decreases with the photon energy for all materials, but aluminum remains highly reflective until ~ 15 eV.

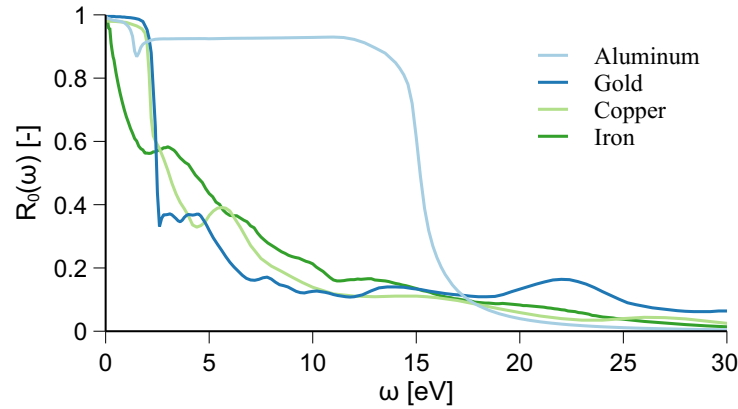


Figure 5.4: Normal reflectance for selected materials as a function of the impacting photon energy [2, 13, 14].

5.3 Analysis of complex geometries

The performance of the model introduced in Sec. 5.1 is assessed in this section employing a complex spacecraft-like electrode assembly and the material properties for aluminum listed in Sec. 5.2.

5.3.1 Experimental setup

The experimental setup pictured in Fig. 5.5 is installed in the ECLIPS vacuum chamber and used in the experiments. It is identical to the one adopted in Sec. 3.2.1, but includes a Hamamatsu L10706-S2D2 UV light source whose normalized spectrum is shown in Fig. 5.6. In addition, the electrode assembly is connected to a Matsusada AU-30R1 high voltage power supply that imposes potentials between -100 and -900 V. The heading of the assembly spans from -40° to 100° , with 0° corresponding to a perfect alignment between the electron beam and the panel electrode. Although the electron beam is not used in this experiment, this reference is kept in consistency with the study performed in Chapter 3. The RPA forms an angle of $\sim 16^\circ$ with the electron beam axis.

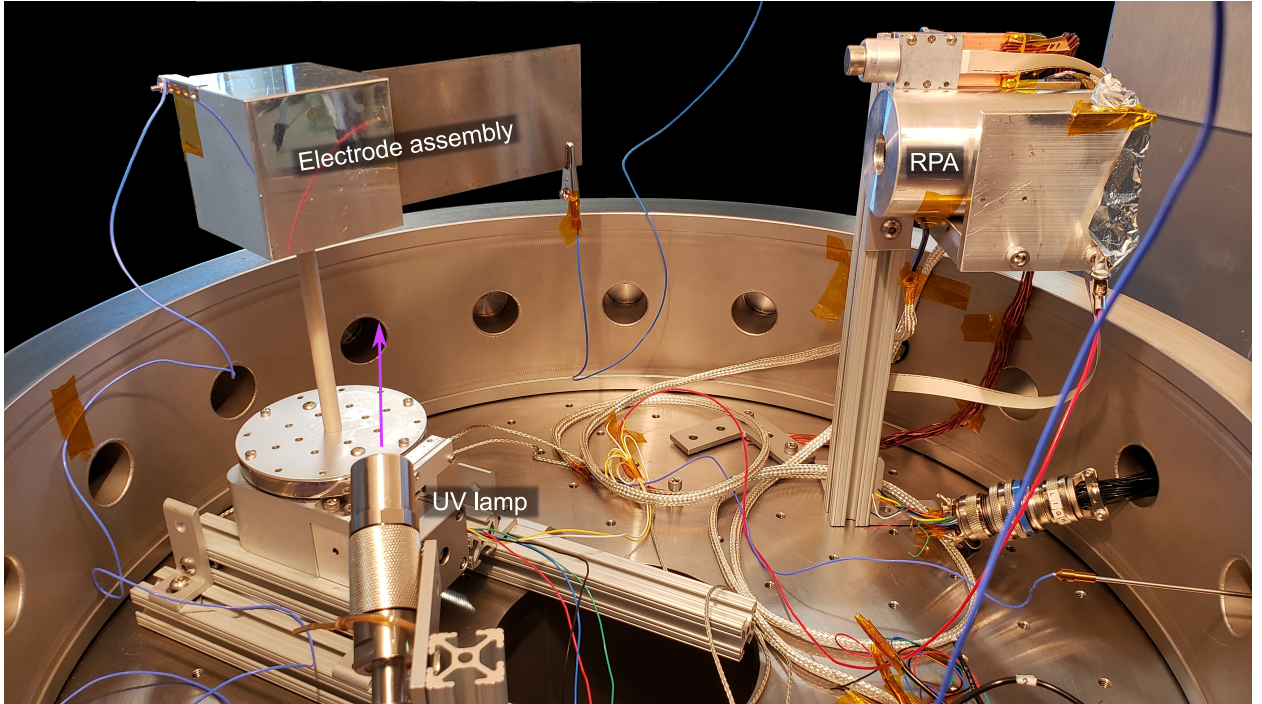


Figure 5.5: Experimental setup.

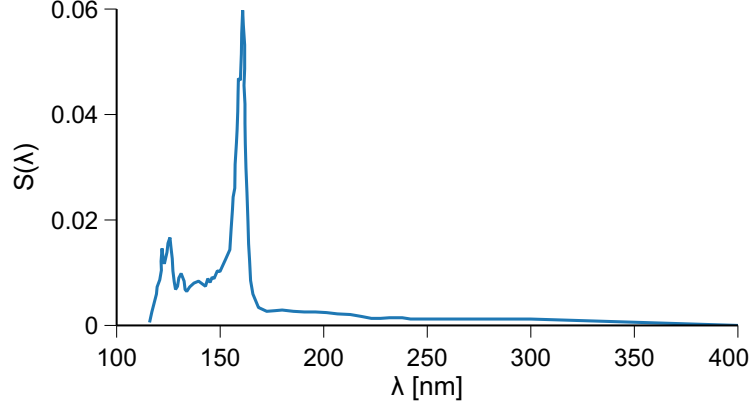


Figure 5.6: Normalized spectrum of the Hamamatsu L10706-S2D2 UV light source [15].

The normalized spectrum of the UV lamp is provided by Hamamatsu in Ref. 15. Private communication with the manufacturer has revealed that the power P_{ph} emitted by the lamp is approximately 1.2 mW, which corresponds to a 160 nm radiant irradiance peak of $0.14 \mu\text{Wcm}^{-2}\text{nm}^{-1}$ at 50 cm from the source.

5.3.2 Configuration of SIMION model

The SIMION model introduced in Sec. 5.1 is configured with the properties listed in Sec. 5.2. As in Chapter 3, the values $E_{\text{max}} \approx 300$ eV, $\delta_{\text{max}} \approx 0.97$ [55], and $\varphi \approx 4$ eV [258] are adopted for the aluminum targets to simulate secondary electron emission. The average photoelectron energy resulting from the spectrum in Fig. 5.6 is $\overline{E}_p \approx 4$ eV, while the effective photoelectron yield becomes $Y_{\text{eff}}^*(0) \approx 5.88 \cdot 10^{-2}$. A scale factor $\kappa = 10$ is considered, which returns a virtual yield $Y_{\text{virt}}^*(0) \approx 5.88 \cdot 10^{-1}$. The reflectivity R_0 of aluminum is assumed to be 0.9, while that of the steel walls of the chamber is limited to 0.1. Once again, it is important to highlight that surface conditions can have a very significant impact on these values [249–252], which should be taken as a rough estimate. 200000 photons are propagated in the simulation.

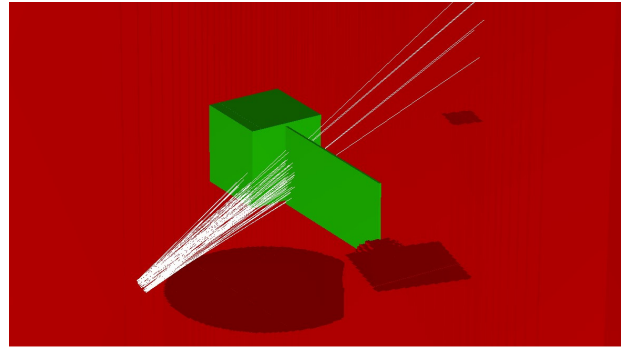
5.3.3 Calibration

Similarly to the electron beam experiments performed in Chapter 3, the geometry of the SIMION domain is adjusted to guarantee that the experimental setup is correctly reproduced. Figure 5.7 pictures the experiment and SIMION for different rotation angles. The electrode assembly is illuminated by the UV light

while the panel is covered by a sheet of paper that eases visualization. An excellent qualitative agreement with the SIMION model is achieved. However, the UV lamp illuminates areas outside the central bright spot and generates a complex radial distribution. This is a significant source of uncertainty that cannot be easily accounted for without dedicated characterization equipment. Alternatively, focused UV lasers may be employed in future works.



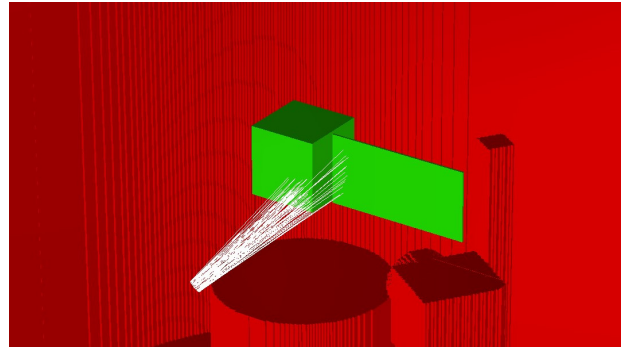
(a) Experiment (30°)



(b) SIMION (30°)



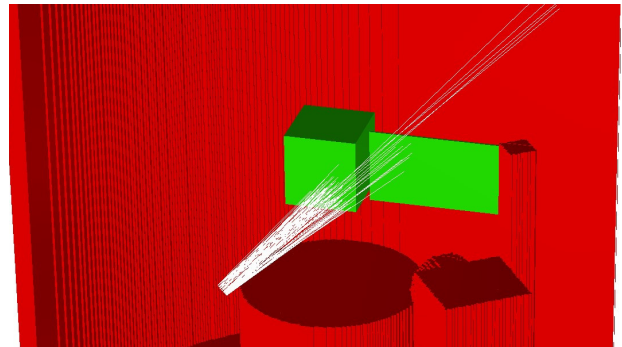
(c) Experiment (50°)



(d) SIMION (50°)



(e) Experiment (70°)



(f) SIMION (70°)

Figure 5.7: Calibration of the position and heading of the UV light.

5.3.4 Results and discussion

5.3.4.1 Overview

The trajectories of 500 randomly sampled photons are propagated in Fig. 5.8 to characterize the flux of photoelectrons coming out of the electrode assembly. A single consecutive photon reflection is considered for -25° to illustrate this effect, but it is then removed from the other cases for clarity. The results obtained in this work are computed with an unlimited number of reflections. A brief study of the plots tells us that photoelectrons will be detected between -25° and 0° and between 75° and 100° . Reflected photons may also induce photoelectron release, but this may be considered a second-order effect due to the spread of particles in the vacuum chamber.

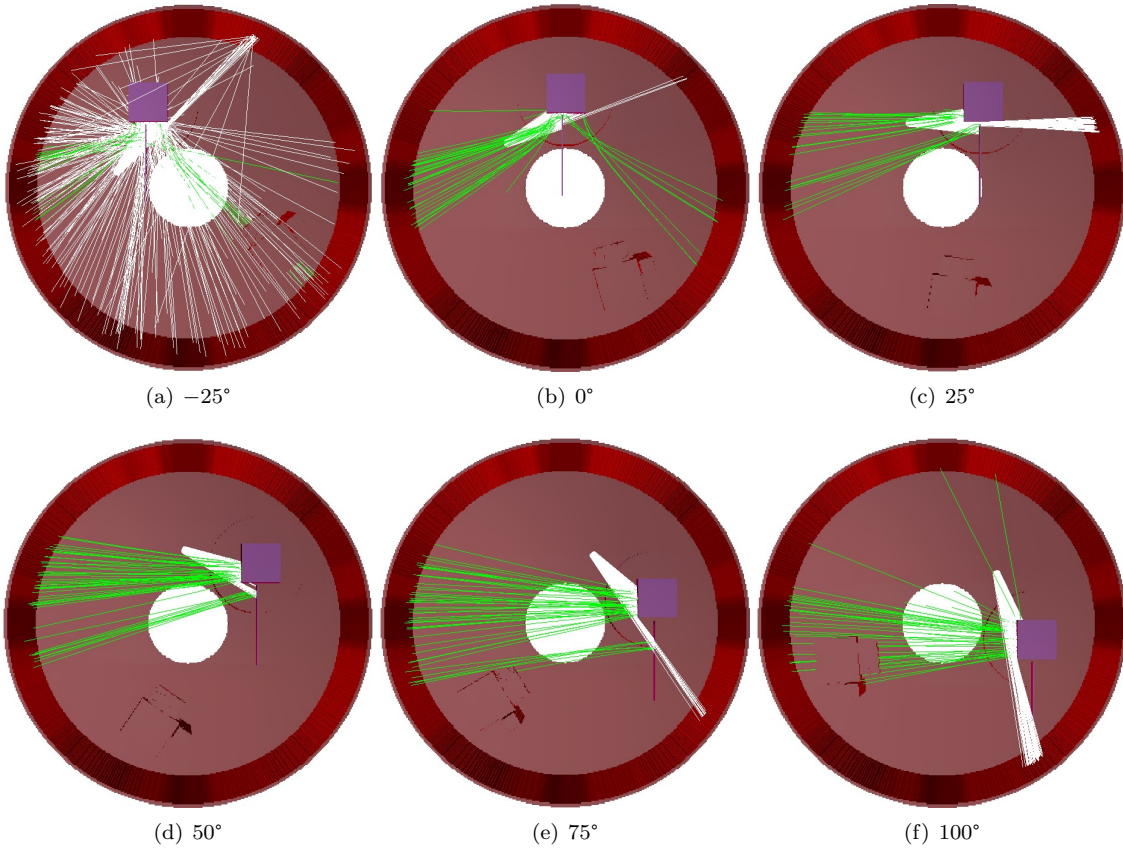


Figure 5.8: Overview of photoelectron trajectories (green) generated by the UV source (white) as a function of the electrode assembly heading angle. The first iteration of reflected photons is shown for -25° and removed for clarity in the other cases.

5.3.4.2 Experiments

The potential of the electrode assembly described in Sec. 5.3.1 is set to -100 to -900 V with steps of -200 V while being irradiated by the UV source. The assembly is rotated in steps of 2.5° and the electron signal is recorded. When detected, photoelectrons appear in the energy spectrum of the RPA as a prominent, isolated peak. Following the same approach as in Chapter 3, RPA currents generated by photoelectrons with energies in the ± 50 eV band around the potential of the electrode assembly are recovered. This approach is much less time consuming than measuring the full energy spectrum for each angle and potential configuration.

Figure 5.9 compares experimental results with numerical simulations performed in SIMION with and without diffuse photon reflections. In both cases, the model is able to identify the angles for which the photoelectron flux is detected, the overall trend with the applied electrode potential, and the order of

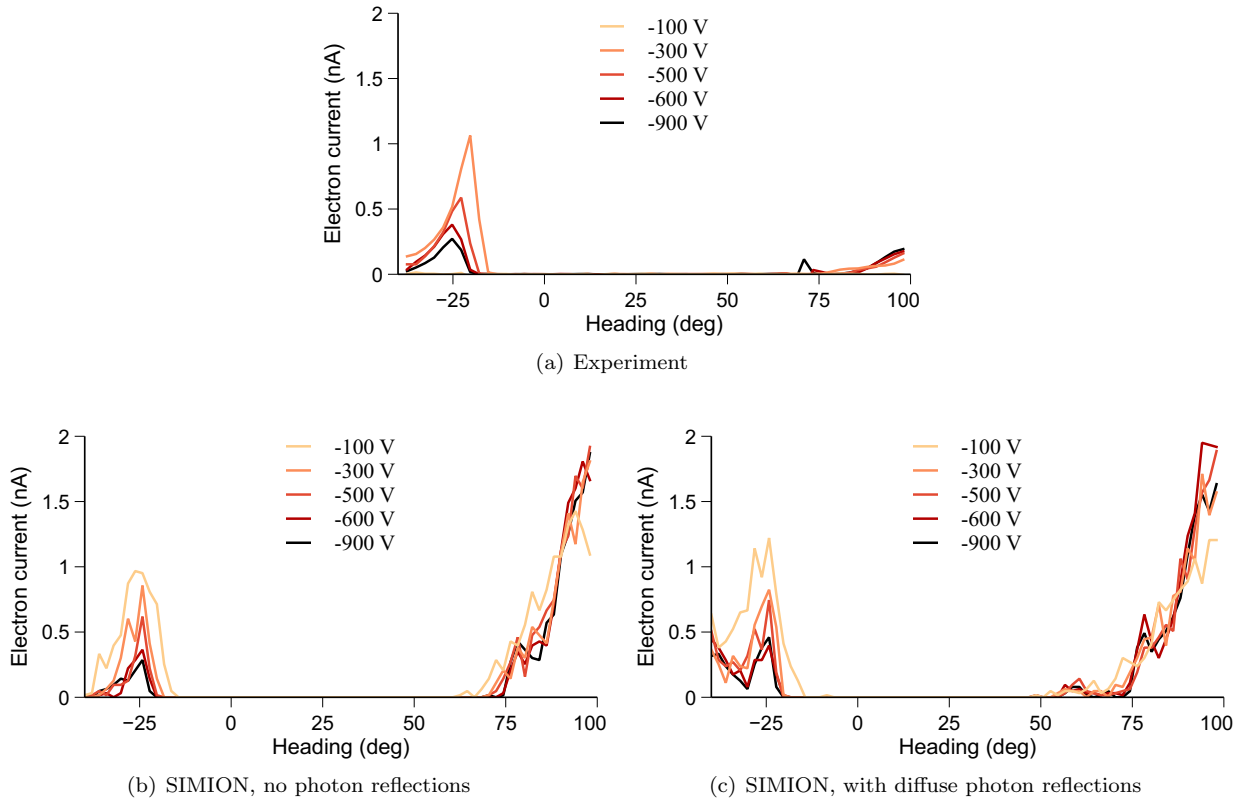


Figure 5.9: Comparison of experimental and simulated currents from the electrode assembly as a function of its potential and heading angle. The currents correspond to the electron flux entering the RPA in the ± 50 eV band around the electrode potential.

magnitude of the signal. Surprisingly, the elimination of photon reflections results in a qualitatively better agreement with the experiments, particularly around -30° and 60° . This is counterintuitive, because the UV light wavelength is so small that diffuse reflections must necessarily take place over the rough aluminum surface employed in the experiments. An additional interesting feature is the photoelectric current decrease with the applied electrode potential for a 25° heading angle. As observed in Fig. 5.8, the panel of the assembly acts in this case as an electrostatic deflector: when the potential decreases, the flux progressively moves away from the RPA and the signal is lost. Most important, however, is to note that the peak between 75° and 100° is largely overestimated in the simulations. The study of Fig. 5.8 shows that this peak corresponds to incidence angles ϕ close to 90° . Either the simplified models presented in Sec. 2.2.2 do not provide a good representation of the photoelectric effect at high incidence angles, or geometrical errors are somehow precipitating the appearance of the peak in the SIMION model. Unfortunately, this hypothesis is hard to validate due to the spatial constraints of the vacuum chamber, and is left as an open question for upcoming works.

5.4 Applications

The analysis presented in Sec. 5.3 shows that particle tracing simulations can be used to compute the detectability of a target spacecraft and an order of magnitude estimate of the photoelectron fluxes when irradiate with a UV source. This opens the possibility of replacing low-energy electron beams by high-energy UV lasers for secondary electron generation. The reasons why this may be an interesting idea are subsequently discussed followed by the description of some of the applications that benefit from this approach.

5.4.1 Critical analysis of previous methods

The surface properties listed in Sec. 5.2 are generally obtained in a controlled laboratory environment with samples that have been thoroughly cleaned with ion sources. Since even the slightest change in surface conditions can alter these values [249–251, 293], surface properties can degrade significantly after a prolonged exposition to the GEO environment [252]. This adds a layer of uncertainty that must be accounted for while

sensing.

In the electron-based method the release of secondary electrons at the target is induced by low-energy electron beams. This choice is motivated by the rapid decay of the secondary electron yield $\delta(E, \phi)$, described by Eq. 2.10, after the peak δ_{\max} located at $E_{\max} < 1000$ eV (see Table 5.1)¹. Chapter 4 has shown that low-energy primary electrons are particularly susceptible to the complex electrostatic environment around the two-spacecraft system and add further uncertainty to the steering and expansion of the electron beam. In addition to δ_{\max} and E_{\max} , the secondary electron flux also depends on the backscattered electron yield $\eta(E, \phi)$. Even though the degradation of these parameters with respect to laboratory conditions can significantly impact the charge balance and secondary electron flux magnitude coming out from the target, Chapter 3 has shown that the spatial detectability of secondaries in a complex electrostatic environment generally remains unaffected.

The operational conditions for the x-rays method, described in Refs. [27, 28], are the exact opposite of the electron-based method. The emission of x-rays is boosted by high-energy primary electron impacts [294], while the emission of secondary electrons is minimized (see Eq. 2.10). The higher electron velocity also increases its gyroradius, leading to quasi-rectilinear (hence, easily predictable) trajectories. Finally, the backscattered electron yield converges to the value given by Eq 2.22, which remains relatively constant with surface degradation, as shown in Fig. 5.2.

Although the x-ray sensing method is particularly robust to changes in the geometry of the problem [28], it is significantly less accurate than the secondary electron method [44], which in turn exhibits large sensitivities to the electrostatic environment [295]. Both approaches are therefore complementary. However, the use of low-energy electron beams in the secondary electron method complicates the measurement process and makes it particularly dependent on the uncertainty in material properties.

¹ However, at high energies the secondary electron yield may follow an extended power law rather than Eq. 2.10. This results in higher yields at energies beyond E_{\max} , which may enable the possibility of using high energy beams that are less susceptible to the ambient electrostatic environment [253, 292].

5.4.2 Touchless potential sensing

Active photoelectron-based sensing makes use of UV lasers to release photoelectrons with energies of the order of few electronvolts (see Eq. 2.21). Commercial lasers are already available for this purpose, with a sample of them being given in Table 5.2. The electrons are then accelerated by the electrostatic environment and reach the servicer with an energy that is approximately equal to the potential difference between the crafts. An RPA is employed to characterize this flux and determine the energy of incoming electrons. Knowing the potential of the servicer, that of the target is finally determined.

The active photoemission approach can be employed alone or in combination with high-energy electron beams. However, the standalone implementation risks increasing the target potential by releasing photoelectrons, eventually preventing their emission. In addition, a concentrated laser beam may locally charge the target and shift its potential [253, 292], inducing further measurement errors. A trade-off study between laser power and RPA sensitivity should be carried out to identify the best operational regime. Close proximity operations may benefit from the accuracy of this method and the compactness of the hardware involved.

Table 5.2: Representative parameters of commercial-off-the-Shelf UV lasers.

Model	Divergence (mrad)	λ (nm)	ω (eV)	P_{ph} (mW)
TOPTICA Photonics CW213	1	190	6.5	20
Photon Systems HeAg-224SL	4	224.3	5.5	50
Opto Engine LLC MPL-N-257	1	257	4.8	15
Photon Systems NeCu 30-248	4	248	5	50

5.4.3 Charge control

The decoupling of the x-ray and secondary electron generation processes and the net negative and positive current fluxes that they respectively impart on the target brings the opportunity of measuring the target potential without significantly altering the measurement. To do so, the positive and negative current fluxes must be balanced.

The photoelectron current induced by a UV laser with photon flux n_{ph} (see Eq. 5.4) is

$$J_{\text{ph}} = Y(\omega, R)n_{\text{ph}}. \quad (5.6)$$

Similarly, the flux of high-energy electrons is

$$j_e = \frac{I_b}{q_e}, \quad (5.7)$$

where I_b is the current of the electron beam. For beam energies E_b of the order of 10s of keV and for most materials, $\delta(E, 0) \ll \eta(Z, E, \phi)$ and the flux of incoming electrons becomes

$$J_e \approx [1 - \eta(Z, \phi)]j_e. \quad (5.8)$$

If follow-up interactions produced by backscattered electrons and reflected photons are ignored, the condition for neutral charging is obtained by equating Eqs. 5.6 and 5.8, resulting in

$$I_b = \frac{q_e}{\omega} \frac{Y(\omega, R)}{[1 - \eta(Z, 0, \phi)]} P_{\text{ph}}, \quad (5.9)$$

which gives the electron beam current I_b required to balance, in first order approximation, the charge induced by a laser with power P_{ph} and photon energy ω for $E_b \gg 1$ keV. If the target material is known, good estimations of the surface properties can be obtained by employing high-energy electron beams and lasers. However, simulation frameworks like the one introduced in Sec. 5.1 are needed to account for backscattered electrons, reflected photons, and, for materials with high yields at high impact energies (e.g. gold), secondary electrons. The exact same approach could be employed in combination with spacecraft charging models to set the target potential to a certain value.

5.4.4 Material identification

The photoelectric effect has been traditionally employed to determine the work function of surfaces in laboratory settings. The material is exposed to a coherent laser beam with predefined wavelength, and the energy of the emitted photoelectrons is characterized with an RPA. The stopping potential, defined as the value that matches the energy of photoelectrons and prevents their collection at the RPA, is obtained. This process is repeated for lasers of various energies, leading to a stopping potential versus laser photon energy plot. Following Eq. 2.21, the y-intercept is the work function of the material [296]. From a remote sensing perspective, the value of the work function can be employed to constrain the range of possible surface materials.

The same process could be utilized to approximately characterize the materials employed at the surface of a target spacecraft. The servicer would utilize UV lasers of varying wavelengths to excite photoelectrons, which are then collected by an RPA. The stopping potential is thus determined, and with it, the work function of the material. However, the flux of photoelectrons arrives at the servicer with an energy equal to the potential difference between the crafts plus the stopping potential. Given that the work function is of the order of 5 eV (see Table 5.1) and that the maximum touchless potential sensing accuracy achieved to date is of the order of 20 V (see Chapter 3), uncertainties in the stopping potential determination may render this approach unfeasible. Instead, multiple lasers with energies between 2 and 10 eV could be employed to sequentially excite the target. The minimum energy that produces a peak in the energy spectrum would become the closest approximation of the work function of the material.

5.5 Collaborators

The results presented in this chapter were obtained in collaboration with Kaylee Champion, whose contributions are gratefully acknowledged.

Part II

Low-gravity magnetohydrodynamics

Chapter 6

Preliminary considerations

The term *low-gravity magnetohydrodynamics* has been identified in Sec. 1.3.1 as the intersection where liquids are subject to relevant surface tension and magnetic polarization forces. Lorentz forces are also included in this definition but, although briefly covered in Chapter 14, are not the main subject of this dissertation. A first important feature of the combination of electromagnetism and low-gravity fluid mechanics is the coupling between fluid and magnetic problems. That is, the presence of a magnetizable volume in a magnetic environment modifies the magnetic field, and such field drives the momentum balance. A second characteristic is the small gravity to surface tension ratio (or Bond number) that, similarly to capillary flows, drives the behavior of the liquid. The low Bond number represents an important difference with respect to most terrestrial fluid systems, and leads by itself to a complex analytical approach to the fluid problem [85]. When magnetic forces are considered, however, the system becomes dependent also on a spatially inhomogeneous magnetic force potential, which invalidates and/or severely complicates most classical solution procedures. Finally, the discontinuity in the Maxwell stress tensor across the interface of a polarized liquid leads to a magnetic normal traction term that complicates the adoption of a potential formulation.

The existing literature on the topic has not devoted sufficient attention to this family of problems, leading to overly simplified application-oriented models. However, ignoring key features like the fluid-magnetic coupling may lead to significant errors, particularly in microgravity and for highly susceptible liquids. Therefore, the goal of Part II is to comprehensively address the problem of low-gravity magnetohydrodynamics.

6.1 Forces on magnetically polarized media

The discovery of diamagnetism dates back to 1778, when A. Brugmans reported the diamagnetic effect on bismuth [297]. In 1845, M. Faraday demonstrated that magnetism is a universal property of matter and carried out the first thorough study of the phenomenon, classifying different materials as “diamagnetic” and “paramagnetic” [298]. Atoms with completely filled shells have a total orbital momentum of $L = 0$ and a spin angular momentum of $S = 0$. The corresponding total angular momentum operator $J = L + S$ is therefore $J = 0$ and the total atomic magnetic moment cancels out. When a magnetic field is applied, it can however still modify the electron’s angular velocity as the electron spins around the atomic nucleus [299]. Considering that an atom has Z electrons, the magnetic dipole can be expressed as

$$\mu_L = \omega_L \frac{Ze}{3c} \langle r^2 \rangle, \quad (6.1)$$

where ω_L is the electron angular velocity, e is the elementary charge, c is the speed of light, and $\langle r^2 \rangle$ is the average squared radius of electron trajectories in a plane perpendicular to the magnetic flux \mathbf{B} . The \mathbf{B} field-based magnetic susceptibility can be directly expressed as the quotient of the magnetization and the magnetic flux modules as

$$\bar{\chi}^{\text{vol}} = \frac{M}{B} = \frac{Ze^2}{6mc^2} \langle r^2 \rangle N, \quad (6.2)$$

with N being the density of atoms and m the electron rest mass. A diamagnetic species responds opposing against a magnetic field via a negative magnetic susceptibility which increases with increasing r^2 . Paramagnetic materials, in contrast, possess finite magnetic dipole moments due to the spin of unpaired electrons. Upon application of an external magnetic field, the dipoles tend to align along the direction of the magnetic field in order to reduce the magnetic energy. This alignment depends on the statistical distribution of the initial orientations and on the temperature. The magnetic susceptibility of a paramagnetic substance is given by

$$\bar{\chi}^{\text{vol}} = N \frac{\mu_A^2}{3k_B T}, \quad (6.3)$$

where μ_A is the finite magnetic dipole of atoms, k_B is the Boltzmann constant, and T is the temperature.

From a macroscopic perspective, diamagnetic and paramagnetic substances are repelled and attracted by a magnetic dipole, respectively. The body force acting on a magnetized medium, named in this case *Kelvin*

force, adopts the form (see Appendix A)

$$\mathbf{f}_m = \mu_0 \mathbf{M} \nabla H, \quad (6.4)$$

where μ_0 is the magnetic permeability of free space, and \mathbf{M} and \mathbf{H} are the magnetization and magnetic fields, respectively. The \mathbf{H} field-based volume magnetic susceptibility of the material, χ^{vol} , is defined through

$$\mathbf{M} = \chi^{\text{vol}} \mathbf{H}, \quad (6.5)$$

and its sign determines whether a substance is diamagnetic or paramagnetic. The \mathbf{H} -based definition of χ^{vol} will be adopted in this work. Ferrofluids are characterized by large susceptibilities and a non-linear dependence between \mathbf{M} and \mathbf{H} . Magnetic susceptibilities are commonly expressed per unit volume (χ^{vol}), mass (χ^{mass}), or mole (χ^{mol}) in the international or CGS systems [300]. In this thesis, symmetrical fluids are considered for which the magnetization and magnetic fields are aligned. Alternating magnetic fields at sufficiently high frequencies or fluids with very large vortex viscosity values may render Eq. 6.5 inappropriate due to the transient misalignment between \mathbf{M} and \mathbf{H} [20]. However, this is not a concern for the problems studied in this dissertation.

Natural liquids exhibit very low susceptibility values. Therefore, the effect of the magnetization field on \mathbf{H} can be neglected and the analysis can be carried out as a function of the external magnetic field in the absence of magnetized media, which is here denoted as \mathbf{H}_0 . Same is true for the magnetic pressure terms that arise at the liquid interface. This effectively uncouples the fluid-magnetic problem and simplifies the modeling of the system.

6.2 Stress tensor and force distribution

The magnetodynamic state of an incompressible continuous medium is described by means of the viscous Maxwell stress tensor, given by [62, 301–303]

$$\mathcal{T} = \mathcal{T}_p + \mathcal{T}_\nu + \mathcal{T}_m, \quad (6.6)$$

where the pressure, viscous, and magnetic terms are

$$\mathcal{T}_p = -p^* \mathbf{I}, \quad (6.7a)$$

$$\mathcal{T}_\nu = \eta [\nabla \mathbf{v} + (\nabla \mathbf{v})^T], \quad (6.7b)$$

$$\mathcal{T}_m = -\frac{\mu_0}{2} H^2 \mathbf{I} + \mathbf{B} \mathbf{H}, \quad (6.7c)$$

and where

$$p^* = p(\nu, T) + \mu_0 \int_0^H \frac{\partial}{\partial \nu} [\nu M] dH' \quad (6.8)$$

is the *composite pressure*, which includes hydrostatic $p(\nu, T)$ and magnetopolarization terms. In these expressions, $\mathbf{B} = \mu_0 (\mathbf{H} + \mathbf{M})$, $\mathbf{I} = \delta_{ij} \mathbf{e}_i \mathbf{e}_j$ is the unit dyadic in the Cartesian \mathbf{e}_i reference system, and \mathbf{v} is the fluid velocity.

The forces per unit volume exerted on the medium in the absence of electric fields are computed as the divergence of the stress tensor given by Eq. 6.6, resulting in [303]

$$\mathbf{f} = \mathbf{f}_p + \mathbf{f}_\nu + \mathbf{f}_m, \quad (6.9)$$

with

$$\mathbf{f}_p = \nabla \cdot \mathcal{T}_p = -\nabla p^*, \quad (6.10a)$$

$$\mathbf{f}_\nu = \nabla \cdot \mathcal{T}_\nu = \nabla \cdot \left\{ \eta [\nabla \mathbf{v} + (\nabla \mathbf{v})^T] \right\}, \quad (6.10b)$$

$$\mathbf{f}_m = \nabla \cdot \mathcal{T}_m = \mu_0 M \nabla H = \mu_0 (\mathbf{M} \cdot \nabla) \mathbf{H}. \quad (6.10c)$$

The reader is referred to the Appendix A for the derivation of Eq. 6.10c, where it is assumed that no internal currents are present in the liquid. If the viscosity coefficient is constant, the viscous term reduces to

$$\mathbf{f}_\nu = \eta_0 \nabla^2 \mathbf{v}. \quad (6.11)$$

6.3 Governing equations for a magnetic, viscous, incompressible fluid

6.3.1 Volume equations

The ferrohydrodynamic mass and momentum conservation equations that derive from the stress tensor in Eq. 6.6 are [303]

$$\nabla \cdot \mathbf{v} = 0, \quad (6.12a)$$

$$\rho \frac{D\mathbf{v}}{Dt} = \rho \mathbf{g} + \mathbf{f}_p + \mathbf{f}_\nu + \mathbf{f}_m, \quad (6.12b)$$

with D denoting the material derivative, and t the time. Applications involving unequilibrated ferrofluid solutions, for which $\mathbf{M} \times \mathbf{H} \neq 0$, should also incorporate the effects resulting from particle rotation. An additional term is then added to the viscous stress tensor \mathcal{T}_ν , and the angular momentum and magnetic relaxation equations also have to be considered [302, 303]. As previously noted, symmetrical fluids are considered in this dissertation, and therefore $\mathbf{M} \times \mathbf{H} = 0$.

The terms \mathbf{f}_p and \mathbf{f}_m are defined by the fields \mathbf{H} , \mathbf{B} , and \mathbf{M} , which have to be computed at each time step by solving the magnetic problem. Assuming a static magnetic configuration without surface currents and electric fields, the magnetostatic equations that determine such fields are [304]

$$\nabla \cdot \mathbf{B} = 0, \quad (6.13a)$$

$$\nabla \times \mathbf{H} = \mathbf{J}_e, \quad (6.13b)$$

where \mathbf{J}_e is the volume density of electric current, which only appear outside the magnetized region.

6.3.2 Boundary conditions

Surface forces are present at the liquid interface as a consequence of the discontinuity in the stress tensor. Those forces are balanced according to the *ferrohydrodynamic incompressible viscous boundary condition*. Assuming a contact between a ferrofluid and a non-magnetic, inviscid gas, the condition is expressed in normal (n) and tangential (t) components as [303]

$$n : \quad p^* - 2\eta \frac{\partial v_n}{\partial x_n} + p_m - p_g = 2\sigma\mathcal{H}, \quad (6.14a)$$

$$t : \quad \eta \left(\frac{\partial v_n}{\partial x_t} + \frac{\partial v_t}{\partial x_n} \right) = 0, \quad (6.14b)$$

with \mathbf{n} being the external normal vector, $p_m = \mu_0 M_n^2/2$ the *magnetic normal traction* (derived in the Appendix A), \mathcal{H} the mean curvature of the interface, v_n and v_t the normal and tangential velocity components, and x_n and x_t the distances along the normal and tangential directions, respectively. These balances should be adapted if multiple liquids with different magnetic properties are considered, as done in Refs. 303 and 3. In addition, the magnetic boundary conditions are

$$\mathbf{n} \cdot [\mathbf{B}] = 0, \quad (6.15a)$$

$$\mathbf{n} \times [\mathbf{H}] = \mathbf{K}_e, \quad (6.15b)$$

with \mathbf{K}_e denoting the electric surface currents, and $[-]$ the difference across the interface. Therefore, the normal component of \mathbf{B} and the tangential component of \mathbf{H} are continuous across the interfaces in the absence of surface currents.

6.4 Formulation of mass-force potentials

Analytical methods rely heavily on potential formulations to simplify the derivation of results. Unlike the inertial acceleration, the magnetic force is spatially inhomogeneous for virtually all scenarios of interest. In spite of this complication, it can be shown that the magnetic force in Eq. 6.4 derives from a potential if the liquid is isothermal [305]. In that case, the mass-force potential Π for inertial and magnetic terms is

$$\Pi = gz + \Pi_m, \quad \text{with} \quad \Pi_m = -\frac{\mu_0}{\rho} \int_0^H M(H) dH \quad (6.16)$$

where the convention $\mathbf{f} = -\nabla\Pi$ has been employed. The mass-force potential can also include a centripetal acceleration term [85], but this possibility is discarded for simplicity.

Chapter 7

An analytical perspective

The complexity of the coupled fluid-magnetic problem described in Chapter 6 may suggest that an analytical approximation to low-gravity magnetohydrodynamics is totally unfeasible. Indeed, previous works in the field rely heavily on numerical simulation frameworks [154, 163–171], somehow renouncing to more classical methods. This chapter shows that an analytical approach to the study of capillary, magnetic liquid interfaces is not only feasible, but also convenient. The derivations here introduced follow the classical literature in low-gravity fluid mechanics (brilliantly summarized by Myshkis and coworkers [85]) and focus on three basic concepts: equilibrium, stability, and modal response. The study is limited to axisymmetric liquid-gas interfaces due to their relevance for space systems and simplified treatment. However, the same fundamental modeling decisions can be applied to a wide variety of problems, from three-dimensional equilibrium shapes to magneto-thermocapillary convection.

7.1 Problem definition

Figure 7.1 sketches the basic problem under study, where a volume V of a magnetically polarizable liquid fills an axisymmetric container and develops a meniscus with contour radius a in partial gravity conditions. The liquid is incompressible, inviscid, with density ρ , specific volume $v = \rho^{-1}$, surface tension σ , and wall contact angle θ_c . An applied inhomogeneous axisymmetric magnetic field is imposed by a magnetic source (e.g. a coil or a permanent magnet) located at the base of the vessel and interacts with the fluid with magnetization $M(H)$. H and M are the modules of the magnetic \mathbf{H} and magnetization \mathbf{M} fields, respectively, which are assumed collinear. A non-reactive gas with pressure p_g fills the free space. In the

gets

$$-\rho\Pi + p_m + c = 2\sigma\mathcal{H}, \quad (7.1)$$

where c is an arbitrary constant. By employing the angle of inclination $\beta(s)$ of a point at the interface profile, the derivatives of the radial and axial coordinates with respect to the arc parameter s become

$$\begin{aligned} r' &= \cos \beta, & f' &= \sin \beta, \\ r'' &= -\beta' z', & f'' &= \beta' r', \end{aligned} \quad (' = d/ds) \quad (7.2)$$

and the curvature of the interface can be expressed as [85]

$$\mathcal{H} = -\frac{1}{2} \left(\beta' + \frac{f'}{r} \right), \quad (7.3)$$

where the liquid is assumed to remain in the z -negative side of the interface. If the liquid was in the z -positive region, a negative sign would precede this expression. By combining Eqs. 7.1-7.3, the equilibrium interface equations become

$$r'' = -f' \left\{ \left[\frac{\rho}{\sigma} \Pi - \frac{p_m}{\sigma} + c \right] - \frac{f'}{r} \right\}, \quad (7.4a)$$

$$f'' = r' \left\{ \left[\frac{\rho}{\sigma} \Pi - \frac{p_m}{\sigma} + c \right] - \frac{f'}{r} \right\}, \quad (7.4b)$$

where the geometrical compatibility condition $r'^2 + f'^2 = 1$ is imposed. These expressions differ with respect to those obtained by Myshkis and coworkers [85] in the addition of the magnetic normal traction p_m and the inclusion of a magnetic potential term. The system can be expressed in the alternative form

$$(rf')' = rr' \left(\frac{\rho}{\sigma} \Pi - \frac{p_m}{\sigma} + c \right), \quad (7.5a)$$

$$r' f'' + f' f'' = 0, \quad (7.5b)$$

by adding up r'' and f'' in Eq. 7.4 and differentiating the geometric compatibility condition. This expression is derived in Ref. 16 from the vertical force balance at the interface, and its non-magnetic equivalent can be found in classical textbooks on low-gravity liquid sloshing [63]. Appropriate boundary conditions should be imposed at the beginning and end of the axisymmetric arc. This task is simplified using a nondimensional formulation of the problem, which is subsequently presented.

7.2.2 Nondimensional formulation

The non-magnetic case of Eq. 7.5 is usually transformed into a nondimensional set of differential equations. In the magnetic problem, this process leads to

$$\frac{d}{d\mathcal{S}} \left(R \frac{dF}{d\mathcal{S}} \right) = R \frac{dR}{d\mathcal{S}} [\lambda + BoF - \bar{\psi}(R)], \quad (7.6a)$$

$$\frac{dF}{d\mathcal{S}} \frac{d^2 F}{d\mathcal{S}^2} + \frac{dR}{d\mathcal{S}} \frac{d^2 R}{d\mathcal{S}^2} = 0, \quad (7.6b)$$

subject to the boundary conditions arising from Fig. 7.1

$$R(0) = F(0) = \frac{dF(0)}{d\mathcal{S}} = 0, \quad \frac{dR(0)}{d\mathcal{S}} = 1, \quad (7.6c)$$

$$\frac{dF(1)}{dR} = \tan \left(\frac{\pi}{2} - \bar{\theta}_c \right), \quad (7.6d)$$

where $R = r/a$, $F = f/a$, $\mathcal{S} = s/a$, $Bo = \rho g a^2 / \sigma$ is the Bond number, $\lambda = ac$, $\bar{\psi}$ includes the magnetic potential and magnetic normal traction through

$$\bar{\psi}(R) = \frac{a\mu_0}{\sigma} \left[\int_{H(0,0)}^{H(R,F(R))} M(H) dH + \frac{M_n^2}{2} \right]_{F(R)}, \quad (7.7)$$

and the static contact angle $\bar{\theta}_c$ with respect to the vertical is given by

$$\bar{\theta}_c = \theta_c + \frac{\pi}{2} - \arctan \left(\left. \frac{dW}{dr} \right|_{C'} \right). \quad (7.8)$$

The axisymmetric meniscus $F(R)$ is computed with an iterative shooting algorithm that accounts for the fluid-magnetic coupling. The algorithm solves the meniscus balance from Eq. 7.6 for a given magnetic field, and then the magnetic field is recomputed in magnetic solver employing the new interface. The process is repeated until the vertex height converges with a prescribed relative variation. When non-trivial magnetic setups are involved, a numerical solver must be included in the loop to compute the magnetic and magnetization fields inside the liquid.

7.3 Stability

The classical literature in low-gravity fluid mechanics has devoted significant attention to the stability of liquid interfaces [85]. Space applications make use of the critical Bond number Bo^* , which determines the

critical load g^* that destabilizes the surface through

$$Bo^* = \frac{\rho g^* a^2}{\sigma}, \quad (7.9)$$

as a design parameter [86]. Although this problem has been comprehensively studied since the Apollo era, its magnetic equivalent remains practically unexplored. Exceptions are the numerical works by Marchetta and coworkers [154, 165–171] where the magnetic field is computed or measured as a fixed external input. Then, the magnetic contribution is either implemented as a source term in the momentum (Eq 6.12b) or energy balances.

Even though the formulation of the problem is complicated by the application of highly inhomogeneous force fields, the meniscus stability analysis can still be carried out by means of quasi-analytical tools for axisymmetric geometries. Referring to Myshkis and coworkers, *“if for a certain position of absolute equilibrium of a liquid the second variation $\delta^2\mathcal{U}$ of the potential energy \mathcal{U} for the mechanical system ‘liquid + vessel wall’ is positive, the position [of the interface] will be stable”* [85]. The potential energy \mathcal{U} is expressed as the sum of energies related to the fluid surface S , liquid wall W , gas wall W_g , and mass-force potential Π , which results in

$$\mathcal{U} = \sigma|S| + \tilde{\sigma}|W| + \sigma_g|W_g| + \rho \int_V \Pi dV, \quad (7.10)$$

where $\tilde{\sigma}$ and σ_g are the surface tensions of the pairs liquid/wall and gas/wall, respectively, and $|\cdot|$ denotes the area of the corresponding surface. By expressing Eq. 7.10 in terms of the geometry of the system and computing its second variation, a quadratic functional $\delta^2\mathcal{U}$ is obtained. The application of the principles of calculus of variations to this functional results in an eigenvalue problem that determines the stability of the interface (i.e. a spectral stability criterion). For axisymmetric problems, it can be split as the sequence of one-dimensional boundary-value problems

$$-\varphi_0'' - \frac{r'}{r}\varphi_0 + a(s)\varphi_0 + \mu = \lambda\varphi_0 \quad \left(0 \leq s \leq s_1; ' = \frac{d}{ds}\right), \quad (7.11a)$$

$$\varphi_0'(s_1) + \chi(s_1)\varphi_0(s_1) = 0, \quad \int_0^{s_1} r\varphi_0(s)ds = 0, \quad (7.11b)$$

$$-\varphi_n'' - \frac{r'}{r}\varphi_n + \left[a(s) + \frac{n^2}{r^2}\right]\varphi_n = \lambda\varphi_n \quad (0 \leq s \leq s_1; n = 1, 2, \dots), \quad (7.12a)$$

$$\varphi'_n(s_1) + \chi(s_1)\varphi_n(s_1) = 0, \quad (7.12b)$$

with s denoting the arc parameter along the axisymmetric meniscus S that starts at the axis ($s = 0$) and ends at s_1 , μ and λ being unknown parameters,

$$a(s) = \frac{\rho}{\sigma} \left(r' \frac{\partial \Pi}{\partial z} - z' \frac{\partial \Pi}{\partial r} \right) - \frac{z'^2}{r^2} - r''^2 - z''^2 \quad (7.13)$$

being a function that depends on the radial r and axial z positions and the normal derivative of Π at the interface, and

$$\chi(s_1) = \frac{k \cos \theta_c - \bar{k}}{\sin \theta_c}, \quad (7.14)$$

representing a boundary parameter where θ_c is the contact angle of the liquid with the wall and k and \bar{k} are, respectively, the radial curvatures of the surface S and tank wall W [85]. The functions φ_0 and φ_n are bounded at the origin and denote the axisymmetric and lateral stability modes with increasing eigenvalues λ_{0i} and λ_{1i} for $i \geq 1$. It can be shown that the *critical eigenvalue* is given by

$$\lambda^* = \min\{\lambda_{01}, \lambda_{11}\}, \quad (7.15)$$

and that the equilibrium state is stable (asymptotically stable, for a viscous liquid) if $\lambda^* > 0$, and unstable if $\lambda^* < 0$ [85]. The nature of the instability is determined by the relative magnitude of the axisymmetric and lateral eigenvalues. For example, if $\lambda_{01} < \lambda_{11}$, the axisymmetric perturbations are *most dangerous*. Alternatively, the stability of the surface can be determined by defining a *critical* $\chi^*(s_1)$ *parameter*, such that if $\chi(s_1) < \chi^*(s_1)$ the equilibrium state is unstable, and if $\chi(s_1) > \chi^*(s_1)$ it is stable. From the computational perspective, the main advantage of this method is that it substitutes the boundary-value problems in Eq. 7.11 and 7.12 by three second-order ordinary differential equations. Further details can be found in Ref. 85.

The magnetic terms can be readily implemented in this procedure by employing the mass-force potential described by Eq. 6.16. If a highly susceptible liquid is considered, the pressure-like term p_m must be included in the derivation of Eqs. 7.11 and 7.12 and a coupled fluid-magnetic simulation framework must be employed to solve the liquid interface. Complex geometries or time-dependent problems may instead be studied by means of numerical frameworks like the one introduced in Chapter 10.

7.4 Modal response

As with any other mechanical system, the analysis of the dynamic response of a liquid surface can be performed through modal analysis. The procedure is conceptually similar in all problems: after finding the equilibrium meniscus, the free surface is perturbed with a linear oscillation. A set of admissible functions is then substituted in the governing equations, resulting in an eigenvalue problem from which the eigenfrequencies and eigenmodes are obtained [86]. The modal analysis of microgravity liquid interfaces was first formulated and solved by Satterlee and Reynolds in 1964 [306], and is significantly more complicated due to the presence of a curved meniscus. However, it is key for developing mechanical analogies that reproduce the forces and torques induced by a sloshing propellant on a spacecraft [63]. The low-gravity magnetic case can be derived in a similar way after considering the fluid-magnetic coupling. Although forced oscillations are addressed in Ref. 16, the discussion that follows is limited to the free surface oscillations problem.

7.4.1 Nonlinear formulation

If an irrotational flow field is assumed, there exists a potential ϕ such that

$$\mathbf{v} = -\nabla\phi = -\frac{\partial\phi}{\partial r}\mathbf{e}_r - \frac{1}{r}\frac{\partial\phi}{\partial\theta}\mathbf{e}_\theta - \frac{\partial\phi}{\partial z}\mathbf{e}_z. \quad (7.16)$$

The velocity potential satisfies Laplace's equation

$$\nabla^2\phi = \frac{\partial^2\phi}{\partial r^2} + \frac{1}{r}\frac{\partial\phi}{\partial r} + \frac{1}{r^2}\frac{\partial^2\phi}{\partial\theta^2} + \frac{\partial^2\phi}{\partial z^2} = 0 \text{ in } V, \quad (7.17)$$

subjected to the non-penetration wall boundary condition

$$\frac{\partial\phi}{\partial r} = 0, \quad \frac{1}{r}\frac{\partial\phi}{\partial\theta} = 0, \quad \frac{\partial\phi}{\partial z} = 0 \text{ on } W. \quad (7.18)$$

An additional boundary condition at the free surface is given by the unsteady ferrohydrodynamic Bernoulli's equation, which for an isothermal system with collinear magnetization field \mathbf{M} adopts the form [20, 307]

$$-\frac{\partial\phi}{\partial t} + \frac{v^2}{2} + \frac{p^*}{\rho} + gw - \frac{\Pi_m}{\rho} = c(t) \text{ on } S, \quad (7.19)$$

where $c(t)$ is an arbitrary function of time. For magnetically diluted systems $M \sim \rho$, where ρ is represented by the magnetic particles concentration for the case of ferrofluids. Under this additional assumption, both pressure-like components are approximately compensated, and hence $p^* \approx p(\rho, T)$ [20].

From Eq. 6.14a, the ferrohydrodynamic boundary condition in the absence of viscous forces becomes

$$p^* = 2\sigma\mathcal{H} + p_g - p_m \text{ on } S, \quad (7.20)$$

with

$$-2\mathcal{H} = \frac{1}{r} \frac{\partial}{\partial r} \left[\frac{rw_r}{\sqrt{1 + w_r^2 + \frac{1}{r^2}w_\theta^2}} \right] + \frac{1}{r^2} \frac{\partial}{\partial \theta} \left[\frac{w_\theta}{\sqrt{1 + w_r^2 + \frac{1}{r^2}w_\theta^2}} \right] \quad (7.21)$$

being the curvature of the surface [86]. Since at Eq. 7.19 only the spatial derivatives of the velocity potential have a physical meaning (e.g. Eq. 7.16), any function of time can be added to ϕ whenever it is convenient. From a physical viewpoint, the absolute value of p remains undetermined under the incompressible flow assumption [307]. The integration variable $c(t)$ can be then absorbed into the definition of ϕ . By arbitrarily selecting $c = p_g/\rho$, the dynamic interface condition is obtained

$$\frac{\partial \phi}{\partial t} - \frac{1}{2} \left[\left(\frac{\partial \phi}{\partial r} \right)^2 + \frac{1}{r^2} \left(\frac{\partial \phi}{\partial \theta} \right)^2 + \left(\frac{\partial \phi}{\partial z} \right)^2 \right] - \frac{2\sigma\mathcal{H}}{\rho} - gw + \frac{\Pi_m}{\rho} + \frac{\mu_0 M_n^2}{2\rho} = 0 \text{ on } S. \quad (7.22)$$

In an inertial reference system, the vertical displacement \bar{w} of a surface point lying at $(\bar{r}, \bar{\theta})$ in the interface $z = w(r, \theta, t)$ is given by

$$\frac{d\bar{w}}{dt} = \frac{\partial w}{\partial t} + \frac{\partial w}{\partial r} \frac{d\bar{r}}{dt} + \frac{\partial w}{\partial \theta} \frac{d\bar{\theta}}{dt} \text{ on } S. \quad (7.23)$$

If the velocity components relative to the tank $d\bar{w}/dt$, $d\bar{r}/dt$ and $\bar{r}d\bar{\theta}/dt$ are expressed as a function of the potential given by Eq. 7.16, the kinematic interface condition that relates the last with the shape of the free surface becomes

$$\frac{\partial w}{\partial t} = -\frac{\partial \phi}{\partial z} + \frac{\partial w}{\partial r} \frac{\partial \phi}{\partial r} + \frac{1}{r^2} \frac{\partial w}{\partial \theta} \frac{\partial \phi}{\partial \theta} \text{ on } S. \quad (7.24)$$

The continuity equation given by Eq. 7.17, together with the kinematic relation in Eq. 7.24 and the boundary conditions at Eq. 7.18 and Eq. 7.22, conform the problem to be solved after imposing the contact angle at the wall (θ_c) and a contact hysteresis parameter that will be described later in the text.

7.4.2 Linear equations

The dynamic and kinematic conditions at Eq. 7.22 and Eq. 7.24 are highly nonlinear. This difficulty can be overcome by linearizing the problem and restricting the analysis to small oscillations. If the wave

position is expressed as the sum of the static equilibrium solution and a small perturbation

$$w(r, \theta, t) = f(r) + h(r, \theta, t), \quad (7.25)$$

it will be possible to express the system of equations and boundary conditions as a Taylor's series expansion around the equilibrium surface S' . After neglecting second-order terms, the boundary-value problem becomes

$$\nabla^2 \phi = 0 \text{ in } V, \quad (7.26a)$$

$$\frac{\partial \phi}{\partial r} = 0, \quad \frac{1}{r} \frac{\partial \phi}{\partial \theta} = 0, \quad \frac{\partial \phi}{\partial z} = 0 \text{ on } W. \quad (7.26b)$$

$$\frac{\partial \phi}{\partial t} + \frac{\sigma}{\rho} \left\{ \frac{1}{r} \frac{\partial}{\partial r} \left[\frac{r(\partial h / \partial r)}{\sqrt{1 + (\partial f / \partial r)^2}} \right] + \frac{1}{r^2} \frac{\partial}{\partial \theta} \left[\frac{\partial h / \partial \theta}{\sqrt{1 + (\partial f / \partial r)^2}} \right] \right\} - \left[g - \frac{\mu_0}{\rho} \left(M \frac{\partial H}{\partial z} + M_n \frac{\partial M_n}{\partial z} \right) \right] h = 0 \text{ on } S', \quad (7.26c)$$

$$\frac{\partial h}{\partial t} = -\frac{\partial \phi}{\partial z} + \frac{\partial f}{\partial r} \frac{\partial \phi}{\partial r} \text{ on } S', \quad (7.26d)$$

$$\frac{\partial h}{\partial r} = \gamma h \text{ on } C'. \quad (7.26e)$$

Equation 7.26e assumes that the slope of the perturbation field at the wall is related to the magnitude of the perturbation at the same point through the parameter γ . The *free-edge condition* is characterized by $\gamma = 0$, while the *stuck-edge condition* is associated with $\gamma \rightarrow \infty$ [17]. This assumption is far from being rock-solid, and has indeed motivated a strong debate in the past. It has been suggested that the contact angle hysteresis condition depends not only on the position of the wave but also on its velocity [308] or the state of the wall [309]. In the absence of a clear criteria, some studies assume the free-edge condition or intermediate approaches, generally obtaining a reasonable agreement with experimental data [310].

The only difference between the previous formulation and the classical problem without magnetic interactions is given by the magnetic term in Eq. 7.26c. The effective gravity acceleration includes both inertial and magnetic components and is given by

$$g^*(r) = g - \frac{\mu_0}{\rho} \left(M \frac{\partial H}{\partial z} + M_n \frac{\partial M_n}{\partial z} \right)_S, \quad (7.27)$$

where it can be observed that the magnetic contribution is a function of the radius. The magnitude and relative importance of the magnetic terms depend on the magnetic configuration and gravity level of the system under analysis.

The magnetic field modifies the effective gravity acceleration of the system and shifts its natural frequencies, as reported in normal-gravity works [160, 311]. If the magnetic term was approximately constant in R , like in the case of a linear magnetic field and a flat surface, the problem would be equivalent to the non-magnetic system [162, 177]. In this analysis, however, an inhomogeneous magnetic field is being considered.

7.4.3 Dimensionless linear equations

In Refs. 306 and 17 it is proposed to split the potentials ϕ and h into spatial and temporary components, the second being a cyclic function of time with a circular frequency ω . The resulting dimensionless boundary-value problem is

$$\nabla^2 \Phi = 0 \text{ in } V, \quad (7.28a)$$

$$\frac{\partial \Phi}{\partial n} = 0 \text{ on } W, \quad (7.28b)$$

$$\Omega^2 \Phi - [Bo + Bo_{\text{mag}}(R)]\mathcal{H} + \frac{1}{R} \frac{\partial}{\partial R} \left[\frac{R(\partial \mathcal{H} / \partial R)}{\sqrt[3]{1 + (\partial F / \partial R)^2}} \right] + \frac{1}{R^2} \frac{\partial}{\partial \theta} \left[\frac{\partial \mathcal{H} / \partial \theta}{\sqrt{1 + (\partial F / \partial R)^2}} \right] = 0 \text{ on } S', \quad (7.28c)$$

$$\mathcal{H} = \frac{\partial \Phi}{\partial Z} - \frac{\partial \Phi}{\partial R} \frac{\partial F}{\partial R} \text{ on } S', \quad (7.28d)$$

$$\frac{\partial \mathcal{H}}{\partial R} = \Gamma \mathcal{H} \text{ on } C', \quad (7.28e)$$

where $R = r/a$, $Z = z/a$, $F = f/a$, $\phi(R, \theta, Z, t) = \sqrt{g_0 a^3} \Phi(R, \theta, Z) \sin(\omega t)$, $h(R, \theta, t) = \sqrt{a g_0 / \omega^2} \mathcal{H}(R, \theta) \cos(\omega t)$, $\Omega^2 = \rho a^3 \omega^2 / \sigma$, $\Gamma = a \gamma$ and g_0 is the acceleration of gravity at ground level [86]. The Magnetic Bond Number is defined as

$$Bo_{\text{mag}}(R) = -\frac{\mu_0 a^2}{\sigma} \left(M \frac{\partial H}{\partial z} + M_n \frac{\partial M_n}{\partial z} \right)_{F(R)}, \quad (7.29)$$

and accounts for the effects of the external magnetic field on the liquid.

7.4.4 Variational formulation

By following the procedure described in [17, 306], it is possible to develop a variational principle equivalent to Eq. 7.28b and Eq. 7.28c as

$$I = \iint_{S'} \left[\frac{(\partial \mathcal{H} / \partial R)^2}{\sqrt[3]{1 + (\partial F / \partial R)^2}} + \frac{1}{R^2} \frac{(\partial \mathcal{H} / \partial \theta)^2}{\sqrt{1 + (\partial F / \partial R)^2}} + (Bo + Bo_{\text{mag}}(R)) \mathcal{H}^2 - \Omega^2 \Phi \mathcal{H} \right] R dR d\theta - \Omega^2 \iint_W \Phi G R dR d\theta - \Gamma \int_{C'} \left[\frac{\mathcal{H}^2}{\sqrt[3]{1 + (\partial F / \partial R)^2}} \right]_{R=1} d\theta = \text{extremum}, \quad (7.30a)$$

subjected to

$$\nabla^2 \Phi = 0 \text{ in } V, \quad (7.30b)$$

$$\mathcal{H} = \frac{\partial \Phi}{\partial Z} - \frac{\partial F}{\partial R} \frac{\partial \Phi}{\partial R} \text{ on } S', \quad (7.30c)$$

$$G = \frac{\partial \Phi}{\partial Z} - \frac{\partial W}{\partial R} \frac{\partial \Phi}{\partial R} \text{ on } W, \quad (7.30d)$$

$$\frac{\partial \mathcal{H}}{\partial R} = \Gamma \mathcal{H} \text{ on } C', \quad (7.30e)$$

where G is a function defined by Eq. 7.30d that accounts for the non-penetration wall boundary condition and that arises naturally after reducing a volume integral in the original form of Eq. 7.30a to a surface integral using Green's theorem, as described in Ref. 17. The obtention of this variational formulation follows the procedure described in Refs. 17 and 312.

7.4.5 Ritz method

The previous set of equations can only be solved analytically for simplified configurations in the absence of magnetic fields, like the case of a cylindrical container with flat bottom and flat fluid surface ($\theta_c = 90^\circ$) [306]. For other physical systems, Ritz approximations [17, 86] or finite differences approaches [313, 314] have been proposed to approximate the eigenfunctions of the problem. The basic formulation of the first approach is subsequently developed based on Refs. 306 and 17.

By following Ritz's method, the eigenfunctions $\Phi^{(n)}$ can be approximated as the linear combination of admissible functions $\bar{\Phi}_i(R, \theta, Z)$ that satisfy the boundary conditions of the problem described by Eq. 7.30b

to Eq. 7.30e. This results in

$$\Phi^{(n)} = \sum_{i=1}^N C_i^{(n)} \bar{\Phi}_i \quad (n=1, \dots, N), \quad (7.31)$$

where N is the size of the set of admissible functions. In the same way, the eigenfunctions $\mathcal{H}_i^{(n)}$ and $G^{(n)}$ are approximated by $\bar{\zeta}_i(R, \theta)$ and $\bar{\xi}_i(R, \theta)$ through

$$\mathcal{H}^{(n)} = \sum_{i=1}^N C_i^{(n)} \bar{\zeta}_i, \quad (7.32)$$

$$G^{(n)} = \sum_{i=1}^N C_i^{(n)} \bar{\xi}_i. \quad (7.33)$$

The sets of admissible functions are linked through Eq. 7.30c and Eq. 7.30d. If $\Phi^{(n)}$, $\mathcal{H}^{(n)}$ and $G^{(n)}$ are continuous functions of $C_i^{(n)}$, the extremum condition represented by Eq. 7.30a requires that

$$\frac{\partial I}{\partial C_i^{(n)}} = 0, \quad (i=1, 2, \dots, N), \quad (7.34)$$

which results in the system of equations

$$\sum_{i=1}^N C_i^{(n)} \left(R_{ij} + Bo \bar{L}_{ij} + \bar{L}_{ij}^{mag} - \Omega_n^2 Q_{ij} \right) = 0, \quad (j=1, 2, \dots, N), \quad (7.35)$$

being

$$R_{ij} = \iint_F \left[\frac{(\partial \bar{\zeta}_i / \partial R)(\partial \bar{\zeta}_j / \partial R)}{\sqrt[3]{1 + (\partial F / \partial R)^2}} + \frac{n^2 (\partial \bar{\zeta}_i / \partial R)(\partial \bar{\zeta}_j / \partial R)}{R^2 \sqrt{1 + (\partial F / \partial R)^2}} \right] R dR d\theta - \Gamma \int_0^{2\pi} \left[\frac{\bar{\zeta}_i \bar{\zeta}_j}{\sqrt[3]{1 + (\partial F / \partial R)^2}} \right]_{R=1} d\theta, \quad (7.36a)$$

$$\bar{L}_{ij} = \iint_F \bar{\zeta}_i \bar{\zeta}_j R dR d\theta, \quad (7.36b)$$

$$\bar{L}_{ij}^{mag} = \iint_F Bo_{mag}(R) \bar{\zeta}_i \bar{\zeta}_j R dR d\theta, \quad (7.36c)$$

$$Q_{ij} = \frac{1}{2} \iint_F (\bar{\Phi}_i \bar{\zeta}_j + \bar{\Phi}_j \bar{\zeta}_i) R dR d\theta + \frac{1}{2} \iint_F (\bar{\Phi}_i \bar{\xi}_j + \bar{\Phi}_j \bar{\xi}_i) R dR d\theta. \quad (7.36d)$$

The system has a nontrivial solution only when its determinant is zero. The eigenvalues Ω_n^2 , and therefore the corresponding modal circular frequencies ω_n , are then computed by means of the characteristic equation

$$||R_{ij} + Bo L_{ij} + L_{ij}^{mag} - \Omega^2 Q_{ij}|| = 0. \quad (7.37)$$

Once solved, the eigenfunctions of the problem are obtained from Eq. 7.31 to Eq. 7.33.

7.4.5.1 Selection of admissible and primitive functions

The set of admissible functions for Φ , \mathcal{H} and G , related through Eq. 7.30c and Eq. 7.30d, satisfy by definition Eq. 7.30b to Eq. 7.30e and form truncated series that approximate the eigenfunctions of the problem. A set of primitives should be previously defined as [306]

$$\vartheta_p = J_n(k_p R) \cos(m\theta) e^{k_p Z} \quad (p=1, \dots, N, N+1), \quad (7.38a)$$

$$\zeta_p = \left(\frac{\partial \vartheta_p}{\partial Z} - \frac{\partial F}{\partial R} \frac{\partial \vartheta_p}{\partial R} \right)_{Z=F(R)}, \quad (7.38b)$$

$$\xi_p = \left(\frac{\partial \vartheta_p}{\partial Z} - \frac{\partial W}{\partial R} \frac{\partial \vartheta_p}{\partial R} \right)_{Z=W(R)}, \quad (7.38c)$$

with k_p being the roots of the equation

$$\left[\frac{d}{dR} J_n(k_i R) \right]_{R=1} = 0, \quad (7.39)$$

where J_n is the Bessel function of first kind and order n . This index is used to study the axisymmetric ($n = 0$) or lateral ($n = 1$) case, while m defines the circumferential symmetry of the problem. Axisymmetric primitive functions will be characterized by $n = m = 0$, while lateral sloshing functions can be obtained with $n = m = 1$.

However, the previous set of primitives does not satisfy Eq. 7.30e. The set of admissible functions is then created as a linear combination of the previous

$$\bar{\Phi}_i = \sum_{p=i}^{N+1} a_{ip} \vartheta_p, \quad \bar{\zeta}_i = \sum_{p=i}^{N+1} a_{ip} \zeta_p, \quad \bar{\xi}_i = \sum_{p=i}^{N+1} a_{ip} \xi_p, \quad (i=1, 2, \dots, N). \quad (7.40)$$

The $N + 1 - p$ coefficients a_{ip} for each i value are determined by imposing (i) a normalization condition, (ii) a contact angle value, and (iii) a Lagrange minimization problem designed to produce Bessel-like functions. These condition are respectively expressed as [306]

$$\sum_{p=i}^{N+1} a_{ip} \zeta_p(1) = 1, \quad (7.41a)$$

$$\sum_{p=i}^{N+1} a_{ip} \frac{\partial \zeta_p}{\partial R}(1) = \Gamma, \quad (7.41b)$$

$$\sum_{p=i}^{N+1} a_{ip}(K_{pj} - k_p^2 L_{pj}) + \lambda_{1i} \frac{\partial \zeta_j}{\partial R}(1) + \lambda_{2i} \zeta_j(1) = 0 \quad (j=i, i+1, \dots, N, N+1), \quad (7.41c)$$

where λ_{1i} and λ_{2i} are the Lagrange multipliers of the minimization problem and

$$\zeta_i(R) = \zeta_i(R, \theta) / \cos(m\theta), \quad (7.42)$$

$$K_{ij} = \iint_F \left(\frac{\partial \zeta_i}{\partial R} \frac{\partial \zeta_j}{\partial R} - \frac{n}{R^2} \zeta_i \zeta_j \right) R dR d\theta. \quad (7.43)$$

$$L_{ij} = \iint_F \zeta_i \zeta_j R dR d\theta. \quad (7.44)$$

Once the system is solved, the admissible set can be used to solve the eigenvalue problem.

The success of this method depends on finding an adequate set of admissible functions $\overline{\Phi}_i$ such that the eigenfunctions $\Phi^{(n)}$ can be represented with a reduced number of elements. The Z term in the primitives ϑ_p , evaluated at the equilibrium surface, grows exponentially when $F(R)$ departs significantly from $Z = 0$. This is the case of low Bond numbers and small contact angles. In [315] it is stated that for contact angles lower than 15° in the case of free-edge condition ($\Gamma = 0$) or lower than 60° for the stuck-edge condition ($\Gamma \rightarrow \infty$) the system may become numerically ill-conditioned. Furthermore, the comparison between this method and a finite differences approach showed significant divergences in the shape of the eigenfunctions $\Phi^{(n)}$ for particular cases.

A possible solution would be finding a set of primitive functions without exponential terms. To the best knowledge of the authors, and considering the attempts made in Ref. 306, an alternative has not yet been proposed. It should also be noted that the magnetic force generally flattens the equilibrium surface, hence mitigating the effect of the exponential term in Eq. 7.38a.

7.4.6 Finite differences method

As previously mentioned, the system defined by Eq. 7.30 can also be solved numerically, as done in the 1960s with the non-magnetic problem using a finite differences approach [313, 314]. This overcomes the difficulties associated with the definition of appropriate primitive functions in the Ritz method.

In order to verify the implementation of Sec. 7.4.5, the numerical approach introduced in Ref. 108 to simulate the nonlinear dynamics and linear stability of capillary fluid systems is adopted in Ref. 316 to study a ferrofluid surface in a cylindrical tank taking the magnetic Bond number and the meniscus profile

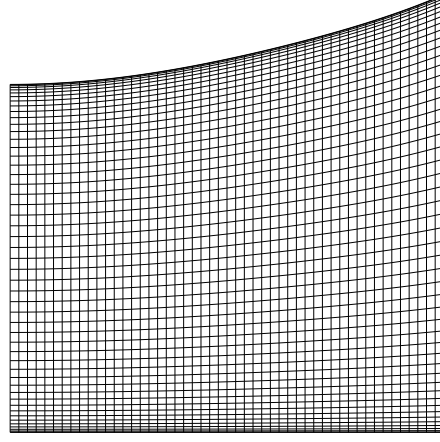


Figure 7.2: Mesh employed to discretize a ferrofluid interface in a cylindrical tank using the finite differences solution procedure.

as inputs. The spatial physical domain is mapped onto a rectangular computational domain by means of a nonsingular mapping. Figure 7.2 shows the mesh produced by this procedure for a particular configuration of interest. The system defined by Eq. 7.26 is discretized using Chebyshev spectral collocation points. The temporal derivatives for the perturbations in h and ϕ are computed assuming an oscillatory behavior of the type $e^{i\omega t}$, with ω being the natural frequency. The generalized eigenvalue problem resulting from the spatial and temporal discretization is finally solved using MATLAB's `EIG` function, returning the different modes of oscillation. For the case under analysis in Ref. 316, the eigenvalues obtained with both methods differ by at most a 0.5%, verifying the implementation of the solve.

7.4.7 Limitations

Although the modal analysis procedure presented in this section is particularly efficient with respect to coupled magnetohydrodynamic simulations, the reader should note that the linearization performed in Sec. 7.4.2 is done for constant magnetic and magnetization fields. In other words, a zero-order approximation to the magnetic field variation with the oscillation of the ferrofluid interface is assumed. The next two chapters will show the impact of this apparently innocent assumption and how fully coupled frameworks, like the one presented in Chapter 10, perform in comparison.

Chapter 8

Bubble dynamics

Gas bubbles are the elemental multiphase flow unit and can be found in virtually all liquid systems in space, ranging from life support to spacecraft propulsion. A vast body of literature has explored their behavior on Earth, unveiling a plethora of phenomena of scientific and technical interest [317]. Even though the models for the equilibrium, stability, and modal response of magnetic liquid interfaces described in Chapter 7 are fully applicable to gas bubbles in liquids, specific features are here addressed.

The evolution of an isolated gas bubble subject to an inhomogeneous magnetic field in low-gravity can be studied as a four-step process, represented in Fig. 8.1: nucleation, growth, detachment, and displacement. The magnetic force does not directly impact the mass balance during the nucleation phase, but the same cannot be said about the rest. Although realistic applications (e.g. low-gravity electrolysis, see Chapter 14) lead to far more complex interactions [216–219], the tools here introduced are still useful to draw fundamental conclusions. A comprehensive chemical analysis of the bubble nucleation process can be found in Ref. 318.

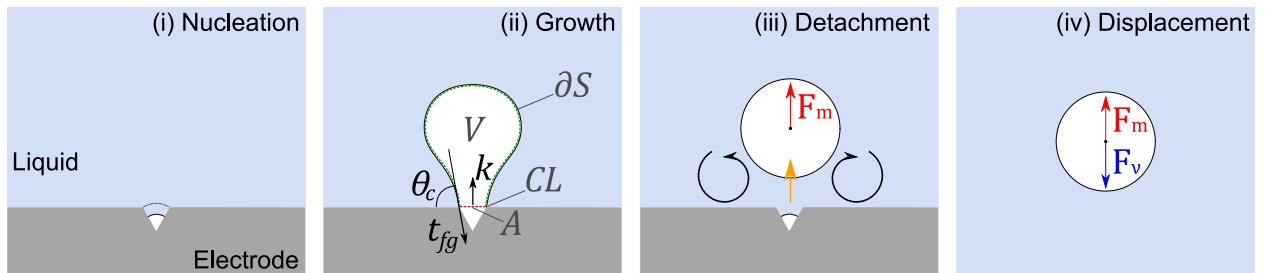


Figure 8.1: Conceptual stages of single bubble evolution when subject to an inhomogeneous magnetic field in microgravity. Detachment occurs when the vertical momentum balance is no longer satisfied, inducing a microconvection flow in the surrounding liquid. The bubble subsequently accelerates until viscous drag F_v compensates the magnetic buoyancy force, reaching the terminal velocity.

8.1 Effective total force

Due to its technical relevance, it is important to clarify how magnetic polarization forces act on a magnetic body (b) immersed in a magnetic environment (me). As shown in Ref. 77, different equivalent formulations can be employed to compute the total magnetic force experienced by such body. One of the most common procedures consists on integrating the volume and surface magnetic force densities as

$$\mathbf{F}_m^{\text{eff}} = \int_V dV \mathbf{f}_m^{V,\text{eff}} + \oint_{\partial V} dS \mathbf{f}_m^S, \quad (8.1)$$

where V and ∂V denote the volume and surface of the body, respectively. Assuming the magnetic polarization forces introduced in Sec. 6.1 and Appendix A, the surface force distribution in ∂V becomes

$$\mathbf{f}_m^S = \frac{\mu_0}{2} (M_{n,b}^2 - M_{n,me}^2) \mathbf{n} \quad (8.2)$$

with \mathbf{n} being the external normal of the body surface ∂V . The *effective* volume force distribution in V is

$$\mathbf{f}_m^{V,\text{eff}} = \mu_0 (\chi_b^{\text{vol}} H \nabla H - \chi_{me}^{\text{vol}} \overline{H} \nabla \overline{H}), \quad (8.3)$$

where \overline{H} is the *virtual* magnetic field that would be present if the volume V was occupied by the environment. The same expression can be obtained by applying the Archimedes' principle.

If the system is in thermodynamic equilibrium, the total force can be also computed by integrating the magnetic stress force in the external contour ∂V^+ [77]. Taking again into account the Archimedes' principle, the effective magnetic force acting on the body can be formulated as

$$\mathbf{F}_m^{\text{eff}} = \oint_{\partial V} dS \mathbf{n} \cdot [\mathbf{T}_m^+ - (\overline{\mathbf{T}}_m)^+], \quad (8.4)$$

where \mathbf{T}_m^+ is the magnetic stress tensor in the external contour ∂V^+ when the volume V is occupied by the medium b , and $(\overline{\mathbf{T}}_m)^+$ is the magnetic stress tensor at the same points computed as if the volume V was part of the environment.

A third equivalent formulation of the effective magnetic force can be obtained by applying the Principle of Virtual Works to the free energy variation of a magnetizable medium caused by changes in the applied magnetic field \mathbf{H}_0 . The result is a well-known expression [62, 77, 301] that modified as before results in

$$\mathbf{F}_m^{\text{eff}} = \mu_0 \int_V dV [(\chi_b^{\text{vol}} \mathbf{H} - \chi_{me}^{\text{vol}} \overline{\mathbf{H}}) \cdot \nabla] \mathbf{H}_0. \quad (8.5)$$

These force formulations represent the Archimedes' principle for the magnetic component of the external fields. The effective inertial forces can be obtained by following the same procedure, giving

$$\mathbf{F}_{\text{in}}^{\text{eff}} = \int_V dV (\rho_b - \rho_{me}) \mathbf{g}. \quad (8.6)$$

These expressions can be particularized for the case of a bubble (non-magnetic body, magnetic environment) or a droplet (magnetic body, non-magnetic environment). The next sections focus on the former.

8.2 Growth

The quasi-static momentum balance is one of the fundamental and most widely extended tools to study bubble growth. Following Fig. 8.1, the problem under study considers a magnetic fluid environment (f) with density ρ_f and a body consisting on a single gas bubble (g) with volume V , density ρ_g , and liquid-gas surface tension σ . The bubble is sitting on an horizontal surface with apparent contact angle θ_c while subject to an inertial acceleration \mathbf{g} . In the absence of dynamic forces, the momentum balance can be obtained as done in Ref. 134 for the electric polarization force, resulting in

$$\int_V dV \rho_g \mathbf{g} + \int_{CL} dL \sigma \mathbf{t}_{fg} + \oint_{\partial V} dS \mathbf{n} \cdot \mathcal{T}_p^+ + \oint_{\partial V} dS \mathbf{n} \cdot \mathcal{T}_m^+ = 0, \quad (8.7)$$

where CL denotes the circular contact line of diameter D_0 and \mathbf{t}_{fg} is the tangent unit vector in the meridian plane, depicted in Fig. 8.1. The pressure and magnetic stress tensors are defined in Eq. 6.6. It should be noted that ∂V , that can be decomposed as a surface ∂S on the liquid face of the gas-liquid interface and surface A delimited by CL in the gas region, denotes a complete surface enclosing the pinned bubble volume V . The pressure term can be expanded as

$$\oint_{\partial V} dS \mathbf{n} \cdot \mathcal{T}_p^+ = - \oint_{\partial V} dS \bar{p}_f^* \mathbf{n} + \int_A dS (\bar{p}_f^* - p_g^*) \mathbf{n}, \quad (8.8)$$

with \bar{p}_f^* being the virtual composite pressure applied to the magnetic fluid if it occupied the bubble volume V (see Eq. 6.8). The term $(\bar{p}_f^* - p_g^*)$ is the virtual fluid overpressure with respect to the gas flow pressure evaluated at the plane A . In quasi-static conditions, the first term in the right equals the inertial and magnetic flotability forces acting on the bubble, and Eq. 8.7 can be reformulated as

$$\int_{CL} dL \sigma \mathbf{t}_{fg} + \int_A dS (\bar{p}_f^* - p_g^*) \mathbf{n} + \mathbf{F}_{\text{in}}^{\text{eff}} + \mathbf{F}_m^{\text{eff}} = 0, \quad (8.9)$$

where $\mathbf{F}_m^{\text{eff}}$ is given by Eq. 8.4 or, equivalently, Eqs. 8.1 or 8.5, and $\mathbf{F}_{\text{in}}^{\text{eff}}$ is defined by Eq. 8.6. For practical purposes, it is useful to project Eq. 8.9 on an axis \mathbf{k} perpendicular to A , which results in

$$F_b + F_p + F_\sigma + F_m = 0, \quad (8.10)$$

with the buoyancy, internal overpressure, surface tension, and magnetic forces being given by

$$F_b = \mathbf{k} \cdot \mathbf{F}_{\text{in}}^{\text{eff}} \approx V (\rho_g - \rho_f) \mathbf{k} \cdot \mathbf{g}, \quad (8.11)$$

$$F_p = \frac{\pi D_0^2}{4} (p_g^* - \bar{p}_f^*), \quad (8.12)$$

$$F_\sigma = \int_{CL} dL \sigma \mathbf{k} \cdot \mathbf{t}_{fg} \approx -\pi D_0 \sigma \sin \theta_c, \quad (8.13)$$

$$F_m = \mathbf{k} \cdot \mathbf{F}_m^{\text{eff}}, \quad (8.14)$$

and where uniform fluid density and overpressure on A have been assumed. For gas bubbles in diamagnetic media, which exhibit susceptibilities of the order of $|\chi^{\text{vol}}| \approx 10^{-6}$, the magnetic fields in Eq. 8.5 can be approximated as $\mathbf{H}, \overline{\mathbf{H}} \approx \mathbf{H}_0$. The total force exerted on a small, spherical, gas bubble is then

$$\mathbf{F}_m^{\text{eff}} \approx \frac{2}{3} \pi R_b^3 \mu_0 \Delta \chi^{\text{vol}} \nabla H_0^2, \quad (8.15)$$

where R_b is the radius of the bubble and with $\Delta \chi^{\text{vol}} = \chi_b^{\text{vol}} - \chi_e^{\text{vol}}$ denoting the differential magnetic susceptibility between gas and the water environment. This approach has been employed in previous works on dielectric manipulation in low-gravity [73, 147]. The momentum balance may also consider a forced viscous shear flow by including the viscous stress tensor and its associated lift and drag expressions [319].

8.3 Detachment

The detachment of the bubble is produced when the balance of vertical forces cannot longer be satisfied with increasing volume [152]. In this context, the magnetic force F_m can be employed to accelerate the detachment process or, equivalently, reduce the critical bubble volume.

Alternative simplified expressions can be developed to estimate the bubble detachment radius. In boiling and heat transfer research, the maximum break-of diameter of a bubble on an upward facing surface

is usually estimated from Fritz's equation [320]

$$d_0 = 1.2\theta_c \sqrt{\frac{\sigma}{g(\rho_f - \rho_g)}}, \quad (8.16)$$

where θ_c is expressed in radians. If the bubble is sufficiently small, the magnetic force may be approximated by a constant, uniform field. The *magnetic Fritz equation* would then be rewritten as

$$d_0 = 1.2\theta_c \sqrt{\frac{\sigma}{f_m + g(\rho_f - \rho_g)}}, \quad (8.17)$$

with $f_m = F_m/V$ being the *overall* magnetic body force density (in N/m³). The departure diameter may deviate from this result due to the microconvection flow associated with the detachment process [320] and the interactions between adjacent bubbles [216, 217, 219].

8.4 Displacement

8.4.1 Dynamic regime

The displacement of bubbles in liquids has historically raised significant attention due to its importance for a wide range of industrial applications. The problem is severely complicated by factors like the bubble radius, shape, and formation method or the liquid purity, viscosity, temperature, and pressure [321]. In spite of this inherent complexity, three distinct dynamic regimes can be observed: viscosity-dominated, surface-tension-dominated, and inertia-dominated [317, 322, 323]. The dynamic regime of a given bubble is determined by the balance between fundamental forces. The Weber number

$$We = \frac{\rho_f V^2 (2R_b)}{\sigma} \quad (8.18)$$

reflects the ratio between Laplace (surface-tension-induced) and inertial pressures. This ratio is much smaller than one for the radii and velocities covered in this work, indicating that bubbles remain almost perfectly spherical. On the other hand, the Reynolds number

$$Re = \frac{\rho_f V (2R_b)}{\eta}, \quad (8.19)$$

where η is the dynamic viscosity of the liquid, describes the ratio of inertial to viscous forces and is usually kept below 100 in unforced low-gravity flows. The combination of low We and moderate Re numbers results

in spherical bubbles with no-zigzag motions. Therefore, due to the weakness of the diamagnetic force and the overwhelming role of surface tension, the case of a free-floating air bubble subject to the influence of a magnet in microgravity falls within the viscosity-dominated bubble displacement regime. In terms of fluid motion, the flow remains attached to the bubble until $Re \approx 20$, where it is separated at the rear stagnation point and a steady wake region is generated until $Re \approx 130$ [317].

8.4.2 Bubble force balance

In the dynamic regime described in Sec. 8.4.1, the movement of a spherical bubble in a liquid is described by the balance

$$m'_b \frac{d^2 \mathbf{x}}{dt^2} = \mathbf{F}_m^{\text{eff}} + \mathbf{F}_d + \mathbf{F}_h, \quad (8.20)$$

with $m'_b = (4/3)\pi R^3(\rho_g + 0.5\rho_l)$ being the virtual mass (that accounts for the surrounding fluid accelerated by the bubble [324]), ρ_g the gas density, \mathbf{x} the position of the bubble, $\mathbf{F}_m^{\text{eff}}$ the magnetic polarization force, \mathbf{F}_d the viscous drag, and \mathbf{F}_h the history (or Basset) force [325]. If a rigid sphere is considered, the Stokes law predicts the drag force [326]

$$\mathbf{F}_d = -6\pi R\eta(d\mathbf{x}/dt), \quad (8.21)$$

which is appropriate in virtually every technical application where the liquid is exposed to impurities and the so-called “Marangoni” effect blocks the bubble surface movement. In particular, water is extremely sensitive to surface contamination [327, 328], and even the contact with the atmosphere can immobilize its surface [329]. Pure liquids exhibit a mobile interface that promotes the circulation of air inside the bubble. In these cases, the Hadamard-Rybczynski drag force [330, 331]

$$\mathbf{F}_d = -4\pi R\eta(d\mathbf{x}/dt), \quad (8.22)$$

validated on Earth using ultra-clean systems [329, 332], should be employed instead. Intermediate formulations with partially mobile surfaces have also been proposed [333].

Both the Hadamard-Rybczynski and Stokes laws neglect the convective terms of the Navier-Stokes equations. Therefore, they are only valid under the Stokes flow approximation ($Re < 1$). For higher Reynolds

numbers, most results are based on experimental or numerical works where the drag force module

$$\mathbf{F}_d = -\frac{1}{2}\rho_l V^2 A C_D \frac{d\mathbf{x}/dt}{\|d\mathbf{x}/dt\|} \quad (8.23)$$

is defined by means of the drag coefficient C_D , with $A = \pi R^2$ being the reference area of the spherical bubble [317].

8.4.3 Terminal velocity

The magnetic terminal velocity is obtained after assuming a steady-state behavior in Eq. 8.20, resulting in [3]

$$v_t \approx \frac{\mu_0 R^2}{9\eta} \Delta\chi^{\text{vol}} |\nabla H_0^2|, \quad Re < 1. \quad (8.24)$$

for a Stokes flow. For higher Reynolds numbers, the drag force defined by Eq. 8.23 must be employed instead. Numerous correlations have been proposed for the range $Re \in [0.01, 100]$, one of the simplest being given by Rumpf

$$C_D = \kappa + \frac{24}{Re}, \quad (8.25)$$

where $\kappa = 2$ for $Re \in [0.01, 10]$ ($\pm 5\%$ error) and $\kappa = 1$ for $Re \in [10, 100]$ ($\pm 20\%$ error) [317]. Although more accurate formulations have been derived [317, 334], this one allows the derivation of a closed-form terminal velocity

$$v_t \approx \frac{-9\eta + \sqrt{3}\sqrt{\kappa\mu_0\rho_l R^3 \Delta\chi^{\text{vol}} |\nabla H_0^2| + 27\eta^2}}{(3/2)R\kappa\rho_l} \quad (8.26)$$

that can be useful for first-order bubble velocity estimations. It is important to emphasize that both Eq. 8.24 and Eq. 8.26 are only valid for steady-state systems. However, the inhomogeneity of the magnetic force and the short duration of diamagnetic-dominated transfers prevent bubbles from reaching their terminal velocity. Still, this value can be employed as an upper speed limit.

8.5 Application to liquid droplets

As pointed out in Sec. 8.1, the expressions derived in this chapter for the growth, detachment, and displacement of bubbles in liquids are fully applicable to the problem of a liquid droplet immersed in a gas. In this case, the condensation of liquids over nucleation surfaces becomes the focus of interest. A key

difference is that liquid droplets experience very small drag forces while they displace at low speeds in a gas, rendering the concept of terminal velocity useless for most applications. Instead, the total force acting on the droplet and its free-floating kinematic analysis acquire a particularly relevant role in technical settings like those covered in Chapters 12 and 13.

The total force acting on the droplet can be computed from Eq. 8.1 or any of its equivalent forms in Sec. 8.1. Newton's second law is then applied to derive the velocity and displacement of the droplet under appropriate magnetic modeling assumptions (see e.g. Ref. 77). However, in order to obtain analytical closed-form results, the simplified problem of a perfectly spherical liquid droplet moving along the symmetry axis of an axisymmetric coil or magnet in a non-magnetic gas is subsequently studied. The droplet is small in comparison with the variation of the magnetic field and exhibits linear magnetization with susceptibility $\chi_b \ll 1$. A soft magnetic liquid with collinear external, internal, and magnetization fields is considered and magnetic surface force terms are neglected. In this simplified framework, the magnetic field generated by a circular coil with n turns, radius R , and current intensity I at a distance z along the symmetry axis \mathbf{e}_z is

$$\mathbf{B} = \mu_0 \frac{InR^2}{2(z^2 + R^2)^{3/2}} \mathbf{e}_z. \quad (8.27)$$

From Eq. 8.1, and noting the collinearity between magnetization and magnetic fields and the negligible role of surface force component (caused by the small magnetic susceptibility $\chi_b \ll 1$), the total force per unit volume induced by the coil on an infinitesimal liquid droplet located in the symmetry axis is

$$\mathbf{F}_m \approx \mu_0 M \frac{\partial H}{\partial z} \mathbf{e}_z. \quad (8.28)$$

Making again use of the assumption $\chi_b \ll 1$, the magnetic flux density due to the immanation of the ferrofluid can be considered negligible, and hence $\mathbf{B} \approx \mu_0 \mathbf{H}_0$ inside the droplet, with \mathbf{H}_0 being the magnetic field in the absence of the droplet. The internal magnetic field can then be approximated as $\mathbf{H} \approx \mathbf{H}_0$. Assuming a linear magnetization curve, where $\mathbf{M} = \chi_b \mathbf{H}$, a simplified expression for the total force is obtained as

$$\mathbf{F}_m \approx \mu_0 \chi_b H_0 \frac{\partial H_0}{\partial z} \mathbf{e}_z, \quad (8.29)$$

but since $\mathbf{H}_0 \approx \mathbf{B}/\mu_0$, the consideration of Eq. 8.27 in Eq. 8.29 results in

$$\mathbf{F}_m \approx -\frac{3\mu_0 \chi (nI)^2 R^4}{4} \frac{z}{(R^2 + z^2)^4} \mathbf{e}_z. \quad (8.30)$$

This expression can be applied to axially magnetized cylindrical magnets with magnetization M_m , radius R and height l by employing an equivalent circular loop with the same radius and current intensity $I = M_m l$.

The simplicity of Eq. 8.30 enables the derivation of a quasi-analytical expression for the time of flight of the droplet. After considering Newton's second law and solving the resulting second-order differential equation with initial position $z(0) = L$ and velocity $\dot{z}(0) = 0$, the duration of the flight becomes

$$t_f(L) = \sqrt{\frac{4\pi\rho_l}{\mu_0\chi(nI)^2 R^4}} \cdot \int_0^L \left[\frac{1}{(z^2 + R^2)^3} - \frac{1}{(L^2 + R^2)^3} \right]^{-1/2} dz, \quad (8.31)$$

where it should be noted that t_f is inversely proportional to nI (or, if a magnet is employed, to $M_m l_m$).

8.6 Collaborators

Many of the magnetic formulations introduced in this chapter were obtained in collaboration with Prof. Gabriel Cano-Gómez, to whom the author expresses his most sincere gratitude.

Chapter 9

Experimental validation

The analytical formulations for the equilibrium, stability, and dynamic response of axisymmetric ferrohydrodynamic interfaces presented in Chapters 7 and 8 involve a number of assumptions that require validation with relevant experimental results. This process must necessarily involve coupled ferrohydrodynamic setups where both surface tension and magnetic forces are relevant (i.e. $Bo \approx 0$, $Bo_{\text{mag}} \approx 1$). Experiments satisfying these characteristics were almost non-existent at the time of starting this thesis. In order to cover this fundamental gap, the European Space Agency (ESA) *Drop Your Thesis!* 2017 *The Ferros* experiment [172, 173] studied the axisymmetric oscillations of water-based ferrofluids in cylindrical tanks when subject to an inhomogeneous magnetic field in microgravity. Lateral oscillations, which have an intrinsic technical value as main sources of attitude disturbances, were explored in the United Nations Office for Outer Space Affairs (UNOOSA) *DropTES* 2019 StELIUM project, whose design is comprehensively described in Refs. 174, 175, and 176.

This chapter summarizes the design and main results of the aforementioned experiments, that helped validate the analytical results derived in Chapter 7 and motivated the development of the numerical interface-tracking simulation framework described in Chapter 10. A brief description of the drop tower of the Center of Applied Space Technology and Microgravity (ZARM), which was thoroughly employed in this work, is also provided.

9.1 ZARM's drop tower

ZARM's drop tower, pictured in Fig. 9.1, is a vacuum-chamber-type microgravity tower located in Bremen, Germany, that provides a gravity residual of approximately $10^{-6}g_0$ for 4.7 s or 9.3 s. This quality level is comparable to on-orbit platforms, which makes it ideal for fundamental physics experiments. The tower features a 120 m vacuum chamber and operates with drop and catapult modes. In the former, the capsule is released from the top providing 4.74 s of microgravity conditions and experiencing a deceleration of approximately $50 g_0$ at the end of the flight. The catapult mode, available since 2007, launches the capsule vertically from the bottom of the tower extending the flight duration to 9.3 seconds. The capsule and its enclosed experiment experience an acceleration of up to $50 g_0$ before the experiment begins. The acceleration profile of both modes is shown in Fig. 9.2. Each launch takes 2 – 3 h and includes the capsule loading, pumping down, experimental, venting, and capsule retrieval phases, allowing for 2-3 drops per working day. Due to its extended microgravity period, the catapult mode was selected for the experiments described in this chapter. However, the drop mode is employed in Chapter 11.

The catapult capsule allows a maximum payload weight of 165 kg and a cylindrical payload volume

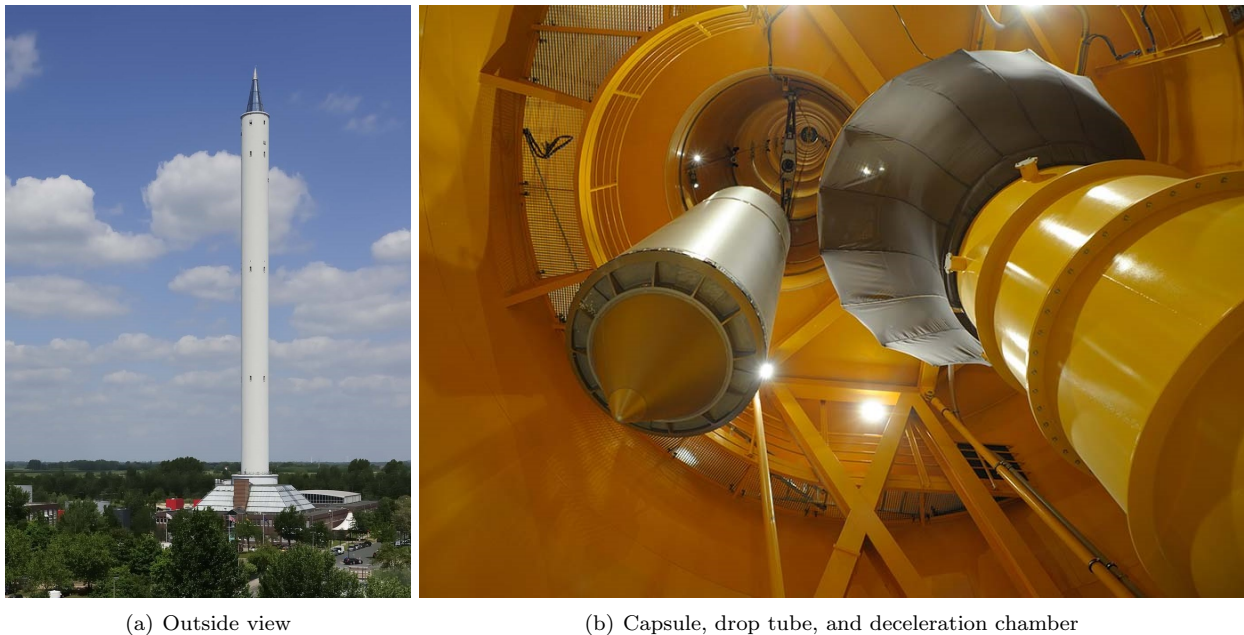


Figure 9.1: ZARM's drop tower.

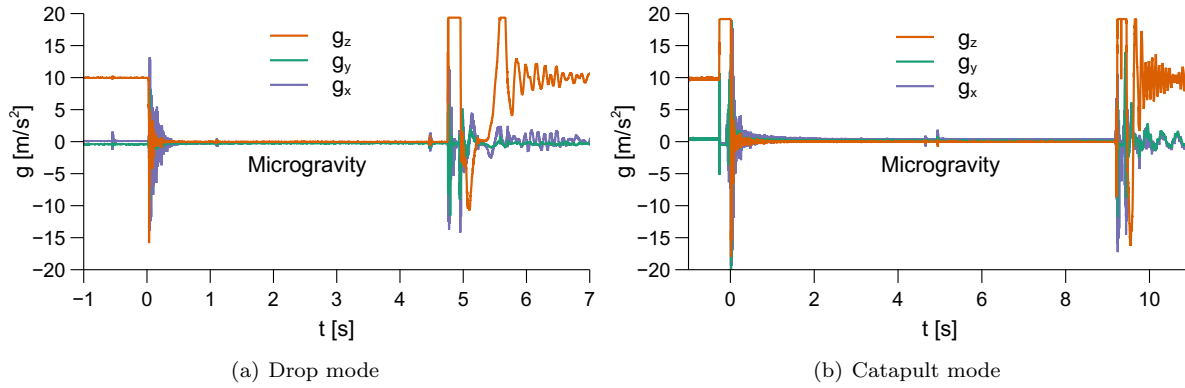


Figure 9.2: Acceleration profile of ZARM's drop tower drop and catapult capsules. Disturbances during the microgravity window are caused by the payload.

with 600 mm diameter and 953 mm height. The system is monitored and automated by the Capsule Control System (CCS), which is connected to an external control room through radio telemetry and telecommand. To ease integration, experiments are mounted on standardized platforms and kept at ambient pressure throughout the drop. Further specifications can be found at ZARM's Drop Tower User Manual [335].

9.2 Axisymmetric free surface oscillations

9.2.1 The ESA *Drop Your Thesis! 2017 - The Ferros* project

Axisymmetric oscillations, although less technically relevant than lateral oscillations, were first studied during the ESA *Drop Your Thesis! 2017 The Ferros* experiment. This decision was aimed at reducing the complexity and sources of uncertainty of the experiment. This data is relevant for the validation of several results presented in Chapter 7. The project team was led by the author, completed with Mr. Tim Hermans and Ms. Lidia Parrilla Benítez, and coordinated by Prof. Elena Castro-Hernández at the University of Seville. It counted with the external support from Prof. Gabriel Cano-Gómez and Prof. Miguel Herrada. The author thanks all of them for their contributions to the project. This section provides a brief description of the experiment and its main results.

9.2.2 Experimental setup

The experimental setup, represented in Fig. 9.3, is composed of mobile and fixed structures. The former slides over the latter by means of two linear actuators, and holds two identical assemblies with equivalent experiments separated 368 mm. Each assembly includes a cylindrical vessel that holds the liquid while a $N = 200$ turns copper coil with 94.25 mm mean radius imposes a static magnetic field. The coils resistance at ambient temperature is approximately $0.86 \, \Omega$. Despite having a high thermal inertia, the temperature of the coils increases during operation, modifying the resistivity of copper. A PicoLAS LDP-CW 120-40 constant current power source is employed to fix the magnetic field intensity for each experiment after wiring the coils in series. Axisymmetric free surface oscillations are first induced by ZARM's drop tower catapult, that launches the experiment from the bottom of the facility, and then by a percussion mechanism that displaces the mobile structure along the rails following a sinusoidal profile 4.5 s after launch. The oscillations of the center of the fluid surface are recorded by a visualization system located on top of each container.

Both transparent Plexiglas cylindrical tanks, depicted with relevant variables in Fig. 9.4 as a par-

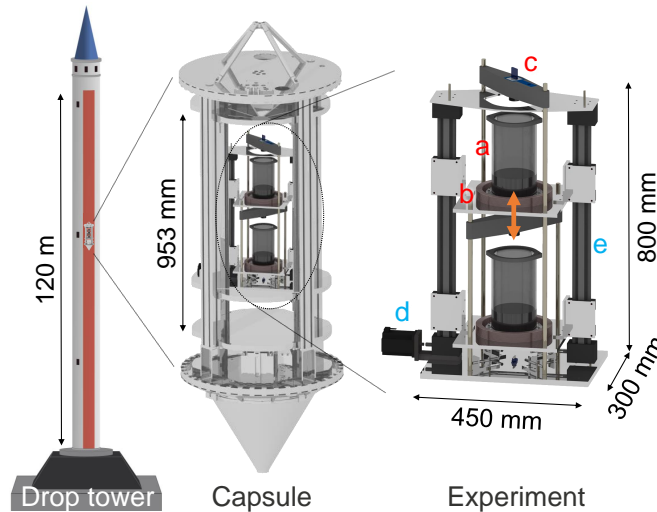


Figure 9.3: From left to right, ZARM's drop tower, drop capsule, and setup of the ESA *Drop Your Thesis! 2017 The Ferros* experiment [3]. The setup has a mobile structure (red labels) with two identical assemblies that include (a) cylindrical ferrofluid containers, (b) magnetic coils, and (c) detection systems. The structure slides over a fixed frame (blue labels) with (d) a stepper engine actuator, and (e) two linear modules, as indicated by the orange arrow.

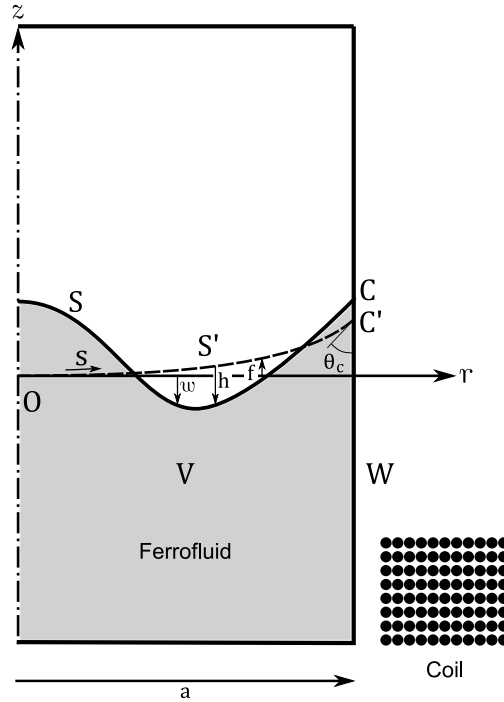


Figure 9.4: Geometry of the ESA *Drop Your Thesis! 2017 The Ferros* liquid tank.

ticularization of Fig. 7.1, have an inner diameter of 11 cm, a height of 20 cm, and are filled up to 5 cm with 475 ml of a 1:10 water solution of the commercial Ferrotec EMG-700 ferrofluid. In order to minimize the visualization issues reported in Ref. 163, the inner surface of the container is treated with Aquapel, a hydrophobic treatment that minimizes stains. Further technical details on the experimental setup can be found in Refs. 173 and 316.

9.2.3 Visualization system

The visualization system consists of a monoscopic fringe reflectometric device and a series of lateral visualization cameras. The former include a Photron Fastcam MC2-10K camera with a SKR KMP-IR CINEGON 8 mm lens located 20 cm above the surface of the fluid and a Picotronic DD635-5-24(16×62)-DOE laser projector. The camera works at 60 fps, a shutter speed of 1/60 s, and a resolution of 512×512 px^2 , and is placed in the symmetry axis of the vessel. The laser projects a pattern of parallel lines over the ferrofluid surface with an inclination of $\alpha = 14^\circ$ with respect to the vertical. The deformation of the ferrofluid surface is perceived in the image plane as a lateral displacement of the laser lines. The system exhibits an

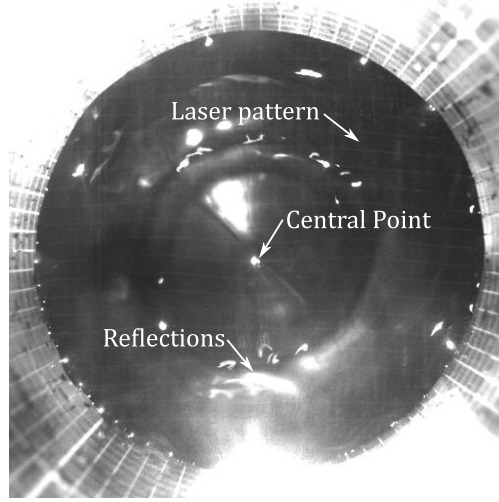


Figure 9.5: Frame of one of the video records. The central point, laser pattern lines and light reflections can be observed.

ideal accuracy of ± 0.9 mm.

The equivalence between in-plane (d_p [px]) and vertical (d_V [mm]) laser displacement is obtained from a simplified pinhole model that neglects the intrinsic non-linear deformation produced by the camera, following

$$d_V = \frac{k d_p}{\tan \alpha + \tan \beta}, \quad (9.1)$$

where $k = 110/430$ mm/px is the horizontal equivalence at the ferrofluid surface and β is the tilting angle of the visual line with respect to the camera axis. In this way, the central pixel has a $\beta = 0^\circ$, while the ones at the top border of the image are associated with $\beta = FOV/2$, with FOV being the field of view of the camera.

Due to strong light reflections, the analysis is limited to the brighter central point and line, depicted in Fig. 9.5. While the point is used to obtain the fundamental and second oscillation frequencies, the line allows computing the axisymmetric equilibrium surface profile $F(R)$, and hence the wall contact angle in microgravity conditions θ_c . The central laser point is selected to perform the modal analysis, as it remains unaffected by residual lateral oscillations. The equilibrium surface is measured 4 seconds after launch, just before the application of the artificial percussion. A semi-automatic image analysis algorithm is employed to extract the position of the laser line in the image plane.

Two measurements, associated with the oscillations induced by catapult and percussion, are obtained per container and drop, but only one is available for $I = 21.3$ A due to a malfunction of the percussion mechanism. A Fast Fourier Transform is applied on the time domain curve to determine the fundamental and second frequency peaks for each case.

9.2.4 Liquid properties

The magnetization curve of the ferrofluid solutions, that determine their magnetic response, were measured after the experimental campaign with a MicroSense EZ-9 Vibrating Sample Magnetometer. Figure 9.6 represents their magnetization curve, characterized by an initial susceptibility $\chi = 0.181$ and saturation magnetization $M_s = 3160 \pm 100$ A/m. The curve is fitted with a function of the form

$$M(H) = \frac{2}{\pi} [a_M \arctan(c_M H) + b_M \arctan(d_M H)], \quad (9.2)$$

where $a_M = 459.70$ A/m, $\kappa_2 = 2747.15$ A/m, $\kappa_3 = 5.73 \cdot 10^{-6}$ m/A and $\kappa_4 = 1.03 \cdot 10^{-4}$ m/A.

Additional properties of the solution are reported in Table 9.1.

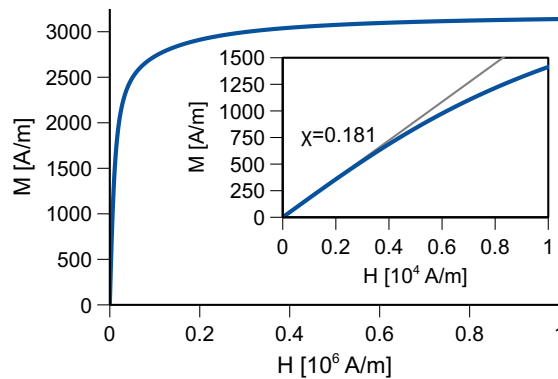


Figure 9.6: Measured magnetization curve of the 1:10 vol EMG-700 ferrofluid solution.

Table 9.1: Physical properties of the ferrofluid solution employed in the ESA *Drop Your Thesis!* 2017 experiment with their standard deviations [3].

Tank	ρ (g/ml)	μ (cP)	σ (mN/m)	θ_c (°)
Upper	1.012 ± 0.008	1.445 ± 0.005	62.39 ± 1.02	67 ± 6
Lower	1.020 ± 0.002	1.448 ± 0.007	61.7 ± 0.95	55 ± 4

9.2.5 Operation

The setup was launched five times at ZARM's drop tower in November 2017 with varying current intensity, as shown in Table 9.2. The operation and characteristics of the facility can be found in Sec. 9.1.

Table 9.2: Current intensities for each drop.

Drop	1	2	3	4	5
I(A)	21.3	10.6	5.7	15.9	10.9

9.2.6 Results

Simulation results from the coupled free surface oscillations model introduced in Sec. 7.4 (abbreviated as *Cou.*) and an uncoupled framework (denoted by *Unc.*) where the magnetic field inside the ferrofluid is approximated as $\mathbf{H} \approx \mathbf{H}_0 - \mathbf{M}$ and \mathbf{H}_0 is computed analytically are subsequently analyzed and compared with experimental measurements for the upper and lower containers.

The first result of technical interest is the equilibrium free surface (or meniscus) profile $f(r)$, which is computed with the coupled magnetic model and shown in Fig. 9.7 for upper and lower containers. Due to the particular magnetic configuration and physical properties of each system, the free surfaces show qualitatively different responses to the magnetic interaction. However, they remain practically unaffected by the external

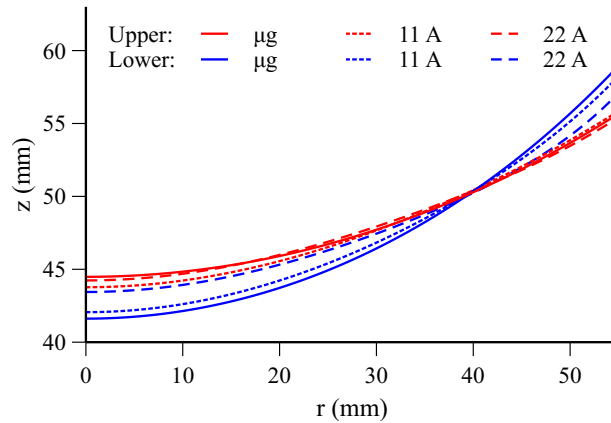


Figure 9.7: Theoretical meniscus profile for upper (red) and lower (blue) containers for 0, 11, and 22 A computed using the coupled equilibrium model (Sec. 7.2).

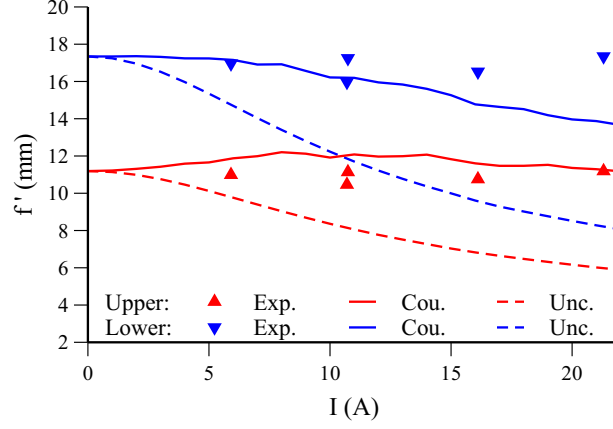


Figure 9.8: Experimental vertex to border vertical distance f' as a function of current intensity I , measured 4 seconds after launch and comparison with coupled (solid) and uncoupled (dashed) theoretical frameworks. The measurements have a resolution of ± 1.8 mm.

magnetic field. This motivates the employment of the relative height f' between the static contact line C' and vertex O as a metric to validate the magnetic free surface predictions.

As described in Sec. 9.2.3, the experimental meniscus is computed from the deformation of the central laser line 4 seconds after launch. The relative height f' is measured and compared with the theoretical models in Fig. 9.8. Due to the limited number of launch opportunities, only 5 experimental data points are available. Each point is subject to the $\pm 2 \times 0.9$ mm pixel resolution of the detection system. Additional sources of error affect the value of f' , but can only be quantified by analyzing repeated experiments. Although at least 3 points would be needed to reach a minimum statistical significance at each current level, the comparison between experimental and theoretical linear slopes is still indicative of the magnetic response of each theoretical framework. This statistic follows a t-student distribution with 3 degrees of freedom, which enables a more robust analysis than individual data points. For the upper container, the linear regression of the experimental points has a slope of $1.29 \cdot 10^{-5}$ mm/A with $[-0.78 \cdot 10^{-4}, 1.03 \cdot 10^{-4}]$ mm/A 95% confidence interval (CI). If the coupled model was assumed to be correct, the resulting measurements would exhibit a linear slope of $-4.78 \cdot 10^{-5}$ mm/A, which falls within the CI. The uncoupled model slope, on the contrary, would be $-2.4 \cdot 10^{-4}$ mm/A, which falls outside the CI. In the lower container, the experimental slope is $2.45 \cdot 10^{-5}$ mm/A with $[-1.46 \cdot 10^{-4}, 1.95 \cdot 10^{-4}]$ mm/A 95% CI, and the coupled model would give $-2.25 \cdot 10^{-4}$ mm/A (outside the CI) while the uncoupled model would return an even more negative slope

of $-4.17 \cdot 10^{-4}$ mm/A (outside the CI). Although these results should be taken with caution due to the limitations of the experimental dataset, the analysis and Fig. 9.8 itself indicate that the uncoupled model performs worse than the coupled framework and that it is unable to predict the deformation of the magnetic meniscus.

The divergence in the predictions from both theoretical models is associated with the characteristics of their magnetic frameworks. The magnetic Bond number at the interface, represented in Fig. 9.9 for a range of current intensities, shows how each model leads to very different magnetic interactions, highlighting the importance of using an appropriate magnetic model for the system under study.

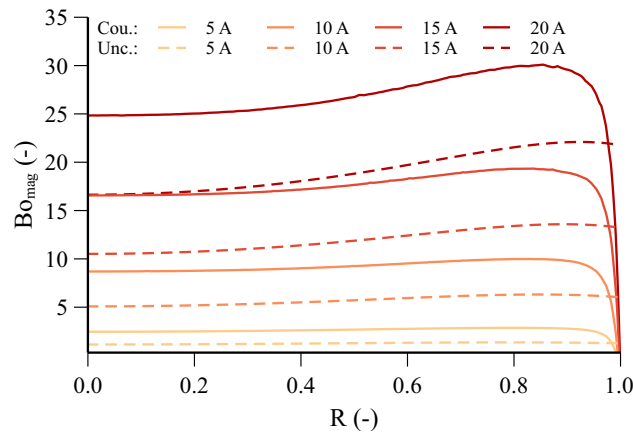


Figure 9.9: Magnetic Bond number Bo_{mag} at the meniscus as a function of the dimensionless radius and coils current intensity for coupled (solid) and uncoupled (dashed) magnetic models.

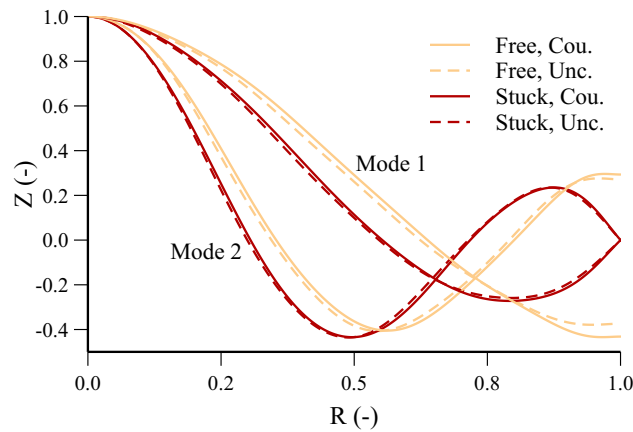


Figure 9.10: Normalized first and second axisymmetric modes as a function of the dimensionless radius R for the free (light) and stuck (dark) edge conditions, the coupled (solid) and uncoupled (dashed) physical models, and $I = 20$ A.

Further results of interest relate to the modal shapes and frequencies of the free surface oscillations problem. Figure 9.10 represents the first two theoretical axisymmetric modes for the free ($\gamma = 0$) and stuck ($\gamma \rightarrow \infty$) edge conditions, and the coupled and uncoupled magnetic models. The hysteresis parameter γ determines the slope of each mode at the wall by following Eq. 7.30e, as observed at $R = 1$. Modal shapes do not diverge significantly between magnetic frameworks, with the observed differences being explained by the different distributions of the Bo_{mag} number reported in Fig. 9.9. Although the $I = 20$ A case is depicted, it should be noted that the magnetic interaction has a marginal effect on the eigenmodes of the system, and so the $I = 0$ A and $I = 20$ A modal shapes are almost identical [16].

The movement of the center of the ferrofluid surface, whose vertical position is computed as described in Sec. 9.2.3, is employed to study the evolution of the axisymmetric modes. Figure 9.11 depicts the fundamental oscillation frequency of this point as a function of current intensity. Experimental measurements are taken from the upper and lower vessels, and are generated by ZARM's drop tower catapult (*Cat.*) or the percussion mechanism (*Per.*). The first sinusoidal wave period is discarded in the analysis to respect the

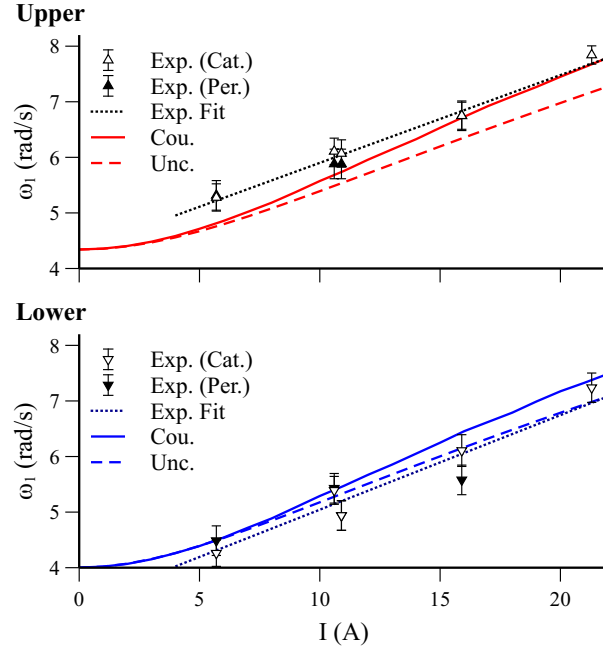


Figure 9.11: Fundamental axisymmetric oscillation frequency for experimental (Exp.), coupled model (solid), and uncoupled model (dashed) values as a function of coils current intensity for upper and lower containers. The error bars denote the standard deviation of the measurements, to which a linear regression (dotted) is superposed. The free edge condition is assumed in the computations.

small displacements assumption of the magnetic sloshing model. Error bands are built by identifying the FFT resolution with the $\pm 3\sigma$ Gaussian interval, and linear regressions of the measurements are fitted for upper and lower tanks. Those fits are shifted by a constant frequency of ≈ 0.9 rad/s, reflecting the small differences in the non-magnetic physical parameters reported in Table 9.1, and possibly others (e.g. filling ratio). Theoretical predictions from the coupled and uncoupled magnetic models are superposed assuming a free-edge condition. It should be noted that the stuck-edge condition produces higher oscillation frequencies, reaching 6.2 rad/s in the upper vessel for $I = 0$ A, which are not observed in the experiment.

Although the limited number of experimental data points limits the scope of the analysis, a good overall agreement between experimental and theoretical values is observed. The uncoupled theoretical model leads to important deviations for high current intensities with respect to the coupled framework due to the mid-range magnetic susceptibility of the ferrofluid solution ($\chi_{\text{ini}} = 0.18$). This behavior reflects the importance of the fluid-magnetic coupling. Experimental results show a slight frequency shift and a smaller slope with respect to the coupled magnetic model. While the first effect may be attributed to the accumulation of errors in the non-magnetic parameters of the system, such as the actual filling ratio or contact angle, the second depends mainly on the magnetic interaction and is hence of particular interest for this work. The experimental slope at the upper container is $0.158 \text{ rad s}^{-1} \text{ A}^{-1}$ with $[0.138, 0.178] \text{ rad s}^{-1} \text{ A}^{-1}$ 95% CI, that does not include the $0.187 \text{ rad s}^{-1} \text{ A}^{-1}$ slope of the coupled magnetic model. In the lower vessel, it results in $0.170 \text{ rad s}^{-1} \text{ A}^{-1}$ with $[0.121, 0.219] \text{ rad s}^{-1} \text{ A}^{-1}$ 95% CI, which includes the $0.186 \text{ rad s}^{-1} \text{ A}^{-1}$ theoretical value. This points out, at least for the upper container, to a significant statistical difference between experimental and theoretical slopes. Several reasons may be behind this divergence: (i) numerical errors in the computation of the theoretical solution, (ii) magnetically-induced viscosity effects, (iii) uncertainty in the determination of the magnetic parameters of the problem, (iv) violation of modeling assumptions, or (v) unmodeled physical effects. Ritz's solution to Eqs. 7.30a-e is verified with a variation of the numerical model presented in Chapter 10 with relative errors in the oscillation frequencies below 0.5% (more details in Ref. 316). The convergence of the underlying magnetic Finite-Elements Model is also confirmed in Appendix B. Liquid viscosity is commonly ignored in low-gravity fluid mechanics research due to its minimal impact on the free oscillation problem [86, 328], and although ferrofluids develop an inhomogeneous viscosity distribution in

the presence of magnetic fields and shear flows [20, 336], this effect is negligible for the concentrations and field intensities employed in this chapter. However, the damping ratios, reported in Table 9.3 and computed by means of the half-power bandwidth method as

$$\xi_n = \frac{1}{2} \frac{\Delta\omega_{-3dB}}{\omega_n}, \quad (9.3)$$

where ω_n is the natural frequency of mode n and $\Delta\omega_{-3dB}$ is the frequency width between the -3 dB points on the FFT spectrum, lead to an estimated viscosity-induced reduction of the natural frequencies of roughly a 1.5% (resulting from a factor $\sqrt{1 - \xi_1^2}$). The second axisymmetric mode has a smaller damping ratio than the first, as $\xi_n \propto \omega_n^{-1}$ and $\omega_2 \gg \omega_1$. In addition, the uncertainty of a $\pm 3\%$ in the saturation magnetization of the ferrofluid solution leads to a maximum error of a 1% in the fundamental frequency at $I = 20A$. These small contributions can explain up to 3% of the difference between experimental and theoretical slopes, but they still leave the theoretical value for the upper container outside the 95% CI of the experimental trend. The reason behind this divergence may be found in a potential violation of modeling assumptions. Issues related to the small displacements framework should be discarded after noting the overall excellent agreement between catapult (low-amplitude) and percussion (high-amplitude) frequencies in Fig. 9.11. Additional unmodeled physical effects may influence the free surface frequencies. For instance, a non-trivial dependence between γ and the magnetic field may be hypothesized. Noting that the theoretical results here presented consider a constant free-edge $\gamma = 0$ value for all current intensities, and that the stuck-edge ($\gamma \rightarrow \infty$) frequencies are much higher than their free-edge counterparts, unexpected variations in γ could potentially have a large impact in the results. This hypothesis will be studied in Sec. 9.3. However, the numerical simulations presented in Chapter 10 unveil an additional, fundamental, source of error: the assumption embedded in the analytical framework in Sec. 7.4 that the magnetic field does not change with the linear oscillations of the liquid. More details on this key aspect are given in Chapter 10.

Experimental observations are in better agreement with the trend of the uncoupled $I - \omega$ curve, that exhibits a slope of $0.160 \text{ rad s}^{-1}\text{A}^{-1}$ at the upper tank, and $0.170 \text{ rad s}^{-1}\text{A}^{-1}$ in the lower container (both within the experimental 95% CI). In spite of this apparently good result, the simplified model violates the magnetohydrodynamic coupling of the problem and is hence, by design, less accurate than the coupled frame-

Table 9.3: Damping ratios for the first two axisymmetric oscillation modes computed by means of the half-power bandwidth method. The uncertainty is represented by the standard deviation.

	ξ_1 (-)	ξ_2 (-)
Upper	0.138 ± 0.038	0.087 ± 0.035
Lower	0.171 ± 0.037	0.093 ± 0.040

work. The errors induced by this approximation seem to compensate the unmodeled effects hypothesized in the previous paragraph. Care should be taken when trying to extrapolate this result, as the compensation may not be reproduced by different systems.

Figure 9.12 depicts the second axisymmetric oscillation frequency as a function of current intensity for those cases where the second mode is observable. The amplitude of the second mode is much smaller than the first, and so harder to detect, but several measurements are still obtained. Experimental values show a slope of $0.136 \text{ rad s}^{-1} \text{ A}^{-1}$ with $[0.049, 0.222] \text{ rad s}^{-1} \text{ A}^{-1}$ 95% CI for the upper container, and $0.202 \text{ rad s}^{-1} \text{ A}^{-1}$ with $[0.054, 0.349] \text{ rad s}^{-1} \text{ A}^{-1}$ 95% CI for the lower. Theoretical slopes from the coupled models

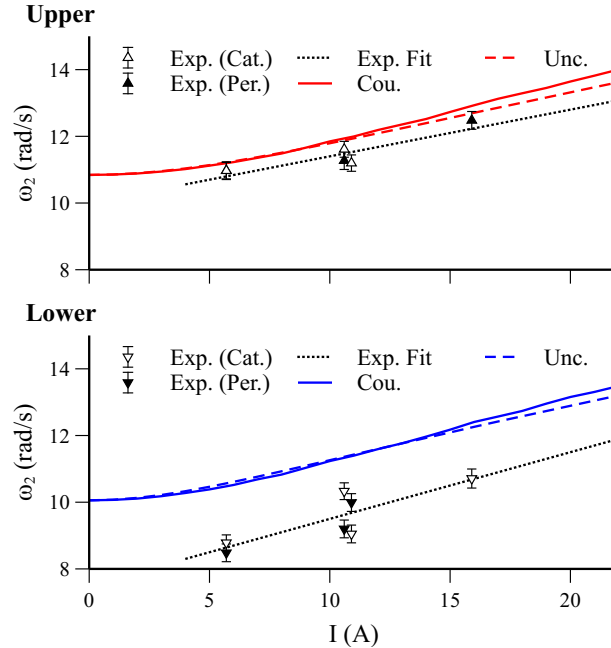


Figure 9.12: Second axisymmetric oscillation frequency for experimental (Exp.), coupled model (solid), and uncoupled model (dashed) values as a function of coils current intensity for upper and lower containers. The error bars denote the standard deviation of the measurements, to which a linear fitting (dotted) is superposed. The free edge condition is assumed in the computations.

are $0.180 \text{ rad s}^{-1}\text{A}^{-1}$ (upper) and $0.190 \text{ rad s}^{-1}\text{A}^{-1}$ (lower), and both fall within their corresponding CI. The frequencies are overestimated at the lower vessel, an effect that could be explained by the accumulation of errors in the non-magnetic parameters of the system and that is also present in Fig. 9.11. The uncoupled and coupled models diverge slightly for high current intensities, but the first only shows a better agreement with the experimental slopes for the upper tank, with trends of $0.151 \text{ rad s}^{-1}\text{A}^{-1}$ (upper), and $0.162 \text{ rad s}^{-1}\text{A}^{-1}$ (lower), both within the CIs. The statistical analysis is hence unable to determine the importance of the fluid-magnetic coupling in the second oscillation mode, reflecting the need for additional data points.

9.3 Lateral free surface oscillations

9.3.1 The UNOOSA DropTES 2019 - *StELIUM* project

The Drop Tower Experiment Series (DropTES) is a fellowship programme of UNOOSA in collaboration with ZARM and the German Aerospace Center (DLR) that provides access to ZARM's drop tower to students from around the world. The author received the 2019 DropTES award together with the *StELIUM* team, completed with Mr. Antonio García-Salcedo, Mr. Francesco Garrone, Ms. Inés Rivoalen, and advised by Prof. Filippo Maggi at Politecnico di Milano. The *StELIUM* project was aimed at complementing the results presented in Sec. 9.2 by studying the lateral oscillations of ferrofluids in cylindrical tanks subject to magnetic polarization forces in microgravity. This data completes the validation of the free surface oscillations framework presented in Sec. 7.4. What follows is a brief description of the experiment and its main results.

9.3.2 Experimental setup

The experimental setup of *StELIUM*, depicted in Fig. 9.13, is a modification of that shown in Fig. 9.3 designed to operate in a 9.3 s catapult launch at ZARM's drop tower. The system, that is thoroughly described in Ref. 174, is subdivided into two identical assemblies that contain a cylindrical Plexiglas container (similar to Fig. 9.4), a surrounding electromagnetic coil, and an horizontal linear slider that imposes a lateral oscillation to the fluid in the middle of the flight. This oscillation induces a lateral sloshing wave that is complemented with the axisymmetric wave started by the initial launch acceleration. A restoring

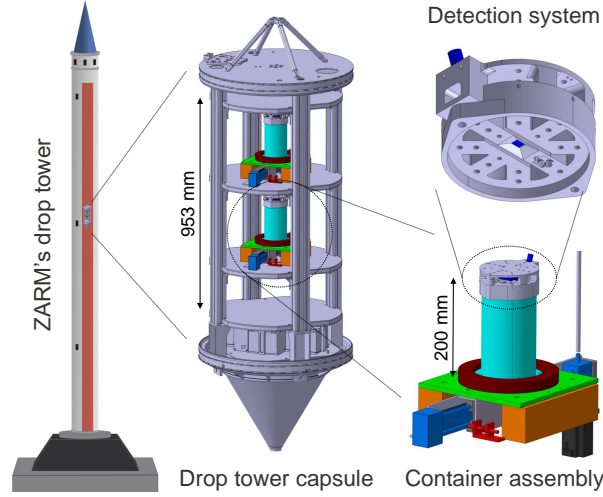


Figure 9.13: Experimental setup (not in scale).

polarization force is applied to the ferrofluid during this process by operating the coils with constant current intensities I ranging from 0 to 20 A. The 20 A level generates an inhomogeneous magnetic force distribution with characteristic meniscus magnetic Bond number and accelerations values of ~ 35 and $\sim 0.71 \text{ m/s}^2$, respectively.

9.3.3 Visualization system

The evolution of the free surface is captured by a sophisticated device located on top of each container whose design is thoroughly described in Refs. 175 and 176. It can be considered an evolution of the one presented in Sec. 9.2.3. A laser line is pointed at the surface of the ferrofluid while a camera records its projection. The deformation of the line is then correlated with the height of the surface using analytical geometry tools and the three-dimensional liquid surface profile is extracted as exemplified in Fig. 9.14. The system is able to compute the axisymmetric meniscus, from which the apparent contact angles θ_c are derived, and the evolution of the axisymmetric and lateral waves along the direction of excitation. A modal projection is subsequently applied to compute the hysteresis parameter Γ defined by Eq. 7.28e from the lateral waves, while a Fast Fourier Transform of the movement of the laser line is employed to extract the modal frequencies plotted in Fig. 9.15. Γ is here assumed to be the same for axisymmetric and lateral modes.

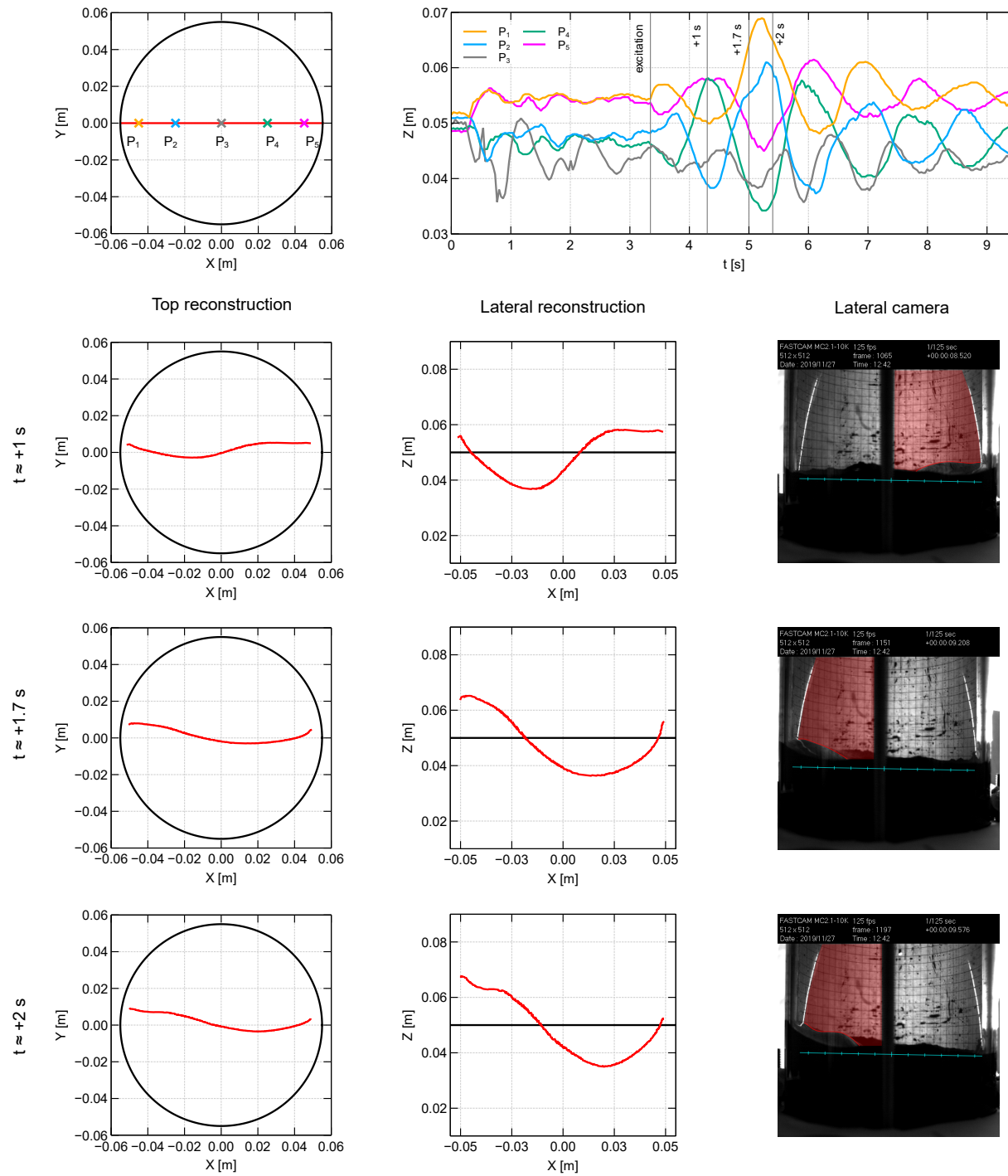


Figure 9.14: Surface line laser evolution of a StELIUM container in microgravity. On the top, the time evolution of different surface points is depicted. The first and second columns represents the top and lateral reconstructions of the ferrofluid surface. On the third column, synchronized lateral images are shown.

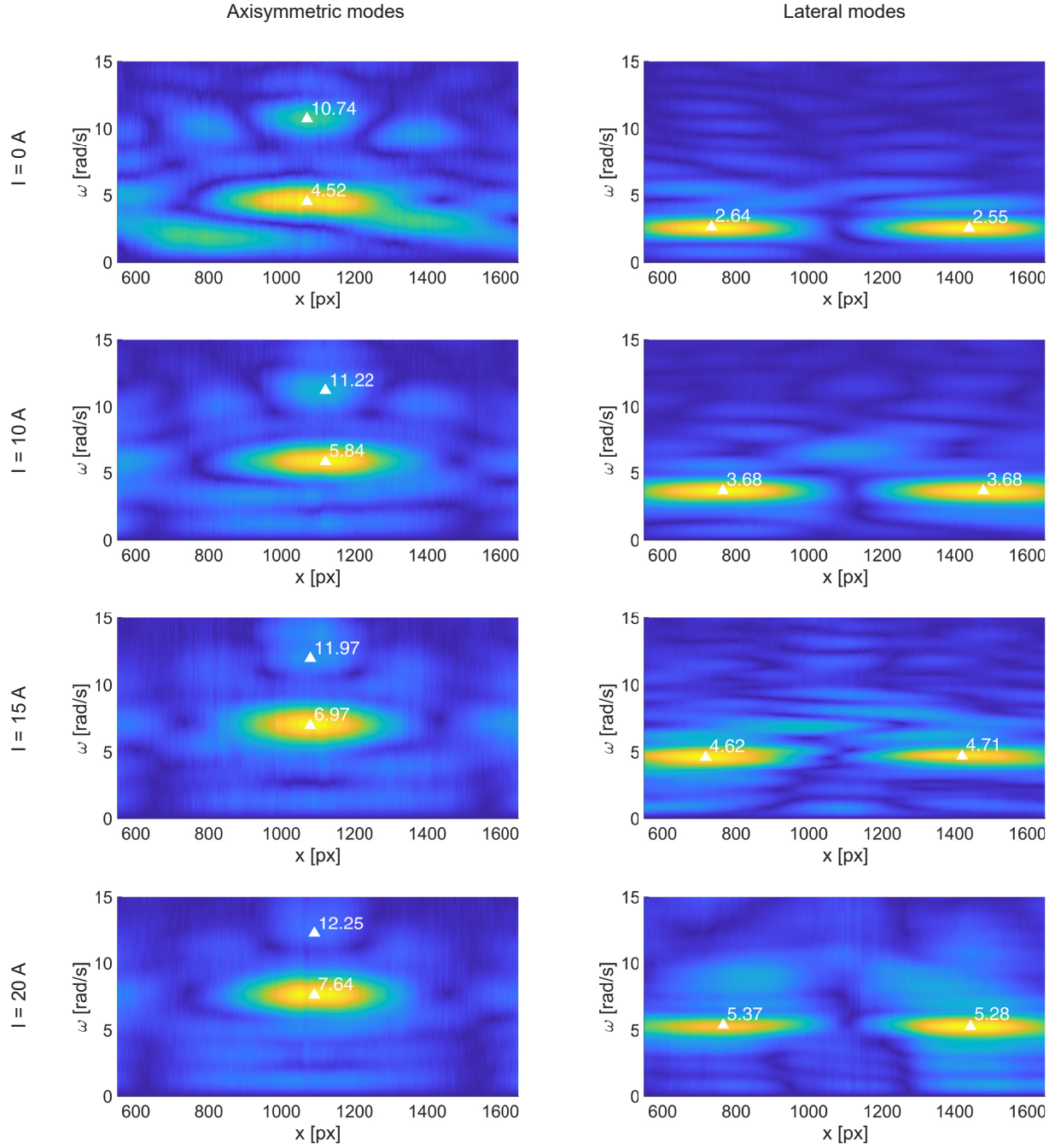


Figure 9.15: Fast Fourier Transform of the laser line for axisymmetric and lateral oscillations of the upper container.

This assumption is motivated by the difficulty in extracting Γ in the axisymmetric case, where magnetic and non-magnetic modal shapes are very similar (see Fig. 9.10). This capability is key to explore the effect

of Γ on the eigenfrequencies of the system hypothesized in Sec. 9.2.6. The interested reader is referred to Refs. 175 and 176 for further details on the design and operation of the detection system.

9.3.4 Liquid properties

The liquid tank has 11 cm diameter and 20 cm height, and is filled up by a 1:5 volume solution of the Ferrotec EMG-700 water-based ferrofluid. Again, an Aquapel treatment was applied to the walls of the container to avoid the visualization issues reported in previous works [163]. The ferrofluid has a density of 1058 kg/m³, surface tension of 55.6 mN/m, a viscosity of 1.448 mPa·s, employs an anionic surfactant, and contains a 1.16% vol concentration of 10 nm magnetic nanoparticles. The magnetization curve of the solution was measured with a MicroSense EZ-9 Vibrating Sample Magnetometer, resulting in an initial magnetic susceptibility $\chi = 0.39$ and saturation magnetization $M_s = 4160 \pm 100$ A/m. The curve is fitted with a function of the form given by Eq. 9.2 with $a_M = 1120.25$ A/m, $b_M = 3103.56$ A/m, $c_M = 8.49 \cdot 10^{-6}$ m/A, and $d_M = 1.94 \cdot 10^{-4}$ m/A.

9.3.5 Operation

The experiment is carried out using only four catapult drops. The response of the liquid is analyzed as a function of the magnetic field intensity (or, equivalently, the coils current intensity I), which changes between drops. During each flight, a single oscillation is induced 3 seconds after launch, when the surface reaches its equilibrium position. The frequency ω_e of such actuation is set between the first and second modes so that both are excited and measured by the detection system.

Table 9.4: StELIUM test matrix.

Drop	ω_e (rad/s)	I(A)
1	6.5	20
2	3.3	10
3	3.3	0
4	5	15

9.3.6 Results

Estimations for the fundamental axisymmetric and lateral frequencies $\omega_{a/l}$, fundamental damping ratios $\xi_{a/l}$, contact angle θ_c , and lateral hysteresis parameter Γ are obtained after analyzing the laser line projection as described in the previous sections. Results are shown in Table 9.5 as a function of current intensity I for upper and lower containers. Data for the lower container at the 20 A drop is recovered from a time-of-flight sensor (see Refs. 175 and 176). Even though they share the same geometry and a very similar magnetic environment, each container has significantly different values of θ_c (two-sample t-test $t(5) = 3.07$, $p = 0.03$), revealing dissimilar wettability conditions. An analogous bias is observed with Γ , although in this case it is not statistically significant ($t(3) = 0.90$, $p = 0.43$). These effects may be attributed to the potentially uneven application of the hydrophobic treatment over the internal walls of the tanks and to the large sensitivity of water to surface contamination [327, 328].

Microgravity facilities are expensive to operate and their access is generally limited. Having only 4 launch opportunities, it was decided to follow the same approach as in Sec. 9.2 and favor the derivation of statistical *trends* rather than statistical *repetitions*. The comparative analysis between individual data points shall thus be treated with care since data dispersion may impair accuracy. Nevertheless, there seems to be a strong dependence between Γ and I when switching between non-magnetic ($I = 0$ A) and magnetic ($I = 10$ A) regimes. A 56.3% and 68.0% drop in Γ is observed for upper and lower containers, respectively,

Table 9.5: Experimental results for contact angle, fundamental oscillation frequency and damping ratios for axisymmetric and lateral waves, and lateral hysteresis parameter.

	I [A]	θ_c [deg]	Γ [-]	$\omega_{a,1}$ [rad/s]	$\xi_{a,1}$ [-]	$\omega_{l,1}$ [rad/s]	$\xi_{l,1}$ [-]
Upper	0	60.52	16.75	4.52	0.19	2.58	0.21
	10	59.87	7.23	5.82	0.15	3.62	0.16
	15	62.36	7.11	7.05	0.14	4.60	0.12
	20	65.67	4.41	7.60	0.13	5.30	0.11
Lower	0	47.52	15.27	3.62	0.23	2.21	0.22
	10	53.07	4.88	5.41	0.16	3.36	0.17
	15	58.15	5.44	5.98	0.17	4.18	0.15
	20	*	*	*	*	4.90	*

* Not available due to a malfunction of the primary detection system.

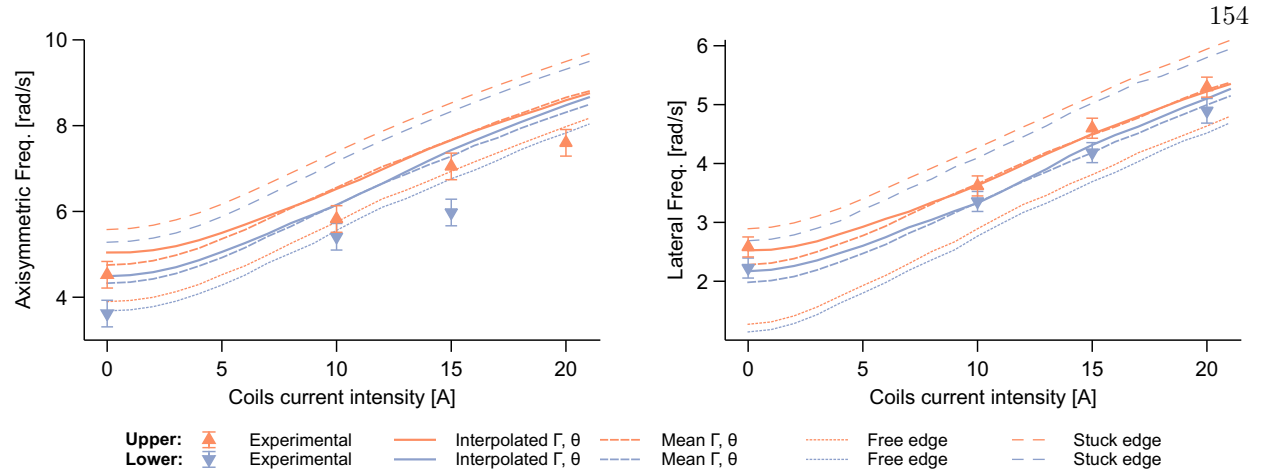


Figure 9.16: Axisymmetric (left) and lateral (right) fundamental frequencies as a function of the coils current intensity.

suggesting the existence of a shift from surface-tension-dominated to magnetic-force-dominated regimes. To the best knowledge of the author, this effect has not been reported before and should be confirmed by future studies.

In spite of the aforementioned limitations, solid statistical conclusions can be drawn through the application of appropriate statistics to the variables of interest, as discussed in Sec. 9.2. Figure 9.16 shows the fundamental axisymmetric and lateral free surface oscillation frequencies as a function of current intensity. Experimental values, whose error bands are derived by identifying the FFT resolution with the $\pm 3\sigma$ Gaussian interval, are superposed with free edge ($\Gamma = 0$) and stuck edge ($\Gamma \rightarrow \infty$) estimations from the model described in Sec. 7.4 using mean contact angle values of 62.15° and 52.91° for upper and lower containers, respectively. The use of mean contact angle values is motivated by the absence of a significant linear correlation between I and θ_c for upper ($r(2) = 0.79$, $p = 0.21$) and lower ($r(1) = 0.99$, $p = 0.10$) containers¹. From a technical perspective, reducing the number of inputs simplifies the characterization and simulation of the system. The free edge condition is associated with the lowest free surface frequency, while the stuck edge case sets the maximum possible value. Although experimental lateral frequencies fall within those boundaries, the same does not seem to happen in the axisymmetric case.

Two more theoretical predictions are superposed in Fig. 9.16: a first one that considers a linear

¹ However, previous works [337–339] have reported a dependence between the apparent contact angle and the applied magnetic field of ferrofluid droplets, an effect that should be explored with larger datasets for the setup employed in this work.

interpolation of the contact angle θ_c and hysteresis Γ values reported in Table 9.5, and a second that assumes average θ_c and magnetic Γ (upper: 6.25, lower: 5.16) results. Both curves are practically identical, exemplifying the small effect of the contact angle variability, but diverge by ~ 0.2 rad/s for $I = 0$. This effect is attributed to the large increase of Γ in the non-magnetic case, confirming the hypothesis from Sec. 9.2.6 that variable Γ values affect the frequency response. The most remarkable feature of these predictions is, however, the excellent agreement with experimental results observed for the lateral frequencies. While the interpolation of Γ and θ_c results in an adjusted coefficient of determination $R_{\text{adj}}^2 = 0.983$ (with 3 explanatory variables, Γ , θ_c , and I) and a mean-squared error of $MSE = 0.01$ rad/s, the use of averaged values returns $R_{\text{adj}}^2 = 0.976$ with a single explanatory variable I and an $MSE = 0.02$ rad/s. Both models lead to normally distributed residuals according to the Saphiro-Wilk test ($p = 0.075$, $W = 0.84$ and $p = 0.49$, $W = 0.93$ for the fitted and averaged models, respectively). Interestingly, if the frequencies are computed with a restoring inertial acceleration equivalent to the mean magnetic acceleration at the interface (which, for $I = 20$ A, is ~ 0.71 m/s²), the deviation at 20 A is just ~ 0.3 rad/s for both the free and stuck lateral cases. The reasons are that (i) $Bo_{\text{mag}}(R)$ remains almost constant along the meniscus for this setup (see Fig. 9.9), and (ii) the meniscus profile is only slightly deformed by the magnetic field. In other words, when these two conditions apply, the frequencies can be roughly estimated by assuming a low-gravity interface subject to an equivalent inertial acceleration.

Results for lateral oscillations are in sharp contrast with the axisymmetric case, where the free-edge model ($R_{\text{adj}}^2 = 0.873$) performs much better than the rest (e.g. the averaged alternative, $R_{\text{adj}}^2 = 0.486$). This is consistent with the analysis reported in Sec. 9.2.6, that assumes the free-edge condition, and with the fact that the Γ values are derived from the shape of the lateral sloshing waves. The magnetic response of the model (i.e. its current-frequency slope) cannot be robustly assessed because, unlike in Sec. 9.2, the small sample size prevents any meaningful comparison. Furthermore, an R_{adj}^2 coefficient of just 0.873 is far from acceptable for confirming or denying the conclusions of said section, where the analytical framework in Sec. 7.4 is shown to overestimate the axisymmetric free surface oscillation frequencies.

The damping ratios reported in Table 9.5 are computed by means of the half-power bandwidth method as described in Eq. 9.3. The division by $\omega_{a/l}$ justifies the decrease of $\xi_{a/l}$ with I . Most importantly, the

excellent agreement between inviscid theoretical and experimental lateral frequencies confirms the negligible impact of fluid viscosity and magnetically-induced viscosity [20, 336] on the sloshing problem for the system under study, as predicted in Sec. 9.2.6.

From a technical perspective, this analysis shows that, given an educated estimate of θ_c and Γ and an appropriate characterization of the geometric and magnetic environments, the inviscid model introduced in Sec. 7.4 is able to predict the lateral sloshing parameters of a highly-susceptible low-viscosity magnetic liquid in microgravity. This is important for future space applications involving magnetic positive positioning or magnetic liquid sloshing (see Chapter 12) because lateral oscillations represent the largest fuel-induced attitude control disturbance. Furthermore, the results confirm the importance of coupling the magnetic and fluid problems for the study of the dynamics of highly susceptible ferrofluids: if the simplified uncoupled model introduced Sec. 9.2.6 was considered instead, the frequencies at 20 A would be underestimated by 1.37 rad/s and 0.74 rad/s for the axisymmetric and lateral cases, respectively, falling well beyond the error bands. The excellent agreement between experimental results and the averaged model, that operates employing a global estimation of θ_c and Γ , makes basic science discussions on the dependence of such parameters on the applied magnetic field less relevant for most applications, at least for the configuration here considered. The same can be said about axisymmetric oscillations, which have a weaker impact on the spacecraft dynamics [63, 86].

In spite of these results, an outstanding open question remains: why does the free surface oscillations model from Sec. 7.4 fail to predict the axisymmetric response of the interface in Sec. 9.2.6? This and other questions are addressed in Chapter 10.

9.4 Free floating ferrofluid droplet

During the fourth drop of the ESA *Drop Your Thesis! 2017 The Ferros* campaign, the vertical percussion produced by the stepper engine generated a ferrofluid jet and a free-floating droplet of 11 mm diameter in the upper assembly. This effect was not observed in the other four drops and is a consequence of the destabilization of the free surface described in Sec. 7.3. Figure 9.17 pictures the formation and breakup of the ferrofluid jet, that generates several droplets of which the one shown in the figure could be tracked

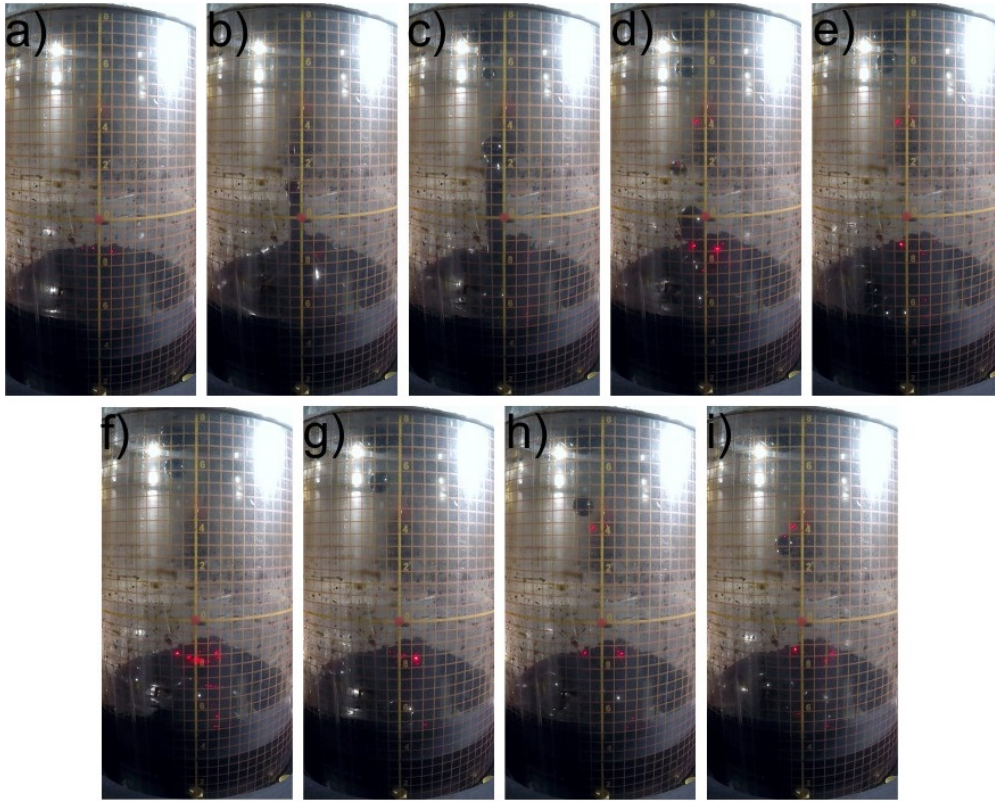


Figure 9.17: Sequence captured by a lateral camera showing the ferrofluid droplet formation and evolution after the application of the vertical percussion. a) -2.5 s; b) -1 s; c) -0.5 s; d) 0 s; e) 0.5 s; f) 1 s; g) 1.5 s; h) 2 s; i) 2.5 s.

with reasonable accuracy. This was a rare opportunity to study an example of magnetic mass transfer in microgravity.

The three-dimensional position of the droplet is triangulated by making use of the two lateral cameras located at opposite sides of each container. A Monte Carlo simulation is carried out to estimate the error of the visualization system and the initial uncertainty in the droplet position and velocity by perturbing every parameter involved in the triangulation process. The magnetic environment is simulated in Comsol Multiphysics employing the model described in the Appendix B, and the magnetic fields inside the droplet are approximated using demagnetization factors. Then, the total magnetic force is computed with the different equivalent formulations listed in Table A.1.

The theoretical vertical displacement of the droplet is integrated starting from its initial position and velocity and compared with experimental measurements in Fig. 9.18. The theoretical error bands are

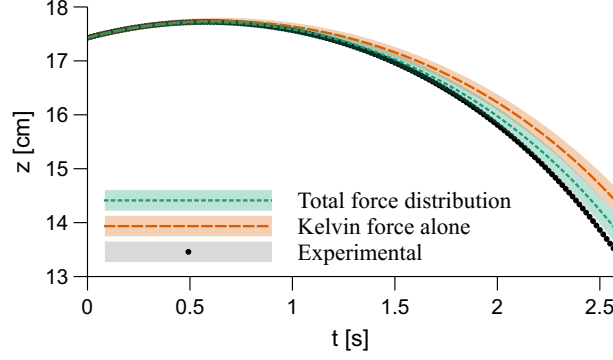


Figure 9.18: Measured and integrated height of the droplet as a function of time for the total force distribution (Eq. A.6 + Eq. A.11) and the Kelvin force alone (Eq. A.6). The error bands represent the standard deviation.

due to the uncertainty in the initial position, while experimental errors are a consequence of the Monte Carlo analysis. The laws of motion $z(t)$ are integrated using a basic momentum balance for (i) the full force distribution arising from Eq. A.6 and Eq. A.11, and (ii) the Kelvin body force in Eq. A.6 alone. This distinction is made to emphasize the importance of the surface force terms defined by Eq. A.11 in ferrofluids, which are generally neglected in previous works [66, 163, 340]. Not surprisingly, the full force formulation shows the best agreement with the experimental results and deviates from the prediction given by the Kelvin force, that falls outside the experimental error band. Greater divergences may be observed with highly concentrated ferrofluids, for which $\chi > 1$ [341, 342].

The results exemplify how the indiscriminate use of Kelvin's body force without the corresponding surface term may lead to large errors when computing the total force. This assumption, common in normal-gravity research [75, 340, 343], has a critical impact in space applications where the magnetic force acquires an overwhelming role due to the absence of gravity. Special care should therefore be taken when modeling, implementing, and describing the magnetic interaction. From the technical perspective, the dynamics of the droplet are predicted with high accuracy in spite of the inherent complexity of the magnetic setup, informing the design of future space systems.

This section has presented a brief summary of the full analysis carried out in Ref. 77, which focuses on the derivation, implementation, and comparison of the total force formulations listed in Table A.1 and derived in collaboration with Prof. Gabriel Cano-Gómez. The selection of the system of forces acting on

ferrofluids is an important fundamental problem. However, once an appropriate force distribution is adopted, the practical differences between different options tend to vanish for most applications. The interested reader is referred to Ref. 77 for a comprehensive discussion.

Chapter 10

Fully coupled interface-tracking magnetohydrodynamic model

Numerical magnetohydrodynamic multiphase simulation frameworks can be used to extend the capabilities of analytical tools beyond the axisymmetric, inviscid flow assumptions. This chapter extends the interface-tracking framework introduced in Ref. 108 to study the equilibrium, linear stability, modal response, and time-dependent deformation of capillary liquid interfaces subject to magnetic polarization. A robust and numerically stable implementation is achieved by employing a fully implicit monolithic approach that solves both problems with essentially the same code. Its implicit nature allows using arbitrarily large time steps on each Newton-Raphson iteration. Symbolic functions and collocation matrices are employed to evaluate the Jacobian of the discretized system of equations and take advantage of the sparsity of the resulting matrix, leading to significant gains in flexibility and computational efficiency with respect to previous approaches.

One of the unique capabilities of the model is its ability to easily compute the modal shapes and frequencies of ferrohydrodynamic interfaces. The validation of this feature is complicated by the fact that previous experiments were mostly concerned with the equilibrium and dynamic evolution of ferrofluid interfaces rather than their modal response. An exception is the European Space Agency (ESA) *Drop Your Thesis!* 2017 *The Ferros* project, whose configuration (described in Chapter 9) is here implemented. Beyond the computational interest in developing interface-tracking magnetohydrodynamic frameworks, an additional technical motivation for this chapter is to shed light on the disagreement reported in Chapter 9 between experimental and quasi-analytical measurements for the axisymmetric free surface frequencies of a ferrofluid interface, thus paving the path for the development of magnetic propellant management devices like those described in Chapter 12.

10.1 Numerical method

10.1.1 Problem formulation

The system under study, represented in Fig. 10.1(a), consists on a partially filled cylindrical tank subject to an inhomogeneous axisymmetric magnetic field. Such field is imposed by either a coil or a magnet. The tank has radius a , height h_B , and holds a volume V of an incompressible, Newtonian, magnetic liquid with density ρ , specific volume $\nu = \rho^{-1}$, shear coefficient of viscosity η , and surface tension σ at temperature T . The static contact angle between the liquid and the wall is θ_c . The free space is filled by a non-reactive inviscid gas at pressure p_g . A vertical inertial acceleration g is also applied to the tank.

The basic theoretical framework described in Sec. 6.3 is particularized for the cylindrical reference system $\{\mathbf{e}_r, \mathbf{e}_\phi, \mathbf{e}_z\}$ depicted in Fig. 10.1(a). Although the model here introduced can be applied to a variety problems, the experimental setup of the ESA *Drop Your Thesis! 2017 The Ferros* project is adopted for verification and validation (see Chapter 9). The goal of the model is to determine the axisymmetric

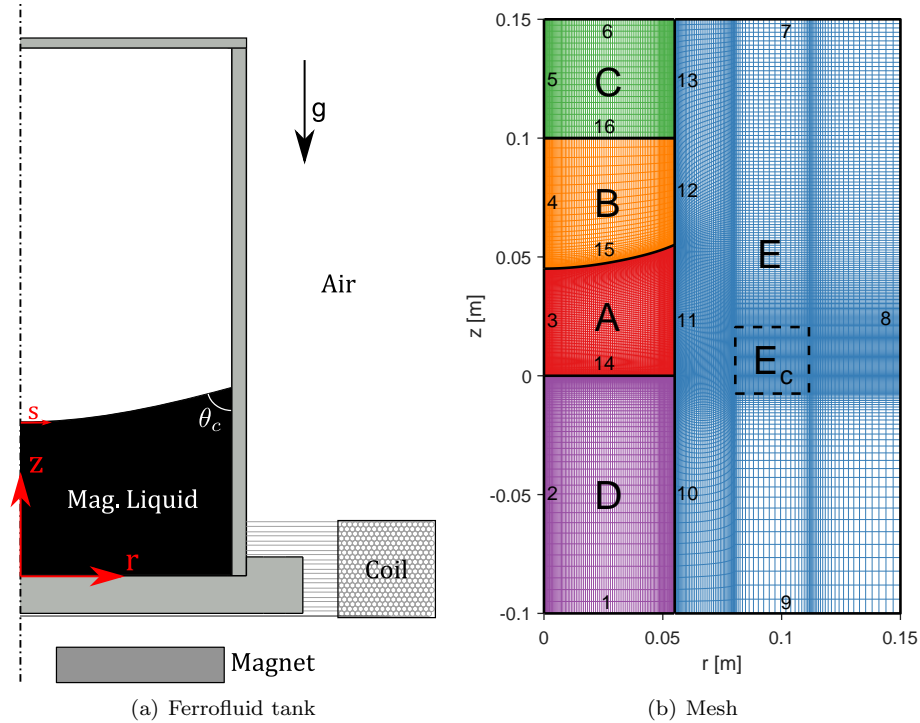


Figure 10.1: Schematic of the problem under study and numerical simulation domain with mapped regions and interfaces. The dashed rectangle E_c denotes the virtual coil domain.

equilibrium, stability, modal response, and nonlinear time evolution of the surface.

Five regions and their corresponding interfaces conform the simulation domain, as shown in Fig. 10.1(b): A (liquid), B (air inside the container), C (air over the container), D (air below the container), and E (surrounding air). The subdivision between regions B and C is not strictly necessary; however, adding a buffer area on top of B allows expanding the simulation domain while easily controlling the mesh density. The magnetic source (e.g. a coil or magnet) is included in E as a subdomain E_c .

10.1.2 Axisymmetric Navier-Stokes equations

The mass and momentum conservation equations defined by Eq. 6.12 should be expressed in the cylindrical reference system after considering the axisymmetry of the problem. This results in

$$\frac{\partial(ru)}{\partial r} + \frac{\partial(rw)}{\partial z} = 0, \quad (10.1a)$$

$$\rho \left(\frac{\partial u}{\partial t} + u \frac{\partial u}{\partial r} + w \frac{\partial u}{\partial z} \right) = -\frac{\partial p^*}{\partial r} + \eta \left(\frac{\partial^2 u}{\partial r^2} + \frac{\partial(u/r)}{\partial r} + \frac{\partial^2 u}{\partial z^2} \right) + \mu_0 \left(M_r \frac{\partial H_r}{\partial r} + M_z \frac{\partial H_r}{\partial z} \right), \quad (10.1b)$$

$$\rho \left(\frac{\partial w}{\partial t} + u \frac{\partial w}{\partial r} + w \frac{\partial w}{\partial z} \right) = \rho g - \frac{\partial p^*}{\partial z} + \eta \left(\frac{\partial^2 w}{\partial r^2} + \frac{1}{r} \frac{\partial w}{\partial r} + \frac{\partial^2 w}{\partial z^2} \right) + \mu_0 \left(M_r \frac{\partial H_z}{\partial r} + M_z \frac{\partial H_z}{\partial z} \right), \quad (10.1c)$$

where r (z) is the radial (axial) coordinate, and u (w) is the radial (axial) velocity component. The axisymmetry of the magnetic problem is taken into account in the previous expressions, so that \mathbf{J}_e has only azimuthal components, and \mathbf{M} and \mathbf{H} lack from them, resulting in $\mathbf{H} = H_r \mathbf{e}_r + H_z \mathbf{e}_z$, and $\mathbf{M} = M_r \mathbf{e}_r + M_z \mathbf{e}_z$. For practical reasons, vertically magnetized magnets will be considered.

10.1.3 Magnetic potentials for axisymmetric problem

Equations 6.13a and 6.13b are rewritten as a function of \mathbf{H} , resulting in

$$\nabla \cdot \mathbf{H} = -\nabla \cdot \mathbf{M}, \quad (10.2a)$$

$$\nabla \times \mathbf{H} = \mathbf{J}_e. \quad (10.2b)$$

Therefore, \mathbf{H} has scalar sources in the magnetized regions and vector sources in the coil. According to Helmholtz's theorem, \mathbf{H} can be expressed in terms of scalar and vector magnetic potentials. Taking into

account the axisymmetry of the problem,

$$H_r = -\frac{1}{r} \frac{\partial \Psi}{\partial z} - \frac{\partial \Phi}{\partial r}, \quad H_z = \frac{1}{r} \frac{\partial \Psi}{\partial r} - \frac{\partial \Phi}{\partial z}, \quad (10.3)$$

where Φ is the scalar potential generated by scalar sources and the stream-like function $\Psi = rA_\phi(r, z)/\mu_0$ is directly related to the azimuthal component $A_\phi(r, z)$ of the vector magnetic potential created by the electric current. The magnetic problem is then formulated and solved in terms of Φ and Ψ after noting that

$$\nabla \cdot \mathbf{H} = - \left[\frac{\partial^2 \Phi}{\partial z^2} + \frac{\partial^2 \Phi}{\partial r^2} + \frac{1}{r} \frac{\partial \Phi}{\partial r} \right], \quad (10.4)$$

$$\nabla \times \mathbf{H} = -\frac{1}{r} \left[\frac{\partial^2 \Psi}{\partial r^2} + \frac{\partial^2 \Psi}{\partial z^2} - \frac{1}{r} \frac{\partial \Psi}{\partial r} \right] \mathbf{e}_\phi. \quad (10.5)$$

In the domain A, $\mathbf{M} = \chi^{\text{vol}}(H)\mathbf{H}$ and Eq. 10.2a becomes

$$\frac{\partial^2 \Phi}{\partial z^2} + \frac{\partial^2 \Phi}{\partial r^2} + \frac{1}{r} \frac{\partial \Phi}{\partial r} = \frac{1}{1 + \chi^{\text{vol}}(H)} \left(H_r \frac{\partial \chi^{\text{vol}}}{\partial r} + H_z \frac{\partial \chi^{\text{vol}}}{\partial z} \right), \quad (10.6)$$

where χ^{vol} also depends on Ψ and Φ through the magnetization law

$$\chi^{\text{vol}}(H) = \frac{2a_M}{\pi H} \arctan(c_M H) + \frac{2b_M}{\pi H} \arctan(d_M H) + e_M, \quad (10.7)$$

with a_M , b_M , c_M , d_M , and e_M being a set of fitting parameters [3]. For domains B-E, Eq. 10.2a is simplified to $\nabla \cdot \mathbf{H} = 0$ due to the absence of inhomogeneous magnetization fields. It should be noted, however, that magnets may be considered in the subdomain E_c . When such subdomain is occupied by a coil,

$$\mathbf{J}_e = \frac{NI}{S_c} \mathbf{e}_\phi, \quad (10.8)$$

with N being the number of wire turns, I the current flowing through each of them, and S_c the cross section of the coil. Consequently, Eq. 10.2b adopts the form

$$-\frac{1}{r} \left[\frac{\partial^2 \Psi}{\partial r^2} + \frac{\partial^2 \Psi}{\partial z^2} - \frac{1}{r} \frac{\partial \Psi}{\partial r} \right] = \frac{NI}{S_c}. \quad (10.9)$$

For domains A-D (and E, when E_c is occupied by a magnet), $\mathbf{J}_e = 0$, and the previous expression simplifies to $\nabla \times \mathbf{H} = \mathbf{0}$. If a magnet with uniform, vertical magnetization field is considered in E_c , the condition $\mathbf{M} = M_m \mathbf{e}_z$ is imposed at such region and the stream-like function has trivial solution $\Psi = 0$.

10.1.4 Boundary conditions

An axisymmetric boundary condition is applied at $r = 0$ for both fluid and magnetic problems, while the wall-liquid interaction is described by the non-penetration and no-slip boundary conditions. This results in

$$3 : \quad u = 0, \quad \frac{\partial w}{\partial r} = 0, \quad (10.10a)$$

$$11 : \quad u = w = 0, \quad (10.10b)$$

$$14 : \quad u = w = 0. \quad (10.10c)$$

The interfacial conditions described by Eq. 6.14 are particularized at the free fluid surface 15 by following a parametrization of the form $z_{\text{in}} = G(s, t)$ and $r_{\text{in}} = F(s, t)$, resulting in the normal balance

$$p^* + p_n - p_0 = \frac{\sigma}{F} \left(\frac{\partial F}{\partial s} \right)^{-1} \frac{\partial}{\partial s} \left[\frac{F \frac{\partial G}{\partial s}}{\sqrt{\left(\frac{\partial F}{\partial s} \right)^2 + \left(\frac{\partial G}{\partial s} \right)^2}} \right] + 2\eta \frac{\frac{\partial u}{\partial r} \left(\frac{\partial G}{\partial s} \right)^2 + \frac{\partial w}{\partial z} \left(\frac{\partial F}{\partial s} \right)^2 - \left(\frac{\partial w}{\partial r} + \frac{\partial u}{\partial z} \right) \frac{\partial F}{\partial s} \frac{\partial G}{\partial s}}{\left(\frac{\partial G}{\partial s} \right)^2 + \left(\frac{\partial F}{\partial s} \right)^2}, \quad (10.11a)$$

tangential balance

$$\frac{\left[\left(\frac{\partial G}{\partial s} \right)^2 - \left(\frac{\partial F}{\partial s} \right)^2 \right] \left(\frac{\partial w}{\partial r} + \frac{\partial u}{\partial z} \right) + 2 \frac{\partial F}{\partial s} \frac{\partial G}{\partial s} \left(\frac{\partial u}{\partial r} - \frac{\partial w}{\partial z} \right)}{\left(\frac{\partial F}{\partial s} \right)^2 + \left(\frac{\partial G}{\partial s} \right)^2} = 0, \quad (10.11b)$$

and the kinematic and geometric compatibility equations

$$\left(u - \frac{\partial F}{\partial t} \right) \frac{\partial G}{\partial s} - \left(w - \frac{\partial G}{\partial t} \right) \frac{\partial F}{\partial s} = 0, \quad (10.11c)$$

$$\frac{\partial G}{\partial s} \frac{\partial^2 G}{\partial s^2} + \frac{\partial F}{\partial s} \frac{\partial^2 F}{\partial s^2} = 0, \quad (10.11d)$$

where s is the arc length coordinate along the interface. The contact angle θ_c is imposed at the wall ($s = 1$) through

$$\frac{\partial F}{\partial s} \tan \left(\frac{\pi}{2} - \theta_c \right) + \frac{\partial G}{\partial s} = 0, \quad \text{and} \quad F = R. \quad (10.11e)$$

The magnetic boundary conditions derive from Eq. 6.15 after considering the axisymmetry of the problem and noting that the liquid is magnetized. Two conditions can be imposed per block and boundary, which leads to four equations per internal connection and two per external boundary. The internal boundary

conditions are

$$11, 14, 15 : \quad \Psi_1 = \Psi_2, \quad \Phi_1 = \Phi_2, \quad (10.12a)$$

$$H_{t,1} = H_{t,2}, \quad B_{n,1} = B_{n,2}, \quad (10.12b)$$

$$10, 12, 13 : \quad \Psi_1 = \Psi_2, \quad \Phi_1 = \Phi_2, \quad (10.12c)$$

$$\frac{\partial \Psi_1}{\partial r} = \frac{\partial \Psi_2}{\partial r}, \quad \frac{\partial \Phi_1}{\partial r} = \frac{\partial \Phi_2}{\partial r}, \quad (10.12d)$$

$$16 : \quad \Psi_1 = \Psi_2, \quad \Phi_1 = \Phi_2, \quad (10.12e)$$

$$\frac{\partial \Psi_1}{\partial z} = \frac{\partial \Psi_2}{\partial z}, \quad \frac{\partial \Phi_1}{\partial z} = \frac{\partial \Phi_2}{\partial z}, \quad (10.12f)$$

where, in order to ensure the continuity of the magnetic field at 10, 12, 13 and 16, the continuity of the potentials Ψ and Φ and their derivatives across the internal boundary are imposed. The continuity of the derivative along the boundary is implicitly enforced by the continuity of the potential. In the fluid-air interfaces 11, 14, and 15, H_t and B_n are expressed as a function of the potentials and the normal and tangent vectors, and the analytical expressions are equaled at both side of the interface. It should be noted that the continuity of the potentials across a magnetized domain or a coil is a consequence of the magnetic field formulation shown in Eq. 10.3. The opposite would lead to a singularity (i.e. a nonphysical solution). This also motivates the modeling of such magnetic sources as subdomains of region E, named E_c , where either the source term \mathbf{J}_e is considered in Eq. 10.9 (and not in the rest of the domain), or a vertical magnetization value is imposed.

Two conditions are applied to the external contours. In the axis,

$$2 - 5 : \quad \Psi = 0, \quad \frac{\partial \Phi}{\partial r} = 0, \quad (10.13)$$

which results in $H_r = 0$ (see Eq. 10.3) and imposes a reference value for Ψ . The potential Ψ is truncated at the external contours (1,6-9) by imposing its analytical solution, which can be easily found as the superposition of magnetic potentials induced by virtual circular loops located in the region of interest. This can be expressed as [304]

$$\Psi(r, z)|_{1,6-9} \approx \frac{NI}{N_i N_j} \sum_{i=1}^{N_i} \sum_{j=1}^{N_j} \Psi_{i,j}(r, z)|_{1,6-9}, \quad (10.14a)$$

$$\Psi_{i,j}(r, z)|_{1,6-9} = \frac{1}{\pi k_{i,j}} \sqrt{r_i r} \left[\left(1 - \frac{k_{i,j}^2}{2} \right) K(k_{i,j}) - E(k_{i,j}) \right], \quad (10.14b)$$

with N being the number of turns of the actual coil, I its current intensity, $k_{i,j}^2 = 4r_i r / [(r_i + r)^2 + (z - z_j)^2]$ an intermediate parameter, r_i (z_j) the virtual loop radius (height), N_i (N_j) the number of virtual loops in the radial (vertical) direction, and $K(k)$ and $E(k)$ the complete elliptic integral of first and second kind, respectively. The potential is shown to converge with errors below 0.001% for $N_i = N_j = 15$, which are adopted for the analysis.

The sources of scalar potential Φ are the magnetically polarizable liquid in A and an hypothetical magnet in E_c . Its value at the external contour can be approximated by the contribution of the dipole terms of the magnet and magnetized liquid, and so the condition

$$\Phi(r, z)|_{1,6-9} \approx \Phi^{\text{dip}}(r, z)|_{1,6-9} \quad (10.15a)$$

is imposed, with

$$\Phi^{\text{dip}}(r, z)|_{1,6-9} = \sum_{k=1}^{N_k} \frac{m_k}{4\pi} \frac{(z - z_k)}{[r^2 + (z - z_k)^2]^{3/2}} \Big|_{1,6-9}, \quad (10.15b)$$

where the N_k magnetized domains are characterized by the dipole moments $\mathbf{m}_k = m_k \mathbf{e}_z$ located at $\mathbf{r}_k = z_k \mathbf{e}_z$. The dipole associated with the magnet can be calculated beforehand, but the position and magnitude of the one deriving from the magnetized liquid needs to be computed by integrating \mathbf{M} in the domain A. Although this Dirichlet boundary condition exhibits excellent numerical stability properties, a Neumann condition with higher spatial convergence rate may be imposed instead by considering the radial and axial derivatives of Φ . The unicity of the solution should then be imposed by setting the value of Φ in an arbitrary point of the external boundary. However, this implies that different conditions are applied along the same line, leading to slight numerical aberrations in the potential field.

It should be noted that, if the system only includes magnets and magnetized liquids, the boundary condition given by Eq. 10.14a becomes unnecessary, since $\Psi_{1,6-9} = 0$. Similarly, it is possible to impose $\Phi_{1,6-9} \approx 0$ when a weakly magnetized liquid and a coil are considered. For very large simulation domains the more practical magnetic insulation condition $\Phi_{1,6-9} = \Psi_{1,6-9} = 0$ may be imposed.

10.1.4.1 $\Phi - \Psi$ uncoupling and virtual magnet substitution

From the structure of Eqs. 10.6 and 10.9 and the magnetic boundary conditions in Eqs. 10.14a and 10.15a, the uncoupling between Ψ and Φ becomes evident. Both fields are computed separately, and Ψ does not depend on the deformation of the ferrofluid volume in the domain A. In other words, Ψ could be calculated at the beginning of the simulation and then implemented as an invariant source term in substitution of Eq. 10.2b. This is advantageous from the computational perspective, as the number of variables of the system is reduced and specific domains or subdomains are no longer needed. The only purpose of the boundary domains B-E would then be to ensure the convergence of Φ to the true solution by imposing the dipole approximation given by Eq. 10.15b sufficiently far away from the ferrofluid. However, this approach also limits the scope and flexibility of the simulation framework, particularly for 3D problems without analytical solutions for Ψ . For this reason, both magnetic potentials are solved numerically in this chapter.

Although Eq. 10.14a provides an exact boundary condition for any axisymmetric current distribution, the Φ field induced by magnetized media has to converge to the dipole approximation given by Eq. 10.15a. Consequently, if E_c is occupied by a magnet, larger simulation domains are required to guarantee convergence. It would be desirable, from a computational perspective, to have an exact boundary condition also in that case, limiting the dipole approximation to the magnetized region A. To overcome this issue, it should be noted that the \mathbf{B}_m flux produced by a magnet can be described by two equivalent magnetic virtual currents: (i) a volume term $\mathbf{J}_m = \nabla \times \mathbf{M}_m$ distributed in the magnet volume, where \mathbf{M}_m is the magnetization field, and (ii) a surface term $\mathbf{K}_m = \mathbf{n} \times [\mathbf{M}_m]$, with \mathbf{n} denoting the normal to the interface and $[\mathbf{M}_m]$ the magnetization jump across it.

For a vertically magnetized cylindrical magnet with uniform magnetization $\mathbf{M}_m = M_m \mathbf{e}_z$, the equivalence results in a system of electrical currents with a volume density term $\mathbf{J}_e = \mathbf{0}$ in E_c and a surface density term $\mathbf{K}_e = M_m \mathbf{e}_\phi$ at the lateral wall. If the magnet has a height h , the equivalent electrical system can be modeled as a homogeneous distribution of $N_j \rightarrow \infty$ circular loops in the lateral wall with current $M_m h / N_j$. The magnetic field induced by this equivalent system is $\mathbf{H}_e = (\mathbf{B}_e / \mu_0)$, with \mathbf{B}_e being the

magnetic flux produced by the circular loops, which is identical to \mathbf{B}_m . Because the magnet induces a field $\mathbf{H}_m = \mathbf{B}_m/\mu_0 - \mathbf{M}_m$ inside the magnetized volume, and $\mathbf{H}_m = \mathbf{B}_m/\mu_0$ outside, \mathbf{H}_e is identical to \mathbf{H}_m outside E_c . In other words, the virtual magnet substitution procedure provides an exact analytical solution outside the magnet volume, leading to important computational advantages and faster model development.

10.1.5 Discretization of the simulation domain

The numerical procedure used in this study is a variation of the interface-tracking method developed in Herrada and Montanero for multiphase flows [108]. As shown in Fig. 10.1(b), the simulation domain is divided into five blocks that implement different discretization methods.

The blocks A, B, C, and D are mapped onto the square computational domains A: $[0 \leq s \leq 1] \times [0 \leq \eta_A \leq 1]$, B: $[0 \leq s \leq 1] \times [0 \leq \eta_B \leq 1]$, C: $[0 \leq s \leq 1] \times [0 \leq \eta_C \leq 1]$ and D: $[0 \leq s \leq 1] \times [0 \leq \eta_D \leq 1]$ by means of the analytical mappings

$$r_A = F(s, t), \quad z_A = G(s, t)\eta_A, \quad (10.16a)$$

$$r_B = F(s, t), \quad z_B = G(s, t) + [h_{BC} - G(s, t)]\eta_B, \quad (10.16b)$$

$$r_C = F(s, t), \quad z_C = h_{BC} + (h_{\text{top}} - h_{BC})\eta_C, \quad (10.16c)$$

$$r_D = F(s, t), \quad z_D = h_{\text{bot}}(1 - \eta_D), \quad (10.16d)$$

where $h_{\text{top}} = 0.15$ m ($h_{\text{bot}} = -0.1$ m) denotes the top (bottom) height of the domain, and $h_B = 0.1$ m defines the transition height between B and C.

The domain E is built following the same approach, but in addition to concentrating points next to the domains A-D and adapting to their deformation, this block also has the functionality of defining the subdomain E_c and concentrating points close to its boundaries. In an early version of this work, these requirements were addressed by means of a meshfree discretization of domains D and E. However, that approach resulted in the ill-conditioning of the nodes that interfaced with blocks A-C, an excessive numerical error, and reduced tolerance to fluid deformation [344]. In the definitive configuration, instead, nonsingular transformations of the form

$$r_E = F_E(s_E), \quad z_E = G_E(s_E, \eta_E, t), \quad (10.17)$$

mapped onto the square computational domain $[0 \leq s_E \leq 1] \times [0 \leq \eta_E \leq 1]$ are implemented in E. The radial and vertical position of the points are fixed with the exception of the subdomain between A-D and E_c, which follows the quasi-elliptical mapping [345]

$$F_E = F_E^*, \quad (10.18a)$$

$$g_{22} \frac{\partial^2 G_E}{\partial s_E^2} + g_{11} \frac{\partial^2 G_E}{\partial \eta_E^2} - 2g_{12} \frac{\partial^2 G_E}{\partial s_E \partial \eta_E} = 0, \quad (10.18b)$$

with boundary conditions

$$8' : \quad \frac{\partial G_E}{\partial s} = 0, \quad (10.19a)$$

$$10 - 13 : \quad G_E = G_{A-D}, \quad (10.19b)$$

$$7 : \quad G_E = h_{\text{top}}, \quad (10.19c)$$

$$9 : \quad G_E = h_{\text{bot}}, \quad (10.19d)$$

where 8' denotes the line parallel to 8 that touches the left wall of E_c, F_E^* is an imposed radial distribution, and the coefficients take the form

$$g_{11} = \left(\frac{\partial G_E}{\partial s_E} \right)^2 + \left(\frac{\partial F_E}{\partial s_E} \right)^2, \quad (10.20a)$$

$$g_{22} = \left(\frac{\partial G_E}{\partial \eta_E} \right)^2 + \left(\frac{\partial F_E}{\partial \eta_E} \right)^2, \quad (10.20b)$$

$$g_{12} = \frac{\partial G_E}{\partial \eta_E} \frac{\partial G_E}{\partial s_E} + \frac{\partial F_E}{\partial \eta_E} \frac{\partial F_E}{\partial s_E}. \quad (10.20c)$$

Because the boundaries with A-D and the rest of E are fixed, this subdomain adopts the role of a sliding mesh, ensuring the connectivity between the magnetic source and the liquid and proper adaptation to fluid deformation.

All the derivatives appearing in the governing equations are expressed in terms of s , η , and t . Then, the resulting equations are discretized in the s direction using fourth-order finite differences with n_s and n_{s_E} stretched points. In the η direction, fourth-order finite differences are also employed with n_{η_A} , n_{η_B} , n_{η_C} , n_{η_D} , and n_{η_E} stretched points. This discretization strategy gives rise to meshes that automatically adapt to any variation of the free liquid interface. The results presented in this work are obtained using $n_s = 101$, $n_{s_E} = 99$, $n_{\eta_A} = 101$, $n_{\eta_B} = 41$, $n_{\eta_C} = 21$, $n_{\eta_D} = 61$, and $n_{\eta_E} = 221$. The employment of

fourth-order finite differences over a second-order approach leads to lower truncation errors with marginal implementation efforts and a reasonable computational penalty. Most importantly, it allows reducing the number of points in the simulation domain. Further details on the finite differences implementation can be found in Sec. 10.1.5.1.

To compute the steady-state solution, all the equations of the system are solved together in a monolithic scheme with a Newton–Raphson approach. Second-order backward differences are used to compute the time derivatives (see Sec. 10.1.5.1), and since the method is fully implicit, the time step is chosen to be sufficiently large to ensure that a steady state is reached in a single iteration. This value is set to 100 s. If the time-dependent interface deformation is explored instead, a time step of 0.01 s is employed to guarantee convergence to the solution (see Sec. 10.3.2). One of the main characteristics of this procedure is that the elements of the Jacobian matrix are obtained by combining analytical functions and the collocation matrices of all subdomains. This allows taking advantage of the sparsity of the resulting matrix to reduce the computational time on each Newton-Raphson iteration, which converges when the norm of the state error vector $d\mathbf{x}$ is smaller than 10^{-3} . It should be noted that the norm of the solution is at least of order 1 [108], and hence the 10^{-3} threshold ensures convergence, as observed in the results. On the other hand, the Newton-Raphson method exhibits quadratic convergence rates close to the final solution, which speeds up the computation

As a reference, the computation of a single Newton-Raphson iteration using an Intel Core i7-7820HQ CPU at 2.90 GHz with 32 Gb RAM takes between 60 and 120 s with the base mesh employed in this work. A single time step usually takes between 3 and 15 iterations to converge. The non-magnetic interface tracking method on which this work is based has already been shown to overcome existing models in terms of computational efficiency in Ref. 108.

Table 10.1: Fourth-order finite difference coefficients.

Type	Order	c_{-4}	c_{-3}	c_{-2}	c_{-1}	c_0	c_1	c_2	c_3	c_4
Forward 1	1					-25/12	4	-3	4/3	-1/4
	2					35/12	-26/3	19/2	-14/3	11/12
Forward 2	1				-1/4	-5/6	3/2	-1/2	1/12	
	2				11/12	-5/3	1/2	1/3	-1/12	
Central	1			1/12	-2/3	0	2/3	-1/12		
	2			-1/12	4/3	-5/2	4/3	-1/12		
Backward $n - 1$	1		-1/12	1/2	-3/2	5/6	1/4			
	2		-1/12	1/3	1/2	-5/3	11/12			
Backward n	1	1/4	-4/3	3	-4	25/12				
	2	11/12	-14/3	19/2	-26/3	35/12				

10.1.5.1 Finite differences framework

The governing equations of the problem are discretized in the uniform s - η computational grids. The first and second fourth-order derivatives of each variable f are computed as

$$\frac{\partial^n f}{\partial x^n}(x_0) = \frac{1}{12\Delta x^n} \sum_{i=-4}^4 [c_i f(x_i)] + O(\Delta x^4), \quad (10.21)$$

with x_i being the spatial coordinate (s or η) at node i and $i = 0$ the node under consideration, Δx the uniform grid space, $f(x_i)$ the value of the variable at x_i , c_i a coefficient given by Table 10.1, and n the order of the derivative. Forward, central, and backward finite differences are implemented depending on whether the node is located in the boundary or bulk of the domain.

Second-order backward finite differences are employed in the time domain using a fixed time step Δt , resulting in

$$\frac{\partial f}{\partial t} = \frac{1}{2\Delta t} [3f(t_0) - 4f(t_{-1}) + f(t_{-2})] + O(\Delta t^2), \quad (10.22)$$

where t_0 denotes the time under consideration. The first time step is computed with a first-order approximation of the derivative assuming an initial steady state.

10.1.6 Sloshing modes and free surface stability

The numerical procedure employed to compute the meniscus and time-dependent interface deformation is essentially the same that is used to determine the linear modes of the system [108]. The time derivatives

are computed assuming that the time-dependent perturbation of any variable $\kappa(r, z, t)$ is of the form

$$\kappa(r, z, t) = \kappa_b(r, z, t) + \epsilon \delta \kappa(r, z, t) e^{-i\omega t} \quad (\epsilon \ll 1), \quad (10.23)$$

with $\kappa_b(r, z, t)$ denoting the steady-state solution, ϵ a small coefficient of perturbation, $\delta \kappa(r, z, t)$ the spatial dependence of the eigenmode for that variable, and $\omega = \text{Re}(\omega) + i\text{Im}(\omega)$ the eigenfrequency. The spatial dependence of the eigenmode is the solution of the generalized eigenvalue problem

$$\mathcal{J}_b^{(p,q)} \delta \kappa^{(q)} = i\omega Q_b^{(p)}, \quad (10.24)$$

where $\mathcal{J}_b^{(p,q)}$ is the Jacobian of the system evaluated at the steady-state solution $\kappa_b^{(q)}$, and $Q_b^{(p,q)}$ accounts for the time dependence of the problem (i.e. contains the time-dependent terms of the Jacobian). The resulting generalized eigenvalue problem is solved using the MATLAB EIGS routine. An example of the eigenfrequencies obtained with this method for $I = 10$ A is shown in Fig. 10.2. A *free-edge* condition with fixed contact angle is assumed in this process (i.e. the vertex A-B-E can move freely in the vertical direction, but keeping a constant θ_c). However, different implementations may consider a *stuck-edge* approach or more complex hysteresis mechanisms, as discussed in Sec. 7.4.2.

The dominant eigenmode is related to the largest growth factor $\text{Im}(\omega)$. If such growth factor is negative, the damping ratio of the mode can be computed as $\zeta = -\text{Im}(\omega)/|\omega|$, with $|\omega|$ being the norm of the eigenvalue. If $\text{Im}(\omega)$ is positive, the meniscus becomes asymptotically unstable. This result is of particular importance for low-gravity magnetic liquid positioning applications, as it can be used to size the magnetic actuators of the system [346]. Further details on the computation of the eigenfrequencies and

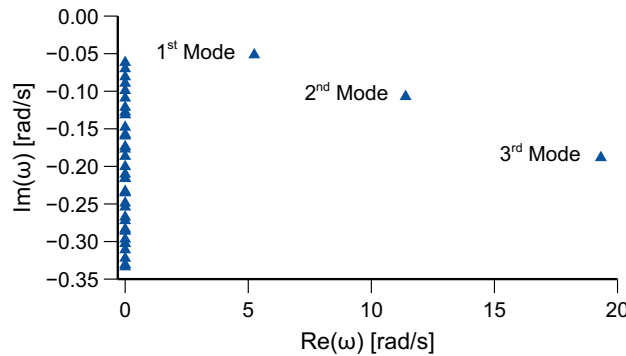


Figure 10.2: Eigenfrequencies spectrum for $I = 10$ A. The first three dynamic modes are labeled.

eigenmodes of the system can be found in Ref. 108.

10.2 Verification and validation

10.2.1 Field-free solution

The dynamic response predicted by the interface-tracking framework on which this work is based has already been validated with experiments on liquid bridges at the International Space Station [108]. For completeness, however, an extended verification is here presented for the axisymmetric non-magnetic liquid sloshing problem. The dimensionless variables

$$\text{Bo} = \frac{\rho g a^2}{\sigma}, \quad \Omega_1^2 = \frac{\rho a^3 [\text{Re}(\omega_1)]^2}{\sigma}, \quad \text{Oh}^2 = \frac{\eta^2}{\rho \sigma a},$$

that correspond to the Bond number, the dimensionless real fundamental frequency, and the Ohnesorge number, respectively, are employed in the validation together with the previously defined damping ratio ζ in consistency with the original sources of data.

Figure 10.3 depicts the dimensionless real fundamental axisymmetric frequency of the tank described in Sec. 10.1.1 for a range of contact angles and Bond numbers. An inviscid liquid is employed to run the simulations, which are then compared with the analytical model developed by Yeh in Ref. 17. The results are in perfect agreement and demonstrate that the implementation of the inviscid non-magnetic terms (in particular, surface tension) are appropriate.

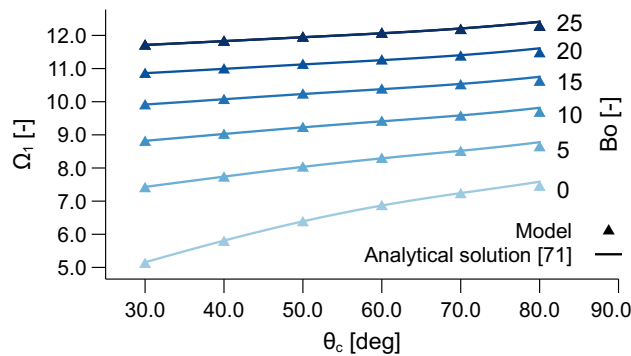


Figure 10.3: Real fundamental axisymmetric frequency as a function of the contact angle and gravity level compared with analytical results from Yeh [17].

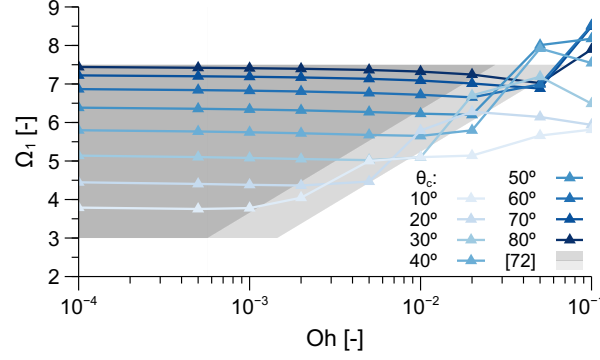


Figure 10.4: Numerical results for the dimensionless frequency as a function of the Ohnesorge number and contact angle compared with envelope data from Gerstmann and Dreyer [18].

Next, the modal response of the liquid is explored for different contact angles and Ohnesorge (viscosity) levels in Fig. 10.4 and compared with free-edge envelope computations from Gerstmann and Dreyer [18]. Following their discussion, gray patches define parametric spaces where surface oscillations are observable, which are bounded by analytical approximations for small Oh at $\theta_c = 0^\circ$ ($\Omega_1^{\min} = 3$), $\theta_c = 90^\circ$ ($\Omega_1^{\max} = 7.5$), and transition limits of the form $\Omega_1 = a + b \ln(Oh)$. The dark and light gray areas denote the viscous damping and boundary layer-dominated regimes, respectively. The second is characterized by the enlargement of the boundary layer and the increase of the frequency with the Ohnesorge number caused by the reduction in the effective liquid radius. The interested reader is referred to Ref. 18 for a comprehensive discussion of these effects. In the context of this section, however, the main conclusion is that numerical results are in perfect agreement with the reference study, validating the implementation of viscous terms and no-slip boundary conditions at the walls of the tank.

The dependence of the damping ratio ζ with the Ohnesorge number and contact angle is finally reported in Fig. 10.5 and compared with the envelope computed by Gerstmann and Dreyer [18]. Again, the results are in perfect agreement and reproduce the transition from linear to non-linear regimes as Oh increases.

The previous results have been expressed in dimensionless variables for consistency with the sources of data. However, it is important to note that the magnetohydrodynamic model introduced in this work is dimensional. There is an inherent benefit in using dimensionless variables in low-gravity fluid mechanic

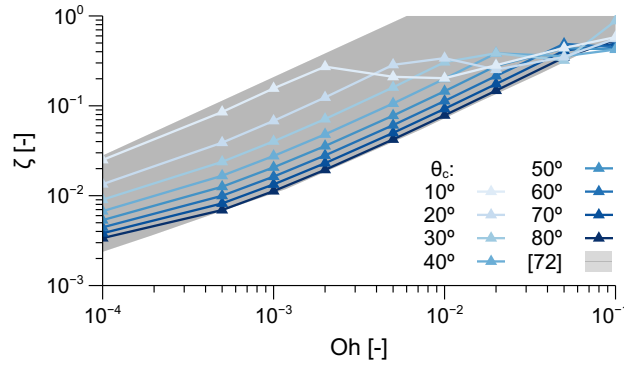


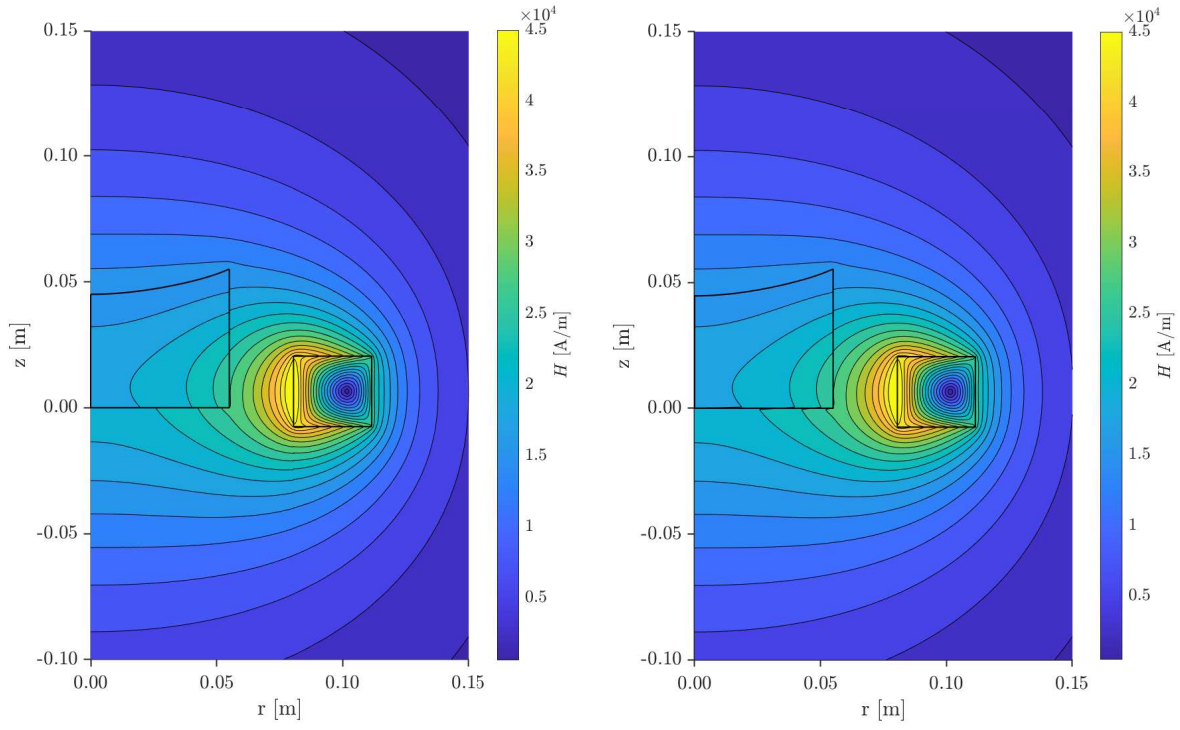
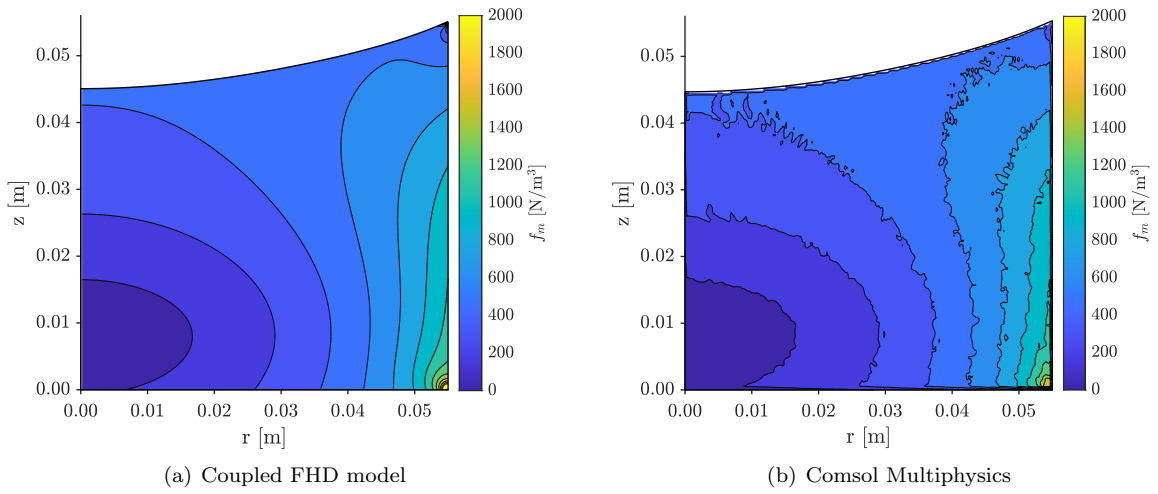
Figure 10.5: Numerical results for the damping ratio as a function of the Ohnesorge number and contact angle compared with envelope data from Gerstmann and Dreyer [18].

(and, in general, capillary) problems, but this practice is far less beneficial in magnetohydrodynamics due to the dependence of the solution on the magnitude, direction, and distribution of the inhomogeneous magnetic force. An excellent review of analytical low-gravity fluid mechanics methods is given by Myshkis and coworkers in Ref. 85.

10.2.2 Magnetic model

The magnetic field \mathbf{H} is first compared in Fig. 10.6 with a finite elements Comsol Multiphysics magnetic model. The model takes the equilibrium ferrofluid interface and, assuming the same materials, computes the magnetic field without solving the Navier-Stokes equations. Further details on its implementation can be found in the Appendix B. Both solutions are in excellent agreement, reflecting the appropriate implementation of Eqs. 6.13 and 6.15 and their axisymmetric formulations in Sec. 10.1.3. Similar levels of agreements are observed when the coil is substituted by a vertically magnetized magnet but, as described in Sec. 10.1.4.1, larger simulation domains are needed.

Figure 10.7 compares the magnetic force density for $I = 20$ A with the control model in Comsol Multiphysics. The distributions are virtually identical, which verifies the implementation of the magnetic force in Eq. 6.10c. The force depends on the spatial derivatives of the magnetic field is then highly sensitive to irregularities in \mathbf{H} and \mathbf{M} . In the figure, however, such irregularities are only observed in the finite elements Comsol Multiphysics model, reflecting the high stability of the fourth-order finite differences scheme employed

Figure 10.6: Magnetic field comparison for $I = 20$ A.Figure 10.7: Force density module comparison for $I = 20$ A.

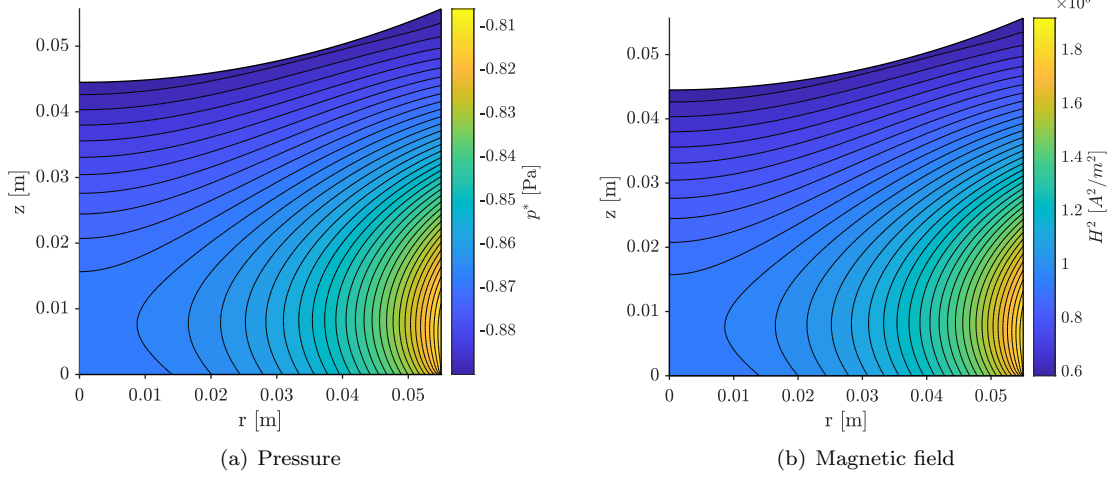


Figure 10.8: Comparison of pressure and magnetic field lines for a paramagnetic fluid with $\chi^{\text{vol}} = 0.1$ at $I = 1$ A.

in this work. The irregularities in the Comsol solution are just a consequence of the gradient computation step and do not reflect an underlying problem with the simulation. The implementation of the magnetic force term in the momentum balance is verified in Fig. 10.8. According to Eq. 6.12b, the steady state pressure lines must be coincident with the constant H^2 lines for a linearly magnetized liquid. After implementing a constant magnetic susceptibility $\chi^{\text{vol}} = 0.1$, the comparison between both plots reflects the desired behavior. Here and in the rest of the chapter, the pressure is referred to the value at the B side of line 15.

Finally, quantitative intermediate results are reported in Table 10.2 for different locations inside domain A as a function of the applied current intensity. The reader may find this useful as a reference for future works.

10.2.3 Equilibrium and virtual magnet substitution

The previous section verifies that (i) the magnetic model produces the desired magnetic field, (ii) such field results in the appropriate magnetic force, and (iii) the magnetic force is properly implemented in the system. The next logical step consists on comparing the equilibrium solution with previous models

In the magnetic sloshing problem, the equilibrium free surface profile - or *meniscus* - defines the steady-state solution of the system. Such profile experiences very small deformations in the ESA *Drop Your*

Table 10.2: Intermediate results for representative positions in domain A as a function of the applied current intensity.

I [A]	r [cm]	z [cm]	ϕ [A]	ψ [A·m]	H [A/m]	F_m [N/m ³]	p^* [Pa]	η [mPa·s]
10	1	1	0.52	-13.38	9612.92	32.77	1.80	1.447
	5	1	14.50	-7.64	12481.52	331.13	7.20	1.448
	5	5	9.81	11.64	8036.53	193.77	-0.78	1.446
15	1	1	0.78	-17.11	14630.95	63.03	4.69	1.448
	5	1	21.76	-9.64	18907.84	593.66	14.64	1.449
	5	5	14.72	14.68	12076.60	385.32	-0.66	1.448
20	1	1	1.04	-19.58	19725.66	96.22	8.09	1.449
	5	1	29.01	-10.93	25390.19	865.30	22.81	1.450
	5	5	19.62	16.69	16135.73	605.11	-0.51	1.449

Thesis! 2017 - *The Ferros* experiment, making it unsuitable for comparison, and so a different setup is chosen. The model and case of analysis introduced in Ref. 16 are analyzed employing the virtual magnet substitution approach introduced in Sec. 10.1.4.1. A 5 cm radius cylindrical tank filled up to 5 cm with the ferrofluid described in Sec. 10.1.1 is exposed to the magnetic field produced by a 28 mm radius, 3 mm height disc cylindrical magnet with a 5 mm hole in its center. This magnet is located 1 mm below the bottom of the container, and is magnetized at $\mathbf{M}_m = 1500 \text{ kA/m}$ along the z-direction. The resulting \mathbf{B} field corresponds to the one produced by an internal virtual surface current $\mathbf{K}_{e,i} = -M_m \mathbf{e}_\phi$ at $r = 2.5 \text{ mm}$, and an external virtual surface current $\mathbf{K}_{e,e} = M_m \mathbf{e}_\phi$ at $r = 28 \text{ mm}$. 20 equispaced circular loops with currents of 375 A are employed on each side to compute the Ψ potential of this equivalent system.

Although the assimilation of virtual magnetization currents as electric currents cannot be adopted in the computation of the magnetic field \mathbf{H} inside the magnet, an exact solution is still obtained in the external domain. Indeed, the magnetic field represented in Fig. 10.9(a), obtained with the virtual magnet substitution procedure, is in excellent agreement with the previous quasi-analytical magnetic sloshing model [16] shown in Fig. 10.9(b). In the second case, the magnetic problem is solved by iterating with the Comsol Multiphysics magnetic model described in the Appendix B. Both solutions show a characteristic protuberance at the center of the meniscus, which results from the tendency of the liquid to follow the constant Bo_{mag} (or \mathbf{H}) lines when surface tension is weakest. Previous works have predicted and reported this behavior [16, 347].

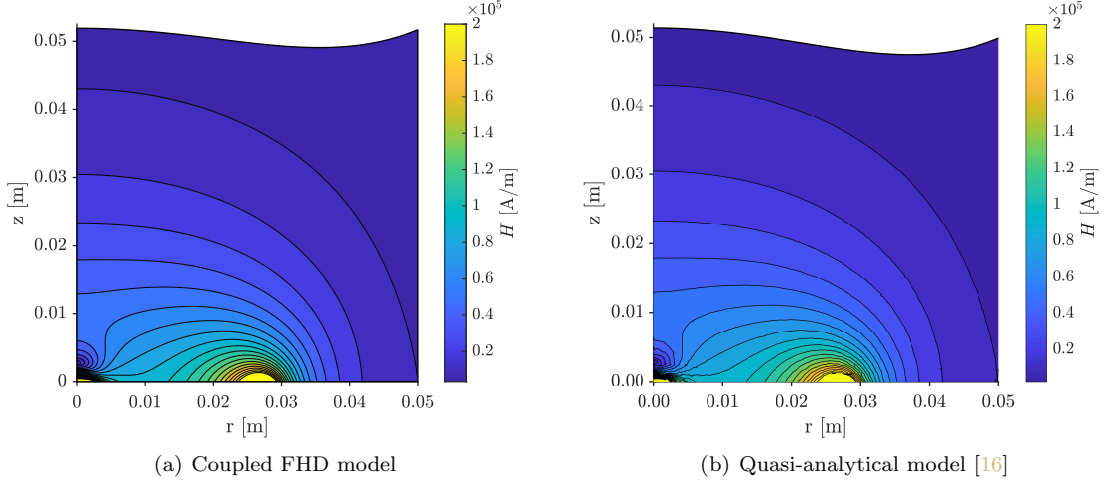


Figure 10.9: Comparison of magnetic fields and meniscus produced by a 3 mm height, 27.5 mm external radius magnet with a central 5 mm radius hole located 1 mm below the container. The virtual magnet substitution method described in Sec. 10.1.4.1 is employed.

10.2.4 Modal shapes

Figure 10.10 compares the shape of the first two axisymmetric modes obtained using the procedure described in Sec. 10.1.6 with predictions from the quasi-analytical model in Sec. 7.4 for $I = 20$ A. The plot shows the normalized modal vertical displacement Z of the surface as a function of the non-dimensional radius r/a . An excellent overall agreement is observed, but small disagreements are produced due to the inherent differences between both methods. While the procedure here presented is based on the numerical solution of an eigenvalue problem, the quasi-analytical solution relies on a set of suitable primitives and

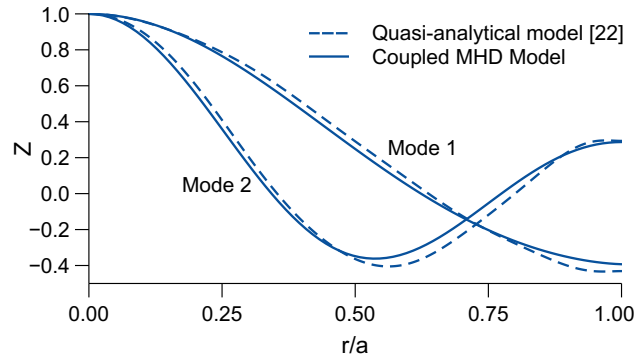


Figure 10.10: Comparison of first two fundamental modes for $I = 20$ A.

admissible functions that are employed in Ritz's method.

10.2.5 Dynamic response

As discussed in Sec. 10.1.1, the geometry and physical properties of the ESA *Drop Your Thesis!* 2017 experiment *The Ferros* [3] are subsequently adopted in the validation of the dynamic response of the model. Among the potential validation metrics, the natural free surface oscillation frequencies arise as the easiest to measure and the most relevant for the development of mechanical analogies [86]. Furthermore, they condense the effect of the magnetic settling force in the fluid system.

The first two axisymmetric free surface oscillation frequencies are reported in Fig. 10.11 for the upper and lower containers of the setup depicted in Fig. 9.3 as a function of the coils current intensity. Predictions from the numerical framework are compared with results from the quasi-analytical inviscid magnetic surface oscillations model in Sec. 7.4 and with experimental data in Chapter 9. The experimental setup has a second coil that is not modeled in the simulation domain (see Figs. 10.1(b) and 9.3), but since its contribution increases the fundamental oscillation frequency in just a 0.45%, it is considered negligible. Two comparison metrics can be extracted from Fig. 10.11: the vertical shift between curves, and their slope. The former is attributed in Chapter 9 to the accumulation of errors in the non-magnetic parameters of the system. This conclusion is backed up by (i) the large uncertainties reported in Table 9.1 for contact angles and surface tension coefficients, (ii) the strong dependence of the natural oscillation frequencies on such parameters, explored in Fig. 10.3, (iii) the linearity of the current-frequency curve, and (iv) the field-independent experimental shift of ~ 0.9 rad/s between the fundamental frequencies of upper and lower containers. This constant shift points to the field-free frequency upon which the magnetic response is built, and hence to the non-magnetic parameters that determine it. It also shows that such initial uncertainty has little or no effect on the frequency-current response of the system because both lines are practically parallel, as quantified in the next paragraph. This is further supported by the fact that the magnetic force is too weak to produce significant deformations on the interface, and thus any potential surface tension or contact angle discrepancy will be unable to alter the magnetic response if the meniscus geometry is kept essentially frozen.

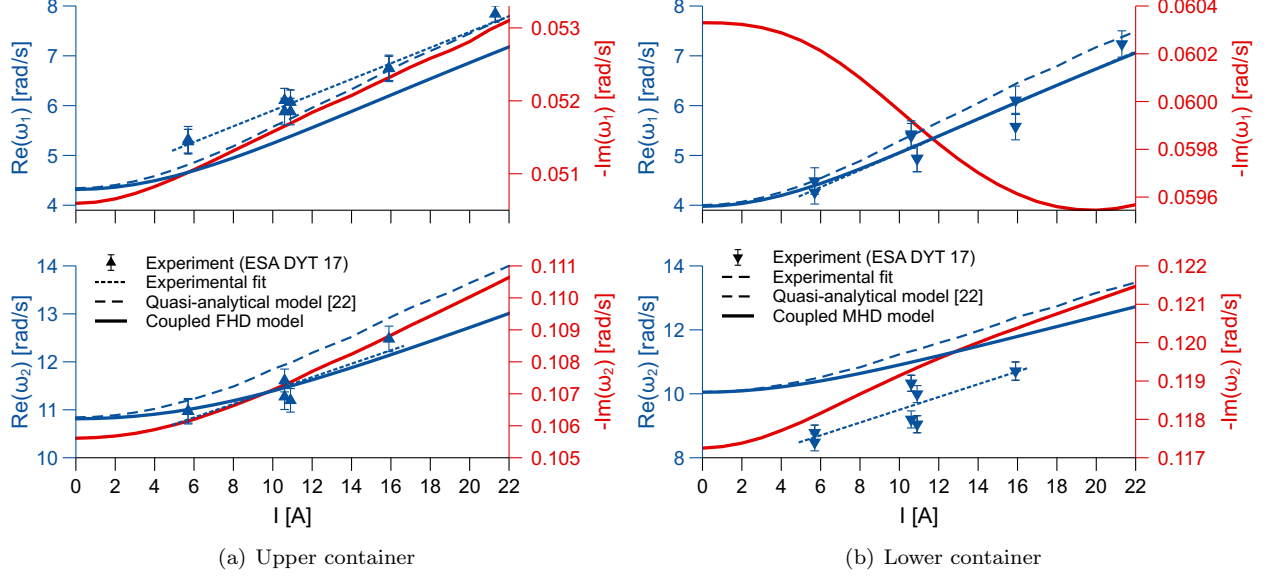


Figure 10.11: First two axisymmetric natural sloshing frequencies compared with the quasi-analytical model Sec. 7.4 and experimental measurements obtained during the ESA *Drop Your Thesis!* 2017 campaign and reported in Chapter 9.

Unlike the vertical frequency shift, the frequency-current slopes reflect the magnetic response of the system. The experimental slope of the fundamental frequency at the upper container is $0.158 \text{ rad s}^{-1}\text{A}^{-1}$ with $[0.138, 0.178] \text{ rad s}^{-1}\text{A}^{-1}$ 95% confidence interval (CI), while in the lower vessel it results in $0.170 \text{ rad s}^{-1}\text{A}^{-1}$ with $[0.121, 0.219] \text{ rad s}^{-1}\text{A}^{-1}$ 95% CI. These CIs do not include the $0.187 \text{ rad s}^{-1}\text{A}^{-1}$ slope of the analytical model at the upper vessel, but include the $0.186 \text{ rad s}^{-1}\text{A}^{-1}$ value of the lower tank. On the contrary, the numerical model presented in this work matches almost perfectly the experimental slopes, with $0.161 \text{ rad s}^{-1}\text{A}^{-1}$ for the upper container and $0.167 \text{ rad s}^{-1}\text{A}^{-1}$ for the lower. As expected from the field-free analysis presented in Fig. 10.3, the non-magnetic solution ($I = 0 \text{ A}$) is also in excellent agreement with the quasi-analytical model.

The second fundamental axisymmetric modes are also reported in Fig. 10.11 for those cases where they are observable. The amplitude of the second mode is much smaller than the first, and so harder to detect. Because in some experiments the second mode could not be recovered, the number of data points is significantly smaller. In addition, its higher oscillation frequency and complex shape makes it more sensitive to disturbances in the contact line. This explains the horizontal bias in the plots and why the experimental

slopes of $0.136 \text{ rad s}^{-1} \text{ A}^{-1}$ with $[0.049, 0.222] \text{ rad s}^{-1} \text{ A}^{-1}$ 95% CI (upper container) and $0.202 \text{ rad s}^{-1} \text{ A}^{-1}$ with $[0.054, 0.349] \text{ rad s}^{-1} \text{ A}^{-1}$ 95% CI (lower container) have such wide CIs. As pointed out in Chapter 9, this large uncertainty effectively renders any comparison with the theoretical slopes statistically meaningless. Still, results are given for completeness.

The differences between inviscid quasi-analytical and numerical results cannot be explained by the effects of liquid viscosity, that accounts for just a 0.6% reduction of the real frequency component. The remaining discrepancy may be attributed to the differences in modal shapes shown in Fig. 10.10, but there is a deeper reason that could cause it and that has already been disclosed in Sec. 7.4.7. While the model in Sec. 7.4 applies a first-order perturbation to an equilibrium solution while considering a constant magnetic environment, the monolithic numerical framework here introduced linearizes the full fluid-magnetic solution around the equilibrium state. Therefore, the magnetic terms are also linearized and contribute to the modal response. If any, this is an important reason for choosing monolithic approaches over partitioned schemes when studying coupled ferromagnetic problems.

The results of the UNOOSA DropTES 2019 StELIUM experiment, shown in Chapter 9, also report an increase in the imaginary component (damping) with the applied magnetic field. However, the damping ratios measured for both the ESA *Drop Your Thesis!* 2017 and the UNOOSA DropTES 2019 StELIUM experiments are one order of magnitude larger than in Fig. 10.11. Because the viscosity of the ferrofluid employed in both experiments was measured with a rheometer under zero-field conditions, the reader may be tempted to attribute this effect to the magnetic interaction. Magnetic nanoparticles, like any magnetic dipole, tend to align with the magnetic field. Although the reorientation is assumed instantaneous in this work, this may not be true for ferrofluids with high vortex viscosity or subject to high-frequency alternating magnetic fields. Such liquids exhibit an apparent increase in the shear viscosity coefficient η [20]. However, the application of Shliomis' shear model [336] to the problem under study results in a viscosity variation of just $\sim 1\%$ at 10^6 A/m , justifying the adoption of the symmetrical constitutive relation in Eq. 6.5. The larger experimental damping may instead be caused by interfacial effects induced by the surfactant. Similar disagreements have been reported in previous experiments with water and hexadecane in Refs. 327 and 328, suggesting a large susceptibility of the effective viscosity of low viscosity liquids to surface contamination.

Table 10.3: Complex fundamental axisymmetric frequencies as a function of mesh density in region A ($n_s \times n_{\eta_A}$) for different current intensities.

	Re(ω_1) [rad/s]			Im(ω_1) [rad/s]		
	91 \times 91	101 \times 101	111 \times 111	91 \times 91	101 \times 101	111 \times 111
0 A	4.3179 (+0.0269%)	4.3168	4.3159 (-0.0216%)	-0.0506 (+0.0046%)	-0.0506	-0.0507 (+0.1878%)
5 A	4.5862 (+0.0243%)	4.5851	4.5842 (-0.0191%)	-0.0510 (+0.1241%)	-0.0509	-0.0510 (+0.1013%)
10 A	5.2454 (+0.0210%)	5.2443	5.2435 (-0.0157%)	-0.0518 (+0.4098%)	-0.0516	-0.0515 (-0.1069%)
15 A	6.0486 (+0.0197%)	6.0474	6.0466 (-0.0139%)	-0.0526 (+0.7670%)	-0.0522	-0.0520 (-0.3681%)
20 A	6.8627 (+0.0193%)	6.8614	6.8605 (-0.0132%)	-0.0534 (+1.1809%)	-0.0528	-0.0525 (-0.5821%)

Table 10.4: Complex second axisymmetric frequencies as a function of mesh density in region A ($n_s \times n_{\eta_A}$) for different current intensities.

	Re(ω_2) [rad/s]			Im(ω_2) [rad/s]		
	91 \times 91	101 \times 101	111 \times 111	91 \times 91	101 \times 101	111 \times 111
0 A	10.8173 (+0.0518%)	10.8117	10.8074 (-0.0403%)	-0.1078 (+2.0552%)	-0.1056	-0.1043 (-1.2539%)
5 A	10.9659 (+0.0509%)	10.9603	10.9560 (-0.0395%)	-0.1083 (+2.1204%)	-0.1060	-0.1046 (-1.3018%)
10 A	11.3980 (+0.0499%)	11.3924	11.3880 (-0.0383%)	-0.1096 (+2.3165%)	-0.1071	-0.1056 (-1.4433%)
15 A	12.0173 (+0.0498%)	12.0113	12.0068 (-0.0376%)	-0.1114 (+2.6019%)	-0.1085	-0.1067 (-1.6841%)
20 A	12.7226 (+0.0506%)	12.7162	12.7115 (-0.0374%)	-0.1132 (+2.9240%)	-0.1100	-0.1079 (-1.8967%)

Real and imaginary frequency components are reported in Tables 10.3 and 10.4 for different current intensities and block A mesh densities. It should be noted that the configuration of block A determines the density of the rest of the simulation domain. The convergence of the base mesh (101 \times 101 nodes) is demonstrated for real and imaginary components with errors below 0.05% and 1.9%, respectively. Furthermore, the error decreases with increasing densities, showing that the solution is mesh-independent. The imaginary terms are more sensitive to the mesh density, as they depend on the discretization of the boundary layer at the walls of the container. This motivates, in first instance, the adoption of the non-uniform node distribution in block A shown in Fig. 10.1(b).

10.3 Extended capabilities

10.3.1 Global stability

As discussed in Sec. 7.3, understanding the stability properties of capillary interfaces is essential for numerous physical systems, from liquid bridges [328, 348] to conduit geometries [124, 349]. Figure 10.12 depicts the evolution of the fundamental axisymmetric frequency of the ESA *Drop Your Thesis!* 2017 problem as a function of the inertial acceleration g along the axis of the container. The transition to an unstable equilibrium regime is characterized by the sudden change of sign and the drop to zero of the

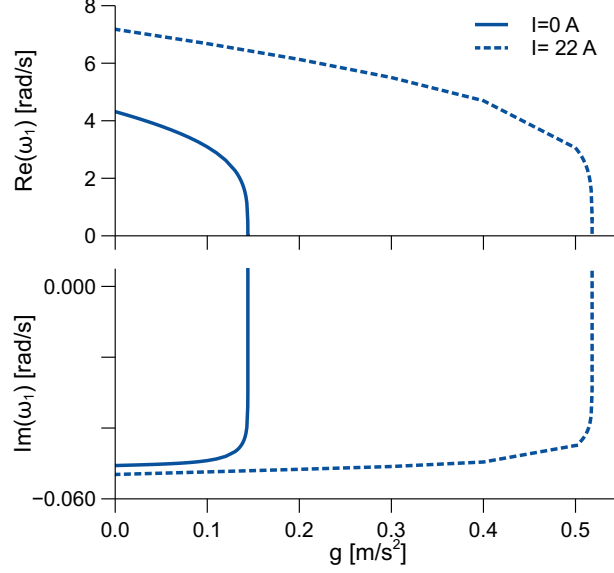


Figure 10.12: Fundamental axisymmetric frequency as a function of the applied destabilizing inertial acceleration for magnetic ($I = 22$ A) and non-magnetic ($I = 0$ A) cases.

imaginary and real components, respectively. While the non-magnetic interface breaks for a critical load of 0.1441 m/s^2 , a value that is in agreement with analytical results from the model described in Sec. 7.3, the magnetic force stabilizes the system and pushes the limit up to 0.518 m/s^2 . This represents a 359.5% critical load increase, and exemplifies how magnetic polarization forces may be employed to enhance the controllability of space propellants. Greater gains should be expected for systems employing high-density permanent magnets, like the magnetic sloshing control devices proposed in Chapters 12 and 13.

10.3.2 Time-dependent analysis

To conclude the presentation of numerical results, Fig. 10.13 depicts the time-dependent vertical displacement z_c of the center of the free surface after the application of 5, 15, and 20 A step loads in microgravity. The response of the surface to a $\sim 0.53 \text{ m/s}^2$ step acceleration in the absence of magnetic fields is shown for comparison. This value corresponds to the mean magnetic acceleration exerted by the coil on the interface at 20 A, which drives the dynamic response of the system according to the quasi-analytical

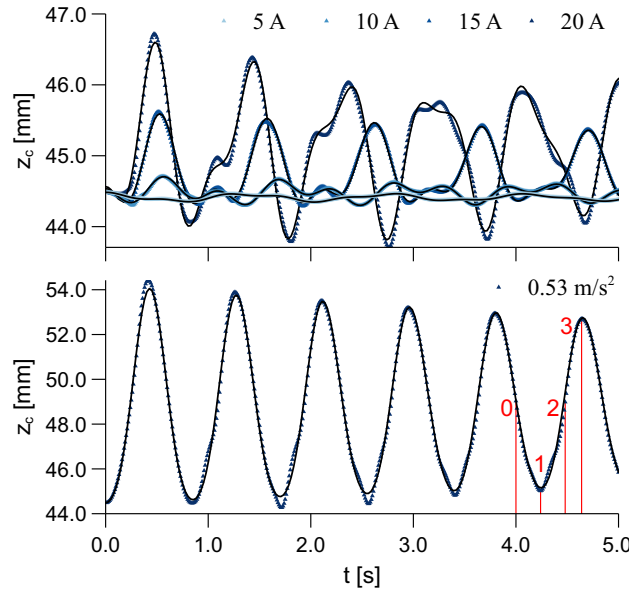


Figure 10.13: Time evolution of the center of the free surface after the application of magnetic (top) and inertial (bottom) step loads in microgravity. The modal fits reported in Eq. 10.25 and Table 10.5 are superposed.

model described in Refs. 16 and 295. If the position of the center is fitted with a function of the form

$$z_c = \sum_{i=1}^2 \left[a_i e^{\text{Im}(\bar{\omega}_i)t} \cos(\text{Re}(\bar{\omega}_i)t + b_i) \right] + k_0 \quad (10.25)$$

where a_i , b_i , $\bar{\omega}_i$, and k_0 are the fitting parameters for mode i , the results reported in Table 10.5 are obtained. It should be noted that $\bar{\omega}_i$ are estimations of the complex eigenfrequencies of the system. As expected, they match the real ($\text{Re}(\omega_i)$) and imaginary ($\text{Im}(\omega_i)$) magnetic frequency components computed in Table 10.3 and 10.4 with minimum errors. Those errors are caused by the inherent difficulties in observing the second eigenmode when superposed to other waves. This result verifies the implementation of the eigensolver described in Sec. 10.1.6 and the consistency of the solution.

As the magnetic step load increases in magnitude, so does the dynamic response of the interface. The 5 and 10 A excitations keep the wave amplitude below ~ 0.25 mm, but this value jumps to ~ 0.5 and ~ 1.5 mm for 15 and 20 A, respectively. It is important to note that the 0.53 m/s^2 inertial load produces a wave that is three times larger than the 20 A counterpart that is supposed to resemble. The reason should be found in a slightly larger inertial load, reflected in its higher eigenfrequencies in Table 10.5, and the curved magnetic field contours at the interface shown in Fig. 10.6, that differ significantly from the horizontal equipotential

Table 10.5: Fitting parameters defined in Eq. 10.25 for the time evolution of the center of the free surface reported in Fig. 10.13 for different step loads.

Step load	a_1 [mm]	$\text{Im}(\bar{\omega}_1)$ [rad/s]	$\text{Re}(\bar{\omega}_1)$ [rad/s]	b_1 [-]	a_2 [mm]	$\text{Im}(\bar{\omega}_2)$ [rad/s]	$\text{Re}(\bar{\omega}_2)$ [rad/s]	b_2 [-]	k_0 [mm]
5 A	$5.158 \cdot 10^{-5}$	-0.0532	4.576	-0.0035	$2.2645 \cdot 10^{-5}$	-0.1180	10.916	-0.0634	0.0444
10 A	$-1.1093 \cdot 10^{-3}$	-0.0567	5.233	-0.0181	$1.2449 \cdot 10^{-4}$	-0.1073	11.345	-0.0611	0.0445
15 A	$-5.462 \cdot 10^{-4}$	-0.0515	6.045	-0.0334	$3.2057 \cdot 10^{-4}$	-0.1213	11.988	-0.0928	0.0448
20 A	$-1.063 \cdot 10^{-3}$	-0.0543	6.843	-0.0135	$-0.5423 \cdot 10^{-3}$	-0.1469	12.640	-0.0252	0.0451
0.53 m/s ²	$-4.866 \cdot 10^{-3}$	-0.0553	7.428	-0.0466	$-0.6506 \cdot 10^{-3}$	-0.1624	14.952	-0.1785	0.0487

lines of the inertial field. Since the horizontal equipotentials are further away from the field-free meniscus, once the excitation is applied the interface will acquire higher potential energies and produce larger amplitude oscillations.

Finally, Fig. 10.14 shows the streamlines associated with the cases covered in Fig. 10.13. Successive time points reflect the approximate first node (0), minimum ($T/4$), second node ($T/2$), and maximum ($3T/4$) of the displacement of the center of the surface. The four points chosen for the inertial wave are highlighted in Fig. 10.13. In the non-magnetic case, the same nodal flow patterns reported in Ref. 18 are observed. However, the magnetic cases also show an apparent boundary layer enlargement at the lower right corner of the container. This is presumably caused by the large localized magnetic forces induced by the coil and seems to be a feature of the magnetic sloshing problem. The minimum and maximum displacement points correspond to transition regimes and lead to more complex flow patterns with respect to the nodal cases. Higher order eigenmodes are clearly visible as counter rotational vortices in several plots (e.g. at $T/4$ for 5 A, 20 A, and the inertial case).

10.4 Generalization

Although the axisymmetric magnetic sloshing problem and the ESA *Drop Your Thesis!* 2017 *The Ferros* configuration described in Sec. 9.2 have been studied in this chapter, the numerical model finds application in several additional scenarios interest. Those include the analysis of microfluidic systems involving highly susceptible magnetic liquids, liquid manipulation devices in space, or bubble/droplet growth, detachment, and displacement problems, among others.

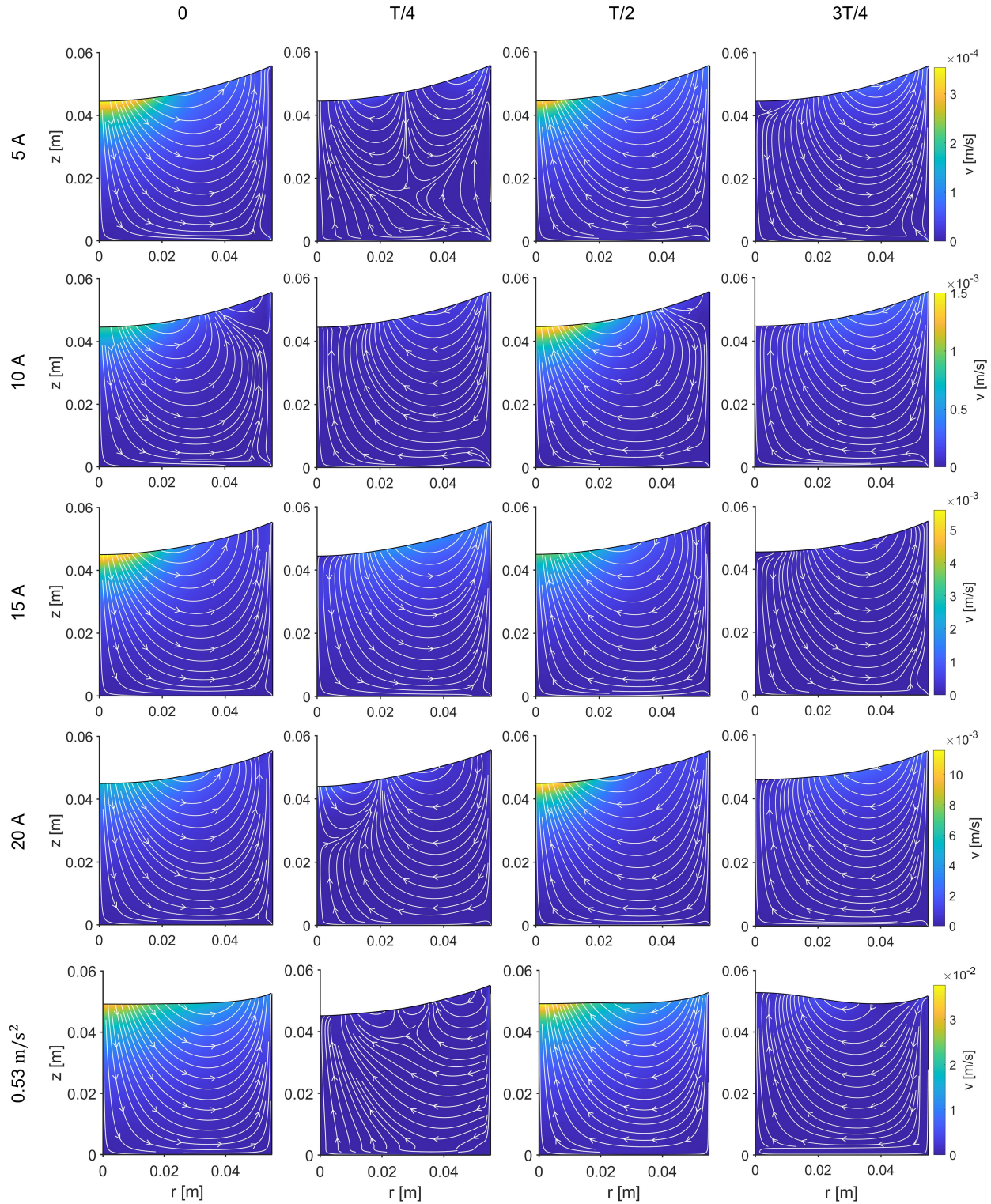


Figure 10.14: Streamlines after the application of magnetic (5-20 A) and inertial (0.53 m/s^2) step loads in microgravity. Successive time points reflect the first node (0), minimum ($T/4$), second node ($T/2$), and maximum ($3T/4$) of the displacement of the center of the surface, as indicated in Fig. 10.13.

At the time of writing this document, progress is being made to study the growth and detachment of gas bubbles in ferrofluids when subject to magnetic polarization forces. The simulation domain sketched in Fig. 10.15 has been developed for that purpose. Experimental [76] and numerical [91, 92, 104] works have recently addressed similar problems. However, they lack the unique capabilities of the interface-tracking approach here introduced, as shown in Sec. 1.3.3. The fundamental understanding of how magnetic fields influence the growth and detachment of gas bubbles over nucleation surfaces is key for the future development of applications like the magnetically enhanced electrolysis concept introduced in Chapter 14. Therefore, future publications will address this and other problems.

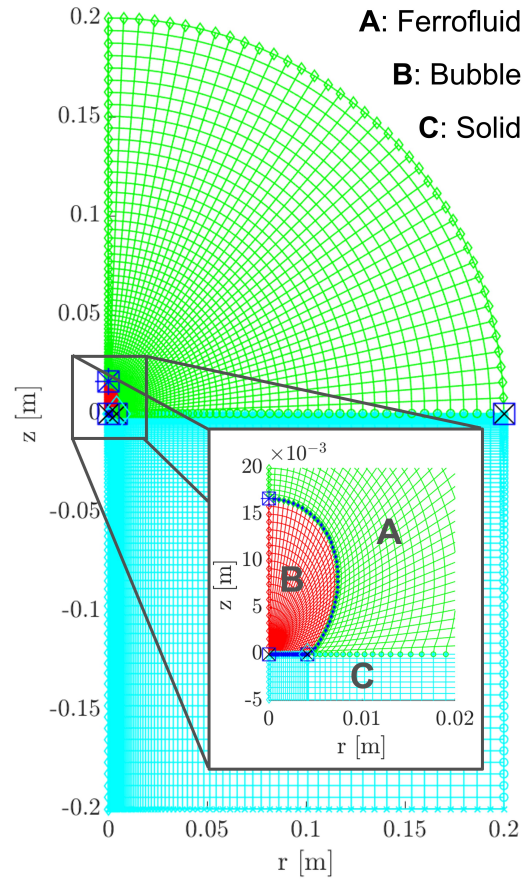


Figure 10.15: Mesh employed in the study of the growth and detachment of bubbles immersed in ferrofluids.

10.5 Collaborators

The numerical framework introduced in this chapter was developed together with Prof. Miguel Herada and with the support from Prof. Gabriel Cano-Gómez. The author thanks both of them for their extraordinary effort and commitment to this project.

Part III

Applications of low-gravity magnetohydrodynamics

Chapter 11

Magnetic phase separation

The third and last part of this dissertation can only start with the most basic low-gravity magnetohydrodynamic application: phase separation. From a systems engineering perspective, dia/paramagnetic phase separators could replace the functionality of existing technologies (reviewed in Sec. 1.4.1) with applications for any combination of phases. The magnetic buoyancy force formulated in Chapter 8 could also be employed in combination with existing systems, such as surface-tension-enabled conduit geometries. This is conceptually represented in Fig. 11.1, where magnetic and combined surface tension/magnetic phase separators are depicted for a diamagnetic liquid. The magnetic phase separator consists of a channel surrounding a magnet that attracts the bubbles from an incoming two-phase flow. The combined phase separator consists of a

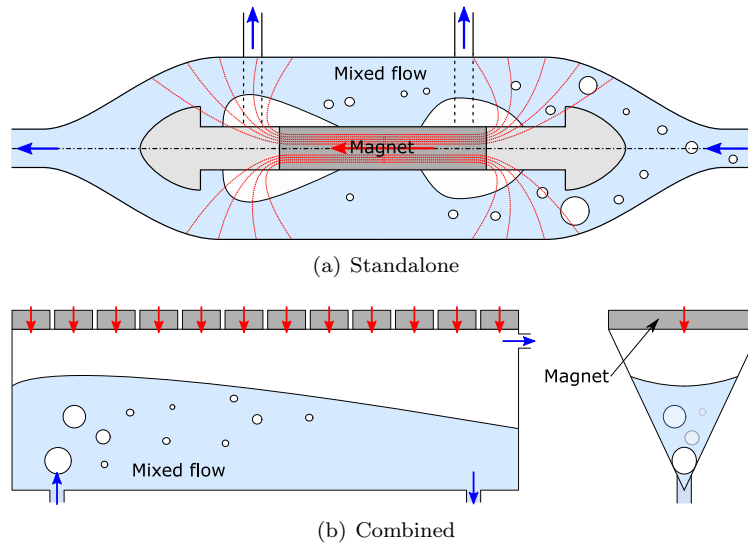


Figure 11.1: Conceptual representation of a magnetic standalone and surface-tension enhanced diamagnetic phase separator. Blue arrows represent the liquid/gas flow, while red arrows denote the magnetization vector.

wedge-shaped channel that pushes large bubbles to the open end as they evolve towards their configuration of minimum energy (spherical geometry). This approach was tested in the Capillary Channel Flow experiment, conducted at the ISS in April 2010 [124]. Magnetic buoyancy may be particularly useful to attract small bubbles that are unlikely to contact the free surface and hence remain within the liquid.

This chapter reports the first comprehensive measurements for magnetically induced buoyancy in microgravity environments generated for 4.7 s at ZARM's drop tower, described in Sec. 9.1. The artificially created buoyancy force is utilized to direct air gas bubbles on specific trajectories through dia- and paramagnetic solutions. The results demonstrate that the inherent magnetic properties of these substances are sufficient to allow the collection and coalescence of gas bubbles at distinct locations of the experiment vessel, providing a proof-of concept that the development of microgravity magnetic phase separators could lead to reliable and lightweight space systems.

11.1 Materials and Methods

11.1.1 Experimental setup

The experimental setup is designed to evaluate the diamagnetic buoyancy effect on three Becton-Dickinson BD Luer-Lok 30 ml syringes that act as sample containers. One syringe is used as a non-magnetic control, while the other two are exposed to the inhomogeneous magnetic field generated by a magnet (see Sec. 11.1.4). The experiment is released in a drop capsule from the top of ZARM's drop tower (described in Sec. 9.1) and experiences ~ 4.7 s of microgravity environment with maximum gravity residuals of $\sim 10^{-5}$ m/s² [335].

At the beginning of the drop, air bubbles are injected into the syringes using a modified Braun-Sterican 0.3 x 12.0 mm cannula depicted in Fig. 11.2(b). The angled tip of the cannula is removed to create a flat air outlet. Its surface is thoroughly cleaned by rinsing with acetone, isopropanol and MilliQ water for 5 s each before hydroxylating the tip for 15 min in a fresh Piranha solution, a 3:1 mixture of sulphuric acid (98%) and hydrogen peroxide (30%) [350]. This procedure is applied to promote the detachment of air bubbles from the tip of the injector. The gas is forced through the cannula by pushing a second syringe connected

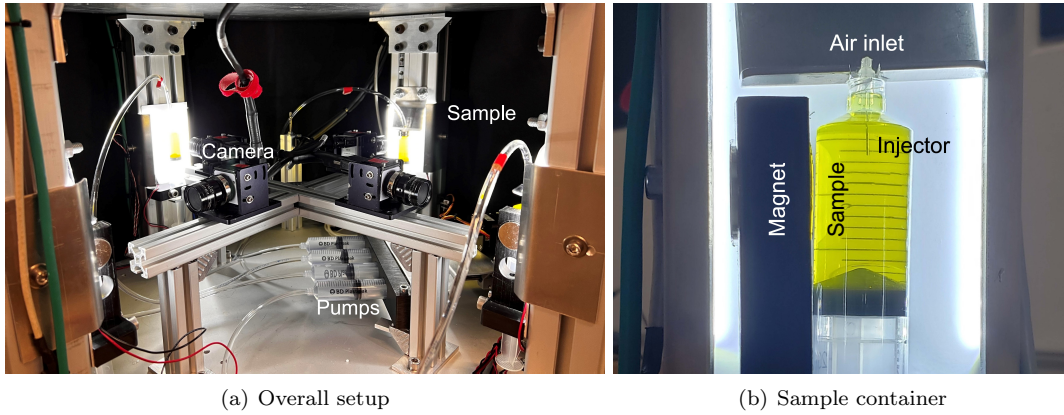


Figure 11.2: Experimental setup and syringe sample container located inside a ZARM's drop tower capsule.

to the sample container through a silicon tube. A programmable stepper motor is used to simultaneously push the syringes from each sample. In order to minimize air compression effects, part of the tube is filled with water. The overall setup is shown in Fig. 11.2(a).

The drops are recorded with three Photon MC-2 Fastcams high-speed cameras mounted in front of each container. The cameras are operated at 500 fps with a resolution of 512×512 px². This high frame rate requires strong illumination, which is made possible by LED strips that diffusely and homogeneously illuminate the liquid container. The flight sequence is commanded from the Capsule Control System described in Ref. [335].

11.1.2 Experimental matrix

Five drops are performed with different carrier liquids as summarized in Table 11.1. The physical properties of MilliQ water are well-known, which motivates the execution of two drop experiments and their use in Sec. 11.2 in the validation of the theoretical framework. An aqueous 0.5 M manganese (II) sulfate solution ($\text{MnSO}_4 \cdot \text{H}_2\text{O}$) was launched in the third drop to demonstrate the paramagnetic buoyancy effect. The fourth drop employed LB (*Lysogeny Broth*) medium (*Miller*) –which is widely used in biological experiments on the International Space Station for the growth of bacteria [351]– to demonstrate how the diamagnetic effect can be used to induce phase separation in such contexts. Finally, extra-virgin olive oil is tested to investigate how phase separation takes place in a complex organic solution.

Table 11.1: Experimental matrix.

ID	Substance	Classification
01	MilliQ Water	Diamagnetic
02	MilliQ Water	Diamagnetic
03	0.5M $\text{MnSO}_4 \cdot \text{H}_2\text{O}(\text{aq})$	Paramagnetic
04	LB Broth	Diamagnetic
05	Extra-virgin olive oil	Diamagnetic

11.1.3 Liquid properties

MilliQ water, LB (Miller) medium, containing 10 g/L tryptone, 10 g/L sodium chloride and 5 g/L yeast extract, and olive oil possess diamagnetic properties, whereas the Mn^{2+} ion has five unpaired 3d electrons and is therefore paramagnetic. MilliQ water is well characterized and exhibits a density $\rho = 998 \text{ kg/m}^3$, dynamic viscosity $\eta = 1.002 \text{ mPa}\cdot\text{s}$, surface tension $\sigma = 72.75 \text{ mN/m}$, and volume magnetic susceptibility $\chi^{\text{vol}} = -9.022 \cdot 10^{-6}$ at 293 K [2]. Therefore, experiments with water are used in this work to validate the formulations derived in Chapter 8. The 0.5M $\text{MnSO}_4 \cdot \text{H}_2\text{O}$ solution is chosen for comparison due to its paramagnetic susceptibility of $\sim 7.7 \cdot 10^{-5}$ [352], while olive oil is characterized by a large dynamic viscosity of $\sim 79 \text{ mPa}\cdot\text{s}$ [353]. Finally, LB Broth is tested due to its widespread application in biological experiments in microgravity and its complex composition [351].

11.1.4 Magnetic environment

The magnetic field is induced by a 19.05 mm height, 25.4 mm diameter, 72.4 g N52 neodymium magnet magnetized at 1150 kA/m and supplied by K&J Magnetics Inc. As shown in Fig. 11.2(b), the magnet is mounted on the side of the syringe. Since the magnetic susceptibility of the liquids employed in this experiment is of the order of $\pm 10^{-5}$, the magnetic properties of the system can be computed without accounting for the influence of the magnetization field on \mathbf{H} .

The magnetic field, diamagnetic acceleration on deionized water, and terminal velocity of a 1 mm diameter bubble computed from Eq. 8.26 and $\kappa = 2$ ($Re < 10$) are shown in Fig. 11.3. Terminal velocities of 1 to 10 mm/s are obtained between the injector and the magnet, indicating that the bubble reaches the magnet in a few seconds. The magnetic solution is computed in a Comsol Multiphysics model that follows

the same design approach as the one presented in the Appendix B.

11.1.5 Bubble tracking algorithm

The characterization of bubbles in transparent liquids is complicated by optical and geometrical challenges that undermine the detection process. Among them, poor illumination conditions, the superposition of different layers of bubbles, or the heterogeneous appearance of the bubble contour [354]. Different methods have been proposed to automatically determine the bubble size distribution of a given image. Optical algorithms are widely extended [355] and may be classified as geometry or appearance-based [354]. In the former, a circle is fitted to the image edge map using voting techniques such as the Hough Transform [356–358] or alternatives like the Concentric Circular Arrangements method [359]. Although geometry-based approaches are particularly susceptible to noise and result in an excessive number of false positives, appearance-based methods require large algorithm training databases [355].

A geometry-based algorithm is developed and implemented in Matlab 2021a to track the trajectory of gas bubbles within the syringe. The code is described in Fig. 11.4 and consists of the following steps:

- (1) **Image conversion:** Firstly, the original video frame is rotated to rectify the camera misalignment

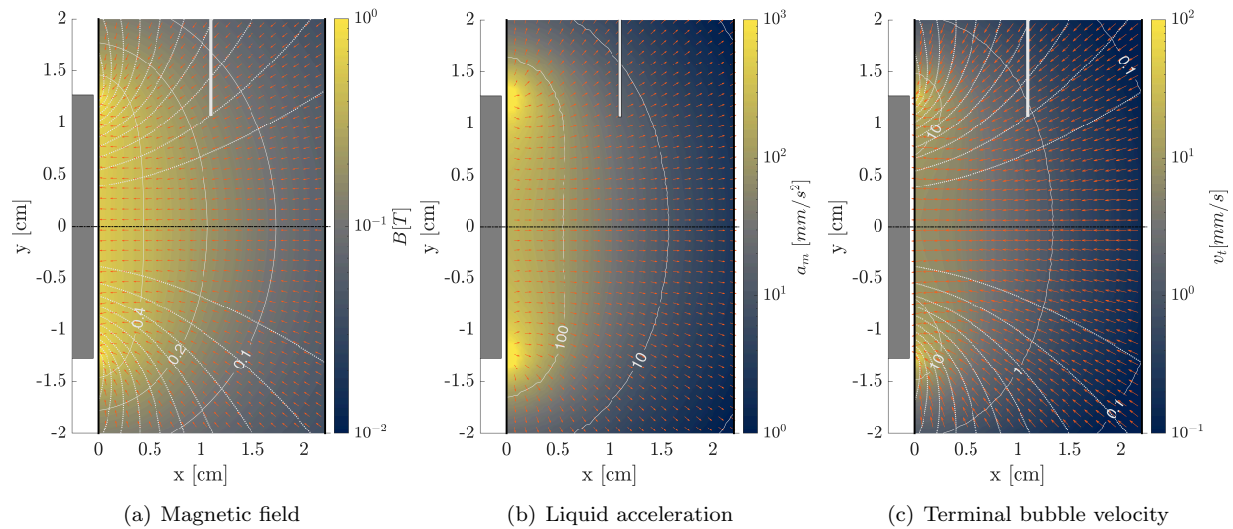


Figure 11.3: Magnetic environment inside the syringe when filled with MilliQ water and 1 mm diameter air bubbles. The white bar at the top represents the gas injector.

and then converted to gray-scale. When the magnet is on the right, the image is flipped to homogenize the comparison between cases.

- (2) **Background removal:** The first frame after the start of the drop is subtracted from the current frame to remove background noise.
- (3) **Binarization:** The contrast of the image is enhanced before binarizing using Otsu's method [360], implemented using Matlab's `imbinarize` function. Then, all objects containing less than 5 px are removed with `bwareaopen`.
- (4) **Circle enhancement:** In order to ease the automatic detection of bubbles, a morphological closing is performed with `imclose` by dilating and eroding the image using a disk shape as structuring element [361].
- (5) **Circle detection:** Finally, circles are detected using the Circular-Hough-Transform-based algorithm implemented in `imfindcircles` [362, 363]. The algorithm is configured with a sensitivity of 0.8 and an edge threshold of 0.2 using a bright object polarity. The curved wall of the syringe elongates the bubble and makes it look elliptical. To correct this visual distortion, a linear transformation is

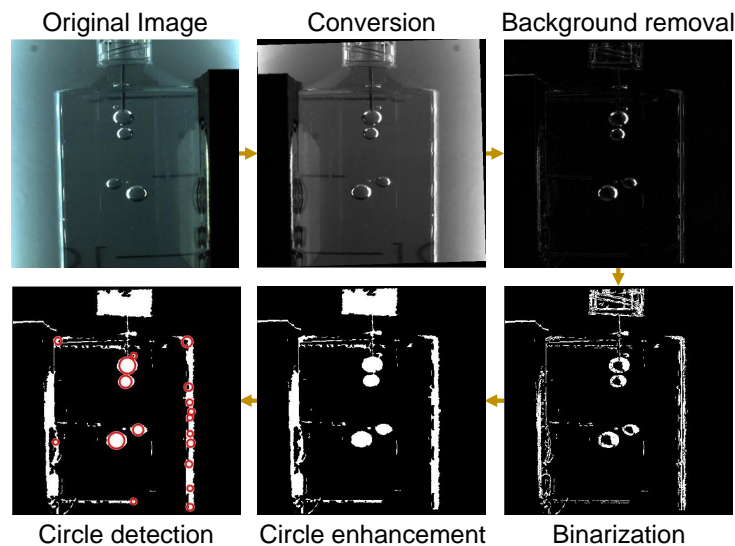


Figure 11.4: Bubble detection algorithm steps applied to the original video frame image.

applied in the horizontal direction before detecting the circle and then reversed to compute its actual position.

The same operations are applied to the rest of the video file until all frames are processed. Even though the bubble detection algorithm returns a large number of false positives, the presence of clear structures in the data enables an effective post-processing. Figure 11.5 represents the detected centroid locations as a function of time, with the size of the marker being proportional to the size of the bubble. To reconstruct its trajectory, a manual estimation of the final position is taken by a point tracking algorithm that looks for the closest point within a certain radius in the next frame. Since the initial position of the bubbles is the same, the tracking algorithm is run backwards in time. The resulting data are smoothed by applying a moving average filter with a window of 0.2 s. Second-order central finite differences are employed to derive the bubble velocity, which is finally smoothed with the same moving average filter.

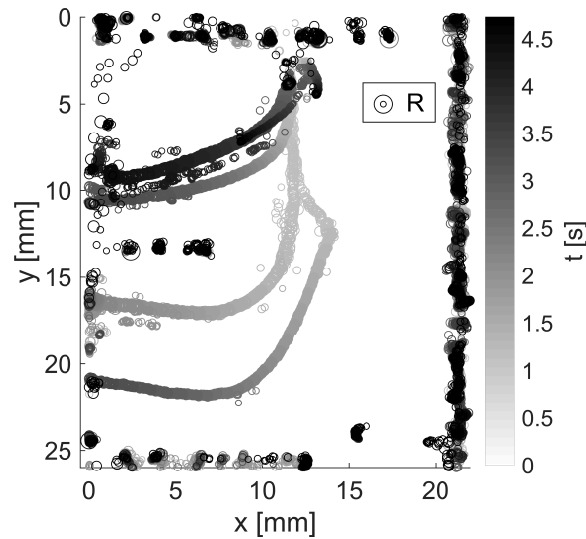


Figure 11.5: Unfiltered bubble trajectories resulting from the application of the bubble detection algorithm to a 4.7 s drop tower experiment. The color of the markers reflects the time of flight. Their size is scaled between 0.35 and 3.4 mm radius as indicated by the legend.

11.2 Results and discussion

11.2.1 Overview

Three samples are analyzed per drop as described in Sec. 11.1.1: two with a magnet and a third one that is used as a control. The control videos are shown in Fig. 11.6 for the first two drops with DI water. A wide range of bubble diameters is generated due to the varying pressure conditions and unsteady nature of the experiment. Rather than supposing a problem, this feature is beneficial to understand how different bubble diameters behave in the presence of the magnetic field. The injection of gas in the syringe leads to a downwards movement that is mostly damped after ~ 3 s. A slight lateral deviation of the flow is observed sometimes due to the small irregularities in the tip of the injector. Similar behaviors can be observed in the other three control videos, that have been omitted for clarity but are accessible in Ref. [364].

Magnetic results for the five drops under study are depicted in Fig. 11.7. The bubbles are collected by the magnets in all diamagnetic cases (01, 02, 04, and 05), while they are pushed away in the paramagnetic scenario (02). Interestingly, complex mixtures like LB Broth and olive oil are significantly affected by the magnetic force. In the second case, the effect is less noticeable (but still visible) due to the high viscosity of the liquid, that increases the drag acting on the bubble. This is an example of how all liquids are subject to magnetic polarization forces and can therefore be employed to induce phase separation in microgravity environments. The determination of such response, represented by the magnetic susceptibility, is relatively straightforward for simple solutions [3, 365]. Complex mixtures, on the contrary, need to be characterized

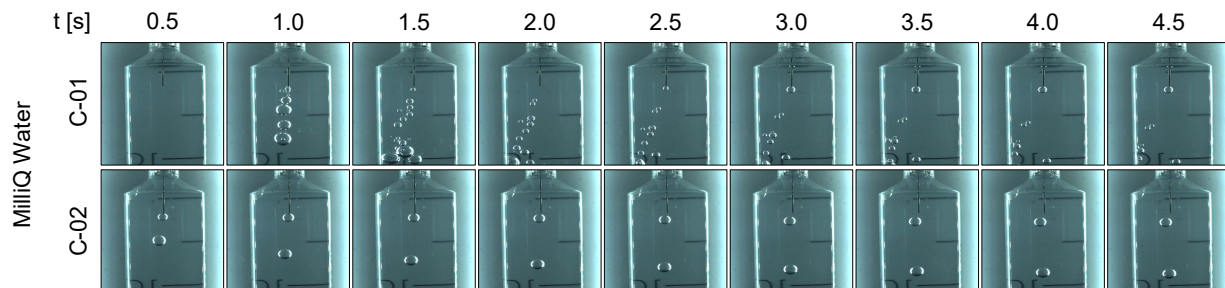


Figure 11.6: Control experiments for MilliQ water showing the injection and displacement of air bubbles in the absence of magnetic forces.

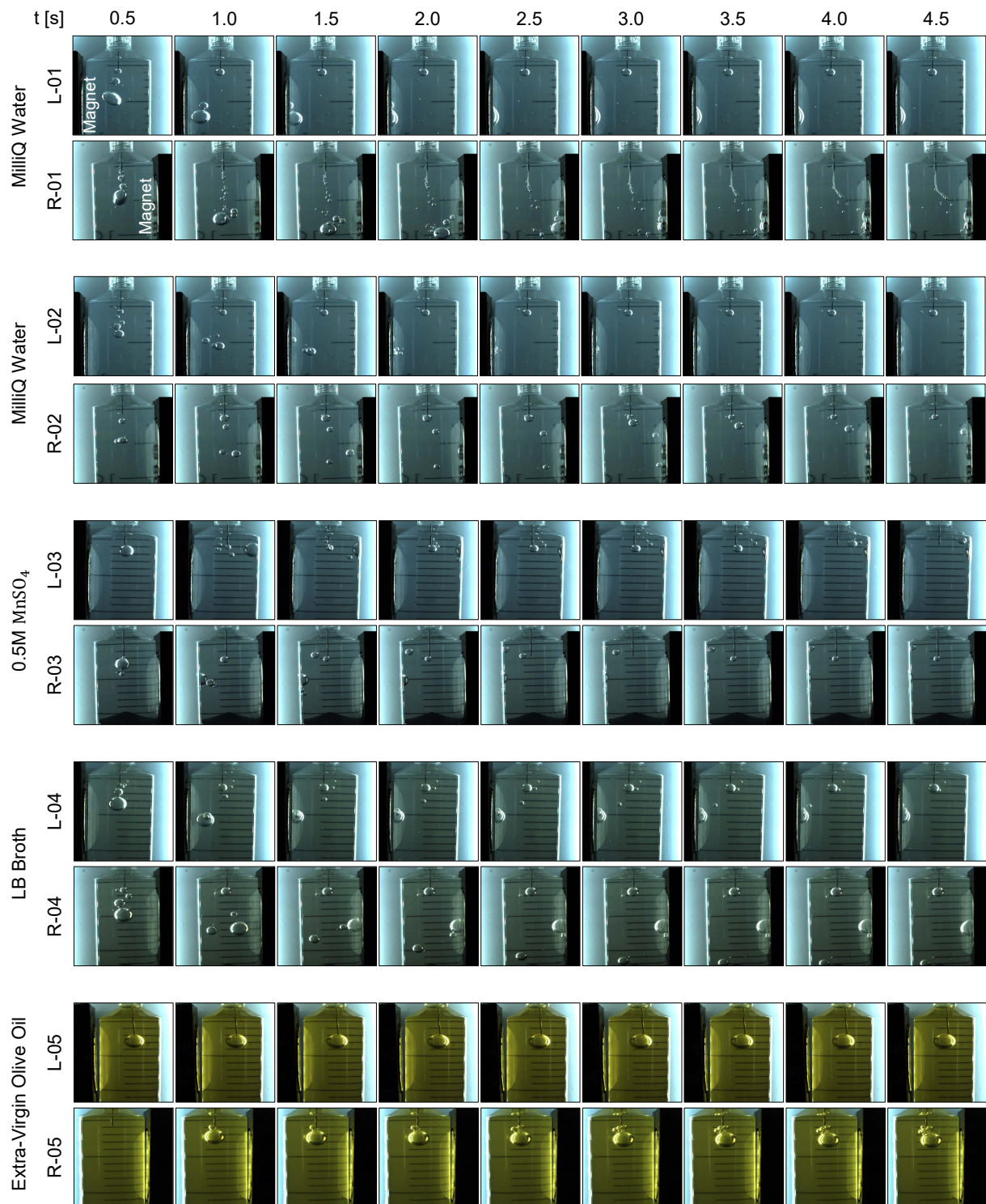


Figure 11.7: Overview of experimental results for the five drop experiments. Videos are labeled depending on whether the magnet is located at the left (L) or right (R) of the image.

with magnetometers.

The experiments reveal a wide variety of wall-bubble and bubble-bubble interactions that are described in detail in Sec. 11.2.3 and Sec. 11.2.4.

11.2.2 Terminal velocity

The magnetic terminal bubble velocity is a powerful metric to characterize the diamagnetic phase separator, but it is derived under the steady-state assumption. This requirement runs in contradiction with the inhomogeneity of the magnetic polarization force, that exposes the bubble to the variable acceleration field represented in Fig. 11.3(b). In order to evaluate the performance of Eqs. 8.24 and 8.26, the radius, maximum and minimum speed, maximum and minimum Reynolds number, and interaction history of 25 air bubbles in water are reported in Table 11.2 after being analyzed with the tracking algorithm described in Sec. 11.1.5. The analysis focuses on the x (“horizontal”) vector components, where magnetic effects are dominant and the injection velocity is negligible. The maximum horizontal bubble velocity is 15.9 mm/s, which corresponds to a Re of 45.1, while the minimum is just 0.1 mm/s. As a consequence of Eqs. 8.24 and 8.26, larger bubbles generally have higher maximum velocities. From a technical perspective, this implies that the diamagnetic phase separator is more effective with large bubbles. Smaller bubbles, on the contrary, are slower but show a higher scattering due to the bubble interaction effects described in Sec. 11.2.4.

Eight bubbles are selected from Table 11.2 based on the following criteria: (i) bubbles that interact

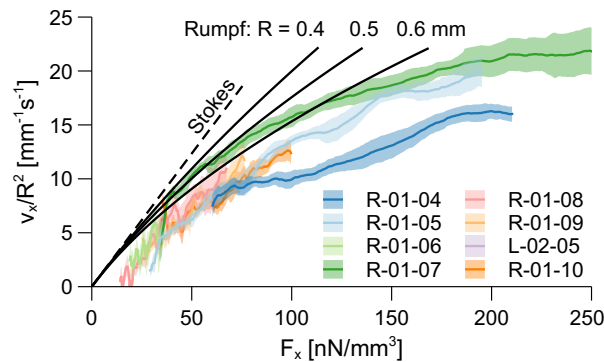


Figure 11.8: Scaled bubble velocities as a function of the horizontal magnetic force compared with Eqs. 8.24 and 8.26 during the 4.7 s microgravity flight. The legend indicates the bubble ID from Table 11.2.

Table 11.2: Bubbles tracked during 4.7 s of free fall. Labels are assigned for the left (L) and right (R) magnets and the first (1) or second (2) experiment with Milli-Q water.

ID	R [mm]	$-v_{x,\min}$ [mm/s]	$-v_{x,\max}$ [mm/s]	Re_{\min} [-]	Re_{\max} [-]	Interacts?
L-01-01	2.55	4.7	15.9	13.4	45.1	Yes
L-01-02	1.26	7.8	12.1	10.9	16.9	Yes
L-01-03	0.37	1.6	2.8	0.6	1.13	No
L-02-01	1.45	-1.5	14.2	0	22.7	Yes
L-02-02	1.06	8.2	11.6	9.6	13.6	Yes
L-02-03	0.67	0.4	7.9	0.3	5.9	Yes
L-02-04	0.50	0.9	7.1	0.5	3.9	Yes
L-02-05	0.43	0.1	0.7	0.1	0.3	No
L-02-06	0.39	0.4	5.3	0.2	2.3	Yes
R-01-01	2.25	-4.1	14.6	0	36.2	Yes
R-01-02	1.42	-1.2	9.9	0	15.5	Yes
R-01-03	0.81	3.1	7.6	2.8	6.9	Yes
R-01-04	0.59	2.2	5.7	1.4	3.7	No
R-01-05	0.54	0.1	6.8	0.1	4.0	No
R-01-06	0.53	0.1	2.9	0.1	1.7	Yes
R-01-07	0.51	0.6	6.2	0.4	3.5	No
R-01-08	0.49	-0.5	3.1	0	1.7	No
R-01-09	0.46	0.5	2.9	0.2	1.5	No
R-01-10	0.45	-2.2	2.8	0	1.4	No
R-01-11	0.41	0.7	2.2	0.3	1.0	Yes
R-02-01	1.29	-0.6	11.7	0	16.7	No
R-02-02	1.24	0.2	13.2	0.2	18.2	Yes
R-02-03	0.95	0.9	9.8	1.0	10.3	No
R-02-04	0.84	2.2	10.0	2.0	9.3	Yes
R-02-05	0.41	1.7	2.4	0.7	1.1	Yes

with other bubbles are discarded, (ii) the maximum bubble diameter is 1.2 mm, and (iii) only MilliQ water is considered. In other words, sources of uncertainty are removed by studying small, isolated bubbles in a well-characterized medium. The resulting bubble velocities are scaled with R^2 and plotted in Fig. 11.8 as a function of the magnetic force in the x axis. The $\pm\sigma$ error bands from the smoothing velocity filter are superposed together with predictions from Eqs. 8.24 and 8.26. Since the latter does not scale with R^2 , a range of bubble radii are represented. None of the cases under study surpasses the upper speed limits, validating the application of the proposed magnetic terminal velocity formulations. The measured velocities are, however, significantly smaller than their terminal values. This should not come as a surprise considering the short duration of the experiment, the non-steady magnetic environment, and the wall-induced drag effect described in Sec. 11.2.3. The same factors will likely appear in space applications and should therefore be considered in future studies.

11.2.3 Wall-bubble interactions

The effective drag acting on the bubbles increases by up to two orders of magnitude as they get closer to the wall [366]. The effects are noticeable already for distances below $\sim 10R$ [325]. In close proximity, bubbles will also experience Van der Waals and electrical double layer forces [367], eventually producing a thin water film between the bubble and the wall. The film drains under the effect of bubble pressure and surface tension, a process that has been successfully modeled by means of force balance-lubrication frameworks [325, 368]. The bubble may also invert its curvature close to the surface creating a so-called dimple [369] and/or bounce back several times before settling [325].

In the experiment, as shown in Fig. 11.3(b), the diamagnetic acceleration induced on MilliQ water can reach $0.1\text{-}1\text{ m/s}^2$ near the magnet. The fundamental processes explored in terrestrial bubbles should be applicable to this experiment by replacing the role of gravity with the diamagnetic force. For instance, the largest bubble from L-01 oscillates several times over the wall of the syringe before being suddenly “absorbed” and starting the film draining process. Such oscillations are relevant for dynamic phase separation approaches and can be studied by means of iterative fluid-magnetic simulations or interface tracking methods like those

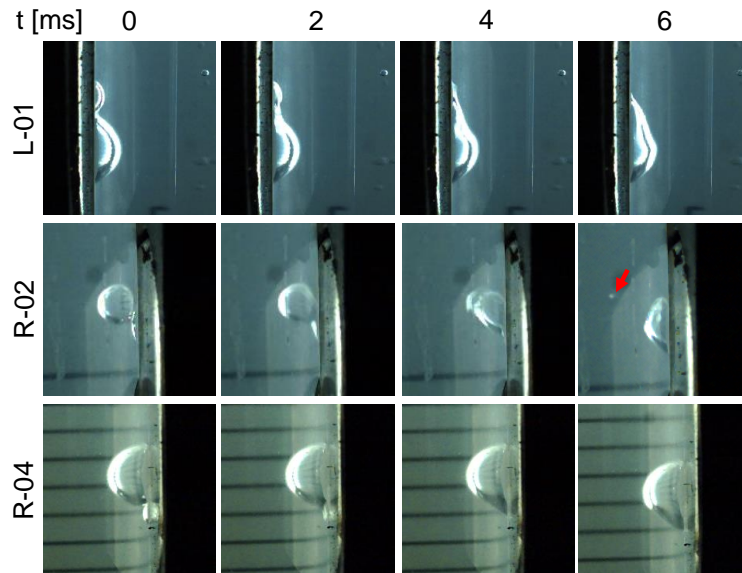


Figure 11.9: Bubble coalescence events at the wall for the L-01, R-02, and R-04 experiments. The red arrow indicates the ejection of a small gas bubble after bubble coalescence.

presented in Chapters 7 and 10. The effect of the diamagnetic force in the eigenfrequencies of the bubble depends on the magnetic Bond number at its interface, as shown in Eq. 7.28c. The “absorption” seems to be related to a change in wettability conditions and can be seen between $t = 1.5$ and $t = 2.0$ s in Fig. 11.7. It is followed by a slow bubble flattening process where the bubble increases its wall diameter. The same behavior is repeated for all liquids, although the sudden wetting is transformed into a gradual flattening for the LB Broth.

Of particular technical relevance are the bubble coalescing events reported in Fig. 11.9 for MilliQ water and LB Broth. The capability to merge several bubbles is key to ensure a pure gas outcome in future diamagnetic phase separators. The process is initiated by the thinning of the interface between the two bubbles, that leads to the formation of a neck. The neck expands very fast and starts a damped oscillatory movement in the new bubble that leads to a new equilibrium configuration [370, 371]. This cycle is reflected in Fig. 11.9 and is also observed in bubble-bubble interactions just after injection (see Fig. 11.7). In some cases, like R-02, a small bubble is ejected due to the violent displacement of the interface. Factors like the concentration of dissolved salts [372, 373] or the bubble collision speed [374] can determine the likelihood of bubble coalescence, and should therefore be considered in the design of future systems.

11.2.4 Bubble-bubble interactions

Equation 8.24 shows that, at least under the Stokes regime, the terminal velocity of bubbles subject to diamagnetic buoyancy scales with R^2 . This characteristic is shared with terrestrial bubbly flows and implies that smaller bubbles will take longer to be separated. However, for $Re \in [20, 130]$ a steady wake is generated behind the bubble with a characteristic length of order R [317]. This structure can be used to generate a liquid flow toward the magnet and enhance the collection process for small bubbles as illustrated in Fig. 11.10 or the interesting stream of bubbles that appear in Fig. 11.7, R-01. This mechanism is of particular relevance for the applications described in Chapter 14. Long-term microgravity experiments are necessary to evaluate this process in a technical setting.

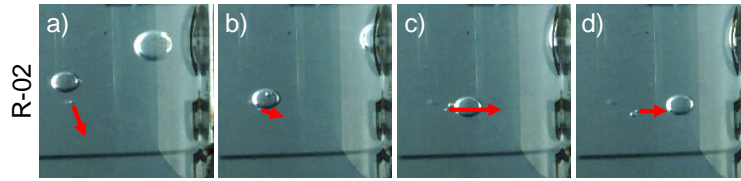


Figure 11.10: Bubble dragging example for the R-02 MilliQ water solution in microgravity. The red arrow indicates the velocity of the smaller bubble as the larger one drags it.

11.3 Collaborators

The experiments presented in this chapter were carried out together with Prof. Katharina Brinkert and Mr. Ömer Akay, to whom the author would like to express his most sincere gratitude.

Chapter 12

Magnetic positive positioning

As outlined in Sec. 1.4.2, the magnetic positive positioning approach makes use of the magnetic polarization properties of liquids to control their position inside a propellant tank. The concept was first introduced by Papell in 1963 [6] and then revisited for the NASA MAPO experiment in the late 1990s motivated by the availability of high-density magnets and superconductors. Recent contributions to the field generated numerical models and feasibility studies of relevance for liquid oxygen [154, 164–171]. Similar forces could be exerted on diamagnetic propellants like liquid hydrogen. Although the TRL of this technology remains below 5, the growing interest in propelled CubeSat platforms and cryogenic propellant management is making this approach more attractive for future missions. This chapter provides new insight into the prospects and challenges of magnetic positive positioning by applying the tools developed in Chapter 7 and reviewing critical processes for ferrofluids and natural liquids.

12.1 Fundamental MP² architectures

The magnetic positive positioning implementations proposed to date may be classified based on two criteria: type of actuation and purpose. This section provides a general description of such categories.

12.1.1 Classification based on type of actuation

Most MP² applications to date focus on what Marchetta and coworkers named *magnetic reorientation* [166]. The basic idea is to locate magnets, electromagnets, or hybrid approaches (e.g. electropermanent magnets) in strategic positions so that the propellant is attracted (para/ferromagnetism) or repelled (dia-

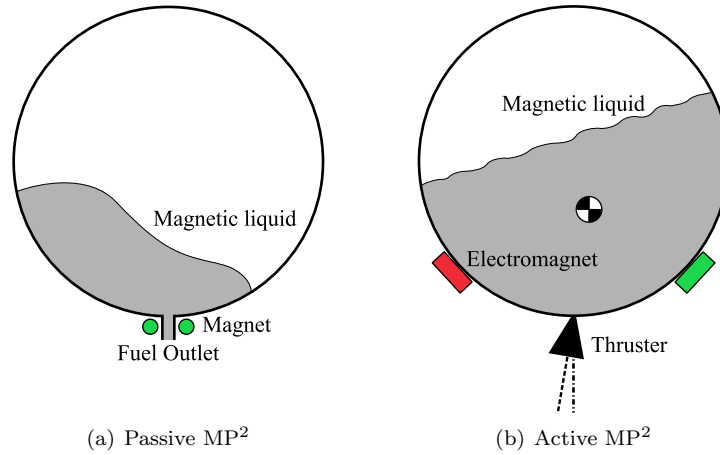


Figure 12.1: Conceptual representation of passive and active MP² devices.

magnetism). For instance, a magnet could be placed at the fuel outlet to hold the propellant and ensure a continuous gas-free supply to the engines, as shown in Fig. 12.1(a). This would replace or reinforce current surface-tension-based PMDs. In contrast with this *passive* approach, the *active* propellant management system represented in Fig. 12.1(b) may be developed. By making use of a series of magnetic actuators, the center of mass of the liquid (and hence, of the spacecraft) could be displaced to the most convenient position. That may serve to correct a potential thrust vector misalignment or generate a prescribed torque during a ΔV firing. In addition, similar mechanisms may also be employed to assist in active fuel flow control [67].

Of these, only the passive magnetic positive positioning approach has been explored in the literature. It was proposed almost simultaneously by the US Air Force [132] and NASA's engineer Steve Papell [6] in the early 1960s. After remaining dormant for decades, the advent of high-temperature superconductors motivated a renewed interest in this technology. Most recent works originate from the NASA MAPO experiment [163], that studied the magnetic reorientation of a ferrofluid solution in a parabolic flight. Computational Volume-of-Fluid models were developed on the basis of the Los Álamos *RIPPLE* code [375] by assuming (i) linear magnetization, (ii) negligible magnetic pressure, (iii) negligible influence of the magnetized liquid on the magnetic field, and (iv) dipolar magnetic field [164]. These first contributions demonstrated the magnetic reorientation concept through numerical simulations [165]. Marchetta and coworkers subsequently generalized these results and explored the dependence between the critical Bond number (Bo^*), the mag-

netic Bond number (Bo_{mag}), the propellant reorientation time, and the the filling ratio for the NASA MAPO tank [166–168]. Subsequent models extend the computational setup to non-linearly magnetized materials and complex geometries [154]. 3D ANSYS Fluent-based simulations have also been built by making use of User-Defined Functions [169, 170]. Alternatively, the retention of LOX in an accelerating environment has been studied by implementing an additional magnetic energy term in the equilibrium model of Surface Evolver [171]. In all cases, the magnetic field generated by the source is computed or measured as a fixed external input. Then, the magnetic contribution is either implemented as a source term in the momentum balance, or as a magnetic energy term added to the energy balance. In both scenarios, the magnetic and hydrodynamic problems are decoupled.

In spite of the aforementioned works, countless scientific and technological questions still remain unsolved. The stability and reorientation time of spherical, ellipsoidal and conformal tanks have to be explored, and the coupled fluid-magnetic problem needs to be solved to study high-density ferrofluids. Furthermore, full-scale implementations and technological demonstrators have not yet been tested. A dedicated feasibility study must be performed in order to identify potential scenarios of application. The existence of an imposed inertial acceleration increases the magnetic control requirements, leads to a larger electromagnet mass and/or current, and restricts the range of application of this technology. Moreover, significant uncertainties should be expected in the estimation and control of the position of the center of mass. One of the key relations to explore is the dependence of Bo^* with Bo_{mag} and the geometry of the system. Such curves naturally lead to the sizing and reachability assessment of the system, as exemplified in Ref. 167 for the NASA MAPO experiment.

12.1.2 Classification based on scope

All previous works focus on moving the liquid to the fuel outlet to ensure a gas-free supply to the engines. This type of MP² devices fall in the *magnetic reorientation* category. However, as exemplified in Chapter 9, a sufficiently powerful magnetic source would be able to reach a significant portion of the tank volume and modify the response of the liquid to external disturbances. This would (i) increase the critical Bond number Bo^* , making the fluid surface less sensitive to external disturbances, (ii) raise the

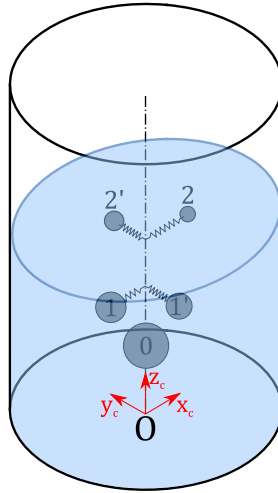


Figure 12.2: Modal spring-mass mechanical analogy for inviscid liquid sloshing.

natural sloshing frequencies and damping ratios and, most importantly, (iii) transform a highly stochastic problem into a predictable system. Standard mechanical analogies, illustrated in Fig. 12.2, could be easily embedded into an external controller to predict and compensate the disturbance torque produced by the liquid, improving pointing accuracy and reducing attitude disturbances. The tools required to study this problem, named *magnetic sloshing control*, can be found in Chapters 7 and 10.

12.2 Performance analysis

The results that follow exploit the analytical tools introduced in Chapter 7 to assess the performance and scalability of the hypothetical system described in Sec. 12.2.1. Complex dynamic environments or multiphase flow patterns are excluded from the analysis and require interface-capturing simulations that fall beyond the scope of this PhD thesis. Therefore, this section should be regarded as a representative example of the power and limitations of such analytical tools.

12.2.1 Case of analysis

For illustrative purposes, a LOX / liquid methane (CH_4) in-space bipropellant propulsion system is considered. This combination has been proposed as a green, long-life, and compact enabler for future missions with in-situ propellant production [376]. An hypothetical liquid methane ferrofluid with a 0.53%

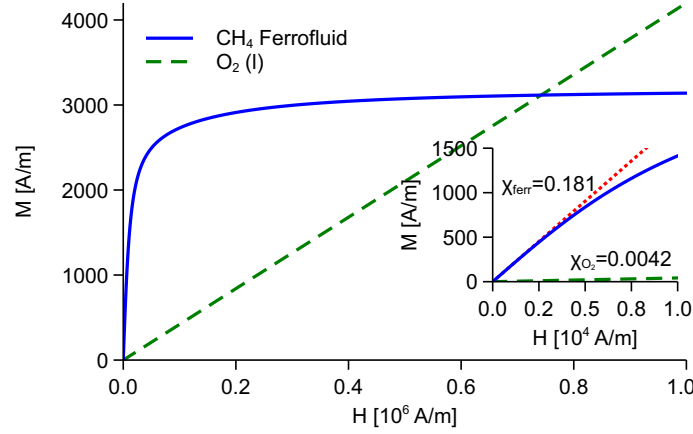


Figure 12.3: Magnetization curves of liquid CH_4 enriched with a 0.53% volume of Fe_3O_4 nanoparticles (ferromagnetic) and liquid O_2 (paramagnetic).

Table 12.1: Physical properties of CH_4 (l) enriched with a 0.53% volume of Fe_3O_4 nanoparticles, and of O_2 (l) at cryogenic storage temperature [2, 4, 5].

Substance	T [K]	P [bar]	ρ [kg/m ³]	σ [mN/m]	χ_{ini}^{vol}
$CH_4(l) + Fe_3O_4(s)$	111	2	448	12.99	Fig. 12.3
$O_2(l)$	90	2	1141	13.2	0.0034

volume concentration of Fe_3O_4 nanoparticles is assumed. This concentration is relatively low in comparison with commercial light-hydrocarbon ferrofluids ($\sim 18\%$, Ferrotec EMG-900¹) but still produces a significant magnetic response without compromising the performance of the propulsion system (see Sec. 12.3.3).

The physical properties of O_2 (l) and CH_4 (l) + Fe_3O_4 (s) are listed in Table 12.1² and Fig. 12.3. The magnetic behavior of the hypothetical CH_4 -based ferrofluid is assumed equivalent to the 1:10 volume solution of the Ferrotec EMG-700 ferrofluid employed in the ESA Drop Your Thesis! 2017 experiment described in Chapter 9. While the increase in density due to the addition of nanoparticles is considered, the surface tension of CH_4 is kept constant.

Propellant and oxidizer are contained in 1U cylindrical tanks with 60 g neodymium magnets surrounding their fuel outlets, as shown in Fig. 12.4. In the nominal configuration, the contact angle θ_c is 60° ,

¹ <https://ferrofluid.ferrotec.com/products/ferrofluid-emg/oil/emg-900/>. Consulted on: 04/25/2022.

² According to Ref. 377, the magnetic susceptibility of liquid oxygen is 0.0042 at 60 K and zero pressure. However, the NASA MAPO experiment [163] and the 84th CRC Handbook of Chemistry and Physics [2] employ 0.0034 at 90 K and atmospheric pressure. Since the actual value is strongly dependent on environmental conditions [377], the first is taken as an upper limit (best-case scenario) for this chapter.

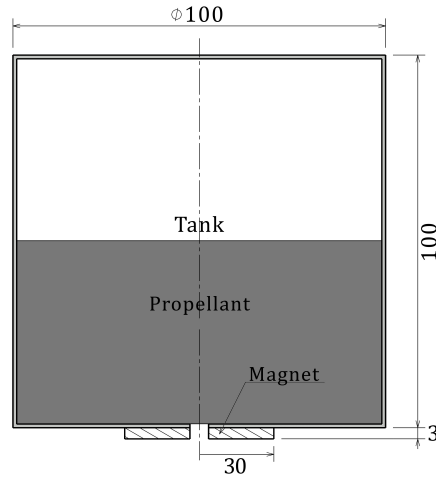


Figure 12.4: Sketch of the 1U propellant tank considered in the analysis. Units in mm.

the inertial acceleration g is set to 0 (microgravity), and the magnet is magnetized in the vertical direction at $M_m = 1500$ kA/m. It should be noted that a larger oxygen tank would be employed in actual systems, since the stoichiometric O/F ratio for this configuration is 2. However, the same volume is kept to facilitate the comparison of results.

12.2.2 Equilibrium, stability, and modal response

The basic low-gravity magnetic liquid sloshing metrics are subsequently studied for the aforementioned case of analysis. Unlike non-magnetic sloshing, a direct generalization of the magnetic results cannot be easily achieved due to the inhomogeneity of the forces involved. In other words, specific configurations have to be analyzed with dedicated simulations. Results are computed with the coupled quasi-analytical models presented in Chapter 7 assuming a free-edge condition ($\Gamma = 0$).

The meniscus and magnetic Bond numbers are represented in Fig. 12.5 as a function of the filling ratio (FR). The filling ratio is usually defined as the portion of the total height or volume of the container occupied by the liquid, which are the same for cylindrical tanks. As the propellant is consumed, the filling ratio decreases and the meniscus and dynamic properties change. The low magnetic susceptibility of LOX gives rise to a smooth meniscus profile with limited changes in curvature. In contrast, the combination of low surface tension and high magnetic susceptibility of the methane-based ferrofluid produces a central

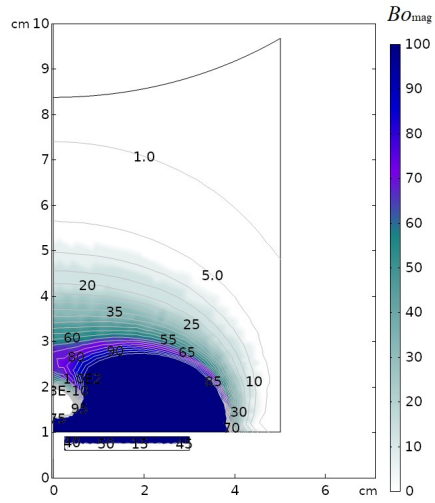
protrusion. The evolution of the meniscus with the filling ratio is represented in Fig. 12.6, where the FR=30% level detaches from the lateral wall and has been removed and the FR=100% is shown as a reference without considering the top end of the cylindrical container. It is important to note that the fluid surface tends to follow the constant Bo_{mag} (or \mathbf{H}) lines, as reported in the literature [347] and Chapter 10. From the physical viewpoint, this is analogous to the tendency of an air balloon to equalize the pressure over its surface. The roles played by air pressure and membrane tension are here assumed by the magnetic force and surface tension, respectively.

An indication of the reachability of the magnet is obtained by analyzing the constant $Bo_{\text{mag}} = 1$ lines, that define the transition from magnetic to surface-tension dominated regimes. While for LOX this line crosses the symmetry axis at a height of approximately 64 mm, in the case of the ferrofluid the crossing is produced at $z > 100$ mm due to its enhanced magnetic properties. However, the magnetic Bond number depends on the position and should then be analyzed along the meniscus. This analysis is given in Fig. 12.7, that illustrates the previous comments and reflects once more the greater susceptibility of the ferrofluid.

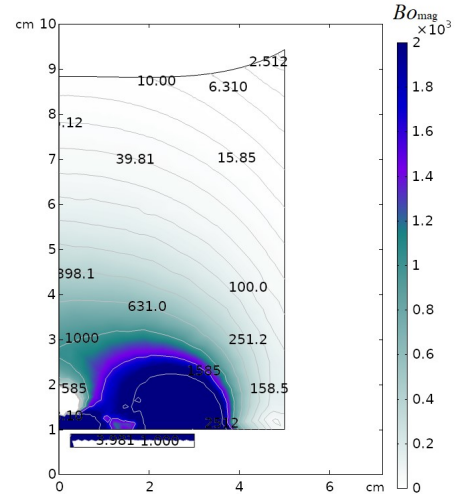
Figure 12.8 depicts the three first sloshing frequencies for both systems as a function of the filling ratio. As expected, the oscillation frequencies increase when the surface is close to the magnet. While only a slight effect is observed for the O_2 (l) tank (negligible for $FR > 60\%$), increases of the fundamental frequency between a 18% and a 786% with respect to the non-magnetic case are observed for the CH_4 -based ferrofluid.

The analytical framework described in Sec. 7.3 is employed in Fig. 12.9 to study the stability of the LOX meniscus for a liquid height of 5 cm. The magnetization of the magnet is increased from 0 to 1500 kA/m and the critical Bond number is computed as the one that makes $\chi(s_1) = \chi^*(s_1)$. The result shows how Bo^* decreases from -3.017 (which matches the non-magnetic value reported in the literature [85]) up to -3.968, increasing the critical load by a 31.5% with the 60 g magnet. As noted in Sec. 7.3, this framework may be extended for ferrofluids to account for the fluid-magnetic coupling. However, the numerical approach followed in Sec. 10.3.1 could also be employed at the expenses of computational efficiency.

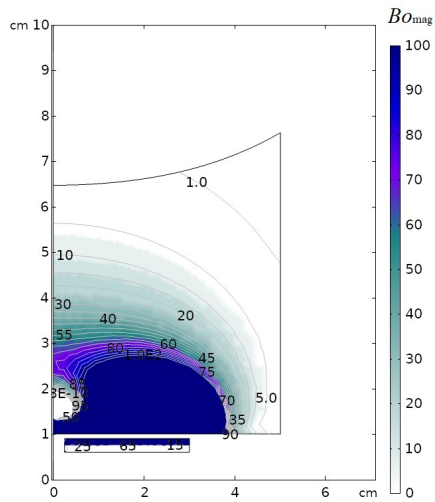
The analysis indicates that ferrofluids may be particularly appropriate for highly demanding magnetic liquid management applications in space, such as active MP² or magnetic sloshing control. Because liquid oxygen has the highest known paramagnetic susceptibility of natural liquids, it is also concluded that non-



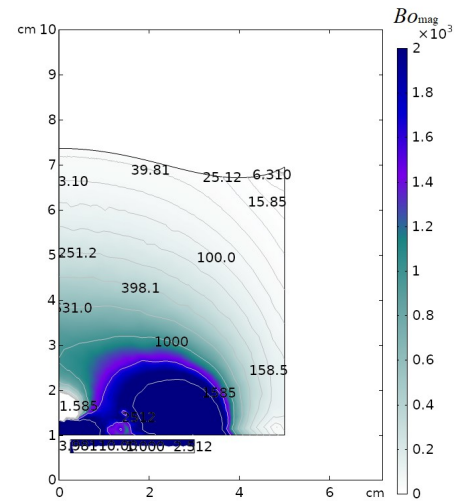
(a) O_2 (l), FR=80%



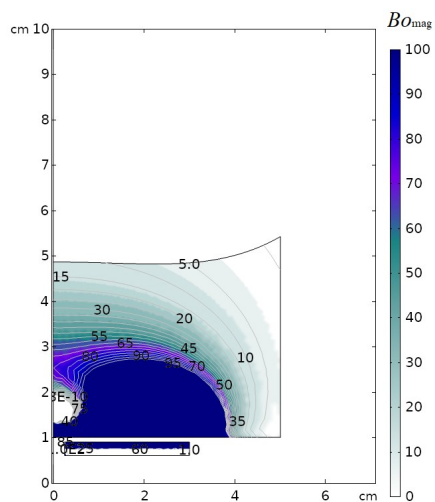
(b) CH_4 -based ferrofluid, FR=80%



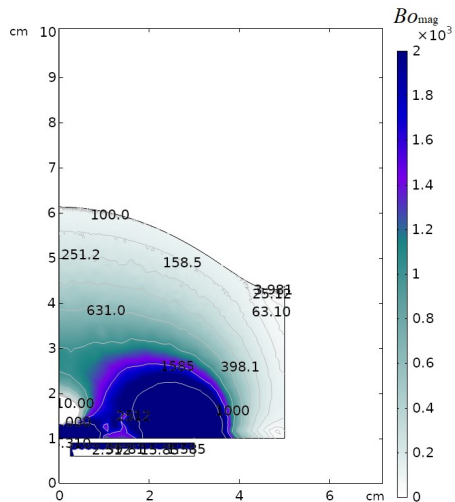
(c) O_2 (l), FR=60%



(d) CH_4 -based ferrofluid, FR=60%



(e) O_2 (l), FR=40%



(f) CH_4 -based ferrofluid, FR=40%

Figure 12.5: Axisymmetric meniscus profile and magnetic Bond number (color scale) for different filling ratios.

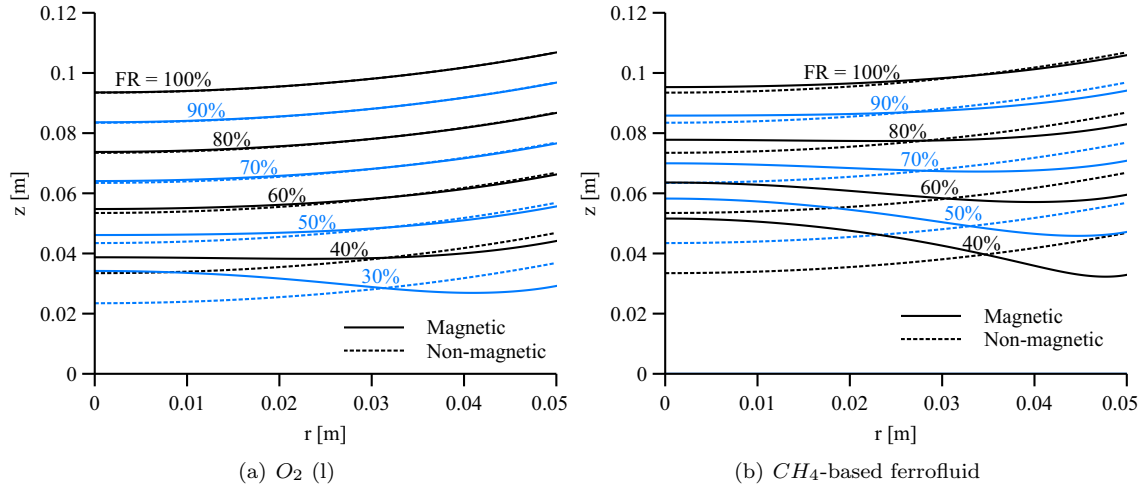


Figure 12.6: Axisymmetric meniscus profile as a function of the filling ratio (FR).

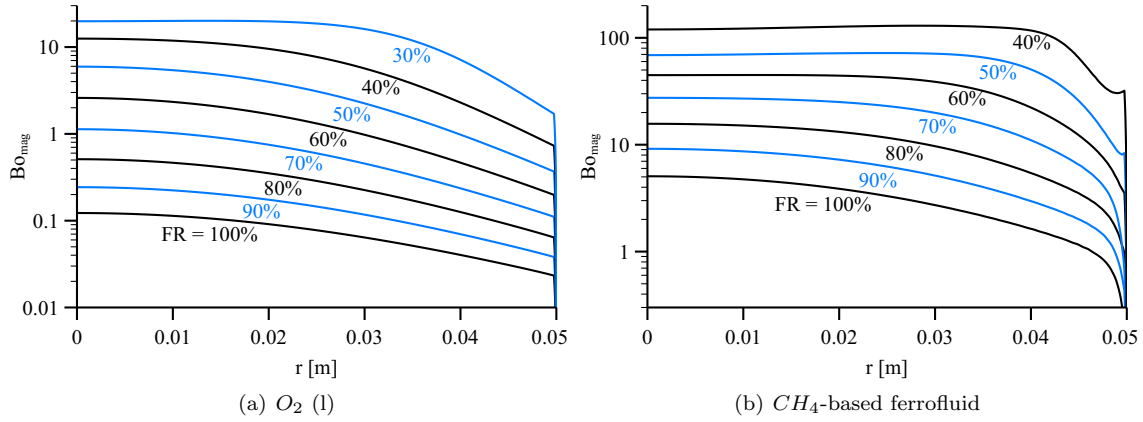


Figure 12.7: Magnetic Bond number at the axisymmetric meniscus as a function of the filling ratio (FR).

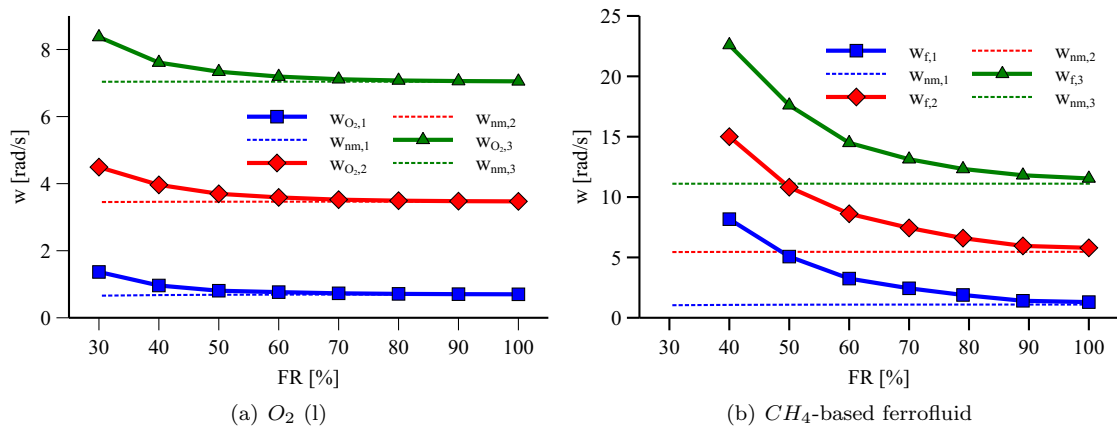


Figure 12.8: Fundamental free-edge sloshing frequencies as a function of the filling ratio (FR).

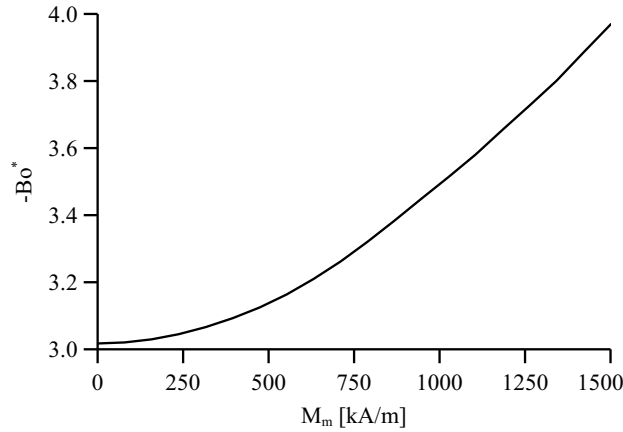


Figure 12.9: Dependence of the critical Bond number with the magnetization of the magnet in Fig. 12.4 for the LOX tank and 5 cm filling height.

ferromagnetic liquids may not be well suited for such applications. From the modeling perspective, the strong dependence of the meniscus profile and oscillation frequencies with the filling ratio should be carefully considered in the development of mechanical analogies and the sizing of space systems.

12.2.3 System scaling

Applications dealing with MP² [163] or magnetic sloshing control [16] traditionally work with either small regions or small propellant tanks due to the rapid decay of magnetic fields. However, a hypothetical design may consider the employment of MP² in larger tanks. The scalability of the system should therefore be addressed.

Although Eq. 8.30 is derived for liquid droplets, the assumption $\chi_b \ll 1$ makes it applicable to the estimation of the force acting on a dia/paramagnetic liquid volume along the symmetry axis of a coil or magnet. The result

$$\mathbf{F}_m \approx -\frac{3\mu_0\chi(nI)^2R^4}{4}\frac{z}{(R^2+z^2)^4}\mathbf{e}_z,$$

reproduced again for convenience, unveils some important features of the system. Before, it should be reminded that this expression can be applied to axially magnetized cylindrical magnets with magnetization M_m , radius R and height l by employing an equivalent circular loop with the same radius and current intensity $I = M_m l$. The evolution of F_m with z is strongly influenced by R . An increase in the radius of the

current loop for constant intensity reduces the force for small z and increases it for large z . Considering a magnet whose mass is conserved with the modification of R , the new equivalent current intensity becomes $I = M_m l_0 R_0^2 / R^2$ and an increase in R reduces the value of F_m for all z . However, the values of F_m outside the symmetry axis benefit from the more homogeneous field generated by wide magnets.

Most importantly, a geometrical scaling of R , l , and z by a factor K multiplies F_m by $1/K$. The scaled ferrofluid meniscus would then be exposed to $1/K$ times the original force. However, because the magnetic Bond number given by Eq. 7.29 is multiplied by the square of the characteristic length, the Bo_{mag} number of the new system scales with K . In other words, an upscaling of the liquid tank requires relatively smaller magnetic sources to produce an equivalent Bo_{mag} distribution at the interface. Assuming that Bo_{mag} is kept constant, the dimensionless natural frequency Ω in the free surface oscillations problem (see Eq. 7.28) remains the same, while the dimensional frequency ω evolves with $1/K^3$. This conclusion is exemplified in Fig. 12.10 after enlarging the nominal CH_4 propellant tank by a factor $K = 10$. The radius of the magnet is then reduced from 30 to 15 cm to approximately recover the original magnetic Bond number distribution, achieving a 75% mass reduction (45 kg for a magnet density of 7100 kg/m^3). Including the weight of the magnetic nanoparticles and the magnet, the total mass of the magnetic control system is 31 kg, representing

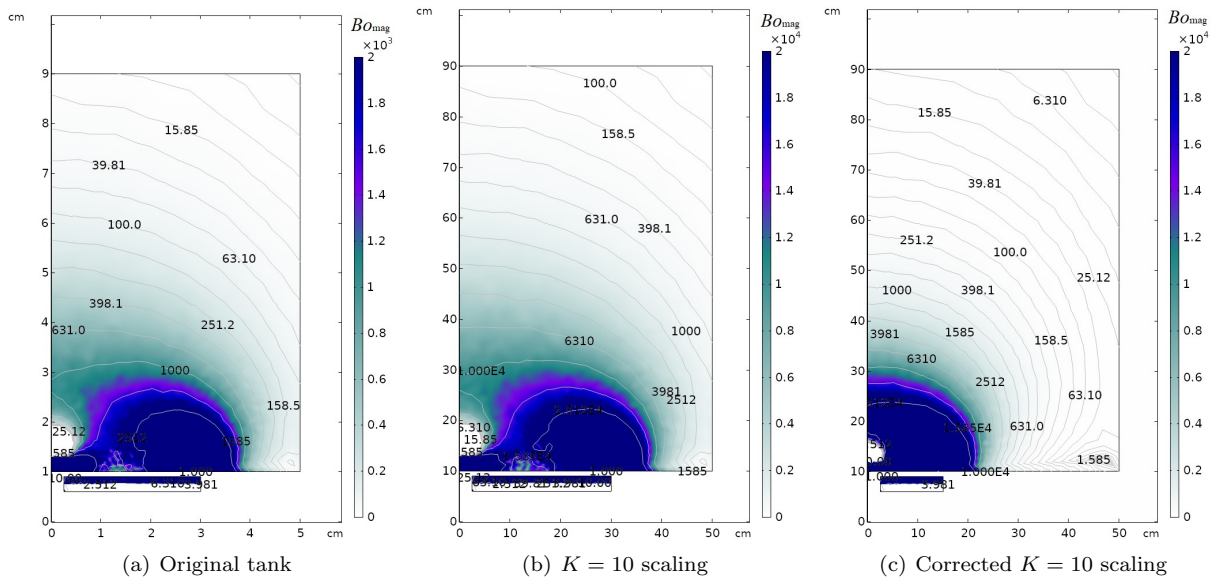


Figure 12.10: Bo_{mag} distribution (color scale) in a CH_4 -based ferrofluid with $FR=80\%$ and a flat surface.

a 12% of the propellant mass (282 kg for 80 cm filling height). This value can be significantly reduced with a dedicated optimization process.

As a final remark, Eq. 7.29 shows that the critical acceleration g^* scales with $1/K^2$ for geometrically similar configurations (i.e. same Bo^*). Even if Bo_{mag} scales with K , g^* will decrease more rapidly, and so a careful selection of critical acceleration loads is required for large tanks.

12.3 Technical feasibility

The use of ferrofluids for MP² applications involves a series of technical challenges that cast doubts on the feasibility of this approach. The most obvious ones are subsequently addressed.

12.3.1 Thermal stability of ferrofluids

Some of the most promising applications of ferrofluids are related to thermal management and space propulsion. These environments may potentially expose the colloid to high temperatures and induce an accelerated agglomeration of the nanoparticles. However, if ferrofluids are sought to be employed in space, their long-term thermal stability must be first guaranteed.

The physicochemical stability of a colloid is determined by the balance between the energetic contributions to the system. Under specific environmental conditions, a sufficiently small particle avoids settling (decantation to the sources of potential) and agglomeration (union of several particles) if an appropriate surfactant is employed to overcome the Van der Waals attraction. The excellent discussion on the stability requirements of ferrofluids provided by Rosensweig in Ref. 20 is summarized in Table 12.2, where the maximum particle diameter that overcomes magnetic and gravitational settling, and dipole-dipole agglomeration, is given. In these expressions, $k = 1.38 \cdot 10^{-23} \text{ JK}^{-1}$, T is the absolute temperature, $\Delta\rho = \rho_{\text{solid}} - \rho_{\text{liquid}}$ is the differential density, L is the elevation in the gravitational field, and $V = \pi d^3/6$ is the volume of the particle.

The dipole-dipole force acts together with the Van der Waals attraction, always present due to the

Table 12.2: Maximum particle diameter as given by key energy balances.

Symbol	Expression	Comment
d_{\max}^m	$\left(\frac{6kT}{\pi\mu_0 MH}\right)^{1/3}$	Addresses settling due to magnetic sources
d_{\max}^g	$\left(\frac{6kT}{\pi\Delta\rho gL}\right)^{1/3}$	Addresses settling due to gravitational energy
d_{\max}^{dd}	$\left(\frac{72kT}{\pi\mu_0 M^2}\right)^{1/3}$	Addresses agglomeration due to dipole-dipole interaction

fluctuating electric dipole-dipole forces. Assuming spherical particles, its associated energy would be

$$E_{V.d.W.} = -\frac{A}{6} \left[\frac{2}{l^2 + 4l} + \frac{2}{(l+2)^2} + \ln \frac{l^2 + 4l}{(l+2)^2} \right], \quad (12.1)$$

with $l = 2s/d$, s being the surface-to-surface separation distance and A the *Hamaker constant*, approximately equal to 10^{-19} for Fe , Fe_2O_3 or Fe_3O_4 in hydrocarbon. Unlike the magnetic dipole-dipole energy, Eq. 12.1 diverges when $s \rightarrow 0$. In other words, the contact between particles must be physically avoided to prevent agglomeration, as thermal energy is unable to prevent it. The problem is commonly solved by adding a surfactant layer made of long chain molecules, producing a mechanism known as *steric* or *entropic* repulsion which follows Mackor's theory [378]. Alternatively, the particles may be charged to induce Coulomb repulsion, producing *ionic* ferrofluids. The agglomeration rate is finally determined by the net potential curve, obtained as the difference between attractive and repulsive energies. For very short separation distances the Van der Waals attraction is dominant; otherwise, the steric repulsion prevents the contact. Consequently, two given particles collide only when their thermal energy is greater than the maximum of the net potential. If this energy barrier is well designed (i.e. only a negligible portion of the critical thermal energy distribution overcomes the steric repulsion barrier), the ferrofluid should remain stable for long periods of time [20].

Space applications dealing with ferrofluids must carefully consider this trade-off analysis. The mission may expose the liquid to (i) launch accelerations of up to $10 g_0$, (ii) long-term microgravity conditions, and (iii) significant thermal gradients. In principle, the first two points represent minor concerns, as the time required to change the equilibrium profile of the colloid is several orders of magnitude larger than the high-gravity window [379, 380] and the process is reversible [20]. On the contrary, colloids subjected to excessive temperatures experience an accelerated thermal aging leading to sedimentation and the degradation of magnetic properties [381].

For the CH_4 -based ferrofluid propellant here considered, $d_{\max}^m = 15$ nm, $d_{\max}^g = 3$ nm and $d_{\max}^{dd} = 149$ nm for a storage temperature $T = 111$ K, maximum magnetic field $H = 10^5$ A/m, maximum magnetization field 2900 A/m, launch acceleration $g = 10g_0$ m/s², differential density $\Delta\rho = 7450$ kg/m³ and elevation length $L = 0.1$ m. The selection of the surfactant is subject to additional requirements (e.g. resistance to low temperatures, space radiation or compatibility with the carrier liquid) and falls beyond the scope of this preliminary analysis. It should be noted that launch accelerations lasts for few minutes and that the condition $d < d_{\max}^g$ may hence be relaxed. This is further supported by the flawless execution of past ferrofluids experiments at the ISS [68].

12.3.2 Radiation stability of ferrofluids

Long-term exposure to space radiation may also degrade the ferrofluid solution and modify its magnetic response. The literature addressing this problem is scarce, focusing mainly on biomedical applications, and can be hardly extended to the space environment due to methodological and application-related issues.

Early studies by Kopčanský *et al.* report strong reductions in the initial susceptibility (13–40%), saturation magnetization (6–25%) and magnetic particles concentration (10–36%) of a stabilized kerosene-based ferrofluid after being exposed to 4.5–17.3 Gy of ^{60}Co γ -radiation with a dose rate of 1.3 $\mu\text{Gy/s}$. This degradation is attributed to the destruction of the long polar chain molecules composing the surfactant. Similar experiments on a non-stabilized Fe_3O_4 diester-based ferrofluid show equivalent reductions of the saturation magnetization and a strong influence in the stabilization process [382]. Bădescu *et al.* also report reductions in initial susceptibility and saturation magnetization of a 5–10% in kerosene-based ferrofluid subjected to 5–20 Gy of γ -radiation. The same effect is not observed for water-based solutions, attributing this behavior to the superficial anisotropy produced by the implantation of free oleic acid molecules on the particle surface [383]. Recent works with Gd_2O_3 -based ferrofluids using CTAB as a surfactant and ethanol as a carrier liquid analyze the development of intragranular defects due to γ -ray radiation doses between 32 Gy and 2635 kGy. Results suggest the existence of a critical dose beyond which the defects tend to saturate [384]. The same group explored the effects of 878 Gy and 2635 kGy γ -radiation doses on the particle size and size distribution dependent spectroscopic and magneto-optic properties of a water-based Fe_3O_4 ferrofluid

solution, finding a clear particle distribution dependence, among other results that fall beyond the scope of this work [385].

The effects of electron irradiation on biocompatible water-based ferrofluids were explored by Tomašovičová *et al.* with sodium oleate and double layer sodium oleate/PEG surfactants [386]. Stable reductions in saturation magnetization of a 50% and a 25% are respectively measured after applying an irradiation dose of 1000 Gy, although most of the loss is already produced for 5 Gy. PEG is shown to behave as a protective surfactant against radiation, with this capability being independent of its molar weight [387]. The degradation process is attributed to the aggregation of particles produced by ionization. Similar experiments with bovine serum albumin (BSA) modified ferrofluids containing sodium oleate stabilized Fe_3O_4 nanoparticles show a dependence between the BSA/ Fe_3O_4 w/w ratio and the stability against radiation [388].

Studies with a technical scope have also been presented. Ferrofluid feedthrough (FF) rotary seals are exposed in Ref. 389 to a mixed radiation environment consisting of fast neutrons (0.2 MGy), protons (2 MGy) and γ -rays (20 MGy). Serious magneto-viscous damages are reported for radiation levels above 2 MGy. Reference 390 reports the negative impact of a 900 MHz 30 W electromagnetic radiation on the discharging current of transformer oil ITO 100. As a last example, in Ref. 391 microwave heating applied during the synthesis of aqueous ferrofluids is shown to increase the saturation magnetization and have a negligible effect on the stability properties.

From the material sciences perspective, none of the previous works can be easily extended to the space environment. This is due to the fact that (i) the space radiation dose is small (of the order of 0.4 Gy/year for the ISS orbit, and 1.2 Gy for a 3-years Mars mission), (ii) the tests are performed with radiation sources whose spectrum differs significantly from the space environment (^{60}Co), and (iii) different types of nanoparticles, coatings, and carrier liquids experience different effects. However, a significant degradation for radiation doses below 5 Gy is observed in some of the previous works, so mid-to-long-term effects on ferrofluids should be expected.

Due to the complete lack of space-oriented studies, further experimental efforts are required to estimate the lifetime of a given solution. Future works should address this problem by making use of either high-energy Earth facilities or long-term flight experiments.

12.3.3 Impact of ferrofluid-enriched propellants on the propulsion subsystem

Slurry fuels is a wide class of liquids consisting of a solid phase in the shape of particles, from the submicrometric to some hundreds of micron, suspended in a fluid medium. The use of metal-based particles in liquid propellants has been analyzed since the 1950s with the perspective to enhance ideal propulsion performance [392]. The stabilization of the suspension can be obtained through liquid gelification, treatment with surfactants, use of dispersants, etc. Proposed applications considered different fields of propulsion (from rocket to air breathing) to obtain lighter and more compact systems. Specific impulse and propellant average density augmentation could be obtained, depending on the peculiar properties of the suspended material. As an example, mixtures of aluminum suspended in gelled kerosene, burned in combination with liquid oxygen, were targeted by NASA. Palaszewsky and Zakany described the experience on aluminum suspensions in kerosene, showing theoretical and experimental results up to metal loads of 55% [393]. In the reported case, gelification of the suspending medium was necessary to stabilize the dispersion. Known issues connected to the use of metal-based slurry fuels are deposition on nozzle and walls, erosion of injectors, and agglomeration of particles during the combustion process. Lifetime of the slurry became a critical aspect for the real application.

Ferrofluids have been associated with space propulsion since their invention. In 1963 Papell already described colloidal suspensions of magnetite on heptane or JP₄ carriers [6]. Water-based ferrofluids may also find application in propulsion systems employing water, like the one described in Ref. 210. Light hydrocarbons are widely employed as carriers in commercial ferrofluids [20]; however, liquid propellant rocket fuels never made use of iron oxide. Iron-based compounds have been used in the past for soot reduction in the combustion of complex hydrocarbons (e.g. diesel, kerosene), finding experimental confirmation of enhanced catalytic effect when nanometric oxide particles are involved in the reaction [394].

There are different forms of iron oxide and catalytic/decomposition properties depend on the exact molecule. Hematite is the most stable, and its stability depends on reaction temperature and atmosphere. The reduction in a methane environment of Fe_2O_3 has been documented by Ghosh and co-authors between 1073 K and 1298 K. An active role is attributed to the molecular hydrogen generated by the decomposition

of the CH_4 molecule [395]. This property has been used in chemical looping combustion processes. As an example, in a paper by Monazam an iron-based compound acts as oxygen carrier between a section of the reactor where Fe_2O_3 oxidizes a fuel and another part where air oxidizes the resulting metal-based material back to hematite. Reportedly, reaction with methane can generate Fe_3O_4 , FeO or Fe depending on the degree of hematite reduction [396]. Out of the iron oxide family, magnetite (Fe_3O_4) is a combination of the two oxidation states Fe(II) and Fe(III). It is an amphoteric compound arranged in mixed octahedral/tetrahedral configuration (inverse spinel). It is featured by ferromagnetic properties and high electric conductivity [397]. For this reason, magnetite is a perfect candidate for ferroluids.

From the rocket propulsion viewpoint, iron oxide is a component characterized by low energy content due to its low formation enthalpy. Thermodynamic computations for a liquid methane / liquid oxygen /magnetite propellant obtained from NASA's CEA [398] are reported in Fig. 12.11. The specific impulse is computed for the oxidizer-to-fuel ratio of 4 at 20 bar, nozzle pressure ratio of 20 with optimal discharge and frozen expansion model. Chemical equilibrium is assumed in the combustion chamber only. The evaluations are performed at the reference iron oxide content of 1% and 10% and are compared against a baseline without the oxide additive. As expected, the specific impulse decreases constantly once the iron oxide is introduced. The decrement is less than 1% when Fe_3O_4 fraction is 1% and becomes about 5% for the 10% additive mass

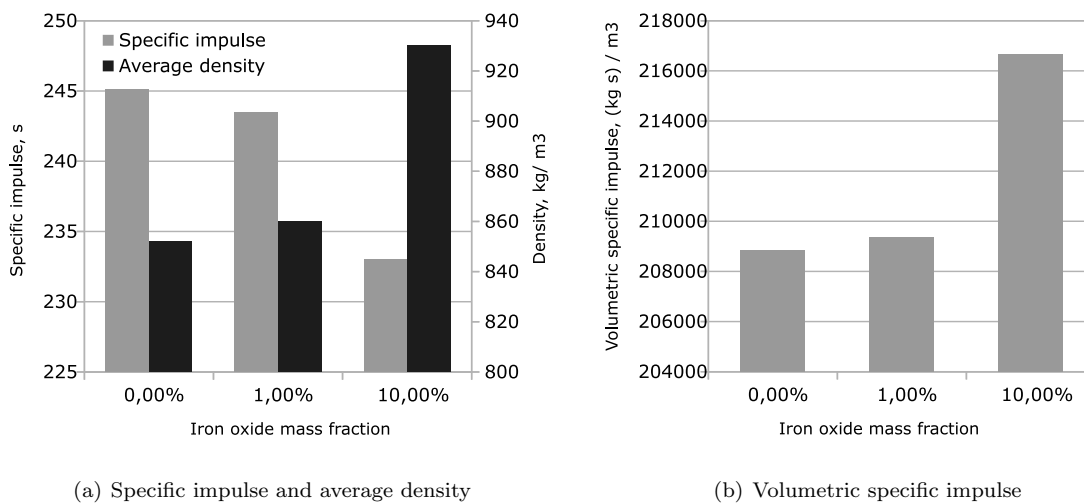


Figure 12.11: Analysis of the combustion of $LCH_4/LOX/Fe_3O_4$.

concentration. The variation is attributed to the reduction of the flame temperature and the increasing value of the molar mass of the mixture [399]. Figure 12.11 reports also the average density of the liquid propellant before combustion. Data are considered for liquid propellants at their respective boiling points. This figure of merit concurs to the definition of the volumetric specific impulse (the product between the specific impulse and the propellant average density) and becomes important to rate the compactness of a propulsion system [400]. A 1% addition of magnetite generates +1% density, and 10% additive content leads to +10% density. This trend attributes a global increase to the volumetric specific impulse, showing that the use of ferrofluid dispersed into the propellant can be beneficial from the compactness viewpoint.

12.4 Collaborators

The author thanks Prof. Filippo Maggi for his key contributions to Sec. 12.3.3.

Chapter 13

Application of magnetic positive positioning to launch vehicle restart

The application of the magnetic positive positioning concept introduced in Chapter 12 has never been proposed or explored for launch vehicles. This is actually not surprising: rockets in general (and rocket sloshing, in particular) are associated in the popular culture with hypergravity operations rather than microgravity conditions, but magnetic control is only feasible in the latter. In addition, the elongated shape of a rocket is not favorable to this application due to the rapid decay of magnetic fields, and high-density magnetic technologies have only been made available since relatively recently. As pointed out in Sec. 1.4.3, however, the in-orbit restart of launch vehicles may benefit from the magnetic positive positioning approach, potentially leading to significant mass savings per launch and stage. The development of such system might be particularly beneficial for new-generation microlaunchers and cryogenics management, which cannot be easily achieved with existing PMDs [194].

This chapter explores for the first time the feasibility and performance of several high-risk-high-return magnetic propellant settling strategies. Three distinct Magnetic Positive Positioning concepts, a hydrogen-peroxide-based Propellant Gasification System, and a hybrid device that combines both approaches are introduced. Although still in a very early stage of development, the analysis aims to promote an open discussion on these ideas in the rocket propulsion community.

13.1 Launcher characteristics

13.1.1 Overview

Although valid for multiple low-gravity propellant settling systems, the discussion that follows applies the magnetic positive positioning concept described in Chapter 12 to the first and second launch stages of a Falcon-9-like LV. The basic parameters of the vehicle are reported in Table 13.1, with the geometrical definitions being depicted in Fig. 13.1. Some of these values are found in SpaceX’s Falcon User’s Guide [198], while others can only be estimated from unofficial sources¹.

¹ See www.spacelaunchreport.com/falcon9ft.html. Consulted on 13/01/2022.

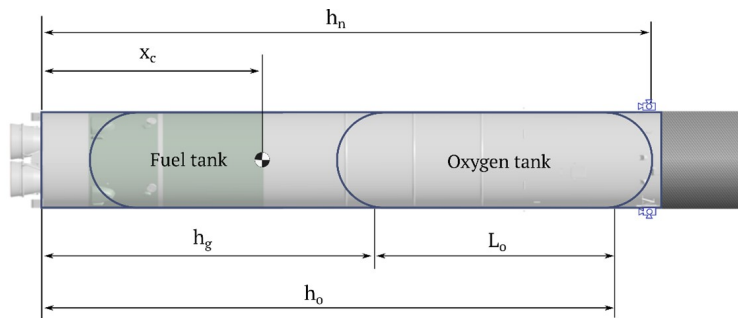


Figure 13.1: Geometrical parameters of a launch vehicle stage.

Table 13.1: Geometrical and inertial parameters of the launch vehicle.

Parameter	First Stage	Second Stage
Propellant type	LOX + RP1	LOX + RP1
Empty mass [t]	22	4.5
Propellant mass [t]	411	111.5
Oxygen tank capacity [t]	287.4	78
Kerosene tank capacity [t]	123.5	33.5
Total mass [t]	433	116
Propellant after separation [t]	13	3.5
Propellant after landing [t]	1	0.3
Thrust (stage total) [kN]	7686	981
Throttle capability [kN]	4381 to 7686	626 to 981
Number of engines	9	1
Diameter [m]	3.66	3.66
LOX tank height L_o [m]	22.5	8.7
Length of 1 stage h_o [m]	29	11.2
Length of fuel tank h_g [m]	19.2	7.4
First stage mass center x_c [m]	14.9	5.7
Moment of inertia [kg·m ²]	$2.68 \cdot 10^6$	$3 \cdot 10^4$
Length to PGS nozzles h_n [m]	39	15

13.1.2 Propellant behavior during stage separation

The acceleration profile experienced by each stage during separation is key to understand the dynamic behavior of the propellant. A simple mechanical model introduced in Ref. 401 and employed to obtain the acceleration curves reported in Fig. 13.2 using representative values. Peak accelerations of $\sim 1 \text{ m/s}^2$ are applied to the system and sustained for less than 1 s. Additional effects that may impact the propellant behavior include the release of strain energy from the walls of the tank, the flow movement induced by engine suction, or thermal convection [196].

Modeling this problem is far from trivial, and experimental data is not easily available because of its consideration as Export-Controlled material. However, a partial recording of Falcon 9's first and second stage liquid oxygen (LOX) tanks during the CRS 5 mission is publicly available², allowing for a qualitative analysis of the problem. Figure 13.3 shows the sequence of video frames for (a) the instant before second-stage engine cut off (SECO), (b) the lateral sloshing wave caused by the structural relaxation after SECO, (c) the cloud of LOX bubbles generated after separation, and (d) the state of the cloud 45 s after separation. It can be readily concluded that (i) the SECO induces a mild lateral sloshing wave, but does not significantly disturb the liquid (at least, for this system), (ii) the stage separation atomizes the residual LOX in a myriad of droplets that reach the top of the tank in less than 40 s (i.e. the droplets move at least at $\sim 20 \text{ cm/s}$), and (iii) the droplets keep moving for at least 6 minutes while coalescing with each other. This behavior is also (briefly) observed in the first stage, where the droplets seem to move at about 0.5 m/s . This value has

² The interested reader is referred to <https://youtu.be/p7x-SumbynI>. Consulted on 13/01/2022.

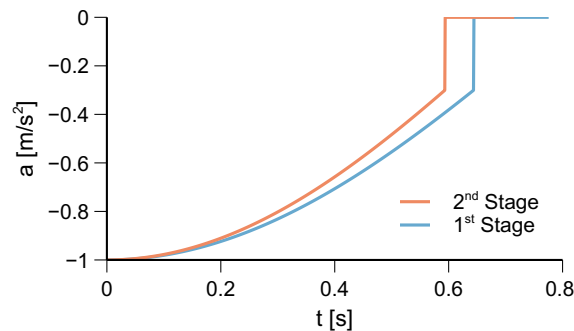


Figure 13.2: Estimated acceleration profile of the 1st and 2nd stages after separation.

been employed in the derivation of the acceleration profiles shown in Fig. 13.2.

13.1.3 Engine restart conditions

The propellant must be settled over the fuel outlet to ensure a safe engine restart. Although this usually implies bringing *all* the liquid back to the bottom of the tank before ignition, the requirement may be instead reformulated by noting that the engines will also accelerate the stage. The goal is thus to have enough propellant at the outlet so that, when the thrust-induced settling brings all the liquid to the bottom of the tank, no gas bubbles have made their way into the engines. This design philosophy is shared by many traditional types of PMDs [194].

The first factor to consider is mass flow rate: higher thrust will settle the propellant droplets faster, but will also require a larger initial mass. The relation between thrust T and mass flow rate \dot{m}_p is given by

$$T = I_{sp} g_0 \dot{m}_p, \quad (13.1)$$

where I_{sp} is the specific impulse and $g_0 = 9.81 \text{ m/s}^2$ is the standard gravity acceleration. For a LOX-RP1 chemical engine with a mass ratio of ~ 2.3 the specific impulse should be around 285 s at sea level [400]. In fact, SpaceX attributes to Falcon 9's Merlin engines the values of 282 s at sea level and 311 s in vacuum.³ The second factor is the propellant settling time, that can be divided into two phases. On the first, the propellant residuals return to the intake device, while on the second, gas bubbles are removed from the liquid. The total settling time can thus be expressed as

$$t_s = t_I + t_{II}. \quad (13.2)$$

³ See web.archive.org/web/20130501002858/http://www.spacex.com/falcon9.php. Consulted on: 13/01/2022.

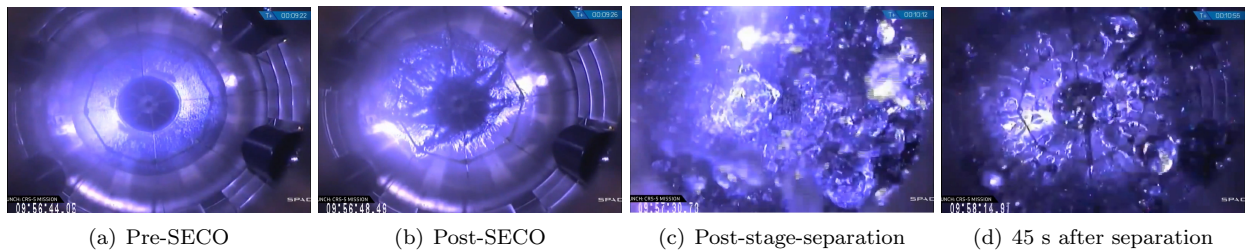


Figure 13.3: Top view of the second-stage LOX tank of SpaceX's Falcon 9 during the CRS-5 mission. Source: www.youtube.com/watch?v=mVAGoWJuDKk.

For a tank of length L , the duration of the first phase is bounded by the kinematic result

$$t_I = \sqrt{\frac{2Lm_0}{T}}, \quad (13.3)$$

with m_0 being the dry mass of the stage. The duration of the second phase, assuming a constant terminal velocity of the bubbles in the liquid, is [402]

$$t_{II} = l \left[\frac{8}{3} \frac{r_b T}{C_d m_t} \left(1 - \frac{\rho_g}{\rho_l} \right) \right]^{-1/2} \quad (13.4)$$

where r_b is the bubble radius, C_d is the drag coefficient, ρ_g is the gas density, ρ_l is the liquid density, m_t is the total mass of the stage after settling, and l is the height of the longest liquid column. Consequently, the initial mass of propellant required to complete the maneuver for a giving thrust level is

$$m_p = \dot{m}_p t_s = \frac{T}{I_{sp} g_0} \left\{ \sqrt{\frac{2Lm_0}{T}} + l \left[\frac{8}{3} \frac{r_b T}{C_d m_t} \left(1 - \frac{\rho_g}{\rho_l} \right) \right]^{-1/2} \right\}, \quad (13.5)$$

which increases with \sqrt{T} , showing that small thrust values are convenient to minimize the mass of propellant required to restart the engines. Table 13.2 reports the stage acceleration, settling time, and initial oxidizer and fuel masses for different thrust configurations of Falcon 9's first and second stages. The values $C_d = 0.47$ (sphere at $Re = 10^3$ to 10^5 [317]), $r_b = 5$ mm, $\rho_g = 0.1785$ kg/m³ (He), $\rho_l = 1141$ kg/m³ (LOX), and $l = m_r/(\pi R^2 \rho_l)$, with R being the tank radius and m_r the residual LOX mass, are employed in combination with those presented in Table 13.1 using the larger LOX tank as a reference. The masses reported in Table 13.2 are the minimum absolute values required near the fuel outlet to initiate the restart maneuver. Unofficial sources claim that Falcon 9's first stage restart acceleration is less than 50 m/s² by employing reverse engineered telemetry data⁴, which indicates that either the central engine at maximum thrust or three outer engines at minimum thrust are actually employed in this process. However, it was not possible to verify this information.

⁴ See <https://github.com/shahar603/SpaceXtract> for a remarkable example of reverse engineering. Consulted on 17/01/2022.

	First Stage				Second Stage			
	g [m/s ²]	t_s [s]	LOX [kg]	RP1 [kg]	g [m/s ²]	t_s [s]	LOX [kg]	RP1 [kg]
Maximum Thrust	350	0.66	1287	401	218	0.39	88	38
Minimum Thrust	200	0.88	971	303	140	0.49	70	30
Single Engine	22	2.63	324	101	140	0.49	70	30

Table 13.2: Stage acceleration, settling time, and minimum initial oxidizer and fuel masses for different restart configurations of Falcon 9’s first and second stages.

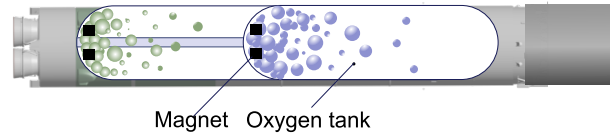


Figure 13.4: Magnetic Positive Positioning.

13.2 Magnetic Positive Positioning

13.2.1 Implementation

As discussed in Chapter 12, the ability of controlling the position of susceptible liquids by means of magnetic fields is of particular interest for in-space propellant management. The passive MP² approach, sketched in Fig. 13.4 for the system under study, seeks to induce a magnetic acceleration that holds, collects, and/or traps the liquid near the fuel outlets. Since both the magnetic field \mathbf{H} and its gradient decay with the distance to the source, the magnetic force vanishes relatively quickly. Therefore, high-density magnets or powerful coils are needed for most applications.

The applicability of MP² methods as part of the operation of LVs remains completely unexplored. Although constrained by the limited access to technical information, this section aims at covering this knowledge gap by exploring the application of MP² to the restart of Falcon 9’s first and second stages. While liquid oxygen is a strong paramagnetic, RP-1 is a diamagnetic that needs to be modified as described in Sec. 13.2.6

13.2.2 Passive retention strategy

The first and most intuitive approach to MP² is the liquid retention strategy, where a magnet or coil is used to hold the paramagnetic liquid in the presence of adverse accelerations that tend to destabilize the free liquid surface. As shown in Sec. 7.3, the critical Bond number determines the critical acceleration load g^* for which surface tension, with coefficient σ , cannot longer stabilize the meniscus. Myshkis and coworkers provide a best-case $Bo^* = -3.32$ for cylindrical tanks at a contact angle of 90° [85], which results in $g^* = 2.9 \cdot 10^{-6} \text{ m/s}^2$ for the LOX tank considered in this work. In other words, surface tension does little or nothing to prevent the atomization of the residual LOX volume observed in Fig. 13.3 under the action of the acceleration loads estimated in Fig. 13.2. A logical follow-up question is whether the magnetic force can hold the liquid against adverse accelerations of $\sim 1 \text{ m/s}^2$.

Marchetta and coworkers explore the problem of magnetic LOX retention in a 12 cm diameter 24 cm height cylindrical tank under the influence of a point dipole of 1.4 cm diameter and an inertial acceleration along its major axis [171]. The dipole strength required to hold $\sim 30 \text{ ml}$ of liquid is shown to be about 10 Am^2 for $g^* = 1 \text{ m/s}^2$. Similarly, in Chapter 12 the analytical model developed in Sec. 7.3 is applied to a 10 cm

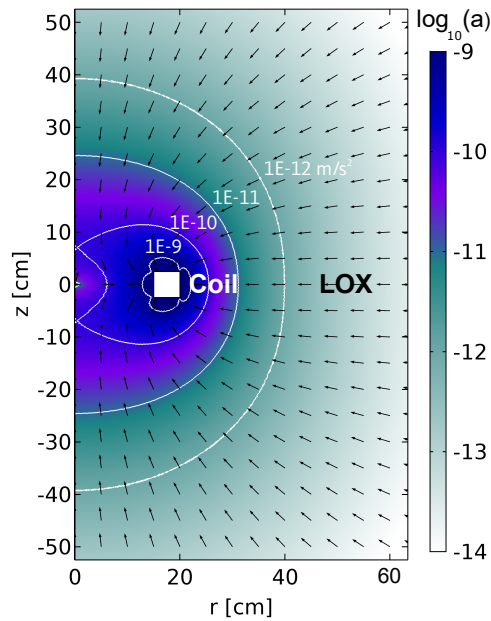


Figure 13.5: Magnetic acceleration contours induced on LOX by a 35 cm diameter coil operating at 1 At.

diameter cylindrical tank, showing that a 60 g magnet can increase the critical load by 31.5%. None of these low-gravity studies can be easily extended to Falcon 9's 3.66 m diameter LOX tank, where the liquid outlet has a diameter of about 90 cm and the maximum estimated acceleration is about 1 m/s^2 . The problem, however, can be easily addressed by plotting the axisymmetric magnetic acceleration contours induced by a 1 A cylindrical coil on the LOX tank volume as done in Fig. 13.5. The figure depicts the magnetic acceleration levels in a logarithmic scale and its direction using black arrows. A coil mean diameter of 35 cm is chosen to ensure that the liquid gets attracted toward the PMD located at the tank outlet. The minimum mass to be retained is 70 kg (second stage), which translates to a LOX sphere of 25 cm radius. The magnetic acceleration at this distance is about 10^{-11} m/s^2 . Since the acceleration scales with the square of the current intensity (see Eq. 8.30), values of $\sim 10^6 \text{ At}$ (i.e. coils current intensity times number of coil turns) would be required to retain the oxidizer against accelerations of 1 to 10 m/s^2 . Further computations are not required to conclude that the mass and/or power requirements of this approach are well beyond reason with existing technologies, particularly for the first stage.

13.2.3 Recovery strategy

The passive magnetic retention strategy sets an upper limit for the magnetic field strength. Because this limit is practically impossible to reach, alternative strategies must be explored. The first of them is here introduced and seeks to collect the LOX droplets after they are atomized rather than holding part of the liquid at the bottom of the tank. In order to evaluate this idea, the time required to settle a LOX droplet is first derived with the simplified framework of analysis introduced in Sec. 8.5.

13.2.3.1 Magnetic settling time

If the settling of the propellant is induced by the magnetic interaction and not by a uniform acceleration g , the derivation of t_s is complicated by the presence of an inhomogeneous acceleration field. A strict approach to the problem would require solving the Navier-Stokes equations with a magnetic force source term. Although less computationally expensive than fully coupled fluid-magnetic simulations, this approach is still prohibitive for a preliminary study. Instead, the movement of a perfectly spherical low-susceptibility

droplet along the symmetry axis of an axisymmetric coil or magnet is analyzed as done in Sec. 8.5, resulting in the time of flight given by Eq. 8.31 that is reproduced here for convenience,

$$t_I(L) = \sqrt{\frac{4\pi\rho_l}{\mu_0\chi^{\text{vol}}(nI)^2R^4}} \cdot \int_0^L \left[\frac{1}{(z^2 + R^2)^3} - \frac{1}{(L^2 + R^2)^3} \right]^{-1/2} dz.$$

Again, it should be noted that t_I is inversely proportional to nI (or, if a magnet is employed, to $M_m l_m$) and R^2 . Of these, only the current intensity can be considered a design parameter, because R is bounded by the fuel intake radius (see Sec. 13.2.2).

The time required to debubble the multiphase mixture near the fuel outlet using the paramagnetic force can be derived in a similar way by integrating Eq. 8.20. However, the magnetic debubbling process is much faster than the droplet settling phase because the liquid is closer to the magnetic source, and hence it is further assumed that $t_s \approx t_I$. Even though the assumptions employed in the derivation of Eq. 8.30 are not appropriate for highly susceptible ferrofluids, the volume magnetic susceptibility of the liquids employed in this work is bounded by that of LOX ($\chi_{\text{LOX}}^{\text{vol}} = 0.0034$ at 90 K and 1 atm [2]). It would not be particularly useful to employ high density ferrofluids in the fuel tank when the most demanding requirements are associated with the LOX tank.

13.2.3.2 Performance analysis

The time of flight of the droplets for a coil diameter of 35 cm is represented in Fig. 13.6 as a function of the initial droplet distance to the coil and the applied current intensity. A LOX settling time of $t_{\text{max}} \approx 6$ minutes, estimated in Sec. 13.1, is superposed and treated as a deadline for the collection process. However, unofficial telemetry data shows that the first stage restarts 2 to 3 minutes after stage separation. As it will be seen, this does not change the qualitative results of the analysis. It is arbitrarily assumed that, after atomization, the LOX droplets are uniformly distributed in the tank volume. In this framework, the vertical lines represent the tank length that needs to be settled for each one of the configurations detailed in Table 13.2 before the LOX droplets stop moving (i.e. get attached to the walls of the tank).

A qualitative difference is first observed between first and second stages. The LOX mass required to restart the engines, listed in Table 13.2, drops by an order of magnitude in the second stage, and thus a

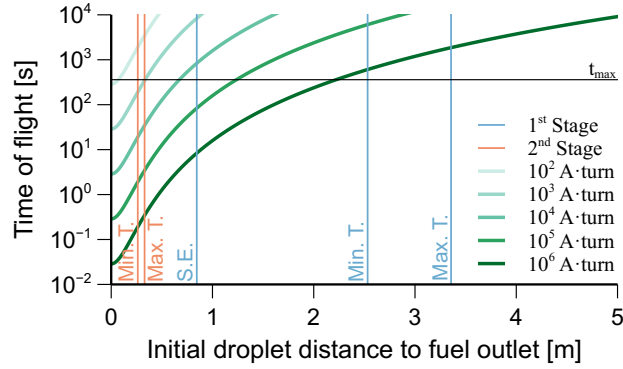


Figure 13.6: Time required by a LOX droplet to reach the bottom of the tank as a function of its distance to the coil and the applied current intensity. The minimum tank settling length required by the single engine (S.E.), minimum thrust (Min. T.) and maximum thrust (Max. T.) configurations is superposed.

smaller tank length needs to be settled. The second factor that should be considered is the density of residual LOX per unit tank length. Although the lower LOX tank is 22.5 m and the upper is just 8.7 m, the density of residual LOX is relatively similar, decreasing from 383.5 kg/m to 267 kg/m, respectively. Figure 13.6 shows that a coil with a configuration of 10^3 A·turn can satisfy the requirements of the second stage. However, 10^4 to 10^5 A·turn are needed to settle the first stage using the single engine restart configuration, with 10^6 to 10^7 A·turn being required for the rest. In other words, the liquid recovery strategy can potentially reduce the coil strength requirements by one order of magnitude in the first stage and three orders of magnitude in the second. These conclusions do not change if t_{\max} drops to 120-180 s for the first stage, as indicated by unofficial telemetry data.

These results should be taken with care due to the number of assumptions employed in the derivation of Eq. 8.31. In particular, fluid-structure interactions have been completely neglected, but Fig. 13.3 shows that, after a few minutes, the liquid droplets tend to get stuck to the walls of the tank. This is a natural consequence of the presence of corner geometries in the interface between PMDs and the walls. The robustness of the liquid recovery strategy may thus be compromised by this effect, which should be evaluated with flight data that is not available to the author. Possible mitigation strategies include the elimination of gaps and corner geometries or the application of a LOX-phobic treatment to the internal surfaces.

13.2.3.3 Liquid lines

The discussion provided in this section focuses on attracting the propellant residuals to the bottom of the tank after stage separation. However, for the system to effectively prevent the ingestion of gas bubbles, conduits connecting the propellant tank to the engines must remain filled with liquid during the whole process. Start baskets, traps, or troughs, whose characteristics and historical heritage are thoroughly described in Ref. 194, may be employed to instantaneously hold the liquid against accelerations of $\sim 1 \text{ m/s}^2$. Retaining the minimum masses computed in Table 13.2 while enabling high cryogenic mass flow rates is far from simple, and it is in this context where the magnet can help reduce the volume of the trap by ensuring that part of the propellant is collected after stage separation.

The employment of cryogenic propellants may lead to additional gas trapping issues in the liquid lines between stage separation and engine restart. For instance, LOX could start boiling over hot surfaces. The relevance and impact of these events depends on environmental factors that are unknown to the author but that must be considered by the designer.

13.2.4 Magnetic trap

As previously noted, capillary PMDs are far less effective in ensuring the safe restart of cryogenic engines in comparison with storable liquids due the low surface tension of the propellant [194]. Furthermore, the presence of meshes or screens can severely increase the pressure drop across PMDs in high flow rate tank outlets, rendering this approach unfeasible for launch vehicles. The magnetic trap system here proposed faces these issues by combining a screen-less clam shell trap aimed at holding the liquid and a magnet employed to induce reorientation in microgravity.

Figure 13.7 depicts a conceptual magnetic trap for Falcon 9's first stage LOX tank. When the engine is in operation, the flux of LOX surrounds the trap and reaches the fuel outlet. Because inertia is dominant, the magnetic force has a marginal effect on the flow. Stage separation triggers the unfavorable acceleration profile estimated in Fig. 13.2 and part of the liquid escapes the trap. The volume of released propellant and the risk of gas injection depends on the geometry of the system and should be quantified numerically. Once the launcher reaches microgravity conditions, the magnet located at the fuel outlet reorients the remaining

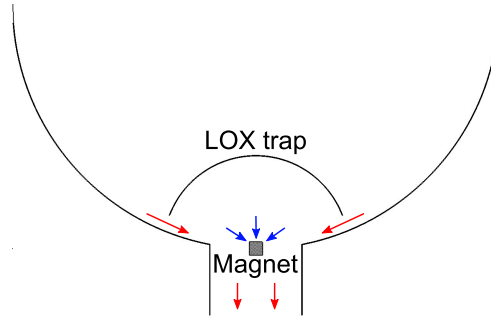


Figure 13.7: Conceptual magnetic trap system for Falcon 9's first stage LOX tank. Red and blue arrows indicate the propellant flux in hyper- and microgravity conditions, respectively.

liquid oxygen and prevents the ingestion of gas bubbles. The trap can be refilled by installing a vent tube on top of the structure [188]. It is important to highlight that, unlike similar capillary systems, the magnetic trap does not prevent the ingestion of gas bubbles in the trap space; instead, it ensures that the required volume of gas-free propellant reaches the fuel outlet by employing a localized magnetic polarization force.

The magnetic acceleration field on LOX of a 5 cm radius, 10 cm height cylindrical magnet magnetized at 1300 kA/m is shown in Fig. 13.8. The geometry differs from that of Fig. 13.5 in the adoption of a smaller radius, which increases the magnetic force close to the source [346] and makes this configuration more suitable for magnetic traps. The magnet volume is chosen to impose an acceleration of 10^{-4} m/s^2 (one order of magnitude larger than microgravity disturbances [196]) at $\sim 40 \text{ cm}$ from the magnet. This leads to the approximate LOX volume that needs to be retained in the single-engine first stage scenario reported in Table 13.2. Although the mass of the magnet is just $\sim 5.5 \text{ kg}$, the total mass would be close to 20 kg after considering ancillary components like the 2.5 mm aluminum LOX trap wall or its supports.

The same system can be applied to the second stage and would require a 25 cm radius LOX volume with a magnet of just 0.5 kg. The mass of the trap would account for $\sim 2.2 \text{ kg}$. That is, the magnetic trap may potentially achieve mass savings of one to two orders of magnitude with respect to current ullage engine approaches.

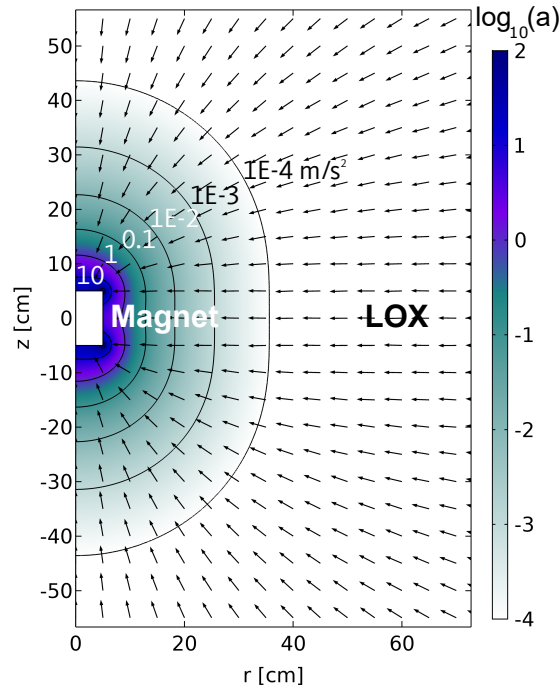


Figure 13.8: Magnetic acceleration field induced by a 5 cm radius 10 cm height praseodymium magnet magnetized at 1300 kA/m.

13.2.5 Magnetic field generation

With the nI parameter already sized for the different engine restart configurations, the next logical step is to determine how to produce the required magnetic fields. Three technologies are considered: copper and aluminum coils, rare earth permanent magnets, and superconducting coils.

The magnetic field generated by a coil is linearly dependent on the nI parameter, that can be increased by adding more wire turns or employing higher currents. Total coil mass and power dissipation are the driving factors of the design. The mass of the coil can be estimated as

$$m = 2\pi R n S \rho_w, \quad (13.6)$$

where S is the cross-section of the wire and ρ_w its density. The heat dissipated by the coil can be derived from Ohm's law, resulting in

$$P = 2\pi R I n \rho_e \frac{I}{S}, \quad (13.7)$$

with ρ_e being the resistivity of the material. In a worst-case scenario this heat is stored in the coil instead

of being dissipated, causing a temperature increase of

$$\Delta T = \frac{Pt_{\max}}{mC_p} = \frac{\rho_e t_{\max}}{\rho_s C_p} \left(\frac{I}{S} \right)^2, \quad (13.8)$$

where C_p is the heat capacity of the wire. In order to constrain the design, the heat dissipated by the coil is limited by considering two worst-case scenarios: in the first, the heat is fully transferred to the residual LOX. The maximum power is arbitrarily set to the one that vaporizes 1 kg of LOX during the 6 minutes operation of the coils. The latent heat of vaporization of LOX is 6.82 kJ/mol (or 213.13 kJ/kg) at atmospheric pressure [2], which results in a maximum coil power of 592 W. Because nI is fixed, the ratio I/S is determined by Eq. 13.7. In the second scenario, the heat is stored in the coil, causing a temperature increase that is arbitrarily limited to 10 K. Therefore, the I/S parameter is extracted from Eq. 13.8. The most restrictive constraint is chosen for each design so that the thermal runaway of the material and the vaporization of the residual LOX volume are avoided. Then, the mass is computed for the I/S value from Eq. 13.6. The second requirement concerns the voltage of the coil, set to 24 V to ease integration with Falcon 9's power subsystem. After inserting the I/S value in Eq. 13.7 and employing Ohm's law, the current intensity of the coil and its resistance are computed. At the boiling temperature of LOX (90 K) the resistivities of copper and aluminum are $3.5 \cdot 10^{-9} \Omega \text{ m}$ and $4.5 \cdot 10^{-9} \Omega \text{ m}$, respectively [403]. Although copper is slightly more conductive than aluminum, its density and heat capacity are 8960 kg/m³ and 0.385 kJ/kgK, while aluminum has a density of 2700 kg/m³ and a heat capacity of 0.89 kJ/kgK. Therefore, aluminum is chosen to minimize the mass of the design.

The second approach focuses on employing rare earth permanent magnets to generate a constant, unpowered magnetic field. Neodymium ($\text{Nd}_2\text{Fe}_{14}\text{B}$) is the most popular rare earth material, has a density of 7008 kg/m³ [2], and exhibits a remanent magnetization of $M_m \approx 1200 \text{ kA/m}$. It is classified as a “hard material”, implying that it can be used to manufacture magnets of any shape [404]. As previously noted, the sizing parameter nI of a cylindrical coil can be translated to the length l_m of an equivalent cylindrical magnet with the same diameter by means of the expression $In = M_m l_m$. Magnet tessellation strategies such as Halbach arrays can be employed to boost the paramagnetic force on one side, while partially canceling it on the other [405]. Halbach arrays have already been proposed for space applications (see Chapter 14)

and would be particularly well suited for the LOX settling problem for two reasons: the reach of the magnet is increased, and the interaction between the LOX magnet and the droplets generated in the fuel tank is reduced.

Neodymium magnets experience a slight increase of their magnetic flux as temperature decreases. At around 135 K, a transition point is reached and the magnet undergoes spin reorientation (i.e. a change in the preferred direction of the magnetization vector) that decreases the flux by no more than a 14%. This process is reverted as soon as the temperature increases [406]. If needed, the transition point could be avoided by isolating the magnet in the LOX tank and actively controlling its temperature. A more elegant solution is, however, to employ praseodymium magnets to avoid the spin reorientation. Praseodymium magnets have been shown to reach a remanent magnetization of ~ 1300 kA/m at 85 K [407, 408], which makes them ideal for LOX control applications.

The design points of the aluminum coil and praseodymium magnet are shown in Table 13.3 as a function of the nI parameter. In all cases but 10^6 At, the design of the coil is driven by the thermal requirement (maximum temperature increase of 10 K). Magnets are orders of magnitude lighter for all nI values, incurring in a – still reasonable– mass penalty of 52 kg at 10^5 At. nI values beyond 10^5 At seem unreachable without incurring in large mass penalties, and it is in this context where high-temperature superconductors (HTC) can become a game-changing alternative. A HTC wire exhibits zero resistance in a certain operational range, resulting in no heat loss and a potential reduction in mass and power requirements. This happens when (i) it is operated below its critical temperature T_c –greater, by definition, than the boiling

Table 13.3: Mass and power budget for different magnetic configurations.

Current · Turns [At]	Aluminum coil ¹					Praseodymium magnet ²	
	I [A]	P [W]	n [# turns]	d [mm]	m [kg]	h [mm]	m [kg]
10^2	$2.51 \cdot 10^{-3}$	0.06	4	$1.62 \cdot 10^{-1}$	2.44	0.08	0.052
10^3	$2.51 \cdot 10^{-2}$	0.60	40	$5.12 \cdot 10^{-1}$	24.4	0.77	0.52
10^4	$2.51 \cdot 10^{-1}$	6.03	405	1.62	244	7.7	5.2
10^5	2.51	60.26	4054	5.12	2438	77	52
10^6	24.67	592	40541	16.2	24814	769	519

¹ Coil of 35 cm diameter operating at 24 V and 90 K.

² Cylindrical magnet of 35 cm diameter magnetized at 1300 kA/m at 90 K.

point of nitrogen (77 K)–, (ii) it is subjected to a magnetic field below the critical field B_c , and (iii) the critical current I_c is not exceeded. The simultaneous satisfaction of these three requirements is far from trivial; in fact, I_c decreases continuously with increasing temperature and magnetic field [409]. For example, Bi2223 ($\text{Bi}_2\text{Sr}_2\text{Ca}_2\text{Cu}_3\text{O}_{10+\delta}$) has a critical temperature of 110 K, but its critical current drops to zero when the material is exposed to a field of less than 1 T. RE-123 ($(\text{RE})\text{Ba}_2\text{Cu}_3\text{O}_7$, where RE stands for Rare Earth element) superconductors (also known as REBCO), on the contrary, can resist up to 10 T, but only well below a critical temperature of around 90 K [410]. It is nowadays feasible to generate very strong magnetic fields at the boiling point of Helium (4.22 K), a good example being the 32 T superconducting magnet [411] of the National High Magnetic Field Laboratory⁵. Reaching similar values at higher temperatures seems, unfortunately, still beyond our technical capabilities. In the application here discussed the superconductor would be immersed in LOX, which would act as a cooling agent only if $T_c \gg 90$ K, and the maximum magnetic field imposed near the coils would be ~ 10 T at $In = 10^6$ At. The results presented in Ref. 409 for different commercial REBCO conductors seem to indicate that such operation point cannot be reached with current technologies. However, the I_c value of 4 mm wide superconductors is shown to be 450–1000 A/mm at 12 T and 77 K, a value that jumps up to 60 kA/mm² at 18 T and 4.2 K. This indicates that cooling mechanisms need to be put in place to reach the 10^6 At configuration with HTCs, which may open an opportunity for multiple-use of the helium tanks employed for tank pressurization. This possibility, although attractive, would require a deeper technical analysis that is beyond the scope of this chapter.

13.2.6 Fuel tank

From the magnetic actuation perspective, LOX determines the design envelope of the system. On one hand, the LOX tank is more than two times larger than the fuel tank, and therefore a given magnetic source will reach a larger portion of the latter. On the other, LOX is a paramagnetic substance with volume magnetic susceptibility $\chi_{\text{LOX}}^{\text{vol}} = 0.0034$ [2], while kerosene is a diamagnetic with $\chi_{\text{Ke}}^{\text{vol}} \approx -8 \cdot 10^{-6}$ [412]. In order to apply the same MP² strategies to the fuel tank, it must be transformed into a para/ferromagnetic by adding magnetic nanoparticles and creating a kerosene-based ferrofluid. With this approach, the susceptibility of

⁵ See <https://nationalmaglab.org/magnet-development/magnet-science-technology/magnet-projects/32-tesla-scm>. Consulted on: 26/12/2021.

the solution is bounded by the concentration of magnetic nanoparticles.

As described in Sec. 12.3.3, the use of metal-based particles in liquid propellants has been analyzed since the 1950s with the perspective to enhance ideal propulsion performance [392]. Kerosene has been employed as a carrier liquid for ferrofluids since their invention in 1963 [6] and kerosene-based ferrofluids are synthesized and used in numerous fields [413–416]. Commercial solutions like Ferrotec’s EMG-905⁶ are now widely available at a relatively low cost. The initial susceptibility of a monodisperse, colloidal ferrofluid can be estimated as [20]

$$\chi_{\text{ini}}^{\text{vol}} = 8\phi\lambda, \quad (13.9)$$

where ϕ is the volume fraction of magnetic solids and λ is the coupling coefficient, given by

$$\lambda = \frac{\mu_0 M_d^2 V}{24kT}, \quad (13.10)$$

with M_d being the saturation moment of the bulk magnetic solid, V the nanoparticle volume, k the Boltzmann constant, and T the absolute temperature. Assuming an iron oxide nanoparticle radius of 5 nm, an absolute temperature of 293 K, and a saturation moment of 446 kA/m [417], the approximate volume fraction required to match the magnetic susceptibility of LOX starting from the value of kerosene would be just $\phi \approx 3.2 \cdot 10^{-4}$. Not surprisingly, this value is within the range tested by Martin and Holt in the NASA MAPO experiment [163].

If the whole kerosene tank volume is magnetized, the magnetic nanoparticles add ~ 40 kg and ~ 11 kg to the first and second stages, respectively, in addition to negligible variations in density and specific impulse (see Sec. 12.3.3). The very low ferrofluid concentration should prevent damage to the engines. Although simple, this approach is expensive and inefficient. A better alternative is to enhance only the volume of kerosene employed to restart the engine by adding a concentrated ferrofluid volume shortly before MECO/SECO. The mass penalty associated with the addition of nanoparticles would be of just 40 to 140 g based on the values presented in Table 13.2.

⁶ See <https://ferrofluid.ferrotec.com/products/ferrofluid-emg/oil/emg-905/>. Consulted on: 28/12/2021.

13.3 Propellant Gasification System

The Propellant Gasification System concept was first proposed in the early 2010s by Trushlyakov and coworkers as a method to vaporize the propellant residual of 2nd launch vehicle stages and provide attitude and orbit control capabilities by means of dedicated vapor-fed thrusters [418–420]. The original idea was to inject the combustion products of two-component propellants (AA and NDMH) in the tank to move the stage from its initial circular orbit to an elliptical orbit. Such orbit would ensure a successful deorbiting in the time frame of 25 years. In 2015, the use of solid fuel instead of a two-component propellant was investigated to simplify the design and improve the energy performance of the PGS. Further analyses on the Soyuz 2.1v launch vehicle showed that the PGS could also lead to launch vehicle characteristic speed enhancements of up to 5% [421]. The PGS baseline design has currently evolved to reduce its mass and environmental impact using a green mono-propellant (hydrogen peroxide) that adds the possibilities of i) controlling the movement of the stage to reach a given drop area, ii) providing conditions for LRE restart by executing the flip around and propellant settling maneuvers, and iii) passivating the propellant after a normal or emergency cutoff of the LRE [422]. Highly concentrated hydrogen peroxide (85%) has already been employed as a green mono-propellant in substitution of hydrazine on the “Soyuz” launch vehicle for the operation of turbo-pump units [423].

The PGS considered in this chapter vaporizes the propellant residuals in the oxidizer tank of the launch vehicle using the catalytic decomposition of hydrogen peroxide, which is placed in an auxiliary tank and used as a heat source. The mono-propellant is passed through a catalyst chamber that leads to the formation of up to 823K hot oxygen and steam. The vapor-gas mixture is then transferred into the oxidizer tank, which leads to vaporization of the liquid phase and a pressure increase. The gas, consisting of vaporized propellant and pressurizing agent (helium), is used to feed a set of gas thrusters that are employed for attitude control and tank settling, as sketched in Fig. 13.9. This approach can be regarded as the active equivalent of the hydrogen venting strategy employed in the Apollo era [196].

The following main subsystems compose the PGS: (i) a hot gas generator that includes a bladder-controlled hydrogen peroxide tank and a catalyst chamber where the exothermic decomposition of hydrogen

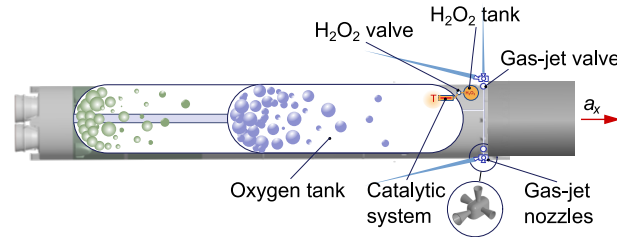


Figure 13.9: Propellant Gasification System.

peroxide happens, producing a high-temperature vapor-gas mixture (VGM) with a 34% H_2O and 66% O_2 composition, (ii) a system of nozzles installed after the catalyst chamber that injects the VGM into the LOX tank minimizing tank wall heating, and (iii) a system of gas nozzles used to discharge the VGM from the tank and produce the required thrust. The PGS provides control over the tank discharge valves, hydrogen peroxide feeding, and gas nozzles. Cold helium gas, which is stored in balloons at the bottom of the oxidizer tank, can also be used to reduce the temperature of the VGM.

Further details on the PGS can be consulted in Ref. 401 and are not reflected here to respect the intellectual ownership of Vladislav Urbansky, Prof. Vadim Yudintsev, and Prof. Valeriy Trushlyakov, inventors and developers of the system. However, the preliminary mass budget arising from the analysis that is carried out in the aforementioned manuscript is left in Table 13.4 as a reference.

13.4 Hybrid Magnetic Gasification

A combination of the MP² and PGS technologies can potentially enhance the robustness and performance of the overall propellant settling system. This hybrid approach, depicted in Fig. 13.10, involves

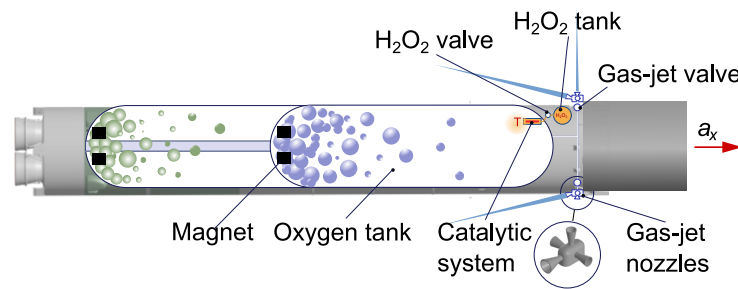


Figure 13.10: Hybrid Propellant Gasification System.

Table 13.4: Mass from different components required for the flip around and settling maneuvers in the first and second stages.

System	Flip around		Settling	
	1 st	2 nd	1 st	2 nd
Time [s]	9.7	5.2	40.3	12.5
Gas, nozzles [kg]	22.9	6.14	305	94.6
Vaporized O_2 [kg]	53.9	15	304	92
PGS [kg]	40	40	-	-
Catalyst [kg]	0.5	0.5	-	-
H_2O_2 balloon [kg]	4.6	1.24	5.8	1.77
H_2O_2 [kg]	42	11.4	53	16.2
Helium [kg]}	0.069	0.02	0.668	0.2

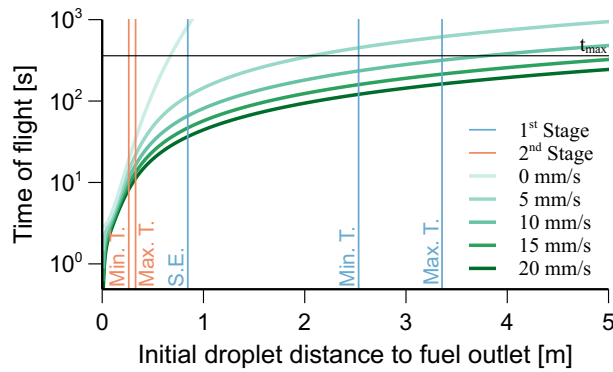


Figure 13.11: Time required by a LOX droplet to reach the bottom of the tank as a function of its initial position and velocity when subject to a 10^4 At coil located at the tank outlet. The minimum tank settling length required by the single engine (S.E.), minimum thrust (Min. T.) and maximum thrust (Max. T.) configurations is superposed.

a permanent magnet located at the fuel outlet and a smaller PGS aimed at carrying out the flip-around phase and the shorter propellant settling maneuver. The initial acceleration induced on the liquid residuals during the settling phase starts a slow movement toward the bottom of the tank, where the magnetic force is stronger and thus able to efficiently collect the liquid droplets.

Figure 13.11 depicts the time required by an LOX droplet to reach the bottom of the tank when subject to the magnetic field generated by a 10^4 At magnet as a function of its initial velocity and distance to the tank outlet. Based on Table 13.3, such magnet has a mass of ~ 5.2 kg. The results are computed from a modified version of Eq. 8.31, and prove that an initial inertial kick can significantly extend the reach of the MP² system. Initial droplet velocities of just 5 to 10 mm/s allow the magnet to collect the necessary residual

Table 13.5: Comparison of different propellant settling approaches and mass budgets for first and second stages.

	Advantages	Disadvantages	Mass, 1 st [kg]	Mass, 2 nd [kg]
Passive Magnetic Retention	- Simple - Robust - Thoroughly studied	- Beyond current technological capabilities - Massive unless stage operation is adapted - Limited control	$\rightarrow \infty$	>1000
Magnetic Recovery	- Lightweight - Simple	- Sensitive to fluid-structure interactions - Slow - Requires tank outlet redesign - Very low TRL	104	1-10
Magnetic Trap	- Lightweight - Simple - Potentially robust	- Requires careful trap design - Requires tank outlet redesign - Very low TRL	40	6
Propellant Gasification System	- Robust - Provides settling and attitude control - Fast to operate - More traditional design	- Complex - Sensitive to liquid movement - Very low TRL	147	71
Hybrid Magnetic Gasification	- Lightweight - More robust than magnetic recovery - Provides settling and attitude control - Fast to operate - Boosts magnet performance	- Complex - Sensitive to liquid movement - Requires tank outlet redesign - Very low TRL	93	58

propellant mass under all engine restart configurations listed in Table 13.2 for both stages assuming that the droplets are uniformly distributed in the tank volume. The 5 kN PGS nozzles, that induce accelerations of $\sim 0.23 \text{ m/s}^2$ in the first stage, would theoretically need to operate for less than 0.05 s to induce these droplet velocities, reducing the propellant settling window in about 40 s. The operation of the nozzles would need to be extended to account for transient effects and fluid-structure interactions, but this would only increase the effectivity of the system. Based on Table 13.4, the associated PGS mass savings would be close to 90 kg and 53 kg in the first and second stages, respectively, resulting in total hybrid system masses of 93 and 58 kg. The gas generated during the turn around phase is considered in this estimation. Further details can be found in Ref. 401.

13.5 Summary

Five novel cryogenic propellant settling approaches have been explored in this chapter: passive magnetic retention, magnetic recovery, magnetic traps, propellant gasification, and hybrid magnetic gasification. The advantages and disadvantages of each of them have been discussed, and preliminary mass budgets have

been derived. Table 13.5 summarizes and extends the main results from the analysis.

While the passive magnetic retention strategy exceeds any reasonable mass budget, the magnetic trap approach can potentially reduce the mass of existing propellant settling systems by one to two orders of magnitude, leading to more than half a million dollar savings per launch and stage. This comes at the cost of higher complexity and modeling efforts, particularly in the fuel tank. Although less efficient, the magnetic recovery system also seems competitive with respect to current technologies. Because this approach depends on the availability of uniformly distributed free-floating propellant droplets, fluid-structure interactions may undermine its performance. The PGS, which represents a relatively more conventional approximation to the problem, can also lead to moderate mass savings that are significantly increased when operated in combination with a magnetic retention system. As with any other low-TRL technology, numerous technical challenges remain that can only be addressed with a more detailed numerical and experimental analysis.

Ullage engines have been employed since the beginning of the space era and are nowadays regarded as a robust active settling solution. However, publicly available data indicates that they also involve significant mass and economic penalties that may be reduced with novel approaches. Such approaches face additional challenges when dealing with cryogenic propellants and must demonstrate the same level of reliability and robustness in order to become competitive. Although the MP² and propellant gasification systems are still in a very early TRL stage, the analysis here presented offers reasons to persevere in their development

13.6 Collaborators

The author gratefully acknowledges the support from Vladislav Urbansky, Dr. Vadim Yudintsev, and Dr. Valeriy Trushlyakov from Omsk Technical State University, project collaborators and inventors/developers of the propellant gasification system that is briefly described in Sec. 13.3.

Chapter 14

Magnetically enhanced electrolysis

Different magnetic actuation strategies have been applied in this dissertation to problems with (i) continuous gas-liquid interfaces, and (ii) free-floating droplets and bubbles. However, processes like boiling, electrolysis, or reduction also involve the bubble nucleation, growth, and detachment mechanisms addressed in Chapter 8. Such processes are key for a wide range of space applications in orbit and partial gravity environments. They can potentially enable several human and robotic missions, and thus deserve further attention.

This final chapter focuses on low-gravity water electrolysis, which plays a central role in environmental control and life support systems [207], space propulsion [208–210], energy storage and conversion [211, 212], and ISRU [213, 214], among others. However, as explained in Sec. 1.4.4, alkaline/acidic cells and PEMs face mass transport issues in microgravity that limit their efficiency and complicate phase separation [216–218]. What follows is the formulation, numerical study, design, development, and testing of magnetically-enhanced low-gravity water electrolysis cells. This effort is aimed at developing assemblies with no moving parts that could potentially exhibit enhanced efficiency and reliability. Even though the focus is placed on water electrolysis, the designs and processes here introduced can also be applied to boiling, condensation, or electrochemical reduction, among others.

14.1 Fundamental architectures

As shown in Chapter 11, magnetic buoyancy can be induced in virtually all liquids of technical interest. Its application may be beneficial for both PEM and alkaline/acidic cells, but one important distinction

should be made between them: while the former employ pure water, the latter require electrolytes with moving charges. The presence of an electrical current leads to a magnetohydrodynamic Lorentz-force that coexists with magnetic polarization forces. Thus, two basic architectures should be considered in microgravity conditions: diamagnetically and Lorentz-force enhanced electrolysis.

14.1.1 Diamagnetically enhanced electrolysis

Diamagnetically enhanced electrolysis architectures employ the magnetic polarization forces tested in Chapter 11 to detach and collect bubbles from the surface of an electrode while they are immersed in a diamagnetic liquid. The concept is illustrated in Fig. 14.1(a) and, as previously mentioned, is applicable to any other conceivable multiphase process (e.g. boiling). Processes of technical relevance, such as the detachment and coalescence of bubbles or their displacement, have already been explored in Secs. 11.2.2, 11.2.3, and 11.2.4.

Although virtually all existing electrolyzers are diamagnetic, paramagnetic or ferromagnetic liquids may also be employed in future applications. This would require the approach sketched in Fig. 14.1(b), where the magnet pushes away the gas bubbles generated over the nucleation surface. Ferrofluids have already been employed to boost the productivity of boiling surfaces on Earth [145, 146] and, in spite of the numerous technical challenges that such approach would face (e.g. thermal stability or particle deposition [424]), future applications should not be discarded.

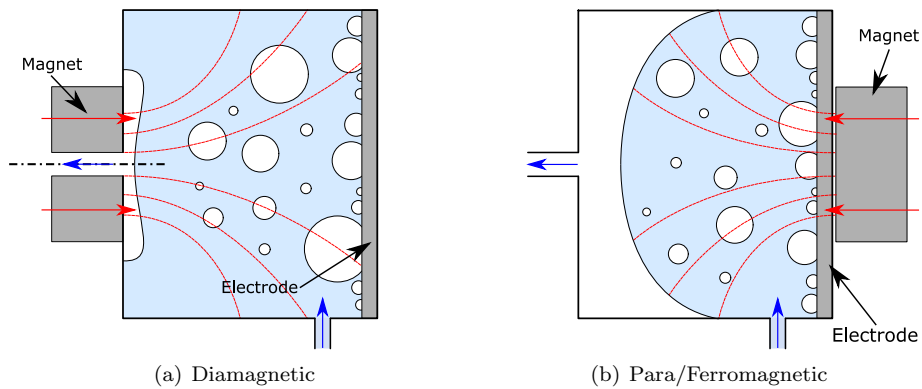


Figure 14.1: Conceptual representation of a magnetically enhanced electrolysis cell. Blue arrows represent the liquid/gas flow, while red arrows denote the magnetization vector.

14.1.2 Lorentz-force enhanced electrolysis

The Lorentz force must be considered when an electromagnetic field is applied to unbalanced electrolyte solutions, and adopts the form

$$\mathcal{L} = \rho_v \mathbf{E} + \mathbf{J}_e \times \mathbf{B}, \quad (14.1)$$

with ρ_v being the free charge density. As with the diamagnetic force, a buoyancy effect is induced on the gas bubbles. However, the Lorentz force also generates a convective liquid flow that opposes the buoyancy effect. In most cases, the forced flow is the driving force acting on the bubbles.

Previous works have explored the effect of magnetic fields applied to the OH^- transport region in the productivity of terrestrial alkaline electrolyzers [425–428], reporting cell current increments above 100% [429]. The basic configuration for the Lorentz-force enhanced electrolysis approach is depicted in Fig. 14.2 and employs two parallel flat electrodes immersed in an alkaline electrolyte to which a magnetic field is imposed. The magnetic field is applied parallel to the plane of the electrode, and since the mean electric current density vector \mathbf{J}_e is perpendicular to such electrode, a vertical force is induced by the magnetic term in Eq. 14.1. The bubbles also modify the local current flow, leading to more complex microfluidic interactions arising from a non-uniform Lorentz force distribution [430, 431]. The same working principle is the foundation of the magnetohydrodynamic drive, which became popular with the 1990 movie “The Hunt

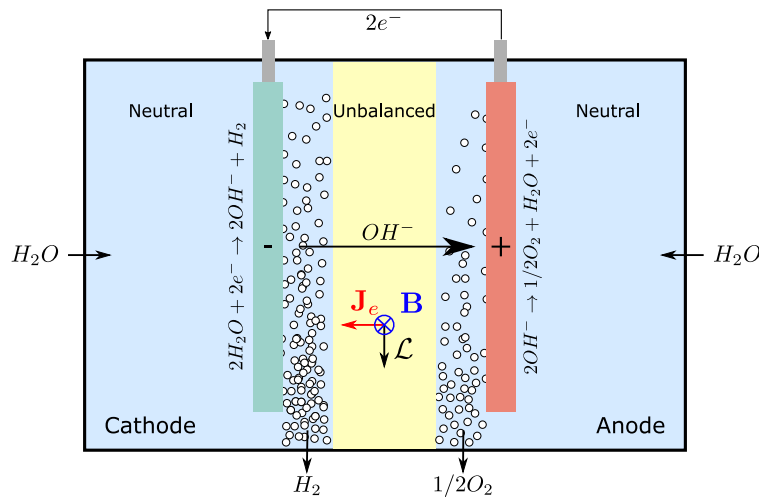


Figure 14.2: Alkaline cell where the charge unbalance in the OH^- transport region leads to a magnetic Lorentz buoyancy effect in the presence of an out-of-plane magnetic field \mathbf{B} .

for Red October” and is usually employed as an educational example¹.

14.2 Numerical study

A series of numerical results are here presented to explore the diamagnetic and Lorentz-force electrolysis concepts. This high-level analysis and system sizing is made based on the results derived in Chapter 8. N52 neodymium magnets magnetized at 1150 kA/m are considered. The physicochemical properties of water, gas hydrogen, and gas oxygen at 25°C and 1 atm employed in the simulations are reported in Table 14.1.

Table 14.1: Relevant physicochemical properties of water, gas hydrogen, and gas oxygen at 25°C and 1 atm [2].

Material	\mathcal{M} [g/mol]	ρ [kg/m ³]	χ^{vol}	η [Pa·s]
H_2O (l)	18.015	997	$-9.1 \cdot 10^{-6}$	0.0009
H_2 (g)	2.016	0.082	$1 \cdot 10^{-10}$	-
O_2 (g)	31.999	1.308	$3.73 \cdot 10^{-7}$	-

14.2.1 Electrically neutral media

The effects of magnetic buoyancy on electrically neutral media are first addressed. This includes pure water in contact with the external face of PEM electrodes and alkaline electrolytes outside the OH^- transport region. Although in the second case the presence of charged electrodes leads to a local distribution of charge, the Debye length [432] of such distribution becomes about 0.1 nm for $NaOH$ and KOH solutions in water in standard conditions. That is, the alkaline electrolyte outside the OH^- transport region can be considered electrically neutral, and hence unaffected by Lorentz’s electric and magnetic force terms (but, still, influenced by the magnetohydrodynamic fluid flow).

Figure 14.3 represents the radial cross-section of the volume force density $f_m^{V,\text{eff}}$ (Eq. 8.3) induced by a cylindrical magnet with 1 cm radius and 0.5 cm height in a O_2 bubble. Finite-element simulations in Comsol Multiphysics are employed with the equations and boundary conditions of the magnetic model described in the Appendix B. Due to the small magnetic susceptibility of water, values of 1 nN/mm³, corresponding to

¹ See <https://youtu.be/bPSowtQ9rjI>. Consulted on: 28/04/2022.

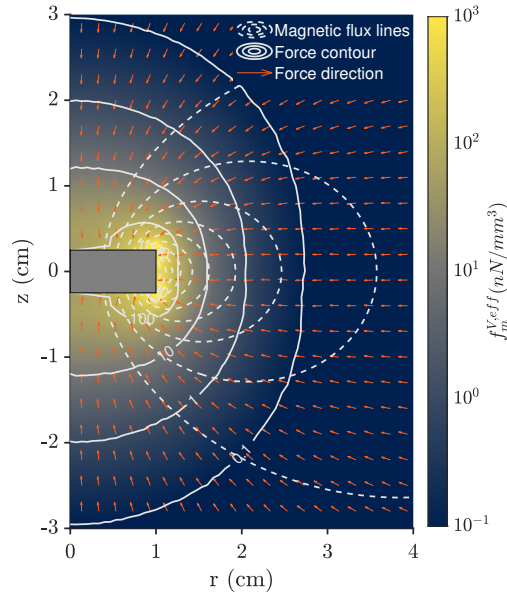


Figure 14.3: Radial cross-section of the magnetic force density induced by a cylindrical magnet in an O_2 gas bubble. The red arrows, solid lines, and dashed lines represent the non-scaled force vector, the constant force contours, and the magnetic flux lines, respectively.

an inertial acceleration of $\approx 1 \text{ mm/s}^2$, are reached at 2 cm from the surface of the magnet. In contrast, an hypothetical square PEM cell with an electrode surface of 2 cm^2 and a potential difference of 1.2 V exerts a dielectric force of 10^{-5} to 10^{-1} nN/mm^3 on a gas bubble sitting on the electrode. It is then justified to neglect the dielectric force for the applications here considered.

Figure 14.4 shows the Stokes terminal velocity field from Eq. 8.24 of a 1 mm radius O_2 bubble immersed in water and subject to the influence of a permanent neodymium magnet in microgravity. The red arrows, solid lines, and dashed lines correspond to the non-scaled velocity vector, the constant velocity contours, and the magnetic flux lines, respectively. Three different cylindrical magnets magnetized along the axis are studied, the first (a) with 10 mm radius and 5 mm height, the second (b) with 20 mm radius and 5 mm height, and the third (c) with 10 mm radius and 20 mm height. The velocity vectors point toward the magnets, which adopt the role of a bubble sink. This effect can be employed to induce the detachment and collection of gas bubbles from an electrode or boiling surface in microgravity, as illustrated in Chapter 11. The performance of the magnets is hampered by the rapid magnetic field decay, leading to terminal velocities

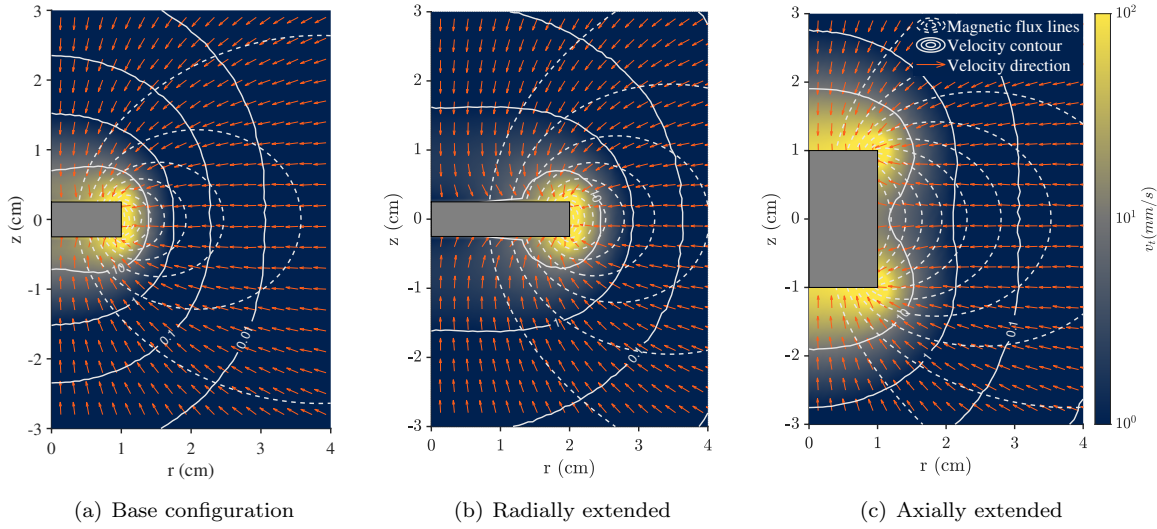


Figure 14.4: Radial cross-section of the Stokes terminal velocity v_t induced by a cylindrical magnet in an O_2 gas bubble with 1 mm radius in water. The red arrows, solid lines, and dashed lines represent the non-scaled velocity vector, the constant velocity contours, and the magnetic flux lines, respectively.

of the order of 1 mm/s at approximately 15 mm from their surface. Larger velocities are experienced in the corners of the magnets, where the magnetic field gradient is maximum. However, the reader should note that terminal velocities above 1 mm/s fall beyond the validity range of the Stokes law and are therefore overestimated (see Sec. 11.2.2).

The magnetic body force is proportional to the gradient of the magnetic field \mathbf{H} and its module. When a quasi-uniform field is generated, as observed near the axis of Fig. 14.4(b), the magnetic forces and terminal velocities are reduced. It is then convenient to select a magnetic configuration that maximizes the force exerted on the bubbles. Similar problems appear in biomedical applications dealing with magnetic drug delivery and targeting [433–436] or magnetic resonance imaging [437, 438], and have been faced by means of Halbach magnet arrays. A Halbach magnet array is an arrangement of permanent magnets that reinforces the magnetic field on one side of the array and cancels it on the other [405]. These characteristics are convenient for space applications, where the performance of the magnet should be maximized, and its electromagnetic interference and mass should be minimized.

Figure 14.5 represents a linear array of five $1 \times 1 \times 0.5 \text{ cm}^3$ neodymium magnets configured considering (a) aligned magnetizations, and (b) Halbach-oriented magnetizations. As in Fig. 14.4, the terminal velocity

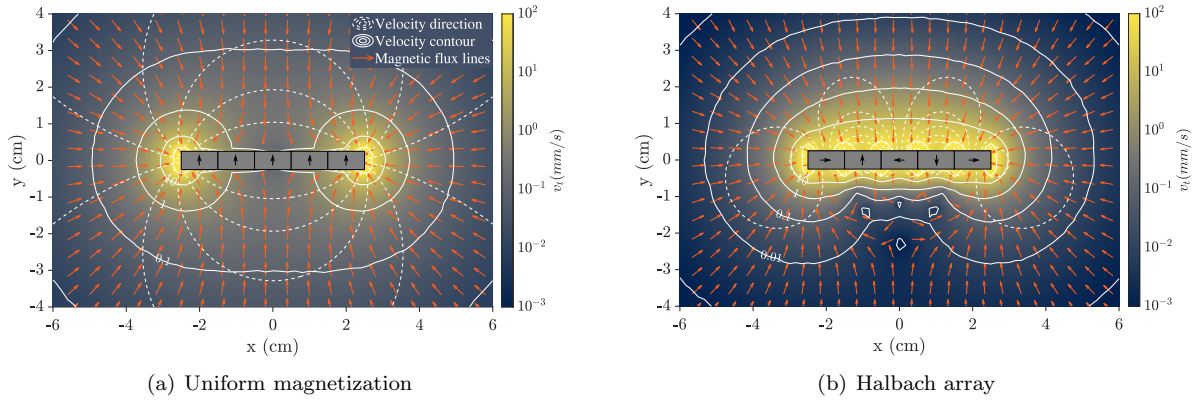


Figure 14.5: Two-dimensional simulation with 1 cm depth of the microgravity terminal velocity v_t induced by an array of magnets in an O_2 gas bubble with 1 mm radius in water. The black arrows, red arrows, solid lines, and dashed lines represent the magnetization direction, non-scaled velocity vector, the constant velocity contours, and the magnetic flux lines, respectively.

map computed with Eq. 8.24 is represented. It can be observed how the Halbach configuration produces an asymmetrical magnetic field and a more homogeneous terminal velocity distribution, with the 1 mm/s contour line staying at approximately 2 cm from the magnets along the x axis. However, the terminal velocity is shown to decay faster than in the linear configuration, as exemplified by the 0.1 mm/s line. This characteristic may guide the design of future phase separators. For instance, the linear configuration may be more suitable for the gas collection process due to the convergence of the velocity vectors toward the extremes of the magnet, while the Halbach array may produce a more homogeneous magnetic force distribution over the electrodes.

These results can be easily extended to KOH or $NaOH$ solutions by noting the linear dependence of the terminal velocity with the volume magnetic susceptibility χ^{vol} . Because this parameter is a 60-80% larger with respect to pure water [3], the performance of the system would be improved. Similar effects would be observed in applications involving ferrofluids, whose magnetic susceptibility can be of the order 10. Without considering the many technical difficulties associated with their operation, such technologies could easily reach magnetic force values equal or larger than the acceleration of gravity. This may lead to large improvements in the productivity of the cell both on Earth and in space.

A second effect of interest arising from the application of an inhomogeneous magnetic field to a

nucleation surface is the potential reduction of the break-of diameter. This is explored in Fig. 14.6 for an isolated bubble by making use of Eq. 8.17. A 10 mm radius, 5 mm height cylindrical magnet is considered in microgravity, assuming a contact angle of $\theta_c = 5^\circ$. The magnetic Fritz equation predicts a reduction of the break-of diameter from 10 cm to few millimeters as the bubble approaches the magnet. Without considering the variations in contact angle and surface tension, the employment of saturated $KOH/NaOH$ solutions would reduce the diameter by a 25% due to the increase in magnetic susceptibility. On the other hand, no significant differences are observed between O_2 or H_2 gas bubbles due to their small magnetic susceptibility. These predictions should however be taken with care, as the magnetic Fritz equation assumes an homogeneous magnetic force in the bubble volume, and this assumption is being violated in a significant portion of the solution domain. Even if this was not the case, the Fritz equation describes the detachment of an isolated bubble. Experimental observations have shown that the break-of diameter in microgravity is actually much smaller due to the interaction between bubbles located in the first layer over the electrodes [216, 217, 219].

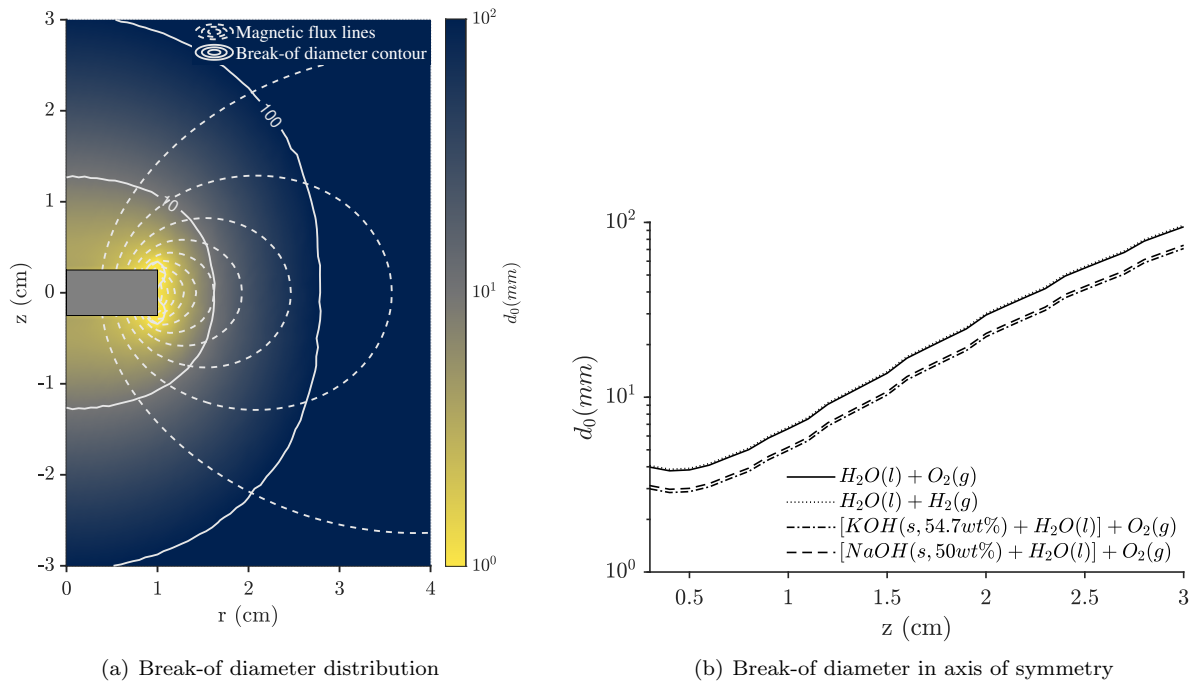


Figure 14.6: (a) Radial cross-section of the break-of diameter d_0 induced by a 10 mm radius, 5 mm height cylindrical magnet in an O_2 gas bubble in water with $\theta_c = 5^\circ$. The solid and dashed lines represent the constant break-of diameter contours and the magnetic flux lines, respectively. (b) Break-of diameter in the axis of symmetry for different gas-liquid combinations.

Numerical simulations based on the framework of analysis presented in Sec. 8.2 and experimental results are then required to shed light on this problem.

Non-magnetic cell components have been considered throughout this discussion. However, electrodes and bipolar plates are made of diamagnetic (carbon), paramagnetic (titanium), or ferromagnetic (nickel, ferritic stainless steel) materials. Those from the third group, with relative permeabilities up to 2000, can be strongly magnetized by external fields and modify significantly their local magnetic force distributions. If not taken into consideration, these disturbances may lead to the undesired accumulation of bubbles at the surface of the electrodes. Although the local effect needs to be evaluated in a case-by-case basis, it can become important for massive, ferromagnetic electrodes subject to strong magnetic fields. In particular, corner geometries will tend to generate magnetic singularities, leading to the generation of bubble sinks (as it happens in the well-known lightning rod effect [304]).

14.2.2 Effect of magnetic field in unbalanced electrolyte

The Lorentz force defined by Eq. 14.1 acts on electrolytic cells in the presence of charge unbalance or electrical currents. As previously discussed, this is the case of alkaline cells. For example, a Lorentz buoyancy force of 5000 nN/mm^3 would be generated with a current density of 0.5 A/cm^2 and a characteristic magnetic field of 1 T . This term is several orders of magnitude larger than the diamagnetic force studied in Sec. 14.2.1 and could lead to disruptive low-gravity applications. From the technical perspective, the need to generate gas bubbles *between* the electrodes may raise safety concerns in space applications, where the recombination of products represents a critical safety hazard. Membranes would be needed to prevent such recombination.

In PEM electrolysis the only space where there is a charge unbalance is the membrane itself, where a highly acidic medium is created in the presence of water. Assuming a current density of 1 A/cm^2 , a magnetic field of 1 T , a potential difference between electrodes of 1.2 V , and a Nafion membrane with $100 \mu\text{m}$ thickness in an acidic solution with pH 1, the electric term dominates over the magnetic term by a factor 10^7 . This factor increases for more acidic solutions, so it can be concluded that the imposed magnetic field has virtually no effect in the solid electrolyte of PEM electrolyzers.

14.2.3 Scale-up process

Many times innovations at the sub-cell or cell levels do not survive the scale-up process from a single cell to full-size stack. It is then convenient to give some hints on how such process should be carried out.

Two basic scale-up strategies may be followed in the diamagnetic case: either a continuous magnetic sheet with Halbach-like arrays (like the one represented in Fig. 14.5(b)) is located in parallel to the electrodes, or a series of magnets are strategically positioned to collect the bubbles. In both cases, the magnetic system can be adapted to any cell surface. However, the second approach may lead to important mass savings. This is shown in Fig. 14.7, where a 1 kg array of twelve $1 \times 1 \times 10 \text{ cm}^3$ magnets is employed to induce diamagnetic buoyancy at the surface of three 100 cm^2 PEMs. The bubble velocity vectors point toward the magnets, that can be used as gas collection points. This design can be largely improved by optimizing the distribution of magnets in the z axis, or by employing anode- and cathode-fed PEM architectures where only one side of the membrane requires phase separation.

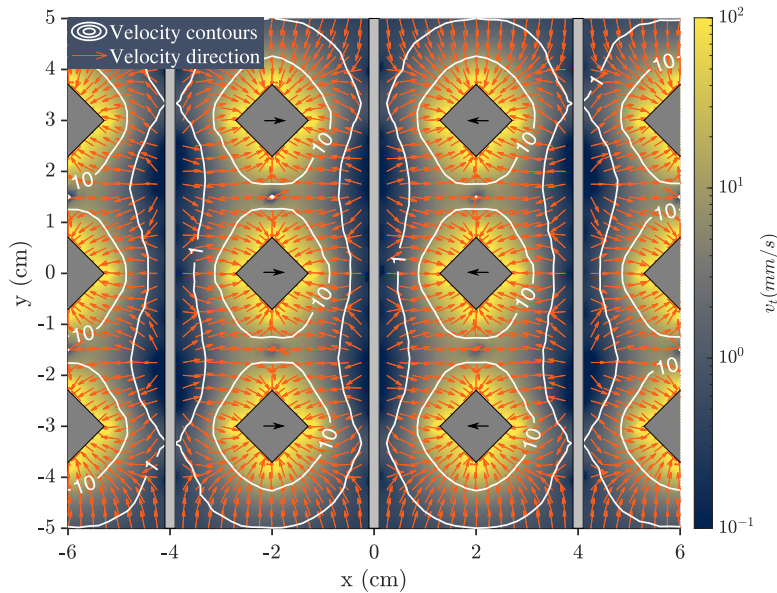


Figure 14.7: Two-dimensional simulation with 10 cm depth of the microgravity terminal velocity v_t induced by an array of magnets in an O_2 gas bubble with 1 mm radius in water. The hypothetical location of the Membrane Electrode Assemblies is represented by light gray areas. Black arrows, red arrows, and solid lines represent the magnetization direction, non-scaled velocity vector, and constant velocity contours, respectively.

In addition to selecting an efficient magnetic architecture, the movement of the bubbles should be constrained by means of an optimized wall (or bipolar plate) profile. Such profile would be adapted to the magnetic force potential to push the bubbles toward specific collection points, where the gas is finally extracted. Hydrophobic and hydrophilic surfaces may be employed to induce the accumulation and coalescence of bubbles.

The same philosophy would be followed in Lorentz-force enhanced cells to scale up the magnetic actuators. However, the resulting flow is far more turbulent and less controllable than in the diamagnetic case, rendering some sort of phase separation mechanism necessary. Given the intense liquid current produced by the magnetohydrodynamic effect, vortical phase separators arise as a natural solution. Still, the resulting cell assembly would leave out moving parts, potentially improving existing implementations.

14.3 ASGSR Ken Souza Magnetically Enhanced Electrolysis Experiment

Even though the foundations of the diamagnetic phase separation concept have been established and validated throughout this dissertation, applications like electrolysis or boiling involve complex multiphase flow mechanisms that can only be addressed with high-quality microgravity experiments. Those include multi-bubble and wall-bubble interactions like those reported in Sec. 11.2.3. In addition, electrolytic cells take minutes to reach steady-state conditions both from a fluid management and electrochemical perspectives, justifying the employment of sounding rockets to expose the system to extended microgravity conditions. These reasons motivated in first instance the development of the Magnetically Enhanced Electrolysis (MEE) experiment, whose design is briefly described in this section.

The American Society for Gravitational and Space Research (ASGSR) Ken Souza Memorial Student Spaceflight Research Program honors the memory of ASGSR's leader by offering young student investigators the opportunity to test their own microgravity research ideas onboard Blue Origin's New Shepard suborbital rocket. The author received this flight award in November 2020 to carry out the Magnetically Enhanced Electrolysis experiment. The proposal was submitted together with Dr. Hanspeter Schaub, Ph.D. advisor, and counted with the support of Connor Nogales, from CU Boulder's Electrical, Computer & Energy Engineering Department, and Dr. Will West and Keith Billings, from NASA JPL's Electrochemical Research,

Technology, & Engineering Group. The author is deeply grateful to every one of them for their support.

14.3.1 Scientific Objectives

The scientific objectives pursued by the MEE experiment are

- (1) Assess the capability of N52 neodymium magnets to induce liquid/gas phase separation in low-gravity and to passively detach H_2 or O_2 bubbles from the electrode of an electrolytic cell.
- (2) Study the impact of magnetohydrodynamic forces on the performance of an electrolytic cell in microgravity.
- (3) Analyze the low-gravity bubble dynamics in the presence of inhomogeneous magnetic fields.

Although the experiment was initially aimed at testing the diamagnetically enhanced electrolysis concept introduced in Sec. 14.1.1, technical considerations arising during the development process pushed the author to adopt a mixed diamagnetic and Lorentz-force approach instead.

14.3.2 Requirements

The Level-1 requirements specify the scientific determinations and/or results required for successful completion of the mission's objectives. They arise from the scientific objectives of the mission listed in Sec. 14.3.1 and are detailed in Table 14.2.

Level-2 requirements are not reported to prevent the disclosure of confidential information about the launch vehicle. However, it is publicly known that mini-payloads flying onboard New Shepard must be formatted as 0.5 kg, 2 units blocks that may contain up to 150 ml of non-hazardous liquids. Chemical, biological, energy, or RF hazards must also be avoided. Payloads shall operate with a 5 V, 0.9 A USB power supply and can be automated with live serial data sent through the USB port. The payload must be sent to Blue Origin for integration no later than 2 weeks before launch and is located inside a NanoRacks module that hosts 12 2U nano-experiments in a rectangular matrix. The module is located inside a payload stack placed inside the New Shepard Crew Capsule. Each nano-experiment must avoid acoustic or electromagnetic interferences with other experiments.

Table 14.2: Level-1 requirements.

ID	Requirement
L1-001	The mission shall observe the growth and detachment of H_2 bubbles from the surface of a representative electrode subject to an inhomogeneous magnetic field in microgravity
L1-002	The mission shall record the movement of the H_2 bubbles after detachment when subject to an inhomogeneous magnetic field in microgravity
L1-003	The mission shall determine whether the H_2 bubbles coalesce after detachment when subject to an inhomogeneous magnetic field in microgravity
L1-004	The mission should pursue requirements L1-001-003 for O_2 bubbles
L1-005	The mission shall measure the time evolution of the electrolytic cell's current in microgravity.
L1-006	The mission shall measure the time evolution of the electrolytic cell's voltage in microgravity.
L1-007	The mission should test the magnetically-enhanced liquid-gas separation using conduit geometries.
L1-008	The mission may address the long-term performance of nanostructured electrodes in 3 minutes microgravity.

14.3.3 Experimental setup

14.3.3.1 Architecture selection

As with any other mission, the requirements listed in Table 14.2 can be satisfied with many different architectures. The restrictions of the facility impose some obvious constraints. For instance, high-density magnets have to be employed instead of electromagnets due to the limitations in power and the strength of the required magnetic fields. Others require a careful trade-off analysis. The most critical decisions are depicted in Fig. 14.8 and subsequently discussed.

In the original experiment proposal, a closed-circuit system with an electrolytic cell and a magnetic phase separator was considered. This system involved a water pump to recirculate the flow and demonstrate the capabilities of the magnetic separator. Although this approach would increase the scientific impact of the experiment, it also has important disadvantages: (i) the water pump must satisfy EMI/EMC compatibility tests and would require a significant fraction of the power budget, (ii) the closed circuit would increase the required liquid volume, which is limited to 150 ml, and (iii) the satisfaction of the scientific objectives may be compromised by splitting the microgravity window in different regimes. Furthermore, from a fundamental science perspective, the removal of the phase separator may be compensated by focusing on the requirements L1-002/003 inside the electrolytic cell. These reasons motivate the elimination of this component.

The second decision focuses on the electrolytic cell itself. Although PEM technologies employ pure

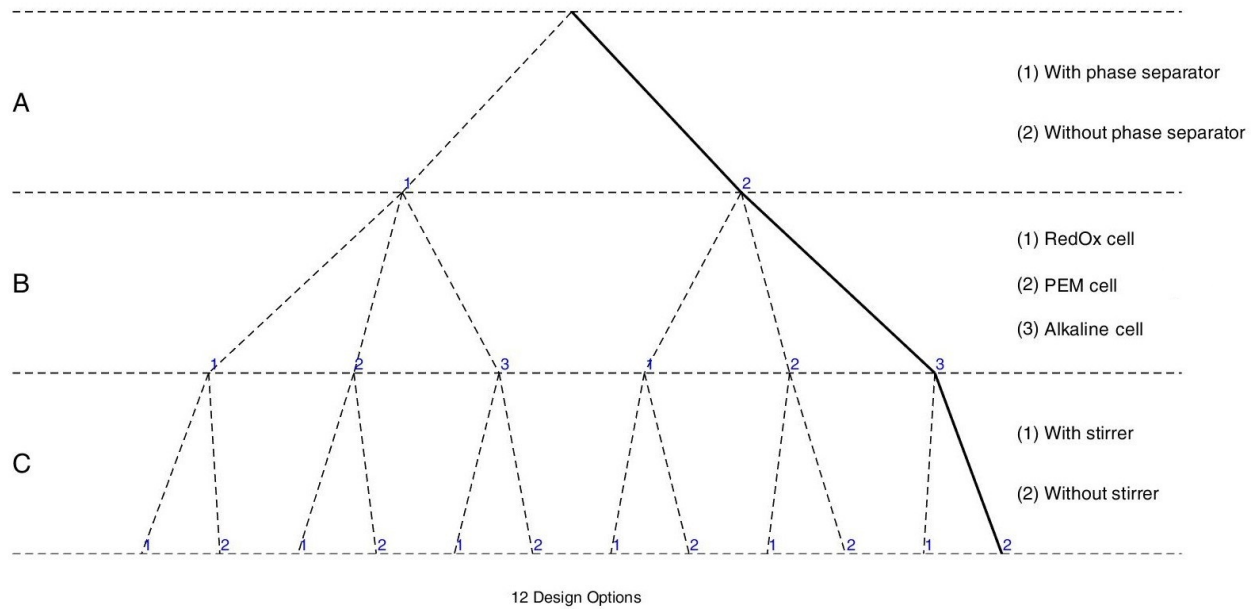


Figure 14.8: Architecture tree.

water and are therefore simpler to study, they also require very high quality microgravity conditions. For instance, magnetic forces around 1 N/m^3 (reported, for instance, at $\sim 2 \text{ cm}$ from the magnet employed in Fig. 14.3) produce accelerations of 10^{-3} m/s^2 , which lead to maximum acceptable gravity residuals of $\sim 10^{-4} g_0$. This value may not be satisfied in a suborbital vehicle like New Shepard, making it safer to adopt a mixed diamagnetic and Lorentz-force enhanced electrolysis approach to boost the magnetic effect during the experiment.

Finally, the preliminary review of the experimental proposal suggested the employment of a stirrer at the surface of the electrodes to promote bubble detachment. This idea is motivated by the potential difficulties in inducing bubble detachment with the weak magnetic buoyancy force. The concept is interesting and may be considered in future technologies, but involves important risks. The first is an increased fluid-dynamic complexity that may result in unwanted dynamics in microgravity. The second is the need for an pump or a liquid accumulator powered by a spring and a switch, which would make EMI/EMC tests necessary (with the subsequent cost in time and resources). The team chose instead to focus on implementing a hydrophilic electrode surface to promote bubble detachment. As shown in Sec. 14.3.4, this was indeed an

appropriate decision.

These considerations led to a preliminary architecture that was iterated until the final experimental setup was defined. For the sake of clarity, this process is skipped in this document, which focuses on the final experiment design.

14.3.3.2 Final configuration

The final configuration of the experimental setup, formatted as a 0.5 kg, 2U box, is depicted in Fig. 14.9. The experiment contains three electrolytic cells: two magnetic units subject to different magnetic field strengths, and a non-magnetic one that serves as a control. The non-magnetic unit is located 9 cm below the magnets to ensure that the diamagnetic acceleration falls below $10^{-6} g_0$. The flow evolution is observed in microgravity with a Raspberry Pi V2 camera located in front the electrodes, which are covered by transparent Plexiglas windows to allow visual inspection. Two flat mirrors ensure that the optical paths from the camera to the cells have approximately the same length, allowing the simultaneous focusing of all surfaces. The camera is wired to a Raspberry Pi Zero microcontroller that, in addition, powers the system

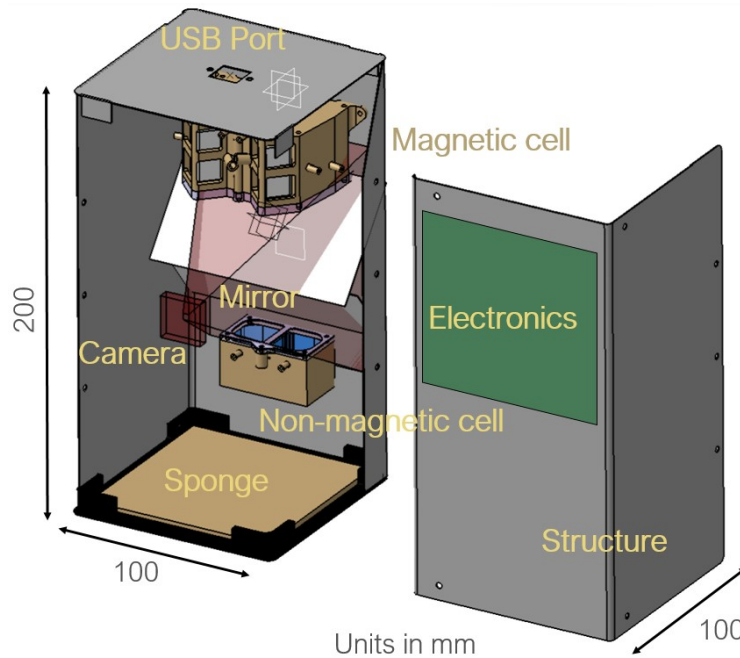


Figure 14.9: Final design of the Magnetically Enhanced Electrolysis experiment.

and automates the flight sequence. The microcontroller interfaces with the USB port to receive power and flight data. Each component is bolted to an aluminum box structure composed of two halves and top and end caps.

Each cell contains two 1 cm^2 platinum electrodes immersed in a 5% mass K_2SO_4 aqueous solution with pH 7. Although not particularly efficient, this electrolyte is chosen to avoid hazardous chemicals. While the non-magnetic cell is relatively simple, the design of the magnetic assembly is depicted in Fig. 14.10(a) and requires further attention. The assembly contains 45 ml of electrolyte stored in a central compartment. The electrodes are located in the same place and are oriented in parallel with the Plexiglas window, as shown in Fig. 14.10(b). Two block N52 neodymium magnets oriented symmetrically and magnetized toward the liquid generate the magnetic environment. When bubbles are released from the electrodes, the diamagnetic force tends to attract them to the magnets as illustrated in Fig. 14.10(b). A conic bubble collector is located just below the magnet and brings the gas to a cylindrical fitting located on top of the cell, from where a silicon tube redirects the gas to an auxiliary surface-tension-based phase separator (even though the diamagnetic force also contributes to the separation process). The phase separator is necessary to prevent the release of residual liquids before a significant gas volume is generated. Finally, the gas exits the phase separator and is stored in an air bag located outside the assembly. The purpose of the magnets is thus to induce the detachment, collection, and coalescence of hydrogen and oxygen bubbles.

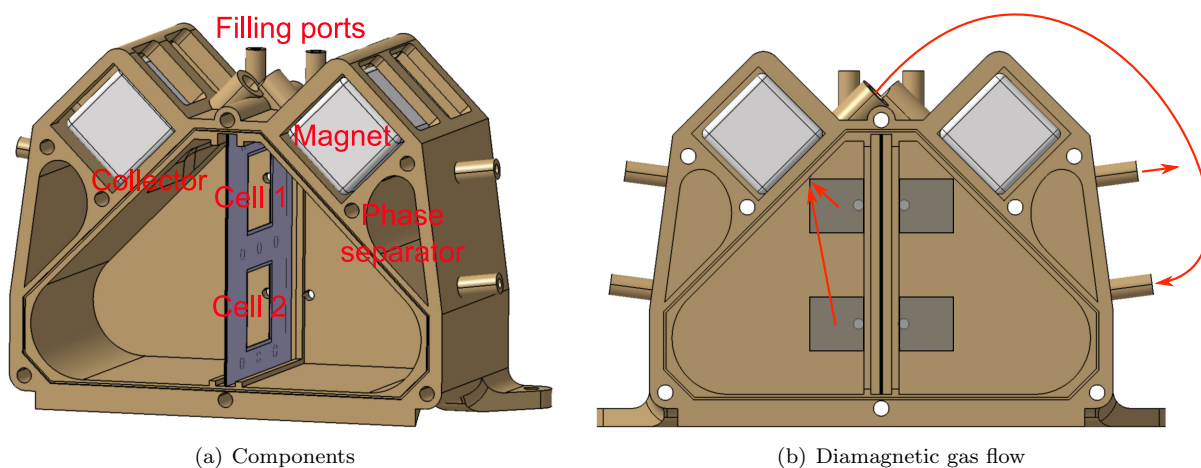


Figure 14.10: Magnetic electrolytic cell assembly.

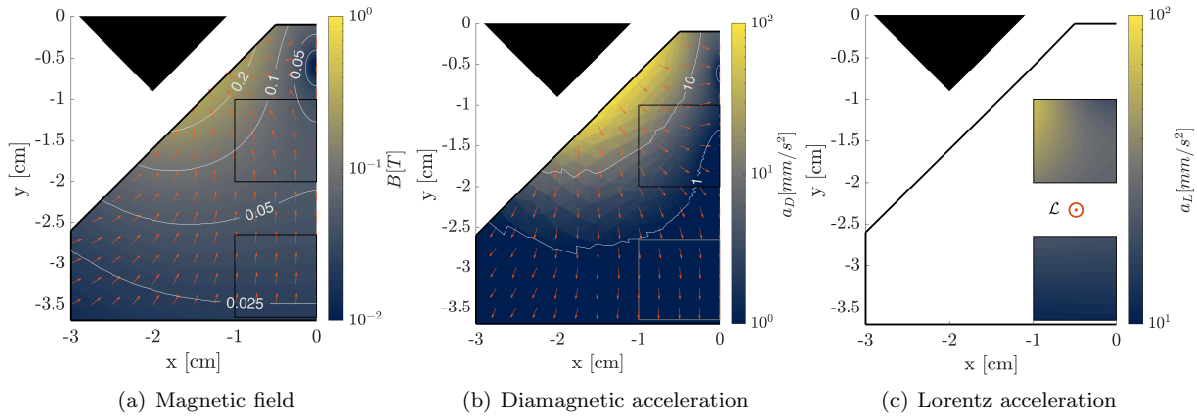


Figure 14.11: Magnetic environment inside the left section of the magnetic cell.

The magnets induce a magnetic flux density of 25 to 200 mT in the cell volume, as shown in Fig. 14.11(a). This leads to the diamagnetic acceleration field applied to the electrolyte that is illustrated in Fig. 14.11(b). Diamagnetic acceleration values range between 1 and 20 mm/s² in the top cell and drop below 1 mm/s² in the bottom one. The out-of-plane Lorentz acceleration exerted on the liquid for current intensities of 50 mA/cm² (to the right) is illustrated in Fig. 14.11(c) and reaches 60 mm/s² in the upper cell, with a minimum of 10 mm/s² in the bottom. In other words, the Lorentz force is about one order of magnitude stronger than the diamagnetic effect. Although useful to remove the bubbles from the electrodes, the Lorentz force lacks the directivity and controllability of the diamagnetic effect, that enables bubble collection. This observation determines the operational profile of the cell in microgravity, described in Sec. 14.3.3.4. The reader should also note that the maximum gravity residual of $\sim 10^{-4} g_0$ is imposed by the diamagnetic force. The application of Lorentz forces of about $\sim 10^{-2} g_0$ ensures that, in a worst-case g-jitter scenario, scientifically valuable data will still be generated by the experiment.

The system is designed to prevent fluid leaks and accommodate for ambient pressure differences while avoiding the explosive recombination of hydrogen and oxygen. Nylon membranes with a porous size of 0.2 μm split the cells in two halves, and medical-graded plastic bags are employed to store the gases during the experiment. In addition, the assembly is stored inside an 8 mil Mylar bag that acts as a second layer of containment.

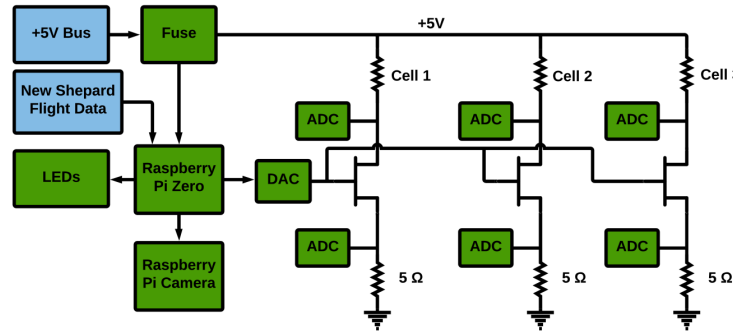


Figure 14.12: Power and electronics subsystem.

14.3.3.3 Power and electronics

The power and electronic subsystem, whose diagram is shown in Fig. 14.12, connects the 5V USB bus to the main PCB. The PCB integrates the Raspberry pi Zero board, three individual current control circuits, and four LED's for general illumination. The current through each cell is controlled by a MOSFET transistor that behaves like a variable resistor. The resistance of the transistor is set by a Digital-Analogue Converter operated by the Raspberry Pi and is incrementally changed until the appropriate current is obtained. An Analogue-Digital Converter samples the voltage across a $5\ \Omega$ resistor and sets the current value. Once the current is set, the voltage drop and current in each cell are measured and referenced back to each individual frame in the video file of the experiment.

The LEDs are tied directly to 3.3V supplied by the raspberry pi and cannot be turned off while the board is powered. In order to protect against short circuits, a 5 A fuse is placed in series with the 5V supply to the board. The maximum measured current draw of the experiment is 0.5 A, which offers a 45% safety margin with respect to the maximum current value. The data is stored on the Raspberry Pi SD card which is epoxied to the board for safety. The built-in Wi-Fi capabilities of the Raspberry Pi are disabled in software to minimize the electromagnetic interference.

The Raspberry Pi interfaces with the V2.0 camera by means of a flex connector, and with the electrolytic cells by means of power lines. All the wires are epoxied to the board at regular intervals and soldering points.

14.3.3.4 Concept of operations

The concept of operations of the mission is determined by the New Shepard nominal acceleration profile depicted in Fig. 14.13. The platform provides about 180 s of high-quality microgravity conditions (E-H). Once the experiment is powered, the microcontroller remains in standby mode with the cameras and electrolytic cells disconnected and the lights on. At liftoff (B) the cameras are switched on for 130 s, and the data is continuously stored on the SD card. The electrolytic cells are switched on at Coast Start (F) and follow a pre-programmed science sequence that lasts for 135 s. Upon release of main parachutes (M), the electrolytic cells are switched on again for 90 s to characterize each cell in Earth gravity conditions. The videos and electrochemical data, composed of current and voltage measurements, are written simultaneously on the SD card.

The science sequence is composed of three 45 s trams where the electrolytic cells operate at a given current level for 25 s followed by 20 s at 0 mA. 15, 30, and 45 mA are tested to evaluate different ratios of diamagnetic to Lorentz forces. The period of 20 s at 0 mA is designed to let the diamagnetic force collect the bubbles without the Lorentz force disturbance and demonstrate the bubble separation and collection effect.

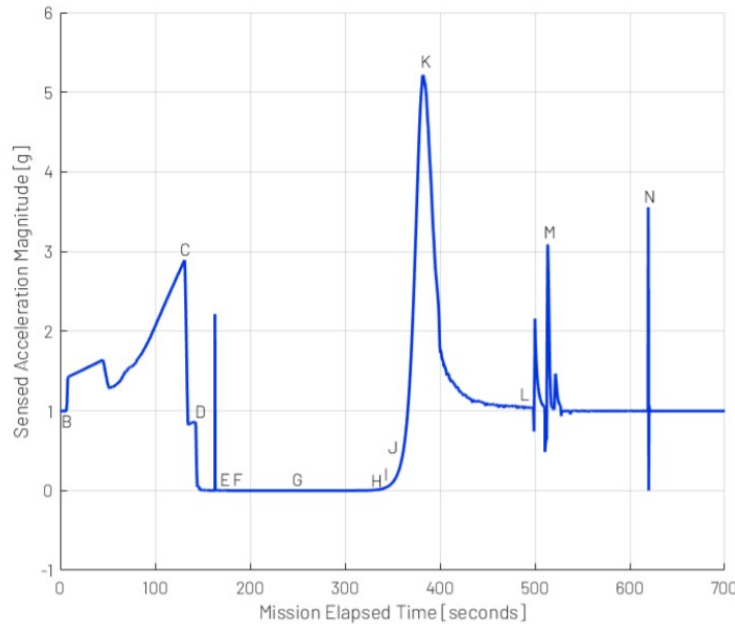


Figure 14.13: Nominal acceleration profile during Blue Origin's New Shepard flight [19].

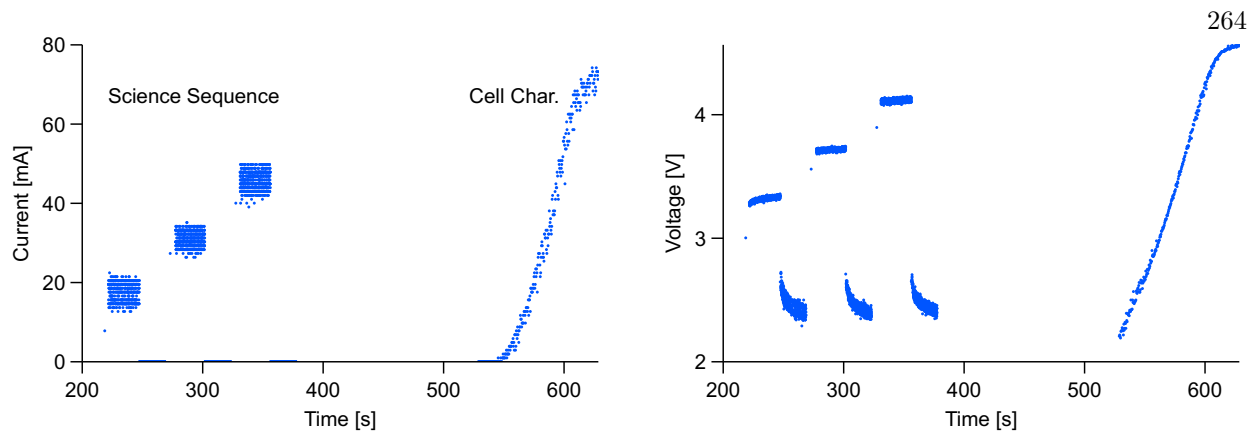


Figure 14.14: Sample electrochemical data from a single cell during on-ground testing.

This experimental plan should highlight the stability of the magnetic cells in contrast with the non-magnetic cell, where gas bubbles accumulate over the electrodes. The effect would be reflected in the gradual increase of cell resistance for the non-magnetic assembly. Sample electrochemical data from a single cell during on-ground pre-flight testing is given in Fig. 14.14 as a reference together with the cell characterization phase.

14.3.3.5 Safety

The major safety risk of the mission is the possibility of explosive recombination of hydrogen and oxygen. The 3 electrolytic cells operate at 15, 30, and 45 mA for 30 s, and at 0 to 80 mA for 90 s. After computing the total charge transferred per cell (6.75 C), a total volume of gas of 3.78 mL (2.52 mL of H_2 , 1.26 mL of O_2) is generated by the three cells during the flight in a perfect conversion efficiency scenario at 1 atm and 293 K. The energy released in case of recombination is 8 J and would reduce the total volume of gases by +50%. Just for comparison, this energy release would increase the temperature of the water volume in the assembly by 0.032°C.

In a worst-case scenario where all the cells operate at 80 mA for 21 minutes, 56.5 mL of gas are generated and 128 J could be potentially released. The gas accumulators are over-dimensioned to hold 100 mL, giving a 44% safety margin over these results. Even when the pressure drops to 0.7 bar inside the capsule, the gas accumulators hold the fluids without building up pressure. Still, the first and second levels of containment are designed and tested to withstand 10 and 5 PSI, respectively.

The recombination of H_2 and O_2 is prevented by a commercial 0.2- μm Nylon membrane and its supporting plates, that separate the two halves of the cells. In the extremely unlikely case where all the gas is released to the mini-payload volume, the concentration of H_2 would be 0.13% (3.78 mL of gas released, standard) or, in a worst-case 21 min operation, 1.9% (57 mL of gas released, worst-case). Both values are well below the 4% Lower Explosive Limit of H_2 in air. However, hydrogen may still accumulate in the 2.5 cm^3 phase separator of the magnetic electrolytic cell, increasing its relative concentration. A worst-case scenario would involve the combustion of the 0.53 cm^3 of O_2 in that volume, but such reaction would only release 11 J of heat and produce a small volume of vapor water, leading to a +50% local decrease in pressure. In order to minimize the risk of combustion, the air chambers of the magnetic electrolytic cell are filled with nitrogen before the flight.

14.3.3.6 Illustrative images

The experiment assembly is almost ready for flight at the time of writing this thesis. As a reference, Figs. 14.15 to 14.19 show the current state of the payload.

14.3.4 Preliminary test

Although at the time of writing the payload has not yet flown in Blue Origin's New Shepard, the author was able to run a 4.7 s test at ZARM's drop tower in December 2021 to explore the operation of the magnetic cell at ~ 100 mA in microgravity. The experiment, summarized in Fig. 14.20, shows that the design is able to (i) detach bubbles from the platinum mesh electrodes, (ii) sweep them away from their surface, and (iii) collect them near the magnets for both the upper and lower cells. However, several vortexes induced by the Lorentz force are superposed to the diamagnetic flow pattern that hamper the collection of bubbles, as predicted in Sec. 14.3.3.2. The observation of this behavior motivates the implementation of the 20 s diamagnetic bubble collection window reflected in Fig. 14.14.

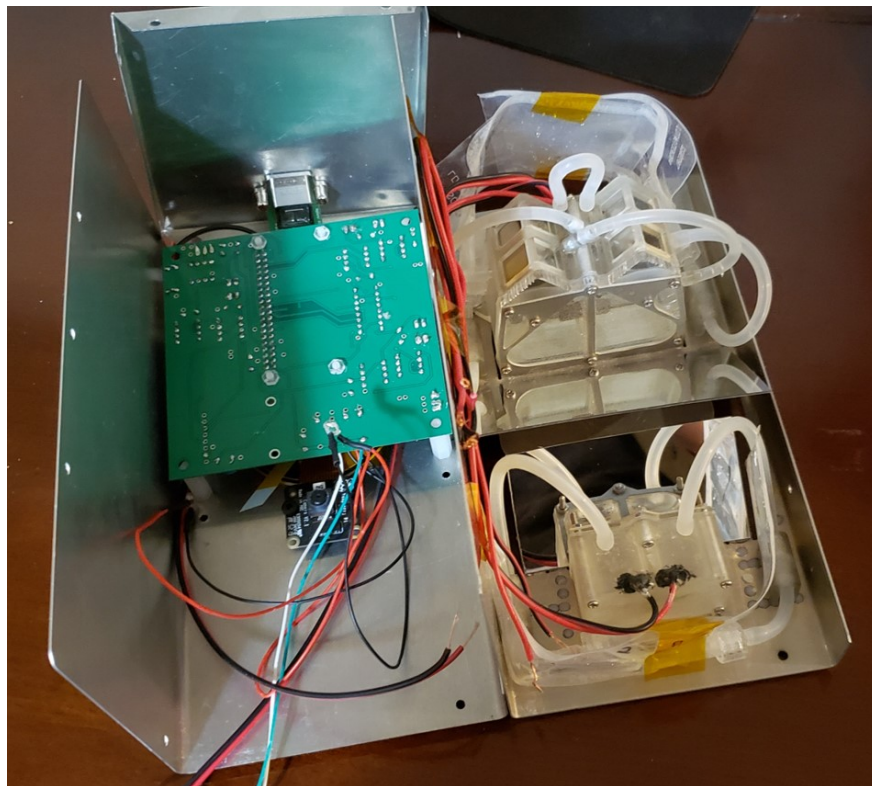


Figure 14.15: Overview of experimental setup before integration.

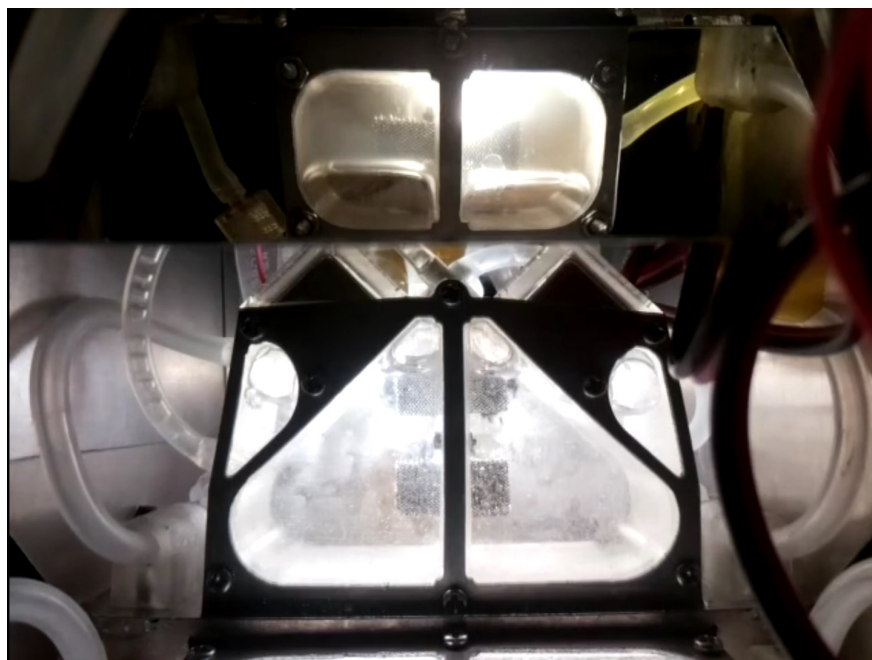


Figure 14.16: Sample camera image during on-ground testing.



Figure 14.17: External structure. The white bolt in subfigure (b) blocks the hydraulic circuit and is removed before flight.

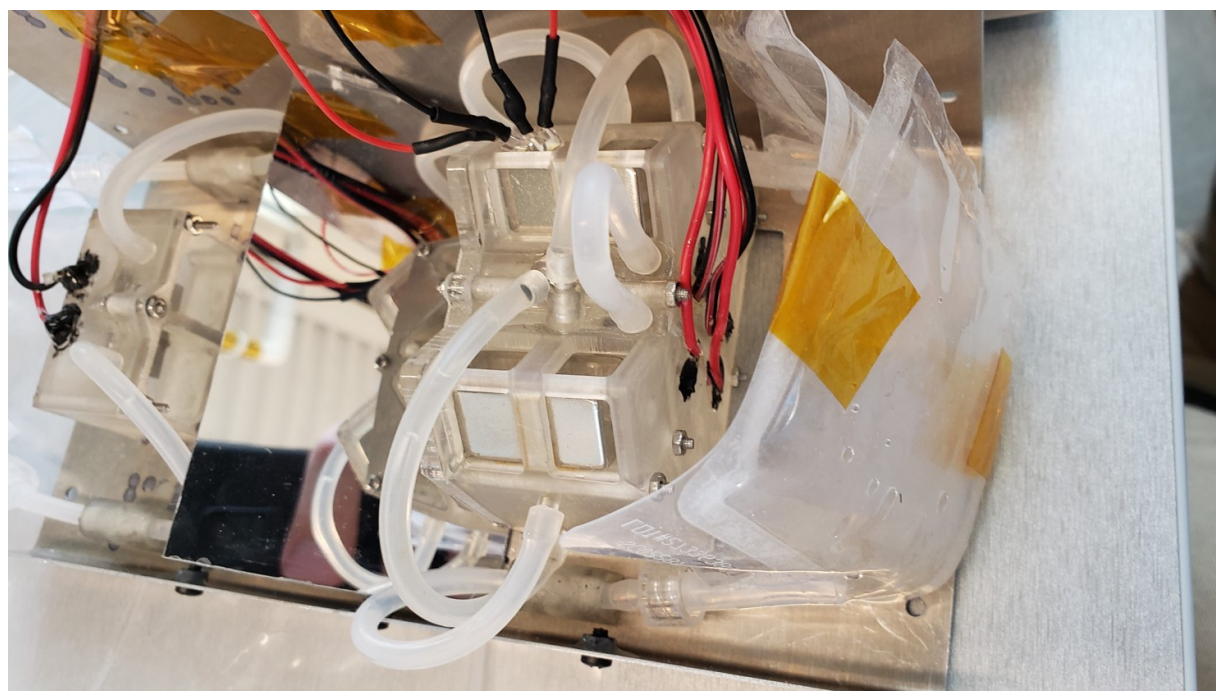
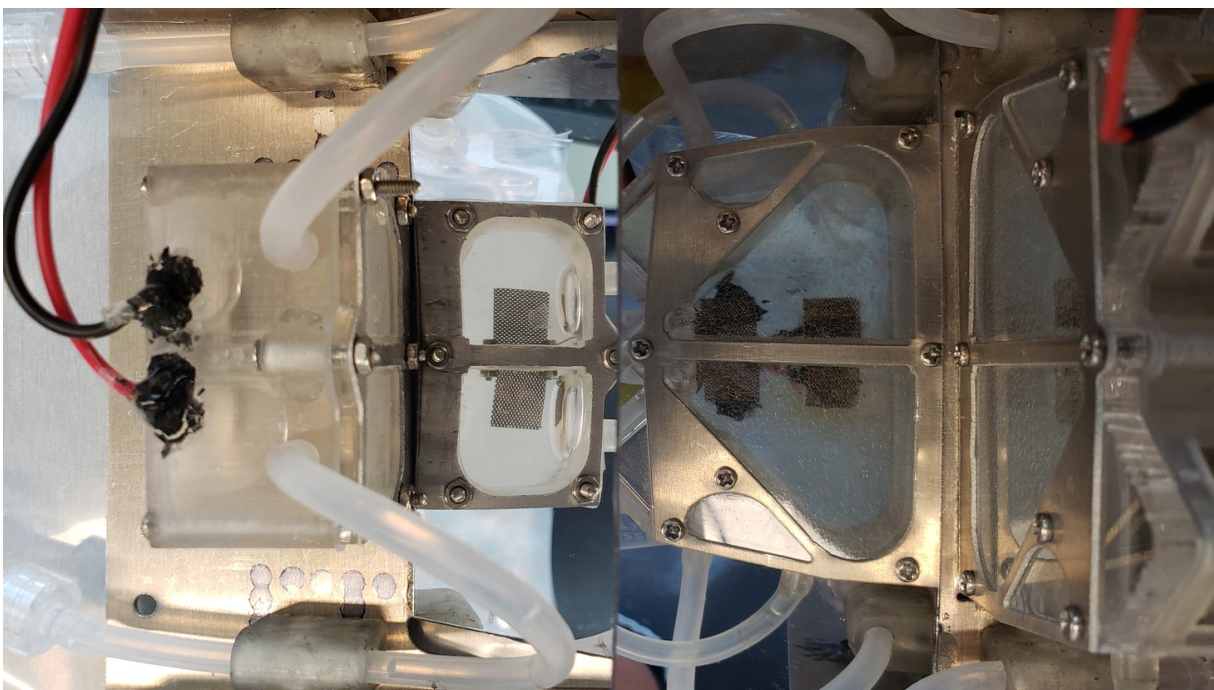


Figure 14.18: Detail of the magnetic cell and gas accumulators.



(a) Mirrors and magnetic cell



(b) Top view of the assembly

Figure 14.19: Detail of the mirrors.

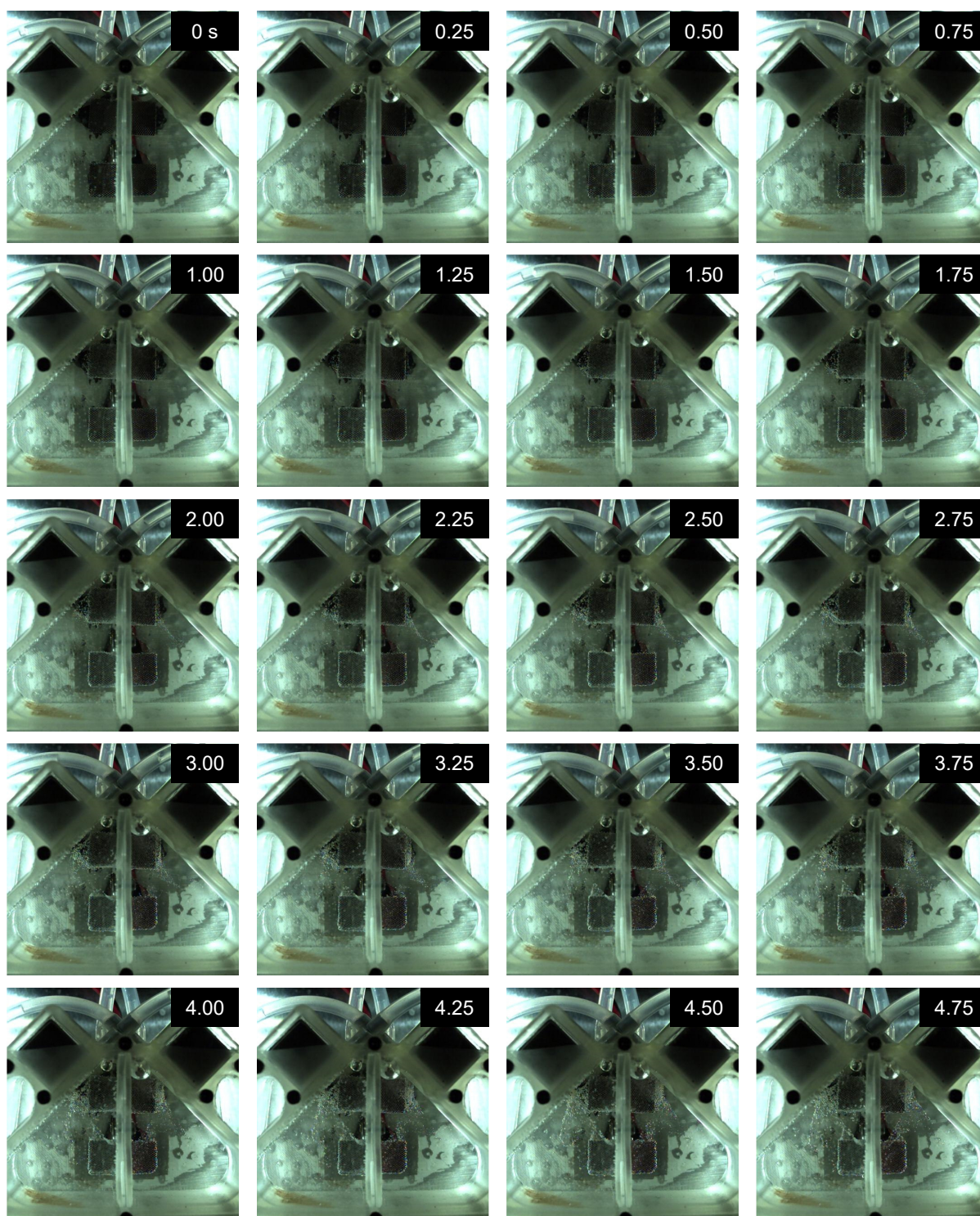


Figure 14.20: Drop tower test of the magnetic electrolytic cell.

14.4 Short-term microgravity experiments

In addition to the ASGSR Ken Souza 2020 experiment, a collaboration was established with Prof. Katharina Brinkert's group to apply the magnetically enhanced electrolysis concept to a series of acidic (pH 0, 1M HClO₄) water electrolysis cells in microgravity. Although those include photoelectrochemical reactors and flat hydrophilic surfaces, the discussion that follows focuses on experiments with platinum foils and hydrophilic mesh electrodes treated with a piranha solution (a 3:1 mixture of sulphuric acid -98%- and hydrogen peroxide -30%- [350]). The rest of data is under study at the time of writing and will be disclosed in a future publication. The author would like to thank Prof. Katharina Brinkert and Mr. Ömer Akay for their invitation to collaborate in this exciting project and for their tireless support.

14.4.1 LiMo Project

LiMo ('Light-induced production of fuels and oxygen in microgravity') is a project funded by the German Aerospace Center (DLR, grant no. #50WM2150) from October 2021 to September 2024 and led by Prof. Katharina Brinkert. It aims at (i) the investigation of photoelectrochemical oxygen production and CO₂ reduction in reduced gravitational environments and (ii) the construction of a monolithic photoelectrochemical water-splitting device which produces simultaneously hydrogen and oxygen stably and at terrestrial efficiencies in microgravity environment. The author joined the project in summer 2021 to support the second goal by applying the magnetically enhanced electrolysis approach.

14.4.2 Experimental setup

The experimental setup of LiMo, illustrated in Fig. 14.21, is composed of two identical cells where a working electrode (W.E.), a counter electrode (C.E.), and a reference electrode (R.E.) operate in a 1M HClO₄ solution (pH 0). The electrodes are connected to a Biologic SP-300 potentiostat that, at least in the cases covered in this section, controls the potential between the C.E. and the W.E. so that the difference between R.E. and W.E. corresponds to the value specified by the user. The potentiostat measures the evolution of the current density while front (1) and lateral (2) cameras observe the electrodes. A Photron Fastcam MC-2 working at 500 fps is employed in the front window. An additional diagonal window is employed to

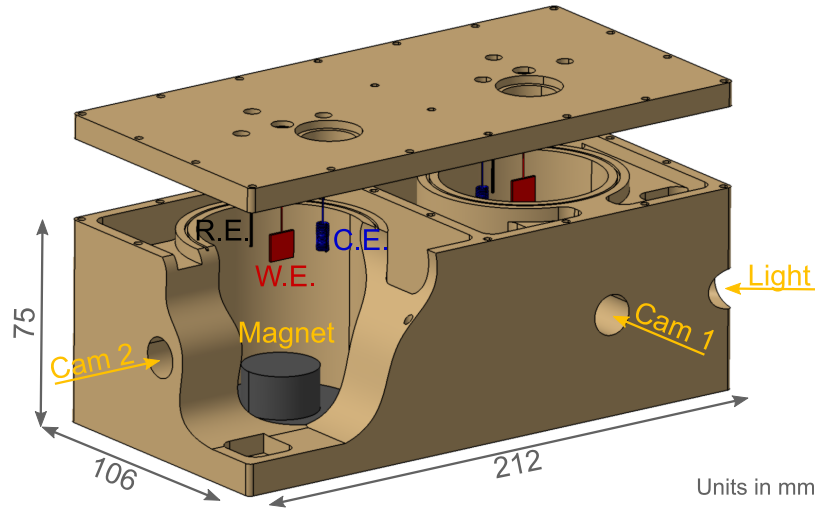


Figure 14.21: Experimental setup of the LIMO experiment.

illuminate the electrode or, in the photoelectrochemical experiments, induce water splitting. The assembly is mounted on a short ZARM capsule together with its support equipment. The catapult mode, which provides up to 9.3 s of microgravity conditions, is employed. Both the type of electrode and operational conditions are tuned for each experiment. Further details on ZARM's drop tower can be found in Sec. 9.1.

Magnetohydrodynamic forces are applied by an axially magnetized 25.4 mm diameter, 19.05 mm length cylindrical N52 neodymium magnet supplied by K&J Magnetics Inc. and located ~ 4 mm below the working electrode. Figure 14.22 characterizes the magnetic environment of the system in the plane defined by the working electrode and the counter electrode. The magnetic flux density distribution, shown in Fig. 14.22(a), reaches ~ 0.6 T over the surface of the magnet. The diamagnetic terminal velocity is depicted in Fig. 14.22(b) and ranges between 0.1 and 2 mm/s over the surface of the electrode for a 0.25 mm radius bubble. Diamagnetic accelerations between 10 and 100 mm/s² are applied to the electrolyte at the same locations, but the Lorentz acceleration is about one order of magnitude larger for current densities of 200 mA/cm². Since the mean electric current density vector \mathbf{J}_e is contained in the plane of the electrode, the Lorentz force pushes the liquid toward the surface, following Eq. 14.1. Although a lateral flow would probably remove bubbles more effectively, this particular configuration enables a direct view of the electrode surface without implementing any modifications to the existing setup.

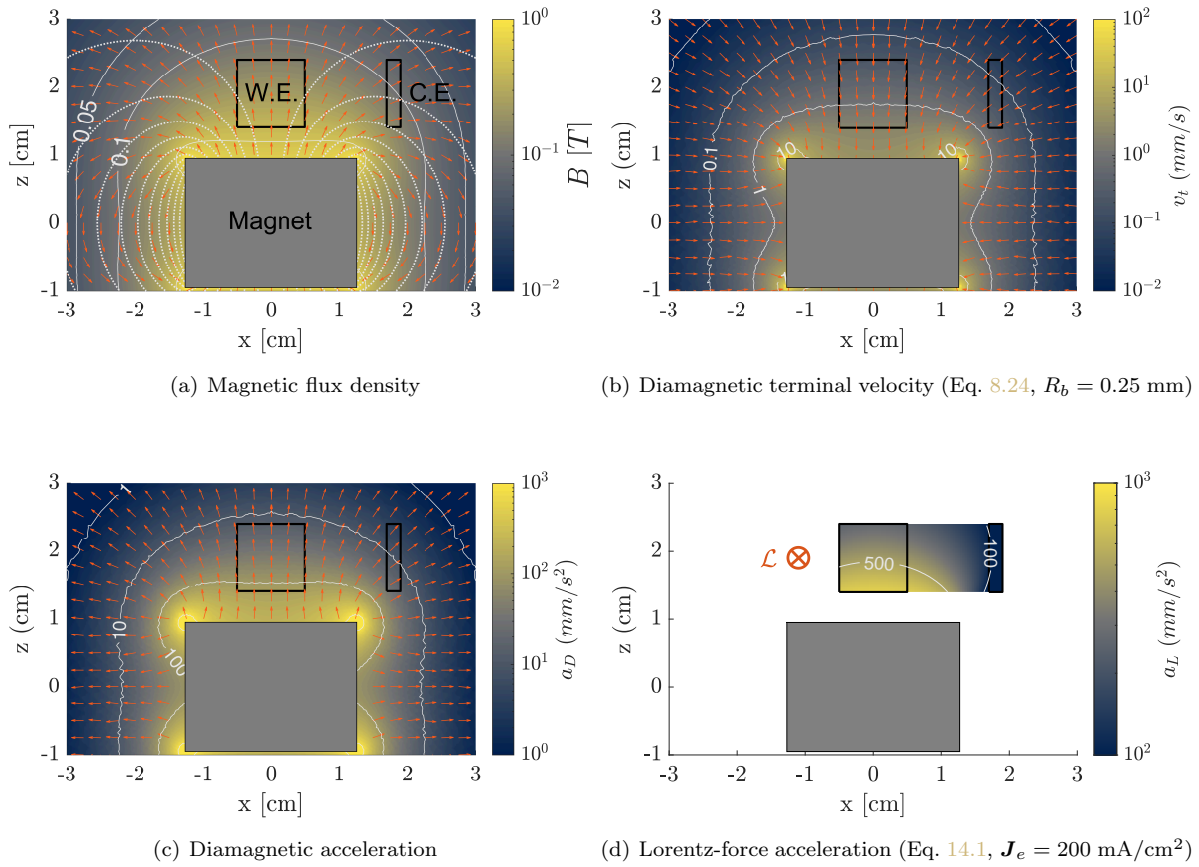


Figure 14.22: Magnetic environment of the LIMO experimental setup in the $y = 0$ plane defined by the working electrode (W.E.) and the counter electrode (C.E.).

14.4.3 Preliminary results

Non-magnetic and magnetic results are reported for platinum foils and platinum meshes operating as hydrogen electrodes at 800 mV. Figures 14.24 to 14.27 summarize the 9.3 s video sequences of each experiment. In the non-magnetic cases (Fig. 14.24 and 14.26) bubbles are continuously generated and create a foam layer over the electrodes. This progressively reduces the effective surface area and current density, as shown in Fig. 14.23. Existing space electrolyzers deal with this problem by means of forced convection, requiring ancillary components such as pumps or phase separators. In the presence of the magnet, small bubbles are removed from the surface of the platinum foil electrode (Fig. 14.25) but surface tension prevents the detachment of larger ones. The problem is solved in Fig. 14.27 by employing an hydrophilic platinum

mesh electrode treated with a piranha solution that effectively detaches large bubbles. The superiority of the platinum mesh may be attributed to its enhanced wettability, which leads to smaller bubble sizes in the non-magnetic case reported in Fig. 14.26 with respect to the platinum foil in Fig. 14.24. In addition, and since the main component of the Lorentz force in Fig. 14.22(d) is applied along the axis perpendicular to the electrode, the mesh does not obstruct the forced magnetohydrodynamic flow. Similarly to the test reported in Sec. 14.3.3.6, numerous Lorentz-force-induced vortices are observed which would ultimately drive the bubble collection process. A careful magnetohydrodynamic design must be implemented in future applications to take advantage of this effect.

The magnetohydrodynamic flow leads to an average $\sim 20\%$ increase of the platinum foil cell current density in Fig. 14.23, where this variable is represented as a function of time during a catapult drop. Two groups (magnetic and non-magnetic) with three independent and randomly sampled electrodes each are tested. The small number of samples is a consequence of the limited access to the platform and represents a recurrent (and not easy to solve) problem in microgravity research. In order to compare them, current density values are extracted at $t = 8.5$ s and reported in Table 14.3. If it is further assumed that the data is normally distributed and that both groups have the same variance, the independent two-sample t-test shows that magnetohydrodynamic forces have a significant effect on the performance of the cells with $\alpha = 0.1$ and $p = 0.069$. The t-test, however, is not appropriate for small samples due to the high risk of violating the

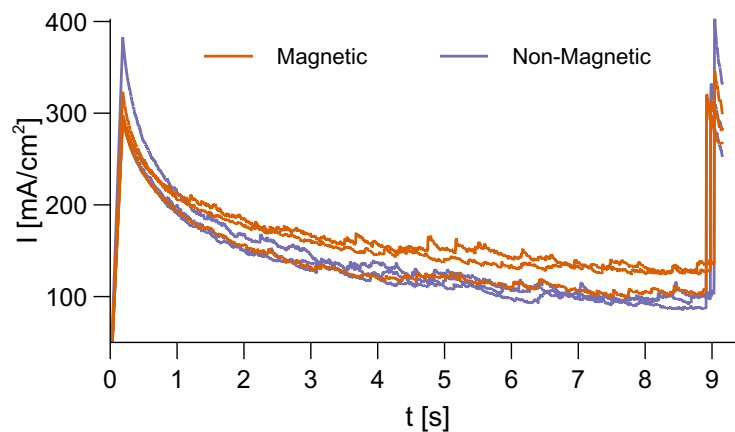


Figure 14.23: Electrochemical performance of platinum foil and mesh electrodes with and without magnetic fields during a 9.3 s catapult drop.

Table 14.3: Quasi-steady-state current density values of independent magnetic and non-magnetic platinum foil electrodes measured after 8.5 s of microgravity conditions.

Magnetic [mA/cm ²]	Non-Magnetic [mA/cm ²]
125.6	99.5
126	104.3
104.4	86.8

aforementioned assumptions. The Mann Whitney U (or Wilcoxon Rank Sum) test is the non-parametric equivalent of the independent two-sample t-test and becomes far more appropriate for this problem. Its application to Table 14.3 also returns a significant effect for $\alpha = 0.1$ and $p = 0.1$. Both results are obtained for a significance level of 10%, implying that the risk of making a Type I error is a 10%. The power of the test for $n = 3$ and $\alpha = 0.1$ is 71.5%, meaning that the probability of a Type II error is 28.5%.

The statistical analysis is obviously limited by the small sample size and should be taken with care. It also motivates the collection of additional data points in future works. However, it hints at the existence of a magnetically-induced enhancement of the cell current density in short-term microgravity experiments. It is important to highlight that, after a few minutes, the layer of bubbles shown in the non-magnetic cases (Figs. 14.24 and 14.26) would completely cover the electrode and almost completely stop the reaction. Based on the magnetic results presented in Fig. 14.27, it is appropriate to assume that the magnetohydrodynamic convection effect would prevent this behavior and stabilize the cell after a long exposition to microgravity.

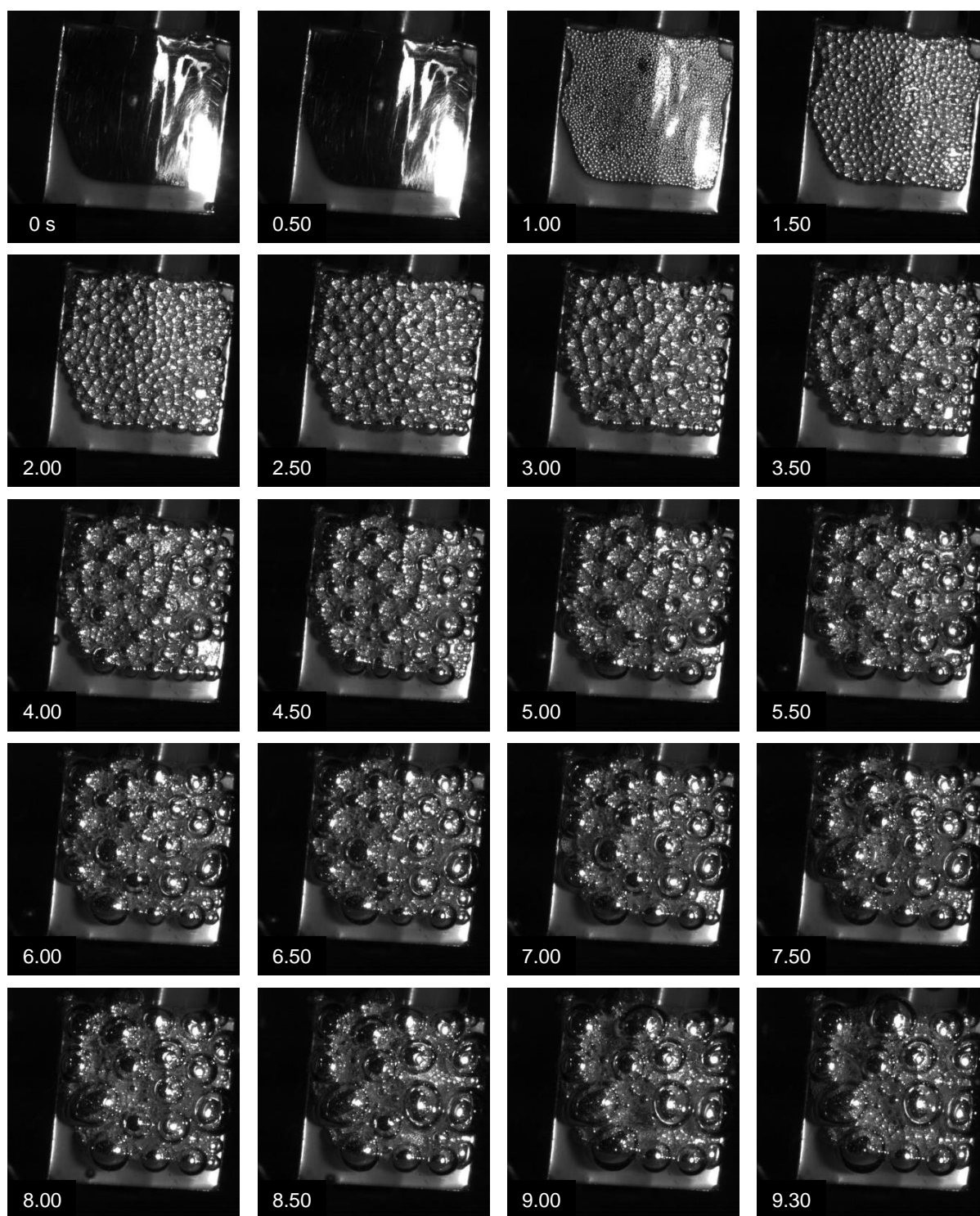


Figure 14.24: Non-magnetic platinum foil electrode with hydrogen bubbles.

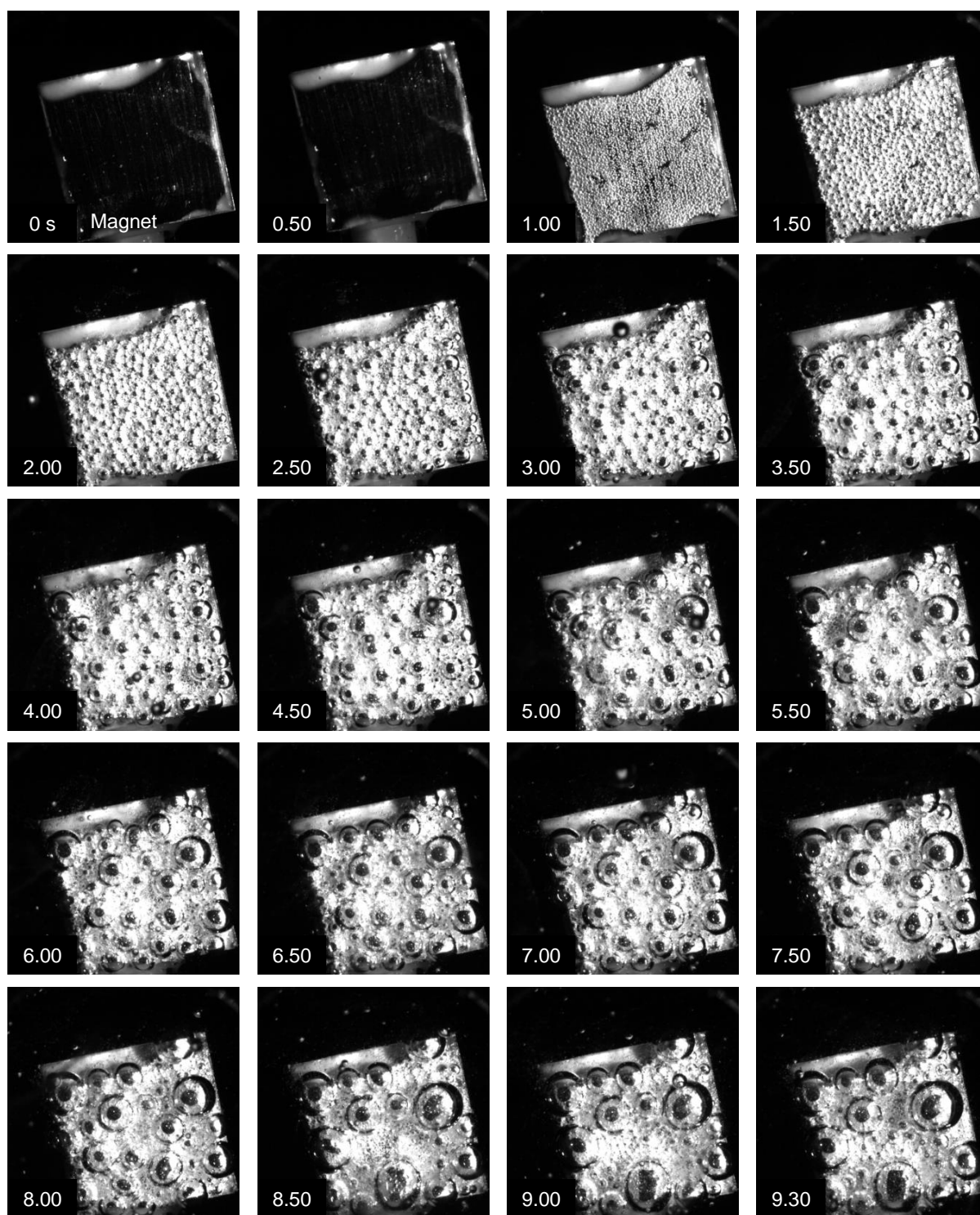


Figure 14.25: Magnetic platinum foil electrode with hydrogen bubbles.

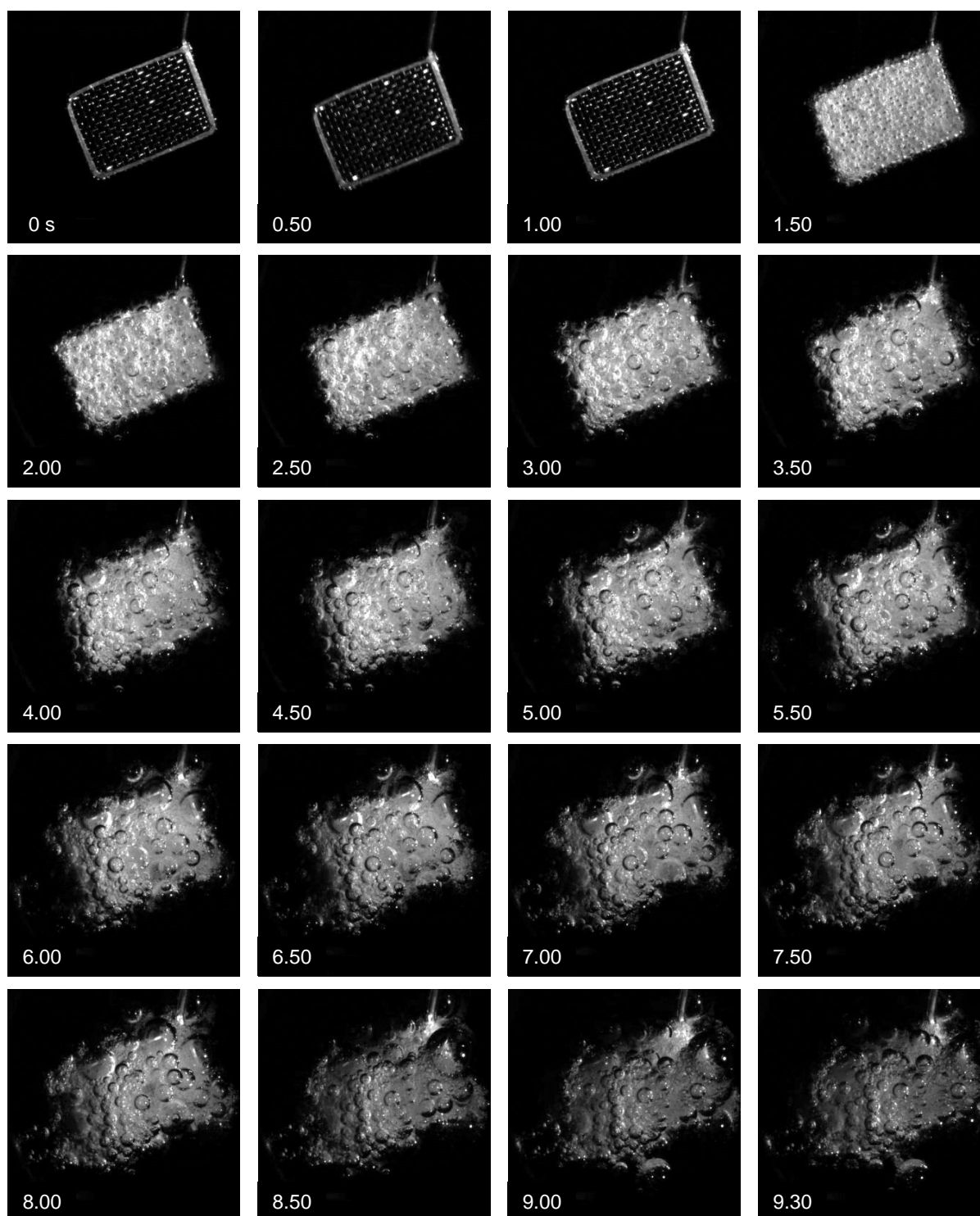


Figure 14.26: Non-magnetic platinum mesh electrode with hydrogen bubbles.

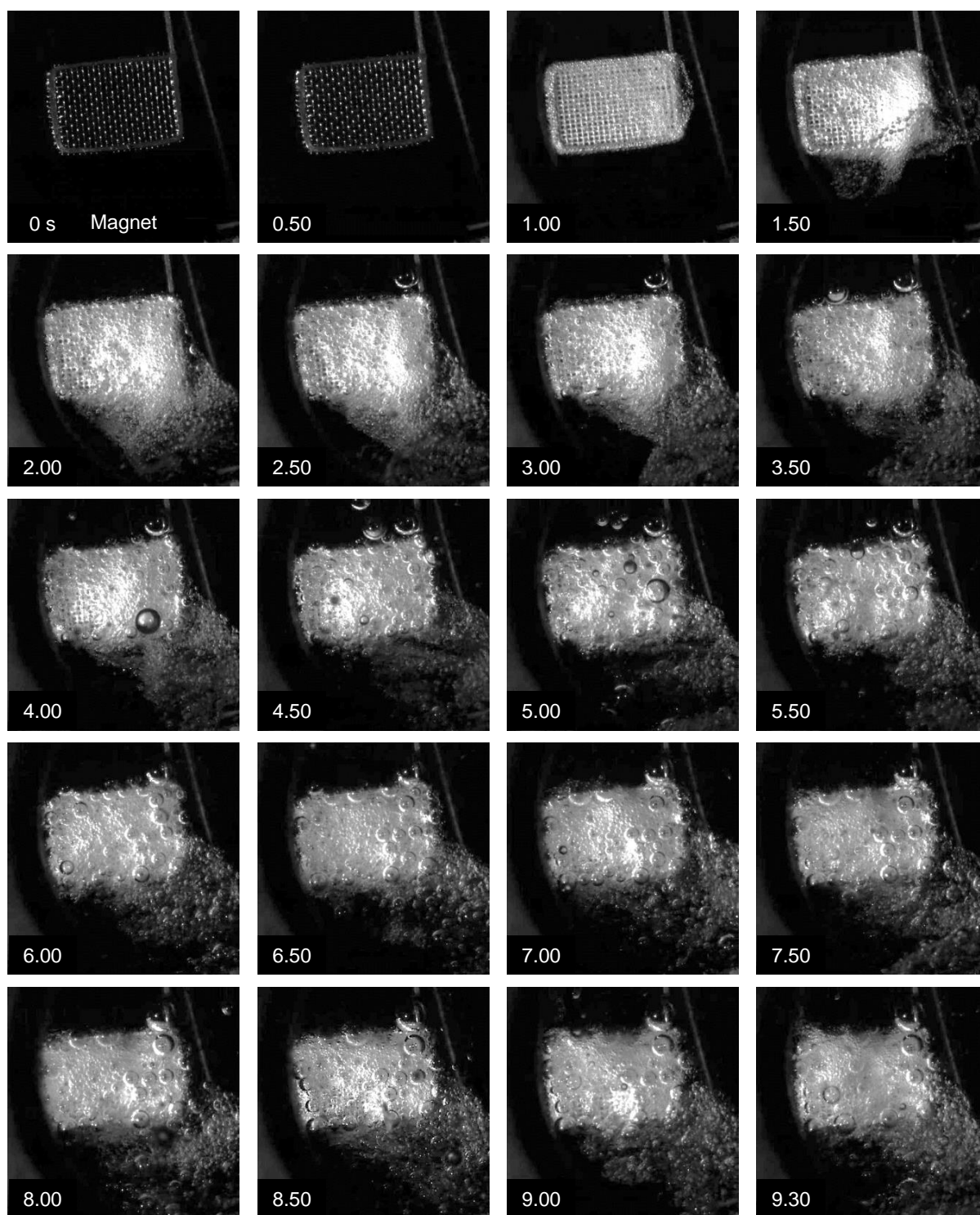


Figure 14.27: Magnetic platinum mesh electrode with hydrogen bubbles.

Conclusions

Overview and main contributions

The use of electromagnetic forces (and electromagnetism, in general) is proposed in this dissertation to enable mid-distance, contactless actuation and sensing in space systems. This approach opens interesting opportunities in the challenging environment brought by planned missions, and can have deep implications in scenarios ranging from close proximity operations to in-situ resource utilization.

Part I explores the use of electron beams and UV photon sources for active electron-based touchless potential sensing. The focus of Chapter 3 is placed on understanding the effect of complex shapes and differential charging on the sensing process. Experiments and numerical simulations show that the detectability of the system is bounded to well-defined regions surrounding the target. However, once the servicer spacecraft is within those regions, the potentials are determined with very high accuracy for both the homogeneous and differential charging scenarios. It is in this context where accurate and efficient particle tracing simulations are needed to determine the source regions of secondary electrons. Such models are introduced and validated with attention to their applicability to ground studies and flight algorithms. In particular, a computationally efficient electron beam model is introduced in Chapter 4 to support the development of future applications. The use of UV lasers alone and in combination with high-energy electron beams is finally proposed in Chapter 5 to minimize the sources of uncertainty and enhance the robustness of the sensing method. The particle tracing simulation framework introduced in Chapter 3 is extended to simulate these problems and compared with experimental results, demonstrating its ability to characterize the location and order of magnitude of the photoelectron flux coming out of a complex target. Additional UV-laser-based applications, ranging from material characterization to charge control, are also proposed.

Part II introduces the fundamentals of *low-gravity magnetohydrodynamics*. The derivation of analytical results for the equilibrium, stability, and modal response of axisymmetric liquid-gas interfaces is achieved in Chapter 7, sometimes by incorporating a first-order approximation to the fluid-magnetic coupling. Specific results are derived for gas bubbles and liquid droplets subject to magnetic polarization forces in Chapter 8. The capabilities of analytical tools are extended in Chapter 10 to viscous flows with an interface-tracking magnetohydrodynamic numerical framework. Chapter 9 validates both approximations with experiments performed at ZARM's drop tower, showing that the numerical model outperforms the analytical solution of the free surface oscillations problem due to the consideration of fully coupled fluid-magnetic problems. In addition, the magnetic mass transport concept is exemplified with a free-floating ferrofluid droplet in microgravity.

Part III applies the analytical results presented in Part II to the study of several novel space applications. First, the dia/paramagnetic phase separation concept is introduced and demonstrated in Chapter 11 using drop tower experiments. Numerous phenomena are reported for the first time, including the displacement, wall interaction, coalescence, and drag-induced motion of bubbles at low-Reynolds. In addition, the experiments validate the magnetic terminal velocity formulations introduced in Part II. Chapter 12 explores the concept of magnetic positive positioning with an hypothetical LOX and CH_4 -based ferrofluid. Magnetic settling forces are shown to enhance the stability and speed up the oscillatory response of the liquid, leading to more predictable propellant management systems for different scales and filling ratios. Chapter 13 applies the magnetic positive positioning concept to develop novel launch vehicle restart strategies in microgravity, showing that the successful development of these technologies could potentially lead to mass savings of hundreds of kilograms and economic gains of several hundred thousand dollars per launch. This approach may be particularly interesting for cryogenic systems due to the enhanced magnetic properties of liquid oxygen and hydrogen. The applications of diamagnetic buoyancy to low-gravity electrolysis, boiling, and reduction is finally explored in Chapter 14 with a focus on the former. Numerical simulations exemplify how modern neodymium magnets induce a significant diamagnetic force in gas-water flows at distances of the order of 2 cm. Drop tower experiments show that the diamagnetic force, in combination with Lorentz's force, induces the early detachment of gas bubbles from the electrodes, increasing the effective surface area and effectively

detaching bubbles from their nucleation surfaces. Preliminary results point to at least a $\sim 20\%$ cell current density increase using a compact magnetic setup.

Directions for future work

The next logical steps to advance the electron-based touchless potential sensing technology in the TRL scale can be divided in two groups: fundamental understanding and technical development. The physical processes that sustain this method were formulated in previous works and have been applied to complex shapes and basic differentially charged objects in this dissertation. It is now possible to characterize the response of a conductive target in a GEO environment and simulate the flux of secondary electrons coming out of it. Still, dielectric materials have been left out of the discussion and should be studied in future works. Complex phenomena like the generation of localized electrostatic barriers in the source region, the effect of higher density plasma on the potential field, the disturbance induced by surface contamination, or the proper modeling of the photoelectric effect at high incidence angles also require further attention. From a technical perspective, one of the main unknowns is the actual differential charging configuration of the target, whose effects on the sensing process should be quantified and bounded based on appropriate measurements. Mitigation strategies like the simultaneous use of secondary electrons and x-rays may need to be implemented in future space systems. The UV-laser-based strategies proposed in Chapter 5 could certainly eliminate some of the major sources of uncertainty. On top of this, closed-loop sensing control algorithms still have to be developed to measure the target potential in dynamic environments, potentially coupling this problem with charged astrodynamics simulations. Neutral charging strategies have an intrinsic interest for many applications and shall therefore be explored in future works.

This dissertation has also introduced the concept of low-gravity magnetohydrodynamics. Although the fundamentals of the field have been established, this work can only be considered the very first chapter of a long (and hopefully fruitful) story. The analytical methods for the equilibrium, stability, and modal response of liquid-gas interfaces should be adapted to cover additional problems with different geometries. A direct transition from those results to mechanical analogies of liquid sloshing would ease the development of propellant management devices and associated preliminary studies. In the numerical realm, magneto-

hydrodynamic interface tracking models are currently being extended to consider lateral oscillations and three-dimensional systems. Applications in nuclear fusion, microfluidics, or magnetic liquid dampers should also be explored. Fully coupled interface-capturing methods represent the next logical step of development that will enable the study of complex multiphase flows.

The low-gravity magnetohydrodynamics implementations presented in Part III, although representative of the field, are just a small subset of all its possibilities. Examples of application include electrochemical reduction, boiling, condensation, plant watering, food processing, or waste management, among others. Dedicated studies must be carried out to quantify the advantages of these technologies with respect to existing systems in terms of mass, power, and reliability. For instance, the magnetic phase separation approach may be implemented with forced water flows, but the maximum flow rate at which the diamagnetic force is able to collect the bubbles needs to be determined with numerical simulations and microgravity experiments. In the case of water electrolysis, long-term microgravity experiments are required to quantify the stabilizing effect of the magnetic force. A maturation process should be conducted to eventually produce a flight-ready electrolyzer, and the same applies to every other system here introduced.

Bibliography

- [1] Olano, L., and Montero, I., “Energy spectra of secondary electrons in dielectric materials by charging analysis,” Results in Physics, Vol. 19, 2020, p. 103456. <https://doi.org/10.1016/j.rinp.2020.103456>.
- [2] Lide, D. R., CRC Handbook of Chemistry and Physics: 84th Edition, CRC Press, 2003.
- [3] Romero-Calvo, A., Schaub, H., and Cano-Gómez, G., “Diamagnetically Enhanced Electrolysis and Phase Separation in Low Gravity,” Journal of Spacecraft and Rockets, Vol. 59, No. 1, 2022, pp. 59–72. <https://doi.org/10.2514/1.A35021>.
- [4] Grayson, G. D., Hand, M. L., and Cady, E. C., “Thermally Coupled Liquid Oxygen and Liquid Methane Storage Vessel,” US Patent 7,568,352 B2, Aug, 4 2009.
- [5] Wohlfarth, C., “Surface tension of methane: Datasheet from Landolt-Börnstein - Group IV Physical Chemistry · Volume 24: “Supplement to IV/16”, ” , 2008. https://doi.org/10.1007/978-3-540-75508-1_20.
- [6] Papell, S., “Low viscosity magnetic fluid obtained by the colloidal suspension of magnetic particles,” , 1963. US Patent 3215572.
- [7] Bengtson, M. T., “Electron Method for Touchless Electrostatic Potential Sensing of Neighboring Spacecraft,” Ph.D. thesis, University of Colorado Boulder, 2020. URL <http://hanspeterschaub.info/Papers/grads/MilesBengtson.pdf>.
- [8] Bengtson, M. T., and Schaub, H., “Electron-Based Touchless Potential Sensing of Shape Primitives and Differentially-Charged Spacecraft,” Journal of Spacecraft and Rockets, Vol. 58, No. 6, 2021, pp. 1847–1857. <https://doi.org/10.2514/1.A35086>.
- [9] Manura, D., and Dahl, D., SIMION (R) 8.1 User Manual, Rev-5, Adaptas Solutions, LLC, Palmer, MA 01069, 2008. URL <http://simion.com/manual/>.
- [10] Assa, A., and El Gomati, M., “Backscattering Coefficients for Low Energy Electrons,” Scanning Microscopy, Vol. 12, No. 1, 1998, pp. 185–192.
- [11] Kawasaki, K., Inoue, S., Ewang, E., Toyoda, K., and Cho, M., “Measurement of electron emission yield by electrons and photons for space aged material,” Proceedings of the 14th Spacecraft Charging Technology Conference, ESA/ESTEC Noordwijk, Netherlands, 2016, pp. 1–7.
- [12] Feuerbacher, B., and Fitton, B., “Experimental Investigation of Photoemission from Satellite Surface Materials,” Journal of Applied Physics, Vol. 43, No. 4, 1972, pp. 1563–1572. <https://doi.org/10.1063/1.1661362>.
- [13] Rodriguez, H., Abercromby, K., Mulrooney, M., and Barker, E., “Optical Properties of Multi-Layered Insulation,” Proceedings of the Advanced Maui Optical and Space Surveillance Technologies Conference, Wailea, Maui, Hawaii, 2007.

- [14] Heaney, J. B., “Evaluation of commercially supplied silver coated Teflon for Spacecraft Temperature Control Usage,” Tech. Rep. TM-X-70488, NASA, 1974.
- [15] Hamamatsu, “S2D2 L10706 VUV Light Source Datasheet,” Tech. Rep. TLSZ1001E03, Hamamatsu Photonics K.K., 2014. URL www.hamamatsu.com/content/dam/hamamatsu-photonics/sites/documents/99_SALES_LIBRARY/etd/L10706_TLSZ1001E.pdf.
- [16] Romero-Calvo, A., Cano Gómez, G., Castro-Hernández, E., and Maggi, F., “Free and Forced Oscillations of Magnetic Liquids Under Low-Gravity Conditions,” *Journal of Applied Mechanics*, Vol. 87, No. 2, 2019, pp. 021–010. <https://doi.org/10.1115/1.4045620>, 021010.
- [17] Yeh, G., “Free and Forced Oscillations of a Liquid in an Axisymmetric Tank at Low-Gravity Environments,” *Journal of Applied Mechanics*, Vol. 34, No. 1, 1967, pp. 23–28. <https://doi.org/10.1115/1.3607644>.
- [18] Gerstmann, J., and Dreyer, M. E., “Axisymmetric Surface Oscillations in a Cylindrical Container with Compensated Gravity,” *Annals of the New York Academy of Sciences*, Vol. 1077, No. 1, 2006, pp. 328–350. <https://doi.org/10.1196/annals.1362.022>.
- [19] Team, N. S. P., “New Shepard Payload User’s Guide,” Tech. Rep. NSPM-MA0002, Rev. F, Blue Origin, 2019.
- [20] Rosensweig, R. E., *Ferrohydrodynamics*, Dover Publications, 1997.
- [21] Youngquist, R. C., Nurge, M. A., Starr, S. O., Leve, F. A., and Peck, M., “A slowly rotating hollow sphere in a magnetic field: First steps to de-spin a space object,” *American Journal of Physics*, Vol. 84, No. 3, 2016, pp. 181–191. <https://doi.org/10.1119/1.4936633>.
- [22] Reinhardt, B. Z., and Peck, M. A., “New Electromagnetic Actuator for On-Orbit Inspection,” *Journal of Spacecraft and Rockets*, Vol. 53, No. 2, 2016, pp. 241–248. <https://doi.org/10.2514/1.A33320>.
- [23] Weis, L. M., and Peck, M., “Chip-Scale Satellite Control with Multiple Electrodynamic Tethers,” *Journal of Guidance, Control, and Dynamics*, Vol. 39, No. 7, 2016, pp. 1643–1646. <https://doi.org/10.2514/1.G001438>.
- [24] Farr, B., Wang, X., Goree, J., Hahn, I., Israelsson, U., and Horányi, M., “Dust mitigation technology for lunar exploration utilizing an electron beam,” *Acta Astronautica*, Vol. 177, 2020, pp. 405–409. <https://doi.org/10.1016/j.actaastro.2020.08.003>.
- [25] Bengtson, M., Wilson, K., Hughes, J., and Schaub, H., “Survey of the electrostatic tractor research for reorbiting passive GEO space objects,” *Astrodynamics*, Vol. 2, No. 4, 2018, pp. 291–305. <https://doi.org/10.1007/s42064-018-0030-0>.
- [26] Bengtson, M. T., Wilson, K. T., and Schaub, H., “Experimental Results of Electron Method for Remote Spacecraft Charge Sensing,” *Space Weather*, Vol. 18, No. 3, 2020, pp. 1–12. <https://doi.org/10.1029/2019SW002341>.
- [27] Wilson, K., and Schaub, H., “X-Ray Spectroscopy for Electrostatic Potential and Material Determination of Space Objects,” *IEEE Transactions on Plasma Science*, Vol. 47, No. 8, 2019, pp. 3858–3866. <https://doi.org/10.1109/TPS.2019.2910576>.
- [28] Wilson, K. T., Bengtson, M. T., and Schaub, H., “X-ray Spectroscopic Determination of Electrostatic Potential and Material Composition for Spacecraft: Experimental Results,” *Space Weather*, Vol. 18, No. 4, 2020, pp. 1–10. <https://doi.org/10.1029/2019SW002342>.
- [29] Wilson, K., Hammerl, J., and Schaub, H., “Using Plasma-Induced X-Ray Emission to Estimate Electrostatic Potentials on Nearby Space Objects,” *Journal of Spacecraft and Rockets*, Vol. 0, No. 0, 2022, pp. 1–4. <https://doi.org/10.2514/1.A35161>.

- [30] Bengtson, M., Hughes, J., and Schaub, H., “Prospects and Challenges for Touchless Sensing of Spacecraft Electrostatic Potential Using Electrons,” *IEEE Transactions on Plasma Science*, Vol. 47, No. 8, 2019, pp. 3673–3681. <https://doi.org/10.1109/TPS.2019.2912057>.
- [31] Schaub, H., and Moorer, D. F., “Geosynchronous Large Debris Reorbiter: Challenges and Prospects,” *The Journal of the Astronautical Sciences*, Vol. 59, No. 1, 2012, pp. 161–176. <https://doi.org/10.1007/s40295-013-0011-8>.
- [32] Casale, F., Schaub, H., and Biggs, J. D., “Lyapunov Optimal Touchless Electrostatic Detumbling of Geostationary Debris Using Surface Multisphere Models,” *AIAA Journal of Spacecraft and Rockets*, Vol. 58, No. 3, 2021, pp. 764–778. <https://doi.org/10.2514/1.A34787>.
- [33] Hughes, J., and Schaub, H., “Prospects of Using a Pulsed Electrostatic Tractor With Nominal Geosynchronous Conditions,” *IEEE Transactions on Plasma Science*, Vol. 45, No. 8, 2017, pp. 1887–1897. <https://doi.org/10.1109/TPS.2017.2684621>.
- [34] Hughes, J. A., and Schaub, H., “Electrostatic Tractor Analysis Using a Measured Flux Model,” *Journal of Spacecraft and Rockets*, Vol. 57, No. 2, 2020, pp. 207–216. <https://doi.org/10.2514/1.A34359>.
- [35] Hammerl, J., and Schaub, H., “Effects of Electric Potential Uncertainty on Electrostatic Tractor Relative Motion Control Equilibria,” *Journal of Spacecraft and Rockets*, Vol. 59, No. 2, 2022, pp. 552–562. <https://doi.org/10.2514/1.A35165>.
- [36] Schaub, H., Parker, G. G., and King, L. B., “Challenges and Prospects of Coulomb Spacecraft Formation Control,” *The Journal of the Astronautical Sciences*, Vol. 52, No. 1, 2004, pp. 169–193. <https://doi.org/10.1007/BF03546427>.
- [37] Parker, G. G., Schaub, H., Natarajan, A., and King, L. B., “Coulomb Force Virtual Space Structures,” *Acta Futura*, Vol. 2, No. ACT-PUB-AFO502, 2006, pp. 39–44. <https://doi.org/10.2420/ACT-BOK-AF02>.
- [38] Stiles, L. A., Schaub, H., Maute, K. K., and Moorer, D. F., “Electrostatically inflated gossamer space structure voltage requirements due to orbital perturbations,” *Acta Astronautica*, Vol. 84, 2013, pp. 109–121. <https://doi.org/10.1016/j.actaastro.2012.11.007>.
- [39] Wilson, K., Romero-Calvo, A., and Schaub, H., “Constrained Guidance for Spacecraft Proximity Operations Under Electrostatic Perturbations,” *Journal of Spacecraft and Rockets*, Vol. 0, No. 0, 2022, pp. 1–13. <https://doi.org/10.2514/1.A35162>.
- [40] Maxwell, J., Harris, A., and Schaub, H., “Balancing differential drag with Coulomb repulsion in low earth orbit plasma wakes,” *Acta Astronautica*, Vol. 194, 2022, pp. 323–333. <https://doi.org/10.1016/j.actaastro.2020.08.021>.
- [41] Ferguson, D. C., Murray-Krezan, J., Barton, D. A., Dennison, J. R., and Gregory, S. A., “Feasibility of Detecting Spacecraft Charging and Arcing by Remote Sensing,” *Journal of Spacecraft and Rockets*, Vol. 51, No. 6, 2014, pp. 1907–1913. <https://doi.org/10.2514/1.A32958>.
- [42] Wilson, K. T., “Remote Electrostatic Potential Determination for Spacecraft Relative Motion Control,” Ph.D. thesis, Aerospace Engineering Sciences Department, University of Colorado, Boulder, CO, 2021. URL <http://hanspeterschaub.info/Papers/grads/KieranWilson.pdf>.
- [43] Wilson, K. T. H., Bengtson, M., and Schaub, H., “Hybrid Method of Remote Sensing of Electrostatic Potential for Proximity Operations,” *IEEE Aerospace Engineering Conference, Big Sky, MO*, 2020, pp. 1–9. <https://doi.org/10.1109/AERO47225.2020.9172772>.
- [44] Wilson, K., Bengtson, M., and Schaub, H., “Remote Electrostatic Potential Sensing for Proximity Operations: Comparison and Fusion of Methods,” *Journal of Spacecraft and Rockets*, 2022. <https://doi.org/10.2514/1.A35071>.

- [45] Parker, L. W., and Whipple Jr., E. C., “Theory of spacecraft sheath structure, potential, and velocity effects on ion measurements by traps and mass spectrometers,” Journal of Geophysical Research (1896-1977), Vol. 75, No. 25, 1970, pp. 4720–4733. <https://doi.org/10.1029/JA075i025p04720>.
- [46] Scime, E. E., Phillips, J. L., and Bame, S. J., “Effects of spacecraft potential on three-dimensional electron measurements in the solar wind,” Journal of Geophysical Research: Space Physics, Vol. 99, No. A8, 1994, pp. 14769–14776. <https://doi.org/10.1029/94JA00489>.
- [47] Miyake, Y., Cully, C. M., Usui, H., and Nakashima, H., “Plasma particle simulations of wake formation behind a spacecraft with thin wire booms,” Journal of Geophysical Research: Space Physics, Vol. 118, No. 9, 2013, pp. 5681–5694. <https://doi.org/10.1002/jgra.50543>.
- [48] Barrie, A. C., Cipriani, F., Escoubet, C. P., Toledo-Redondo, S., Nakamura, R., Torkar, K., Sternovsky, Z., Elkington, S., Gershman, D., Giles, B., and Schiff, C., “Characterizing spacecraft potential effects on measured particle trajectories,” Physics of Plasmas, Vol. 26, No. 10, 2019, p. 103504. <https://doi.org/10.1063/1.5119344>.
- [49] Romero-Calvo, A., Cano-Gómez, G., and Schaub, H., “Simulation and uncertainty quantification of electron beams in active spacecraft charging scenarios,” Journal of Spacecraft and Rockets, Vol. 59, No. 3, 2022, pp. 739–750. <https://doi.org/10.2514/1.A35190>.
- [50] Garrett, H. B., and Whittlesey, A. C., “Spacecraft Design Guidelines,” Guide to Mitigating Spacecraft Charging Effects, John Wiley & Sons, Ltd, 2012, Chap. 3, pp. 26–61. <https://doi.org/10.1002/9781118241400.ch3>.
- [51] Olsen, R. C., McIlwain, C. E., and Whipple Jr., E. C., “Observations of differential charging effects on ATS 6,” Journal of Geophysical Research: Space Physics, Vol. 86, No. A8, 1981, pp. 6809–6819. <https://doi.org/10.1029/JA086iA08p06809>.
- [52] Grard, R., Knott, K., and Pedersen, “Spacecraft charging effects,” Space Science Reviews, Vol. 34, No. 3, 1983, pp. 289–304. <https://doi.org/10.1007/BF00175284>.
- [53] Roeder, J. L., and Fennell, J. F., “Differential Charging of Satellite Surface Materials,” IEEE Transactions on Plasma Science, Vol. 37, No. 1, 2009, pp. 281–289. <https://doi.org/10.1109/TPS.2008.2004765>.
- [54] Ferguson, D., White, S., Rast, R., and Holeman, E., “The Case for Global Positioning System Arcing and High Satellite Arc Rates,” IEEE Transactions on Plasma Science, Vol. 47, No. 8, 2019, pp. 3834–3841. <https://doi.org/10.1109/TPS.2019.2922556>.
- [55] Lai, S. T., Fundamentals of Spacecraft Charging: Spacecraft Interactions with Space Plasmas, Princeton University Press, 2012.
- [56] Wilson, K., Álvaro Romero-Calvo, Bengtson, M., Hammerl, J., Maxwell, J., and Schaub, H., “Development and characterization of the ECLIPS space environments simulation facility,” Acta Astronautica, Vol. 194, 2022, pp. 48–58. <https://doi.org/10.1016/j.actaastro.2021.12.037>.
- [57] Olsen, R., and Cohen, H., “Electron beam experiments at high altitudes,” Advances in Space Research, Vol. 8, No. 1, 1988, pp. 161–164. [https://doi.org/10.1016/0304-3886\(87\)90085-4](https://doi.org/10.1016/0304-3886(87)90085-4).
- [58] Melzner, F., Metzner, G., and Antrack, D., “The GEOS electron beam experiment,” Space Science Instrumentation, Vol. 4, 1978, pp. 45–55.
- [59] Paschmann, G., Boehm, M., Höfner, H., Frenzel, R., Parigger, P., Melzner, F., Haerendel, G., Kletzing, C. A., Torbert, R. B., and Sartori, G., “The Electron Beam Instrument (F6) on Freja,” Space Science Reviews, Vol. 70, No. 3, 1994, pp. 447–463. <https://doi.org/10.1007/BF00756881>.

- [60] Paschmann, G., Melzner, F., Frenzel, R., Vaith, H., Parigger, P., Pagel, U., Bauer, O. H., Haerendel, G., Baumjohann, W., Scopke, N., Torbert, R. B., Briggs, B., Chan, J., Lynch, K., Morey, K., Quinn, J. M., Simpson, D., Young, C., McIlwain, C. E., Fillius, W., Kerr, S. S., Mahieu, R., and Whipple, E. C., "The Electron Drift Instrument for Cluster," *Space Science Reviews*, Vol. 79, No. 1, 1997, pp. 233–269. <https://doi.org/10.1023/A:1004917512774>.
- [61] Torbert, R. B., Vaith, H., Granoff, M., Widholm, M., Gaidos, J. A., Briggs, B. H., Dors, I. G., Chutter, M. W., Macri, J., Argall, M., Bodet, D., Needell, J., Steller, M. B., Baumjohann, W., Nakamura, R., Plaschke, F., Ottacher, H., Hasiba, J., Hofmann, K., Kletzing, C. A., Bounds, S. R., Dvorsky, R. T., Sigsbee, K., and Kooi, V., "The Electron Drift Instrument for MMS," *Space Science Reviews*, Vol. 199, No. 1, 2016, pp. 283–305. <https://doi.org/10.1007/s11214-015-0182-7>.
- [62] Landau, L., and Lifshitz, E., *Electrodynamics of Continuous Media*, Pergamon Press, 1960.
- [63] Dodge, F., *The New Dynamic Behavior of Liquids in Moving Containers*, Southwest Research Institute, 2000.
- [64] Wakayama, N. I., "Magnetic buoyancy force acting on bubbles in nonconducting and diamagnetic fluids under microgravity," *Journal of Applied Physics*, Vol. 81, No. 7, 1997, pp. 2980–2984. <https://doi.org/10.1063/1.364330>.
- [65] Wakayama, N. I., "Utilization of magnetic force in space experiments," *Advances in Space Research*, Vol. 24, No. 10, 1999, pp. 1337–1340. [https://doi.org/10.1016/S0273-1177\(99\)00743-7](https://doi.org/10.1016/S0273-1177(99)00743-7), gravitational Effects in Materials and Fluid Sciences.
- [66] Boulware, J. C., Ban, H., Jensen, S., and Wassom, S., "Experimental studies of the pressures generated by a liquid oxygen slug in a magnetic field," *Journal of Magnetism and Magnetic Materials*, Vol. 322, No. 13, 2010, pp. 1752–1757. <https://doi.org/10.1016/j.jmmm.2009.12.022>.
- [67] Kinefuchi, K., and Kobayashi, H., "Theoretical and experimental study of the active control of bubble point pressure using a magnetic field and its applications," *Physics of Fluids*, Vol. 30, No. 6, 2018, p. 062101. <https://doi.org/10.1063/1.5034222>.
- [68] Causevica, A., Sahli, P., Hild, F., Grunwald, K., Ehresmann, M., and Herdrich, G., "PAPELL: Interaction Study of Ferrofluid with Electromagnets of an Experiment on the International Space Station," *Proceedings of the 69th International Astronautical Congress*, 2018, pp. 1–5.
- [69] Ludovisi, D., Cha, S. S., Ramachandran, N., and Worek, W. M., "Heat transfer of thermocapillary convection in a two-layered fluid system under the influence of magnetic field," *Acta Astronautica*, Vol. 64, No. 11, 2009, pp. 1066–1079. <https://doi.org/10.1016/j.actaastro.2009.01.018>.
- [70] Bozhko, A., and Putin, G., "Thermomagnetic Convection as a Tool for Heat and Mass Transfer Control in Nanosize Materials Under Microgravity Conditions," *Microgravity Science and Technology*, Vol. 21, No. 1, 2009, pp. 89–93. <https://doi.org/10.1007/s12217-008-9059-7>.
- [71] Jackson, B. A., Terhune, K. J., and King, L. B., "Ionic liquid ferrofluid interface deformation and spray onset under electric and magnetic stresses," *Physics of Fluids*, Vol. 29, No. 6, 2017, p. 064105. <https://doi.org/10.1063/1.4985141>.
- [72] Lemmer, K., "Propulsion for CubeSats," *Acta Astronautica*, Vol. 134, 2017, pp. 231–243. <https://doi.org/10.1016/j.actaastro.2017.01.048>.
- [73] Scarl, E., and Houston, J., "Two-phase magnetic fluid manipulation in microgravity environments," *Proceedings of the 37th Aerospace Sciences Meeting and Exhibit*, 1999, pp. 1–5. <https://doi.org/10.2514/6.1999-844>.
- [74] Tillotson, B. J., Torre, L. P., and Houston, J. D., "Method for Manipulation of Diamagnetic Objects in a Low-Gravity Environment," , 2000. US Patent 6162364.

- [75] Poesio, P., and Wang, E., “Resonance induced wetting state transition of a ferrofluid droplet on superhydrophobic surfaces,” Experimental Thermal and Fluid Science, Vol. 57, 2014, pp. 353–357. <https://doi.org/10.1016/j.expthermflusci.2014.02.012>.
- [76] Yamasaki, H., Kishimoto, T., Tazawa, T., and Yamaguchi, H., “Dynamic behavior of gas bubble detached from single orifice in magnetic fluid,” Journal of Magnetism and Magnetic Materials, Vol. 501, 2020, p. 166446. <https://doi.org/10.1016/j.jmmm.2020.166446>.
- [77] Romero-Calvo, A., Cano-Gómez, G., Hermans, T. H., Benítez, L. P., Gutiérrez, M. A. H., and Castro-Hernández, E., “Total magnetic force on a ferrofluid droplet in microgravity,” Experimental Thermal and Fluid Science, Vol. 117, 2020, p. 110124. <https://doi.org/10.1016/j.expthermflusci.2020.110124>.
- [78] Tan, S.-H., Nguyen, N.-T., Yobas, L., and Kang, T. G., “Formation and manipulation of ferrofluid droplets at a microfluidic T-junction,” Journal of Micromechanics and Microengineering, Vol. 20, No. 4, 2010, p. 045004. <https://doi.org/10.1088/0960-1317/20/4/045004>.
- [79] Wu, Y., Fu, T., Ma, Y., and Li, H. Z., “Active control of ferrofluid droplet breakup dynamics in a microfluidic T-junction,” Microfluidics and Nanofluidics, Vol. 18, No. 1, 2015, pp. 19–27. <https://doi.org/10.1007/s10404-014-1414-y>.
- [80] Aboutalebi, M., Bijarchi, M. A., Shafii, M. B., and Kazemzadeh Hannani, S., “Numerical investigation on splitting of ferrofluid microdroplets in T-junctions using an asymmetric magnetic field with proposed correlation,” Journal of Magnetism and Magnetic Materials, Vol. 447, 2018, pp. 139–149. <https://doi.org/10.1016/j.jmmm.2017.09.053>.
- [81] Bibo, A., Masana, R., King, A., Li, G., and Daqaq, M., “Electromagnetic ferrofluid-based energy harvester,” Physics Letters A, Vol. 376, No. 32, 2012, pp. 2163–2166. <https://doi.org/10.1016/j.physleta.2012.05.033>.
- [82] Alazemi, S. F., Bibo, A., and Daqaq, M. F., “A ferrofluid-based energy harvester: An experimental investigation involving internally-resonant sloshing modes,” The European Physical Journal Special Topics, Vol. 224, No. 14, 2015, pp. 2993–3004. <https://doi.org/10.1140/epjst/e2015-02602-9>.
- [83] Alazmi, S., Xu, Y., and Daqaq, M. F., “Harvesting energy from the sloshing motion of ferrofluids in an externally excited container: Analytical modeling and experimental validation,” Physics of Fluids, Vol. 28, No. 7, 2016, p. 077101. <https://doi.org/10.1063/1.4954787>.
- [84] ALFVÉN, H., “Existence of Electromagnetic-Hydrodynamic Waves,” Nature, Vol. 150, No. 3805, 1942, pp. 405–406. <https://doi.org/10.1038/150405d0>.
- [85] Myshkis, A., Babitskii, V., Kopachevskii, N., Slobozhanin, L., and Tyuptsov, A., Low-gravity fluid mechanics: mathematical theory of capillary phenomena, Springer, 1987. ISBN: 978-35-401-6189-9.
- [86] Reynolds, W. C., and Satterlee, H. M., “Ch. 11 - Liquid Propellant Behavior at Low and Zero g,” The Dynamic Behavior of Liquids in Moving Containers, Vol. SP-106, NASA SP-106, 1966, Chaps. 11 - Liquid Propellant Behavior at Low and Zero g, pp. 387–440.
- [87] Dodge, F., and Garza, L., “Experimental and Theoretical Studies of Liquid Sloshing at Simulated Low Gravity,” Journal of Applied Mechanics, Vol. 34, No. 3, 1967, pp. 555–562. <https://doi.org/10.1115/1.3607743>.
- [88] Dodge, F., and Garza, L., “Equivalent Mechanical Model of Propellant Sloshing in the Workshop Configuration of the Saturn S-IVB,” Tech. Rep. CR-102615, NASA - Southwest Research Institute, 1969.
- [89] Collicott, S. H., and Weislogel, M. M., “Computing Existence and Stability of Capillary Surfaces Using Surface Evolver,” AIAA Journal, Vol. 42, No. 2, 2004, pp. 289–295. <https://doi.org/10.2514/1.9093>.

- [90] Singh, C., Das, A. K., and Das, P. K., “Flow restrictive and shear reducing effect of magnetization relaxation in ferrofluid cavity flow,” Physics of Fluids, Vol. 28, No. 8, 2016, p. 087103. <https://doi.org/10.1063/1.4960085>.
- [91] Shafiei Dizaji, A., Mohammadpourfard, M., and Aminfar, H., “A numerical simulation of the water vapor bubble rising in ferrofluid by volume of fluid model in the presence of a magnetic field,” Journal of Magnetism and Magnetic Materials, Vol. 449, 2018, pp. 185–196. <https://doi.org/10.1016/j.jmmm.2017.10.010>.
- [92] Ling, K., Guo, K.-K., Zhang, S., and Tao, W.-Q., “A numerical investigation on dynamics of ferrofluid droplet in nonuniform magnetic field,” Numerical Heat Transfer, Part A: Applications, Vol. 75, No. 10, 2019, pp. 690–707. <https://doi.org/10.1080/10407782.2019.1609277>.
- [93] Li, X., Dong, Z.-Q., Yu, P., Niu, X.-D., Wang, L.-P., Li, D.-C., and Yamaguchi, H., “Numerical investigation of magnetic multiphase flows by the fractional-step-based multiphase lattice Boltzmann method,” Physics of Fluids, Vol. 32, No. 8, 2020, p. 083309. <https://doi.org/10.1063/5.0020903>.
- [94] Abicalil, V. G. e., Abdo, R. F., da Cunha, L. H. P., and de Oliveira, T. F., “On the magnetization of dilute ferrofluid emulsions in shear flows,” Physics of Fluids, Vol. 33, No. 5, 2021, p. 053313. <https://doi.org/10.1063/5.0050643>.
- [95] Khan, A., Zhang, S.-T., Li, Q.-P., Zhang, H., Wang, Y.-Q., and Niu, X.-D., “Wetting dynamics of a sessile ferrofluid droplet on solid substrates with different wettabilities,” Physics of Fluids, Vol. 33, No. 4, 2021, p. 042115. <https://doi.org/10.1063/5.0047553>.
- [96] Selimefendigil, F., and Öztop, H. F., “Mixed convection of ferrofluids in a lid driven cavity with two rotating cylinders,” Engineering Science and Technology, an International Journal, Vol. 18, No. 3, 2015, pp. 439–451. <https://doi.org/10.1016/j.jestch.2015.03.003>.
- [97] Sheikholeslami, M., and Rashidi, M. M., “Ferrofluid heat transfer treatment in the presence of variable magnetic field,” The European Physical Journal Plus, Vol. 130, No. 6, 2015, p. 115. <https://doi.org/10.1140/epjp/i2015-15115-4>.
- [98] Liu, Q., Alazemi, S. F., Daqaq, M. F., and Li, G., “A ferrofluid based energy harvester: Computational modeling, analysis, and experimental validation,” Journal of Magnetism and Magnetic Materials, Vol. 449, 2018, pp. 105–118. <https://doi.org/10.1016/j.jmmm.2017.09.064>.
- [99] Heil, M., Hazel, A. L., and Boyle, J., “Solvers for large-displacement fluid–structure interaction problems: segregated versus monolithic approaches,” Computational Mechanics, Vol. 43, No. 1, 2008, pp. 91–101. <https://doi.org/10.1007/s00466-008-0270-6>.
- [100] Markert, B., Heider, Y., and Ehlers, W., “Comparison of monolithic and splitting solution schemes for dynamic porous media problems,” International Journal for Numerical Methods in Engineering, Vol. 82, No. 11, 2010, pp. 1341–1383. <https://doi.org/10.1002/nme.2789>.
- [101] Küttler, U., Gee, M., Förster, C., Comerford, A., and Wall, W. A., “Coupling strategies for biomedical fluid–structure interaction problems,” International Journal for Numerical Methods in Biomedical Engineering, Vol. 26, No. 3-4, 2010, pp. 305–321. <https://doi.org/10.1002/cnm.1281>.
- [102] Mayr, M., Klöppel, T., Wall, W. A., and Gee, M. W., “A Temporal Consistent Monolithic Approach to Fluid-Structure Interaction Enabling Single Field Predictors,” SIAM Journal on Scientific Computing, Vol. 37, No. 1, 2015, pp. B30–B59. <https://doi.org/10.1137/140953253>.
- [103] Hu, Y., Li, D., and Niu, X., “Phase-field-based lattice Boltzmann model for multiphase ferrofluid flows,” Phys. Rev. E, Vol. 98, 2018, p. 033301. <https://doi.org/10.1103/PhysRevE.98.033301>.

- [104] Huang, Y., Zhang, Y., Xu, M., Lei, J., Li, Z., and Ye, W., “A numerical investigation of bubble dynamics in a ferrofluid by improved multicomponent multiphase pseudopotential lattice Boltzmann model coupled with magnetic field solver,” *Physics of Fluids*, Vol. 33, No. 9, 2021, p. 097110. <https://doi.org/10.1063/5.0066572>.
- [105] Zhu, C.-S., Hu, Z., and Wang, K.-M., “Multi-bubble motion behavior of uniform magnetic field based on phase field model,” *Chinese Physics B*, Vol. 29, No. 3, 2020, p. 034702. <https://doi.org/10.1088/1674-1056/ab6839>.
- [106] Popinet, S., “Numerical Models of Surface Tension,” *Annual Review of Fluid Mechanics*, Vol. 50, No. 1, 2018, pp. 49–75. <https://doi.org/10.1146/annurev-fluid-122316-045034>.
- [107] Mirjalili, S., Jain, S. S., and Dodd, M. S., “Interface-capturing methods for two-phase flows: An overview and recent developments,” *Annual Research Briefs, Center for Turbulence Research, Stanford University*, 2017, pp. 117–135.
- [108] Herrada, M., and Montanero, J., “A numerical method to study the dynamics of capillary fluid systems,” *Journal of Computational Physics*, Vol. 306, 2016, pp. 137–147. <https://doi.org/10.1016/j.jcp.2015.11.048>.
- [109] Erickson, R. J., Howe, J., Kulp, G. W., and Van Keuren, S. P., “International Space Station United States Orbital Segment Oxygen Generation System On-orbit Operational Experience,” *International Conference On Environmental Systems, 2008-01-1962*, 2008. <https://doi.org/10.4271/2008-01-1962>.
- [110] Samplatsky, D. J., and Dean, W. C., “Development of a Rotary Separator Accumulator for Use on the International Space Station,” *International Conference On Environmental Systems*, SAE International, 2002. <https://doi.org/10.4271/2002-01-2360>.
- [111] Tilton, D. E., and Tilton, C. L., “Entrained droplet separator,” , 1994. US Patent 5314529.
- [112] Hoyt, N., Kamotani, Y., Kadambi, J., McQuillen, J., and Sankovic, J., “Computational Investigation of the NASA Cascade Cyclonic Separation Device,” *46th AIAA Aerospace Sciences Meeting and Exhibit*, 2008. <https://doi.org/10.2514/6.2008-809>, AIAA Paper 2008-809.
- [113] Hoyt, N. C., Kang, M.-F., Lee, K.-L., Kharraz, A., Kadambi, J., and Kamotani, Y., “Study of Steady and Dynamic Behavior of Gas Core of Passive Cyclonic Separator for Space Applications,” *Microgravity Science and Technology*, Vol. 25, No. 3, 2013, pp. 187–200. <https://doi.org/10.1007/s12217-013-9346-9>.
- [114] Xu, X., Yang, Q., yang Wang, C., ling Ge, X., and lin Wang, H., “Dissolved gas separation using the pressure drop and centrifugal characteristics of an inner cone hydrocyclone,” *Separation and Purification Technology*, Vol. 161, 2016, pp. 121–128. <https://doi.org/10.1016/j.seppur.2016.01.006>.
- [115] Wu, X., Loraine, G., Hsiao, C.-T., and Chahine, G. L., “Development of a passive phase separator for space and earth applications,” *Separation and Purification Technology*, Vol. 189, 2017, pp. 229–237. <https://doi.org/10.1016/j.seppur.2017.08.017>.
- [116] Browning, W. L., “S-4B/5 Auxiliary Propulsion System 90-day Recycle Capability Test Report, Module 1,” Tech. Rep. DAC-56728, McDonnell Douglas Astronautics Company, 1969. URL ntrs.nasa.gov/citations/19700026606.
- [117] Coates, K., and Donald, E., “Investigation of SA-501 S-4B Auxiliary Propulsion System Flight Anomalies,” Tech. Rep. TN D-5207, NASA, 1969. URL ntrs.nasa.gov/citations/19690016846.
- [118] Weislogel, M. M., and Collicott, S. H., “Capillary Rewetting of Vaned Containers: Spacecraft Tank Rewetting Following Thrust Resettling,” *AIAA Journal*, Vol. 42, No. 12, 2004, pp. 2551–2561. <https://doi.org/10.2514/1.3394>.

- [119] Sakurai, M., Shima, A., Sone, Y., Ohnishi, M., Tachihara, S., and Ito, T., “Development of Oxygen Generation Demonstration on JEM (KIBO) for Manned Space Exploration,” 44th International Conference on Environmental Systems, Tucson, Arizona, 2014, pp. 1–7.
- [120] Sakurai, M., Terao, T., and Sone, Y., “Development of Water Electrolysis System for Oxygen Production Aimed at Energy Saving and High Safety,” 45th International Conference on Environmental Systems, Bellevue, Washington, 2015, pp. 1–8.
- [121] Weislogel, M. M., Thomas, E. A., and Graf, J. C., “A Novel Device Addressing Design Challenges for Passive Fluid Phase Separations Aboard Spacecraft,” Microgravity Science and Technology, Vol. 21, No. 3, 2008, p. 257. <https://doi.org/10.1007/s12217-008-9091-7>.
- [122] Weislogel, M., and Jenson, R., “Passive no moving parts capillary solutions for spacecraft life support systems,” 49th International Conference On Environmental Systems, Boston, Massachusetts, 2019.
- [123] Kichatov, B. V., Mikhalev, A. P., and Polyayev, V. M., “Study of evaporation in a capillary phase separator,” High Temperature, Vol. 38, No. 3, 2000, pp. 460–466. <https://doi.org/10.1007/BF02756007>.
- [124] Jenson, R. M., Wollman, A. P., Weislogel, M. M., Sharp, L., Green, R., Canfield, P. J., Klatte, J., and Dreyer, M. E., “Passive phase separation of microgravity bubbly flows using conduit geometry,” International Journal of Multiphase Flow, Vol. 65, 2014, pp. 68–81. <https://doi.org/10.1016/j.ijmultiphaseflow.2014.05.011>.
- [125] Weislogel, M. M., and McCraney, J. T., “The symmetric draining of capillary liquids from containers with interior corners,” Journal of Fluid Mechanics, Vol. 859, 2019, p. 902–920. <https://doi.org/10.1017/jfm.2018.848>.
- [126] Torres, L. J., and Weislogel, M. M., “The ejection of large non-oscillating droplets from a hydrophobic wedge in microgravity,” npj Microgravity, Vol. 7, No. 1, 2021, p. 52. <https://doi.org/10.1038/s41526-021-00182-4>.
- [127] Beheshti Pour, N., and Thiessen, D. B., “A novel arterial Wick for gas–liquid phase separation,” AICHE Journal, Vol. 65, No. 4, 2019, pp. 1340–1354. <https://doi.org/10.1002/aic.16499>.
- [128] Beheshti Pour, N., and Thiessen, D. B., “Equilibrium configurations of drops or bubbles in an eccentric annulus,” Journal of Fluid Mechanics, Vol. 863, 2019, p. 364–385. <https://doi.org/10.1017/jfm.2018.1010>.
- [129] TeGrotenhuis, W. E., and Stenkamp, V. S., “Normal Gravity Testing of a Microchannel Phase Separator for In Situ Resource Utilization,” Tech. Rep. CR-2001-210955, NASA, 2001. URL ntrs.nasa.gov/citations/20010069258.
- [130] Scovazzo, P., Illangasekare, T. H., Hoehn, A., and Todd, P., “Modeling of two-phase flow in membranes and porous media in microgravity as applied to plant irrigation in space,” Water Resources Research, Vol. 37, No. 5, 2001, pp. 1231–1243. <https://doi.org/10.1029/2000WR900311>.
- [131] Hasan, M., Khan, L., Nayagam, V., and Balasubramaniam, R., “Conceptual Design of a Condensing Heat Exchanger for Space Systems using Porous Media,” 35th International Conference on Environmental Systems, Rome, Italy, 2005. <https://doi.org/10.4271/2005-01-2812>.
- [132] Chipchark, D., “Development of expulsion and orientation systems for advanced liquid rocket propulsion systems,” Tech. Rep. RTD-TDR-63-1048, Contract AF04 (611)-8200, USAF, 1963.
- [133] Pearson, M. R., and Seyed-Yagoobi, J., “Numerical Study of Dielectric Fluid Bubble Behavior Within Diverging External Electric Fields,” Journal of Heat Transfer, Vol. 130, No. 3, 2008, p. 032901. <https://doi.org/10.1115/1.2804937>.

- [134] Di Marco, P., “The Use of Electric Force as a Replacement of Buoyancy in Two-phase Flow,” Microgravity Science and Technology, Vol. 24, No. 3, 2012, pp. 215–228. <https://doi.org/10.1007/s12217-012-9312-y>.
- [135] Ma, R., Lu, X., Wang, C., Yang, C., and Yao, W., “Numerical simulation of bubble motions in a coaxial annular electric field under microgravity,” Aerospace Science and Technology, Vol. 96, 2020, p. 105525. <https://doi.org/10.1016/j.ast.2019.105525>.
- [136] Feng, Y., and Seyed-Yagoobi, J., “Control of liquid flow distribution utilizing EHD conduction pumping mechanism,” IEEE Transactions on Industry Applications, Vol. 42, No. 2, 2006, pp. 369–377. <https://doi.org/10.1109/TIA.2005.863909>.
- [137] Crum, L. A., “Bjerknes forces on bubbles in a stationary sound field,” The Journal of the Acoustical Society of America, Vol. 57, No. 6, 1975, pp. 1363–1370. <https://doi.org/10.1121/1.380614>.
- [138] Luo, X., Cao, J., Gong, H., Yan, H., and He, L., “Phase separation technology based on ultrasonic standing waves: A review,” Ultrasonics Sonochemistry, Vol. 48, 2018, pp. 287–298. <https://doi.org/10.1016/j.ultsonch.2018.06.006>.
- [139] Oeftering, R. C., Chato, D. J., and Mann, A., “Liquid Propellant Manipulated Acoustically,” Tech. Rep. 20050215041, NASA, 2003.
- [140] Suñol, F., Ochoa, D. A., Granados, M., González-Cinca, R., and García, J. E., “Performance Assessment of Ultrasonic Waves for Bubble Control in Cryogenic Fuel Tanks,” Microgravity Science and Technology, Vol. 32, No. 4, 2020, pp. 609–613. <https://doi.org/10.1007/s12217-020-09795-y>.
- [141] Fili, T., Gòdia, F., and González-Cinca, R., “Trade-off analysis of phase separation techniques for advanced life support systems in space,” Acta Astronautica, Vol. 178, 2021, pp. 571–583. <https://doi.org/10.1016/j.actaastro.2020.09.052>.
- [142] Porter, J., Salgado Sánchez, P., Shevtsova, V., and Yasnou, V., “A review of fluid instabilities and control strategies with applications in microgravity,” Math. Model. Nat. Phenom., Vol. 16, 2021, p. 24. <https://doi.org/10.1051/mmnp/2021020>.
- [143] Fernández, J., Tinao, I., Porter, J., and Laverón-Simavilla, A., “Instabilities of vibroequilibria in rectangular containers,” Physics of Fluids, Vol. 29, No. 2, 2017, p. 024108. <https://doi.org/10.1063/1.4976719>.
- [144] Salgado Sánchez, P., Gaponenko, Y. A., Porter, J., and Shevtsova, V., “Finite-size effects on pattern selection in immiscible fluids subjected to horizontal vibrations in weightlessness,” Phys. Rev. E, Vol. 99, 2019, p. 042803. <https://doi.org/10.1103/PhysRevE.99.042803>.
- [145] Junhong, L., Jianming, G., Zhiwei, L., and Hui, L., “Experiments and mechanism analysis of pool boiling heat transfer enhancement with water-based magnetic fluid,” Heat and Mass Transfer, Vol. 41, No. 2, 2004, pp. 170–175. <https://doi.org/10.1007/s00231-004-0529-1>.
- [146] Abdollahi, A., Salimpour, M. R., and Etesami, N., “Experimental analysis of magnetic field effect on the pool boiling heat transfer of a ferrofluid,” Applied Thermal Engineering, Vol. 111, 2017, pp. 1101–1110. <https://doi.org/10.1016/j.applthermaleng.2016.10.019>.
- [147] Tillotson, B., Houston, J., Tillotson, B., and Houston, J., “Diamagnetic manipulation for microgravity processing,” Proceedings of the 35th Aerospace Sciences Meeting and Exhibit, 1997, pp. 1–10. <https://doi.org/10.2514/6.1997-887>.
- [148] Eswaran, M., and Saha, U. K., “Sloshing of liquids in partially filled tanks - a review of experimental investigations,” Ocean Systems Engineering, Vol. 1, No. 2, 2011, pp. 131–155. <https://doi.org/10.12989/ose.2011.1.2.131>.

- [149] Collicott, S. H., Beckman, E. A., and Srikanth, P., “Conformal Tanks: Small-Sat Propellant Management Technology,” *AIAA Propulsion and Energy 2019 Forum*, 2019. <https://doi.org/10.2514/6.2019-3874>, AIAA Paper 2019-3874.
- [150] Lee, A. Y., and Stupik, J., “In-Flight Characterization of the Cassini Spacecraft Propellant Slosh Modes,” *Journal of Spacecraft and Rockets*, Vol. 54, No. 2, 2017, pp. 417–425. <https://doi.org/10.2514/1.A33636>.
- [151] Ogata, J., and Yabe, A., “Augmentation of boiling heat transfer by utilizing the EHD effect—EHD behaviour of boiling bubbles and heat transfer characteristics,” *International Journal of Heat and Mass Transfer*, Vol. 36, No. 3, 1993, pp. 783–791. [https://doi.org/10.1016/0017-9310\(93\)80054-X](https://doi.org/10.1016/0017-9310(93)80054-X).
- [152] Di Marco, P., “Influence of Force Fields and Flow Patterns on Boiling Heat Transfer Performance: A Review,” *Journal of Heat Transfer*, Vol. 134, No. 3, 2012, p. 030801. <https://doi.org/10.1115/1.4005146>.
- [153] Patel, V. K., and Seyed-Yagoobi, J., “Combined Dielectrophoretic and Electrohydrodynamic Conduction Pumping for Enhancement of Liquid Film Flow Boiling,” *Journal of Heat Transfer*, Vol. 139, No. 6, 2017, p. 061502. <https://doi.org/10.1115/1.4035709>.
- [154] Marchetta, J., and Winter, A., “Simulation of magnetic positive positioning for space based fluid management systems,” *Mathematical and Computer Modelling*, Vol. 51, No. 9, 2010, pp. 1202–1212. <https://doi.org/10.1016/j.mcm.2010.01.002>.
- [155] Kaneko, S., Ishiyama, T., and Sawada, T., “Effect of an applied magnetic field on sloshing pressure in a magnetic fluid,” *Journal of Physics: Conference Series*, Vol. 412, No. 1, 2013, p. 012018. <https://doi.org/10.1088/1742-6596/412/1/012018>.
- [156] Ohaba, M., and Sudo, S., “Liquid surface behavior of a magnetic liquid in a container subjected to magnetic field and vertical vibration,” *Journal of Magnetism and Magnetic Material*, Vol. 149, 1995, pp. 38–41. [https://doi.org/10.1016/0304-8853\(95\)00332-0](https://doi.org/10.1016/0304-8853(95)00332-0).
- [157] Sudo, S., Nishiyama, H., Katagiri, K., and Tani, J., “Interactions of Magnetic Field and the Magnetic Fluid Surface,” *Journal of Intelligent Material Systems and Structures*, Vol. 10, No. 6, 1999, pp. 498–504. <https://doi.org/10.1106/N3PX-57EL-F43B-L4AO>.
- [158] Ishiyama, T., Kaneko, S., Takemoto, S., and Sawada, T., “Relation between Dynamic Pressure and Displacement of Free Surface in Two-Layer Sloshing between a Magnetic Fluid and Silicone Oil,” *Materials Science Forum*, Vol. 792, 2014, pp. 33–38. <https://doi.org/10.4028/www.scientific.net/MSF.792.33>.
- [159] Sawada, T., Ohira, Y., and Houda, H., “Sloshing motion of a magnetic fluid in a cylindrical container due to horizontal oscillation,” *Energy Conversion and Management*, Vol. 43, No. 3, 2002, pp. 299–308. [https://doi.org/10.1016/S0196-8904\(01\)00103-0](https://doi.org/10.1016/S0196-8904(01)00103-0).
- [160] Ohno, K., Shimoda, M., and Sawada, T., “Optimal design of a tuned liquid damper using a magnetic fluid with one electromagnet,” *Journal of Physics: Condensed Matter*, Vol. 20, No. 20, 2008, p. 204146. <https://doi.org/10.1088/0953-8984/20/20/204146>.
- [161] Ohno, K., Suzuki, H., and Sawada, T., “Analysis of liquid sloshing of a tuned magnetic fluid damper for single and co-axial cylindrical containers,” *Journal of Magnetism and Magnetic Materials*, Vol. 323, No. 10, 2011, pp. 1389–1393. <https://doi.org/10.1016/j.jmmm.2010.11.052>.
- [162] Dodge, F. T., and Garza, L. R., “Free-Surface Vibrations of a Magnetic Liquid,” *Journal of Engineering for Industry*, Vol. 94, No. 1, 1972, pp. 103–108. <https://doi.org/10.1115/1.3428097>.
- [163] Martin, J., and Holt, J., “Magnetically Actuated Propellant Orientation Experiment, Controlling fluid Motion With Magnetic Fields in a Low-Gravity Environment,” *Tech. Rep. TM-2000-210129, M-975, NAS 1.15:210129*, NASA, 2000. URL ntrs.nasa.gov/citations/20000036592.

- [164] Hochstein, J., R. Warren, J., George Schmidt, J., Hochstein, J., R. Warren, J., and George Schmidt, J., "Magnetically Actuated Propellant Orientation (MAPO) Experiment - Pre-flight flow field predictions," 35th Aerospace Sciences Meeting and Exhibit, 1997, pp. 1–11. <https://doi.org/10.2514/6.1997-570>, AIAA Paper 1997-570.
- [165] Marchetta, J., and Hochstein, J., "Fluid capture by a permanent ring magnet in reduced gravity," Proceedings of the 37th Aerospace Sciences Meeting and Exhibit, Reno, NV, USA, American Institute of Aeronautics and Astronautics, 1999, pp. 1–14. <https://doi.org/10.2514/6.1999-845>, AIAA Paper 1999-845.
- [166] Marchetta, J., and Hochstein, J., "Simulation and dimensionless modeling of magnetically induced re-orientation," Proceedings of the 38th Aerospace Sciences Meeting and Exhibit, Renno, NV, USA, American Institute of Aeronautics and Astronautics, 2000, pp. 1–13. <https://doi.org/10.2514/6.2000-700>, AIAA Paper 2000-700.
- [167] Marchetta, J., Hochstein, J., Sauter, D., and Simmons, B., "Modeling and prediction of magnetic storage and reorientation of LOX in reduced gravity," 40th AIAA Aerospace Sciences Meeting & Exhibit, American Institute of Aeronautics and Astronautics, 2002, pp. 1–19. <https://doi.org/10.2514/6.2002-1005>, AIAA Paper 2002-1005.
- [168] Marchetta, J. G., "Simulation of LOX reorientation using magnetic positive positioning," Microgravity - Science and Technology, Vol. 18, No. 1, 2006, p. 31. <https://doi.org/10.1007/BF02908417>.
- [169] Marchetta, J., and Roos, K., "A Three-Dimensional Computational Simulation of Magnetic Positive Positioning," 45th AIAA Aerospace Sciences Meeting and Exhibit, 2007, pp. 1–11. <https://doi.org/10.2514/6.2007-956>, AIAA Paper 2007-956.
- [170] Marchetta, J., and Roos, K., "Simulating Magnetic Positive Positioning of Liquids in a Transient Acceleration Field," 46th AIAA Aerospace Sciences Meeting and Exhibit, 2007, pp. 1–11. <https://doi.org/10.2514/6.2008-820>, AIAA Paper 2008-820.
- [171] Marchetta, J. G., Simmons, B. D., and Hochstein, J. I., "Magnetic retention of LO2 in an accelerating environment," Acta Astronautica, Vol. 62, No. 8, 2008, pp. 478–490. <https://doi.org/10.1016/j.actaastro.2008.01.016>.
- [172] Romero-Calvo, A., Hermans, T. H., Gómez, G. C., Benítez, L. P., Gutiérrez, M. H., and Castro-Hernández, E., "Ferrofluid Dynamics in Microgravity Conditions," Proceedings of the 2nd Symposium on Space Educational Activities, Budapest, Hungary, 2018, pp. 1–5.
- [173] Romero-Calvo, A., Hermans, T. H., Benítez, L. P., and Castro-Hernández, E., Drop Your Thesis! 2017 Experiment Report - Ferrofluids Dynamics in Microgravity Conditions, European Space Agency - Erasmus Experiment Archive, 2018.
- [174] Romero-Calvo, A., García-Salcedo, A., Garrone, F., Rivoalen, I., Cano-Gómez, G., Castro-Hernández, E., Gutiérrez, M. H., and Maggi, F., "StELIUM: A student experiment to investigate the sloshing of magnetic liquids in microgravity," Acta Astronautica, Vol. 173, 2020, pp. 344–355. <https://doi.org/10.1016/j.actaastro.2020.04.013>.
- [175] Romero-Calvo, A., García-Salcedo, A., Garrone, F., Rivoalen, I., Gomez, G. C., Castro-Hernández, E., and Maggi, F., "Free surface reconstruction of opaque liquids in microgravity. Part 1: design and on-ground testing," Acta Astronautica, Vol. 189, 2021, pp. 250–259. <https://doi.org/10.1016/j.actaastro.2021.08.029>.
- [176] Romero-Calvo, A., Garrone, F., García-Salcedo, A., Rivoalen, I., Cano-Gómez, G., Castro-Hernández, E., and Maggi, F., "Free surface reconstruction of opaque liquids in microgravity. Part 2: Drop tower campaign," Acta Astronautica, Vol. 189, 2021, pp. 269–277. <https://doi.org/10.1016/j.actaastro.2021.07.020>.

- [177] Romero-Calvo, A., García-Salcedo, A., Garrone, F., Rivoalen, I., and Maggi, F., “Lateral and axisymmetric ferrofluid oscillations in a cylindrical tank in microgravity,” AIAA Journal, Vol. 60, No. 4, 2022, pp. 2707–2712. <https://doi.org/10.2514/1.J061351>.
- [178] Inter-Agency Space Debris Coordination Committee, “IACD Space Debris Mitigation Guidelines,” Tech. Rep. IADC-02-01, IADC, 2020. URL orbitaldebris.jsc.nasa.gov/library/iadc-space-debris-guidelines-revision-2.pdf.
- [179] Anselmo, L., and Pardini, C., “Ranking upper stages in low Earth orbit for active removal,” Acta Astronautica, Vol. 122, 2016, pp. 19–27. <https://doi.org/10.1016/j.actaastro.2016.01.019>.
- [180] Liou, J. C., “An active debris removal parametric study for LEO environment remediation,” Advances in Space Research, Vol. 47, No. 11, 2011, pp. 1865–1876. <https://doi.org/10.1016/j.asr.2011.02.003>.
- [181] McKnight, D., Witner, R., Letizia, F., Lemmens, S., Anselmo, L., Pardini, C., Rossi, A., Kunstadter, C., Kawamoto, S., Aslanov, V., Dolado Perez, J.-C., Ruch, V., Lewis, H., Nicolls, M., Jing, L., Dan, S., Dongfang, W., Baranov, A., and Grishko, D., “Identifying the 50 statistically-most-concerning derelict objects in LEO,” Acta Astronautica, Vol. 181, 2021, pp. 282–291. <https://doi.org/10.1016/j.actaastro.2021.01.021>.
- [182] Trushlyakov, V., and Shatrov, Y., “Improving of technical characteristics of launch vehicles with liquid rocket engines using active onboard de-orbiting systems,” Acta Astronautica, Vol. 138, 2017, pp. 19–27. <https://doi.org/10.1016/j.actaastro.2017.05.018>.
- [183] Lednev, S., Koroleva, T., Krechetov, P., Sharapova, A., Semenov, I., and Karpachevskiy, A., “Revegetation of areas disturbed by rocket impact in Central Kazakhstan,” Ecoscience, Vol. 25, No. 1, 2018, pp. 25–38. <https://doi.org/10.1080/11956860.2017.1396100>.
- [184] Koroleva, T. V., Krechetov, P. P., Semenov, I. N., Sharapova, A. V., Lednev, S. A., Karpachevskiy, A. M., Kondratyev, A. D., and Kasimov, N. S., “The environmental impact of space transport,” Transportation Research Part D: Transport and Environment, Vol. 58, 2018, pp. 54–69. <https://doi.org/10.1016/j.trd.2017.10.013>.
- [185] Patera, R. P., Bohman, K. R., Landa, M. A., Pao, C. D., Urbano, R. T., Weaver, M. D., and White, D. C., “DMSP-17 Upper Stage Controlled Reentry Disposal,” Tech. Rep. ATR-2007(8083)-1, The Aerospace Corporation, 2006.
- [186] Trushlyakov, V. I., Shalay, V. V., and Shatrov, Y. T., “Reduction of the technogenic impact of launch vehicles on the liquid toxic components of rocket fuel on the environment,” Tech. rep., Omsk State Technical University, 2004.
- [187] Giacalone, P., “Detail design of the surface tension propellant management device for the Intelsat VII communication satellite,” AIAA 29th Joint Propulsion Conference and Exhibit, 1993. <https://doi.org/10.2514/6.1993-1802>, AIAA Paper 1993-1802.
- [188] D Jaekle, r., “Propellant management device conceptual design and analysis - Traps and troughs,” 31st Joint Propulsion Conference and Exhibit, 1995. <https://doi.org/10.2514/6.1995-2531>, AIAA Paper 1995-2531.
- [189] Tam, W., Drey, M., D. Jaekle, J., and Larsson, L., “Design and manufacture of an oxidizer tank assembly,” 37th Joint Propulsion Conference and Exhibit, 2001. <https://doi.org/10.2514/6.2001-3825>, AIAA Paper 2001-3825.
- [190] Behruzi, P., “Concept Analysis of PMD Designs for Future Upper Stages,” 54th International Astronautical Congress of the International Astronautical Federation, the International Academy of Astronautics, and the International Institute of Space Law, 2003. <https://doi.org/10.2514/6.IAC-03-S.1.07>.

- [191] Behruzzi, P., and Michaelis, M., “Development of a Propellant Management Device (PMD) for Restartable Future Cryogenic Upper Stages,” 42nd AIAA/ASME/SAE/ASEE Joint Propulsion Conference & Exhibit, 2006. <https://doi.org/10.2514/6.2006-5053>, AIAA Paper 2006-5053.
- [192] Burge, G., and Blackmon, J., “Study and design of cryogenic propellant acquisition systems. Volume 1: Design studies,” Tech. Rep. CR-120300/MDC-G5038-VOL-1, NASA, 1973. URL ntrs.nasa.gov/citations/19740021091.
- [193] Boraas, S., and LaBruna, A. J., “In-Space Propellant Acquisition with Pleated Screen Tubes,” Journal of Spacecraft and Rockets, Vol. 13, No. 6, 1976, pp. 377–384. <https://doi.org/10.2514/3.57101>.
- [194] Hartwig, J. W., “Propellant Management Devices for Low-Gravity Fluid Management: Past, Present, and Future Applications,” Journal of Spacecraft and Rockets, Vol. 54, No. 4, 2017, pp. 808–824. <https://doi.org/10.2514/1.A33750>.
- [195] Darr, S. R., Camarotti, C. F., Hartwig, J. W., and Chung, J. N., “Hydrodynamic model of screen channel liquid acquisition devices for in-space cryogenic propellant management,” Physics of Fluids, Vol. 29, No. 1, 2017, p. 017101. <https://doi.org/10.1063/1.4973671>.
- [196] Platt, G. K., “Space vehicle low gravity fluid mechanics problems and the feasibility of their experimental investigation,” Tech. Rep. TM X-53589, NASA, 1967. URL ntrs.nasa.gov/citations/19670031036.
- [197] Austad, K., “The Common Centaur upper stage,” 37th Joint Propulsion Conference and Exhibit, 2001. <https://doi.org/10.2514/6.2001-3842>, AIAA Paper 2001-3842.
- [198] Space Exploration Technologies Corporation, “Falcon User’s Guide,” , September 2021. URL www.spacex.com/media/falcon-users-guide-2021-09.pdf.
- [199] Anz-Meador, P., “Root Cause Classification of Breakup Events 1961-2018,” First International Orbital Debris Conference, Houston, TX, 2019. URL www.hou.usra.edu/meetings/orbitaldebris2019/orbital2019paper/pdf/6040.pdf.
- [200] Saturn Flight Evaluation Working Group, Marshall Space Flight Center, “Saturn 5 launch vehicle flight evaluation report-AS-511 Apollo 16 mission,” Tech. Rep. TM-X-69535, NASA, 1972. URL ntrs.nasa.gov/citations/19730025090.
- [201] Adzhan, A. P., Akim, E. L., and Alifanov, O. M., “Rocket and space technology,” Engineering Encyclopedia, Vol. 4, 2012, p. 925.
- [202] Jones, H., “The Recent Large Reduction in Space Launch Cost,” 48th International Conference on Environmental Systems, Albuquerque, NM, 2018. URL hdl.handle.net/2346/74082.
- [203] Trushlyakov, V. I., Urbansky, V. A., and Yuditsev, V. V., “Reducing Environmental Damage After Emergency Engine Cutoff of the Launch Vehicle,” Journal of Spacecraft and Rockets, Vol. 58, No. 3, 2021, pp. 685–696. <https://doi.org/10.2514/1.A34912>.
- [204] de Levie, R., “The electrolysis of water,” Journal of Electroanalytical Chemistry, Vol. 476, No. 1, 1999, pp. 92–93. [https://doi.org/10.1016/S0022-0728\(99\)00365-4](https://doi.org/10.1016/S0022-0728(99)00365-4).
- [205] Trasatti, S., “Water electrolysis: who first?” Journal of Electroanalytical Chemistry, Vol. 476, No. 1, 1999, pp. 90–91. [https://doi.org/10.1016/S0022-0728\(99\)00364-2](https://doi.org/10.1016/S0022-0728(99)00364-2).
- [206] Newman, D., “Water electrolysis reaction control system,” Proc. of the 7th Liquid Propulsion Symposium, Chemical Propulsion Information Agency Publications, Vol. 72, 1965, pp. 105–114.
- [207] Roy, R., “Backwards Runs the Reaction,” Mechanical Engineering, Vol. 130, No. 04, 2008, pp. 32–36. <https://doi.org/10.1115/1.2008-APR-3>.

- [208] Papale, W., and Roy, R., “A Water-Based Propulsion System for Advanced Spacecraft,” Space 2006, 2006, pp. 1–13. <https://doi.org/10.2514/6.2006-7240>.
- [209] James, K., Moser, T., Conley, A., Slostad, J., and Hoyt, R., “Performance Characterization of the HYDROS Water Electrolysis Thruster,” Proc. of the Small Satellite Conference 2015, 2015, pp. 1–7. Paper SSC15-XI-5.
- [210] Doyle, K. P., and Peck, M. A., “Water Electrolysis Propulsion as a Case Study in Resource-Based Spacecraft Architecture,” IEEE Aerospace and Electronic Systems Magazine, Vol. 34, No. 9, 2019, pp. 4–19. <https://doi.org/10.1109/MAES.2019.2923312>.
- [211] Burke, K., “Small Portable PEM Fuel Cell Systems for NASA Exploration Missions,” Tech. Rep. TM-2005-213994, NASA, 2005.
- [212] Bents, D., Scullin, V., Chang, B., Johnson, D., and snf I.J. Jakupca, C. G., “Hydrogen-Oxygen PEM Regenerative Fuel Cell Development at NASA Glenn Research Center,” Vol. 2006, 2006, pp. 12–14. [https://doi.org/10.1016/S1464-2859\(06\)70909-9](https://doi.org/10.1016/S1464-2859(06)70909-9).
- [213] Lee, K., “Water electrolysis for in-situ resource utilization (ISRU),” AIAA Houston Section Annual Technical Symposium (ATS 2016), 2016.
- [214] Sowers, G. F., and Dreyer, C. B., “Ice Mining in Lunar Permanently Shadowed Regions,” New Space, Vol. 7, No. 4, 2019, pp. 235–244. <https://doi.org/10.1089/space.2019.0002>.
- [215] Millet, P., and Grigoriev, S., “Chapter 2 - Water Electrolysis Technologies,” Renewable Hydrogen Technologies, edited by L. M. Gandía, G. Arzamendi, and P. M. Diéguez, Elsevier, Amsterdam, 2013, pp. 19–41. <https://doi.org/10.1016/B978-0-444-56352-1.00002-7>.
- [216] Matsushima, H., Nishida, T., Konishi, Y., Fukunaka, Y., Ito, Y., and Kuribayashi, K., “Water electrolysis under microgravity: Part 1. Experimental technique,” Electrochimica Acta, Vol. 48, No. 28, 2003, pp. 4119–4125. [https://doi.org/10.1016/S0013-4686\(03\)00579-6](https://doi.org/10.1016/S0013-4686(03)00579-6).
- [217] Matsushima, H., Fukunaka, Y., and Kuribayashi, K., “Water electrolysis under microgravity: Part II. Description of gas bubble evolution phenomena,” Electrochimica Acta, Vol. 51, No. 20, 2006, pp. 4190–4198. <https://doi.org/10.1016/j.electacta.2005.11.046>.
- [218] Kiuchi, D., Matsushima, H., Fukunaka, Y., and Kuribayashi, K., “Ohmic Resistance Measurement of Bubble Froth Layer in Water Electrolysis under Microgravity,” Journal of The Electrochemical Society, Vol. 153, No. 8, 2006, pp. 138–143. <https://doi.org/10.1149/1.2207008>.
- [219] Iwasaki, A., Kaneko, H., Abe, Y., and Kamimoto, M., “Investigation of electrochemical hydrogen evolution under microgravity condition,” Electrochimica Acta, Vol. 43, No. 5, 1998, pp. 509–514. [https://doi.org/10.1016/S0013-4686\(97\)00096-0](https://doi.org/10.1016/S0013-4686(97)00096-0).
- [220] Holder, D. W., O’Connor, E. W., Zagaja, J., and Murdoch, K., “Investigation into the Performance of Membrane Separator Technologies used in the International Space Station Regenerative Life Support Systems: Results and Lessons Learned,” 31st International Conference On Environmental Systems, SAE International, 2001, pp. 1–14. <https://doi.org/10.4271/2001-01-2354>.
- [221] Samsonov, N. M., Bobe, L. S., Gavrilov, L. I., Korolev, V. P., Novikov, V. M., Farafonov, N. S., Soloukhin, V. A., Romanov, S. J., Andrejchuk, P. O., Protasov, N. N., Rjabkin, A. M., Telegin, A. A., Sinjak, J. E., and Skuratov, V. M., “Water Recovery and Oxygen Generation by Electrolysis Aboard the International Space Station,” International Conference On Environmental Systems, SAE International, 2002. <https://doi.org/10.4271/2002-01-2358>.
- [222] Williams, D. E., and Gentry, G. J., “International Space Station Environmental Control and Life Support System Status: 2004 - 2005,” SAE Transactions, Vol. 114, 2005, pp. 64–75.

- [223] Williams, D. E., and Gentry, G. J., "International Space Station Environmental Control and Life Support System Status: 2005 - 2006," International Conference On Environmental Systems, SAE International, 2006. <https://doi.org/10.4271/2006-01-2055>.
- [224] Williams, D. E., and Gentry, G. J., "International Space Station Environmental Control and Life Support System Status: 2006 - 2007," International Conference On Environmental Systems, SAE International, 2007. <https://doi.org/10.4271/2007-01-3098>.
- [225] Takada, K., Velasquez, L. E., Keuren, S. V., Baker, P. S., and McDougale, S. H., "Advanced Oxygen Generation Assembly for Exploration Missions," 49th International Conference On Environmental Systems, Boston, Massachusetts, 2019.
- [226] Sakurai, M., Sone, Y., Nishida, T., Matsushima, H., and Fukunaka, Y., "Fundamental study of water electrolysis for life support system in space," Electrochimica Acta, Vol. 100, 2013, pp. 350–357. <https://doi.org/10.1016/j.electacta.2012.11.112>.
- [227] Sakurai, M., Terao, T., and Sone, Y., "Development of Water Electrolysis System for Oxygen Production Aimed at Energy Saving and High Safety," 45th International Conference on Environmental Systems, Bellevue, Washington, 2016.
- [228] Sakurai, M., Terao, T., and Sone, Y., "Study on Water Electrolysis for Oxygen Production -Reduction of Water Circulation and Gas-Liquid Separator-," 47th International Conference on Environmental Systems, Charleston, South Carolina, 2017.
- [229] Sakai, Y., Oka, T., Waseda, S., Arai, T., Suehiro, T., Ito, T., Shima, A., and Sakurai, M., "Development status of air revitalization system in JAXA closed ECLSS for future crew module," 48th International Conference on Environmental Systems, Albuquerque, New Mexico, 2018.
- [230] Powell, J., Schubert, F., and Jensen, F., "Static feed water electrolysis module," Tech. Rep. CR-137577, NASA, 1974. URL ntrs.nasa.gov/citations/19750012429.
- [231] Schubert, F., Wynveen, R., Jensen, F., and Quattrone, P., "Development of an advanced static feed water electrolysis module," Proc. of the Intersociety Conference on Environmental Systems, 1975. URL www.jstor.org/stable/44470316.
- [232] Fortunato, F. A., Kovach, A. J., and Wolfe, L. E., "Static Feed Water Electrolysis System for Space Station Oxygen and Hydrogen Generation," SAE Transactions, Vol. 97, 1988, pp. 190–198. URL www.jstor.org/stable/44470316.
- [233] Powell, J., Schubert, F., and Lee, M., "Impact of low gravity on water electrolysis operation," Tech. Rep. CR-185521, NASA, 1989. URL ntrs.nasa.gov/citations/19900012554.
- [234] Davenport, R. J., Schubert, F. H., and Grigger, D. J., "Space water electrolysis: space station through advanced missions," Journal of Power Sources, Vol. 36, No. 3, 1991, pp. 235–250. [https://doi.org/10.1016/0378-7753\(91\)87004-U](https://doi.org/10.1016/0378-7753(91)87004-U), proceedings of the Third Space Electrochemical Research and Technology Conference.
- [235] Schubert, F., "Electrolysis Performance Improvement Concept Study (EPICS) Flight Experiment-Reflight," Tech. Rep. CR-205554, TR-1415-57, NASA, 1997. URL ntrs.nasa.gov/citations/19970040610.
- [236] Knorr, W., Tan, G., and Witt, J., "The FAE Electrolyser Flight Experiment FAVORITE: Current Development Status and Outlook," International Conference On Environmental Systems, SAE International, 2004. <https://doi.org/10.4271/2004-01-2490>.
- [237] Fahr, Hans J., and Heyl, M., "Debye screening under non-equilibrium plasma conditions," Astronomy & Astrophysics, Vol. 589, 2016, p. A85. <https://doi.org/10.1051/0004-6361/201628082>.

- [238] Seubert, C. R., Stiles, L. A., and Schaub, H., “Effective Coulomb force modeling for spacecraft in Earth orbit plasmas,” *Advances in Space Research*, Vol. 54, No. 2, 2014, pp. 209–220. <https://doi.org/10.1016/j.asr.2014.04.005>.
- [239] Thiébaud, B., Hilgers, A., Sasot, E., Laakso, H., Escoubet, P., Génot, V., and Forest, J., “Potential barrier in the electrostatic sheath around a magnetospheric spacecraft,” *Journal of Geophysical Research: Space Physics*, Vol. 109, No. A12, 2004, p. 12207. <https://doi.org/10.1029/2004JA010398>.
- [240] Engwall, E., Eriksson, A. I., and Forest, J., “Wake formation behind positively charged spacecraft in flowing tenuous plasmas,” *Physics of Plasmas*, Vol. 13, No. 6, 2006, p. 062904. <https://doi.org/10.1063/1.2199207>.
- [241] Ergun, R. E., Malaspina, D. M., Bale, S. D., McFadden, J. P., Larson, D. E., Mozer, F. S., Meyer-Vernet, N., Maksimovic, M., Kellogg, P. J., and Wygant, J. R., “Spacecraft charging and ion wake formation in the near-Sun environment,” *Physics of Plasmas*, Vol. 17, No. 7, 2010, p. 072903. <https://doi.org/10.1063/1.3457484>.
- [242] Guillemant, S., Génot, V., Vélez, J.-C. M., Sarrailh, P., Hilgers, A., and Louarn, P., “Simulation Study of Spacecraft Electrostatic Sheath Changes With the Heliocentric Distances From 0.044 to 1 AU,” *IEEE Transactions on Plasma Science*, Vol. 41, No. 12, 2013, pp. 3338–3348. <https://doi.org/10.1109/TPS.2013.2246193>.
- [243] Wang, X., Pilewskie, J., Hsu, H.-W., and Horányi, M., “Plasma potential in the sheaths of electron-emitting surfaces in space,” *Geophysical Research Letters*, Vol. 43, No. 2, 2016, pp. 525–531. <https://doi.org/10.1002/2015GL067175>.
- [244] Seely, S., “Work Function and Temperature,” *Phys. Rev.*, Vol. 59, 1941, pp. 75–78. <https://doi.org/10.1103/PhysRev.59.75>, URL link.aps.org/doi/10.1103/PhysRev.59.75.
- [245] Pomerantz, M. A., “The Temperature Dependence of Secondary Electron Emission from Oxide-Coated Cathodes,” *Phys. Rev.*, Vol. 70, 1946, pp. 33–40. <https://doi.org/10.1103/PhysRev.70.33>, URL link.aps.org/doi/10.1103/PhysRev.70.33.
- [246] Zeng, L., Zhou, X., Cheng, R., Wang, X., Ren, J., Lei, Y., Ma, L., Zhao, Y., Zhang, X., and Xu, Z., “Temperature and energy effects on secondary electron emission from SiC ceramics induced by Xe¹⁷⁺ ions,” *Scientific Reports*, Vol. 7, No. 1, 2017, p. 6482. <https://doi.org/10.1038/s41598-017-06891-9>.
- [247] Wertz, J., and Larson, W., *Space Mission Analysis and Design*, Space Technology Library, Springer Netherlands, 1999.
- [248] Sanders, N. L., and Inouye, G. T., “Secondary emission effects on spacecraft charging: Energy distribution considerations,” *Spacecraft Charging Technology*, 1978, pp. 747–755. NASA-2071, ADA-084626.
- [249] Baglin, V., Bojko, J., Gröbner, O., Henrist, B., Hilleret, N., Scheuerlein, C., and Taborrelli, M., “The secondary electron yield of technical materials and its variation with surface treatments,” *Proceedings of 7th European Particle Accelerator Conference, Vienna, Austria*, 2000, pp. 217–221.
- [250] Robertson, S., Sternovsky, Z., and Walch, B., “Reduction of asymmetry transport in the annular Penning trap,” *Physics of Plasmas*, Vol. 11, No. 5, 2004, pp. 1753–1756. <https://doi.org/10.1063/1.1688337>.
- [251] Jin, C., Ottaviano, A., and Raites, Y., “Secondary electron emission yield from high aspect ratio carbon velvet surfaces,” *Journal of Applied Physics*, Vol. 122, No. 17, 2017, p. 173301. <https://doi.org/10.1063/1.4993979>.
- [252] Reyes, J. A., Fulford, K. W., Plis, E. A., Hoffmann, R. C., Murray, V. J., Cowardin, H. M., Cone, D., Ferguson, D. C., Bengtson, M. T., Shah, J. R., and Engelhart, D. P., “Spectroscopic behavior of various materials in a GEO simulated environment,” *Acta Astronautica*, Vol. 189, 2021, pp. 576–583. <https://doi.org/10.1016/j.actaastro.2021.09.014>.

- [253] Christensen, J., “Electron Yield Measurements of High-Yield, Low-Conductivity Dielectric Materials,” Ph.D. thesis, Utah State University, 2017. <https://doi.org/10.26076/7417-7547>.
- [254] Darlington, E. H., and Cosslett, V. E., “Backscattering of 0.5-10 keV electrons from solid targets,” *Journal of Physics D: Applied Physics*, Vol. 5, No. 11, 1972, pp. 1969–1981. <https://doi.org/10.1088/0022-3727/5/11/305>.
- [255] Laframboise, J., and Kamitsuma, M., “The threshold temperature effect in high voltage spacecraft charging,” *Proceedings of Air Force Geophysics Workshop on Natural Charging of Large Space Structures in Near Earth Polar Orbit*, 1983, pp. 293–308. AFRL-TR-83-0046, ADA-134-894.
- [256] Bruining, H., *Physics and Applications of Secondary Electron Emission*, New York: McGraw-Hill Book Co., Inc. London: Pergamon Press Ltd., 1954. Chapter 7: Theory of Secondary Electron Emission; Discussion of Some Properties of Secondary Electrons.
- [257] Greenwood, J., “The correct and incorrect generation of a cosine distribution of scattered particles for Monte-Carlo modelling of vacuum systems,” *Vacuum*, Vol. 67, No. 2, 2002, pp. 217–222. [https://doi.org/10.1016/S0042-207X\(02\)00173-2](https://doi.org/10.1016/S0042-207X(02)00173-2).
- [258] Chung, M. S., and Everhart, T. E., “Simple calculation of energy distribution of low-energy secondary electrons emitted from metals under electron bombardment,” *Journal of Applied Physics*, Vol. 45, No. 2, 1974, pp. 707–709. <https://doi.org/10.1063/1.1663306>.
- [259] Jeanneret, J., “Photoemission in LHC - A simple model,” Tech. Rep. Note 97-48 (AP), CERN, 1997. URL citeseerx.ist.psu.edu/viewdoc/download?doi=10.1.1.17.5847&rep=rep1&type=pdf.
- [260] POWELL, C. J., “Analysis of Optical- and Inelastic-Electron-Scattering Data. III. Reflectance Data for Beryllium, Germanium, Antimony, and Bismuth,” *J. Opt. Soc. Am.*, Vol. 60, No. 2, 1970, pp. 214–220. <https://doi.org/10.1364/JOSA.60.000214>.
- [261] Lai, S., and Tautz, M., “Aspects of Spacecraft Charging in Sunlight,” *IEEE Transactions on Plasma Science*, Vol. 34, No. 5, 2006, pp. 2053–2061. <https://doi.org/10.1109/TPS.2006.883362>.
- [262] Bennett, H., and Porteus, J., “Relation between surface roughness and specular reflectance at normal incidence,” *JOSA*, Vol. 51, No. 2, 1961, pp. 123–129. <https://doi.org/10.1364/JOSA.51.000123>.
- [263] Lai, S. T., “Charging of mirror surfaces in space,” *Journal of Geophysical Research: Space Physics*, Vol. 110, No. A01204, 2005. <https://doi.org/10.1029/2002JA009447>.
- [264] Everhart, T. E., “Simple Theory Concerning the Reflection of Electrons from Solids,” *Journal of Applied Physics*, Vol. 31, No. 8, 1960, pp. 1483–1490. <https://doi.org/10.1063/1.1735868>.
- [265] Cooper, R., and Hoffman, R., “Jumbo Space Environment Simulation and Spacecraft Charging Chamber Characterization,” Technical report, Air Force Research Laboratory, Space Vehicles Directorate, Albuquerque, New Mexico, 4 2015. URL apps.dtic.mil/sti/pdfs/AD1000521.pdf.
- [266] Paulmier, T., Dirassen, B., Belhaj, M., Inguibert, V., Duzellier, S., Pons, C., Rémaury, S., and Payan, D., “Experimental Test Facilities for Representative Characterization of Space Used Materials,” *14th Spacecraft Charging Technology Conference*, Noordwijk, Netherlands, 2016.
- [267] Dennison, J., Thomson, C., Kite, J., Zavyalov, V., and Corbridge, J., “Materials Characterization at Utah State University: Facilities and Knowledgebase of Electronic Properties of Materials Applicable to Spacecraft Charging,” *8th Spacecraft Charging Technology Conference*, Huntsville, Alabama, 2003.
- [268] Mcernan, J. K., Bilén, S. G., and Krause, L. H., “Facility for Real-time Test and Verification of LEO Space Plasma Phenomena,” *Applied Space Environments Conference*, Huntsville, AL, 2017.
- [269] Kuegler, H., “Performance improvement of the magnetic field simulation facility MFSA,” *Proceedings of the 5th International Symposium on Environmental Testing for Space Programmes*, Noordwijk (ESA SP-558, June 2004), 2004, pp. 407–414.

- [270] Vernier, R., Bonalosky, T., and Slavin, J., “Goddard Space Flight Center Spacecraft Magnetic Test Facility Restoration Project,” 23rd Space Simulation Conference Proceedings, 2004. NASA/CP-2005-212775.
- [271] Knuth, D., The Art of Computer Programming, 3rd ed., Vol. 2, Addison-Wesley Longman Publishing Co., Inc., Boston, MA, USA, 1997.
- [272] Hammerl, J., Romero-Calvo, A., López, A., and Schaub, H., “Touchless potential sensing of complex differentially-charged shapes using X-rays,” Proceedings of the AIAA SciTech 2022 Forum and Exposition, 2022, pp. 1–13. <https://doi.org/10.2514/6.2022-2312>, AIAA Paper 2022-2312.
- [273] Okuda, H., and Berchem, J., “Injection and propagation of a nonrelativistic electron beam and spacecraft charging,” Journal of Geophysical Research: Space Physics, Vol. 93, No. A1, 1988, pp. 175–195. <https://doi.org/10.1029/JA093iA01p00175>.
- [274] Okuda, H., and Ashour-Abdalla, M., “Propagation of a nonrelativistic electron beam in three dimensions,” Journal of Geophysical Research: Space Physics, Vol. 95, No. A3, 1990, pp. 2389–2404. <https://doi.org/10.1029/JA095iA03p02389>.
- [275] Okuda, H., and Ashour-Abdalla, M., “Injection of an overdense electron beam in space,” Journal of Geophysical Research: Space Physics, Vol. 95, No. A12, 1990, pp. 21307–21311. <https://doi.org/10.1029/JA095iA12p21307>.
- [276] Winglee, R. M., “Simulations of pulsed electron beam injection during active experiments,” Journal of Geophysical Research: Space Physics, Vol. 96, No. A2, 1991, pp. 1803–1817. <https://doi.org/10.1029/90JA02102>.
- [277] Koga, J., and Lin, C. S., “A simulation study of radial expansion of an electron beam injected into an ionospheric plasma,” Journal of Geophysical Research: Space Physics, Vol. 99, No. A3, 1994, pp. 3971–3983. <https://doi.org/10.1029/93JA02230>.
- [278] Harting, E., and F.H., R., Electrostatic Lenses, Elsevier Publishing Company, Amsterdam, 1976.
- [279] Read, F. H., Chalupka, A., and Bowering, N. J., “Charge-tube method for space charge in beams,” Charged Particle Optics IV, Vol. 3777, edited by E. Munro, International Society for Optics and Photonics, SPIE, 1999, pp. 184 – 191. <https://doi.org/10.1117/12.370129>.
- [280] Renau, A., Read, F. H., and Brunt, J. N. H., “The charge-density method of solving electrostatic problems with and without the inclusion of space-charge,” Journal of Physics E: Scientific Instruments, Vol. 15, No. 3, 1982, pp. 347–354. <https://doi.org/10.1088/0022-3735/15/3/025>.
- [281] Humphries, S., Charged Particle Beams, Wiley, 1990. Chapter 5: Introduction to Beam-Generated Forces.
- [282] Gendrin, R., “Initial expansion phase of an artificially injected electron beam,” Planetary and Space Science, Vol. 22, No. 4, 1974, pp. 633–636. [https://doi.org/10.1016/0032-0633\(74\)90097-X](https://doi.org/10.1016/0032-0633(74)90097-X).
- [283] Stevenson, D., and Schaub, H., “Multi-Sphere Method for modeling spacecraft electrostatic forces and torques,” Advances in Space Research, Vol. 51, No. 1, 2013, pp. 10–20. <https://doi.org/10.1016/j.asr.2012.08.014>.
- [284] Lewellen, J. W., Buechler, C. E., Carlsten, B. E., Dale, G. E., Holloway, M. A., Patrick, D. E., Storms, S. A., and Nguyen, D. C., “Space-Borne Electron Accelerator Design,” Frontiers in Astronomy and Space Sciences, Vol. 6, 2019, p. 35. <https://doi.org/10.3389/fspas.2019.00035>.
- [285] Smythe, W., Static and Dynamic Electricity, 3rd ed., McGraw-Hill, 1968.
- [286] Hughes, J. A., and Schaub, H., “Heterogeneous Surface Multisphere Models Using Method of Moments Foundations,” Journal of Spacecraft and Rockets, Vol. 56, No. 4, 2019, pp. 1259–1266. <https://doi.org/10.2514/1.A34434>.

- [287] Qin, H., Zhang, S., Xiao, J., Liu, J., Sun, Y., and Tang, W. M., “Why is Boris algorithm so good?” Physics of Plasmas, Vol. 20, No. 8, 2013, p. 084503. <https://doi.org/10.1063/1.4818428>.
- [288] Shampine, L. F., and Reichelt, M. W., “The MATLAB ODE Suite,” SIAM Journal on Scientific Computing, Vol. 18, No. 1, 1997, pp. 1–22. <https://doi.org/10.1137/S1064827594276424>.
- [289] Wilson, K., and Schaub, H., “Impact of Electrostatic Perturbations on Proximity Operations in High Earth Orbits,” Journal of Spacecraft and Rockets, Vol. 58, No. 5, 2021, pp. 1293–1302. <https://doi.org/10.2514/1.A35039>.
- [290] Cannavó, F., “Sensitivity analysis for volcanic source modeling quality assessment and model selection,” Computers & Geosciences, Vol. 44, 2012, pp. 52–59. <https://doi.org/10.1016/j.cageo.2012.03.008>.
- [291] Wilson, K. T. H., and Schaub, H., “An X-ray Spectroscopic Approach to Remote Space Object Potential Determination: Experimental Results,” AIAA SciTech, Orlando, Florida, 2020. <https://doi.org/10.2514/6.2020-0049>, AIAA Paper 2020-0049.
- [292] Hoffmann, R. C., “Electron-Induced Electron Yields of Uncharged Insulating Material,” Ph.D. thesis, Physics Department, Utah State University, 2010. <https://doi.org/10.26076/1e55-9dc9>.
- [293] Diaz-Aguado, M. F., Bonnell, J. W., Bale, S. D., Rezvani, S. J., Koshmak, K., Giglia, A., Nannarone, S., and Gruntman, M., “Experimental Investigation of Total Photoemission Yield from New Satellite Surface Materials,” Journal of Spacecraft and Rockets, Vol. 56, No. 1, 2019, pp. 248–258. <https://doi.org/10.2514/1.A34245>.
- [294] Van Grieken, R. E., and Markowicz, A. A., Handbook of X-Ray Spectrometry, Marcel Dekker Inc., 2001. Second Edition.
- [295] Álvaro Romero Calvo, Hammerl, J., and Schaub, H., “Touchless Potential Sensing of Differentially-Charged Spacecraft Using Secondary Electrons,” Journal of Spacecraft and Rockets, 2022. <https://doi.org/10.2514/1.A35355>, *in press*.
- [296] Powell, R., “Photoelectric effect: Back to basics,” American Journal of Physics, Vol. 46, No. 10, 1978, pp. 1046–1051. <https://doi.org/10.1119/1.11493>.
- [297] Küstler, G., “Diamagnetic Levitation - Historical Milestones,” Revue Roumaine des Sciences Techniques - Électrotechnique et Électroénergétique, Vol. 52, 2007, pp. 265–282.
- [298] Jackson, R., “John Tyndall and the Early History of Diamagnetism,” Annals of science, Vol. 72, No. 4, 2015, pp. 435–489. <https://doi.org/10.1080/00033790.2014.929743>.
- [299] Iadonisi, G., Cantele, G., and Chiofalo, M. L., Introduction to Solid State Physics and Crystalline Nanostructures, Springer, 2014. <https://doi.org/10.1007/978-88-470-2805-0>.
- [300] Kuchel, P., Chapman, B., Bubb, W., Hansen, P., Durrant, C., and Hertzberg, M., “Magnetic susceptibility: Solutions, emulsions, and cells,” Concepts in Magnetic Resonance Part A, Vol. 18A, No. 1, 2003, pp. 56–71. <https://doi.org/10.1002/cmr.a.10066>.
- [301] Engel, A., and Friedrichs, R., “On the electromagnetic force on a polarizable body,” American Journal of Physics, Vol. 70, No. 4, 2002, pp. 428–432. <https://doi.org/10.1119/1.1432971>.
- [302] Rosensweig, R. E., “Continuum equations for magnetic and dielectric fluids with internal rotations,” The Journal of Chemical Physics, Vol. 121, No. 3, 2004, pp. 1228–1242. <https://doi.org/10.1063/1.1755660>.
- [303] Rosensweig, R. E., “Stress Boundary-Conditions in Ferrohydrodynamics,” Industrial & Engineering Chemistry Research, Vol. 46, No. 19, 2007, pp. 6113–6117. <https://doi.org/10.1021/ie060657e>.

- [304] Jackson, J. D., Classical electrodynamics, 3rd ed., Wiley, New York, NY, 1999.
- [305] Neuringer, J. L., and Rosensweig, R. E., “Ferrohydrodynamics,” The Physics of Fluids, Vol. 7, No. 12, 1964, pp. 1927–1937. <https://doi.org/10.1063/1.1711103>.
- [306] Satterlee, H. M., and Reynolds, W. C., “The Dynamics of Free Liquid Surface in Cylindrical Containers Under Strong Capillary and Weak Gravity Conditions,” Stanford University Mechanical Engineering Department, Vol. Report LG-2, No. LG-2, 1964.
- [307] Lamb, H., Hydrodynamics, Cambridge University Press, 1895.
- [308] Dodge, F. T., and Garza, L. R., “Experimental and Theoretical Studies of Liquid Sloshing at Simulated Low Gravity,” Journal of Applied Mechanics, Vol. 34, No. 3, 1967, pp. 555–562. <https://doi.org/10.1115/1.3607743>.
- [309] Salzman, J. A., and Masica, W. J., “Lateral Sloshing in Cylinders Under Low-Gravity Conditions,” Tech. Rep. TN D-5058, NASA, 1969.
- [310] Dodge, F., “Further Studies of Propellant Sloshing Under Low-Gravity Conditions,” Tech. Rep. CR-119892, NASA, 1971. URL ntrs.nasa.gov/citations/19720007133.
- [311] Sawada, T., Kikura, H., and Tanahashi, T., “Kinematic characteristics of magnetic fluid sloshing in a rectangular container subject to non-uniform magnetic fields,” Experiments in Fluids, Vol. 26, No. 3, 1999, pp. 215–221. <https://doi.org/10.1007/s003480050282>.
- [312] Hildebrand, F., Methods of applied mathematics, Prentice-Hall, 1965.
- [313] P. Concus, G. C., and Satterlee, H., “Small amplitude lateral sloshing in a cylindrical tank with a hemispherical bottom under low gravitational conditions,” Tech. Rep. CR-54700, LMSC-A852007, NASA, January 1967. URL ntrs.nasa.gov/citations/19670017255.
- [314] P. Concus, G. C., and Satterlee, H., “Small amplitude lateral sloshing in spheroidal containers under low gravitational conditions,” NASA Technical Note, Vol. NASA-CR-72500, LMSC-A944673, No. CR-72500, 1969.
- [315] Concus, P., and Crane, G. E., “Discussion: ”Free and Forced Oscillations of a Liquid in an Axisymmetric Tank at Low-Gravity Environments”,” Journal of Applied Mechanics, Vol. 34, No. 4, 1967, pp. 1051–1052. <https://doi.org/10.1115/1.3607829>.
- [316] Romero-Calvo, A., Herrada, M. A., Hermans, T. H., P. Benítez, L., Cano-Gómez, G., and Castro-Hernández, E., “Axisymmetric ferrofluid oscillations in a cylindrical tank in microgravity,” Microgravity Science and Technology, Vol. 33, No. 50, 2021. <https://doi.org/10.1007/s12217-021-09894-4>.
- [317] Roland, C., John R., G., and Martin E., W., Bubbles, Drops and Particles, Academic Press, 1978.
- [318] Angulo, A., [van der Linde], P., Gardeniers, H., Modestino, M., and Rivas], D. F., “Influence of Bubbles on the Energy Conversion Efficiency of Electrochemical Reactors,” Joule, Vol. 4, No. 3, 2020, pp. 555–579. <https://doi.org/10.1016/j.joule.2020.01.005>.
- [319] Duhar, G., and Colin, C., “Dynamics of bubble growth and detachment in a viscous shear flow,” Physics of Fluids, Vol. 18, No. 7, 2006, p. 077101. <https://doi.org/10.1063/1.2213638>.
- [320] Stephan, K., Physical Fundamentals of Vapor Bubble Formation, Springer Berlin Heidelberg, Berlin, Heidelberg, 1992. https://doi.org/10.1007/978-3-642-52457-8_10.
- [321] Kulkarni, A. A., and Joshi, J. B., “Bubble Formation and Bubble Rise Velocity in Gas-Liquid Systems: A Review,” Industrial & Engineering Chemistry Research, Vol. 44, No. 16, 2005, pp. 5873–5931. <https://doi.org/10.1021/ie049131p>.

- [322] Tomiyama, A., Celata, G., Hosokawa, S., and Yoshida, S., “Terminal velocity of single bubbles in surface tension force dominant regime,” *International Journal of Multiphase Flow*, Vol. 28, No. 9, 2002, pp. 1497–1519. [https://doi.org/10.1016/S0301-9322\(02\)00032-0](https://doi.org/10.1016/S0301-9322(02)00032-0).
- [323] Liu, L., Yan, H., Zhao, G., and Zhuang, J., “Experimental studies on the terminal velocity of air bubbles in water and glycerol aqueous solution,” *Experimental Thermal and Fluid Science*, Vol. 78, 2016, pp. 254–265. <https://doi.org/10.1016/j.expthermflusci.2016.06.011>.
- [324] Landau, L., and Lifshitz, E., “Chapter I - Ideal Fluids,” *Fluid Mechanics (Second Edition)*, edited by L. LANDAU and E. LIFSHITZ, Pergamon, 1987, second edition ed., pp. 30–31. <https://doi.org/10.1016/B978-0-08-033933-7.50009-X>.
- [325] Manica, R., Klaseboer, E., and Chan, D. Y., “The hydrodynamics of bubble rise and impact with solid surfaces,” *Advances in Colloid and Interface Science*, Vol. 235, 2016, pp. 214–232. <https://doi.org/10.1016/j.cis.2016.06.010>.
- [326] Stokes, G., *Mathematical and Physical Papers*, Cambridge University Press, 1880.
- [327] Nicolás, J. A., and Vega, J. M., “A note on the effect of surface contamination in water wave damping,” *Journal of Fluid Mechanics*, Vol. 410, 2000, pp. 367–373. <https://doi.org/10.1017/S002211209900823X>.
- [328] Herrada, M. A., Montanero, J. M., and Vega, J. M., “The effect of surface shear viscosity on the damping of oscillations in millimetric liquid bridges,” *Physics of Fluids*, Vol. 23, No. 8, 2011, p. 082102. <https://doi.org/10.1063/1.3623425>.
- [329] Kelsall, G. H., Tang, S., Smith, A. L., and Yurdakul, S., “Measurement of rise and electrophoretic velocities of gas bubbles,” *J. Chem. Soc., Faraday Trans.*, Vol. 92, 1996, pp. 3879–3885. <https://doi.org/10.1039/FT9969203879>.
- [330] Hadamard, J., “Mouvement permanent lent d’une sphère liquide et visqueuse dans un liquide visqueux,” *C. R. Acad. Sci.*, Vol. 152, 1911, pp. 1735–1752.
- [331] Hadamard, J., “On the translatory motion of a fluid sphere in a viscous medium,” *Bull. Acad. Sci., Cracow*, Vol. A, 1911, p. 40.
- [332] Parkinson, L., Sedev, R., Fornasiero, D., and Ralston, J., “The terminal rise velocity of 10-100 microm diameter bubbles in water,” *J Colloid Interface Sci*, Vol. 322, No. 1, 2008, pp. 168–172. <https://doi.org/10.1016/j.jcis.2008.02.072>.
- [333] Sadhal, S. S., and Johnson, R. E., “Stokes flow past bubbles and drops partially coated with thin films. Part 1. Stagnant cap of surfactant film – exact solution,” *Journal of Fluid Mechanics*, Vol. 126, 1983, p. 237–250. <https://doi.org/10.1017/S0022112083000130>.
- [334] Kure, I. K., Jakobsen, H. A., La Forgia, N., and Solsvik, J., “Experimental investigation of single bubbles rising in stagnant liquid: Statistical analysis and image processing,” *Physics of Fluids*, Vol. 33, No. 10, 2021, p. 103611. <https://doi.org/10.1063/5.0061581>.
- [335] ZARM, *ZARM Drop Tower User Manual*, ZARM FABmbH, 2011. URL www.zarm.uni-bremen.de/fileadmin/images/droptower/downloads/Users_Manual_0611.pdf, drop Tower Operation and Service Company.
- [336] Shliomis, M., “Effective Viscosity of Magnetic Suspensions,” *Soviet Physics JETP*, Vol. 34, 1972, pp. 1291–1294.
- [337] Rigoni, C., Pierno, M., Mistura, G., Talbot, D., Massart, R., Bacri, J.-C., and Abou-Hassan, A., “Static Magnetowetting of Ferrofluid Drops,” *Langmuir*, Vol. 32, No. 30, 2016, pp. 7639–7646. <https://doi.org/10.1021/acs.langmuir.6b01934>.

- [338] Souza, P., Lira, S., and de Oliveira, I., “Wetting dynamics of ferrofluids on substrates with different hydrophilicity behaviors,” *Journal of Magnetism and Magnetic Materials*, Vol. 483, 2019, pp. 129–135. <https://doi.org/10.1016/j.jmmm.2019.03.069>.
- [339] Guba, S., Horváth, B., and Szalai, I., “Examination of contact angles of magnetic fluid droplets on different surfaces in uniform magnetic field,” *Journal of Magnetism and Magnetic Materials*, Vol. 498, 2020, p. 166181. <https://doi.org/10.1016/j.jmmm.2019.166181>.
- [340] Shi, D., Bi, Q., He, Y., and Zhou, R., “Experimental investigation on falling ferrofluid droplets in vertical magnetic fields,” *Experimental Thermal and Fluid Science*, Vol. 54, No. April, 2014, pp. 313–320. <https://doi.org/10.1016/j.expthermflusci.2014.01.010>.
- [341] Bakuzis, A. F., Chen, K., Luo, W., and Zhuang, H., “Magnetic Body Force,” *International Journal of Modern Physics B*, Vol. 19, No. 07n09, 2005, pp. 1205–1208. <https://doi.org/10.1142/S0217979205030074>.
- [342] Petit, M., Kedous-Lebouc, A., Avenas, Y., Tawk, M., and Arteaga, E., “Calculation and analysis of local magnetic forces in ferrofluids,” *Przegląd Elektrotechniczny (Electrical Review)*, Vol. 87, 2011, pp. 115–119. URL pe.org.pl/articles/2011/9b/27.pdf.
- [343] Moghadam, M. E., Shafii, M. B., and Dehkordi, E. A., “Hydromagnetic Micropump and Flow Controller. Part A: Experiments with nickel particles added to the water,” *Experimental Thermal and Fluid Science*, Vol. 33, 2009, pp. 1021–1028. <https://doi.org/10.1016/j.expthermflusci.2009.05.004>.
- [344] Romero-Calvo, A., Herrada, M., Cano-Gómez, G., and Schaub, H., “Advanced numerical simulation of magnetic liquid sloshing in microgravity,” *Proceedings of the International Astronautical Congress, The CyberSpace Edition*, 2020, pp. 1–8.
- [345] Dimakopoulos, Y., and Tsamopoulos, J., “A quasi-elliptic transformation for moving boundary problems with large anisotropic deformations,” *Journal of Computational Physics*, Vol. 192, No. 2, 2003, pp. 494–522. <https://doi.org/10.1016/j.jcp.2003.07.027>.
- [346] Romero-Calvo, A., Maggi, F., and Schaub, H., “Magnetic Positive Positioning: Toward the application in space propulsion,” *Acta Astronautica*, Vol. 187, 2021, pp. 348–361. <https://doi.org/10.1016/j.actaastro.2021.06.045>.
- [347] Berkovsky, B. M., and Smirnov, N. N., “Capillary hydrodynamic effects in high magnetic fields,” *Journal of Fluid Mechanics*, Vol. 187, 1988, p. 319–327. <https://doi.org/10.1017/S0022112088000448>.
- [348] Lin, P., Lin, X., Johns, L. E., and Narayanan, R., “Stability of a static liquid bridge knowing only its shape,” *Phys. Rev. Fluids*, Vol. 4, 2019, p. 123904. <https://doi.org/10.1103/PhysRevFluids.4.123904>.
- [349] White, N. C., and Troian, S. M., “Why capillary flows in slender triangular grooves are so stable against disturbances,” *Phys. Rev. Fluids*, Vol. 4, 2019, p. 054003. <https://doi.org/10.1103/PhysRevFluids.4.054003>.
- [350] Qi, L., and Christopher, G. F., “Effects of non-ionic surfactant on the formation of pellicles by *Pseudomonas aeruginosa*,” *Rheologica Acta*, Vol. 61, No. 1, 2022, pp. 59–68. <https://doi.org/10.1007/s00397-021-01313-0>.
- [351] Wilson, J. W., Ott, C. M., zu Bentrup, K. H., Ramamurthy, R., Quick, L., Porwollik, S., Cheng, P., McClelland, M., Tsapralis, G., Radabaugh, T., Hunt, A., Fernandez, D., Richter, E., Shah, M., Kilcoyne, M., Joshi, L., Nelman-Gonzalez, M., Hing, S., Parra, M., Dumars, P., Norwood, K., Bober, R., Devich, J., Ruggles, A., Goulart, C., Rupert, M., Stodieck, L., Stafford, P., Catella, L., Schurr, M. J., Buchanan, K., Morici, L., McCracken, J., Allen, P., Baker-Coleman, C., Hammond, T., Vogel, J., Nelson, R., Pierson, D. L., Stefanyshyn-Piper, H. M., and Nickerson, C. A., “Space Flight Alters Bacterial Gene Expression and Virulence and Reveals a Role for Global Regulator Hfq,” *Proceedings of the National Academy of Sciences of the United States of America*, Vol. 104, No. 41, 2007, pp. 16299–16304. URL www.jstor.org/stable/25449309.

- [352] Yang, X., Tschulik, K., Uhlemann, M., Odenbach, S., and Eckert, K., “Magnetic Separation of Paramagnetic Ions From Initially Homogeneous Solutions,” IEEE Transactions on Magnetics, Vol. 50, No. 11, 2014, pp. 1–4. <https://doi.org/10.1109/TMAG.2014.2324284>.
- [353] Sahasrabudhe, S. N., Rodriguez-Martinez, V., O’Meara, M., and Farkas, B. E., “Density, viscosity, and surface tension of five vegetable oils at elevated temperatures: Measurement and modeling,” International Journal of Food Properties, Vol. 20, No. sup2, 2017, pp. 1965–1981. <https://doi.org/10.1080/10942912.2017.1360905>.
- [354] Strokina, N., Juránek, R., Eerola, T., Lensu, L., Zemčík, P., and Kälviäinen, H., “Comparison of Appearance-Based and Geometry-Based Bubble Detectors,” Computer Vision and Graphics, edited by L. J. Chmielewski, R. Kozera, B.-S. Shin, and K. Wojciechowski, Springer International Publishing, Cham, 2014, pp. 610–617.
- [355] Ilonen, J., Juránek, R., Eerola, T., Lensu, L., Dubská, M., Zemčík, P., and Kälviäinen, H., “Comparison of bubble detectors and size distribution estimators,” Pattern Recognition Letters, Vol. 101, 2018, pp. 60–66. <https://doi.org/10.1016/j.patrec.2017.11.014>.
- [356] Duda, R. O., and Hart, P. E., “Use of the Hough Transformation to Detect Lines and Curves in Pictures,” Commun. ACM, Vol. 15, No. 1, 1972, p. 11–15. <https://doi.org/10.1145/361237.361242>.
- [357] Kyrki, V., and Kälviäinen, H., “Combination of Local and Global Line Extraction,” Real-Time Imaging, Vol. 6, No. 2, 2000, pp. 79–91. <https://doi.org/10.1006/rtim.1999.0183>.
- [358] Mukhopadhyay, P., and Chaudhuri, B. B., “A survey of Hough Transform,” Pattern Recognition, Vol. 48, No. 3, 2015, pp. 993–1010. <https://doi.org/10.1016/j.patcog.2014.08.027>.
- [359] Strokina, N., Matas, J., Eerola, T., Lensu, L., and Kälviäinen, H., “Detection of bubbles as concentric circular arrangements,” Machine Vision and Applications, Vol. 27, No. 3, 2016, pp. 387–396. <https://doi.org/10.1007/s00138-016-0749-7>.
- [360] Otsu, N., “A Threshold Selection Method from Gray-Level Histograms,” IEEE Transactions on Systems, Man, and Cybernetics, Vol. 9, No. 1, 1979, pp. 62–66. <https://doi.org/10.1109/TSMC.1979.4310076>.
- [361] van den Boomgaard, R., and van Balen, R., “Methods for fast morphological image transforms using bitmapped binary images,” CVGIP: Graphical Models and Image Processing, Vol. 54, No. 3, 1992, pp. 252–258. [https://doi.org/10.1016/1049-9652\(92\)90055-3](https://doi.org/10.1016/1049-9652(92)90055-3).
- [362] Yuen, H., Princen, J., Illingworth, J., and Kittler, J., “Comparative study of Hough Transform methods for circle finding,” Image and Vision Computing, Vol. 8, No. 1, 1990, pp. 71–77. [https://doi.org/10.1016/0262-8856\(90\)90059-E](https://doi.org/10.1016/0262-8856(90)90059-E).
- [363] Atherton, T., and Kerbyson, D., “Size invariant circle detection,” Image and Vision Computing, Vol. 17, No. 11, 1999, pp. 795–803. [https://doi.org/10.1016/S0262-8856\(98\)00160-7](https://doi.org/10.1016/S0262-8856(98)00160-7).
- [364] Romero-Calvo, A., Akay, O., Schaub, H., and Brinkert, K., “Magnetic phase separation in microgravity,” npj microgravity, 2022. *in press*.
- [365] Pickering, W. F., Modern analytical chemistry, New York-Dekker, 1971.
- [366] Brenner, H., “The slow motion of a sphere through a viscous fluid towards a plane surface,” Chemical Engineering Science, Vol. 16, No. 3, 1961, pp. 242–251. [https://doi.org/10.1016/0009-2509\(61\)80035-3](https://doi.org/10.1016/0009-2509(61)80035-3).
- [367] Manica, R., Parkinson, L., Ralston, J., and Chan, D. Y. C., “Interpreting the Dynamic Interaction between a Very Small Rising Bubble and a Hydrophilic Titania Surface,” The Journal of Physical Chemistry C, Vol. 114, No. 4, 2010, pp. 1942–1946. <https://doi.org/10.1021/jp911104b>.

- [368] Hendrix, M. H. W., Manica, R., Klaseboer, E., Chan, D. Y. C., and Ohl, C.-D., "Spatiotemporal Evolution of Thin Liquid Films during Impact of Water Bubbles on Glass on a Micrometer to Nanometer Scale," *Phys. Rev. Lett.*, Vol. 108, 2012, p. 247803. <https://doi.org/10.1103/PhysRevLett.108.247803>.
- [369] Derjaguin, B., and Kussakov, M., "An experimental investigation of polymolecular solvate (adsorbed) films as applied to the development of a mathematical theory of the stability of colloids," *Progress in Surface Science*, Vol. 40, No. 1, 1992, pp. 26–45. [https://doi.org/10.1016/0079-6816\(92\)90031-C](https://doi.org/10.1016/0079-6816(92)90031-C).
- [370] Marrucci, G., "A theory of coalescence," *Chemical Engineering Science*, Vol. 24, No. 6, 1969, pp. 975–985. [https://doi.org/10.1016/0009-2509\(69\)87006-5](https://doi.org/10.1016/0009-2509(69)87006-5).
- [371] Saavedra Moreno, Y., Bournival, G., and Ata, S., "Analysis of Bubble Coalescence Dynamics and Postrupture Oscillation of Capillary-Held Bubbles in Water," *Industrial & Engineering Chemistry Research*, Vol. 56, No. 50, 2017, pp. 14781–14792. <https://doi.org/10.1021/acs.iecr.7b03197>.
- [372] Lessard, R. R., and Zieminski, S. A., "Bubble Coalescence and Gas Transfer in Aqueous Electrolytic Solutions," *Industrial & Engineering Chemistry Fundamentals*, Vol. 10, No. 2, 1971, pp. 260–269. <https://doi.org/10.1021/i160038a012>.
- [373] Craig, V. S. J., Ninham, B. W., and Pashley, R. M., "The effect of electrolytes on bubble coalescence in water," *The Journal of Physical Chemistry*, Vol. 97, No. 39, 1993, pp. 10192–10197. <https://doi.org/10.1021/j100141a047>.
- [374] Yaminsky, V. V., Ohnishi, S., Vogler, E. A., and Horn, R. G., "Stability of Aqueous Films between Bubbles. Part 1. The Effect of Speed on Bubble Coalescence in Purified Water and Simple Electrolyte Solutions," *Langmuir*, Vol. 26, No. 11, 2010, pp. 8061–8074. <https://doi.org/10.1021/la904481d>.
- [375] Kothe, D. B., and Mjolsness, R. C., "RIPPLE - A new model for incompressible flows with free surfaces," *AIAA Journal*, Vol. 30, No. 11, 1992, pp. 2694–2700. <https://doi.org/10.2514/3.11286>.
- [376] Hulbert, E. A., Whitley, R., Klem, M. D., Johnson, W., Alexander, L., D'Aversa, E., Ruault, J.-M., and Manfretti, C., "International Space Exploration Coordination Group Assessment of Technology Gaps for LOx/Methane Propulsion Systems for the Global Exploration Roadmap," *Proc. of the AIAA Space Forum 2016*, 2016, pp. 1–17. <https://doi.org/10.2514/6.2016-5280>, AIAA Paper 2016-5280.
- [377] Meier, R. J., Schinkel, C. J., and de Visser, A., "Magnetisation of condensed oxygen under high pressures and in strong magnetic fields," *Journal of Physics C: Solid State Physics*, Vol. 15, No. 5, 1982, pp. 1015–1024. <https://doi.org/10.1088/0022-3719/15/5/019>.
- [378] Mackor, E., "A theoretical approach of the colloid-chemical stability of dispersions in hydrocarbons," *Journal of Colloid Science*, Vol. 6, No. 5, 1951, pp. 492–495. [https://doi.org/10.1016/0095-8522\(51\)90019-0](https://doi.org/10.1016/0095-8522(51)90019-0).
- [379] Elfimova, E. A., Ivanov, A. O., Lakhtina, E. V., Pshenichnikov, A. F., and Camp, P. J., "Sedimentation equilibria in polydisperse ferrofluids: critical comparisons between experiment, theory, and computer simulation," *Soft Matter*, Vol. 12, 2016, pp. 4103–4112. <https://doi.org/10.1039/C6SM00304D>.
- [380] Luigjes, B., Thies-Weesie, D. M. E., Philipse, A. P., and Ern , B. H., "Sedimentation equilibria of ferrofluids: I. Analytical centrifugation in ultrathin glass capillaries," *Journal of Physics: Condensed Matter*, Vol. 24, No. 24, 2012, p. 245103. <https://doi.org/10.1088/0953-8984/24/24/245103>.
- [381] Kurimsk , J., Rajn k, M., Bartko, P., Paulovi ov , K., Cimbala, R., Medve , D., D zamov , M., Timko, M., and Kop ansk , P., "Experimental study of AC breakdown strength in ferrofluid during thermal aging," *Journal of Magnetism and Magnetic Materials*, Vol. 465, 2018, pp. 136–142. <https://doi.org/10.1016/j.jmmm.2018.05.083>.
- [382] Kop ansk , P.,  ern k, J., Tima, T., Zentko, A., Timko, M., and Slan o, P., " -Radiation induced sedimentation of magnetic particles in magnetic fluids," *Journal of Magnetism and Magnetic Materials*, Vol. 85, No. 1, 1990, pp. 103–106. [https://doi.org/10.1016/0304-8853\(90\)90030-T](https://doi.org/10.1016/0304-8853(90)90030-T).

- [383] Badescu, V., Craciun, V., and Calugaru, G., "The effect of irradiation on the properties of some ferrofluids used in hyperthermia," 2002 IEEE International Magnetism Conference (INTERMAG), 2002, pp. FU7-. <https://doi.org/10.1109/INTMAG.2002.1001376>.
- [384] Devi, M., Paul, N., Mohanta, D., and Saha, A., "Characteristic spectroscopic properties of γ -irradiated rare-earth oxide-based ferrofluids," Journal of Experimental Nanoscience, Vol. 7, No. 5, 2012, pp. 586–595. <https://doi.org/10.1080/17458080.2010.548408>.
- [385] Devi, M., Das, R., Mohanta, D., Baruah, K. K., and Saha, A., "Enhanced magneto-optic activity of magnetite-based ferrofluids subjected to γ - irradiation," Applied Physics A, Vol. 106, No. 3, 2012, pp. 757–763. <https://doi.org/10.1007/s00339-011-6678-4>.
- [386] Tomašovičová, N., Závišová, V., Kováč, J., Koneracká, M., Timko, M., Haysak, I., Koneracká, M., Zavisova, V., Kopčanský, P., Haysak, I., Okunev, A., Parlag, A., and Fradkin, A., "Radiation stability of biocompatible magnetic fluid," , 2010. <https://doi.org/10.48550/arXiv.1004.3448>.
- [387] Tomašovičová, N., Haysak, I., Koneracká, M., Kováč, J., Timko, M., Závišová, V., Okunev, A., Parlag, A., Fradkin, A., Sakhno, V., and P.Kopčanský, "Magnetic Properties of Biocompatible Magnetic Fluid after Electron Irradiation," Proceedings of the European Conference Physics of Magnetism 2011 (PM-11), Poznań, Vol. 121, 2012, pp. 1302–1304. <https://doi.org/10.12693/APhysPolA.121.1302>.
- [388] Tomašovičová, N., Haysak, I., Kováč, J., Kubovčíková, M., Závišová, V., Timko, M., Okunev, A., Zorkovská, A., and P.Kopčanský, "Radiation Stability of the BSA Modified Biocompatible Magnetic Fluid," Proceedings of the 15th Czech and Slovak Conference on Magnetism, Košice, Slovakia, Vol. 126, 2014, pp. 262–263. <https://doi.org/10.12693/APhysPolA.126.262>.
- [389] Simos, N., Fernandes, S., Mittag, W., Pellemoine, F., Avilov, M., Kostin, M., Mausner, L., Ronningen, R., Schein, M., and Bollen, G., "Performance degradation of ferrofluidic feedthroughs in a mixed irradiation field," Nuclear Instruments and Methods in Physics Research Section A: Accelerators, Spectrometers, Detectors and Associated Equipment, Vol. 841, 2017, pp. 144–155. <https://doi.org/10.1016/j.nima.2016.10.007>.
- [390] Pavlík, M., Kruželák, L., Mikita, M., Špes, M., Bucko, S., Lisoň, L., Kosterec, M., Beňa, L., and Liptai, P., "The impact of electromagnetic radiation on the degradation of magnetic ferrofluids," Archives of Electrical Engineering, Vol. vol. 66, No. No 2 June, 2017. <https://doi.org/10.1515/ae-2017-0027>.
- [391] Bhattacharya, S., Jenamoni, K., and Nayar, S., "Stability of biomimetic ferrofluids established by a systematic study using microwave 21 irradiation at defined wattages," Journal of Magnetism and Magnetic Materials, Vol. 324, No. 20, 2012, pp. 3261–3266. <https://doi.org/10.1016/j.jmmm.2012.05.001>.
- [392] Choudhury, P. R., "Slurry fuels," Progress in Energy and Combustion Science, Vol. 18, No. 5, 1992, pp. 409–427. [https://doi.org/10.1016/0360-1285\(92\)90008-O](https://doi.org/10.1016/0360-1285(92)90008-O).
- [393] Palaszewsky, B., and Zakany, J., "Metallized Gelled Propellants: Oxygen/RP-1/aluminum Rocket Combustion Experiments," 31st Joint Propulsion Conference and Exhibit; San Diego, CA; United States, 1995, pp. 1–32. <https://doi.org/10.2514/6.1996-2622>, AIAA Paper 95-2435.
- [394] Stelmachowski, P., Kopacz, A., Legutko, P., Indyka, P., Wojtasik, M., Ziemiański, L., Żak, G., Sojka, Z., and Kotarba, A., "The role of crystallite size of iron oxide catalyst for soot combustion," Catalysis Today, Vol. 257, 2015, pp. 111–116. <https://doi.org/10.1016/j.cattod.2015.02.018>, air and Water Pollution Abatement Catalysis (AWPAC 2014).
- [395] Ghosh, D., Roy, A. K., and Ghosh, A., "Reduction of Ferric Oxide Pellets with Methane," Transactions of the Iron and Steel Institute of Japan, Vol. 26, No. 3, 1986, pp. 186–193. <https://doi.org/10.2355/isijinternational1966.26.186>.

- [396] Monazam, E. R., Breault, R. W., Siriwardane, R., Richards, G., and Carpenter, S., “Kinetics of the reduction of hematite (Fe_2O_3) by methane (CH_4) during chemical looping combustion: A global mechanism,” *Chemical Engineering Journal*, Vol. 232, 2013, pp. 478–487. <https://doi.org/10.1016/j.cej.2013.07.091>.
- [397] Maggi, F., Dossi, S., Paravan, C., Galfetti, L., Rota, R., Cianfanelli, S., and Marra, G., “Iron oxide as solid propellant catalyst: A detailed characterization,” *Acta Astronautica*, Vol. 158, 2019, pp. 416–424. <https://doi.org/10.1016/j.actaastro.2018.07.037>.
- [398] Gordon, S., and McBride, B., “Computer Program for Calculation of Complex Chemical Equilibrium Compositions and Applications,” Tech. Rep. RP-1311, 1994. URL ntrs.nasa.gov/citations/19950013764.
- [399] Glassman, I., and Sawyer, R., *The performance of chemical propellants*, AGARDograph ; no.129, Technivision Services, Slough, England, 1970.
- [400] Sutton, G., and Biblarz, O., *Rocket Propulsion Elements*, 8th ed., John Wiley & Sons, 2010.
- [401] Romero-Calvo, A., Urbansky, V., Yudinsev, V., Schaub, H., and Trushlyakov, V., “Novel strategies for liquid rocket engine restart in microgravity,” *Acta Astronautica*, 2022. *under review*.
- [402] Vasilev, A. P., Kudryavtsev, V. M., Kuznetsov, V. A., Kurpatenkov, V. D., and Obelnitskii, A. M., *Fundamentals of the theory and calculation of liquid propellant rocket engines*, 4th ed., Vol. 2, Kudryavtsev M.V., 1993.
- [403] Campbell, J., Eldridge, E., and Thompson, J., “Handbook on Materials for Superconducting Machinery,” Tech. Rep. HB-04, MCIC, 1974. URL ntrl.ntis.gov/NTRL/dashboard/searchResults/titleDetail/ADA002698.xhtml.
- [404] Trench, A., and Sykes, J. P., “Rare Earth Permanent Magnets and Their Place in the Future Economy,” *Engineering*, Vol. 6, No. 2, 2020, pp. 115–118. <https://doi.org/10.1016/j.eng.2019.12.007>.
- [405] Halbach, K., “Design of permanent multipole magnets with oriented rare earth cobalt material,” *Nuclear Instruments and Methods*, Vol. 169, No. 1, 1980, pp. 1–10. [https://doi.org/10.1016/0029-554X\(80\)90094-4](https://doi.org/10.1016/0029-554X(80)90094-4).
- [406] Trout, S. R., and Constantinides, S., “Using Permanent Magnets at Low Temperature,” Tech. Rep. TN 0302, Arnold Magnetic Technologies, 2021. URL www.arnoldmagnetics.com/wp-content/uploads/2017/10/TN_0302_rev_150715.pdf.
- [407] Uestuener, K., Katter, M., Blank, R., Benedikt, D., Bahrtdt, J., Gaupp, A., Klemke, B., Grüner, F., and Weingartner, R., “Sintered (Pr,Nd)-Fe-B permanent magnets with $(\text{BH})_{\text{max}}$ of 520.kJ/m³ at 85 K for cryogenic applications,” *20th International Workshop on Rare-Earth and Future Permanent Magnets and their Applications*, 2008.
- [408] Huang, J.-C., Kitamura, H., Yang, C.-S., Yang, C.-K., Mizumoto, S., Chang, C.-H., Chang, C.-H., and Hwang, C.-S., “Development of cryogenic permanent magnet undulators at NSRRC,” *AIP Conference Proceedings*, Vol. 2054, No. 1, 2019, p. 030022. <https://doi.org/10.1063/1.5084585>.
- [409] Tsuchiya, K., Wang, X., Fujita, S., Ichinose, A., Yamada, K., Terashima, A., and Kikuchi, A., “Superconducting properties of commercial REBCO-coated conductors with artificial pinning centers,” *Supercond. Sci. Technol*, Vol. 34, 2021, p. 105005. <https://doi.org/10.1088/1361-6668/ac1e65>.
- [410] Fietz, W., Heller, R., Schlachter, S., and Goldacker, W., “Application of high temperature superconductors for fusion,” *Fusion Engineering and Design*, Vol. 86, No. 6, 2011, pp. 1365–1368. <https://doi.org/10.1016/j.fusengdes.2010.11.018>, proceedings of the 26th Symposium of Fusion Technology (SOFT-26).

- [411] Weijers, H., Markiewicz, W., Abraimov, D., Bai, H., Hilton, D., Gavrilin, A., Larbalestier, D., Lu, J., Murphy, T. P., and A. J. Voran, P. N., and NHMFL, “Testing of prototype coils for the NHMFL 32 T superconducting user magnet,” Applied Superconductivity Conference, Charlotte, NC, 2014.
- [412] Ivakhnenko, O. P., and Potter, D. K., “Magnetic susceptibility of petroleum reservoir fluids,” Physics and Chemistry of the Earth, Parts A/B/C, Vol. 29, No. 13, 2004, pp. 899–907. <https://doi.org/10.1016/j.pce.2004.06.001>, paleo, Rock and Environmental Magnetism.
- [413] Hong, C.-Y., Jang, I. J., Horng, H. E., Hsu, C. J., Yao, Y. D., and Yang, H. C., “Ordered structures in Fe₃O₄ kerosene-based ferrofluids,” Journal of Applied Physics, Vol. 81, No. 8, 1997, pp. 4275–4277. <https://doi.org/10.1063/1.364800>.
- [414] Ghasemi, E., Mirhabibi, A., Edrissi, M., Aghababazadeh, R., and Brydson, R. M., “Study on the Magnetorheological Properties of Maghemite-Kerosene Ferrofluid,” Journal of Nanoscience and Nanotechnology, Vol. 9, No. 7, 2009, pp. 4273–4278. <https://doi.org/doi:10.1166/jnn.2009.M45>.
- [415] Zubko, V. I., Dikanskii, Y. I., Zubko, D. V., Kunikin, S. A., and Sitsko, G. I., “Electrical and Magnetic Properties of a Kerosene-Based Magnetic Fluid Subjected to the Action of Electric and Magnetic Fields,” Journal of Engineering Physics and Thermophysics, Vol. 91, No. 3, 2018, pp. 806–811. <https://doi.org/10.1007/s10891-018-1803-2>.
- [416] Susan-Resiga, D., Malaescu, I., Marinica, O., and Marin, C., “Magnetorheological properties of a kerosene-based ferrofluid with magnetite particles hydrophobized in the absence of the dispersion medium,” Physica B: Condensed Matter, Vol. 587, 2020, p. 412150. <https://doi.org/10.1016/j.physb.2020.412150>.
- [417] Maldonado-Camargo, L., Unni, M., and Rinaldi, C., “Magnetic Characterization of Iron Oxide Nanoparticles for Biomedical Applications,” Methods in molecular biology (Clifton, N.J.), Vol. 1570, 2017, pp. 47–71. https://doi.org/10.1007/978-1-4939-6840-4_4.
- [418] Trushlyakov, V., Shalay, V., Shatrov, J., Jakovlev, M., and Kostantino, A., “Active de-orbiting onboard system from LEO of upper stages of launchers,” 5th European Conference on Space Debris, Darmstadt, 2009.
- [419] Yutkin, E., Trushlyakov, V., Maggi, F., Galfetti, L., and De Luca, L. T., “Active onboard deorbiting system for the second stage of Cosmos 3M: a preliminary study,” 4th European Conference for Aerospace Sciences (EUCASS), 2011, pp. 1–9. <https://doi.org/10.13140/2.1.1418.4009>.
- [420] Maggi, F., Galfetti, L., De Luca, L., Trushlyakov, V. I., Kudentsov, V. Y., and Lempert, D. B., “Thermochemical Considerations in Support of ADOS Propulsion,” Space Debris Mitigation Workshop, 2010.
- [421] Trushlyakov, V. I., Lempert, D. B., and Bel’kova, M. E., “Possibility of using gas-generating compositions for increasing the rocket propulsion efficiency,” Combustion, Explosion, and Shock Waves, Vol. 51, No. 3, 2015, pp. 326–332. <https://doi.org/10.1134/S0010508215030077>.
- [422] Trushlyakov, V. I., Urbansky, V. A., and Pustovoy, N. V., “Study of the unusable liquid propellant residues evaporation processes parameters in the tanks of the launch vehicle expended stage in microgravity,” Journal of Physics: Conference Series, Vol. 1441, 2020, p. 012121. <https://doi.org/10.1088/1742-6596/1441/1/012121>.
- [423] Arianespace, “Soyuz User’s Manual,” , March 2012. URL www.arianespace.com/wp-content/uploads/2015/09/Soyuz-Users-Manual-March-2012.pdf, Issue 2, Revision 0.
- [424] Vatani, A., Woodfield, P. L., Dinh, T., Phan, H.-P., Nguyen, N.-T., and Dao, D. V., “Degraded boiling heat transfer from hotwire in ferrofluid due to particle deposition,” Applied Thermal Engineering, Vol. 142, 2018, pp. 255–261. <https://doi.org/10.1016/j.applthermaleng.2018.06.064>.

- [425] Wang, M., Wang, Z., Gong, X., and Guo, Z., “The intensification technologies to water electrolysis for hydrogen production – A review,” *Renewable and Sustainable Energy Reviews*, Vol. 29, 2014, pp. 573–588. <https://doi.org/10.1016/j.rser.2013.08.090>.
- [426] Koza, J. A., Mühlenhoff, S., Żabiński, P., Nikrityuk, P. A., Eckert, K., Uhlemann, M., Gebert, A., Weier, T., Schultz, L., and Odenbach, S., “Hydrogen evolution under the influence of a magnetic field,” *Electrochimica Acta*, Vol. 56, No. 6, 2011, pp. 2665–2675. <https://doi.org/10.1016/j.electacta.2010.12.031>.
- [427] Lin, M. Y., and Hourng, L. W., “Effects of magnetic field and pulse potential on hydrogen production via water electrolysis,” *International Journal of Energy Research*, Vol. 38, No. 1, 2014, pp. 106–116. <https://doi.org/10.1002/er.3112>.
- [428] Lin, M. Y., Hourng, L. W., and Hsu, J. S., “The effects of magnetic field on the hydrogen production by multielectrode water electrolysis,” *Energy Sources, Part A: Recovery, Utilization, and Environmental Effects*, Vol. 39, No. 3, 2017, pp. 352–357. <https://doi.org/10.1080/15567036.2016.1217289>.
- [429] Garcés-Pineda, F. A., Blasco-Ahicart, M., Nieto-Castro, D., López, N., and Galán-Mascarós, J. R., “Direct magnetic enhancement of electrocatalytic water oxidation in alkaline media,” *Nature Energy*, Vol. 4, No. 6, 2019, pp. 519–525. <https://doi.org/10.1038/s41560-019-0404-4>.
- [430] Liu, H., ming Pan, L., Huang, H., Qin, Q., Li, P., and Wen, J., “Hydrogen bubble growth at micro-electrode under magnetic field,” *Journal of Electroanalytical Chemistry*, Vol. 754, 2015, pp. 22–29. <https://doi.org/10.1016/j.jelechem.2015.06.015>.
- [431] Hu, Q., bo Liu, H., Liu, Z., Zhong, D., Han, J., and ming Pan, L., “A pair of adjacent bubbles evolution at micro-electrode under electrode-normal magnetic field,” *Journal of Electroanalytical Chemistry*, Vol. 880, 2021, p. 114886. <https://doi.org/10.1016/j.jelechem.2020.114886>.
- [432] Kohonen, M. M., Karaman, M. E., and Pashley, R. M., “Debye Length in Multivalent Electrolyte Solutions,” *Langmuir*, Vol. 16, No. 13, 2000, pp. 5749–5753. <https://doi.org/10.1021/la991621c>.
- [433] Sarwar, A., Nemirovski, A., and Shapiro, B., “Optimal Halbach Permanent Magnet Designs for Maximally Pulling and Pushing Nanoparticles,” *Journal of magnetism and magnetic materials*, Vol. 324, No. 5, 2012, pp. 742–754. <https://doi.org/10.1016/j.jmmm.2011.09.008>, 23335834.
- [434] Shapiro, B., Kulkarni, S., Nacev, A., Sarwar, A., Preciado, D., and Depireux, D., “Shaping Magnetic Fields to Direct Therapy to Ears and Eyes,” *Annual Review of Biomedical Engineering*, Vol. 16, No. 1, 2014, pp. 455–481. <https://doi.org/10.1146/annurev-bioeng-071813-105206>, PMID: 25014789.
- [435] Barnsley, L. C., Carugo, D., Owen, J., and Stride, E., “Halbach arrays consisting of cubic elements optimised for high field gradients in magnetic drug targeting applications,” *Physics in Medicine and Biology*, Vol. 60, No. 21, 2015, pp. 8303–8327. <https://doi.org/10.1088/0031-9155/60/21/8303>.
- [436] Subramanian, M., Miaskowski, A., Jenkins, S. I., Lim, J., and Dobson, J., “Remote manipulation of magnetic nanoparticles using magnetic field gradient to promote cancer cell death,” *Applied Physics A*, Vol. 125, No. 4, 2019, p. 226. <https://doi.org/10.1007/s00339-019-2510-3>.
- [437] Bashyam, A., Li, M., and Cima, M. J., “Design and experimental validation of Unilateral Linear Halbach magnet arrays for single-sided magnetic resonance,” *Journal of Magnetic Resonance*, Vol. 292, 2018, pp. 36–43. <https://doi.org/10.1016/j.jmr.2018.05.004>.
- [438] Cooley, C. Z., Haskell, M. W., Cauley, S. F., Sappo, C., Lapierre, C. D., Ha, C. G., Stockmann, J. P., and Wald, L. L., “Design of sparse Halbach magnet arrays for portable MRI using a genetic algorithm,” *IEEE Transactions on Magnetics*, Vol. 54, No. 1, 2018, p. 5100112. <https://doi.org/10.1109/TMAG.2017.2751001>.
- [439] Brown, W. F., “Electric and Magnetic Forces: A Direct Calculation. I,” *American Journal of Physics*, Vol. 19, No. 5, 1951, pp. 290–304. <https://doi.org/10.1119/1.1932805>.

- [440] Cano-Gómez, G., and Romero-Calvo, Á., “Comment on ‘The magnetic body force in ferrofluids’,” Journal of Physics D: Applied Physics, Vol. 55, No. 12, 2022, p. 128002. <https://doi.org/10.1088/1361-6463/ac4180>.
- [441] Rinaldi, C., and Brenner, H., “Body versus surface forces in continuum mechanics: Is the Maxwell stress tensor a physically objective Cauchy stress?” Phys. Rev. E, Vol. 65, 2002, p. 036615. <https://doi.org/10.1103/PhysRevE.65.036615>.
- [442] Liu, M., and Stierstadt, K., Colloidal Magnetic Fluids, Springer, 2009. <https://doi.org/10.1007/978-3-540-85387-9>.
- [443] Odenbach, S., and M.Liu, “Invalidation of the Kelvin Force in Ferrofluids,” Physical Review Letters, Vol. 86, 2001, p. 328. <https://doi.org/10.1103/PhysRevLett.86.328>.
- [444] Engel, A., “Comment on “Invalidation of the Kelvin Force in Ferrofluids”,” Phys. Rev. Lett., Vol. 86, 2001, pp. 4978–4978. <https://doi.org/10.1103/PhysRevLett.86.4978>.
- [445] Liu, M., “Liu replies,” Phys. Rev. Lett., Vol. 86, 2001, p. 4979. <https://doi.org/10.1103/PhysRevLett.86.4979>.
- [446] Lange, A., “Kelvin force in a layer of magnetic fluid,” Journal of Magnetism and Magnetic Materials, Vol. 241, No. 2, 2002, pp. 327 – 329. [https://doi.org/10.1016/S0304-8853\(01\)01368-3](https://doi.org/10.1016/S0304-8853(01)01368-3).

Appendix A

Magnetic force distribution

The calculation of the forces exerted by electromagnetic fields on electrically or magnetically polarizable continuous media has been a subject of recurrent debate since the invention of ferrofluids [77, 439, 440]. The discussion has been particularly intense in what refers to the distribution of forces within a magnetic fluid. While some authors consider that the action of an external field produces forces throughout the medium [441], others conclude that only the liquid interface experiences a force with true physical meaning [442]. Further considerations on how magnetic fields contribute to the energy variation result in different formulations of this interaction [342, 442–446]. A larger consensus exists regarding the different formulations of the *total magnetic force*, that were revisited in 2001 when the validity of the Kelvin force expression in ferrofluids was contested [443] leading to a significant response in the physics community [301, 341, 442, 444, 446]. This discussion, which is covered in depth in Ref. [77], is particularly relevant for space applications where electromagnetic polarization forces become dominant and apparently insignificant modeling errors lead to qualitative differences. Although the debate is not concluded, what follows can be considered the most widespread formulation of the body and surface force components acting on magnetically polarizable media [20, 301, 439].

The magnetic stress tensor \mathcal{T}_m has been widely used in classical and recent works to obtain the local distributions of magnetic forces on magnetically polarizable bodies [20, 62, 301–303]. The canonical form of the magnetic work per unit volume done to magnetize the polarizable medium, $\mathbf{H} \cdot \delta \mathbf{B}$, leads to

$$\mathcal{T}_m = -\frac{\mu_0}{2} H^2 \mathbf{I} + \mathbf{B} \mathbf{H}. \quad (\text{A.1})$$

The local effect of magnetic fields on the continuous magnetizable medium can be formulated in terms of both volume (\mathbf{f}_m^V) and surface (\mathbf{f}_m^S) magnetic force densities. The force per unit volume, or magnetic body force, is determined by the divergence of magnetic stress tensor

$$\mathbf{f}_m^V = \nabla \cdot \mathcal{T}_m = -\mu_0 H \nabla H + \nabla \cdot (\mathbf{B}\mathbf{H}), \quad (\text{A.2})$$

By noting $\mathbf{B} = \mu_0(\mathbf{H} + \mathbf{M})$ as well as the solenoidal nature of the magnetic induction field ($\nabla \cdot \mathbf{B} = 0$), the dyadic product $\mathbf{B}\mathbf{H}$ becomes

$$\nabla \cdot (\mathbf{B}\mathbf{H}) = (\mathbf{B} \cdot \nabla) \mathbf{H} = \mu_0 (\mathbf{H} \cdot \nabla) \mathbf{H} + \mu_0 (\mathbf{M} \cdot \nabla) \mathbf{H}. \quad (\text{A.3})$$

When this expression is substituted in Eq. A.2, and taking into account the general result

$$H \nabla H = (\mathbf{H} \cdot \nabla) \mathbf{H} + \mathbf{H} \times (\nabla \times \mathbf{H}), \quad (\text{A.4})$$

the general expression

$$\mathbf{f}_m^V = -\mu_0 \mathbf{H} \times (\nabla \times \mathbf{H}) + \mu_0 (\mathbf{M} \cdot \nabla) \mathbf{H} \quad (\text{A.5})$$

is obtained [77].

In the problems of interest for this thesis, no electric current are applied to the involved magnetic media. Therefore, \mathbf{H} is an irrotational field. On the other hand, the constitutive relation that is assumed for these media implies that the fields \mathbf{M} and \mathbf{H} are aligned, so that $\mathbf{M} = (M/H)\mathbf{H}$. If both conditions (together with Eq. A.4) are taken into account in the above general expression, the relations

$$\mathbf{f}_m^V = \mu_0 (\mathbf{M} \cdot \nabla) \mathbf{H} = \mu_0 M \nabla H \quad (\text{A.6})$$

are finally derived. The equivalence between the above expressions is due to the collinearity that is assumed for the fields M and H , regardless of the characteristic constitutive relationship of the medium. The result is commonly known as the Kelvin body force.

The imantation field \mathbf{M} is discontinuous between the internal (∂V^-) and external (∂V^+) faces of the surface ∂V bounding the magnetized media, since $\mathbf{M}^+ = \mathbf{0}$ and $\mathbf{M}^- \neq \mathbf{0}$. In consequence, the magnetic stress tensor also has a discontinuity through ∂V , and a magnetic traction force arises at said interface

[20, 77, 301, 303], which is described by the surface density

$$\mathbf{f}_m^S = \mathbf{n} \cdot \mathcal{T}_m^+ - \mathbf{n} \cdot \mathcal{T}_m^-, \quad (\text{A.7})$$

with

$$\mathbf{n} \cdot \mathcal{T}_m^\pm = -\frac{\mu_0}{2}(H^\pm)^2 \mathbf{n} + B_n^\pm \mathbf{H}^\pm \quad (\text{A.8})$$

and \mathbf{n} being the external normal vector at ∂V . According to Gauss's law, the normal component of the induction field is continuous through ∂V ($B_n^+ = B_n^- = B_n$). In addition, the absence of electrical surface currents in ∂V results in the continuity of the tangential magnetic field component ($H_t^+ = H_t^- = H_t$). Therefore, Eq. A.7 becomes

$$\mathbf{f}_m^S = -\frac{\mu_0}{2} [(H_n^+)^2 - (H_n^-)^2] \mathbf{n} + B_n(H_n^+ - H_n^-) \mathbf{n}. \quad (\text{A.9})$$

Using the definition of the magnetic field \mathbf{H} on the external and internal faces of ∂V ,

$$H_n^+ = \frac{B_n}{\mu_0}; \quad H_n^- = \frac{B_n}{\mu_0} - M_n^- \quad (\text{A.10})$$

the result for the surface distribution of magnetic force at ∂V is

$$\mathbf{f}_m^S = p_m = \frac{\mu_0}{2}(M_n^-)^2 \mathbf{n}. \quad (\text{A.11})$$

In this Ph.D. thesis, Eqs. A.6 and A.11 have been considered for the body and surface magnetic force terms acting on magnetically polarizable liquids. However, the expressions summarized in Table A.1 produce the same total force and are left as a reference. The interested reader is encouraged to read Ref. 77 for further details.

Table A.1: Equivalent total magnetic force expressions.

ID	Volume term	Surface term
Tensor formulation	-	$\mathbf{n} \cdot \mathcal{T}_m^+$
\mathbf{H} -field distribution	$\mu_0 M \nabla H$	$\mu_0 M_n^2 \mathbf{n} / 2$
\mathbf{B} -field distribution	$M \nabla B$	$-\mu_0 M_t^2 \mathbf{n} / 2$
Virtual works scheme	$\mu_0 (\mathbf{M} \cdot \nabla) \mathbf{H}_0$	-

Appendix B

Magnetic Comsol Multiphysics model

In order to verify the magnetic field and force from the simulation for a given meniscus profile and coils current intensity, the problem is reproduced in Comsol Multiphysics by solving the stationary Maxwell equations

$$\nabla \times \mathbf{H} = \mathbf{J}, \quad (\text{B.1})$$

$$\mathbf{B} = \nabla \times \mathbf{A}, \quad (\text{B.2})$$

$$\mathbf{J} = \bar{\sigma} \mathbf{E}, \quad (\text{B.3})$$

where \mathbf{J} is the current field, \mathbf{A} is the magnetic vector potential produced by the current in the coil and the magnetized materials, $\bar{\sigma}$ is the conductivity of the coil, and \mathbf{E} is the electric displacement field. The constitutive relation

$$\mathbf{B} = \mu_0 \mu_r \mathbf{H}, \quad (\text{B.4})$$

with μ_r being the relative permeability of the material, is applied to the aluminum plates ($\mu_r^{Al} = 1.000022$), surrounding air ($\mu_r^{air} = 1$) and copper coils ($\mu_r^{Cu} = 1$). Within the ferrofluid volume, the constitutive relation is defined by the magnetization curve $M = f(H)$ depicted in Figure 9.6, that results in

$$\mathbf{B} = \mu_0 \left(1 + \frac{f(H)}{H} \right) \mathbf{H}, \quad (\text{B.5})$$

where H is the module of the magnetic field \mathbf{H} . The current field is computed through

$$\mathbf{J} = \frac{NI}{A} \mathbf{u}_\theta, \quad (\text{B.6})$$

with $N = 200$ being the number of turns, I the current intensity flowing through each wire, $A = 509 \text{ mm}^2$ the coils cross section and \mathbf{e}_θ the circumferential vector.

The simulation domain is a rectangular $1 \times 3 \text{ m}$ region enclosing the assemblies. An axisymmetric boundary condition is applied to the symmetry axis, while the tangential magnetic potential is imposed at the external faces through $\mathbf{n} \times \mathbf{A} = \mathbf{n} \times \mathbf{A}_d$. \mathbf{A}_d is the dipole term of the magnetic vector potential generated by the current in the coils and the magnetization fields of the ferrofluid volumes. Consequently, \mathbf{A}_d is computed as the potential vector generated by four point dipoles applied at the centers of the magnetization distributions and whose moments are those of said distributions. While the dipoles associated to the coils can be calculated beforehand, the ferrofluid dipoles need to be approximated iteratively by integrating \mathbf{M} in the ferrofluid volume. The relative error in the magnetic vector potential due the dipole approximation is estimated to be below 1.0% at the boundary of the domain with respect to the exact value generated by equivalent circular loops.

The mesh is composed of 167755 irregular triangular elements, as shown in Figure B.1 for the $I = 20 \text{ A}$ case. Mean and minimum condition numbers of 0.985 and 0.527 are obtained. The governing equations are solved using Comsol's magnetic fields physics module with a stationary solver and a fully coupled implementation. The termination criterion set to "Solution or Residual" with a residual factor of 10^3 .

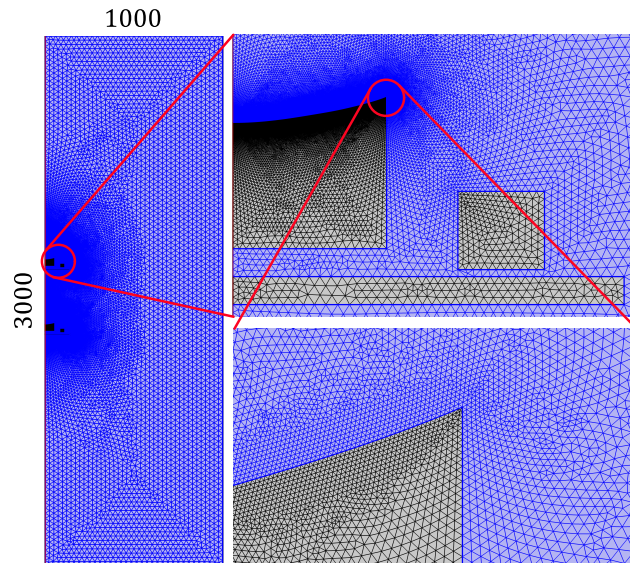


Figure B.1: Mesh employed by the magnetic Comsol Multiphysics model.